Intelligent Agents via Representation Learning

by

Tongzhou Wang

B.A., University of California Berkeley (2017)
M.S., Massachusetts Institute of Technology (2022)

Submitted to the Department of Electrical Engineering and Computer Science
in Partial Fulfillment of the Requirements for the Degree of

Doctor of Philosophy

at the

MASSACHUSETTS INSTITUTE OF TECHNOLOGY

September 2024

Authored By: Tongzhou Wang
Department of Electrical Engineering and Computer Science
August 9, 2024

Certified By: Phillip Isola
Associate Professor of Electrical Engineering and Computer Science
Thesis Supervisor

Certified By: Antonio Torralba
Professor of Electrical Engineering and Computer Science
Thesis Supervisor

Accepted By: Leslie A. Kolodziejski
Professor of Electrical Engineering and Computer Science
Chair, Department Committee on Graduate Students

Intelligent Agents via Representation Learning

by

Tongzhou Wang

Submitted to the Department of Electrical Engineering and Computer Science
on August 9, 2024, in Partial Fulfillment of the
Requirements for the Degree of
Doctor of Philosophy

Abstract

The effectiveness of deep learning is often attributed to the ability of neural networks to perform *representation learning*, a transformation that maps input data into a vector representation (usually $\in \mathbb{R}^d$ with small d much lower than the data dimension). Such representation spaces can reorganize data with inductive structures (*e.g.*, representation distances correlating with perceptual similarity) that make solving general new tasks much easier (*e.g.*, groundtruth semantic classification function is smoother w.r.t. a good representation space). This dissertation focuses on the core skills of general intelligent agents—perception and decision making. We show how these capabilities can be reduced to learning good representations that capture various structures of the world. In particular, we solve reinforcement learning problems via representation learning alone, thus making a step forward towards building intelligent agents by learning good representations. Moreover, we study the convergent trend of strong representations from different models and modalities, and propose the *Platonic Representation Hypothesis*: stronger models better approximate a Platonic representation fit to the structures of our reality. We argue that this representation is a critical component in building better models and intelligent artificial agents. Finally, we outline several future directions towards learning this Platonic representation via pretraining and adaptation.

Thesis Supervisor: Phillip Isola
Title: Associate Professor of Electrical Engineering and Computer Science

Thesis Supervisor: Antonio Torralba
Title: Professor of Electrical Engineering and Computer Science

To Lexi, Wenjuan, Guangbin, Andrew, Tabby, and Mochi

Acknowledgments

My advisors, Phillip Isola and Antonio Torralba, taught me how to research, write, present, and share.

When I first discussed graduate school with Phil in 2018, he told me he was shifting focus from computer vision to artificial general intelligence (AGI). At that time, I had worked with Phil remotely on a computer vision project for almost a year, but was still pretty junior in research. So, I joined Phil's lab. Phil gave us a lot of freedom and was always excited to talk about AI, helping me gradually understand AGI and form my research interests. I am really grateful to Phil for guiding me in AI research, for introducing me to best practices for writing and presenting, and for helping me become a better researcher.

I have always been amazed by Antonio's constant stream of crazy yet cool ideas and how often they turn out to be valuable and widely recognized. My first time working with Antonio was in 2017, on *Dataset Distillation*, an idea of Antonio's and Alyosha Efros'. The goal was to compress datasets of hundreds of thousands of images into just tens of images that are still effective in training neural networks. I submitted it to three conferences over two years, each time with major improvements, but didn't get in any of them. However, that arXiv report is now my second most cited paper, with over 550 citations and several workshops dedicated to this topic. Over my time at MIT, I have heard many stories of Antonio's ideas that no students wanted to work on but turned out to be gold. Prospective students often ask me, "What topics does Antonio focus on?" For many years, I didn't know how to answer. Now I tell them, "Antonio is the most curiosity-driven person I know; it feels fortunate and special to work with him because that means working on some of the most unique and influential ideas ahead of the field's time." It has changed my view of the world and enabled me to explore things I never would have otherwise.

I would also like to thank my other committee members, Leslie Kaelbling and Stefanie Jegelka.

Throughout my PhD, I have learned so much from Leslie about big problems in

decision-making and different approaches to it. Leslie was one of the instructors for the *Embodied Intelligence* seminar that first properly introduced me to decision-making. Leslie has always been nice, patient, and extremely sharp, making time to meet me whenever I needed advice for research and career. I am grateful for the discussions we had and the advice Leslie gave me.

I first learned about Stefanie's lab when I visited MIT as a prospective admitted student. I did not come during the regular visit days, but Stefanie still made an effort to arrange a meeting for me with her lab, even though she was on leave at the time. The lab was focusing on many interesting topics such as learning dynamics and expressive power. What was most inspiring to me was the many mathematically-grounded yet practical insights Stefanie's research produced. Over my time at MIT, I gladly found my research increasingly overlapping with Stefanie's works on representation learning. I am fortunate and thankful to have learned so much from Stefanie and her students over many impromptu discussions.

My gratitude also goes to the many collaborators I have had throughout my PhD. I have had fantastic collaborators with whom I wrote many papers over many years. I've also had many great short collaboration experiences that I truly enjoyed. I learned something exciting from each of my collaborators, without whom none of my research would be possible. For that, I am truly grateful.

There are many more people in the academic research community who helped my research beyond academic collaborations. With others, I had stimulating conversations that led to productive projects. I am really happy that I became a part of the research community, and many thanks go to everyone who welcomed me and helped me grow.

I was fortunate to be a member of two labs at MIT. During my five and a half years here, we had many wonderful events, from lab dinners to retreats. One of my favorites is the Isola lab's retreat to Arcadia. One night, we gathered around the fire, drank wine, made marshmallows, forgot about specific research problems for a moment, and talked about our lives and philosophical ideas. Each member adds a bit of their own identity, making the labs a colorful, fun, and unique place to be.

In academic labs, people come and go. At the time of my graduation, my labs are

composed of mostly different members than when I joined five years ago. However, even though the people are different, to some extent, the labs feel the same. Antonio, Phillip, and Fern have spent a lot of effort to maintain a welcoming atmosphere where everyone can achieve what they want. I am certain they will keep the labs a great space for research and learning whenever I return to visit the Torralba lab and the Isola lab.

I have made some of my best friends during my PhD. When I graduated from my undergraduate degree and moved to New York City alone for work, I found it very difficult to make friends, even harder to make good friends. I kept thinking about the night before I left California and said goodbye to my friends, wishing I was closer to them.

When I came for graduate school, I thought it would be just the same—hard to make friends and I would still miss my old friends. Not soon after, I realized I was very wrong both about research and friends. Graduate school has been a roller coaster of stress, excitement, depression, and happiness. Through this roller coaster, I became friends with the most amazing group of people I have met in my life. We talked for hours about research and life late into the night, sometimes with a little alcohol to stay hydrated. We were on the same emotional roller coaster of graduate school, helped each other, and shared important life moments, including my wedding. I will always cherish the time we spent together. Many of my PhD friends and pre-PhD friends are in California. I look forward to moving there and seeing them frequently again.

Being an international student with a 12-hour time difference from home has not been easy. Fortunately, my family made efforts to visit me as much as they could. Since starting my PhD in January 2019, I have not been back to China even once. My family visited me in Hawaii, Boston, and California. Thank you, Mom, Dad, and Andrew, for always being there and supporting me. Your love means a lot to me and has made me who I am today.

Throughout the years, I have also received great love and support from my cousin's family and my wife's parents. I showed them around Boston and enjoyed talking with them either in person or via video chat.

Especially, I want to thank Lexi, my wife, and the most important person in my life. Together we have shared many defining moments. For some time, we lived separately, in different countries, then on different coasts, then in different cities, until Lexi moved to Boston in 2020, in support of my PhD. Together we have lived and traveled through many amazing places: Shanghai, Chengdu, Qingdao, Seattle, San Francisco Bay Area, New York City, Williamsburg, Charlottesville, Washington DC, Shenandoah, Acadia, Japan, and many more.

We spent many hours together doing fun activities—going to museums, enjoying nature (especially the ocean), playing badminton, table tennis, and video games, cooking, and eating great food. You made this life meaningful, worthwhile, and so much more enjoyable, and it motivated me to do my best in life and work. Lexi, I am forever grateful for your love and support, and I will continue to give my best support and love to you.

My love also goes to our cats, Tabby and Mochi. They joined our family at the height of the pandemic. In 2021, they arrived at our tiny apartment at just three months old. At age three, they are now five times heavier, five times larger, and, I really think, 20 times louder. There are numerous times I stayed late at the lab just to enjoy some time without their constant "meows." I am pretty sure they reduced my work efficiency by half, but I do not regret it one bit. They have brought so much more love and happiness to us. Their carefree lifestyle is something I aspire to every single day. The PhD would have been so much harder without them. I wish their lives to be always healthy and full of love.

Contents

List of Figures

List of Tables

Chapter 1

Introduction

Modern machine learning systems are pipelines. Raw data is first transformed into intermediate representations, often through the use of powerful pretrained neural network models. These representations are then used for making complex decisions in specific downstream tasks. Such pipelines are increasingly popular across various domains, ranging from recommendation systems powered by learned embeddings of users and products, to robotic control based on estimated 3D environment mapping. In particular, this dissertation focuses on a particular complex pipeline—artificial intelligence (AI) agents that use machine learning models to process various inputs and to interact with the world with its decisions.

The deciding factor in such a complex system's performance is *its intermediate representations* from the learned neural networks. These representations geometrically organize input data in a way that determines the effectiveness of learning and decision-making on top of them. Indeed, large pretrained models that provide good representations of data are already the cornerstones of modern machine learning. Specialized systems, such as medical condition classifiers, are now usually built via learning a prediction head on top of pretrained representations, along with possible finetuning of the pretrained model (Steiner and Pilgrim, 2024; Xu et al., 2024).

The goal of this dissertation is to explore the extent that **strong perceptual and decision-making capabilities can be directly obtained from good representations without requiring much agent-specific or task-specific learning**.

We study how the structure of learned representations can make downstream tasks easy, and sometimes trivial. For example, a representation *invariant to imperceptible variations* in model input greatly improves sample efficiency of solving perceptual problems (*e.g.*, image classification) (Chapter 2). A representation space where *distances align with decision costs* offers a powerful heuristic for planning behaviors over long horizons (Chapters 3 and 4). Conversely, a poorly chosen structure may obscure critical signals, and lead to a failed system (Chapter 5).

One important contribution of this dissertation is that we make the connection between *representation learning* and *reinforcement learning* (or decision-making). While many reinforcement learning methods have used auxiliary losses to promote good representations (Ni et al., 2024; Laskin et al., 2020a; Zhang et al., 2020a), we instead solve the reinforcement learning problem by *representation learning* alone without any other objectives in Chapters 3 and 4. Furthermore, in Chapter 5, we show that good representations can automatically identify the abstract easy-to-solve reinforcement learning problems from the noisy complex world.

Perception and decision-making are core capabilities for building intelligent artificial agents. After formulating them as representation learning tasks, we take one step further, and hypothesize an *ultimate representation* that all strong machine learning models are converging to, and that working towards learning this representation will make the most important progress to intelligent agents (Chapter 6).

1.1 Representations in Neural Networks

In this dissertation, we restrict our attention to representations that are *vector embeddings* (*i.e.*, latents) induces by neural networks (sometimes referred to as *encoders*). Such neural networks are often pre-trained with supervised or self-supervised objectives, such as a truncated classification network, or a next-token predictor transformer network. In particular, for input data $x \in \mathcal{X}$ and a neural network $f\colon \mathcal{X} \to \mathbb{R}^n$, we say that $f(x)$ is the (vector) embedding of data x.

Our study focuses on the geometric structures induced by this embedding of f. For

example, the similarity between $x_1 \in \mathcal{X}$ and $x_2 \in \mathcal{X}$ can be defined as $\langle f(x_1), f(x_2) \rangle$; the distance between them can be defined as $\|f(x_1) - f(x_2)\|_2$ (or $d(f(x_1), f(x_2))$ for some non-Euclidean d). In other words, a neural network f defines a *geometry* over data $\mathcal{X}$ in its representation space ; and learning f is essentially about identify the desired geometry in a data-driven way. In this dissertation, we study the representation geometric structures indued by neural networks, and how they relate to perception and decision-making capabilities of artificial agents.

1.2 Dissertation Outline

The dissertation consists of three parts:

1. Part I: Perception as Representation Learning;
2. Part II: Decision-Making as Representation Learning;
3. Part III: The Platonic Representation Hypothesis.

We outline each part below in subsections.

1.2.1 Part I: Perception as Representation Learning

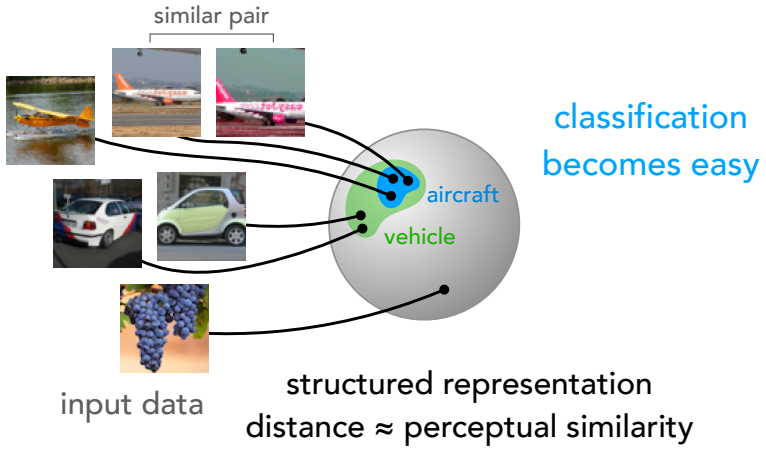

Figure 1-1: Similarity structure improves perception.

Chapter 2: Contrastive Representation Learning of Perceptual Relationships No image is an island. Perception requires contextualizing each piece of information in its connection with the rest of the world through a graph of perceptual similarity, co-occurrence, and other relationships (James, 1890; Isola, 2015b). However, these relationships are tricky to model. Images with significant pixel variations can still be perceived similarly (*e.g.*, the similar pair in Figure 1-1).

We present a geometric approach to train and evaluate encoder models that transform data to a structured representation space, where distance approximates perceptual similarity and co-occurrence. These learned structures can enhance many perception tasks, such as classification (Figure 1-1). We formulate *perceptual relationships* with two quantifiable *geometric* properties of representation space: **alignment**, which ensures related pairs map to nearby representations, and **uniformity**, which preserves data information in the representation space. We show that downstream performance strongly agrees with both geometric properties across diverse tasks in vision and language. We conduct a geometric analysis of contrastive representation learning, a method driving many recent advances like text-to-image synthesis. In distinction from prior information-theoretic approaches, we prove that contrastive learning essentially optimizes for alignment and uniformity with realistic assumptions and empirical validations.

1.2.2 Part II: Decision-Making as Representation Learning

Chapters 3 and 4: Reinforcement Learning as Quasimetric Representation Learning The machine learning revolution will not be single-task. Many recent advances are powered by generalist systems whose behavior is controllable by user-specified goals (*e.g.*, instruction-following language models). For decision-making, strategies for reaching different goals are not isolated. For example, knowing how to "`open fridge`" makes it easy to "`get milk`". Such dependencies highlight an important *asymmetric* structure in decision-making, where some goals lead to others, but not vice versa, due to the inherent *asymmetry* of our world (*e.g.*, time and gravity). However, previous decision-making methods often overlook such goal structures, resulting in

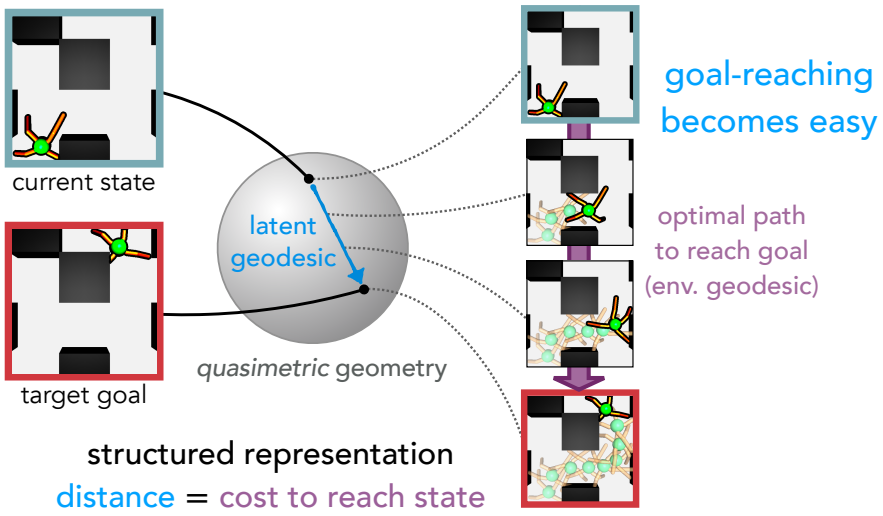

Figure 1-2: Distance structure guides agent to reach goals.

poor sample efficiency, or incorrectly assume symmetry, failing to make effective decisions in the asymmetric world Chapter 5.

We use *quasimetric* geometry, the asymmetric relaxation of metric geometry, to model decision-making structures. By accurately capturing decision costs among different states, *quasimetric* geometry directly produces optimal goal-reaching agents (Figure 1-2). We establishe learning foundations for *quasimetrics* (Chapter 4), and develop a *quasimetric*-based algorithm that advanced the frontier of goal-reaching agents (Chapter 5).

In particular, we address several key challenges in the *modeling* and *learning* of *quasimetric* distance structures:

- *Modeling* (Chapter 3): We conduct the first learning-theoretical analyses on *quasimetrics*. With mathematical tools from extremal combinatorics, we prove that *quasimetrics* are not learnable by the unconstrained neural network architectures commonly used for goal-reaching decision-making. We designe new architectures that encode data into a *quasimetric representation space*, with strong theoretical guarantees and empirical performances.
- *Learning* (Chapter 4): I developed a decision-making algorithm that at its core learns a *quasimetric* representation space to guide goal-reaching agents (Figure 1-2). In distinction to common approaches, it is based on *quasimetric* geometry of the

decision-making problem, and efficiently learns optimal behavior from suboptimal data with theoretical guarantees under diverse problem settings (*e.g.*, continuous action space). Over goal-reaching benchmarks, our algorithm robustly recovers *quasimetric* structures of the environment, and beats prior art by 43% in performance and by up to 3.9× in sample efficiency.

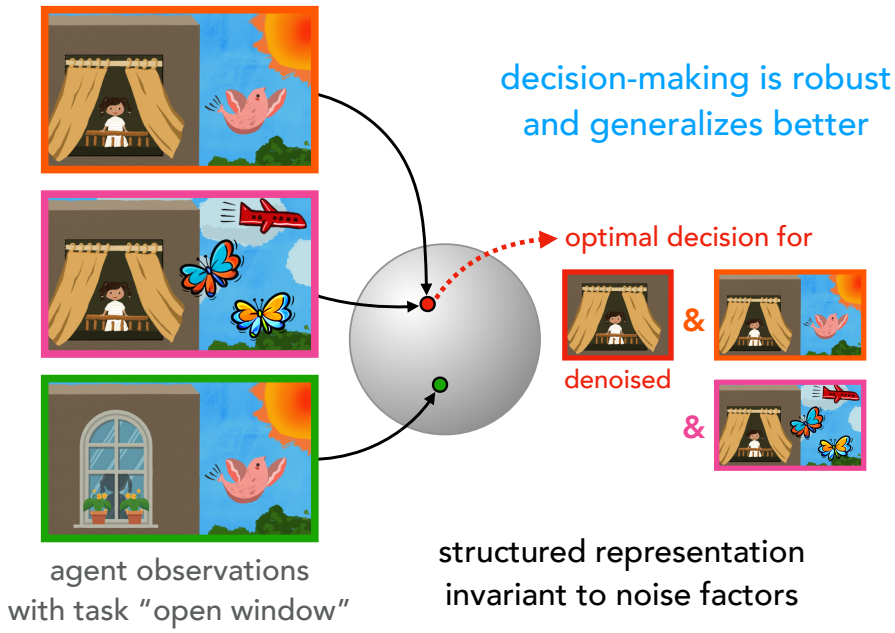

Figure 1-3: Abstraction structure enables robust decisions that are invariant to noises and generalize to equivalent scenarios.

Chapter 5: Denoised MDPs: Learning Latent World Models Better Than the World Itself Abstract reasoning is key to intelligence. Even with a good perceptual representation, autonomous agents are often provided more than enough information for their task, and must extract task-specific signals from rich observations. However, the typical framework for sequential decision making, *Markov Decision Process (MDP)*, models the entire agent observation in an unstructured way, and falls short for any separation between signal and noise. To address these shortcomings, we reformulate the MDP framework with a *factorized* model of agent observations. We show that the factorization structure explicitly identifies information necessary for optimal decision-making without loss of generality.

We develop an algorithm to extract such decision-critical signals via a structured representation space (Figure 1-3) without requiring additional supervision. Our method can denoise observations for any decision-making algorithm, yielding 25%-60% performance gain on various benchmark tasks.

1.2.3 Part III: The Platonic Representation Hypothesis

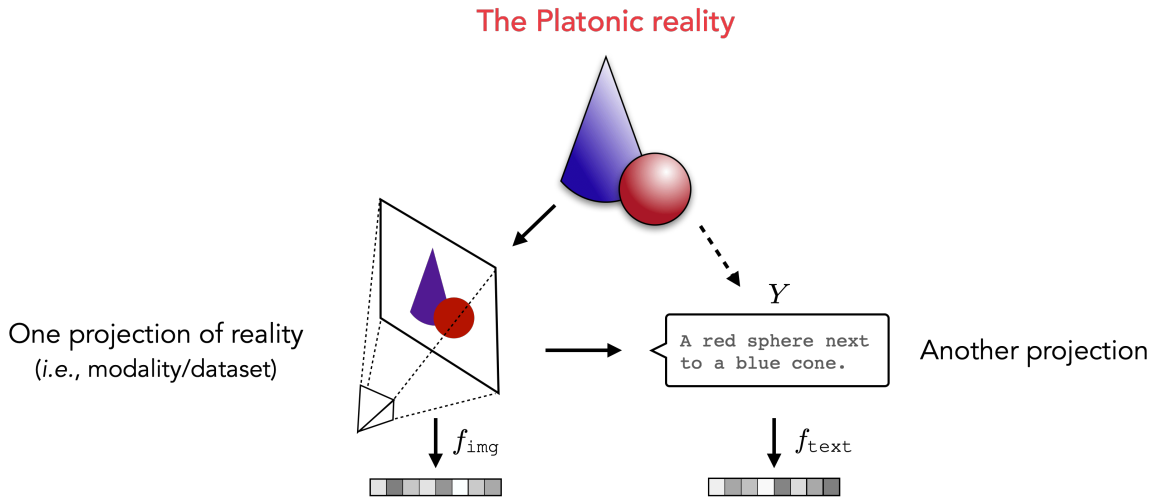

Figure 1-4: **The Platonic Representation Hypothesis:** Neural networks, trained with different objectives on different data and modalities, are converging to a shared statistical model of reality in their representation spaces.

Chapter 6: The Platonic Representation Hypothesis Strong representations can solve diverse tasks in perception and decision-making by capturing some fundamental statistical structures of the world (Chapters 2, 4 and 5). Do these have to be different representations? Can one representation rule them all? We empirically study the current best foundation models, and found that *all strong models converge towards the same way of representing the world regardless of data, objective, or modality*. Based on this convergence, we conjecture the *Platonic Representation Hypothesis* that this unique representation captures the core (statistical) structure of the world by learning on various projections (*e.g.*, modalities, datasets) of it (Figure 1-4). Further more, we argue that *recovering this Platonic representations is an crucial part of building intelligent agents* that can solve diverse interactive tasks.

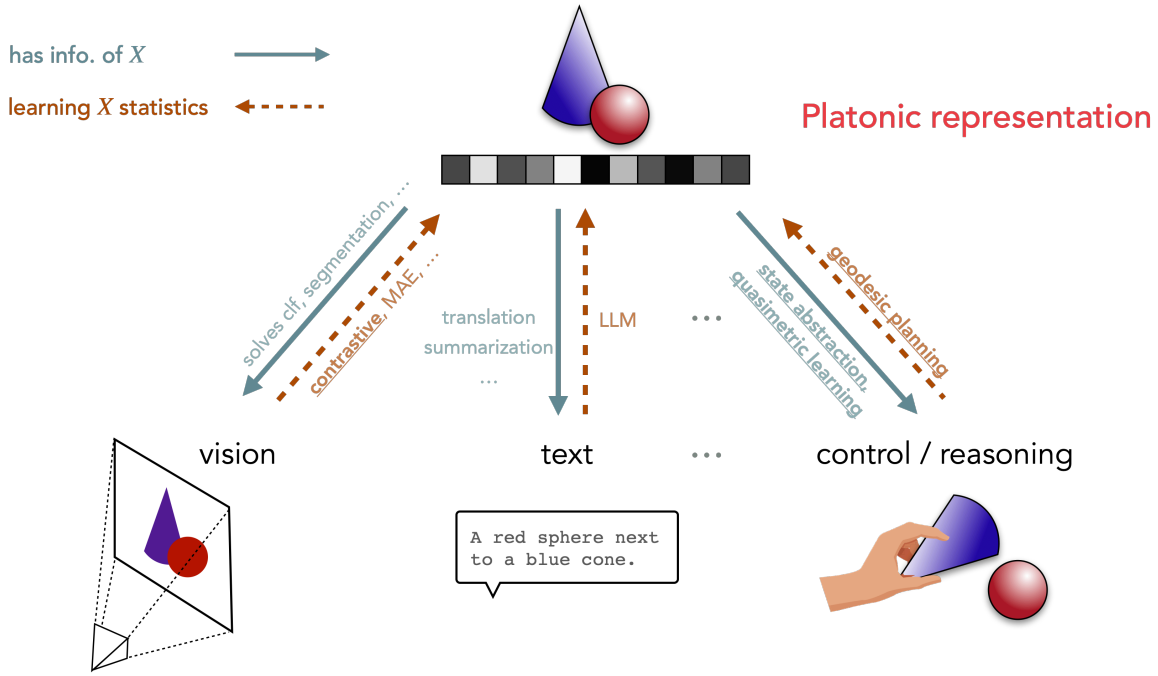

Figure 1-5: Recovering the Platonic representation from different sources (projections). This dissertation explored multiple parts of the arrows (**bold and underlined**).

We argue that working towards recovering the Platonic representation is one of the most important future goals. This dissertation has explored various methods that allow us to learn from individual projections (Figure 1-5). However, in order to combine different sources, we must explore effective methods to integrate new information into existing representations, and adapt them to more modalities/projections. In Chapter 7, we propose several important questions in this aspect for future research.

Part I

Perception as Representation Learning

Chapter 2

Contrastive Representation Learning of Perceptual Relationships

Contrastive representation learning has been outstandingly successful in practice. In this chapter, we identify two key *geometric* properties related to the contrastive loss: (1) *alignment* (closeness) of features from perceptually similar positive pairs, and (2) *uniformity* of the induced distribution of the (normalized) features on the hypersphere. We prove that, asymptotically, the contrastive loss optimizes these properties, and analyze their positive effects on downstream tasks. Empirically, we introduce an optimizable metric to quantify each property. Extensive experiments on standard vision and language datasets confirm the strong agreement between *both* metrics and downstream task performance. Directly optimizing for these two metrics leads to representations with comparable or better performance at downstream tasks than contrastive learning.

This chapter is based on published work:

1. *Understanding Contrastive Representation Learning Through Alignment and Uniformity on the Hypersphere* with co-author Phillip Isola at the International Conference on Machine Learning (ICML) 2020 (Wang and Isola, 2020).

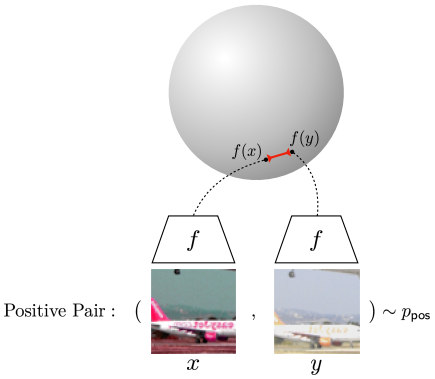

Alignment: Similar samples have similar features.
(Figure inspired by Tian et al. (2020b).)

Uniformity: Preserve maximal information.

Figure 2-1: Illustration of alignment and uniformity of feature distributions on the output unit hypersphere. STL-10 (Coates et al., 2011) images are used for demonstration.

2.1 Introduction

A vast number of recent empirical works learn representations with a unit ℓ_2 norm constraint, effectively restricting the output space to the unit hypersphere (Parkhi et al., 2015; Schroff et al., 2015; Liu et al., 2017; Hasnat et al., 2017; Wang et al., 2017; Bojanowski and Joulin, 2017; Mettes et al., 2019; Hou et al., 2019; Davidson et al., 2018; Xu and Durrett, 2018), including many unsupervised contrastive representation learning methods (Wu et al., 2018; Bachman et al., 2019; Tian et al., 2020b; He et al., 2019; Chen et al., 2020a).

Intuitively, having the features live on the unit hypersphere leads to several desirable traits. Fixed-norm vectors are known to improve training stability in modern machine learning where dot products are ubiquitous (Xu and Durrett, 2018; Wang et al., 2017). Moreover, if features of a class are sufficiently well clustered, they are linearly separable with the rest of feature space (see Figure 2-2), a common criterion used to evaluate representation quality.

While the unit hypersphere is a popular choice of feature space, not all encoders that map onto it are created equal. Recent works argue that representations should additionally be invariant to unnecessary details, and preserve as much information as possible (Oord et al., 2018; Tian et al., 2020b; Hjelm et al., 2018; Bachman et al.,

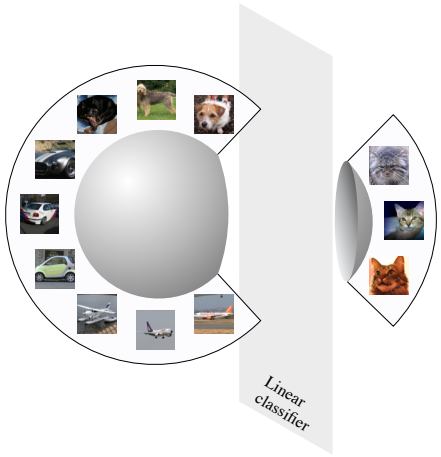

Figure 2-2: **Hypersphere:** When classes are well-clustered (forming spherical caps), they are linearly separable. The same does not hold for Euclidean spaces.

2019). Let us call these two properties *alignment* and *uniformity* (see Figure 2-1). *Alignment* favors encoders that assign similar features to similar samples. *Uniformity* prefers a feature distribution that preserves maximal information, *i.e.*, the uniform distribution on the unit hypersphere.

In this work, we analyze the *alignment* and *uniformity* properties. We show that a currently popular form of contrastive representation learning in fact directly optimizes for these two properties in the limit of infinite negative samples. We propose theoretically-motivated metrics for alignment and uniformity, and observe strong agreement between them and downstream task performance. Remarkably, directly optimizing for these two metrics leads to comparable or better performance than contrastive learning.

Our main contributions are:

- We propose quantifiable metrics for *alignment* and *uniformity* as two measures of representation quality, with theoretical motivations.

- We prove that the contrastive loss optimizes for alignment and uniformity asymptotically.

- Empirically, we find strong agreement between *both* metrics and downstream task performance.

- Despite being simple in form, our proposed metrics, when directly optimized with no other loss, empirically lead to comparable or better performance at downstream tasks than contrastive learning.

2.2 Related Work

Unsupervised Contrastive Representation Learning has seen remarkable success in learning representations for image and sequential data (Logeswaran and Lee, 2018; Wu et al., 2018; Oord et al., 2018; Hénaff et al., 2019; Tian et al., 2020b; Hjelm et al., 2018; Bachman et al., 2019; Tian et al., 2020b; He et al., 2019; Chen et al., 2020a). The common motivation behind these work is the InfoMax principle (Linsker, 1988), which we here instantiate as maximizing the mutual information (MI) between two views (Tian et al., 2020b; Bachman et al., 2019; Wu et al., 2020). However, this interpretation is known to be inconsistent with the actual behavior in practice, *e.g.*, optimizing a tighter bound on MI can lead to worse representations (Tschannen et al., 2019). What the contrastive loss exactly does remains largely a mystery. Analysis based on the assumption of latent classes provides nice theoretical insights (Saunshi et al., 2019), but unfortunately has a rather large gap with empirical practices: the result that representation quality suffers with a large number of negatives is inconsistent with empirical observations (Wu et al., 2018; Tian et al., 2020b; He et al., 2019; Chen et al., 2020a). In this chapter, we analyze and characterize the behavior of contrastive learning from the perspective of alignment and uniformity properties, and empirically verify our claims with standard representation learning tasks.

Representation learning on the unit hypersphere. Outside contrastive learning, many other representation learning approaches also normalize their features to be on the unit hypersphere. In variational autoencoders, the hyperspherical latent space has been shown to perform better than the Euclidean space (Xu and Durrett, 2018; Davidson et al., 2018). Directly matching uniformly sampled points on the unit hypersphere is known to provide good representations (Bojanowski and Joulin,

2017), agreeing with our intuition that uniformity is a desirable property. Mettes et al. (2019) optimizes prototype representations on the unit hypersphere for classification. Hyperspherical face embeddings greatly outperform the unnormalized counterparts (Parkhi et al., 2015; Liu et al., 2017; Wang et al., 2017; Schroff et al., 2015). Its empirical success suggests that the unit hypersphere is indeed a nice feature space. In this work, we formally investigate the interplay between the hypersphere geometry and the popular contrastive representation learning.

Distributing points on the unit hypersphere. The problem of uniformly distributing points on the unit hypersphere is a well-studied one. It is often defined as minimizing the total pairwise potential w.r.t. a certain kernel function (Borodachov et al., 2019; Landkof, 1972), *e.g.*, the Thomson problem of finding the minimal electrostatic potential energy configuration of electrons (Thomson, 1904), and minimization of the Riesz s-potential (Götz and Saff, 2001; Hardin and Saff, 2005; Liu et al., 2018). The uniformity metric we propose is based on the Gaussian potential, which can be used to represent a very general class of kernels and is closely related to the universally optimal point configurations (Borodachov et al., 2019; Cohn and Kumar, 2007). Additionally, the best-packing problem on hyperspheres (often called the Tammes problem) is also well studied (Tammes, 1930).

2.3 Preliminaries on Unsupervised Contrastive Representation Learning

The popular unsupervised contrastive representation learning method (often referred to as *contrastive learning* in this chapter) learns representations from unlabeled data. It assumes a way to sample *positive pairs*, representing similar samples that should have similar representations. Empirically, the positive pairs are often obtained by taking two independently randomly augmented versions of the same sample, *e.g.* two crops of the same image (Wu et al., 2018; Hjelm et al., 2018; Bachman et al., 2019; He et al., 2019; Chen et al., 2020a).

Let $p_{\mathsf{data}}(\cdot)$ be the data distribution over $\mathbb{R}^n$ and $p_{\mathsf{pos}}(\cdot,\cdot)$ the distribution of positive pairs over $\mathbb{R}^n \times \mathbb{R}^n$. Based on empirical practices, we assume the following property.

Assumption 2.3.1. Distributions p_{data} and p_{pos} should satisfy

- Symmetry: $\forall x, y,\ p_{\mathsf{pos}}(x,y) = p_{\mathsf{pos}}(y,x)$.
- Matching marginal: $\forall x,\ \int p_{\mathsf{pos}}(x,y)\,\mathrm{d}y = p_{\mathsf{data}}(x)$.

We consider the following specific and widely popular form of contrastive loss for training an encoder $f\colon \mathbb{R}^n \to \mathcal{S}^{m-1}$, mapping data to ℓ_2 normalized feature vectors of dimension m. This loss has been shown effective by many recent representation learning methods (Logeswaran and Lee, 2018; Wu et al., 2018; Tian et al., 2020b; He et al., 2019; Hjelm et al., 2018; Bachman et al., 2019; Chen et al., 2020a).

$$\mathcal{L}_{\mathsf{contrastive}}(f;\tau,M) \triangleq \mathop{\mathbb{E}}_{\substack{(x,y)\sim p_{\mathsf{pos}} \\ \{x_i^-\}_{i=1}^M \overset{\text{i.i.d.}}{\sim} p_{\mathsf{data}}}} \left[-\log \frac{e^{f(x)^\mathsf{T} f(y)/\tau}}{e^{f(x)^\mathsf{T} f(y)/\tau} + \sum_i e^{f(x_i^-)^\mathsf{T} f(y)/\tau}} \right], \tag{2.1}$$

where $\tau > 0$ is a scalar temperature hyperparameter, and $M \in \mathbb{Z}_+$ is a fixed number of negative samples.

The term *contrastive loss* has also been generally used to refer to various objectives based on positive and negative samples, *e.g.*, in Siamese networks (Chopra et al., 2005; Hadsell et al., 2006). In this work, we focus on the specific form in Equation (2.1) that is widely used in modern unsupervised contrastive representation learning literature.

Necessity of normalization. Without the norm constraint, the `softmax` distribution can be made arbitrarily sharp by simply scaling all the features. Wang et al. (2017) provided an analysis on this effect and argued for the necessity of normalization when using feature vector dot products in a cross entropy loss, as is in Eqn. (2.1). Experimentally, Chen et al. (2020a) also showed that normalizing outputs leads to superior representations.

The InfoMax principle. Many empirical works are motivated by the InfoMax principle of maximizing $I(f(x); f(y))$ for $(x, y) \sim p_{\mathsf{pos}}$ (Tian et al., 2020b; Bachman et al., 2019; Wu et al., 2020). Usually they interpret $\mathcal{L}_{\mathsf{contrastive}}$ in Eqn. (2.1) as a lower bound of $I(f(x); f(y))$ (Oord et al., 2018; Hjelm et al., 2018; Bachman et al., 2019; Tian et al., 2020b). However, this interpretation is known to have issues in practice, *e.g.*, maximizing a tighter bound often leads to worse downstream task performance (Tschannen et al., 2019). Therefore, instead of viewing it as a bound, we investigate the exact behavior of directly optimizing $\mathcal{L}_{\mathsf{contrastive}}$ in the following sections.

2.4 Feature Distribution on the Hypersphere

The contrastive loss encourages learned feature representation for positive pairs to be similar, while pushing features from the randomly sampled negative pairs apart. Conventional wisdom says that representations should extract the most shared information between positive pairs and remain invariant to other noise factors (Linsker, 1988; Tian et al., 2020b; Wu et al., 2020; Bachman et al., 2019). Therefore, the loss should prefer two following properties:

- *Alignment*: two samples forming a positive pair should be mapped to nearby features, and thus be (mostly) invariant to unneeded noise factors.
- *Uniformity*: feature vectors should be roughly uniformly distributed on the unit hypersphere $\mathcal{S}^{m-1}$, preserving as much information of the data as possible.

To empirically verify this, we visualize CIFAR-10 (Torralba et al., 2008; Krizhevsky et al., 2009) representations on $\mathcal{S}^1$ ($m = 2$) obtained via three different methods:

- Random initialization.
- Supervised predictive learning: An encoder and a linear classifier are jointly trained from scratch with cross entropy loss on supervised labels.
- Unsupervised contrastive learning: An encoder is trained w.r.t. $\mathcal{L}_{\mathsf{contrastive}}$ with $\tau = 0.5$ and $M = 256$.

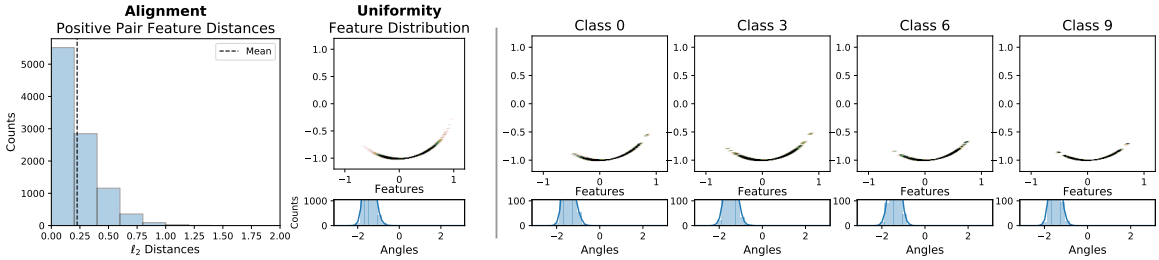

(a) **Random Initialization.** Linear classification validation accuracy: 12.71%.

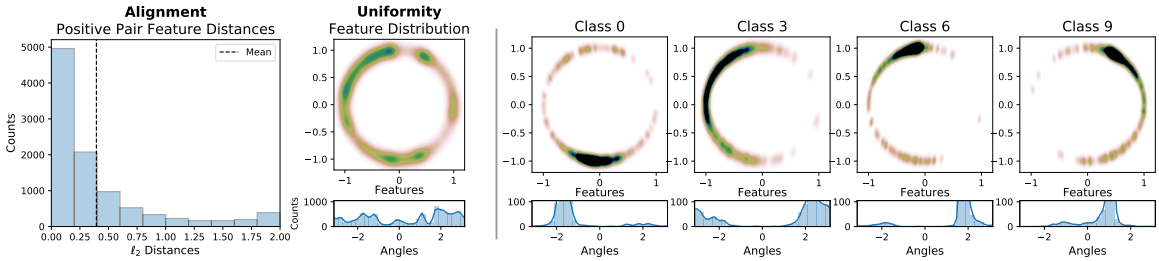

(b) **Supervised Predictive Learning.** Linear classification validation accuracy: 57.19%.

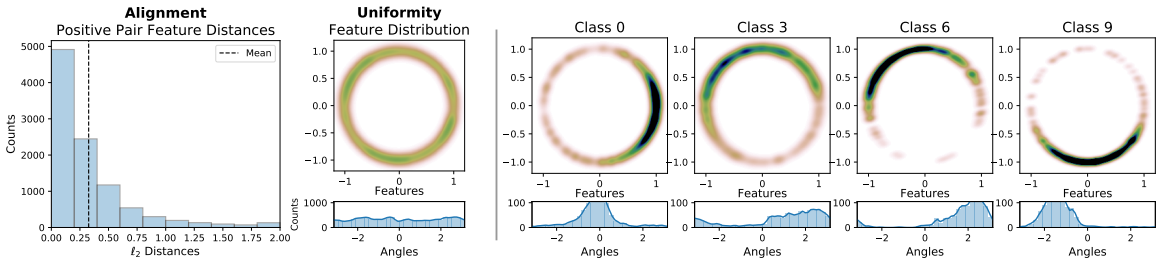

(c) **Unsupervised Contrastive Learning.** Linear classification validation accuracy: 28.60%.

Figure 2-3: Representations of CIFAR-10 validation set on $\mathcal{S}^1$. **Alignment analysis:** We show distribution of distance between features of positive pairs (two random augmentations). **Uniformity analysis:** We plot feature distributions with Gaussian kernel density estimation (KDE) in $\mathbb{R}^2$ and von Mises-Fisher (vMF) KDE on angles (*i.e.*, $\arctan2(y, x)$ for each point $(x, y) \in \mathcal{S}^1$). **Four rightmost plots** visualize feature distributions of selected specific classes. Representation from contrastive learning is both *aligned* (having low positive pair feature distances) and *uniform* (evenly distributed on $\mathcal{S}^1$).

All three encoders share the same AlexNet based architecture (Krizhevsky et al., 2012), modified to map input images to 2-dimensional vectors in $\mathcal{S}^1$. Both predictive and contrastive learning use standard data augmentations to augment the dataset and sample positive pairs.

Figure 2-3 summarizes the resulting distributions of validation set features. Indeed, features from unsupervised contrastive learning (bottom in Figure 2-3) exhibit the most uniform distribution, and are closely clustered for positive pairs.

The form of the contrastive loss in Eqn. (2.1) also suggests this. We present informal arguments below, followed by more formal treatment in Section 2.4.2. From

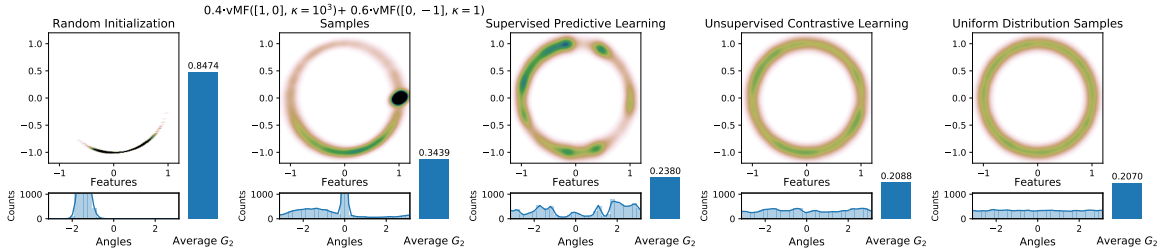

Figure 2-4: Average pairwise G_2 potential as a measure of uniformity. Each plot shows 10000 points distributed on $\mathcal{S}^1$, obtained via either applying an encoder on CIFAR-10 validation set (same as those in Figure 2-3) or sampling from a distribution on $\mathcal{S}^1$, as described in plot titles. We show the points with Gaussian KDE and the angles with vMF KDE.

the symmetry of p, we can derive

$$\mathcal{L}_{\mathsf{contrastive}}(f;\tau,M) = \mathop{\mathbb{E}}_{(x,y)\sim p_{\mathsf{pos}}}\left[-f(x)^\mathsf{T} f(y)/\tau\right] + \mathop{\mathbb{E}}_{\substack{(x,y)\sim p_{\mathsf{pos}} \\ \{x_i^-\}_{i=1}^M \overset{\text{i.i.d.}}{\sim} p_{\mathsf{data}}}}\left[\log\left(e^{f(x)^\mathsf{T} f(y)/\tau} + \sum_i e^{f(x_i^-)^\mathsf{T} f(x)/\tau}\right)\right].$$

Because the $\sum_i e^{f(x_i^-)^\mathsf{T} f(x)/\tau}$ term is always positive and bounded below, the loss favors smaller $\mathbb{E}\left[-f(x)^\mathsf{T} f(y)/\tau\right]$, *i.e.*, having more aligned positive pair features. Suppose the encoder is perfectly aligned, *i.e.*, $\mathbb{P}\left[f(x) = f(y)\right] = 1$, then minimizing the loss is equivalent to optimizing

$$\mathop{\mathbb{E}}_{\substack{x\sim p_{\mathsf{data}} \\ \{x_i^-\}_{i=1}^M \overset{\text{i.i.d.}}{\sim} p_{\mathsf{data}}}}\left[\log\left(e^{1/\tau} + \sum_i e^{f(x_i^-)^\mathsf{T} f(x)/\tau}\right)\right],$$

which is akin to maximizing pairwise distances with a `LogSumExp` transformation. Intuitively, pushing all features away from each other should indeed cause them to be roughly uniformly distributed.

2.4.1 Quantifying Alignment and Uniformity

For further analysis, we need a way to measure alignment and uniformity. We propose the following two metrics (losses).

Alignment

The alignment loss is straightforwardly defined with the expected distance between positive pairs:

$$\mathcal{L}_{\mathsf{align}}(f;\alpha) \triangleq \mathop{\mathbb{E}}_{(x,y)\sim p_{\mathsf{pos}}} \left[\|f(x)-f(y)\|_2^{\alpha}\right], \quad \alpha > 0.$$

Uniformity

We want the uniformity metric to be both asymptotically correct (*i.e.*, the distribution optimizing this metric should converge to uniform distribution) and empirically reasonable with finite number of points. To this end, we consider the Gaussian potential kernel (also known as the Radial Basis Function (RBF) kernel) $G_t \colon \mathcal{S}^d \times \mathcal{S}^d \to \mathbb{R}_+$ (Cohn and Kumar, 2007; Borodachov et al., 2019):

$$G_t(u,v) \triangleq e^{-t\|u-v\|_2^2} = e^{2t\cdot u^{\mathsf{T}}v-2t}, \quad t > 0,$$

and define the uniformity loss as the logarithm of the average pairwise Gaussian potential:

$$\begin{aligned}\mathcal{L}_{\mathsf{uniform}}(f;t) &\triangleq \log \mathop{\mathbb{E}}_{x,y \overset{\text{i.i.d.}}{\sim} p_{\mathsf{data}}} \left[G_t(u,v)\right] \\ &= \log \mathop{\mathbb{E}}_{x,y \overset{\text{i.i.d.}}{\sim} p_{\mathsf{data}}} \left[e^{-t\|f(x)-f(y)\|_2^2}\right], \quad t > 0.\end{aligned}$$

The average pairwise Gaussian potential is nicely tied with the uniform distribution on the unit hypersphere.

Definition 2.4.1 (Uniform distribution on $\mathcal{S}^d$)**.** σ_d denotes the normalized surface area measure on $\mathcal{S}^d$.

First, we show that the uniform distribution is the unique distribution that minimize the expected pairwise potential.

Proposition 2.4.2. For $\mathcal{M}(\mathcal{S}^d)$ the set of Borel probability measures on $\mathcal{S}^d$, σ_d is

the unique solution of

$$\min_{\mu \in \mathcal{M}(\mathcal{S}^d)} \int_u \int_v G_t(u, v) \, \mathrm{d}\mu \, \mathrm{d}\mu.$$

Proof. See Appendix A.1.1. □

In addition, as number of points goes to infinity, distributions of points minimizing the average pairwise potential converge weak* to the uniform distribution. Recall the definition of the weak* convergence of measures.

Definition 2.4.3 (Weak* convergence of measures)**.** A sequence of Borel measures $\{\mu_n\}_{n=1}^{\infty}$ in $\mathbb{R}^p$ converges weak* to a Borel measure μ if for all continuous function $f \colon \mathbb{R}^p \to \mathbb{R}$, we have

$$\lim_{n \to \infty} \int f(x) \, \mathrm{d}\mu_n(x) = \int f(x) \, \mathrm{d}\mu(x).$$

Proposition 2.4.4. For each $N > 0$, the N point minimizer of the average pairwise potential is

$$\mathbf{u}_N^* = \operatorname*{arg\,min}_{u_1, u_2, \ldots, u_N \in \mathcal{S}^d} \sum_{1 \le i < j \le N} G_t(u_i, u_j).$$

The normalized counting measures associated with the $\{\mathbf{u}_N^*\}_{N=1}^{\infty}$ sequence converge weak* to σ_d.

Proof. See Appendix A.1.1. □

Designing an objective minimized by the uniform distribution is in fact nontrivial. For instance, average pairwise dot products or Euclidean distances is simply optimized by any distribution that has zero mean. Among kernels that achieve uniformity at optima, the Gaussian kernel is special in that it is closely related to the universally optimal point configurations and can also be used to represent a general class of other kernels, including the Riesz s-potentials. We refer readers to Borodachov et al. (2019) and Cohn and Kumar (2007) for in-depth discussions on these topics. Moreover, as we show below, $\mathcal{L}_{\mathsf{uniform}}$, defined with the Gaussian kernel, has close connections with $\mathcal{L}_{\mathsf{contrastive}}$.

Empirically, we evaluate the average pairwise potential of various finite point collections on $\mathcal{S}^1$ in Figure 2-4. The values nicely align with our intuitive understanding of uniformity.

We further discuss properties of $\mathcal{L}_{\mathsf{uniform}}$ and characterize its optimal value and range in Appendix A.1.1.

2.4.2 Limiting Behavior of Contrastive Learning

In this section, we formalize the intuition that contrastive learning optimizes alignment and uniformity, and characterize its asymptotic behavior. We consider optimization problems over all measurable encoder functions from the p_{data} measure in $\mathbb{R}^n$ to the Borel space $\mathcal{S}^{m-1}$.

We first define the notion of optimal encoders for each of these two metrics.

Definition 2.4.5 (Perfect Alignment)**.** We say an encoder f is *perfectly aligned* if $f(x) = f(y)$ a.s. over $(x, y) \sim p_{\mathsf{pos}}$.

Definition 2.4.6 (Perfect Uniformity)**.** We say an encoder f is *perfectly uniform* if the distribution of $f(x)$ for $x \sim p_{\mathsf{data}}$ is the uniform distribution σ_{m-1} on $\mathcal{S}^{m-1}$.

Realizability of perfect uniformity. We note that it is not always possible to achieve perfect uniformity, *e.g.*, when the data manifold in $\mathbb{R}^n$ is lower dimensional than the feature space $\mathcal{S}^{m-1}$. Moreover, in the case that p_{data} and p_{pos} are formed from sampling augmented samples from a finite dataset, there cannot be an encoder that is *both* perfectly aligned and perfectly uniform, because perfect alignment implies that all augmentations from a single element have the same feature vector. Nonetheless, perfectly uniform encoder functions do exist under the conditions that $n \geq m - 1$ and p_{data} has bounded density.

We analyze the asymptotics with infinite negative samples. Existing empirical work has established that larger number of negative samples consistently leads to better downstream task performances (Wu et al., 2018; Tian et al., 2020b; He et al., 2019; Chen et al., 2020a), and often uses very large values (*e.g.*, $M = 65536$ in He et al.

(2019)). The following theorem nicely confirms that optimizing w.r.t. the limiting loss indeed requires both alignment and uniformity.

Theorem 2.4.7 (Asymptotics of $\mathcal{L}_{\mathsf{contrastive}}$). For fixed $\tau > 0$, as the number of negative samples $M \to \infty$, the (normalized) contrastive loss converges to

$$\lim_{M\to\infty} \mathcal{L}_{\mathsf{contrastive}}(f;\tau,M) - \log M = \\ -\frac{1}{\tau}\mathop{\mathbb{E}}_{(x,y)\sim p_{\mathsf{pos}}}\left[f(x)^\top f(y)\right] + \mathop{\mathbb{E}}_{x\sim p_{\mathsf{data}}}\left[\log \mathop{\mathbb{E}}_{x^-\sim p_{\mathsf{data}}}\left[e^{f(x^-)^\top f(x)/\tau}\right]\right]. \tag{2.2}$$

We have the following results:

1. The first term is minimized iff f is perfectly aligned.

2. If perfectly uniform encoders exist, they form the exact minimizers of the second term.

3. For the convergence in Equation (2.2), the absolute deviation from the limit decays in $\mathcal{O}(M^{-1/2})$.

Proof. See Appendix A.1.2. □

Relation with $\mathcal{L}_{\mathsf{uniform}}$. The proof of Theorem 2.4.7 in the Appendix A.1.2 connects the asymptotic $\mathcal{L}_{\mathsf{contrastive}}$ form with minimizing average pairwise Gaussian potential, *i.e.*, minimizing $\mathcal{L}_{\mathsf{uniform}}$. Compared with the second term of Equation (2.2), $\mathcal{L}_{\mathsf{uniform}}$ essentially pushes the log outside the outer expectation, without changing the minimizer (perfectly uniform encoders). However, due to its pairwise nature, $\mathcal{L}_{\mathsf{uniform}}$ is much simpler in form and avoids the computationally expensive `softmax` operation in $\mathcal{L}_{\mathsf{contrastive}}$ (Goodman, 2001; Bengio et al.; Gutmann and Hyvärinen, 2010; Grave et al., 2017; Chen et al., 2018).

Relation with feature distribution entropy estimation. When p_{data} is uniform over finite samples $\{x_1, x_2, \ldots, x_N\}$ (*e.g.*, a collected dataset), the second term in Equation (2.2) can be alternatively viewed as a resubstitution entropy estimator of

$f(x)$ (Ahmad and Lin, 1976), where x follows the underlying distribution p_{nature} that generates $\{x_i\}_{i=1}^N$, via a von Mises-Fisher (vMF) kernel density estimation (KDE):

$$\begin{aligned}
\mathop{\mathbb{E}}_{x\sim p_{\mathsf{data}}}\left[\log \mathop{\mathbb{E}}_{x^-\sim p_{\mathsf{data}}}\left[e^{f(x^-)^\top f(x)/\tau}\right]\right] &= \frac{1}{N}\sum_{i=1}^N \log\left(\frac{1}{N}\sum_{j=1}^N e^{f(x_i)^\top f(x_j)/\tau}\right) \\
&= \frac{1}{N}\sum_{i=1}^N \log \hat{p}_{\mathsf{vMF\text{-}KDE}}(f(x_i)) + \log Z_{\mathsf{vMF}} \\
&\triangleq -\hat{H}(f(x)) + \log Z_{\mathsf{vMF}}, \qquad x \sim p_{\mathsf{nature}} \\
&\triangleq -\hat{I}(x; f(x)) + \log Z_{\mathsf{vMF}}, \qquad x \sim p_{\mathsf{nature}},
\end{aligned}$$

where

- $\hat{p}_{\mathsf{vMF\text{-}KDE}}$ is the KDE based on samples $\{f(x_j)\}_{j=1}^N$ using a vMF kernel with $\kappa = \tau^{-1}$,
- Z_{vMF} is the normalization constant for vMF distribution with $\kappa = \tau^{-1}$,
- $\hat{H}$ denotes the resubstitution entropy estimator,
- $\hat{I}$ denotes the mutual information estimator based on $\hat{H}$, since f is a deterministic function.

Relation with the InfoMax principle. Many empirical works are motivated by the InfoMax principle, *i.e.*, maximizing $I(f(x); f(y))$ for $(x, y) \sim p_{\mathsf{pos}}$. However, the interpretation of $\mathcal{L}_{\mathsf{contrastive}}$ as a lower bound of $I(f(x); f(y))$ is known to be inconsistent with its actual behavior in practice (Tschannen et al., 2019). Our results instead analyze the properties of $\mathcal{L}_{\mathsf{contrastive}}$ itself. Considering the identity $I(f(x); f(y)) = H(f(x)) - H(f(x) \mid f(y))$, we can see that while uniformity indeed favors large $H(f(x))$, alignment is stronger than merely desiring small $H(f(x) \mid f(y))$. In particular, both Theorem 2.4.7 and the above connection with maximizing an entropy estimator provide alternative interpretations and motivations that $\mathcal{L}_{\mathsf{contrastive}}$ optimizes for *aligned* and *information-preserving* encoders.

Finally, even for the case where only a single negative sample is used (*i.e.*, $M = 1$), we can still prove a weaker result, which we describe in details in the Appendix A.1.2.

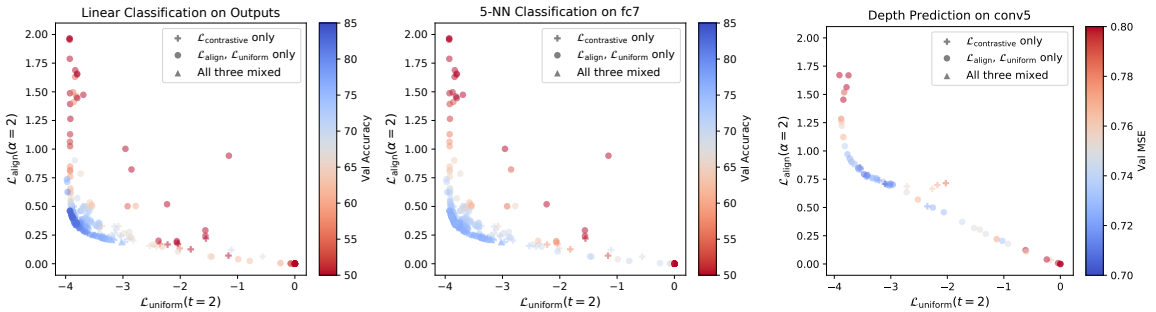

(a) 304 STL-10 encoders are evaluated with linear classification on output features and 5-nearest neighbor (5-NN) on fc7 activations. Higher accuracy (blue color) is better.

(b) 64 NYU-Depth-V2 encoders are evaluated with CNN depth regressors on conv5 activations. Lower MSE (blue color) is better.

Figure 2-5: Metrics and performance of STL-10 and NYU-Depth-V2 experiments. Each point represents a trained encoder, with its x- and y-coordinates showing $\mathcal{L}_{\text{align}}$ and $\mathcal{L}_{\text{uniform}}$ metrics and color showing the performance on validation set. **Blue** is better for both tasks. Encoders with low $\mathcal{L}_{\text{align}}$ and $\mathcal{L}_{\text{uniform}}$ are consistently the better performing ones (lower left corners).

```
# bsz : batch size (number of positive pairs)
# d   : latent dim
# x   : Tensor, shape=[bsz, d]
#       latents for one side of positive pairs
# y   : Tensor, shape=[bsz, d]
#       latents for the other side of positive pairs
# lam : hyperparameter balancing the two losses

def lalign(x, y, alpha=2):
    return (x - y).norm(dim=1).pow(alpha).mean()

def lunif(x, t=2):
    sq_pdist = torch.pdist(x, p=2).pow(2)
    return sq_pdist.mul(-t).exp().mean().log()

loss = lalign(x, y) + lam * (lunif(x) + lunif(y)) / 2
```

Figure 2-6: PyTorch implementation of $\mathcal{L}_{\text{align}}$ and $\mathcal{L}_{\text{uniform}}$.

2.5 Experiments

In this section, we empirically verify the hypothesis that alignment and uniformity are desired properties for representations. Recall that our two metrics are

$$\mathcal{L}_{\text{align}}(f; \alpha) \triangleq \mathbb{E}_{(x,y)\sim p_{\text{pos}}} \left[\|f(x) - f(y)\|_2^{\alpha} \right]$$
$$\mathcal{L}_{\text{uniform}}(f; t) \triangleq \log \mathbb{E}_{x,y \overset{\text{i.i.d.}}{\sim} p_{\text{data}}} \left[e^{-t\|f(x)-f(y)\|_2^2} \right].$$

We conduct extensive experiments with convolutional neural network (CNN) and recurrent neural network (RNN) based encoders on four popular representation learning

benchmarks with distinct types of downstream tasks:

- STL-10 (Coates et al., 2011) classification on AlexNet-based encoder outputs or intermediate activations with a linear or k-nearest neighbor (k-NN) classifier.
- NYU-Depth-V2 (Nathan Silberman and Fergus, 2012) depth prediction on CNN encoder intermediate activations after convolution layers.
- ImageNet and ImageNet-100 (random 100-class subset of ImageNet) classification on CNN encoder penultimate layer activations with a linear classifier.
- BookCorpus (Zhu et al., 2015) RNN sentence encoder outputs used for Moview Review Sentence Polarity (MR) (Pang and Lee, 2005) and Customer Product Review Sentiment (CR) (Wang and Manning, 2012) binary classification tasks with logisitc classifiers.

For image datasets, we follow the standard practice and choose positive pairs as two independent augmentations of the same image. For BookCorpus, positive pairs are chosen as neighboring sentences, following Quick-Thought Vectors (Logeswaran and Lee, 2018).

We perform majority of our analysis on STL-10 and NYU-Depth-V2 encoders, where we calculate $\mathcal{L}_{\mathsf{contrastive}}$ with negatives being other samples within the minibatch following the standard practice (Hjelm et al., 2018; Bachman et al., 2019; Tian et al., 2020b; Chen et al., 2020a), and $\mathcal{L}_{\mathsf{uniform}}$ as the logarithm of average pairwise feature potentials also within the minibatch. Due to their simple forms, these two losses can be implemented in PyTorch (Paszke et al., 2019) with less than 10 lines of code, as shown in Figure 2-6.

To investigate *alignment* and *uniformity* properties on recent contrastive learning methods and larger datasets, we also analyze ImageNet and ImageNet-100 encoders trained with Momentum Contrast (MoCo) (He et al., 2019; Chen et al., 2020b), and BookCorpus encoders trained with Quick-Thought Vectors (Logeswaran and Lee, 2018), with these methods modified to also allow $\mathcal{L}_{\mathsf{align}}$ and $\mathcal{L}_{\mathsf{uniform}}$.

	Loss Formula	Validation Set Accuracy ↑			
		Output + Linear	Output + 5-NN	fc7 + Linear	fc7 + 5-NN
Best $\mathcal{L}_{\mathsf{contrastive}}$ only	$\mathcal{L}_{\mathsf{contrastive}}(\tau{=}0.19)$	80.46%	78.75%	83.89%	76.33%
Best $\mathcal{L}_{\mathsf{align}}$ and $\mathcal{L}_{\mathsf{uniform}}$ only	$0.98 \cdot \mathcal{L}_{\mathsf{align}}(\alpha{=}2) + 0.96 \cdot \mathcal{L}_{\mathsf{uniform}}(t{=}2)$	**81.15%**	78.89%	**84.43%**	**76.78%**
Best among all encoders	$\mathcal{L}_{\mathsf{contrastive}}(\tau{=}0.5) + \mathcal{L}_{\mathsf{uniform}}(t{=}2)$	81.06%	**79.05%**	84.14%	76.48%

Table 2.1: STL-10 encoder evaluations. Numbers show linear and 5-nearest neighbor (5-NN) classification accuracies on the validation set. The best result is picked by encoder outputs linear classifier accuracy from a 5-fold training set cross validation, among all 150 encoders trained from scratch with 128-dimensional output and 768 batch size.

	Loss Formula	Validation Set MSE ↓	
		conv5	conv4
Best $\mathcal{L}_{\mathsf{contrastive}}$ only	$0.5 \cdot \mathcal{L}_{\mathsf{contrastive}}(\tau{=}0.1)$	0.7024	**0.7575**
Best $\mathcal{L}_{\mathsf{align}}$ and $\mathcal{L}_{\mathsf{uniform}}$ only	$0.75 \cdot \mathcal{L}_{\mathsf{align}}(\alpha{=}2) + 0.5 \cdot \mathcal{L}_{\mathsf{uniform}}(t{=}2)$	**0.7014**	0.7592
Best among all encoders	$0.75 \cdot \mathcal{L}_{\mathsf{align}}(\alpha{=}2) + 0.5 \cdot \mathcal{L}_{\mathsf{uniform}}(t{=}2)$	**0.7014**	0.7592

Table 2.2: NYU-Depth-V2 encoder evaluations. Numbers show depth prediction mean squared error (MSE) on the validation set. The best result is picked based on conv5 layer MSE from a 5-fold training set cross validation, among all 64 encoders trained from scratch with 128-dimensional output and 128 batch size.

We optimize a total of 304 STL-10 encoders, 64 NYU-Depth-V2 encoders, 45 ImageNet-100 encoders, and 108 BookCorpus encoders without supervision. The encoders are optimized w.r.t. weighted combinations of $\mathcal{L}_{\mathsf{contrastive}}$, $\mathcal{L}_{\mathsf{align}}$, and/or $\mathcal{L}_{\mathsf{uniform}}$, with varying

- (possibly zero) weights on the three losses,
- temperature τ for $\mathcal{L}_{\mathsf{contrastive}}$,
- $\alpha \in \{1, 2\}$ for $\mathcal{L}_{\mathsf{align}}$,
- $t \in \{1, 2, \ldots, 8\}$ for $\mathcal{L}_{\mathsf{uniform}}$,
- batch size (affecting the number of (negative) pairs for $\mathcal{L}_{\mathsf{contrastive}}$ and $\mathcal{L}_{\mathsf{uniform}}$),
- embedding dimension,
- number of training epochs and learning rate,
- initialization (from scratch vs. a pretrained encoder).

See Appendix A.2 for more experiment details and the exact configurations used.

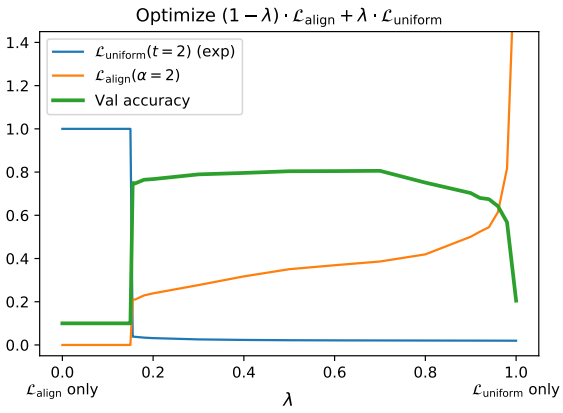

Figure 2-7: Effect of optimizing different weighted combinations of $\mathcal{L}_{\text{align}}(\alpha{=}2)$ and $\mathcal{L}_{\text{uniform}}(t{=}2)$ for STL-10. For each encoder, we show the $\mathcal{L}_{\text{align}}$ and $\mathcal{L}_{\text{uniform}}$ metrics, and validation accuracy of a linear classifier trained on encoder outputs. $\mathcal{L}_{\text{uniform}}$ is exponentiated for plotting purposes.

$\mathcal{L}_{\text{align}}$ and $\mathcal{L}_{\text{uniform}}$ strongly agree with downstream task performance. For each encoder, we measure the downstream task performance, and the $\mathcal{L}_{\text{align}}$, $\mathcal{L}_{\text{uniform}}$ metrics on the validation set. Figure 2-5 visualizes the trends between both metrics and representation quality. We observe that the two metrics strongly agrees the representation quality overall. In particular, the best performing encoders are exactly the ones with low $\mathcal{L}_{\text{align}}$ and $\mathcal{L}_{\text{uniform}}$, *i.e.*, the lower left corners in Figure 2-5.

Directly optimizing only $\mathcal{L}_{\text{align}}$ and $\mathcal{L}_{\text{uniform}}$ can lead to better representations. As shown in Tables 2.1 and 2.2, encoders trained with only $\mathcal{L}_{\text{align}}$ and $\mathcal{L}_{\text{uniform}}$ consistently outperform their $\mathcal{L}_{\text{contrastive}}$-trained counterparts, for both tasks. Theoretically, Theorem 2.4.7 showed that $\mathcal{L}_{\text{contrastive}}$ optimizes alignment and uniformity asymptotically with infinite negative samples. This empirical performance gap suggests that directly optimizing these properties can be superior in practice, when we can only have finite negatives.

Both alignment and uniformity are necessary for a good representation. Figure 2-7 shows how the final encoder changes in response to optimizing differently weighted combinations of $\mathcal{L}_{\text{align}}$ and $\mathcal{L}_{\text{uniform}}$ on STL-10. The trade-off between the $\mathcal{L}_{\text{align}}$ and $\mathcal{L}_{\text{uniform}}$ indicates that perfect alignment and perfect uniformity are likely hard to simultaneously achieve in practice. However, the inverted-U-shaped accuracy

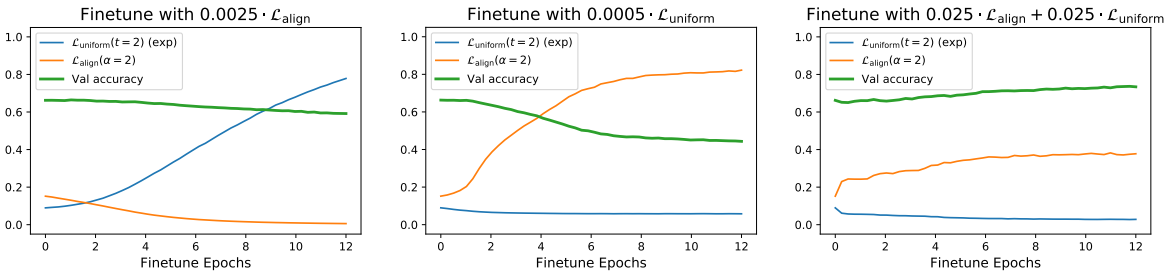

Figure 2-8: Finetuning trajectories from a STL-10 encoder trained with $\mathcal{L}_{\text{contrastive}}$ using a suboptimal temperature $\tau = 2.5$. Finetuning objectives are weighted combinations of $\mathcal{L}_{\text{align}}(\alpha{=}2)$ and $\mathcal{L}_{\text{uniform}}(t{=}2)$. For each intermediate checkpoint, we measure $\mathcal{L}_{\text{align}}$ and $\mathcal{L}_{\text{uniform}}$ metrics, as well as validation accuracy of a linear classifier trained from scratch on the encoder outputs. $\mathcal{L}_{\text{uniform}}$ is exponentiated for plotting purpose. **Left and middle:** Performance degrades if only one of alignment and uniformity is optimized. **Right:** Performance improves when both are optimized.

curve confirms that both properties are indeed necessary for a good encoder. When $\mathcal{L}_{\text{align}}$ is weighted much higher than $\mathcal{L}_{\text{uniform}}$, degenerate solution occurs and all inputs are mapped to the same feature vector ($\exp \mathcal{L}_{\text{uniform}} = 1$). However, as long as the ratio between two weights is not too large (*e.g.*, < 4), we observe that the representation quality remains relatively good and insensitive to the exact weight choices.

$\mathcal{L}_{\text{align}}$ and $\mathcal{L}_{\text{uniform}}$ causally affect downstream task performance. We take an encoder trained with $\mathcal{L}_{\text{contrastive}}$ using a suboptimal temperature $\tau = 2.5$, and finetune it according to $\mathcal{L}_{\text{align}}$ and/or $\mathcal{L}_{\text{uniform}}$. Figure 2-8 visualizes the finetuning trajectories. When only one of alignment and uniformity is optimized, the corresponding metric improves, but both the other metric and performance degrade. However, when both properties are optimized, the representation quality steadily increases. These trends confirm the causal effect of alignment and uniformity on the representation quality, and suggest that directly optimizing them can be a reasonable choice.

Alignment and uniformity also matter in other contrastive representation learning variants. MoCo (He et al., 2019) and Quick-Thought Vectors (Logeswaran and Lee, 2018) are contrastive representation learning variants that have nontrivial differences with directly optimizing $\mathcal{L}_{\text{contrastive}}$ in Equation (2.1). MoCo introduces a memory queue and a momentum encoder. Quick-Thought Vectors uses two different

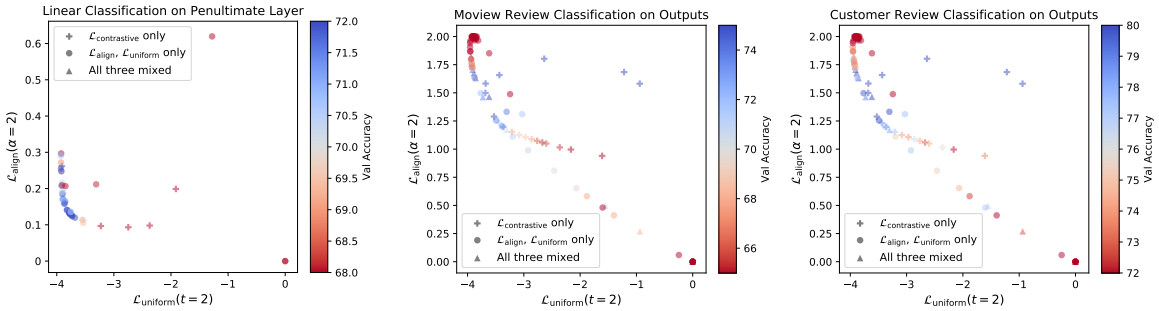

(a) 45 ImageNet-100 encoders are trained with MoCo-based methods, and evaluated with linear classification.

(b) 108 BookCorpus encoders are trained with Quick-Thought-Vectors-based methods, and evaluated with logistic binary classification on Movie Review Sentence Polarity and Customer Product Review Sentiment tasks.

Figure 2-9: Metrics and performance of ImageNet-100 and BookCorpus experiments. Each point represents a trained encoder, with its x- and y-coordinates showing $\mathcal{L}_{\text{align}}$ and $\mathcal{L}_{\text{uniform}}$ metrics and color showing the validation accuracy. **Blue** is better. Encoders with low $\mathcal{L}_{\text{align}}$ and $\mathcal{L}_{\text{uniform}}$ consistently perform well (lower left corners), even though the training methods (based on MoCo and Quick-Thought Vectors) are different from directly optimizing the contrastive loss in Equation (2.1).

encoders to encode each sentence in a positive pair, only normalizes encoder outputs during evaluation, and does not use random sampling to obtain minibatches. After modifying them to also allow $\mathcal{L}_{\text{align}}$ and $\mathcal{L}_{\text{uniform}}$, we train these methods on ImageNet-100 and BookCorpus, respectively. Figure 2-9 shows that $\mathcal{L}_{\text{align}}$ and $\mathcal{L}_{\text{uniform}}$ metrics are still correlated with the downstream task performances. Tables 2.3 and 2.4 show that directly optimizing them also leads to comparable or better representation quality. Table 2.5 also shows improvements on full ImageNet when we use $\mathcal{L}_{\text{align}}$ and $\mathcal{L}_{\text{uniform}}$ to train MoCo v2 (Chen et al., 2020b) (an improved version of MoCo). These results suggest that alignment and uniformity are indeed desirable properties for representations, for *both* image and text modalities, and are likely connected with general contrastive representation learning methods.

2.6 Discussion

Alignment and *uniformity* are often alluded to as motivations for representation learning methods (see Figure 2-1). However, a thorough understanding of these properties is lacking in the literature.

	Loss Formula	Validation Set Accuracy ↑	
		top1	top5
Best $\mathcal{L}_{\text{contrastive}}$ only	$\mathcal{L}_{\text{contrastive}}(\tau{=}0.07)$	72.80%	91.64%
Best $\mathcal{L}_{\text{align}}$ and $\mathcal{L}_{\text{uniform}}$ only	$3 \cdot \mathcal{L}_{\text{align}}(\alpha{=}2) + \mathcal{L}_{\text{uniform}}(t{=}3)$	**74.60%**	**92.74%**
Best among all encoders	$3 \cdot \mathcal{L}_{\text{align}}(\alpha{=}2) + \mathcal{L}_{\text{uniform}}(t{=}3)$	**74.60%**	**92.74%**

Table 2.3: ImageNet-100 encoder evaluations. Numbers show validation set accuracies of linear classifiers trained on encoder penultimate layer activations. The encoders are trained using MoCo-based methods. The best result is picked based on top1 accuracy from a 3-fold training set cross validation, among all 45 encoders trained from scratch with 128-dimensional output and 128 batch size.

	MR Classification		CR Classification	
	Loss Formula	Val. Set Accuracy ↑	Loss Formula	Val. Set Accuracy ↑
Best $\mathcal{L}_{\text{contrastive}}$ only	$\mathcal{L}_{\text{contrastive}}(\tau{=}0.075)$	**77.51%**	$\mathcal{L}_{\text{contrastive}}(\tau{=}0.05)$	**83.86%**
Best $\mathcal{L}_{\text{align}}$ and $\mathcal{L}_{\text{uniform}}$ only	$0.9 \cdot \mathcal{L}_{\text{align}}(\alpha{=}2) + 0.1 \cdot \mathcal{L}_{\text{uniform}}(t{=}5)$	73.76%	$0.9 \cdot \mathcal{L}_{\text{align}}(\alpha{=}2) + 0.1 \cdot \mathcal{L}_{\text{uniform}}(t{=}5)$	80.95%
Best among all encoders	$\mathcal{L}_{\text{contrastive}}(\tau{=}0.075)$	**77.51%**	$\mathcal{L}_{\text{contrastive}}(\tau{=}0.05)$	**83.86%**

Table 2.4: BookCorpus encoder evaluations. Numbers show Movie Review Sentence Polarity (MR) and Customer Product Sentiment (CR) validation set classification accuracies of logistic classifiers fit on encoder outputs. The encoders are trained using Quick-Thought-Vectors-based methods. The best result is picked based on accuracy from a 5-fold training set cross validation, individually for MR and CR, among all 108 encoders trained from scratch with 1200-dimensional output and 400 batch size.

Loss Formula	Validation Set top1 Accuracy ↑
$\mathcal{L}_{\text{contrastive}}(\tau{=}0.2)$ (MoCo v2 Chen et al. (2020b))	$67.5\% \pm 0.1\%$
$3 \cdot \mathcal{L}_{\text{align}}(\alpha{=}2) + \mathcal{L}_{\text{uniform}}(t{=}3)$	**67.69%**

Table 2.5: ImageNet encoder evaluations with MoCo v2, and its variant with $\mathcal{L}_{\text{align}}$ and $\mathcal{L}_{\text{uniform}}$. MoCo v2 results are from the MoCo v2 official implementation (Chen et al., 2020c), with mean and standard deviation across 5 runs. Both settings use 200 epochs of unsupervised training.

Are they in fact related to the representation learning methods? Do they actually agree with the representation quality (measured by downstream task performance)?

In this work, we have presented a detailed investigation on the relation between these properties and the popular paradigm of contrastive representation learning. Through theoretical analysis and extensive experiments, we are able to relate the contrastive loss with the alignment and uniformity properties, and confirm their strong connection with downstream task performances. Remarkably, we have revealed that directly optimizing our proposed metrics often leads to representations of better quality.

Below we summarize several suggestions for future work.

Niceness of the unit hypersphere. Our analysis was based on the empirical observation that representations are often ℓ_2 normalized. Existing works have motivated this choice from a manifold mapping perspective (Liu et al., 2017; Davidson et al., 2018) and computation stability (Xu and Durrett, 2018; Wang et al., 2017). However, to our best knowledge, the question of why the unit hypersphere is a nice feature space is not yet rigorously answered. One possible direction is to formalize the intuition that connected sets with smooth boundaries are nearly linearly separable in the hyperspherical geometry (see Figure 2-2), since linear separability is one of the most widely used criteria for representation quality and is related to the notion of disentanglement (Higgins et al., 2018).

Beyond contrastive learning. Our analysis focused on the relationship between contrastive learning and the alignment and uniformity properties on the unit hypersphere. However, the ubiquitous presence of ℓ_2 normalization in the representation learning literature suggests that the connection may be more general. In fact, several existing empirical methods are directly related to uniformity on the hypersphere (Bojanowski and Joulin, 2017; Davidson et al., 2018; Xu and Durrett, 2018). We believe that relating a broader class of representations to uniformity and/or alignment on the hypersphere will provide novel insights and lead to better empirical algorithms.

Part II

Decision-Making as Representation Learning

Chapter 3

Learning Representations of Quasimetric Distances

Our world is full of asymmetries. Gravity and wind can make reaching a place easier than coming back. Social artifacts such as genealogy charts and citation graphs are inherently directed. In reinforcement learning and control, optimal goal-reaching strategies are rarely reversible (symmetrical). Distance functions supported on these asymmetrical structures are called *quasimetrics*. Despite their common appearance, little research has been done on the learning of quasimetrics.

Our theoretical analysis reveals that a common class of learning algorithms, including unconstrained multilayer perceptrons (MLPs), provably fails to learn a quasimetric consistent with training data. In contrast, our proposed Poisson Quasimetric Embedding (PQE) is the first quasimetric learning formulation that both is learnable with gradient-based optimization and enjoys strong performance guarantees. Experiments on random graphs, social graphs, and offline Q-learning demonstrate its effectiveness over many common baselines.

This chapter is based on published works:

1. *On The Learning and Learnability of Quasimetrics* with co-author Phillip Isola at the International Conference on Learning Representations (ICLR) 2022 (Wang and Isola, 2022b);

2. *Improved Representation of Asymmetrical Distances with Interval Quasimetric Embeddings* with co-author Phillip Isola at the Workshop on Symmetry and Geometry in Neural Representations at NeurIPS 2022 (Wang and Isola, 2022a).

3.1 Introduction

Learned *symmetrical* metrics have been proven useful for innumerable tasks including dimensionality reduction (Tenenbaum et al., 2000), clustering (Xing et al., 2002), classification (Weinberger et al., 2006; Hoffer and Ailon, 2015), and information retrieval (Wang et al., 2014). However, the real world is largely *asymmetrical*, and *symmetrical* metrics can only capture a small fraction of it.

Generalizing metrics, *quasimetrics* (Definition 3.2.1) allow for *asymmetrical* distances and can be found in a wide range of domains (see Figure 3-1). Ubiquitous physical forces, such as gravity and wind, as well as human-defined rules, such as one-way roads, make the traveling time between places a quasimetric. Furthermore, many of our social artifacts are directed graphs— genealogy charts, follow-relation on Twitter (Leskovec and Krevl, 2014), citation graphs (Price, 2011), hyperlinks over the Internet, *etc.* Shortest paths on these graphs naturally induce quasimetric spaces. In fact, we can generalize to Markov Decision Processes (MDPs) and observe that optimal goal-reaching plan costs (*i.e.*, universal value/Q-functions (Schaul et al., 2015; Sutton et al., 2011)) always form a quasimetric (Bertsekas and Tsitsiklis, 1991; Tian et al., 2020a). Moving onto more abstract structures, quasimetrics can also be found as expected hitting times in Markov chains, and as conditional Shannon entropy $H(\cdot \mid \cdot)$ in information theory. (See the appendix for proofs and discussions of these quasimetrics.)

In this work, we study the task of *quasimetric learning*. Given a sampled training set of pairs and their quasimetric distances, we ask: how well can we learn a quasimetric that fits the training data? We define *quasimetric learning* in analogy to metric learning: whereas metric learning is the problem of learning a metric function, quasimetric learning is the problem of learning a quasimetric function. This may involve searching

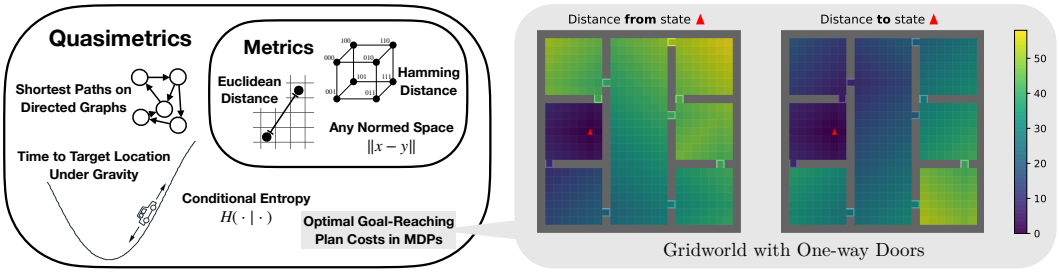

Figure 3-1: Examples of quasimetric spaces. The car drawing is borrowed from Sutton and Barto (2018).

over a hypothesis space constrained to only include quasimetric functions (which is what our method does) or it could involve searching for approximately quasimetric functions (we compare to and analyze such approaches). Successful formulations have many potential applications, such as structural priors in reinforcement learning (Schaul et al., 2015; Tian et al., 2020a), graph learning (Rizi et al., 2018) and causal relation learning (Balashankar and Subramanian, 2021).

Towards this goal, our contributions are

- We study the quasimetric learning task with two goals: (1) fitting training data well and (2) respecting quasimetric constraints (Section 3.3);

- We prove that a large family of algorithms, including unconstrained networks trained in the Neural Tangent Kernel (NTK) regime (Jacot et al., 2018), fail at this task, while a learned embedding into a latent quasimetric space can potentially succeed (Section 3.4);

- We propose Poisson Quasimetric Embeddings (PQEs), the first quasimetric embedding formulation learnable with gradient-based optimization that also enjoys strong theoretical guarantees on approximating arbitrary quasimetrics (Section 3.5);

- Our experiments complement the theory and demonstrate the benefits of PQEs on random graphs, social graphs and offline Q-learning (Section 3.5.5).

3.2 Preliminaries on Quasimetrics and Poisson Processes

Quasimetric space is a generalization of metric space where all requirements of metrics are satisfied, except that the distances can be asymmetrical.

Definition 3.2.1 (Quasimetric Space)**.** A *quasimetric space* is a pair $(\mathcal{X}, d)$, where $\mathcal{X}$ is a set of points and $d\colon \mathcal{X} \times \mathcal{X} \to [0, \infty]$ is the quasimetric, satisfying the following conditions:

$$\forall x, y \in \mathcal{X}, \qquad x = y \iff d(x, y) = 0, \quad \text{(Identity of Indiscernibles)}$$
$$\forall x, y, z \in \mathcal{X}, \qquad d(x, y) + d(y, z) \geq d(x, z). \qquad \text{(Triangle Inequality)}$$

Being asymmetric, quasimetrics are often thought of as (shortest-path) distances of some (possibly infinite) weighted directed graph. A natural way to quantify the complexity of a quasimetric is to consider that of its underlying graph. *Quasimetric treewidth* is an instantiation of this idea.

Definition 3.2.2 (Treewidth of Quasimetric Spaces (Mémoli et al., 2018))**.** Consider a quasimetric space M as shortest-path distances on a positively-weighted directed graph. *Treewidth* of M is the minimum over all such graphs' treewidths.

Poisson processes are commonly used to model events (or points) randomly occurring across a set A (Kingman, 2005) , *e.g.*, raindrops hitting a windshield, photons captured by a camera. The number of such events within a subset of A is modeled as a Poisson distribution, whose mean is given by a measure μ of A that determines how "frequently the events happen at each location".

Definition 3.2.3 (Poisson Process)**.** For nonatomic measure μ on set A, a *Poisson process* on A with *mean measure* μ is a random countable subset $P \subset A$ (*i.e.*, the random events / points) such that

- for any disjoint measurable subsets $A_1, \ldots, A_n$ of A, the random variables $N(A_1), \ldots, N(A_n)$ are independent, where $N(B) \triangleq \#\{P \cap B\}$ is the number

of points of P in B, and

- $N(B)$ has the Poisson distribution with mean $\mu(B)$, denoted as $\mathrm{Pois}(\mu(B))$.

Fact 3.2.4 (Differentiability of $\mathbb{P}[N(A_1) \le N(A_2)]$)**.** For two measurable subsets A_1, A_2,

$$\mathbb{P}[N(A_1) \le N(A_2)] = \mathbb{P}\big[\underbrace{\mathrm{Pois}(\mu(A_1 \setminus A_2)) \le \mathrm{Pois}(\mu(A_2 \setminus A_1))}_{\text{two } \textit{independent} \text{ Poissons}}\big]. \tag{3.1}$$

Furthermore, for independent $X \sim \mathrm{Pois}(\mu_1)$, $Y \sim \mathrm{Pois}(\mu_2)$, the probability $\mathbb{P}[X \le Y]$ is *differentiable w.r.t.* μ_1 *and* μ_2. In the special case where μ_1 or μ_2 is zero, we can simply compute

$$\begin{aligned}\mathbb{P}[X \le Y] &= \begin{cases} \mathbb{P}[0 \le Y] = 1 & \text{if } \mu_1 = 0 \\ \mathbb{P}[X \le 0] = \mathbb{P}[X = 0] = e^{-\mu_1} & \text{if } \mu_2 = 0 \end{cases} \qquad \text{(Pois(0) is always 0)} \\ &= \exp\left(-(\mu_1 - \mu_2)^+\right), \end{aligned} \tag{3.2}$$

where $x^+ \triangleq \max(0, x)$. For general μ_1, μ_2, this probability and its gradients can be obtained via a connection to noncentral χ^2 distribution (Johnson, 1959). We derive the formulas in the appendix.

Therefore, if A_1 and A_2 are parametrized by some θ such that $\mu(A_1 \setminus A_2)$ and $\mu(A_2 \setminus A_1)$ are differentiable w.r.t. θ, so is $\mathbb{P}[N(A_1) \le N(A_2)]$.

3.3 Quasimetric Learning

Consider a quasimetric space $(\mathcal{X}, d)$. The *quasimetric learning* task aims to infer a quasimetric from observing a training set $\{(x_i, y_i, d(x_i, y_i))\}_i \subset \mathcal{X} \times \mathcal{X} \times [0, \infty]$. Naturally, our goals for a learned predictor $\hat{d}\colon \mathcal{X} \times \mathcal{X} \to \mathbb{R}$ are: respecting the quasimetric constraints and fitting training distances.

Crucially, we are not simply aiming for the usual sense of *generalization*, *i.e.*, low population error. Knowing that true distances have a quasimetric structure, we can better evaluate predictors and desire ones that fit the training data and are

(approximately) quasimetrics. These objectives also indirectly capture generalization because a predictor failing either requirement must have large error on some pairs, whose true distances follow quasimetric constraints. We formalize this relation in Theorem 3.4.3.

3.3.1 Learning Algorithms and Hypothesis Spaces

Ideally, quasimetric learning should scale well with data, potentially generalize to unseen samples, and support integration with other deep learning systems (*e.g.*, via differentiation).

Relaxed hypothesis spaces. One can simply learn a generic function approximator that maps the (concatenated) input pair to a scalar as the prediction of the pair's distance, or its transformed version (*e.g.*, log distance). This approach has been adopted in learning graph distances (Rizi et al., 2018) and plan costs in MDPs (Tian et al., 2020a). When the function approximator is a deep neural network, we refer to such methods as *unconstrained networks*. While they are known to fit training data well (Jacot et al., 2018), in this paper we also investigate whether they learn to be (approximately) quasimetrics.

Restricted hypothesis spaces. Alternatively, we can encode each input to a latent space $\mathcal{Z}$, where a latent quasimetric d_z gives the distance prediction. This guarantees learning a quasimetric over data space $\mathcal{X}$. Often d_z is restricted to a subset unable to approximate all quasimetrics, *i.e.*, an **overly restricted hypothesis space**, such as metric embeddings and the recently proposed DeepNorm and WideNorm (Pitis et al., 2020). While our proposed Poisson Quasimetric Embedding (PQE) (specified in Section 3.5) is also a latent quasimetric, it can approximate arbitrary quasimetrics (and is differentiable). PQE thus searches in **a space that approximates all quasimetrics and only quasimetrics**.

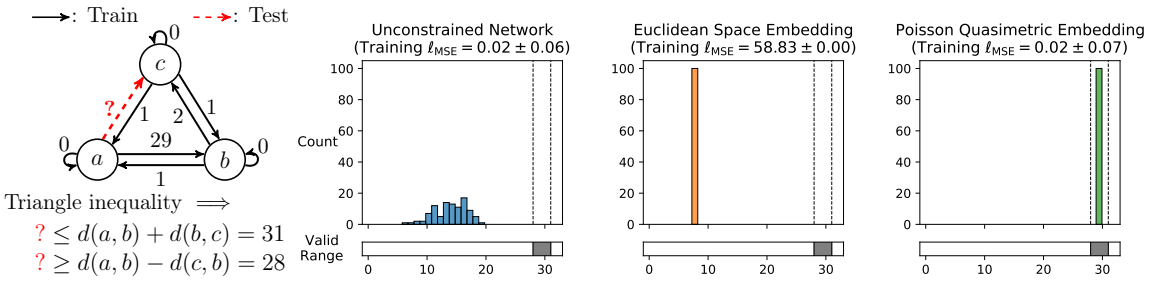

Figure 3-2: Quasimetric learning on a 3-element space. **Leftmost:** Training set contains all pairs except for (a, c). Arrow labels show quasimetric distances (rather than edge weights). A quasimetric $\hat{d}$ should predict $\hat{d}(a, c) \in [28, 30]$. **Right three:** Different formulations are trained to fit training pairs distances, and then predict on the test pair. Plots show distribution of the prediction over 100 runs.

3.3.2 A Toy Example

To build up intuition on how various algorithms perform according to our two goals, we consider a toy quasimetric space with only 3 elements in Figure 3-2. The space has a total of 9 pairs, 8 of which form the training set. Due to quasimetric requirements (*esp.* triangle inequality), knowing distances of these 8 pairs restricts valid values for the heldout pair to a particular range (which is $[28, 31]$ in this case). If a model approximates 8 training pairs well *and* respects quasimetric constraints well, its prediction on that heldout pair should fall into this range.

We train three models w.r.t. mean squared error (MSE) over the training set using gradient descent:

- Unconstrained deep network that predicts distance,
- Metric embedding into a latent Euclidean space with a deep encoder,
- Quasimetric embedding into a latent PQE space with a deep encoder (our method from Section 3.5).

The three approaches exhibit interesting qualitative differences. Euclidean embedding, unable to model asymmetries in training data, fails to attain a low training error. While both other methods approximate training distances well, unconstrained networks greatly violate quasimetric constraints; only PQEs respect the constraints and consistently predicts within the valid range.

Here, the structural prior of embedding into a quasimetric latent space appears

important to successful learning. Without any such prior, unconstrained networks fail badly. In the next section, we present a rigorous theoretical study of the quasimetric learning task, which confirms this intuition.

3.4 Theoretical Analysis of Various Learning Algorithms

In this section, we define concrete metrics for the two quasimetric learning objectives stated above, and present positive and negative theoretical findings for various learning algorithms.

Overview. Our analysis focuses on data-agnostic bounds, which are of great interests in machine learning (*e.g.*, VC-dimension (Vapnik and Chervonenkis, 2015)). We prove a strong negative result for a general family of learning algorithms (including unconstrained MLPs trained in NTK regime, k-nearest neighbor, and min-norm linear regression): they may arbitrarily badly fail to fit training data or respect quasimetric constraints (Theorem 3.4.6). Our informative construction reveals the core reason of their failure. Quasimetric embeddings, however, enjoy nice properties as long as they can approximate arbitrary quasimetrics, which motivates searching for "universal quasimetrics". The next section presents PQEs as such universal approximators and states their theoretical guarantees.

Assumptions. We consider quasimetric spaces $(\mathcal{X}, d)$ with $\mathcal{X} \subset \mathbb{R}^d$, finite size $n = |X| < \infty$, and finite distances (*i.e.*, d has range $[0, \infty)$). It allows discussing deep networks which can't handle infinities well. This mild assumption can be satisfied by simply capping max distances in quasimetrics. For training, $m < n^2$ pairs are uniformly sampled as training pairs $S \subset \mathcal{X} \times \mathcal{X}$ without replacement.

In the appendix, we provide all full proofs, further discussions of our assumptions and presented results, as well as additional results concerning specific learning algorithms and settings.

3.4.1 Distortion and Violation Metrics for Quasimetric Learning

We use *distortion* as a measure of how well the distance is preserved, as is standard in embedding analyses (*e.g.*, Bourgain (1985)). In this work, we especially consider *distortion over a subset of pairs*, to quantify how well a predictor $\hat{d}$ approximates distances over the training subset S.

Definition 3.4.1 (Distortion)**.** Distortion of $\hat{d}$ over a subset of pairs $S \subset \mathcal{X} \times \mathcal{X}$ is $\mathsf{dis}_S(\hat{d}) \triangleq \left(\max_{(x,y)\in S, x\neq y} \frac{\hat{d}(x,y)}{d(x,y)}\right)\left(\max_{(x,y)\in S, x\neq y} \frac{d(x,y)}{\hat{d}(x,y)}\right)$, and its overall distortion is $\mathsf{dis}(\hat{d}) \triangleq \mathsf{dis}_{\mathcal{X}\times\mathcal{X}}(\hat{d})$.

For measuring consistency w.r.t. quasimetric constraints, we define the *(quasimetric) violation* metric. Violation focuses on *triangle inequality*, which can often be more complex (*e.g.*, in Figure 3-2), compared to the relatively simple *non-negativity* and *Identity of Indiscernibles*.

Definition 3.4.2 (Quasimetric Violation)**.** *Quasimetric violation* (*violation* for short) of $\hat{d}$ is $\mathsf{vio}(\hat{d}) \triangleq \max_{A_1,A_2,A_3\in\mathcal{X}} \frac{\hat{d}(A_1,A_3)}{\hat{d}(A_1,A_2)+\hat{d}(A_2,A_3)}$, where we define $\frac{0}{0} = 1$ for notation simplicity.

Both distortion and violation are nicely agnostic to scaling. Furthermore, assuming *non-negativity* and *Identity of Indiscernibles*, $\mathsf{vio}(\hat{d}) \geq 1$ always, with equality iff $\hat{d}$ is a quasimetric.

Distortion and violation also capture generalization. Because the true distance d has optimal training distortion (on S) and violation, a predictor $\hat{d}$ that does badly on either must also be far from truth.

Theorem 3.4.3 (Distortion and Violation Lower-Bound Generalization Error). For non-negative $\hat{d}$, $\mathsf{dis}(\hat{d}) \geq \max(\mathsf{dis}_S(\hat{d}), \sqrt{\mathsf{vio}(\hat{d})})$, where $\mathsf{dis}(\hat{d})$ captures generalization over the entire $\mathcal{X}$ space.

3.4.2 Learning Algorithms Equivariant to Orthogonal Transforms

For quasimetric space $(\mathcal{X}, d)$, $\mathcal{X} \subset \mathbb{R}^d$, we consider applying general learning algorithms by concatenating pairs to form inputs $\in \mathbb{R}^{2d}$ (*e.g.*, unconstrained networks). While straightforward, this approach means that algorithms are generally *unable to relate the same element appearing as 1st or 2nd input.* As we will show, this is sufficient for a wide family of learning algorithms to fail badly– ones **equivariant to orthogonal transforms** (OrthEquiv algorithms; Definition 3.4.4).

For an OrthEquiv algorithm, training on orthogonally transformed data does not affect its prediction, as long as test data is identically transformed. In fact, many standard learning algorithms are OrthEquiv, including unconstrained MLP trained in NTK regime (Lemma 3.4.5).

Definition 3.4.4 (Equivariant Learning Algorithms)**.** Given training set $\mathcal{D} = \{(z_i, y_i)\}_i$, where $z_i \in \mathcal{Z}$ are inputs and $y_i \in \mathcal{Y}$ are targets, a learning algorithm Alg produces a function $\mathsf{Alg}(\mathcal{D})\colon \mathcal{Z} \to Y$ such that $\mathsf{Alg}(\mathcal{D})(z')$ is the function's prediction on sample z'. Consider $\mathcal{T}$ a set of transformations $\mathcal{Z} \to \mathcal{Z}$. Alg is equivariant to $\mathcal{T}$ iff for all transform $T \in \mathcal{T}$, training set $\mathcal{D}$, $\mathsf{Alg}(\mathcal{D}) = \mathsf{Alg}(T\mathcal{D}) \circ T$, where $T\mathcal{D} = \{(Tz, y)\colon (z, y) \in \mathcal{D}\}$ is the training set with transformed inputs.

Lemma 3.4.5 (Examples of OrthEquiv Algorithms). k-nearest-neighbor with Euclidean distance, dot-product kernel ridge regression (including min-norm linear regression and MLP trained with squared loss in NTK regime) are OrthEquiv.

Failure case. These algorithms treat the concatenated inputs as generic vectors. If a transform fundamentally changes the quasimetric structure but is not fully reflected in the learned function (*e.g.*, due to equivariance), learning must fail. The two training sets in Figure 3-3 are sampled from two different quasimetrics over the same 6 elements An orthogonal transform links both training sets *without affecting the test pair*, which is constrained differently in two quasimetrics. An OrthEquiv algorithm, necessarily predicting the test pair identically seeing either training set, must thus fail on one. In

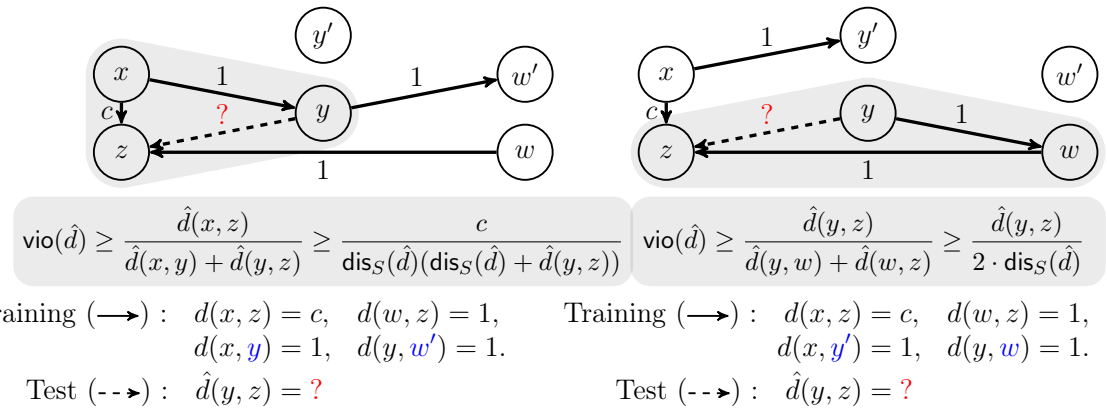

Figure 3-3: Two training sets pose incompatible constraints ( ) for the test pair distance $d(y,z)$. With one-hot features, an orthogonal transform can exchange $(*,y) \leftrightarrow (*,y')$ and $(*,w) \leftrightarrow (*,w')$, leaving the test pair (y,z) unchanged, but transforming the training set from one scenario to the other. Given either set, an OrthEquiv algorithm must attain same training distortion and predict identically on (y,z). For appropriate c, this implies large distortion (not fitting training set) or violation (not approximately a quasimetric) in one of these cases.

the appendix, we empirically verify that unconstrained MLPs indeed *do fail* on this construction.

Extending to larger quasimetric spaces, we consider graphs containing many copies of *both* patterns in Figure 3-3. With high probability, our sampled training set fails in the same way—the learning algorithm can not distinguish it from another training set with different quasimetric constraints.

Theorem 3.4.6 (Failure of OrthEquiv Algorithms). Let $(f_n)_n$ be an *arbitrary* sequence of large values. There is an infinite sequence of quasimetric spaces $((\mathcal{X}_n, d_n))_n$ with $|\mathcal{X}_n| = n$, $\mathcal{X}_n \subset \mathbb{R}^n$ such that, over a random training set S of size m, any OrthEquiv algorithm outputs a predictor $\hat{d}$ that

- $\hat{d}$ fails *non-negativity*, or
- $\max(\mathsf{dis}_S(\hat{d}), \mathsf{vio}(\hat{d})) \geq f_n$ (*i.e.*, $\hat{d}$ approximates training S badly or is far from a quasimetric),

with probability $1/2 - o(1)$, as long as S does not contain almost all of the pairs $1 - m/n^2 = \omega(n^{-1/3})$, and does not only include few pairs $m/n^2 = \omega(n^{-1/2})$.

Furthermore, standard NTK results show that unconstrained MLPs trained in NTK regime converge to a function with zero training loss. By the above theorem, the limiting function is not a quasimetric with nontrivial probability. In the appendix,

we formally state this result. Despite their empirical usages, these results suggest that unconstrained networks are likely not suited for quasimetric learning.

3.4.3 Quasimetric Embeddings

A quasimetric embedding consists of a mapping f from data space $\mathcal{X}$ to a latent quasimetric space $(\mathcal{Z}, d_z)$, and predicts $\hat{d}(x, y) \triangleq d_z(f(x), f(y))$. Therefore, they always respect all quasimetric constraints and attain optimal violation of value 1, *regardless of training data*.

However, unlike deep networks, their distortion (approximation) properties depend on the specific latent quasimetrics. If the latent quasimetric is not overly restrictive and can approximate *any* quasimetric (with flexible learned encoders), we have nice guarantees for both distortion and violation.

In the section below, we present Poisson Quasimetric Embedding (PQE) as such a latent quasimetric, along with its theoretical distortion and violation guarantees.

3.5 Poisson Quasimetric Embeddings (PQEs)

Motivated by above theoretical findings, we aim to find a latent quasimetric space $(\mathbb{R}^d, d_z)$ with a deep network encoder $f\colon \mathcal{X} \to \mathbb{R}^d$, and a quasimetric d_z that is both *universal* and *differentiable*:

- (universality) for any data quasimetric $(\mathcal{X}, d)$, there exists an encoder f such that $d_z(f(x), f(y)) \approx d(x, y)$;
- (differentiability) d_z is differentiable (for optimizing f and possible integration with other gradient-based systems).

Notation 3.5.1. We use x, y for elements of the data space $\mathcal{X}$, u, v for elements of the latent space $\mathbb{R}^d$, upper-case letters for random variables, and $(\cdot)_z$ for indicating functions in latent space (*e.g.*, d_z).

An existing line of machine learning research learns *quasipartitions*, or *partial orders*, via Order Embeddings (Vendrov et al., 2015). Quasipartitions are in fact

special cases of quasimetrics whose distances are restricted to be binary, denoted as π. An Order Embedding is a representation of a quasipartition, where $\pi^{\mathsf{OE}}(x, y) = 0$ (*i.e.*, x is related to y) iff $f(x) \leq f(y)$ coordinate-wise:

$$\pi^{\mathsf{OE}}(x, y) \triangleq \pi_z^{\mathsf{OE}}(f(x), f(y)) \triangleq 1 - \prod_j \mathbf{1}_{f(x)_j - f(y)_j \leq 0}. \tag{3.3}$$

Order Embedding is *universal* and can model *any quasipartition* (see appendix and Hiraguchi (1951)).

Can we extend this discrete idea to general continuous quasimetrics? Quite naïvely, one may attempt a straightforward soft modification of Order Embedding:

$$\pi_z^{\mathsf{SoftOE}}(u, v) \triangleq 1 - \prod_j \exp\big(-(u_j - v_j)^+\big) = 1 - \exp\Big(-\sum_j (u_j - v_j)^+\Big), \tag{3.4}$$

which equals 0 if $u \leq v$ coordinate-wise, and increases to 1 as some coordinates violate this condition more. However, it is unclear whether this gives a quasimetric.

A more principled way is to parametrize a (scaled) *distribution of latent quasipartitions* Π_z, whose expectation naturally gives a continuous-valued quasimetric:

$$d_z(u, v; \Pi_z, \alpha) \triangleq \alpha \cdot \mathbb{E}_{\pi_z \sim \Pi_z}\left[\pi_z(u, v)\right], \qquad \alpha \geq 0. \tag{3.5}$$

Poisson Quasimetric Embedding (PQE) gives a general recipe for constructing such Π_z distributions so that d_z is *universal* and *differentiable*. Within this framework, we will see that π_z^{SoftOE} is actually a quasimetric based on such a distribution and is (almost) sufficient for our needs.

3.5.1 Distributions of Latent Quasipartitions

A random latent quasipartition $\pi_z \colon \mathbb{R}^d \times \mathbb{R}^d \to \{0, 1\}$ is a difficult object to model, due to complicated quasipartition constraints. Fortunately, the Order Embedding representation (Equation (3.3)) is without such constraints. If, instead of fixed latents

u, v, we have *random latents* $R(u), R(v)$, we can compute:

$$\mathbb{E}_{\pi_z}\left[\pi_z(u,v)\right] = \mathbb{E}_{R(u),R(v)}\left[\pi_z^{\mathsf{OE}}(R(u),R(v))\right] = 1 - \mathbb{P}\left[R(u) \leq R(v) \text{ coordinate-wise}\right]. \tag{3.6}$$

In this view, we represent a random π_z via a joint distribution of random vectors[1] $\{R(u)\}_{u\in\mathbb{R}^d}$, *i.e.*, a *stochastic process*. To easily compute the probability of this coordinate-wise event, we assume that each dimension of random vectors is from an independent process, and obtain

$$\mathbb{E}_{\pi_z}\left[\pi_z(u,v)\right] = 1 - \prod_j \mathbb{P}\left[R_j(u) \leq R_j(v)\right]. \tag{3.7}$$

The choice of stochastic process is flexible. Using *Poisson processes* (with Lebesgue mean measure; Definition 3.2.3) that count random points on half-lines[2] $(-\infty, a]$, we can have $R_j(u) = N_j((\infty, u_j])$, the (random) count of events in $(\infty, u_j]$ from j-th Poisson process:

$$\mathbb{E}_{\pi_z\sim\Pi_z}\left[\pi_z(u,v)\right] = 1 - \prod_j \mathbb{P}\big[N_j((-\infty,u_j]) \leq N_j((-\infty,v_j])\big] \tag{3.8}$$

$$= 1 - \prod_j \exp\big(-(u_j - v_j)^+\big) = \pi_z^{\mathsf{SoftOE}}(u,v), \tag{3.9}$$

where we used Fact 3.2.4 and the observation that one half-line is either subset or superset of another. Indeed, π_z^{SoftOE} is an expected quasipartition (and thus a quasimetric), and is *differentiable*.

Considering a mixture of such distributions for expressiveness, the full latent quasimetric formula is

$$d_z^{\mathsf{PQE\text{-}LH}}(u,v;\alpha) \triangleq \sum_i \alpha_i \cdot \Big(1 - \exp\big(-\sum_j (u_{i,j} - v_{i,j})^+\big)\Big), \tag{3.10}$$

[1] In general, these random vectors $R(u)$ do not have to be of the same dimension as $u \in \mathbb{R}^d$, although the dimensions do match in the PQE variants we experiment with.

[2] Half-lines has Lebesgue measure ∞. More rigorously, consider using a small value as the lower bounds of these intervals, which leads to same result.

where we slightly abuse notation and consider latents u and v as (reshaped to) 2-dimensional. We will see that this is a special PQE case with **L**ebesgue measure and **h**alf-lines, and thus denoted PQE-LH.

3.5.2 General PQE Formulation

We can easily generalize the above idea to independent Poisson processes of general mean measures μ_j and (sub)set parametrizations $u \to A_j(u)$, and obtain an expected quasipartition as:

$$\begin{aligned}
&\mathbb{E}_{\pi_z \sim \Pi_z^{\mathsf{PQE}}(\mu, A)}[\pi_z(u, v)] && (3.11)\\
\triangleq &1 - \prod_j \mathbb{P}\left[N_j(A_j(u)) \leq N_j(A_j(v))\right] && (3.12)\\
= &1 - \prod_j \mathbb{P}\Big[\mathrm{Pois}(\underbrace{\mu_j(A_j(u) \setminus A_j(v))}_{\text{Poisson rate of points landing only in } A_j(u)}) \leq \mathrm{Pois}(\mu_j(A_j(v) \setminus A_j(u)))\Big], && (3.13)
\end{aligned}$$

which is *differentiable* as long as the measures and set parametrizations are (after set differences). Similarly, considering a mixture gives us an expressive latent quasimetric.

A general PQE latent quasimetric is defined with $\{(\mu_{i,j}, A_{i,j})\}_{i,j}$ and weights $\alpha_i \geq 0$ as:

$$\begin{aligned}
&d_z^{\mathsf{PQE}}(u, v; \mu, A, \alpha)\\
\triangleq &\sum_i \alpha_i \cdot \mathbb{E}_{\pi_z \sim \Pi_z^{\mathsf{PQE}}(\mu_i, A_i)}\left[\pi_z(u, v)\right] && (3.14)\\
= &\sum_i \alpha_i \Big(1 - \prod_j \mathbb{P}\Big[\mathrm{Pois}(\mu_{i,j}(A_{i,j}(u) \setminus A_{i,j}(v))) \leq \mathrm{Pois}(\mu_{i,j}(A_{i,j}(v) \setminus A_{i,j}(u)))\Big]\Big),
\end{aligned}$$

whose optimizable parameters include $\{\alpha_i\}_i$, possible ones from $\{(\mu_{i,j}, A_{i,j})\}_{i,j}$ (and encoder f).

This general recipe can be instantiated in many ways. Setting $A_{i,j}(u) \to (-\infty, u_{i,j}]$ and Lebesgue $\mu_{i,j}$, recovers PQE-LH. In Appendix B.3.2, we consider a form with **G**aussian-based measures and **G**aussian-shapes, denoted as PQE-GG. Unlike PQE-LH, PQE-GG always gives nonzero gradients.

Implementation Techniques for PQEs In Appendix B.3.4, we discuss several implementation techniques that empirically improve stability, including learning α_i's with deep linear networks, a formulation that outputs discounted distance, *etc.* These techniques are also implemented in our GitHub repository: https://github.com/quasimetric-learning/torch-quasimetric.

3.5.3 Continuous-valued Stochastic Processes

But why Poisson processes over more common choices such as Gaussian processes? It turns out that common continuous-value processes fail to give a *differentiable* formula.

Consider a non-degenerate process $\{R(u)\}_u$, where $(R(u), R(v))$ has bounded density if $u \neq v$. Perturbing $u \to u + \delta$ leaves $\mathbb{P}\left[R(u) = R(u+\delta)\right] = 0$. Then one of $\mathbb{P}\big[R(u) \leq R(u+\delta)\big]$ and $\mathbb{P}\big[R(u+\delta) \leq R(u)\big]$ must be far away from 1 (as they sum to 1), breaking differentiability at $\mathbb{P}\left[R(u) \leq R(u)\right] = 1$. (This argument is formalized in the appendix.) Discrete-valued processes, however, can leave most probability mass on $R(u) = R(u+\delta)$ and thus remain differentiable.

3.5.4 Theoretical Guarantees

Our PQEs bear similarity with the algorithmic quasimetric embedding construction in Mémoli et al. (2018). Extending their analysis to PQEs, we obtain the following distortion and violation guarantees.

Theorem 3.5.2 (Distortion and violation of PQEs). Under the assumptions of Section 3.4, *any* quasimetric space with size n and treewidth t admits a PQE-LH and a PQE-GG with distortion $\mathcal{O}(t \log^2 n)$ and violation 1, with an expressive encoder (*e.g.*, a ReLU network with ≥ 3 layers and polynomial width).

In fact, these guarantees apply to any PQE formulation that satisfies a mild condition. Informally, any PQE with $h \times k$ Poisson processes (*i.e.*, h mixtures) enjoys the above guarantees if it can approximate the discrete counterpart: mixtures of h Order Embeddings, each specified with k dimensions. In the appendix, we make this

condition precise and provide a full proof of the above theorem.

3.5.5 Experiments

Our experiments are designed to (1) confirm our theoretical findings and (2) compare PQEs against a wider range of baselines, across different types of tasks. In all experiments, we optimize γ-discounted distances (with $\gamma \in \{0.9, 0.95\}$), and compare the following five families of methods:

- **PQEs (2 formulations):** PQE-LH and PQE-GG with techniques mentioned in Section 3.5.2.
- **Unconstrained networks (20 formulations):** Predict raw distance (directly, with exp transform, and with $(\cdot)^2$ transform) or γ-discounted distance (directly, and with a sigmoid-transform). Each variant is run with a possible triangle inequality regularizer $\mathbb{E}_{x,y,z}\big[\max(0, \gamma^{\hat{d}(x,y)+\hat{d}(y,z)} - \gamma^{\hat{d}(x,z)})^2\big]$ for each of 4 weights $\in \{0, 0.3, 1, 3\}$.
- **Asymmetrical dot products (20 formulations):** On input pair (x, y), encode each into a feature vector with a *different* network, and take the dot product. Identical to unconstrained networks, the output is used in the same 5 ways, with the same 4 triangle inequality regularizer options.
- **Metric encoders (4 formulations):** Embed into Euclidean space, ℓ_1 space, hypersphere with (scaled) spherical distance, or a mixture of all three.
- **DeepNorm (2 formulations) and WideNorm (3 formulations):** Quasimetric embedding methods that often require significantly more parameters than PQEs (often on the order of $10^6 \sim 10^7$ more effective parameters; see the appendix for detailed comparisons) but can only approximate a subset of all possible quasimetrics (Pitis et al., 2020).

We show average results from 5 runs. The appendix provides experimental details, full results (including standard deviations), additional experiments, and ablation studies.

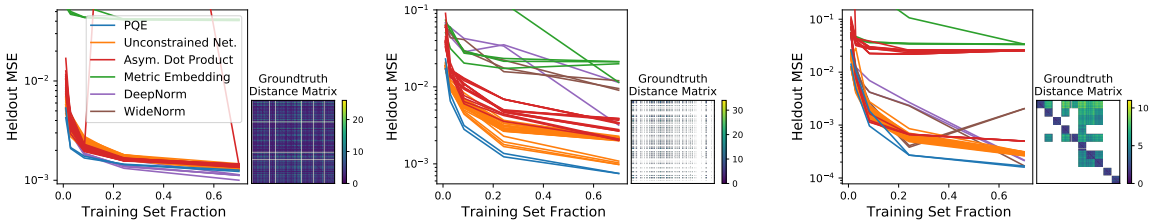

(a) A dense graph. (b) A sparse graph. (c) A sparse graph with block structure.

Figure 3-4: Comparison of PQE and baselines on quasimetric learning in random directed graphs.

Random directed graphs. We start with randomly generated directed graphs of 300 nodes, with 64-dimensional node features given by randomly initialized neural networks. After training with MSE on discounted distances, we test the models' prediction error on the unseen pairs (*i.e.*, generalization), measured also by MSE on discounted distances. On three graphs with distinct structures, PQEs significantly outperform baselines across almost all training set sizes (see Figure 3-4). Notably, while DeepNorm and WideNorm do well on the dense graph quasimetric, they struggle on the other two, attaining both high test MSE (Figure 3-4) and train MSE (not shown). This is consistent with the fact that they can only approximate a subset of all quasimetrics, while PQEs can approximate all quasimetrics.

Large-scale social graph. We choose the Berkeley-Stanford Web Graph (Leskovec and Krevl, 2014) as the real-wold social graph for evaluation. This graph consists of 685,230 pages as nodes, and 7,600,595 hyperlinks as directed edges. We use 128-dimensional node2vec features (Grover and Leskovec, 2016) and the landmark method (Rizi et al., 2018) to construct a training set of 2,500,000 pairs, and a test set of 150,000 pairs. PQEs generally perform better than other methods, accurately predicting finite distances while predicting high values for infinite distances (see Table 3.1). DeepNorms and WideNorms learn finite distances less accurately here, and also do much worse than PQEs on learning the (quasi)metric of an *undirected* social graph (shown in the appendix).

	Triangle inequality regularizer	MSE w.r.t. γ-discounted distances ($\times 10^{-3}$) $\downarrow$	L1 Error when true $d < \infty \downarrow$	Prediction $\hat{d}$ when true $d = \infty \uparrow$
PQE-LH	✗	3.043	1.626	69.942
PQE-GG	✗	3.909	1.895	101.824
Best Unconstrained Net.	✗	3.086	2.115	59.524
	✓	2.813	2.211	61.371
Best Asym. Dot Product	✗	48.106	2.520×10^{11}	2.679×10^{11}
	✓	48.102	2.299×10^{11}	2.500×10^{11}
Best Metric Embedding	✗	17.595	7.540	53.850
Best DeepNorm	✗	5.071	2.085	120.045
Best WideNorm	✗	3.533	1.769	124.658

Table 3.1: Quasimetric learning on large-scale web graph. "Best" is selected by *test* MSE w.r.t. γ-discounted distances.

Offline Q-learning. Optimal goal-reaching plan costs in MDPs are quasimetrics (Bertsekas and Tsitsiklis, 1991; Tian et al., 2020a) (see also the appendix). In practice, optimizing deep Q-functions often suffers from stability and sample efficiency issues (Henderson et al., 2018; Fujimoto et al., 2018). As a proof of concept, we use PQEs as goal-conditional Q-functions in offline Q-learning, on the grid-world environment with one-way doors built upon `gym-minigrid` (Chevalier-Boisvert et al., 2018) (see Figure 3-1 right), following the algorithm and data sampling procedure described in Tian et al. (2020a). Adding strong quasimetric structures greatly improves sample efficiency and greedy planning success rates over popular existing approaches such as unconstrained networks used in Tian et al. (2020a) and asymmetrical dot products used in Schaul et al. (2015) (see Figure 3-5). As an interesting observation, some metric embedding formulations work comparably well.

3.6 Interval Quasimetric Embeddings (IQEs)

In this section, we further improve PQEs by introducing Interval Quasimetric Embeddings (IQEs). IQEs enjoy all nice theoretical properties of PQEs, but also drastically reduces parameter counts and satisfy latent positive homogeneity for easier optimization.

The main issue with PQE is that its components are bounded in $[0, 1)$ and suffer

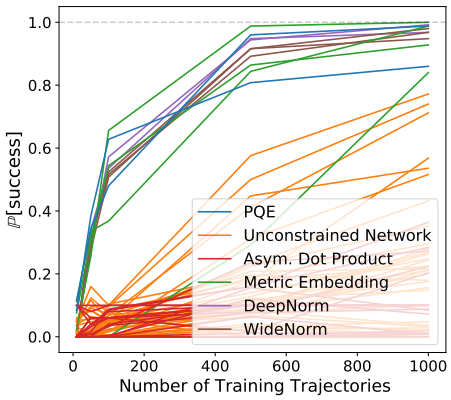

Figure 3-5: Offline Q-learning results with PQE and baseline architectures as Q-function parametrizations.

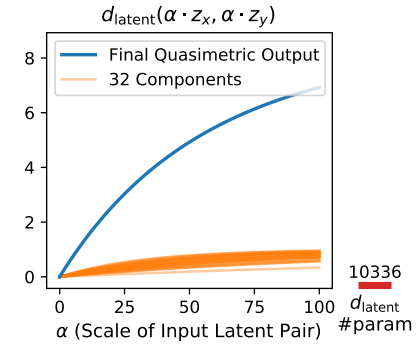

(a) Poisson Quasimetric Embedding.

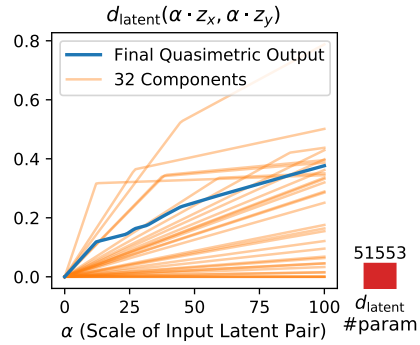

(b) Deep Norm (Pitis et al., 2020).

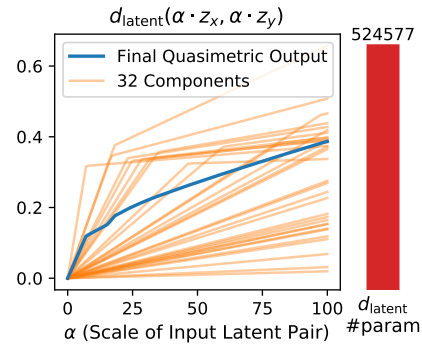

(c) Wide Norm (Pitis et al., 2020).

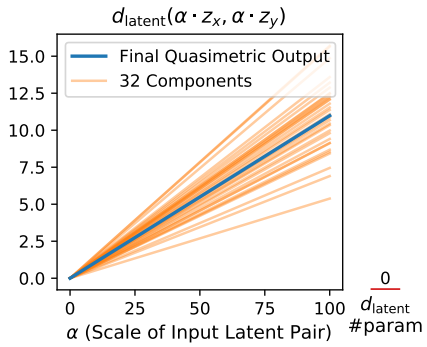

(d) Interval Quasimetric Embedding.

Figure 3-6: Different latent quasimetrics d_{latent}. Plots show how predicted distances (and components forming them) change as two latent vectors move apart. Red bars show the number of trainable parameters in d_{latent}. (a) PQE suffers from diminishing gradients. (b,c) Deep Norm and Wide Norm require expensive latent quasimetric head, and have complex relations between latents and predictions (due to its learned concave transformations). (d) IQE uses a simple head and does not suffer from gradient optimization issues. (a-d) Plots are computed at random initializations, with Deep Norm and Wide concave transformation parameters scaled to emphasize the non-linearity.

from diminishing gradients (Figure 3-6a). Special reparametrization tricks are necessary for successful optimization Section 3.5. We propose Interval Quasimetric Embeddings (IQE) to directly address this drawback. Appendix B.5 derives IQE via a modified PQE framework.

IQE is a new encoder-based quasimetric model, where a (learned) encoder maps data into some latent space, where our latent IQE quasimetric d_{IQE} outputs a quasimetric distance between two given latents.

IQE Components. Similar to PQE, IQE considers input latents as two-dimensional matrices (via reshaping). For input latents $u, v \in \mathbb{R}^{k \times l}$, IQE is formed by components that capture the total size (*i.e.*, Lebesgue measure) of unions of several intervals on the real line:

$$\forall i = 1, 2, \ldots, k, \qquad d_i(u, v) \triangleq \underbrace{\left| \bigcup_{j=1}^{l} \underbrace{\big[u_{ij}, \max(u_{ij}, v_{ij})\big]}_{\text{interval on the real line}} \right|}_{\text{size of the set formed from union of } l \text{ intervals}}. \tag{3.15}$$

Figure 3-7 provides a graphical illustration on how to compute these components.

Combining IQE Components. Unlike PQE, IQE components are positive homogeneous and can be arbitrarily scaled (Figure 3-6d), and thus do not require special reparametrization in combining them. Simply summing yields the most basic yet effective IQE formulation, IQE-sum:

$$d_{\mathsf{IQE\text{-}sum}}(u, v) \triangleq \sum_{i=1}^{k} d_i(u, v) \tag{3.16}$$

Using the maxmean reduction from prior work (Pitis et al., 2020), we obtain IQE-maxmean with a single extra parameter $\alpha \in [0, 1]$ (parametrized via a `sigmoid`

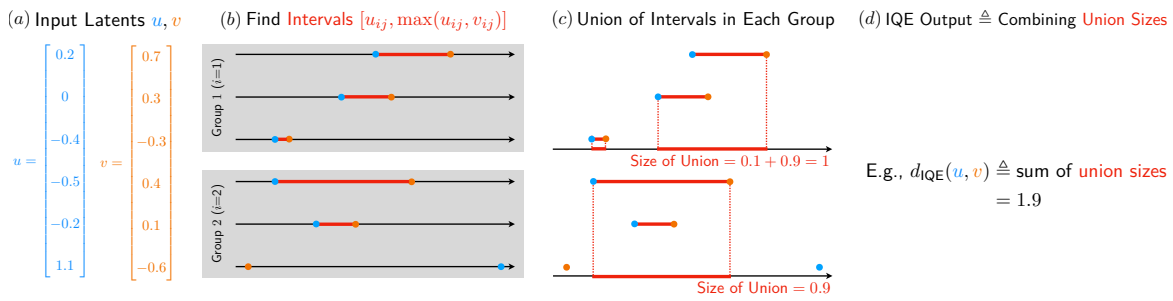

Figure 3-7: Computing IQE quasimetric from latent $u \in \mathbb{R}^{2\times 3}$ to latent $v \in \mathbb{R}^{2\times 3}$.

transform):

$$
\begin{aligned}
d_{\text{IQE-maxmean}}(u, v; \alpha) &\triangleq \text{maxmean}(d_1(u, v), \ldots, d_k(u, v); \alpha) \\
&\triangleq \alpha \cdot \max(d_1(u, v), \ldots, d_k(u, v)) \\
&\quad + (1 - \alpha) \cdot \text{mean}(d_1(u, v), \ldots, d_k(u, v))
\end{aligned} \tag{3.17}
$$

Prior methods often require expensive predictor heads (*e.g.*, MRN, Deep Norm and Wide Norm) and/or complex initialization and reparametrization (*e.g.*, PQEs). In contrast, both IQE formulations have very simple forms. Next, we will see that IQEs are not only simple, but also practically effective.

3.6.1 Evaluating IQE on Modelling Social Graphs

We evaluate IQE on the same experiment in Table 3.1 that learns quasimetric graph distances over the large real-world social graph, Berkeley-Stanford Web Graph (Leskovec and Krevl, 2014). For both IQE and PQE, we tune the parameters: component size $l \in \{8, 16, 32, 64\}$ (and thus correspondingly number of components $k \in \{64, 32, 16, 8\}$). For other baselines, we tune their parameters in the same fashion as the experiment in Table 3.1.

IQEs significantly improve modeling large real-world graphs. We train various quasimetric models to approximate the training distances by minimizng MSE w.r.t. γ-discounted distance with $\gamma = 0.9$. In Table 3.2, both IQEs greatly outperform all baselines, attaining lowest MSE, accurately predicting finite distances, and outputting

		Validation Set Metrics		
		MSE w.r.t. γ-discounted distances ($\times 10^{-3}$) $\downarrow$	ℓ_1 error when true $d < \infty$ $\downarrow$	Predicted distance when true $d = \infty$ $\uparrow$
IQE-sum		**1.078** $\pm$ **0.053**	**1.303** $\pm$ **0.031**	118.244 $\pm$ 5.412
IQE-maxmean		1.488 $\pm$ 0.307	1.333 $\pm$ 0.218	89.635 $\pm$ 1.726
PQE-LH		2.921 $\pm$ 0.187	1.659 $\pm$ 0.048	71.390 $\pm$ 0.436
PQE-GG		3.872 $\pm$ 0.136	2.121 $\pm$ 0.146	∞ (overflow)
Wide Norm		3.533 $\pm$ 0.212	1.769 $\pm$ 0.021	124.658 $\pm$ 2.868
Deep Norm		5.071 $\pm$ 0.135	2.085 $\pm$ 0.063	120.045 $\pm$ 4.353
MRN		10.820 $\pm$ 0.817	2.882 $\pm$ 0.205	129.528 $\pm$ 4.237
Best Metric Embedding		17.595 $\pm$ 0.267	7.540 $\pm$ 0.074	53.850 $\pm$ 3.843
Best Unconstrained Net.	(No Regularizer)	3.086 $\pm$ 0.039	2.115 $\pm$ 0.024	59.524 $\pm$ 0.370
	(+ Δ-Ineq. Regularizer)	2.813 $\pm$ 0.063	2.211 $\pm$ 0.034	61.371 $\pm$ 0.394
Best Asym. Dot Product	(No Regularizer)	48.106 $\pm$ 0.006	2.520×10^{11} $\pm 2.175 \times 10^{11}$	2.679×10^{11} $\pm 2.540 \times 10^{11}$
	(+ Δ-Ineq. Regularizer)	48.102 $\pm$ 0.000	2.299×10^{11} $\pm 9.197 \times 10^{10}$	2.500×10^{11} $\pm 1.446 \times 10^{11}$

Table 3.2: Modeling the large-scale Berkeley-Stanford Web Graph with different quasimetric models. For some **baseline** families, we show the best method picked w.r.t. validation set MSE.

high predictions for infinite (unreachable) pairs. Compared to the prior best methods, the simple IQE-sum has a 61% improvement on MSE and a 16% improvement on ℓ_1 error (on finite distances).

In the full paper for IQE (Wang and Isola, 2022a), additional experiments on random graphs and offline Q-learning shows the superior performance of IQE over general settings. We refer the reader to that paper for more details.

3.6.2 Theoretical Results on Universal Approximation

Following PQEs (Section 3.5.4) and prior works (Liu et al., 2022; Pitis et al., 2020), we assume that the target quasimetric $(\mathcal{X}, d)$ has only finite distances. Here we present strong universal approximation gurantees for IQEs. All full proofs are in Appendix B.6.

Theorem 3.6.1 (IQE Universal Approximation; Finite Case). For any finite quasimetric space $(\mathcal{X}, d)$ with $|\mathcal{X}| = n < \infty$, there exists encoders f_1, f_2 such that $(f_1, d_{\mathsf{IQE\text{-}maxmean}})$ exactly represents d, and $(f_2, d_{\mathsf{IQE\text{-}sum}})$ approximates d with distortion $\mathcal{O}(t \log^2 n)$, where t is a complexity measure of $(\mathcal{X}, d)$ (called treewidth).

Sketch. IQE-maxmean can exactly represent function $d_{\mathsf{asym}}(u, v) = \max_i (v_i - u_i)^+$.

Rewriting $d(x, y) = \max_{z \in \mathcal{X}}(d(x, z) - d(y, z))^+$ leads a desired encoder f_1.

For IQE-sum, each IQE component can exactly represent any quasimetric that takes in binary values (called quasipartitions) with arbitrary scaling. The desired distortion can be achieved with a convex combination of quasipartitions (Lemma B.3.5), and thus also with IQE-sum. □

Theorem 3.6.2 (IQE Universal Approximation; General Case). Consider any quasimetric space $(\mathcal{X}, d)$ where $\mathcal{X}$ is compact and d is continuous. $\forall \epsilon > 0$, with sufficiently large m, there exists some continuous encoder $f\colon \mathcal{X} \to \mathbb{R}^m$ such that

$$\forall x \in \mathcal{X}, y \in \mathcal{X}, \quad |d_{\mathsf{IQE\text{-}maxmean}}(f(x), f(y)) - d(x, y)| \leq \epsilon. \tag{3.18}$$

Relation with PQE. IQE-maxmean guarantees are strictly stronger than those of PQEs (and IQE-sum), which is only a distortion bound on the finite case using polynomial-sized encoders. With the same encoder, IQE-maxmean exactly represents any finite quasimetric.

Relation with MRN. Our IQE-maxmean analysis is largely inspired by the MRN results. In Appendix B.6, full proofs reduce the MRN asymmetrical component to an IQE-maxmean.

Deep Norm and Wide Norm. Also using a connection to MRN, we are the first to prove that Deep Norm and Wide Norm universally approximate any *quasimetric*.

Theorem 3.6.3 (Deep Norm and Wide Norm Universal Approximation). Deep Norm and Wide Norm enjoy the same approximation gaurantees as stated for IQE-maxmean in Theorems 3.6.1 and 3.6.2.

3.7 Related Work

Metric learning. Metric learning aims to approximate a target metric/similarity function, often via a learned embedding into a metric space. This idea has successful

applications in dimensionality reduction (Tenenbaum et al., 2000), information retrieval (Wang et al., 2014), clustering (Xing et al., 2002), classification (Weinberger et al., 2006; Hoffer and Ailon, 2015), *etc.* While asymmetrical formulations have been explored, they either ignore quasimetric constraints (Oord et al., 2018; Logeswaran and Lee, 2018; Schaul et al., 2015), or are not general enough to approximate arbitrary quasimetric (Balashankar and Subramanian, 2021), which is the focus of the present paper.

Isometric embeddings. Isometric (distance-preserving) embeddings is a highly influential and well-studied topic in mathematics and statistics. Fundamental results, such as Bourgain's random embedding theorem (Bourgain, 1985), laid important ground work in understanding and constructing (approximately) isometric embeddings. While most such researches concern metric spaces, Mémoli et al. (2018) study an algorithmic construction of a quasimetric embedding via basic blocks called *quasi-partitions*. Their approach requires knowledge of quasimetric distances between all pairs and thus is not suitable for learning. Our formulation takes inspiration from the form of their embedding, but is fully learnable with gradient-based optimization over a training subset.

Quasimetrics and partial orders. Partial orders (quasipartitions) are special cases of quasimetrics (see Section 3.5). A line of machine learning research studies embedding partial order structures into latent spaces for tasks such as relation discovery and information retrieval (Vendrov et al., 2015; Suzuki et al., 2019; Hata et al., 2020; Ganea et al., 2018). Unfortunately, unlike PQEs, such formulations do not straightforwardly generalize to arbitrary quasimetrics, which are more than binary relations. Similar to PQEs, DeepNorm and WideNorm are quasimetric embedding approaches learnable with gradient-based optimization (Pitis et al., 2020). Theoreically, they universally approximates a subset of quasimetrics (ones induced by asymmetrical norms). Despite often using many more parameters, they are restricted to this subset and unable to approximate general quasimetrics like PQEs do (Figure 3-4).

3.8 Implications

In this work, we study quasimetric learning via both theoretical analysis and empirical evaluations.

Theoretically, we show strong negative results for a common family of learning algorithms, and positive guarantees for our proposed Poisson Quasimetric Embedding (PQE). Our results introduce the novel concept of equivariant learning algorithms, which may potentially be used for other learnability analyses with algorithms such as deep neural networks. Additionally, a thorough average-case or data-dependent analysis would nicely complement our results, and may shed light on conditions where algorithms like deep networks can learn decent approximations to quasimetrics in practice.

PQEs are the first quasimetric embedding formulation that can be learned via gradient-based optimization. Empirically, PQEs show promising performance in various tasks. Furthermore, PQEs are fully differentiable, and (implicitly) enforce a quasimetric structure in any latent space. They are particularly suited for integration in large deep learning systems, as we explore in the Q-learning experiments. This can potentially open the gate to many practical applications such as better embedding for planning with MDPs, efficient shortest path finding via learned quasimetric heuristics, representation learning with quasimetric similarities, causal relation learning, *etc.*

Finally, we proposed Interval Quasimetric Embedding (IQE) with both strong theoretical guarantees and improved empirical performance over PQE. We believe that IQE's simple yet powerful form can enable more machine learning applications of quasimetrics in modeling asymmetrical geometric structures, and that our four criteria are helpful in developing novel and better quasimetric structures.

Chapter 4

Reinforcement Learning as Quasimetric Representation Learning

In goal-reaching reinforcement learning (RL), the optimal value function has a particular geometry, called *quasimetric* structure. This chapter introduces Quasimetric Reinforcement Learning (QRL), a new RL method that utilizes quasimetric models to learn *optimal* value functions. Distinct from prior approaches, the QRL objective is specifically designed for quasimetrics, and provides strong theoretical recovery guarantees. Empirically, we conduct thorough analyses on a discretized `MountainCar` environment, identifying properties of QRL and its advantages over alternatives. On offline and online goal-reaching benchmarks, QRL also demonstrates improved sample efficiency and performance, across both state-based and image-based observations.

This chapter is based on published work:

1. *Optimal Goal-Reaching Reinforcement Learning via Quasimetric Learning* with co-authors Antonio Torralba, Phillip Isola, and Amy Zhang at the International Conference on Machine Learning (ICML) 2023 (Wang et al., 2023).

4.1 Introduction

Modern decision-making problems often involve dynamic programming on the cost-to-go function, also known as the value function. This function allows for bootstrapping,

where a complicated decision is broken up into a series of subproblems. Once a subproblem is solved, its subgraph can be collapsed into a single node whose cost is summarized by the value function. This approach appears in nearly all contemporary RL and planning algorithms.

In deep RL, value functions are modeled with general neural nets, which are universal function approximators. Further, most RL algorithms focus on optimizing toward a single goal. In this setting, the value function $V^*(s)$ reports the (optimal) cost-to-go to achieve that single goal from state $s \in \mathcal{S}$. It is known that V^* can be any function $V^* \colon \mathcal{S} \to \mathbb{R}$, that is, for any $V^* \colon \mathcal{S} \to \mathbb{R}$, there exists a Markov Decision Process (MDP) for which that V^* is the desired optimal value function.

However, an additional structure emerges when we switch to the multi-task setting, where the (goal-conditioned) value function $V^*(s; g) \colon \mathcal{S} \times \mathcal{S} \to \mathbb{R}$ is the cost-to-go to a given goal state g (Figure 4-1). In this case, the optimal value function, for *any* MDP, is always a quasimetric function (Chapter 3; Proposition B.1.4; Sontag (1995); Tian et al. (2020a); Liu et al. (2022)), which is a generalization of metric functions to allow asymmetry while still respecting the triangle inequality.

Given this structure, it is natural to constrain value function search to the space of quasimetrics. This approach searches within a much smaller subset of the space of all functions $\mathcal{S} \times \mathcal{S} \to \mathbb{R}$, ensuring that the true value function is guaranteed to be present within this subspace. Differentiable parametric quasimetric modelshave already enabled a number of studies to explore the use of these models in standard RL algorithms, resulting in improved performance in some cases (Section 3.5.5; Pitis et al. (2020); Liu et al. (2022)) .

However, traditional RL algorithms (such as Q-learning (Watkins, 1989)) were designed for large unconstrained function spaces, and their performance may severely degrade with restricted spaces (Wang et al., 2020, 2021). Instead of constraining the search space, they encourage quasimetric properties via the objective function. For example, the Bellman update partly enforces the triangle inequality on the current state, next state, and target goal. With the advent of differentiable parametric quasimetric models, these properties come for free with the architecture, and we aim

to design a new RL algorithm specifically geared towards learning quasimetric value functions.

In this work, we propose *Quasimetric Reinforcement Learning* (QRL). QRL is in the family of geometric approaches to value function learning, which model the value function as some distance metric, or, in our case, a quasimetric. Obtaining local distance estimates is easy because the cost of a single transition is by definition given by the reward function, and can be learned via regression towards observed rewards. However, capturing global relations is hard. This is a problem studied in many fields such as metric learning (Roweis and Saul, 2000; Tenenbaum et al., 2000), contrastive learning (Oord et al., 2018; Wang and Isola, 2020), *etc.* A general principle is to find a model where local relationships are captured and otherwise states are spread out.

We argue that a similar idea can be used for value function learning. QRL finds a *quasimetric* value function in which *local distances are preserved*, but otherwise states are *maximally spread out*. All *three properties* are essential in accurately learning the function. Intuitively, a quasimetric function that maximizes the separation of states s_0 and s_1, subject to the constraint that it *captures cost* for each adjacent pair of states, gives exactly the cost of the shortest path from s_0 to s_1. It can't be longer than that due to triangle inequality from *quasimetric* and *preservation of local distances*. It can't be shorter than that due to the *maximal spreading*. Analogously, consider a chain with several links. If one pushes the chain ends apart, then the distance between the ends is exactly equal to the length of all the links.

These *three properties* (which we will indicate with the three text colors above) make our method distinct from other contrastive approaches to RL, and ensure that QRL *provably* learns the *optimal* value function. Some alternatives use symmetrical metrics that cannot capture complex dynamics (Yang et al., 2020; Ma et al., 2022; Sermanet et al., 2018). Others do not enforce how much adjacent states are pulled together nor how much states are pushed apart, and rely on carefully weighting loss terms and specific sample distributions to estimate on-policy (rather than optimal) values (Eysenbach et al., 2022; Oord et al., 2018).

In summary, our contributions in this paper are

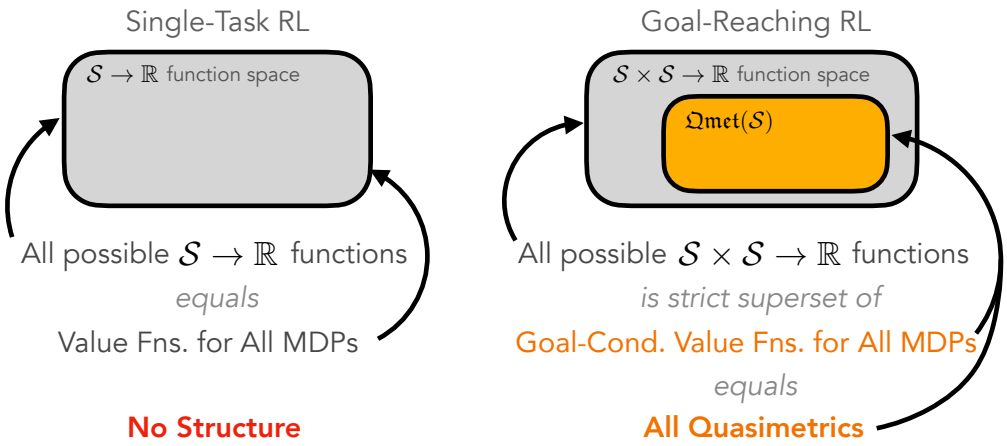

Figure 4-1: In multi-goal RL, the set of all possible (optimal) value functions is exactly the set of *quasimetrics*. In single-task RL, there is no similar structure and value functions can be any function.

- Based on the connection between value functions and quasimetrics (Section 4.2), we propose QRL, a new RL framework that utilizes *quasimetric* models to learn *optimal* goal-reaching value functions (Section 4.3).

- We provide theoretical guarantees (Section 4.3.1) as well as thorough empirical analysis on a discretized `MountainCar` environment (Section 4.3.3), highlighting qualitative differences with many existing methods.

- We augment the proposed method to (optionally) also learn optimal Q-functions and/or policies (Section 4.3.4).

- On offline `maze2d` tasks, QRL performs well in single-goal and multi-goal evaluations, improving $> 37\%$ over the best baseline and $> 46\%$ over the `d4rl` handcoded reference controller Fu et al. (2020) (Section 4.5.1).

- Our learned value functions can be directly used in conjunction with trajectory modeling and planning methods, improving their performances (Section 4.5.1).

- On online goal-reaching settings, QRL shows up to 4.9× improved sample efficiency and performance in both state-based and imaged-based observations, outperforming baselines including Contrastive RL (Eysenbach et al., 2022) and

plugging quasimetric Q-function models into existing RL algorithms (Liu et al., 2022) (Section 4.5.2).

4.2 Value Functions are Quasimetrics

This section covers the preliminaries on goal-reaching RL settings, value functions, and quasimetrics. We also present a new result showing an equivalence between the latter two.

4.2.1 Goal-Reaching Reinforcement Learning

We focus on the goal-reaching RL tasks in the form of Markov Decision Processes (MDPs): $(\mathcal{S}, \mathcal{A}, P, R)$, where $\mathcal{S}$ is the state space, $\mathcal{A}$ is the action space, $P\colon \mathcal{S} \times \mathcal{A} \to \Delta(\mathcal{S})$ is the transition function, and $R\colon \mathcal{S} \times \mathcal{S} \to [R_{\mathsf{min}}, 0]$ is the reward (cost) function for performing a transition between two states. $\Delta(A)$ denotes the set of distributions over set A.

Given a target state $s_{\mathsf{goal}} \in \mathcal{S}$, a goal-conditioned agent $\pi(a \mid s; s_{\mathsf{goal}})$ is tasked to reach s_{goal} as soon as possible from the current state s. Formally, until the agent reaches the goal, it receives a negative reward (cost) $r(s, s')$ for each transition (s, s'). The agent π aims to maximize the expected total reward given any s and s_{goal}, which equals the negated total cost. We call this quantity the (goal-conditioned) on-policy value function $V^\pi(s; s_{\mathsf{goal}})$ for π.

There exists an optimal policy π^* that is universally optimal:

$$\forall s, s_{\mathsf{goal}}, \quad V^{\pi^*}(s; s_{\mathsf{goal}}) = \max_\pi V^\pi(s; s_{\mathsf{goal}}). \tag{4.1}$$

We thus define the optimal value function $V^* \triangleq V^{\pi^*}$.

Similarly, we can define the optimal state-action value function, *i.e.*, Q-function:

$$Q^*(s, a; s_{\mathsf{goal}}) \triangleq \mathbb{E}_{s' \sim P(s,a)} \left[R(s, s') + V^*(s'; s_{\mathsf{goal}}) \right].$$

4.2.2 Value-Quasimetric Equivalence

Regardless of the underlying MDP, some *fundamental* properties of optimal value V^* always hold.

Triangle Inequality. As observed in Chapter 3 and prior works (Liu et al., 2022; Pitis et al., 2020; Durugkar et al., 2021), the optimal value V^* always obeys the triangle inequality (due to optimality and Markov property):

$$\forall s_1, s_2, s_3, \quad V^*(s_1; s_2) + V^*(s_2; s_3) \leq V^*(s_1; s_3). \tag{4.2}$$

Intuitively, $V^*(s_1, s_3)$ is the highest value among all plans from s_1 to s_3; and $V^*(s_1; s_2) + V^*(s_2; s_3)$ is the highest among all plans from s_1 to s_2 and then to s_3, a more restricted set. Thus, Equation (4.2) holds, and $-V^*$ is just like a metric function on $\mathcal{S}$, except that it may be *asymmetrical*.

Quasimetrics are a generalization of metrics in that they do not require symmetry. For a set $\mathcal{X}$, a quasimetric is a function $d\colon \mathcal{X} \times \mathcal{X} \to \mathbb{R}_{\geq 0}$ such that

$$\forall x_1, x_2, x_3, \quad d(x_1, x_2) + d(x_2, x_3) \geq d(x_1, x_3) \tag{4.3}$$

$$\forall x, \quad d(x, x) = 0. \tag{4.4}$$

We use $\mathfrak{Qmet}(\mathcal{X})$ to denote all such quasimetrics over $\mathcal{X}$.

Equation (4.2) shows that $-V^* \in \mathfrak{Qmet}(\mathcal{S})$. In fact, the other direction also holds: for any $d \in \mathfrak{Qmet}(\mathcal{S})$, $-d$ is the optimal value function for some MDP defined on $\mathcal{S}$.

Theorem 4.2.1 (Value-Quasimetric Equivalence).

$$\mathfrak{Qmet}(\mathcal{S}) \equiv \{-V^*\colon V^* \text{ is the optimal value of an MDP on } \mathcal{S}\}. \tag{4.5}$$

Generally, on-policy value $-V^\pi$ may not be a quasimetric.

All proofs are deferred to the appendix.

Structure emerges in multi-goal settings. The space of quasimetrics is the *exact* function class for goal-reaching RL. In contrast, a specific-goal value function $V^*(\,\cdot\,; s_{\mathsf{goal}})$ can be any *arbitrary* function $\mathcal{S} \to \mathbb{R}$. In other words, going from single-task RL to multi-task RL may be a harder problem, but also has much more structure to utilize (Figure 4-1).

4.2.3 Quasimetric Models and RL

Quasimetric Models refer to parametrized models of quasimetrics $d_\theta \in \mathfrak{Qmet}(\mathcal{X})$, where θ is the parameter to be optimized. Many recent quasimetric models are based on neural networks (Chapter 3; Pitis et al. (2020)), can be optimized w.r.t. any *differentiable* objective, and can potentially generalize to unseen inputs (due to neural networks). Many such models can universally approximate any quasimetric and is capable of learning large-scale and complex quasimetric structures Section 3.6.

An Overview of Quasimetric Models. A quasimetric model d_θ usually consists of (1) a deep encoder mapping inputs in $\mathcal{X}$ to a generic latent space $\mathbb{R}^d$ and (2) a differentiable latent quasimetric head $d_{\mathsf{latent}} \in \mathfrak{Qmet}(\mathbb{R}^d)$ that computes the quasimetric distance for two input latents. θ contains both the parameters of the encoder and parameters of the latent head d_{latent}, if any. Recent works have proposed many choices of d_{latent}, which have different properties and performances. See Section 3.6 for an in-depth treatment of such models.

Subtleties of Using Quasimetric Models in RL. It is tempting to parametrize goal-conditioned value functions with quasimetric models in standard RL algorithms, which optimizes for $V^* \in \mathfrak{Qmet}(\mathcal{S})$. However, these algorithms usually use temporal-difference learning or policy iteration, whose success relies on accurate representation of intermediate results (*e.g.*, on-policy values; Theorem 4.2.1) (Wang et al., 2020, 2021)) that are *not* quasimetrics. Indeed, simply using quasimetric models in such

algorithms may yield only minor benefits (Chapter 3) or require significant relaxations of quasimetric inductive bias (Liu et al., 2022).

Can we directly learn V^* without those iterative procedures? Fortunately, the answer is *yes*, with the help of *quasimetrics*.

4.3 Quasimetric Reinforcement Learning

Quasimetric Reinforcement Learning (QRL) at its core learns the *optimal* goal-conditioned value function V^* that is parametrized by a quasimetric model $d_\theta \subset \mathfrak{Qmet}(\mathsf{S})$.

Similar to many recent RL works (Kumar et al., 2019; Ghosh et al., 2019; Janner et al., 2022, 2021; Emmons et al., 2021; Chen et al., 2021; Paster et al., 2022; Yang et al., 2022), our method is derived with the assumption that the environment dynamics P are *deterministic*.

Given ways to sample (*e.g.*, from a dataset / replay buffer)

$$(s, a, s', r) \sim p_{\mathsf{transition}} \quad \text{(transitions)}$$

(s: current state, s': next state, a: action, r: reward ≤ 0)

$$s \sim p_{\mathsf{state}} \quad \text{(random state)}$$

$$s_{\mathsf{goal}} \sim p_{\mathsf{goal}}, \quad \text{(random goal)}$$

QRL optimizes a quasimetric model d_θ as following:

$$\begin{aligned} &\max_\theta \ \mathbb{E}_{\substack{s\sim p_{\mathsf{state}} \\ g\sim p_{\mathsf{goal}}}}[d_\theta(s, g)] \\ &\text{subject to } \mathbb{E}_{(s,a,s',r)\sim p_{\mathsf{transition}}}[\mathtt{relu}(d_\theta(s, s') + r)^2] \le \epsilon^2, \end{aligned} \tag{4.6}$$

where $\epsilon > 0$ is small, and $\mathtt{relu}(x) \triangleq \max(x, 0)$ prevents $d_\theta(s, s')$ from exceeding the transition cost $-r \ge 0$.

After optimization, we take $-d_\theta$ as our estimate of V^*. Section 4.3.4 discusses extensions that learn optimal Q-functions Q^* and policies, making QRL suitable both

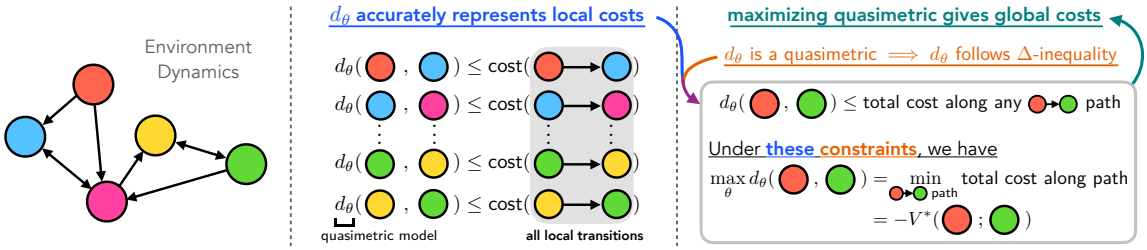

Figure 4-2: QRL objective finds length of the shortest path connecting two states, *i.e.*, the *optimal value* V^*.

as a standalone RL method or in conjunction with other RL methods.

4.3.1 QRL Learns the Optimal Value Function

By using *quasimetric models* d_θ to parametrize value functions, we inherently satisfy the triangle-inequality constraints. What additional constraints should we add in order to find the optimal value function for a specific MDP?

A Physical Analogy. Consider two objects connected by multiple chains. Each chain is formed by several links. If we *pull them apart*, their distance will be limited by the shortest of all chains. Then, simply measuring the distance between the two objects gives the length of that "optimal" chain. This argument relies on (1) the *triangle inequality* of our Euclidean physical space and (2) that each link of the chains has *a fixed length unaffected by our pulling*.

QRL works by the same principles, but in a *quasimetric* space that both satisfies the triangle inequality and can capture any asymmetrical MDP dynamics (Figure 4-2):

- **Locally**, we constrain searching of V^* to d_θ's that are *consistent with local costs, i.e., not overestimating them*:

$$\forall \text{ transition } (s, a, s', r), \quad d_\theta(s, s') \le -r. \tag{4.7}$$

We ensure this because d_θ should approximate $-V^*$ and

$$-V^*(s; s') \le \text{cost of specific path } s \xrightarrow{\text{action } a} s' = -r.$$

- **Globally**, since d_θ is a *quasimetric* that satisfies the triangle inequality and Equation (4.7), for *every state* s *and goal* g, any path $s \to g$ places a constraint on $d_\theta(s, g)$:

$$d_\theta(s, g) \leq \textsf{total cost of path connecting } s \textsf{ to } g.$$

  Optimal cost from s to g is given by *pulling them apart*:

$$\begin{aligned} \max_\theta d_\theta(s, g) &= \textsf{cost of shortest path connecting } s \textsf{ to } g \\ &= -V^*(s; g). \end{aligned} \tag{4.8}$$

Optimal quasimetric $-V^*$ achieves this maxima for all (s, g) pairs. Therefore, we maximize $d_\theta(s, g)$ simultaneously for all (s, g) pairs:

$$\begin{aligned} \theta^* = \arg\max_\theta \mathbb{E}_{\substack{s \sim p_{\textsf{state}} \\ g \sim p_{\textsf{goal}}}}[d_\theta(s, g)] \\ \textsf{subject to } \forall (s, a, s', r) \textsf{ transition}, d_\theta(s, s') \leq -r. \end{aligned} \tag{4.9}$$

This gives exactly the *optimal value*:

$$d_{\theta^*}(s, g) = -V^*(s; g), \qquad \forall s, g, \tag{4.10}$$

(assuming that $p_{\textsf{state}}$ and $p_{\textsf{goal}}$ having sufficient coverage).

The linear programming characterization of V^* (Manne, 1960; Denardo, 1970) is similar to Equation (4.9). However, instead of enforcing triangle inequalities via $|\mathcal{A}||\mathcal{S}|^2$ constraints, our *quasimetric models* automatically satisfy them.

Theoretical Guarantees

We now formally state the recovery guarantees for QRL in both the ideal setting (*i.e.*, optimizing over entire $\mathfrak{Qmet}(\mathcal{S})$) and the function approximation setting.

The proofs of the following results are mostly formalizations of the ideas above.

All proofs are presented in Appendix C.2.

Theorem 4.3.1 (Exact Recovery). If Equation (4.9) optimizes d_θ over the entire $\mathfrak{Qmet}(\mathcal{S})$, then for $s \sim p_{\mathsf{state}}, g \sim p_{\mathsf{goal}}$, we have $d_{\theta^*}(s, g) = -V^*(s; g)$ almost surely.

In the more realistic case, we use a quasimetric family that is not quite as big as the entire $\mathfrak{Qmet}(\mathcal{S})$ but flexible enough to have universal approximation (*e.g.*, IQE Section 3.6). Using a relaxed constraint, we still have a strong guarantee of recovering true V^*, ensuring a small error even for (s, g) pairs that are far apart.

Theorem 4.3.2 (Function Approximation; Informal). Consider a quasimetric model family $\{d_\theta\}_\theta$ that is a universal approximator of $\mathfrak{Qmet}(\mathcal{S})$ (in terms of L_∞ error). If we solve Equation (4.9) with a relaxed constraint, where

$$\forall (s, a, s', r)\ \mathsf{transition}, \quad \texttt{relu}(d_\theta(s, s') + r) \le \epsilon, \tag{4.11}$$

for small $\epsilon > 0$. Then, for $s \sim p_{\mathsf{state}}, g \sim p_{\mathsf{goal}}$, we have

$$\left| d_{\theta^*}(s, g) + (1 + \epsilon) V^*(s; g) \right| \in [-\sqrt{\epsilon}, 0],$$

i.e., $d_{\theta^*}(s, g)$ recovers $-V^*(s; g)$ up to a known scale, with probability $1 - \mathcal{O}(-\sqrt{\epsilon} \cdot \mathbb{E}[V^*])$.

4.3.2 A Practical Implementation

Quasimetric Model. We use Interval Quasimetric Embeddings (IQE; Section 3.6) as our quasimetric model family $\{d_\theta\}_\theta$. IQEs have convincing empirical results in learning various quasimetric spaces, and enjoy strong approximation guarantees (as needed in Theorem 4.3.2).

Constrained Optimization is done via dual optimization and jointly updating a Lagrange multiplier $\lambda \ge 0$ (Eysenbach et al., 2021). We use a relaxed constraint that local costs are properly modeled in expectation.

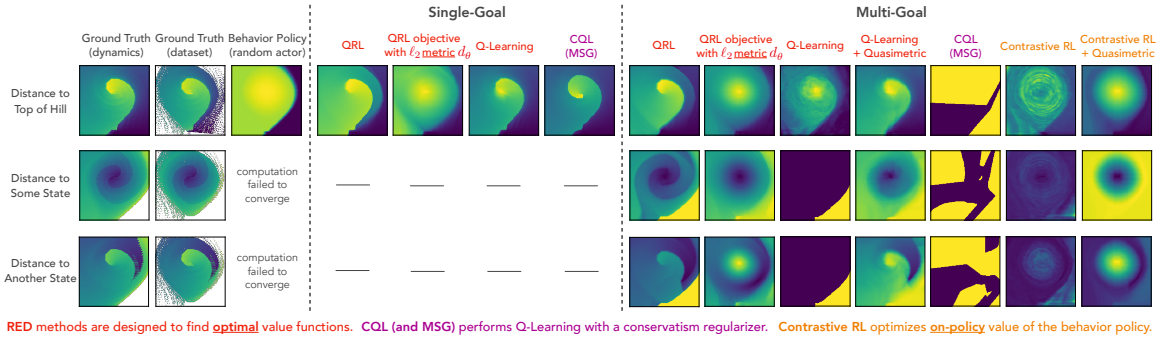

Figure 4-3: Learned value functions on offline `MountainCar`. Each plot shows the estimated values from every state towards a single goal (indicated in the leftmost column) as a 2-dimensional image (velocity as x-axis, position as y-axis). **Left**: Ground truth distances, as well as the (expected) distance for the behavior policy that generated training data. **Middle**: Learned value functions for single-goal methods. **Right**: Learned value functions for multi-goal methods. Only QRL accurately recovers the ground truth distance structure in both settings, which crucially relies on the asymmetry of quasimetrics. Q-learning methods generally fail in multi-goal settings. Their learned values, while improved with quasimetric models, cannot capture the fine details. Contrastive RL only inaccurately estimates the on-policy values.

Stable Maximization of d_θ. In practice, maximizing $\mathbb{E}[d_\theta(s, g)]$ via gradient descent tends to increase the weight norms of the late layers in d_θ. This often leads to slow convergence since λ needs to constantly catch up. Therefore, we instead place a smaller weight on distances $d_\theta(s, g)$ that are already large and optimize $\mathbb{E}[\phi(d_\theta(s, g))]$, where ϕ is a monotonically increasing convex function (*e.g.*, affine-transformed softplus). This is similar to the discount factor in Q-learning, which causes its MSE loss to place less weight on transitions of low value.

Full Objective. Putting everything together, we implement QRL to jointly update (θ, λ) according to

$$\min_{\theta} \max_{\lambda \geq 0} -\mathbb{E}_{\substack{s \sim p_{\text{state}} \\ g \sim p_{\text{goal}}}}[\phi(d_\theta^{\mathsf{IQE}}(s, g))] + \lambda \left(\mathbb{E}_{(s,a,s',r) \sim p_{\text{transition}}}[\texttt{relu}(d_\theta^{\mathsf{IQE}}(s, s') + r)^2] - \epsilon^2 \right). \tag{4.12}$$

4.3.3 Analyses and Comparisons via Discretized `MountainCar`

We empirically analyze QRL and compare to previous works via experiments on the `MountainCar` environment with a discretized state space. In this environment, the agent observes the location and velocity of a car, and controls it to reach the top of a hill. Due to gravity and velocity, the dynamics are highly asymmetrical. We discretize the 2-dimensional state space into 160×160 bins so that we can compute the ground truth value functions. We collected an offline dataset by running a uniform random policy, and evaluated the learning result of various methods, including

- **QRL**, our method;
- Using **QRL** objective to train a **symmetrical ℓ_2 distance** value function;
- **Q-Learning** with regular unconstrained Q function class;
- **Q-Learning with quasimetric** function class;
- **Contrastive RL** (Eysenbach et al., 2022), which uses a contrastive objective but estimates on-policy values;
- **Contrastive RL** with quasimetric function class;
- **Conservative Q-Learning (CQL)** (Kumar et al., 2020), which regularizes Q-Learning to reduce over-confidence in out-of-distribution regions;
- **Model Standard-deviation Gradients (MSG)** (Ghasemipour et al., 2022), a state-of-the-art offline RL algorithm using an ensemble of up to 64 CQL value functions to estimate uncertainty and train policy;
- **Diffuser** (Janner et al., 2022), a representative trajectory modelling methods with goal-conditioned sampling.

QRL can be used for both single-goal and multi-goal settings by specifying p_{goal}. For methods that are not designed for multi-goal settings (MSG and Q-Learning), we use Hindsight Experience Replay (HER; Andrychowicz et al. (2017)) to train the goal-conditioned value functions.

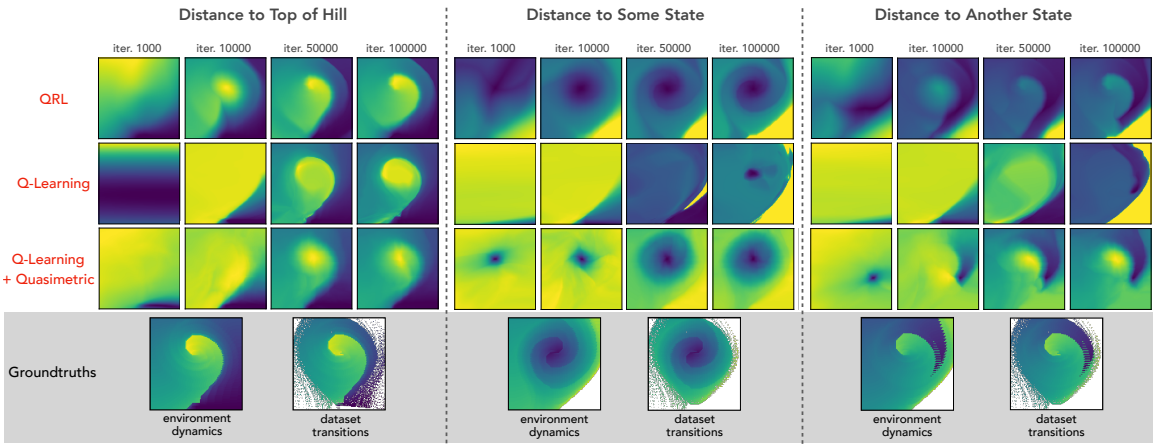

Figure 4-4: Learning dynamics on the offline `MountainCar` setting. Each plot shows the learned values from every state towards a single goal (indicated at the top) as a 2-dimensional image (velocity as x-axis, position as y-axis). Yellow is greater distance (lower value function). Bottom row shows the ground truth distances based on true environment dynamics, and ground truth distances based on transitions appearing in dataset. QRL generally learns the target value function structures much earlier than Q-learning methods.

Evaluation. Visually, we compare the learned values against ground truths (Figures 4-3 and 4-4). We test the agents' control performances in both reaching the original goal, top of the hill, as well as 9 distinct states (Table 4.1). A diverse set of goals allows us to evaluate how well the value functions capture the true environment dynamics structure. For QRL and Q-Learning, agents take the action that greedily maximizes the estimated value for simplicity. We describe how to obtain Q-values for QRL later in Section 4.3.4.

Q-Learning is the standard way to train optimal value functions for such discrete-action space environments. Despite its popularity, many issues have been identified with its temporal-difference training, such as slow convergence (Lyle et al., 2022; Fujimoto et al., 2022). Figure 4-4 visualizes the learning dynamics of Q-Learning and QRL, where vanilla Q-Learning indeed learns very slowly. While using a quasimetric Q-function helps significantly, QRL still learns the V^* structure much faster, and better captures the true target V^* even after training concludes (Figure 4-3). In planning (Table 4.1), vanilla Q-Learning and (Q-Learning based) MSG struggle in multi-goal settings. While Q-Learning with quasimetrics achieves comparable planning

performance with QRL, the higher-quality V^* estimate from QRL is likely important in more complex environments. Furthermore, with continuous action spaces, Q-Learning requires a jointly learned actor, which (1) reduces to on-policy value learning and (2) can have complicated training dynamics as the actor's on-policy values may not be a quasimetric (Theorem 4.2.1). QRL is exempt from such issues. In later sections with experiments on online learning in more complex environments, simply using quasimetric in traditional value training indeed greatly underperforms QRL (Section 4.5.2).

Contrastive RL uses an arguably similar contrastive objective. However, it samples positive pairs from the same trajectory, and does not enforce exact representation of local costs. Hence, it estimates the on-policy values that generated the data (random actor in this case). Indeed, Figure 4-3 shows that the Contrastive RL value functions mostly resemble that of a random actor, and fails to capture the boundaries separating states that have distinct values under *optimal* actors. As shown in Table 4.1, this indeed leads to much worse control results.

Ablations. We highlight three ablation studies here:

- **Asymmetry.** QRL objective with symmetrical value functions underperforms QRL greatly, suggesting the importance of *asymmetry from quasimetrics*.
- **Optimality.** Contrastive RL with quasimetric can be seen as a method that uses quasimetric to train *on-policy* values. Thus, the learned values fail to capture optimal decision structures. QRL instead enforces *consistency with observed local costs* and *maximal spreading of states*, which leads to *optimal values* and better performance.
- **QRL Objective.** While Q-Learning with quasimetrics plans comparably well here , it learns more slowly than QRL (Figure 4-4) and fails to capture finer value function details (Figure 4-3). As discussed above, Q-Learning (with or without quasimetrics) also has potential issues with complex dynamics and/or

Method	Method Configuration	Task	
		Reach Top of Hill	Reach 9 States
QRL	Single-Goal	**97.69** ± **0.26**	—
	Multi-Goal	**95.89** ± **0.55**	**85.55** ± **3.57**
Q-Learning	—	**98.74** ± **0.19**	—
	+ Relabel	89.27 ± 11.69	22.06 ± 8.72
Contrastive RL	—	83.91 ± 8.04	53.75 ± 32.93
MSG	—	**97.44** ± **0.22**	—
	+ Relabel	14.30 ± 0.00	37.80 ± 8.20
Diffuser	—	19.78 ± 3.03	36.41 ± 1.44
QRL Objective with Symmetric ℓ_2 Distance	Single-Goal	**95.42** ± **0.16**	—
	Multi-Goal	**96.13** ± **0.12**	73.27 ± 0.84
Contrastive RL + Quasimetric Q-Function	—	83.90 ± 8.73	72.28 ± 4.63
Q-Learning + Quasimetric Q-Function	+ Relabel	**96.33** ± **0.37**	**85.53** ± **3.69**
Oracle (Full Dynamics)	—	100.00	100.00
Oracle (Dataset Transitions)	—	69.22	75.89

Table 4.1: Control results on `MountainCar`. Scores are normalized returns to reach the desired goal within 200 steps, averaged across all 160×160 starting states. Each row shows evaluations of a method in a specific configuration with standard deviations from 5 seeds. We highlight results that are $\geq 95\%$ of the best method.

continuous action space, while QRL does not have such problems and attain much superior performance in such settings (see later Section 4.5.2).

Compared to existing approaches, QRL efficiently and accurately finds optimal goal-conditioned value functions, showing the importance of both the quasimetric structure and the novel learning objective. In the next section, we describe extensions of QRL, followed by more extensive experiments on offline and online goal-reaching benchmarks in Section 4.5.

4.3.4 From V^* to Q^* and Policy

QRL's optimal value V^* estimate may be used directly in planning to control an agent. A more common approach is to train a policy network w.r.t. to a Q-function estimate (Hafner et al., 2019a). This section describes simple extensions to QRL that learn the *optimal* Q-function Q^* and a policy.

Transition and Q-Function Learning. We augment the quasimetric model d_θ to include an *encoder* $f\colon \mathcal{S} \to \mathcal{Z}$:

$$d_{\theta=(\theta_1,\theta_2)}(s_0, s_1) \triangleq d^z_{\theta_1}(f_{\theta_2}(s_0), f_{\theta_2}(s_1)). \tag{4.13}$$

Since d_θ captures V^*, finding the Q-function $Q^*(s, a; g)$ only requires knowing the transition result, which we model by a learned latent transition $T\colon \mathcal{Z} \times \mathcal{A} \to \mathcal{Z}$. In this section, for notation simplicity, we will drop the $()_{\theta_*}$ subscript, and use $z \triangleq f(s)$, $z' \triangleq f(s')$, $\hat{z}' \triangleq T(z, a)$, and $z_g \triangleq f(g)$.

Once with a well trained T, we can estimate $Q^*(s, a; g)$ as

$$d^z(\underbrace{T(z,a)}_{\text{latent transition}}, z_g) \underbrace{- r}_{\text{transition cost}} = d^z(\hat{z}', z_g) - r \approx -Q^*(s, a; g). \tag{4.14}$$

(In our experiments, transition cost $-r$ is a constant, and thus omitted. Generally, T can be extended to estimate r.)

Transition loss. Given transition (s, a, s'), we define:

$$\mathcal{L}_{\mathsf{transition}}(s, a, s'; T, d_\theta) \triangleq \frac{1}{2}\big(d^z(\hat{z}', z')^2 + d^z(z', \hat{z}')^2\big),$$

which is used to optimize both d_θ and T in conjunction with the QRL objective in Equation (4.12).

$\mathcal{L}_{\mathsf{transition}}$ encourages the predicted next latent $\hat{z}'$ to be close to the actual next latent z' w.r.t. the learned quasimetric function d^z. This is empirically superior to a simple regression loss on $\mathcal{Z}$, whose scale is meaningless.

More importantly, the quasimetric properties allow us to directly relate $\mathcal{L}_{\mathsf{transition}}$ values to Q-function error:

Suppose $d^z(\hat{z}', z')^2 + d^z(z', \hat{z}')^2 \le \delta^2$, which means

$$d^z(\hat{z}', z') \le \delta \text{ and } d^z(z', \hat{z}') \le \delta. \tag{4.15}$$

For any goal g with latent z_g, the triangle inequality implies

$$|\underbrace{d^z(\hat{z}', z_g)}_{\text{estimated } Q^*(s,a;g)} - \underbrace{d_\theta(s', g)}_{\text{estimated } V^*(s';g)}| = |d^z(\hat{z}', z_g) - d^z(z', z_g)| \leq \delta.$$

In other words, if d_θ accurately estimates V^*, our estimated $Q^*(s, a; g)$ has bounded error, *for any* goal g, even though we train with a local objective $\mathcal{L}_{\text{transition}}$. Hence, simply training the transition loss *locally* ensures that Q-function error is bounded *globally*, thanks to using *quasimetrics*.

Based on this argument, our theoretical guarantees for recovering V^* (Theorems 4.3.1 and 4.3.2) can be potentially extended to Q^* and thus to optimal policy. We leave this as future work.

Policy Learning. We train policy $\pi\colon \mathcal{S} \to \Delta(\mathcal{A})$ to maximize the estimated Q-function (Equation (4.14)):

$$\min_{\pi} \mathbb{E}_{\substack{s\sim p_{\text{state}} \\ g\sim p_{\text{goal}}}}[d^z(T(f(s), a), f(g))]. \tag{4.16}$$

Additionally, we follow standard RL techniques, training two critic functions and optimizing the policy to maximize rewards from the minimum of them (Fujimoto and Gu, 2021; Eysenbach et al., 2022). In online settings, we also use an adaptive entropy regularizer (Haarnoja et al., 2018).

4.4 Related Work

Contrastive Approaches to RL. As discussed in Section 4.1, our objective bears similarity to those of contrastive approaches. However, we also differ with them in that we rely on (1) *quasimetric models*, (2) *consistency with observed local costs*, and (3) *maximal spreading of states* to learn the optimal value function. Most contrastive methods satisfy none of these properties, and instead pull together states sampled from the same trajectory for capturing on-policy value/information (Eysenbach et al., 2022; Ma et al., 2022; Sermanet et al., 2018; Oord et al., 2018). Yang et al. (2020)

ensures exact representation of local cost, but also enforces non-adjacent states to have distance 2 via a *metric* function, and thus cannot learn optimal values. Another related line of work trains contrastive models to estimate the alignment between current state and some abstract goal (*e.g.*, text), which are then used as reward for RL training (Fan et al., 2022). Despite the similar goal-reaching setting, their trained model is potentially sensitive to training data, and estimates a density ratio rather than the optimal cost-to-go.

Quasimetric Approaches to RL. Micheli et al. (2020) consider using quasimetrics for multi-task planning, but does not use models that enforce quasimetric properties. Liu et al. (2022) use quasimetric models to parametrize the Q-function, and shows improved performance with DDPG (Lillicrap et al., 2015) and HER (Andrychowicz et al., 2017) on goal-reaching tasks. These prior works mostly only estimate *on-policy* value functions, and rely on iterative policy improvements to train policies. Zhang et al. (2020b) use a similar quasimetric definition, but does not use quasimetric models and focuses on hierarchy learning. In contrast, our work utilizes the full quasimetric geometry to directly estimate V^* and produce high-quality goal-reaching agents. Additionally, the Wasserstein-1 distance induced by the MDP dynamics is also a quasimetric. Durugkar et al. (2021) utilize its dual form to derive a similar training objective for reward shaping, but essentially employ a different 1-dimensional Euclidean geometry for each goal state and forgo much of the quasimetric structure in V^*.

Metrics and Abstractions in RL. Many works explored learning different state-space geometric structures. In particular, bisimulation metric also relates to optimality, but is defined for single tasks where its metric distance bounds the value difference Castro (2020); Ferns and Precup (2014); Zhang et al. (2020a). Generally speaking, any state-space abstraction can be viewed as a form of distance structure, including state embeddings that are related to value functions (Schaul et al., 2015; Bellemare et al., 2019), transition dynamics (Mahadevan and Maggioni, 2007; Lee et al., 2020), factorized dynamics (Chapter 5; (Fu et al., 2021)), *etc.* While our method also uses

	Environment	QRL	Contrastive RL	MSG (#critic = 64)	MSG + HER (#critic = 64)	MPPI with GT Dynamics	MPPI with QRL Value	Diffuser	Diffuser with QRL Value Guidance	Diffuser with Handcoded Controller
Single-Goal	`large`	**191.52** ± 18.28	81.65 ± 43.79	159.30 ± 49.40	59.26 ± 46.70	5.1	19.32 ± 22.97	7.98 ± 1.54	10.08 ± 2.97	128.13 ± 2.59
	`medium`	**163.59** ± 9.70	10.11 ± 0.99	57.00 ± 17.20	75.77 ± 9.02	10.2	58.06 ± 42.79	9.48 ± 2.21	10.71 ± 4.59	127.64 ± 1.47
	`umaze`	71.72 ± 26.21	95.11 ± 46.23	**101.10** ± 26.30	55.64 ± 31.82	33.2	74.85 ± 21.30	44.03 ± 2.25	42.30 ± 3.87	113.91 ± 3.27
	Average	**142.27**	62.29	105.80	63.56	16.17	50.74	20.50	21.03	123.23
Multi-Goal	`large`	**187.71** ± 7.62	172.64 ± 5.13	—	44.57 ± 25.30	8	37.73 ± 16.67	13.09 ± 1.00	21.26 ± 2.95	146.94 ± 2.50
	`medium`	**150.51** ± 3.77	137.01 ± 6.26	—	99.76 ± 9.83	15.4	56.79 ± 7.66	19.21 ± 3.56	33.39 ± 2.78	119.97 ± 1.22
	`umaze`	**150.60** ± 5.32	142.43 ± 11.99	—	27.90 ± 10.39	41.2	87.49 ± 9.72	56.22 ± 3.90	69.96 ± 2.39	128.53 ± 1.00
	Average	**162.94**	150.69	—	57.41	21.53	60.67	29.51	41.54	131.81

Table 4.2: Planning results on `maze2d`. Scores represent average normalized episode return, where 100 represents comparable performance with the `d4rl` reference handcoded controller. Each column show evaluations of the same method configuration. *E.g.*, we train goal-reaching QRL agents and evaluate them in both single-goal and multi-goal settings. We highlight results that are $\geq 95\%$ of the best method. In both evaluations, QRL agents significantly outperform baselines, including MSG + HER with the ground truth reward function, and MPPI with the ground truth environment dynamics. QRL value functions can also be used with planning methods (MPPI) or trajectory sampling methods (Diffuser), and improve their performances. MPPI with GT Dynamics scores are copied from Janner et al. (2022).

an encoder, our focus is to learn a quasimetric that directly outputs the optimal value V^* to reach any goal, rather than bounding it for a single task.

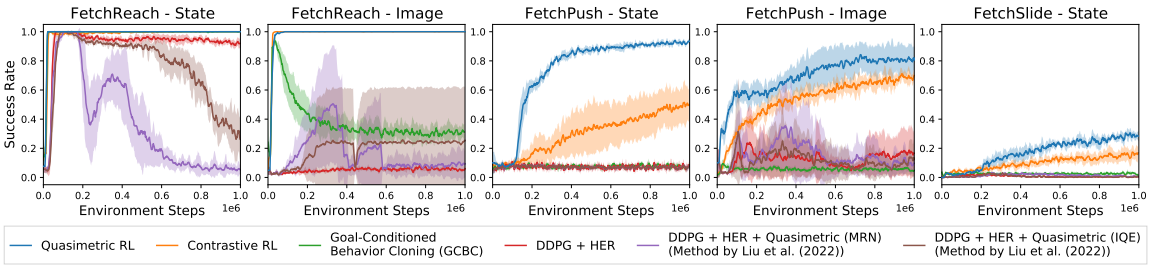

Figure 4-5: Online learning performance on GCRL benchmarks. No method has access to ground truth reward function. QRL learns faster and better than the baseline methods across all environments for both state-based and image-based observations.

4.5 Benchmark Experiments

We evaluate QRL learned policies on standard goal-reaching benchmarks in both offline and online settings. All results show means and standard deviations from 5 seeds. See Appendix C.3 for all experiment details.

4.5.1 Offline Goal-Reaching `d4rl maze2d`

Following Diffuser (Janner et al., 2022), we use `maze2d` environments from `d4rl` (Fu et al., 2020), and evaluate the learned policies' performance in (1) reaching the original fixed single goal defined in `d4rl` as well as (2) reaching goals randomly sampled from the state space. Similar to many offline works (*e.g.*, Contrastive RL (Eysenbach et al., 2022)), we adopt an additional behavior cloning loss for QRL policy optimization in this offline setting.

QRL is a strong method for offline goal-reaching RL. In Table 4.2, QRL significantly outperforms all baselines in both single-goal and multi-goal settings. MSG uses a 64-critic ensemble and is computationally expensive. With only 2 critics, QRL outperforms MSG by 20% on single-goal tasks and 188% on multi-goal tasks. The Diffuser original paper reported results from a handcoded controller with sampled states as input waypoints. We also report planning using Diffuser's sampled actions, which attains a much worse result. Regardless, QRL outperforms both Diffuser settings, without using any external information/controller. Compared with Contrastive RL, QRL again sees a big improvement, especially in the single-goal setting. Since the dataset is not generated by agents trying to reach that goal, the on-policy values estimated by Contrastive RL are likely much worse than the optimal values from QRL.

QRL learned value function improves planning and trajectory sampling methods. Given the high quality of QRL value functions, we can use it to improve other methods. MPPI (Williams et al., 2015) is a model-based planning method. When planning with QRL Q-function, MPPI greatly improves over using ground truth dynamics. We also experiment using QRL Q-function to guide Diffuser's goal-conditioned sampling, and obtain consistent and non-trivial improvements, especially in multi-goal settings.

4.5.2 Online Goal-Reaching RL

Following Contrastive RL (Eysenbach et al., 2022) and Metric Residual Networks (MRN; Liu et al. (2022)), we use the `Fetch` robot environments from the GCRL benchmark (Plappert et al., 2018), where we experiment with both state-based observation as well as image-based observation.

QRL quickly achieves high performance in online RL. Across all environments, QRL exhibits strong sample-efficiency, and learns the task much faster than the alternatives. Only QRL and Contrastive RL learn in the two more challenging state-based settings, `FetchPush` and `FetchSlide`. Compared to Contrastive RL, QRL has 4.9× sample efficiency on state-based `FetchPush` and 2.7× sample efficiency on state-based `FetchSlide`. Strictly speaking, image-based observation only contains partial information of the true state, and thus has stochastic dynamics, which violates the assumption of QRL. However, QRL still shows strong performance on image-based settings, suggesting that QRL can potentially also be useful in other partially observable and/or stochastic environments.

QRL outperforms Q-Learning with quasimetric models in complex environments. Following the approach by Liu et al. (2022), we train standard DDPG (Lillicrap et al., 2015) with relabelling and a quasimetric model Q-function. Essentially, this jointly optimizes a quasimetric Q-function with Q-Learning and a deterministic policy w.r.t. the Q-function. While similar approaches worked well on the simple `MountainCar` environment (Section 4.3.3), they fail miserably here on more complex continuous-control settings, as Q-Learning must estimate *on-policy* Q-function that may not be a quasimetric (Theorem 4.2.1). DDPG with quasimetrics are the slowest to learn on state-based `FetchReach`, and generally are among the least-performing methods. The same pattern holds for two different quasimetric models: IQE and MRN (proposed also by Liu et al. (2022)). In comparison, QRL (which also uses IQE in our implementation) quickly learns the tasks. QRL is more general and scales far better than simply using Q-Learning with quasimetrics.

4.6 Implications

In this work, we introduce a novel RL algorithm, QRL, that utilizes the equivalence between optimal value functions and quasimetrics. In contrast to most RL algorithms that optimize generic function classes, QRL is designed for using *quasimetric models* to parametrize value functions. Combining quasimetric models with an objective that *captures local distances* and *maximally spreads out states* (Section 4.3.1), QRL provably recovers the *optimal* value function (Section 4.3.1) without temporal-difference or policy iteration, making it distinct from many prior approaches.

From thorough analyses on `MountainCar`, we empirically confirm the importance of different components in QRL, and observe that QRL can learn value functions faster and better than alternatives (Section 4.3.3). Our experiments on additional benchmarks echo these findings, showing better control results in both online and offline settings (Section 4.5). QRL can also be used to directly improve other RL methods, and demonstrates strong sample efficiency in online settings.

These QRL results highlight the usefulness of quasimetrics in RL, as well as the benefit of incorporating quasimetric structures into *designing* RL algorithms.

Below we summarize several exciting future directions.

QRL as Representation and World Model Learning. QRL can be also viewed as learning a decision-aware representation (via encoder f) and a latent world model (via latent dynamics T). In this work, for fair comparison, we did not utilize such properties much. However, combining QRL with techniques from these areas (*e.g.*, estimating multi-step return, auxiliary loss training) may yield even stronger performances and/or more general QRL variants (*e.g.*, better support for partial observability and stochasticity).

Quasimetric Structures in Searching and Exploration. QRL results show that quasimetrics can flexibly model distinct environments and greatly boost sample efficiency. Such learned (asymmetrical) state-space distances potentially have further uses in long-range planning and exploration. A *locally distance-preserving* quasimetric

is always a *consistent and admissible* heuristic (Pearl, 1984), which guarantees optimality in search algorithms like A* (Hart et al., 1968). Perhaps such exploration ideas may be incorporated in a quasimetric-aware actor, or even for solvers of general searching and planning problems.

Better Exploration for Structure Learning. In our and most RL works, online exploration is done via noisy actions from the learned policy. Arguably, if an agent is learning the structure of the environment, it should instead smartly and actively probe the environment to improve its current estimate. Consider QRL as an example. If current quasimetric estimate $d_\theta(s_0, s_1)$ is small but no short path connecting s_0 to s_1 was observed, the agent should test if they are actually close w.r.t. the dynamics. Additionally, one may use uncertainty/errors in learned quasimetric distances/dynamics to derive new intrinsic exploration methods. Such advanced exploration may speed up learning the geometric structures of the world, and thus better generalist agents.

More Quasimetric-Aware RL Algorithms. To our best knowledge, QRL is the first RL method designed for quasimetric models. We hope the strong performance of QRL can inspire more work on RL algorithms that are aware of quasimetric and/or other geometric structures in RL.

Chapter 5

Denoised MDPs: Learning Latent World Models Better Than the World Itself

Quasimetric Reinforcement Learning (QRL) solves a given decision-making task (Chapter 4), but it is only a half of the problem. The arguably more important half is to formulate which decision-making task to solve.

The ability to separate signal from noise, and reason with clean abstractions, is critical to intelligence. With this ability, humans can efficiently perform real world tasks without considering all possible nuisance factors. How can artificial agents do the same? What kind of information can agents safely discard as noises? In this chapter, we categorize information out in the wild into four types based on controllability and relation with reward, and formulate useful information as that which is both *controllable* and *reward-relevant*. This framework clarifies the kinds information removed by various prior work on representation learning in reinforcement learning (RL), and leads to our proposed approach of learning a *Denoised MDP* in a *representation space* that explicitly factors out certain noise distractors. Instead of trying to solve the noisy real world, decision-making w.r.t. this *Denoised MDP* is thus much simpler, more efficient and also more effective. Extensive experiments on variants of DeepMind Control Suite and `RoboDesk` demonstrate superior performance

of our denoised world model over using raw observations alone, and over prior works, across policy optimization control tasks as well as the non-control task of joint position regression.

This chapter is based on published work:

1. *Denoised MDPs: Learning World Models Better Than the World Itself* with co-authors Simon S. Du, Antonio Torralba, Phillip Isola, Amy Zhang, and Yuandong Tian at the International Conference on Machine Learning (ICML) 2022 (Wang et al., 2022).

5.1 Introduction

The real world provides us a plethora of information, from microscopic physical interactions to abstracted semantic signals such as the latest COVID-19 news. Fortunately, processing each and every signal is unnecessary (and also impossible). In fact, any particular reasoning or decision often only relies on a small portion of information.

Imagine waking up and wanting to embrace some sunlight. As you open the curtain, a nearby resting bird is scared away and you are pleasantly met with a beautiful sunny day. Far away, a jet plane is slowly flying across the sky.

This may seem a simple activity, but in fact highlights four distinct types of information (see Figure 5-1), with respect to the goal of letting in as much sunlight as possible:

- **Controllable and reward-relevant**: curtain, influenced by actions and affecting incoming sunlight;
- **Controllable and reward-irrelevant**: bird, influenced by actions but not affecting sunlight;
- **Uncontrollable and reward-relevant**: weather, independent with actions but affecting sunlight;
- **Uncontrollable and reward-irrelevant**: plane, independent with both actions and the sunlight.

Our optimal actions towards the goal, however, only in fact depend on information

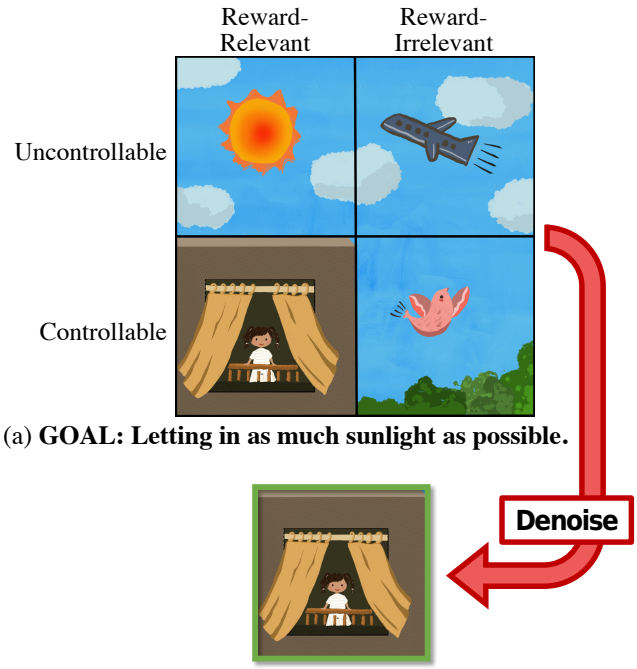

(a) **GOAL: Letting in as much sunlight as possible.**

(b) Optimal control only relies on information that is **both controllable and reward-relevant**. Good world models should ignore other factors as noisy distractors.

Figure 5-1: **Illustrative example: (a)** Four distinct kinds of information in the scenario described in Section 5.1, where the person desires to increase the amount of sunlight let into the room. Their opening of the curtain scares away the bird. **(b)** A denoised world model only includes a small subset of all information.

that is **controllable and reward-relevant**, and the three other kinds of information are merely *noise distractors*. Indeed, no matter how much natural sunlight there is outside, or how the plane and the bird move, the best plan is always to open up the curtain.

When performing a particular task, we humans barely think about the other three types of information, and usually only plan on how our actions affect information that is **controllable and reward-relevant**. Our mental model is an abstract and condensed version of the real world that is actually *better* suited for the task.

The notion of better model/data is ubiquitous in data science and machine learning. Algorithms rarely perform well on raw noisy real data. The common approach is to perform data cleaning and feature engineering, where we manually select the useful signals based on prior knowledge and/or heuristics. Years of research have identified ways to extract good features for computer vision (Lowe, 1999; Donahue et al., 2014), natural language processing (Elman, 1990; Mikolov et al., 2013), reinforcement learning (RL) (Mahadevan and Maggioni, 2007; Bellemare et al., 2019), *etc.* Similarly, system identification aligns real observation with a predefined set of abstract signals/states. Yet for tasks in the wild (in the general form of (partially observable) Markov Decision Processes), there can be very little prior knowledge of the optimal set of signals. In this work, we ask: can we infer and extract these signals automatically, in the form of a learned world model?

The general idea of a mental world model have long been under active research in philosophy and social science (Craik, 1952; Dennett, 1975), cognitive science, where an intuitive physics model is hypothesized to be core in our planning capabilities (Spelke and Kinzler, 2007), and in reinforcement learning, where various methods investigate state abstractions for faster and better learning (Sutton, 1991, 1981).

In this work, we explore this idea within the context of machine learning and reinforcement learning, where we aim to make concrete the different types of information in the wild, and automatically learn a world model that removes noise distractors and is beneficial for both control (*i.e.*, policy optimization) and non-control tasks. Toward this goal, our contributions are

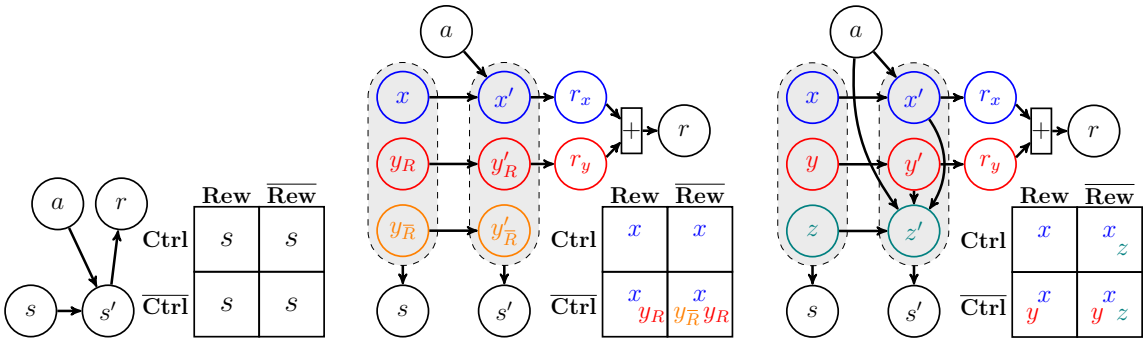

(a) Transition without useful structure. s may contain any type of information.

(b) Transition that factorizes out uncontrollable information in $y_{\overline{R}}$ and y_R.

(c) Transition that factorizes out uncontrollable y and reward-irrelevant z.

Figure 5-2: MDP transition structures consisting of dynamics and reward functions. Unlike the regular structure of **(a)**, **(b, c)** factorized (yet still general) structures inherently separate information into controllable (**Ctrl**) versus uncontrollable ($\overline{\textbf{Ctrl}}$), and reward-relevant (**Rew**) versus reward-irrelevant ($\overline{\textbf{Rew}}$). Presence of a variable in a cell means *possible* containing of respective information. *E.g.*, in **(c)**, z can only contain reward-irrelevant information. In **(b, c)**, the x dynamics form an MDP with less noise and sufficient for optimal planning. Our Denoised MDP (see Section 5.3) is based on these two factorizations.

- We categorize information into four distinct kinds as in Figure 5-1, and review prior approaches under this framework (Section 5.2).
- Based on the above framework, we propose Denoised MDPs, a method for learning world models with certain distractors removed (Section 5.3).
- Through experiments in DeepMind Control Suite and `RoboDesk` environments, we demonstrate superior performance of policies learned our method, across many distinct types of noise distractors (Sections 5.5.1 and 5.5.2).
- We show that Denoised MDP is also beneficial beyond control objectives, improving the supervised task of robot joint position regression (Section 5.5.1).

5.2 Different Types of Information in the Wild

In Section 5.1, we illustrated the four types of information available in the wild w.r.t. a task. Here we make these notions more concrete, and relate them to existing works.

For generality, we consider tasks in the form of Markov Decision Processes (MDPs),

described in the usual manner: $\mathcal{M} \triangleq (\mathcal{S}, \mathcal{A}, R, P, p_{s_0})$ (Puterman, 1994), where $\mathcal{S}$ is the state space, $\mathcal{A}$ is the action space, $R\colon \mathcal{S} \to \Delta([0, r_{\mathsf{max}}])$ defines the reward random variable $R(s')$ received for arriving at state $s' \in \mathcal{S}$, $P\colon \mathcal{S} \times \mathcal{A} \to \Delta(\mathcal{S})$ is the transition dynamics, and $p_{s_0} \in \Delta(\mathcal{S})$ defines the distribution of initial state. We use $\Delta(A)$ to denote the set of all distributions over A. P and R define the most important components of a MDP: the transition dynamics $\mathbb{P}[s' \mid s, a]$ and the reward function $\mathbb{P}[r \mid s']$. Usually, the objective is to find a policy $\pi\colon \mathcal{S} \to \Delta(\mathcal{A})$ acting based on current state, that maximizes the expected cumulative (discounted) reward.

Indeed, MDPs provide a general formulation that encompasses many tasks. In fact, the entire real world may be viewed as an MDP with a rich state/observation space $\mathcal{S}$ that contains all possible information/signal. For an artificial agent to successfully perform real world tasks, it must be able to process observations that are incredibly rich and high-dimensional, such as visual or audio signals.

We characterize different types of information in such observations by considering two intuitive notions of "noisy and irrelevant" signals: (1) uncontrollable information and (2) reward-irrelevant information. Such factors can often be ignored without affecting optimal control, and are referred to as *noise distractors*.

To understand their roles in MDPs, we study different formulations of the transition dynamics and reward functions, and show how different structures naturally leads to decompositions that may help identify such distractors. Removing these distractors can thus *transform the original noisy MDP to a clean denoised one*, to be used in downstream tasks.

For starters, the most generic transition model in Figure 5-2a has little to no structure. The state s can contain both the useful signals and noise distractors. Therefore, it is not directly useful for extracting important information.

5.2.1 Controllability

Intuitively, if something is not controllable, an agent might be able to do well without considering it. Yet it is not enough to only require some variable to be unaffected by actions (*e.g.*, wind directions should not be ignored while sailing). Instead, we focus

on factors that simply evolve on their own, without influencing or being influenced by others.

Not all such information can be safely ignored, as they still may affect reward (*e.g.*, traffic lights when driving). Fortunately, in the usual objective of maximizing expected return, we can ignore ones that only additively affect reward.

Concretely, if an MDP transition can be represented in the form of Figure 5-2b, we say variables $y_{\overline{R}}$ and y_R are *uncontrollable* information, as they evolve independently of actions and do not affect *controllable* x. Here y_R (additively) affects reward, but can be ignored. One can safely discard both $y_{\overline{R}}$ and y_R as *noise distractors*. Operating with the compressed MDP of only x is sufficient for optimal control.

5.2.2 Reward-Relevance

Among controllable information, there can still be some that is completely unrelated to reward. In Figure 5-1, the bird is affected by the opening curtain, but is irrelevant to the task of letting in sunlight. In such cases, the information can be safely discarded, as it does not affect the objective.

If an MDP transition can be represented in the form of Figure 5-2c, we say z is *reward-irrelevant* because it evolves by potentially using everything (*i.e.*, all latent variables and actions), but crucially *does not affect anything but itself*.

Similar to uncontrollable information, z (and y) is a *noise distractor* that can be discarded. The compressed MDP of only x contains all signals needed for optimal control.

5.2.3 Which Information Do Existing Methods Learn?

In RL, many prior work have explored state abstractions in some form. Here we cast several representative ones under the framework described above, and show which kinds of information they learn to remove, summarized in Figure 5-3, together with our proposed method (explained in Section 5.3). Below we discuss each prior work in detail.

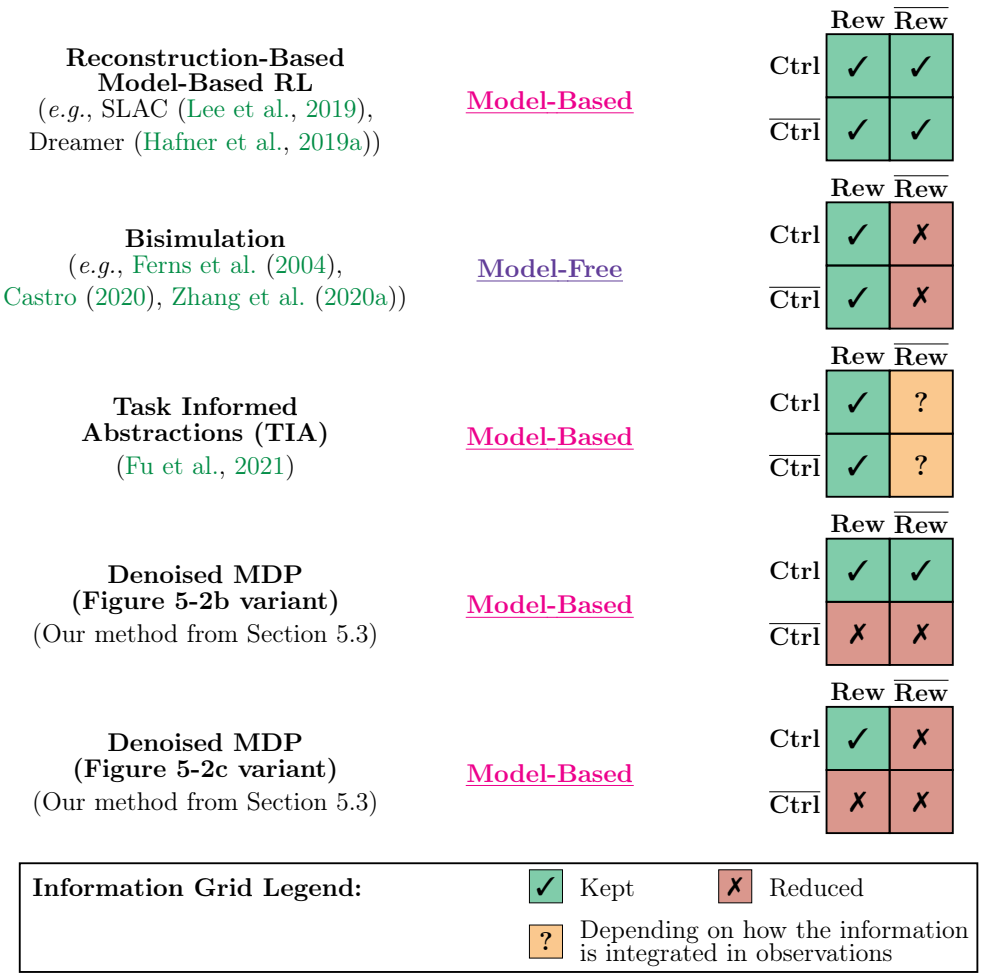

Figure 5-3: Categorization of information learned and removed by various methods with distinct formulations.

Reconstruction-Based Model-Based RL. Many model-based RL methods learn via reconstruction from a single latent code, often as a result of a variational formulation (Hafner et al., 2019a,b; Lee et al., 2019). The latent code must try to compress all information present in the observation, and necessarily contains all types of information.

Bisimulation. Bisimulation defines a state abstraction where states aggregated together must have the same expected return and transition dynamics up to the abstraction (Givan et al., 2003), and is known to optimally ignore reward-irrelevant information (Ferns et al., 2004). While its continuous version, bisimilation metric, is gaining popularity, learning them is computationally difficult (Modi et al., 2020). Even with many additional assumptions, it is generally only possible to learn an on-policy

variant that loses the above guarantee (Castro, 2020; Zhang et al., 2020a).

Task Informed Abstractions (TIA). TIA (Fu et al., 2021) extends Dreamer by modelling two independent latent MDPs, representing signal and noise. The noise latent is enforced to be independent with reward and reconstruct the observation as well as possible. Reconstructions from each latent are composed together using an inferred mask in pixel-space, to form the full reconstruction for the reconstruction loss. Because of its special structure, TIA can remove *reward-irrelevant* noise distractors that are present via pixel-wise composing two images from *independent* processes (*e.g.*, agent moving on a noisy background), but not general ones (*e.g.*, a shaky camera affecting both the agent and the noisy background).

Predictive Information, Data Augmentation, etc. Another set of researches learn state representation that only contains information useful for predicting future states (*e.g.*, CPC (Oord et al., 2018) and PI-SAC (Lee et al., 2020)) or augmented views of the current state (*e.g.*, CURL (Laskin et al., 2020a)). These methods *do not guarantee* removal of any of the three redundant piece of information identified above. Non-i.i.d. noises (*e.g.*, people moving in background) are predictive of future and may be kept by CPC and PI-SAC. The performance of augmentation-based methods can critically rely on specific types of augmentation used and relevance to the tasks. As we show in experiments (see Section 5.5), indeed they struggle to handle certain noise types.

5.2.4 Possible Extensions to Further Factorizations

The above framework is sufficient for characterizing most prior work and related tasks, and can also be readily extended with further factorized transition structures. *E.g.*, if an independent process confounds a signal process and a noise process, fitting the Figure 5-2c structure must group all three processes into x (to properly model the dependencies). However, a further factorization shows that only considering the signal and the confounding processes is theoretically sufficient for control. We leave such

extensions as future work.

5.3 Denoised MDPs

Figures 5-2b and 5-2c show two special MDP structures that automatically identify certain information that can be ignored, leaving x as the useful information (which also forms an MDP). This suggests a naïve approach: directly fitting such structures to collected trajectories, and then extract x.

However, the same MDP dynamics and rewards can be decomposed as Figures 5-2b and 5-2c in many different ways. In the extreme case, x may even contain all information in the raw state s, and such extraction may not help at all. Instead, we desire a fit with the *minimal* x, defined as being least informative of s (so that removal of the other latent variables discards the most information possible). Concretely, we aim for a fit with least $I(\{x_t\}_{t=1}^T; \{s_t\}_{t=1}^T \mid \{a_t\}_{t=1}^T)$, the mutual information x contains about s over T steps. Then from this fit, we can extract a minimal *Denoised MDP* of only x. For notation simplicity, we use bold symbols to denote variable sequences, and thus write, *e.g.*, $I(\boldsymbol{x}; \boldsymbol{s} \mid \boldsymbol{a})$.

Practically, we consider regularizing model-fitting with $I(\boldsymbol{x}; \boldsymbol{s} \mid \boldsymbol{a})$. As we show below, this amounts to a modification to the well-established variational objective (Hafner et al., 2019a). The resulting method is easy-to-implement yet effective, enabling clean removal of various noise distractors the original formulation cannot handle (see Section 5.5).

We instantiate this idea with the structure in Figure 5-2c. The Figure 5-2b formulation can be obtained by simply removing the z components and viewing y as combined y_R and $y_{\overline{R}}$.

The transition structure is modeled with components:

$$
\begin{aligned}
p_\theta^{(x_t)} &\triangleq p_\theta(x_t \mid x_{t-1}, a) && (x \text{ dynamics}) \\
p_\theta(r_x \mid x_t) && (x \text{ reward}) \\
p_\theta^{(y_t)} &\triangleq p_\theta(y_{t-1} \mid y_{t-1}) && (y \text{ dynamics}) \\
p_\theta(r_y \mid y_t) && (y \text{ reward}) \\
p_\theta^{(z_t)} &\triangleq p_\theta(z_t \mid x_t, y_t, z_{t-1}, a) && (z \text{ dynamics}) \\
p_\theta(s_t \mid x_t, y_t, z_t). && (\text{obs. emission})
\end{aligned}
$$

Consider training data in the form of trajectory segments $\boldsymbol{s}, \boldsymbol{a}, \boldsymbol{r}$ sampled from some data distribution p_{data} (*e.g.*, stored agent experiences from a replay buffer). We perform model learning by minimizing the negative log likelihood:

$$
\mathcal{L}_{\mathsf{MLE}}(\theta) \triangleq -\mathbb{E}_{\boldsymbol{s},\boldsymbol{a},\boldsymbol{r}\sim p_{\mathsf{data}}}\big[\log p_\theta\left(\boldsymbol{s}, \boldsymbol{r} \mid \boldsymbol{a}\right)\big].
$$

To obtain a tractable form, we jointly learn three variational posterior components (*i.e.*, encoders):

$$
\begin{aligned}
q_\psi^{(x_t)} &\triangleq q_\psi(x_t \mid x_{t-1}, y_{t-1}, z_{t-1}, s_t, a_t) && (x \text{ posterior}) \\
q_\psi^{(y_t)} &\triangleq q_\psi(y_t \mid x_{t-1}, y_{t-1}, z_{t-1}, s_t, a_t) && (y \text{ posterior}) \\
q_\psi^{(z_t)} &\triangleq q_\psi(z_t \mid x_t, y_t, s_t, a_t), && (z \text{ posterior})
\end{aligned}
$$

whose product defines the posterior $q_\psi(\boldsymbol{x}, \boldsymbol{y}, \boldsymbol{z} \mid \boldsymbol{s}, \boldsymbol{a})$[1]. We choose this factorized form based on the forward (prior) model structure of Figure 5-2c.

Then, the model can be optimized w.r.t. the standard variational bound on log

[1]Following Dreamer (Hafner et al., 2019a), we define posterior of first-step latents $q_\psi(x_1, y_1, z_1 \mid s_1) \triangleq q_\psi(\cdot, \cdot, \cdot \mid \mathbf{0}, \mathbf{0}, \mathbf{0}, s_1, \mathbf{0})$, where $\mathbf{0}$ is the all zeros vector of appropriate size.

likelihood:

$$\mathcal{L}_{\mathsf{MLE}}(\theta) = \min_{\psi} \mathop{\mathbb{E}}_{\boldsymbol{s},\boldsymbol{a},\boldsymbol{r}} \mathop{\mathbb{E}}_{\substack{\boldsymbol{x},\boldsymbol{y},\boldsymbol{z}\sim \\ q_\psi(\cdot\mid \boldsymbol{s},\boldsymbol{a},\boldsymbol{r})}} \Bigg[\underbrace{-\log p_\theta(\boldsymbol{s},\boldsymbol{r} \mid \boldsymbol{x},\boldsymbol{y},\boldsymbol{z},\boldsymbol{a})}_{\triangleq \mathcal{L}_{\mathsf{recon}}(\theta,\psi)} + \underbrace{\sum_{t=1}^{T} D_{\mathsf{KL}}\big(q_\psi^{(x_t)} \,\|\, p_\theta^{(x_t)}\big)}_{\triangleq \mathcal{L}_{\mathsf{KL}\text{-}x}(\theta,\psi)} + \underbrace{\sum_{t=1}^{T} D_{\mathsf{KL}}\big(q_\psi^{(y_t)} \,\|\, p_\theta^{(y_t)}\big)}_{\triangleq \mathcal{L}_{\mathsf{KL}\text{-}y}(\theta,\psi)} + \underbrace{\sum_{t=1}^{T} D_{\mathsf{KL}}\big(q_\psi^{(z_t)} \,\|\, p_\theta^{(z_t)}\big)}_{\triangleq \mathcal{L}_{\mathsf{KL}\text{-}z}(\theta,\psi)} \Bigg], \tag{5.1}$$

where equality is attained by optimal q_ψ that is compatible with p_θ, *i.e.*, q_ψ is the exact posterior of p_θ.

The mutual information regularizer $I(\boldsymbol{x};\boldsymbol{s} \mid \boldsymbol{a})$, using a variational formulation, can be written as

$$I(\boldsymbol{x};\boldsymbol{s} \mid \boldsymbol{a}) = \min_{\theta} \mathcal{L}_{\mathsf{KL}\text{-}x}(\theta,\psi), \tag{5.2}$$

with equality attained when q_ψ and p_θ are compatible. The appendix describes this derivation in detail.

Therefore, for a regularizer weight of $c \geq 0$, we can optimize Equations (5.1) and (5.2) together as

$$\begin{aligned} &\min_{\theta} \mathcal{L}_{\mathsf{MLE}}(\theta) + c \cdot I(\boldsymbol{x};\boldsymbol{s} \mid \boldsymbol{a}) \\ &= \min_{\theta,\psi} \mathcal{L}_{\mathsf{recon}}(\theta,\psi) + (1+c) \cdot \mathcal{L}_{\mathsf{KL}\text{-}x}(\theta,\psi) \\ &\qquad + \mathcal{L}_{\mathsf{KL}\text{-}y}(\theta,\psi) + \mathcal{L}_{\mathsf{KL}\text{-}z}(\theta,\psi). \end{aligned} \tag{5.3}$$

Recall that we fit to the true MDP with the structure of Figure 5-2c, which inherently guarantees all useful information in the x latent variable. As the regularizer ensures learning the *minimal* x latents, the learned model extracts an MDP of condensed useful information with $\mathcal{X}$ as the *denoised* state space, $p_\theta(x' \mid x, a)$ as the transition dynamics, $p_\theta(r_x \mid x')$ as the reward function. This MDP is called the *Denoised MDP*, as it discards the noise distractors contained in y and z. Additionally, we also obtain

Algorithm 1 Denoised MDP

Input: Model p_θ. Posterior encoder q_ψ. Policy $\pi\colon \mathcal{X} \to \Delta(\mathcal{A})$.
Policy optimization algorithm PI-OPT.
Output: Denoised MDP of x in p_θ. Encoder q_ψ. Policy π.

while training **do**
  // Exploration
  Collect trajectories with π acting on q_ψ encoded outputs
  // Model learning
  Sample a batch of $(\boldsymbol{s}, \boldsymbol{a}, \boldsymbol{r})$ segments from reply buffer
  Train p_θ and q_ψ with Equation (5.4) on $(\boldsymbol{s}, \boldsymbol{a}, \boldsymbol{r})$
  // Policy optimization
  Sample $\boldsymbol{x} \sim q_\psi(\boldsymbol{x} \mid \boldsymbol{s}, \boldsymbol{a})$
  Compute $\overline{\boldsymbol{r}_{\boldsymbol{x}}} = \mathbb{E}\left[p_\theta(\boldsymbol{r}_{\boldsymbol{x}} \mid \boldsymbol{x})\right]$
  Train π by running PI-OPT on $(\boldsymbol{x}, \boldsymbol{a}, \overline{\boldsymbol{r}_{\boldsymbol{x}}})$
end while

$q_\psi(\boldsymbol{x} \mid \boldsymbol{s}, \boldsymbol{a})$ as the encoder mapping from raw noisy observation s to the denoised x.

A loss variant for improved stability. When using a large $c \geq 0$ (*e.g.* when the environment is expected to be very noisy), Equation (5.3) contains to a term with a large weight. Thus Equation (5.3) often requires learning rates to be tuned for different c. To avoid this, we use the following loss form that empirically has better training stability and does not require tuning learning rates w.r.t. other hyperparameters:

$$\min_{\theta,\psi} \mathcal{L}_{\mathsf{recon}} + \alpha \cdot \left(\mathcal{L}_{\mathsf{KL}\text{-}x} + \beta\mathcal{L}_{\mathsf{KL}\text{-}y} + \beta\mathcal{L}_{\mathsf{KL}\text{-}z}\right), \tag{5.4}$$

where θ, ψ in arguments are omitted, and the hyperparameters are $\alpha > 0$ and $0 < \beta \leq 1$. Here β is bounded, where $\beta = 1$ represents no regularization. α is also generally small and simply chosen according to the state-space dimensionality (see the appendix; $\alpha \in \{1, 2\}$ in our experiments). This form is justified from the observation that in practice we use isotropic Gaussians with fixed variance to parameterize the distributions of observation $p_\theta(s \mid \dots)$ and reward $p_\theta(r \mid \dots)$, where scaling log likelihoods is essentially changing the variance hyperparameter. Thus, Equation (5.4) is effectively a scaled Equation (5.3) with different variance hyperparameters.

Online algorithm with policy optimization. The model fitting objective of Equation (5.4) can be used in various settings, *e.g.*, offline over a collected trajectory dataset. Without assuming existing data, we explore an online setting, where the training process iteratively performs (1) exploration, (2) model-fitting, and (3) policy optimization, as shown in Algorithm 1. The policy $\pi\colon \mathcal{X} \to \Delta(\mathcal{A})$ soley operates on the Denoised MDP of x, which has all information sufficient for control. For policy optimization, the learned posterior encoder $q_\psi(\boldsymbol{x} \mid \boldsymbol{s}, \boldsymbol{a})$ is used to extract $\boldsymbol{x}$ information from the raw trajectory $(\boldsymbol{s}, \boldsymbol{a}, \boldsymbol{r})$, obtaining transition sequences in $\mathcal{X}$ space. Paired with the $p_\theta(\boldsymbol{r}_{\boldsymbol{x}} \mid \boldsymbol{x})$ rewards, we obtain $(\boldsymbol{x}, \boldsymbol{a}, \boldsymbol{r}_{\boldsymbol{x}})$ as trajectories collected from the Denoised MDP on x. Any general-purpose MDP policy optimization algorithm may be employed on these data, such as Stochastic Actor-Critic (SAC) (Haarnoja et al., 2018). We can also utilize the learned *differentiable* Denoised MDP, *e.g.*, optimizing policy by backpropagating through additional roll-outs from the model, as is done in Dreamer.

While presented in the fully observable setting, Denoised MDP readily handles partial observability without extra changes. In the appendix, we discuss this point in details, and provide a guideline for choosing hyperparameters α, β.

5.4 Related Work

Model-Based Learning for Control jointly learns a world model and a policy. Such methods often enjoy good sample efficiency on RL tasks with rich observations. Some formulations rely on strong assumptions, *e.g.*, deterministic transition in DeepMDP (Gelada et al., 2019) and bilinear transition in FLAMBE (Agarwal et al., 2020). Most general-setting methods use a reconstruction-based objective (Hafner et al., 2019b; Kim et al., 2020; Ha and Schmidhuber, 2018; Lee et al., 2019). Among them, Dreamer (Hafner et al., 2019a) trains world models with a variational formulation and optimizes policies by backpropagating through latent-space rollouts. It has proven effective across a variety of environments with image observations. However, such reconstruction-based approaches can struggle with the presence of noise distractors.

TIA (Fu et al., 2021) partially addresses this limitation (see Section 5.2.3) but can not handle general distractors, unlike our method.

Representation Learning and Reinforcement Learning. Our work automates selecting useful signals from noisy MDPs by learning denoised world models, and can be viewed as an approach for learning general representations (Donahue et al., 2014; Mikolov et al., 2013; He et al., 2019; Huh et al., 2016). In model-free RL, various methods learn state embeddings that are related to value functions (Schaul et al., 2015; Bellemare et al., 2019), transition dynamics (Mahadevan and Maggioni, 2007; Lee et al., 2020), recent action (Pathak et al., 2017), bisimulation structure (Ferns et al., 2004; Castro, 2020; Zhang et al., 2020a), data augmentations (Laskin et al., 2020a) *etc.* While most methods adopt self-predictive auxiliary losses to learn representations (Ni et al., 2024), our work primarily uses the factorized *world model* structure to extract good abstractions. Recently, Eysenbach et al. (2021) proposes a regularizer similar to ours but for the different purpose of robust compressed policies. The theoretical work by Efroni et al. (2021) is closest to our setting but concerns a more restricted set of distractors (ones both uncontrollable and reward-irrelevant). Unlike Denoised MDP, their proposed algorithm is largely impractical and does not produce a generative model of observations (*i.e.*, no decoder).

System Identification. Our work is related to system identification, where an algorithm infers from real world an abstract state among a predefined limited state space, *e.g.*, pose estimation (Rıza Alp Güler, 2018; Yen-Chen et al., 2021) and material estimation (Hahn et al., 2019). Such results are useful for robotic manipulation (Manuelli et al., 2019), image generation (Gu et al., 2019), *etc.* Our setting is not limited to a predefined abstract state space, but instead focuses on automatic discovery of such valuable states.

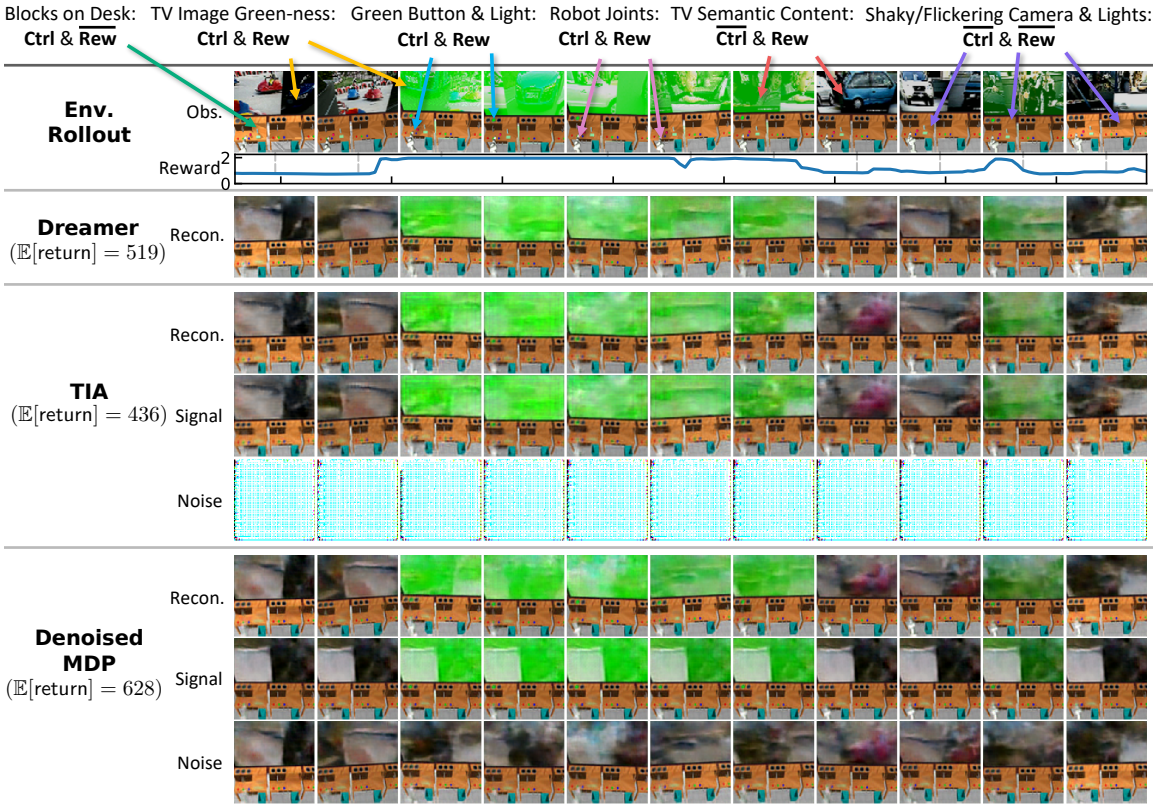

Figure 5-4: Visualization of learned models for `RoboDesk` by using decoders to reconstruct from encoded latents. For TIA and Denoised MDP, we visualize how they separate information as signal versus noise. In each row, *what changes over frames is the information modeled by the corresponding latent component. E.g.*, in the bottom row, only the TV content, camera pose and lighting condition change, so Denoised MDP considers these factors as noises, while modelling the TV hue as signal. See our website for clearer video visualizations.

5.5 Experiments

In this section, we contrast our method with existing approaches on environments with image observations and many distinct types of noise distractors. Our experiments are designed to include a variety of noise distractors and to confirm our analysis on various methods in Section 5.2.3.

Environments. We choose DeepMind Control (DMC) Suite (Tunyasuvunakool et al., 2020) (Section 5.5.2) and `RoboDesk` (Kannan et al., 2021) (Section 5.5.1) with image observations, where we explore adding various noise distractors. Information types in all evaluated environments are categorized in Table D.1 of the appendix. Tasks include control (policy optimization) and a non-control task of regressing robot

joint position from `RoboDesk` image observations.

Methods. We compare not only model-based RL methods, but also model-free algorithms and general representation learning approaches, when the task is suited:

- **Model Learning**: Denoised MDP (our method), Dreamer (Hafner et al., 2019a), and TIA (Fu et al., 2021);
- **Model-Free**: DBC (Zhang et al., 2020a), CURL (Laskin et al., 2020a), PI-SAC (Lee et al., 2020) (without data augmentation for a fair comparison of its core predictive information regularization against other non-augmenting methods), and SAC on true state-space (Haarnoja et al., 2018) (instead of using image observations, this is roughly an "upper bound");
- **General Image Representation Learning for Non-Control Tasks**: Contrastive learning with the Alignment+Uniformity loss (Wang and Isola, 2020) (a form of contrastive loss theoretically and empirically comparable to the popular InfoNCE loss (Oord et al., 2018)).

Model-learning methods can be used in combination with any policy optimization algorithm. For a complete comparison for general control, we compare the models trained with these two policy learning choices: (1) backpropagating via the learned dynamics and (2) SAC on the learned latent space (which roughly recovers SLAC (Lee et al., 2019) when used with an unfactorized model such as Dreamer).

Most compared methods do not apply data augmentations, which is known to strongly boost performance (Yarats et al., 2021; Laskin et al., 2020b). Therefore, for a fair comparison, we run PI-SAC *without augmentation* to highlight its main contribution—representation of only predictive information.

All results are aggregated from 5 runs, showing mean and standard deviations. The appendix contains more details, hyperparameter studies, and additional results. Our website presents videos showing clearer video visualizations.

For Denoised MDP, we use the Figure 5-2b variant. Empirically, the Figure 5-2c variant leads to longer training time and sometimes inferior performance (perhaps

due to having to optimize extra components and fit a more complex model). The appendix provides a comparison between them.

5.5.1 RoboDesk with Various Noise Distractors

We augment RoboDesk environment with many noise distractors that models realistic noises (*e.g.*, flickering lights and shaky camera). Most importantly, we place a large TV in the scene, which plays natural RGB videos. A green button on the desk controls the TV's hue (and a light on the desk). The agent is tasked with using this button to shift the TV to a green hue. Its reward is directly affected by how green the TV image is. The first row of Figure 5-4 shows a trajectory with various distractors annotated. All four types of information exist (see Table D.1), with the controllable and reward-relevant information being the robot arm, the green button, the light on the desk, and the TV screen green-ness.

Only Denoised MDP learns a clean denoised model. Using learned decoders, Figure 5-4 visualizes how the models captures various information. As expected, Dreamer model captures all information. TIA also fails to separate any noise distractors out (the Noise row fails to capture anything), likely due to its limited ability to model different noises. In contrast, Denoised MDP cleanly extracts all controllable and reward-relevant information as signals—the Signal row only *tracks changes* in robot arms, green button and light, and the TV screen green-ness. All other information is modeled as noises (see the Noise row). We recommend viewing video visualizations on our website.

Denoised models improve policy learning. Figure 5-4 also shows the total episode return achieved by policies learned with each of the three models, where the cleanest model from Denoised MDP achieves the best performance. Aggregating over 5 runs, the complete comparison in Figure 5-5 shows that Denoised MDP (with backpropagating via dynamics) generally outperforms all baselines, suggesting that its clean models are helpful for control.

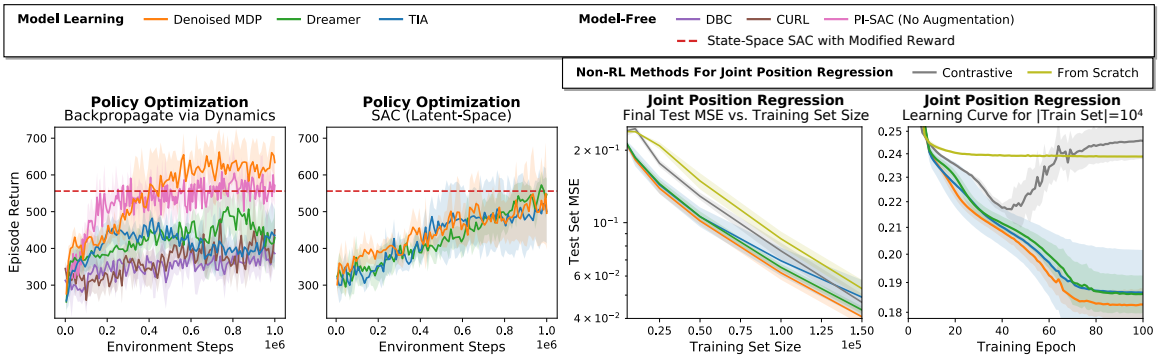

Figure 5-5: Policy optimization on RoboDesk. We give state-space SAC a less noisy reward so it can learn (see appendix).

Figure 5-6: Performance of finetuning various encoders to infer joint position from RoboDesk image observation.

	Policy Learning: Backprop via Dynamics			**Policy Learning:** SAC (Latent-Space)			DBC	PI-SAC (No Aug.)	CURL (Use Aug.)	State-Space SAC (Upper Bound)
	Denoised MDP	TIA	Dreamer	Denoised MDP	TIA	Dreamer				
Noiseless	801.4 ± 96.6	769.7 ± 97.1	**848.6 ± 137.1**	**587.1 ± 98.7**	480.2 ± 125.5	575.4 ± 146.2	297.4 ± 72.5	246.4 ± 56.6	417.3 ± 183.2	910.3 ± 28.2
Video Background	**597.7 ± 117.8**	407.1 ± 225.4	227.8 ± 102.7	309.8 ± 153.0	**318.1 ± 123.7**	188.7 ± 78.2	188.0 ± 67.4	131.7 ± 20.1	478.0 ± 113.5	910.3 ± 28.2
Video Background + Noisy Sensor	**563.1 ± 143.0**	261.2 ± 200.4	212.4 ± 89.7	**288.2 ± 123.4**	197.3 ± 124.2	218.2 ± 58.1	79.9 ± 36.0	152.5 ± 12.6	354.3 ± 119.9	919.8 ± 100.7
Video Background + Camera Jittering	**254.1 ± 114.2**	151.7 ± 160.5	98.6 ± 27.7	**186.8 ± 47.7**	126.5 ± 125.6	105.2 ± 33.8	68.0 ± 38.4	91.6 ± 7.6	**390.4 ± 64.9**	910.3 ± 28.2

Table 5.1: DMC policy optimization results. For each variant, we aggregate performance across three tasks (Cheetah Run, Walker Walk, Reacher Easy) by averaging. Denoised MDP performs well across all four variants with distinct noise types. **Bold numbers** show the best model-learning result for specific policy learning choices, or the best overall result. On **Camera Jittering**, Denoised MDP greatly outperforms all other methods except for CURL, which potentially benefits from its specific data augmentation choice (random crop) on this task, and can be seen as using extra information (*i.e.*, knowing the noise distractor form). In fact, Denoised MDP is the only method that consistently performs well across all tasks and noise variants, which can be seen from the full results in the appendix.

Denoised models benefit non-control tasks. We evaluate the learned representations on a *supervised non-control* task—regressing the robot arm joint position from observed images. Using various pretrained encoders, we finetune on a labeled training set, and measure mean squared error (MSE) on a heldout test set. In addition to RL methods, we compare encoders learned via general contrastive learning on the same amount of data. In Figure 5-6, Denoised MDP representations lead to best converged solutions across a wide range of training set sizes, achieve faster training, and avoid overfitting when the training set is small. DBC, CURL and PI-SAC encoders, which take in stacked frames, are not directly comparable and thus absent from Figure 5-6. In the appendix, we compare them with running Denoised MDP encoder on each frame

and concatenating the output features, where Denoised MDP handily outperforms both DBC and CURL by a large margin.

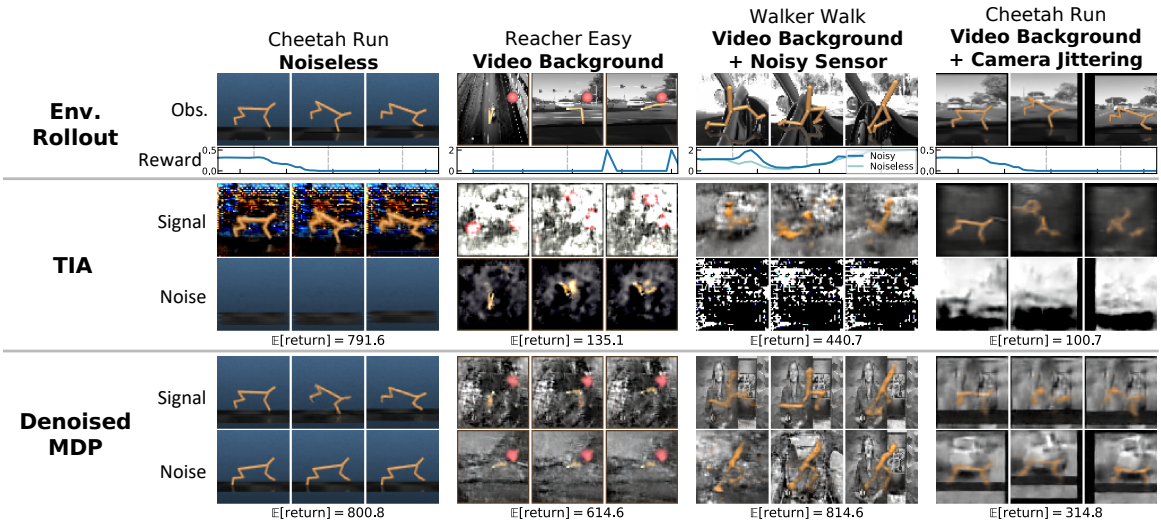

Figure 5-7: Visualization of the different DMC variants and factorizations learned by TIA and Denoised MDP. *E.g.*, bottom Noise row often shows a static agent but varying background, indicating that only the background is modeled as noises in Denoised MDP. Visualizations of full reconstructions are in appendix. See our website for clearer video visualizations.

5.5.2 DeepMind Control Suite (DMC)

To evaluate a diverse set of noise distractors, we consider four variants for each DMC task (see Figure 5-7 top row):

- **Noiseless**: Original environment without distractors.
- **Video Background**: Replacing noiseless background with natural videos (Zhang et al., 2020a) ($\overline{\textbf{Ctrl}} + \overline{\textbf{Rew}}$).
- **Video Background + Sensor Noise**: Imperfect sensors sensitive to intensity of a background patch ($\overline{\textbf{Ctrl}} + \textbf{Rew}$).
- **Video Background + Camera Jittering**: Shifting the observation by a smooth random walk ($\overline{\textbf{Ctrl}} + \overline{\textbf{Rew}}$).

Denoised MDP consistently removes noise distractors. In Figure 5-7, TIA struggles to learn clean separations in many settings. Consistent with analysis in Section 5.2.3, it cannot handle **Sensor Noise** or **Camera Jittering**, as the former is reward-relevant noise that it cannot model, and the latter (although reward-irrelevant) cannot be represented by masking. Furthermore, it fails on Reacher Easy with **Video Background**, where the reward is given by the distance between the agent and a randomly-located ball. TIA encourages its noise latent to be independent of reward, but does not prevent it from capturing the controllable agent. These failures lead to either TIA trying to model everything as useful signals, or a badly-fit model (*e.g.*, wrong agent pose in the last column). In contrast, Denoised MDP separates out noise in all cases, obtaining a clean and accurate MDP (its Signal rows only have the agent moving).

Denoised models consistently improve policy learning. We evaluate the learned policies in Table 5.1, where results are aggregated by the noise distractor variant. Other methods, while sometimes handling certain noise types well, struggle to deal with all four distinct variants. TIA, as expected, greatly underperforms Denoised MDP under **Noisy Sensor** or **Camera Jittering**. CURL, whose augmentation choice potentially helps handling **Camera Jittering**, underperforms in other three variants. In contrast, Denoised MDP policies *consistently* perform well for all noisy variants and also the noiseless setting, regardless of the policy optimizer.

Model-based approaches have a significant lead over the model-free ones, as seen from the DBC results in Table 5.1 and the well-known fact that direct model-free learning on raw image observations usually fails (Laskin et al., 2020b; Kostrikov et al., 2020; Yarats et al., 2021). These results show that learning in a world model is useful, and that learning in a denoised world model is even better.

5.6 Implications

In this work we explore learning denoised and compressed world models in the presence of environment noises.

As a step towards better understanding of such noises, we categorize of information in the wild into four types (Section 5.2). This provides a framework to contrast and understand various methods, highlighting where they may be successful and where they will suffer (Section 5.2.3). Insights gained this way empirically agrees with findings from extensive experiments (Section 5.5). It can potentially assist better algorithm design and analysis of new MDP representation methods, as we have done in designing Denoised MDP (Section 5.3). We believe that this categorization will be a useful framework for investigation on learning under noises, revealing not just the (conceptual) success scenarios, but also the failure scenarios at the same time. Additionally, the framework can be readily extended with more sophisticated factorizations (Section 5.2.4), which can lead to corresponding Denoised MDP variants and/or new algorithms.

Based on the framework, our proposed Denoised MDP novelly can remove *all* noise distractors that are *uncontrollable or reward-irrelevant*, in distinction to prior works. Empirically, it effectively identifies and removes a diverse set of noise types, obtaining clean denoised world models (Section 5.5). It may serve as an important step towards efficient learning of general tasks in the noisy real world. Our experiments also highlight benefits of cleanly denoised world models on both standard control tasks as well as non-control tasks. The success in both cases highlights the general usefulness of such models. Given the generality of MDPs, this opens up the possibility of casting non-RL tasks as MDPs and automatically learn representations from denoised world models, as an alternative to manual feature engineering.

Part III

The Platonic Representation Hypothesis

Chapter 6

The Platonic Representation Hypothesis

This section is partially based on published work:

1. *The Platonic Representation Hypothesis* with co-authors Minyoung Huh, Brian Cheung, and Phillip Isola at the International Conference on Machine Learning (ICML) 2024 (Huh et al., 2024).

We argue that representations in AI models, particularly deep networks, are converging. First, we survey many examples of convergence in the literature: over time and across multiple domains, the ways by which different neural networks represent data are becoming more aligned. Next, we demonstrate convergence across data modalities: as vision models and language models get larger, they measure distance between datapoints in a more and more alike way. We hypothesize that this convergence is driving toward a shared statistical model of reality, akin to Plato's concept of an ideal reality. We term such a representation the *platonic representation* and discuss several possible selective pressures toward it. Finally, we discuss the implications of these trends, their limitations, and counterexamples to our analysis.

6.1 Introduction

AI systems are rapidly evolving into highly multifunctional entities. For example, whereas in the past we had special-purpose solutions for different language processing tasks (*e.g.*, sentiment analysis, parsing, dialogue), modern large language models (LLMs) are competent at all these tasks using a single set of weights (Srivastava et al., 2022). Unified systems are also being built across data modalities: instead of using a different architecture for processing images versus text, recent models, such as GPT4-V (OpenAI, 2023), Gemini (Google, 2023), and LLaVA (Liu et al., 2023), handle both modalities with a combined architecture. More and more systems are built off of general-purpose pretrained backbones, sometimes called foundation models (Bommasani et al., 2021), that support a large range of tasks, including robotics (Driess et al., 2023; Brohan et al., 2023), bioinformatics (Ma et al., 2024), and healthcare (Steinberg et al., 2021). In short, AI systems are becoming increasingly homogeneous in both their architectures and their capabilities.

This chapter explores one aspect of this trend: representational convergence. We argue that there is a growing similarity in how datapoints are represented in different neural network models. This similarity spans across different model architectures, training objectives, and even data modalities.

What has led to this convergence? Will it continue? And ultimately, where does it end?

Our central hypothesis, stated above in Figure 6-1, is that there is indeed an endpoint to this convergence and a principle that drives it: different models are all trying to arrive at a *representation of reality*, meaning a representation of the joint distribution over events in the world that generate the data we observe. Figure 6-1 conveys this hypothesis: there exists a real world (labeled Z), which we measure with various sensors, such as the camera shown to the left (X). Other *projections* of these measurements, such as the textual description shown, can be produced from the first set of measurements or mediated by some other set of measurements, *e.g.*,

The Platonic Representation Hypothesis

Neural networks, trained with different objectives on different data and modalities, are converging to a shared statistical model of reality in their representation spaces.

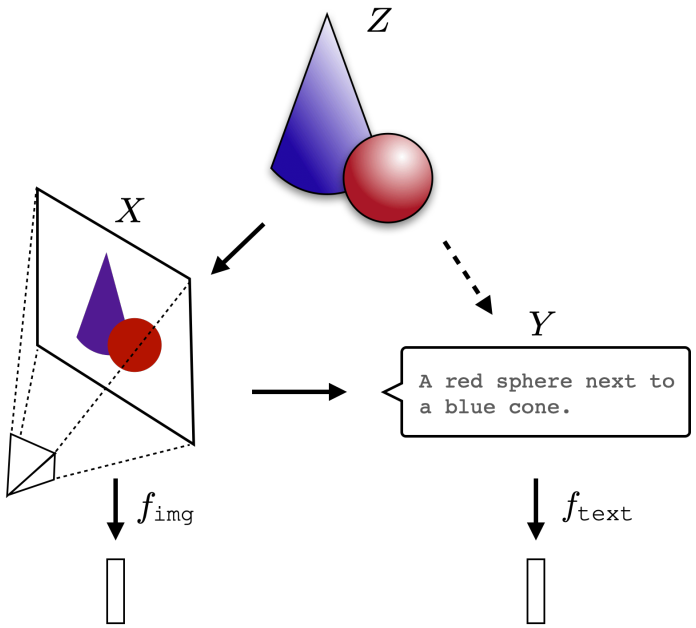

Figure 6-1: **The Platonic Representation Hypothesis:** Images (X) and text (Y) are projections of a common underlying reality (Z). We conjecture that representation learning algorithms will converge on a shared representation of Z, and scaling model size, as well as data and task diversity, drives this convergence.

touch or other camera views (dotted arrow from X to Y)[1]. Representation learning algorithms find vector embeddings that statistically model the various measurements and projections. The resulting vector embeddings are all derived from the underlying reality in Z and thereby become aligned. As models are trained on more data and for more tasks, they require representations that capture more and more information about Z, and hence alignment toward Z increases toward a convergent point as a function of scale.

We call this converged hypothetical representation the "platonic representation" in reference to Plato's Allegory of the Cave (Plato, c. 375 BC), and his idea of an

[1]Touch could convey the shapes in this example but not the colors. This is an important limitation to our hypothesis that we discuss at several points in the chapter: different sensors and views might capture different information, which may limit their potential to converge to identical representations.

ideal reality that underlies our sensations. The training data for our algorithms are shadows on the cave wall, yet, we hypothesize, models are recovering ever better representations of the actual world outside the cave. This idea is not unique to Plato; our hypothesis is also related to the notion of "convergent realism" (Newton-Smith, 1981; Putnam, 1982; Doppelt, 2007; Hardin and Rosenberg, 1982) in the philosophy of science (*i.e.*, that science is converging on truth), and to many arguments that have been put forth in the representation learning literature (*e.g.*, Tian et al. (2020b); Zimmermann et al. (2021); Richens and Everitt (2024); Cao and Yamins (2024)).

Also closely related to our hypothesis is the "Anna Karenina scenario" described by Bansal et al. (2021), referring to the possibility that all well-performing neural nets represent the world in the same way. We discuss the evidence they give for this possibility in Section 6.2[2]. The platonic representation hypothesis refers to the situation where we are in an Anna Karenina scenario *and* the "happy representation" that is converged upon is one that reflects a statistical model of the underlying reality. We discuss the potential nature of this statistical model in more detail in Section 6.4.

6.2 Representations are converging

Preliminaries We restrict our attention to representations that are *vector embeddings*. We characterize such a representation by the similarity structure it induces, referred to as its kernel. Kernels are commonly used to assess representations (Kornblith et al., 2019; Klabunde et al., 2023); this can be justified by the fact that they capture the relative structures among data samples, which are also the learning signal for many machine learning algorithms (Aronszajn, 1950; Smola and Schölkopf, 1998). Following prior literature, we define *representational alignment* as a measure of the similarity of the similarity structures induced by two representations, *i.e.*, a similarity metric over kernels. We give the mathematical definition of these concepts below:

- A **representation** is a function $f\colon \mathcal{X} \to \mathbb{R}^n$ that assigns a feature vector to each

[2]Borrowed from Tolstoy (1877), similar analogies have been made in other domains, such as the "Anna Karenina principle" popularized by Diamond (1998) to explain animal domestication.

input in some data domain $\mathcal{X}$.

- A **kernel**, $K\colon \mathcal{X}\times\mathcal{X} \to \mathbb{R}$, characterizes how a representation measures distance/similarity between datapoints. $K(x_i, x_j) = \langle f(x_i), f(x_j)\rangle$, where $\langle \cdot\,, \cdot \rangle$ denotes inner product, $x_i, x_j \in \mathcal{X}$ and $K \in \mathcal{K}$.
- A **kernel-alignment metric**, $m\colon \mathcal{K}\times\mathcal{K} \to \mathbb{R}$, measures the similarity between two kernels, *i.e.*, how similar is the distance measure induced by one representation to the distance measure induced by another. Examples include Centered Kernel Distance (CKA) (Kornblith et al., 2019), SVCCA (Raghu et al., 2017), and nearest-neighbor metrics (Klabunde et al., 2023).

In our experiments, we use a *mutual nearest-neighbor metric* that measures the mean intersection of the k-nearest neighbor sets induced by two kernels, K_1 and K_2, normalized by k. This metric is a variant of those proposed in Park et al. (2024), Klabunde et al. (2023) and Oron et al. (2017). See Appendix E.1 for the exact definition and Appendix E.2 for comparisons with alternative alignment metrics.

Next, we explore several ways in which representations are converging. First, we argue that different neural networks are converging to aligned representations. Then, we show that this continues to hold across modalities, where image embeddings in vision models align with text embeddings in language models.

6.2.1 Different models, with different architectures and objectives, can have aligned representations

One indication of representational convergence is the rising number of systems built on top of pre-trained foundation models. These models are becoming standard backbones across a growing spectrum of tasks. Their versatility across numerous applications implies a level of universality in the way they represent data.

While this trend implies convergence toward a relatively small set of foundation models, it does not imply that *different* foundation models will arrive at the same representation. Yet that is what has been observed by several recent papers.

Lenc and Vedaldi (2015) conducted one such study, in which they measured

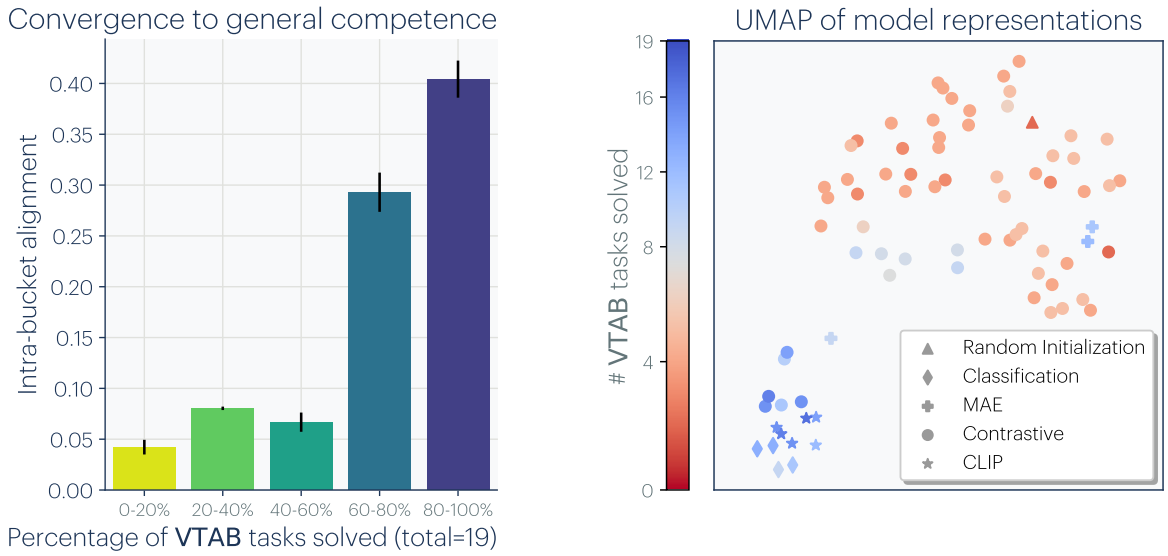

Figure 6-2: **VISION models converge as COMPETENCE increases:** We measure alignment among 78 models using mutual nearest-neighbors on Places-365 (Zhou et al., 2017), and evaluate their performance on downstream tasks from the Visual Task Adaptation Benchmark (VTAB; Zhai et al. (2019)). **LEFT:** Models that solve more VTAB tasks tend to be more aligned with each other. Error bars show standard error. **RIGHT:** We use UMAP to embed *models* into a 2D space, based on $\text{distance} \triangleq -\log(\text{alignment})$. More competent and general models (blue) have more similar representations.

representational similarity through a technique called *model stitching*. Given two models, f and g, each composed of multiple layers ($f = f_1 \circ \cdots \circ f_n$, $g = g_1 \circ \cdots \circ g_m$), an intermediate representation from f is integrated into g via a learned affine stitching layer h, resulting in a new stitched model $F = f_1 \circ \cdots \circ f_k \circ h \circ g_{k+1} \circ \cdots \circ g_m$. If F has good performance, it indicates that f and g have compatible representations at layer k, up to the transform h.

In their study, Lenc and Vedaldi (2015) made two notable findings: (1) A vision model trained on ImageNet (Russakovsky et al., 2015) can be aligned with a model trained on Places-365 (Zhou et al., 2017) while maintaining good performance; (2) The early layers of these convolutional networks are more interchangeable than later layers. The first finding illustrates a level of data independence where distinct image datasets lead to similar representations. The second finding agrees with extensive research that oriented Gabor-like filters are common in both artificial and biological vision systems. This suggests a convergence to a similar initial layer of representation

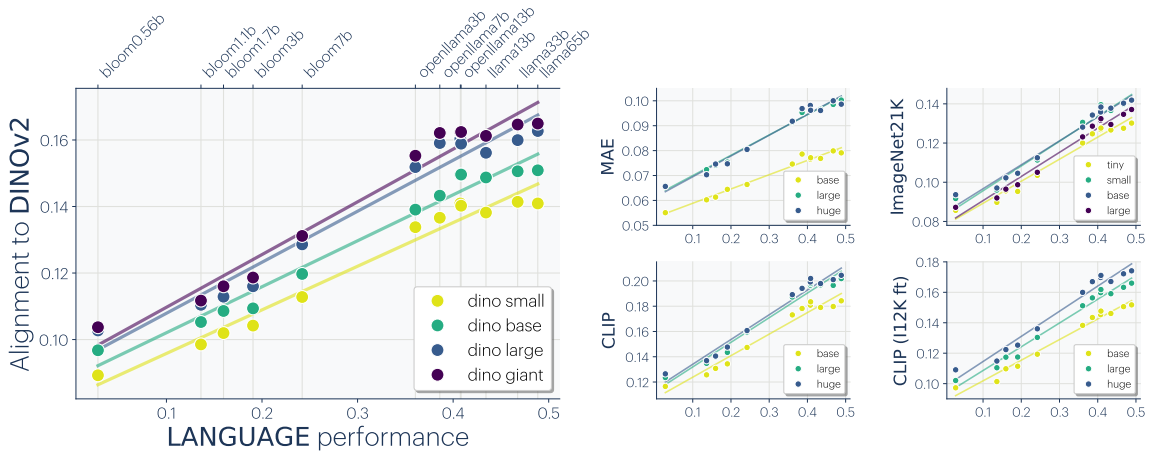

Figure 6-3: **LANGUAGE and VISION models align:** We measure alignment using mutual nearest-neighbor on the Wikipedia caption dataset (WIT) (Srinivasan et al., 2021). The x-axis is the language model performance measured over 4M tokens from the OpenWebText dataset (Gokaslan and Cohen, 2019) (see Appendix E.2 for plots with model names). We measure performance using $1 - \texttt{bits-per-byte}$, where `bits-per-byte` normalizes the cross-entropy by the total bytes in the input text string. The results show a linear relationship between language-vision alignment and language modeling score, where a general trend is that more capable language models align better with more capable vision models. We find that CLIP models, which are trained with explicit language supervision, exhibit a higher level of alignment. However, this alignment decreases after being fine-tuned on ImageNet classification (labeled CLIP (I12K ft)).

across various neural network architectures (Olshausen and Field, 1996; **?**). Bansal et al. (2021) expanded on the idea of model stitching, showing that models trained using self-supervised objectives align closely with their supervised counterparts.

Moschella et al. (2022) further demonstrated the feasibility of "zero-shot" model stitching without learning a stitching layer. Despite the fact that different text models were trained on different modalities, they found that the models often embed data in remarkably similar ways. In particular, they considered the kernel K defined by learned representations and showed that K serves as a bridge between models, allowing an encoder trained in one language, like English, to work effectively with a decoder in another, like French.

Dravid et al. (2023) extended this idea to individual neurons, and found "Rosetta Neurons" that are activated by the same pattern across a range of vision models. Such neurons form a common dictionary independently discovered by all models.

6.2.2 Alignment increases with scale and performance

Kornblith et al. (2019) and Roeder et al. (2021) observed model alignment not only exists but also increases with model scale and dataset size. On CIFAR-10 classification, Krizhevsky et al. (2009) found that larger models exhibit greater alignment with each other compared to smaller ones. Theoretically, Balestriero and Baraniuk (2018) showed that models with similar outputs (*e.g.*, as a result of having high performance) also have similar internal activations. With the continuing trend of models scaling up, this suggests model alignment will increase over time – we might expect that the next generation of bigger, better models will be even more aligned with each other.

We expand upon this observation by evaluating the transfer performance of 78 vision models. These models were trained with varying architectures, training objectives, and datasets (detailed in Appendix E.3.1). In Figure 6-2 (left), we bin these models based on their average transfer performance on the VTAB dataset (Zhai et al., 2019), and then measure the average kernel alignment of the models within each bin. The results indicate that models with high transfer performance form a tightly clustered set of representations, while models with weak performance have more variable representations. We further visualize this structure with UMAP (McInnes et al., 2018) over models representation in Figure 6-2 (right). This suggests that models that are competent all represent data in a similar way. Echoing Bansal et al. (2021) and Tolstoy (1877), we might say: all strong models are alike, each weak model is weak in its own way.

The discussion so far indicates that various models are aligning toward a unified representation. But does the convergence extend to model weights? While models with different architectures might not have compatible weight spaces, there exists ample evidence that models with the same architecture will often converge to the same basin of weights (Nagarajan and Kolter, 2019; Garipov et al., 2018; Lubana et al., 2023). This holds even for models with different initializations, up to permutations over weight space (Ainsworth et al., 2022). Because of this, it is possible to merge separately trained models of the same architecture, and achieve some of the capabilities

of all models in the mixture (Stoica et al., 2023; Jordan et al., 2022; Wortsman et al., 2022).

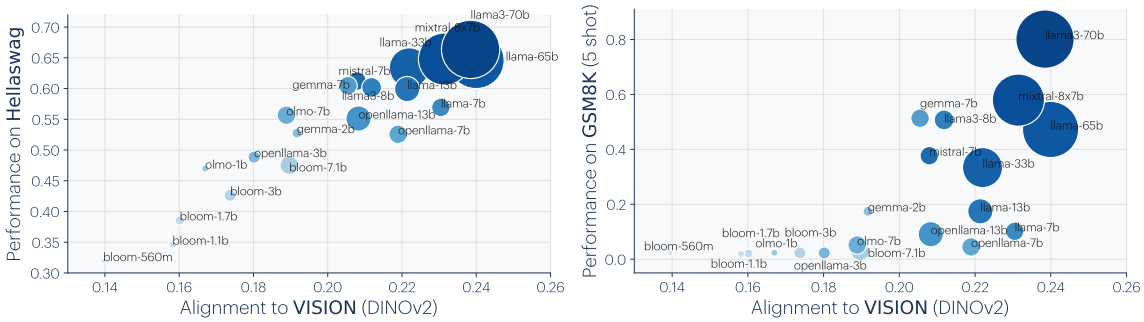

Figure 6-4: **Alignment predicts downstream performance:** We visualize correlation between LLM alignment score to DINOv2 (Oquab et al., 2023) and downstream task performance on Hellaswag (common-sense) (Zellers et al., 2019) and GSM8K (math) (Cobbe et al., 2021). LLMs are plotted with radii proportional to the size of the model, and color-coded by their rank order in language modeling scores ($1 - \texttt{bits-per-byte}$). We observe that models aligned more closely with vision also show better performance on downstream language tasks. For Hellaswag, there is a linear relationship with alignment score, while GSM8K exhibits an "emergence"-esque trend.

6.2.3 Representations are converging across modalities

Do models trained on different data modalities also converge? Several works indicate that the answer is *yes*.

Merullo et al. (2022) extended model stitching to the cross-modal setting, finding that a single linear projection is sufficient to stitch a vision model to an LLM and achieve good performance on visual question answering and image captioning. Koh et al. (2023) showed that linear stitching can also work in the opposite direction, aligning text inputs to visual outputs. In fact, many recent language-vision models stitch pre-trained language and vision models together. For example, LLaVA (Liu et al., 2023) demonstrated state-of-the-art results by projecting visual features into a language model with a 2-layer MLP.

Other works show further kinds of evidence of cross-modal synergy. OpenAI (2023) found that jointly training a language model with a vision model improves performance on language tasks, compared to training the language model on its own. Sorscher et al. (2022) show a setting in which word embeddings of visual concept names can

be isometrically mapped to image embeddings for those same concepts. In work concurrent to ours, Maniparambil et al. (2024) show well-trained vision encoders on large datasets exhibit high semantic similarity with language encoders regardless of the training paradigm (supervised, self-supervised, or language-supervised). Sharma et al. (2024) probed the visual knowledge of LLMs trained *only* on language data, by converting images into code that an LLM can process. They found that LLMs have rich knowledge of visual structures, to the extent that decent visual representations can be trained on images generated solely by querying an LLM to produce code and rendering the response. In visual generation, LLMs show abilities to augment captions with visual structures (*e.g.*, bounding boxes) and improve generation quality (Betker et al., 2023; Lian et al., 2023a,b; Wu et al., 2023). Over other modalities, Ngo and Kim (2024) showed auditory models are also roughly aligned with LLMs up to a linear transformation, and Ng et al. (2023) demonstrated the effectiveness of using pre-trained LLMs for facial motion prediction.

We set out to address these claims in a broader scope to determine whether models are indeed learning an increasingly modality-agnostic representation of the world. We sampled a variety of models trained either solely on vision or solely on language, and compared their representations as they became larger and more competent over many tasks.

In Figure 6-3, we assess alignment between a suite of language models and vision models. So far we have only defined alignment for two kernels defined over the same input space. To measure cross-modal alignment, we use paired datasets to bridge the two modalities. For vision and text, we use the Wikipedia captions dataset $\{(x_i, y_i)\}_i$ (Srinivasan et al., 2021), composed of images from Wikipedia (x_i) and their corresponding captions (y_i). We then measure alignment between a language model $f_{\texttt{text}}$ and a vision model $f_{\texttt{img}}$ as the alignment of the two following kernels:

$$K_{\texttt{img}}(i, j) = \langle f_{\texttt{img}}(x_i), f_{\texttt{img}}(x_j) \rangle \tag{6.1}$$

$$K_{\texttt{text}}(i, j) = \langle f_{\texttt{text}}(y_i), f_{\texttt{text}}(y_j) \rangle. \tag{6.2}$$

Using this analysis, we find that the better an LLM is at language modeling, the more it tends to aligns with vision models, as shown in Figure 6-3. The converse effect also holds: the better a vision models is, the more it tends to align with LLMs. See Appendix E.3.2 for more details.

6.2.4 Models are increasingly aligning to brains

Neural networks also show substantial alignment with biological representations in the brain (Yamins et al., 2014). This commonality may be due to similarities in the task and data constraints both systems are confronted with. Even though the mediums may differ – silicon transistors versus biological neurons – the fundamental problem faced by brains and machines is the same: efficiently extracting and understanding the underlying structure in images, text, sounds, *etc.* (Barlow et al., 1961; Olshausen and Field, 1997). Sorscher et al. (2022) developed a theoretical framework for how the efficient extraction of novel concepts occurs for both the human visual system and deep networks. The tasks that the human visual system has been honed to perform through evolution – like segmentation, detection, and whole-image classification – are also the ones that we train our neural nets to perform. Yamins et al. (2014) went as far as to title their work in the spirit that performance over such tasks implies brain alignment. Antonello and Huth (2024) posited that it is less the particular task and more the generality of the representations that explain their alignment with biological representations. Further, Conwell et al. (2022) showed that training data plays a large role in alignment. Psychophysical studies have also shown agreement between how humans perceive visual similarity and how models do, even when the models are trained on tasks, such as self-supervised prediction, that are seemingly unrelated to mimicking human perception (Zhang et al., 2018).

6.2.5 Does alignment predict downstream performance?

If models are converging towards a more accurate representation of reality, we expect that alignment should correspond to improved performance on downstream tasks.

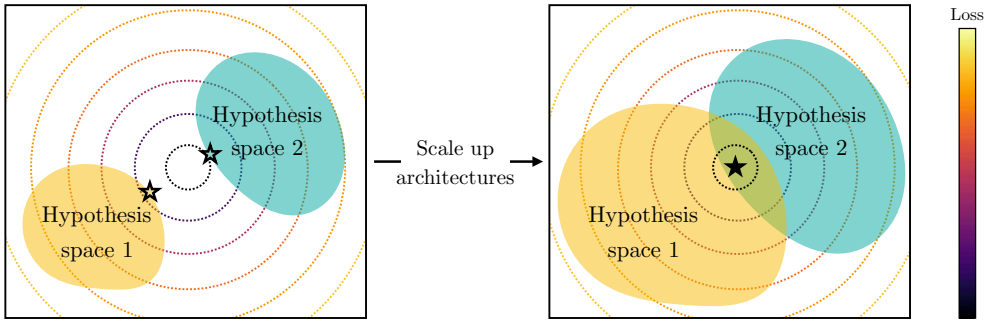

Figure 6-5: **The Capacity Hypothesis:** If an optimal representation exists in function space, larger hypothesis spaces are more likely to cover it. **LEFT:** Two small models might not cover the optimum and thus find *different* solutions (marked by outlined ☆). **RIGHT:** As the models become larger, they cover the optimum and converge to the same solution (marked by filled ★).

Figure 6-4 supports this hypothesis by demonstrating improved performance on commonsense reasoning (Hellaswag; Zellers et al. (2019)) and mathematical problem solving (GSM8K; Cobbe et al. (2021)) as alignment improves.

6.3 Why are representations converging?

Modern machine learning models are generally trained to minimize the empirical risk with possible implicit and/or explicit regularization:

$$\underbrace{f^*}_{\text{trained model}} = \arg\min_{f \in \underbrace{\mathcal{F}}_{\text{function class}}} \mathbb{E}_{x \sim \text{dataset}} [\underbrace{\mathcal{L}}_{\text{training objective}}(f, x)] + \underbrace{\mathcal{R}}_{\text{regularization}}(f)$$

In the following sections, we lay out how each colored component in this optimization process potentially plays a role in facilitating representational convergence.

6.3.1 Convergence via Task Generality

Each training datapoint and objective (task) places an additional constraint on the model. As data and tasks scale, the volume of representations that satisfy these constraints must proportionately grow smaller, as visualized in Figure 6-6 and stated below:

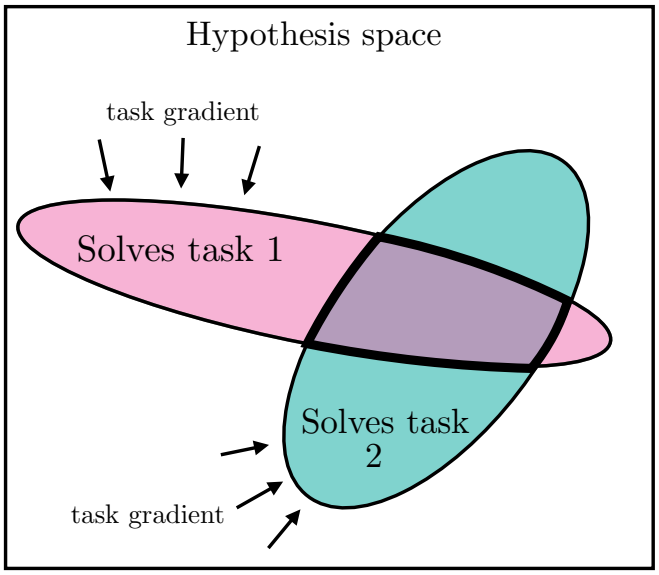

Figure 6-6: **The Multitask Scaling Hypothesis:** Models trained with an increasing number of tasks are subjected to pressure to learn a representation that can solve all the tasks.

The Multitask Scaling Hypothesis

There are fewer representations that are competent for N tasks than there are for $M < N$ tasks. As we train more general models that solve more tasks at once, we should expect fewer possible solutions.

This has been previously termed as the Contravariance principle by Cao and Yamins (2024), which states that the set of solutions to an easy goal is large, while the set of solutions to a challenging goal is comparatively smaller. Moreover, we argue that this narrower solution set also generalizes better. As data scales, models that optimize the empirical risk $\mathbb{E}_{x\sim\text{dataset}}[\mathcal{L}(f,x)]$ also improve on the population risk $\mathbb{E}_{x\sim\text{reality}}[\mathcal{L}(f,x)]$, and become better at capturing statistical structures of the true data generating process (reality).

Recent work has demonstrated a power law relationship between data scale and model performance (Hestness et al., 2017). This implies that with enough data (*e.g.*, consisting of the entire internet and all offline scientific measurements) one ought to converge to a very small solution set with irreducible error – the inherent epistemic

uncertainty of the world. As more models are trained on internet-scale data, the set of solutions that satisfies all data constraints must become relatively small.

In addition to data-scaling, many modern representation learning objectives $\mathcal{L}(f, x)$ directly optimize for multi-task solving. Contrastive learning finds a distance structure over data samples that optimizes many classification tasks (Chapter 2; Arora et al. (2019c); Tian et al. (2020c)). Masked Autoencoders (He et al., 2021) optimize randomly sampled reconstruction tasks. In fact, autoregressive language modeling can also be seen as optimizing a diverse set of tasks (Radford et al., 2019). Such multi-task objectives may be more effective than single-task ones (*e.g.*, ImageNet classification) due to the fact that they impose more task constraints on the representation, leading to a smaller and higher-quality solution space (Chen et al., 2020a; He et al., 2020; Radford et al., 2017, 2019).

6.3.2 Convergence via Model Capacity

Suppose there is a globally optimal representation for standard learning objectives. Then, under sufficient data, *scaling* a model (*i.e.*, using larger function classes $\mathcal{F}$), as well as improved optimization, should be more effective at finding better approximations to this optimum, as illustrated in Figure 6-5. With the same training objective, larger models, even of different architectures, will thus tend to converge toward this optimum. When different training objectives share similar minimizers, larger models are better at finding these minimizers, and will train to similar solutions over the training tasks. We summarize this hypothesis as follows:

The Capacity Hypothesis

Bigger models are more likely to converge to a shared representation than smaller models.

6.3.3 Convergence via Simplicity Bias

Arriving at the same mapping on the *training data* does not prohibit the models from developing distinct internal representations. It is not unreasonable to posit that the representations used to detect a dog in a 1M parameter model could be quite different than that used by a 1B parameter model. What would stop a billion-parameter (and counting) model from learning an overly complicated and distinct representation? One key factor might be simplicity bias:

The Simplicity Bias Hypothesis

Deep networks are biased toward finding simple fits to the data, and the bigger the model, the stronger the bias. Therefore, as models get bigger, we should expect convergence to a smaller solution space.

Such simplicity bias could be coming from explicit regularization $\mathcal{R}(f)$ commonly used in deep learning (*e.g.*, weight decay and dropout). However, even in the absence of external influences, deep networks naturally adhere to Occam's razor, implicitly favoring simple solutions that fit the data (Solomonoff, 1964; Gunasekar et al., 2018; Arora et al., 2019a; Valle-Perez et al., 2019; Huh et al., 2023; Dingle et al., 2018; Goldblum et al., 2023). Figure 6-7 visualizes how simplicity bias can drive convergence.

6.4 What representation are we converging to?

By now, we hope to have convinced the reader that task and data pressures, combined with increasing model capacity, can lead to convergence. We next turn our attention to *what* exactly is the endpoint of all this convergence.

Our central hypothesis, stated in Figure 6-1, is that the representation we are converging toward is a statistical model of the underlying reality that generates our observations. Consistent with the multitask scaling hypothesis, such a representation would naturally be useful toward many tasks (or at least toward any task grounded in

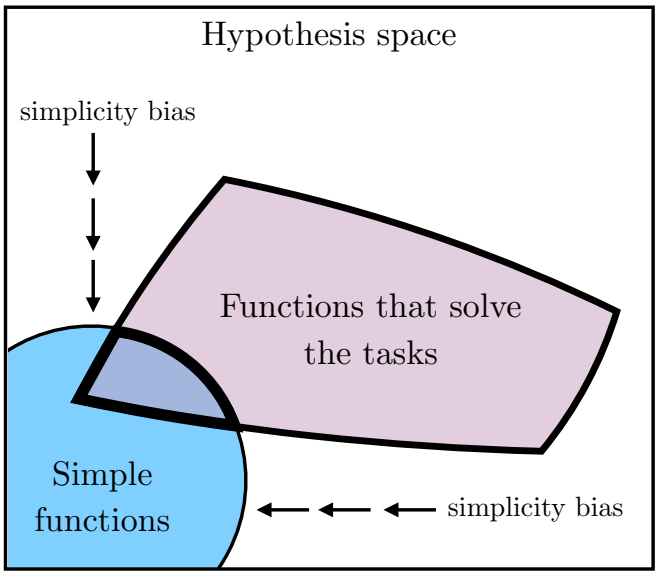

Figure 6-7: **The Simplicity Bias Hypothesis:** Larger models have larger coverage of all possible ways to fit the same data. However, the implicit simplicity biases of deep networks encourage larger models to find the simplest of these solutions.

reality). Additionally, this representation might be relatively simple, assuming that scientists are correct in suggesting that the fundamental laws of nature are indeed simple functions (Gell-Mann, 1995), in line with the simplicity bias hypothesis.

But what exactly do we mean by "a statistical model of the underlying reality." In this section, we formalize one definition with concrete mathematical statements. *Importantly*, this section should be read as just one concrete candidate for the form of the platonic representation; other candidates could be arrived at from other modeling assumptions.

6.4.1 An idealized world

We consider a world that works as follows, consistent with the cartoon in Figure 6-1. The world consists of a sequence of T discrete events, denoted as $\mathbf{Z} \triangleq [z_1, \ldots, z_T]$, sampled from some unknown distribution $\mathbb{P}(\mathbf{Z})$. Each event can be observed in various ways. An observation is a bijective, deterministic function $\texttt{obs} : \mathcal{Z} \to \cdot$ that maps events to an arbitrary measurement space, such as pixels, sounds, mass, force, torque, words, etc. Later, in Section 6.6, we discuss limitations and potential extensions to

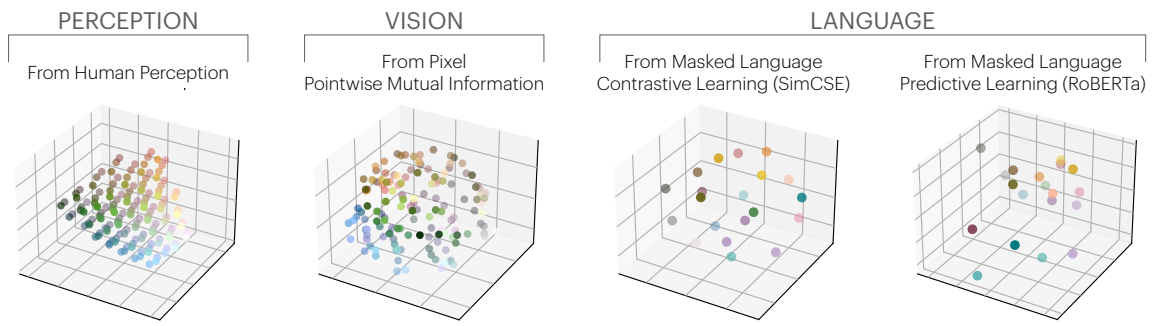

Figure 6-8: **Color cooccurrence in VISION and LANGUAGE yields perceptual organization:** Similar representations of color are obtained via, **from LEFT to RIGHT**, the perceptual layout from CIELAB color space, cooccurrence in CIFAR-10 images, and language cooccurrence modeling (Gao et al. (2021); Liu et al. (2019); computed roughly following Abdou et al. (2021)). Details in Appendix E.4.

continuous and unbounded worlds, and stochastic observations, that could yield a model that better reflects real learning scenarios.

One can think of an event as corresponding to the state of the world at some point in time[3], but it is also fine to simply consider an event as any variable that indexes observations, with no further physical meaning[4].

In this idealized world, knowing $\mathbb{P}(\mathbf{Z})$ would be useful for many kinds of predictions; this would constitute a world model over the events that cause our observations (Werbos, 1987; Ha and Schmidhuber, 2018; Richens and Everitt, 2024). We will next show that a particular representation of $\mathbb{P}(\mathbf{Z})$ is recovered by certain contrastive learners.

6.4.2 A family of contrastive learners converge to a representation of $\mathbb{P}(\mathbf{Z})$

Consider a contrastive learner that models observations that *cooccur* together. For simplicity, we ground our discussion with the following definition of the *cooccurrence probability*, P_{coor}, of two observations x_a and x_b both occurring within some window

[3]Here we only analyze temporal sequences, but note that the same could be done with respect to events laid out in space instead.

[4]This latter interpretation may be more consistent with Plato's intent. Scholars have argued that his allegory of the cave rejects any notion of a true world state (Nettleship, 1897). Instead, we could say that the joint distribution of observation indices is *itself* the platonic reality.

T_{window}:

$$P_{\mathsf{coor}}(x_a, x_b) \quad \propto \sum_{(t,t')\colon |t-t'| \le T_{\mathsf{window}}} \mathbb{P}(X_t = x_a, X_{t'} = x_b).$$

Analogously, we can define P_{coor} for $\mathbf{Z}$ and other observation modalities. Note that P_{coor} is symmetric.

Consider *positive pairs* as two observations nearby in time (sampled from P_{coor}) and *negative pairs* as observations drawn from any point in time (sampled independently from the marginal). Our contrastive learner tries to classify if a pair is positive or negative by learning a representation $f_X \colon X \to \mathbb{R}^d$ such that the dot-product kernel approximates the log odds ratio up to some offset:

$$\langle f_X(x_a), f_X(x_b) \rangle \approx \log \frac{\mathbb{P}(\mathsf{pos} \mid x_a, x_b)}{\mathbb{P}(\mathsf{neg} \mid x_a, x_b)} + \tilde{c}_X(x_a) \tag{6.3}$$

$$= \log \frac{P_{\mathsf{coor}}(x_a \mid x_b)}{P_{\mathsf{coor}}(x_a)} + c_X(x_a) \tag{6.4}$$

$$= K_{\mathsf{PMI}}(x_a, x_b) + c_X(x_a), \tag{6.5}$$

where K_{PMI} is the pointwise mutual information (PMI) kernel, and $c_X(x_a)$ is constant in x_b. We note that this is a common setting for self-supervised contrastive learners with NCE objectives (Gutmann and Hyvärinen, 2010; Oord et al., 2018), including SimCLR (Chen et al., 2020a) and SimCSE (Gao et al., 2021). (See Oord et al. (2018) and Appendix E.6.1 for detailed derivations.)

Under mild conditions that the world is smooth enough (see Appendix E.6.2), a choice of f_X can exactly represent K_{PMI}:

$$\langle f_X(x_a), f_X(x_b) \rangle = K_{\mathsf{PMI}}(x_a, x_b) + c_X, \tag{6.6}$$

where we observed that $c_X(x_a)$ from Equation (6.5) must be a constant since both sides are symmetric.

Therefore, the contrastive learners we consider are minimized by a representation f_X whose kernel is K_{PMI} (up to a constant offset). With sufficient data and optimization,

we will observe convergence to this point.

Thus we have convergence to a representation of the statistics of X, but what about Z? Recall that our idealized world consists of *bijective* observation functions, which, over discrete random variables, preserve probabilities. So we have:

$$P_{\mathsf{coor}}(x_a, x_b) = P_{\mathsf{coor}}(z_a, z_b)$$
$$K_{\mathsf{PMI}}(x_a, x_b) = K_{\mathsf{PMI}}(z_a, z_b),$$

where we use P_{coor} and K_{PMI} in a modality-agnostic way to emphasize that different modalities share the same these quantities.

All these arguments hold not just for X but also for Y (or any other bijective, discrete modality), implying:

$$K_{\mathsf{PMI}}(z_a, z_b) = \langle f_X(x_a), f_X(x_b) \rangle - c_X \tag{6.7}$$
$$= \langle f_Y(y_a), f_Y(y_b) \rangle - c_Y. \tag{6.8}$$

Therefore, for any modality in our idealized world, we observe representational convergence to the same kernel, which represents certain pairwise statistics of $\mathbb{P}(\mathbf{Z})$.

This analysis suggests that certain representation learning algorithms may boil down to a simple rule: *find an embedding in which similarity equals PMI*. We note that this idea is consistent with prior works that have used PMI as a similarity measure for clustering in vision and language (*e.g.*, Isola et al. (2014); Isola (2015a); Isola et al. (2016); Chambers and Jurafsky (2008)).

A study in color We conduct a case study to verify that convergence does happen on real data. Abdou et al. (2021) discovered that color distances in learned language representations, when trained to predict cooccurrences in *text* (Devlin et al., 2018), closely mirror human perception of these distances, which we reproduce in Figure 6-8 with both contrastive and predictive models. Interestingly, they noted an increasing similarity as models scale larger and become better at modeling *text* cooccurrences. In Figure 6-8, we also learn representations of color based on K_{PMI} from cooccurrences

in *images*. Indeed, learning cooccurrence statistics in either domain recovers roughly the *same* perceptual representation. Details of this experiment are described in Appendix E.4.

We believe that our simple model encapsulates essential aspects of complex real-world systems, and offers a path toward understanding the representation that models are converging to—a unified model that is proficient across various domains and modalities, grounded in the statistical properties of the underlying world. Section 6.6 further elaborates some limitations.

6.5 What are the implications of convergence?

Scaling is sufficient, but not necessarily efficient Our arguments are roughly in line with the claim that "scale is all you need" to reach high levels of intelligence. We have argued that as resources are scaled (# parameters, # datapoints, # flops), representations are converging, regardless of other modeling choices and even data modality. Does this mean that scale is all that matters? Not quite: different methods can scale with different levels of *efficiency* (Hestness et al., 2017; Kaplan et al., 2020), and successful methods must still satisfy some general requirements (*e.g.*, be a consistent estimator, model pairwise statistics of $\mathbb{P}(\mathbf{Z})$).

Training data can be shared across modalities Suppose you have access to N images and M sentences, and want to learn the best representation. If there is indeed a modality-agnostic platonic representation, then *both* image and language data should help find it. The implication is that if you want to train the best vision model, you should train not just on N images but also on M sentences. This is already becoming common practice (OpenAI, 2023; Radford et al., 2021). Many vision models are finetuned from pre-trained LLMs. The other direction is less common, but also is implied by our hypothesis: if you want to build the best LLM, *you should also train on image data*. Indeed, OpenAI (2023) showed that training on images improved performance on text. In theory, there should be some conversion ratio: a pixel is worth

a words for training LLMs, and a word is worth b pixels for training vision models.

Ease of translation and adaptation across modalities When two representations are aligned, transitioning from one to the other should be a simple function that's easily obtained. Our hypothesis could explain the phenomenon that conditional generation is easier than unconditional (Mirza and Osindero, 2014; Liu et al., 2020; Sauer et al., 2022), as the data we condition on may have the same platonic structure as the data we are generating. In line with this, recent work has found that representation-conditioning is even easier (Li et al., 2023). Similarly, representational convergence could act as a bridge that lets us find mappings between domains even without paired data; this may underlie the success of unpaired translation in vision (Zhu et al., 2017; Shi et al., 2024; Xie et al., 2022) and language (Tran et al., 2017; Lample et al., 2018). We emphasize that this doesn't mean that models trained on a single modality (*e.g.*, language) can immediately process raw data from another (*e.g.*, vision). What makes them adaptable to the new modalities is that they share a common modality-agnostic representation, and can readily process *representations* of new modalities. Furthermore, this implies that language models would achieve some notion of grounding in the visual domain even in the absence of cross-modal data[5]. The primary advantage of cross-modal data could then simply be sample efficiency.

Scaling may reduce hallucination and bias A prominent shortcoming of current LLMs is their propensity to hallucinate, or output false statements. If models are indeed converging toward an accurate model of reality, and scale powers this convergence, then we may expect hallucinations to decrease with scale. Of course, our hypothesis is conditioned on the training data for future models constituting a sufficiently lossless and diverse set of measurements. This may not come to pass, but it is an implication of our hypothesis worth pointing out. A similar argument can be made about certain

[5]In 1688, William Molyneux asked if a person born blind, upon gaining sight, could distinguish shapes by vision alone (Locke, 1690). Our arguments suggest they could not do so immediately, but after some visual experience, they could easily map shapes to their prior touch-based representations. Empirical data supports this, showing that congenitally blind children given sight can quickly learn these abilities (Held et al., 2011).

kinds of bias. It has been shown that large models can exacerbate existing biases present in their training data (Hall et al., 2022). Our hypothesis implies that, while this may be true, we should expect *larger* models to amplify bias *less*. This does not mean bias will be removed, rather that the model's biases will more accurately reflect the data's biases, rather than exacerbating them.

6.6 Counterexamples and limitations

Different modalities may contain different information One immediate objection to our hypothesis is: what about the information that is unique to a given modality? Can language really describe the ineffable experience of watching a total solar eclipse? Or, how could an image convey the a concept like "I believe in the freedom of speech," which is easy to write in English? Two different models cannot converge to the same representation if they have access to fundamentally different information.

More precisely, our mathematical argument in Section 6.4 only strictly holds for bijective projections of $\mathbf{Z}$, so that the information in all the projections is equivalent to the information in the underlying world. This will not hold true for either lossy or stochastic observation functions. Nonetheless, similar arguments have been made theoretically and empirically that cooccurrence relations are learned by practical contrastive (Chapter 2; Zimmermann et al. (2021)) and predictive learners (Papyan et al., 2020; Roeder et al., 2021). Lu et al. (2021) and Mirchandani et al. (2023) also showed that models trained to autoregressively generate text also capture statistical relations in many other modalities, including symbolic reasoning, vision, protein folding, and robotics.

A more nuanced version of our hypothesis will need to be developed to handle the case of non-bijective observations and abstract concepts. A starting point could be: different models will converge to the same representation *when the input signals are sufficiently high information and the models are sufficiently high capacity*; when they are not, the lower-information representation will only align with the higher-

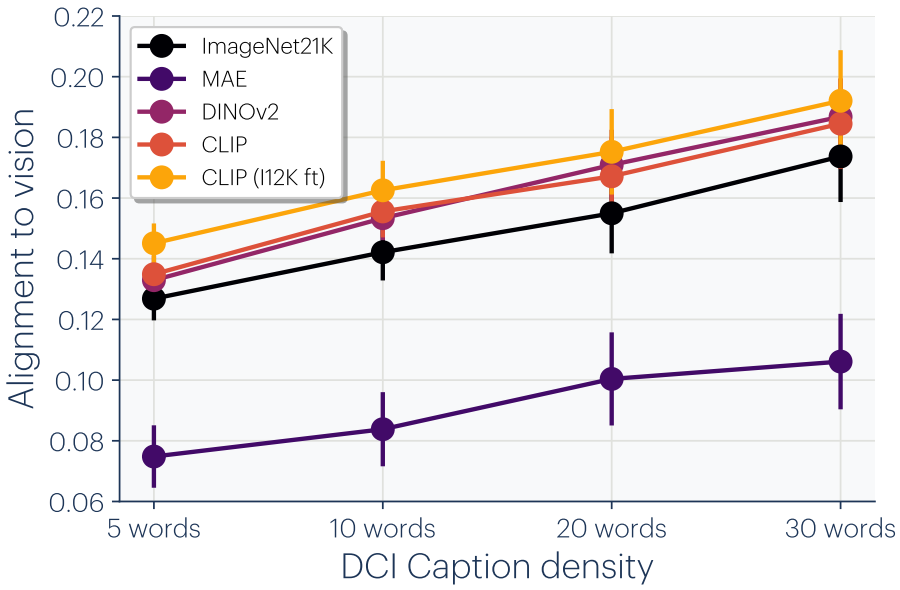

Figure 6-9: **Increasing caption density improves alignment:** We vary caption length using the Densely-Captioned-Images (DCI) dataset (Urbanek et al., 2023). Starting from a dense caption, we used LLaMA3-8B-Instruct (Meta, 2024) to summarize and generate coarse-grained captions. We compute the average alignment score across all vision and language models with standard deviation measured over the language models we evaluated. With denser captions, the mapping may become more bijective, leading to improved language-vision alignment scores.

information one up to a level capped by the mutual information between the input signals and by the capacity of each model. This cap might or might not be practically important. Popular representations like CLIP are explicitly optimized to only capture the shared information between vision and language, yet are highly successful on many pure vision tasks. We perform a preliminary test of the effect of information level in Figure 6-9 (detailed in Appendix E.5), and find that the more descriptive (higher information) a caption is, the better its LLM representation aligns with the visual representation of the corresponding image.

Not all representations are presently converging Our argument has mainly focused on two modalities: vision and language. While we do expect other modalities will follow similar trends, we have yet to see the same level of convergence across all domains. For example, in robotics there is not yet a standardized approach to representing world states in the same way as there is for representing images and text.

One limitation lies in the hardware used in robotics, which is often expensive and slow. This creates a bottleneck in the quantity and diversity of training data.

Sociological bias in producing AI models Researcher bias and collective preferences within the AI community have shaped the trajectory of model development. There is often an explicit or implicit goal of designing AI systems that mimic human reasoning and performance, and this could lead to convergence toward human-like representations even if other kinds of intelligence are in fact possible. Additionally, the "hardware lottery" (Hooker, 2021) suggests that the success of AI models can also depend on the compatibility of their design with available computational architectures, further contributing to convergent trends.

Special-purpose intelligences might not converge Different intelligent systems can be designed to accomplish different tasks. For instance: A bioinformatics systems might predict protein structure; an autonomous vehicle might follow lanes on highways. It's possible that not much is shared between these two narrow tasks. Our argument only holds for intelligences that are optimized to perform well on *many* tasks. We have argued that a representation of *reality* is a structure that is useful across many tasks, but for any special purpose there may be shortcuts, or even effective representations detached from reality. Such shortcuts may be more efficient and necessary for continued improvements in specific domains. This will become more relevant if continued scaling comes up against boundary conditions around resources like energy and compute.

How do we measure alignment? We focused on one particular alignment measure, mutual nearest-neighbor, in our experiments, and cited experiments using several others. However, there is active debate on the merits and deficiencies of all these ways of measuring alignment (Bansal et al., 2021; Sucholutsky et al., 2023). We discuss our choice and show results for other alignment metrics in Appendix E.1.

Lots left to explain We have shown results where different models arrive at *similar* but not the *same* representations. For example, in Figure 6-3, alignment

clearly increases but only reaches a score of 0.16, according to our mutual nearest-neighbor metric. The maximum theoretical value for this metric is 1. Is a score of 0.16 indicative of strong alignment with the remaining gap being "noise" or does it signify poor alignment with major differences left to explain? We leave this as an open question.

Chapter 7

Epilogue: Towards the Platonic Representation via Pretraining and Adaptation

If the Platonic representation is an important missing piece in intelligent agents, how can we work towards recovering it? To make progress, we need to combine different sources and modalities, which are different projections about the reality (Figure 7-1). However, simultaneously training on all projections is both impractical and infeasible. Handling different projections requires different training paradigms, and some projections come in the form of interaction (*e.g.*, reinforcement learning problems) where a pretrained agent need to interact with and adapt to the world. Furthermore, current best vision language models (VLMs) are obtained via finetuning a text-only pretrained model (Liu et al., 2023). Therefore, we argue that the most promising approach would require adapting pretrained models to new concepts and associations, and adaptation are the biggest challenges towards Platonic representation for intelligent agents. Towards this goal, we highlight several important questions focused on pretrained models and adaptation as future directions.

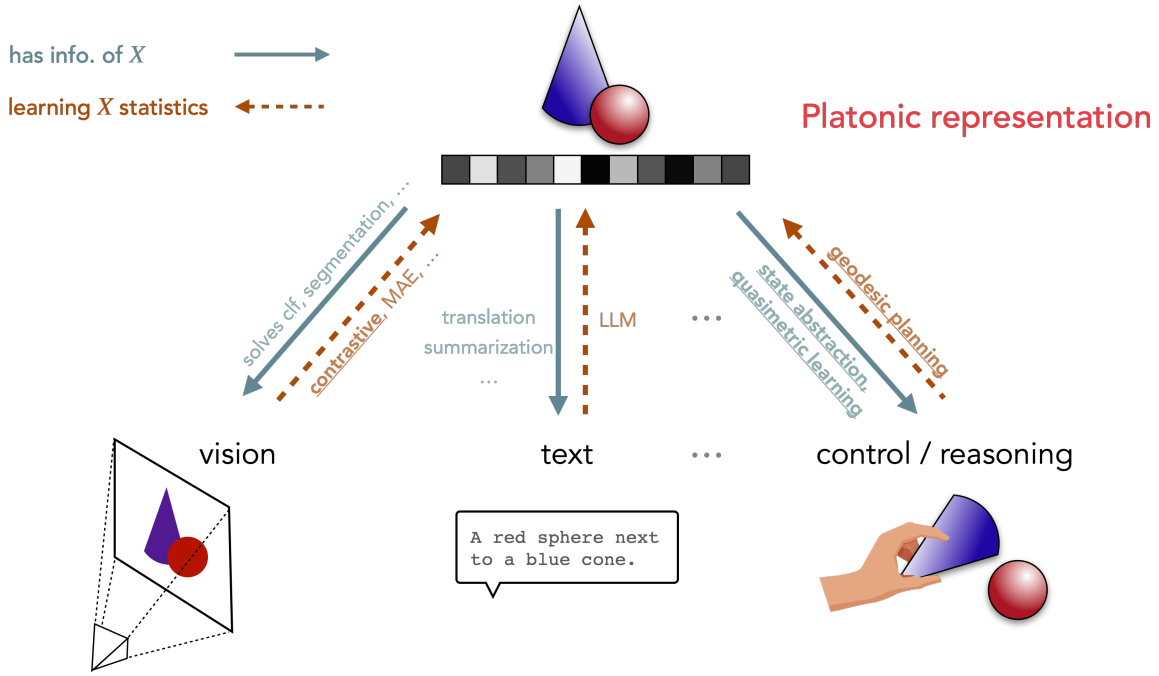

Figure 7-1: Recovering the Platonic representation by combining different sources (projections) and adapting to new ones. This dissertation explored multiple parts of the arrows (**bold and underlined**). Figure is repeated from Figure 1-1.

7.1 Understand what is missing in pretrained models

Pretraining is powerful but is generally limited to specific projections (*i.e.*, datasets and modalities), and does not capture the full statistical structure of reality. To explore what is missing, we can probe *the information delta between different projections*:

> **Q:** If we take a model trained for one projection (*i.e.*, task, modality and/or objective) and try to extract representation or knowledge for another task or domain, how can we quantify what is missing?

Towards better understanding, some specific questions we can ask are:

1. Does a vision model understand "I believe in freedom of speech"?
2. Does an LLM know decision-making structures (*e.g.*, value function V, invariances, symmetry)?
3. Does a video prediction model capture real world dynamics well enough for planning?

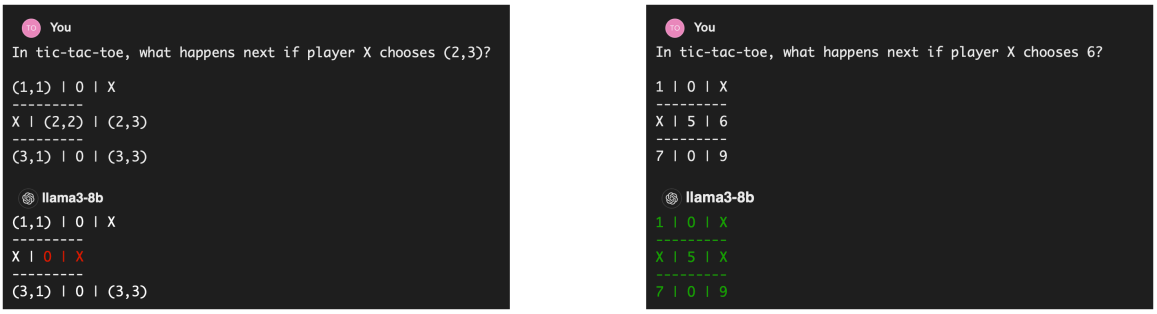

Figure 7-2: Current LLMs fail to recognize invariances in game playing. Example shows LLaMA-3 8B with Tic-Tac-Toe. Similar failures are observed over GPT-4.

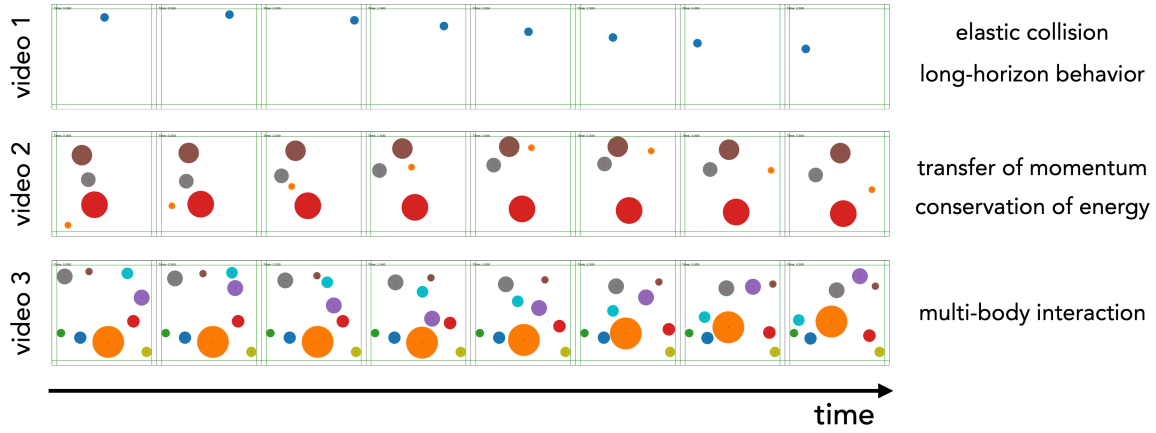

Figure 7-3: **The Billiard-2D synthetic video dataset.** We design synthetic video data where objects evolve following simple physics-like rules in a 2-D plane. Our dataset generation process is highly configurable, producing videos of various complexities, as shown above. This flexible and controlled process enables us to analyze different world modeling approaches on (1) their scaling properties of recovering the underlying "physics laws", and (2) the planning capabilities for building general goal-directed agents.

One way to approach these questions is to create synthetic tasks that capture their essence but also allows full access to control and extract the groundtruth information. For example, to explore the capability of current video prediction models, we created a synthetic 2D dataset Figure 7-3 where the full access to data generation allows us to explore various planning, modeling, and conditioning scenarios. Similarly, we can use controlled game-playing tasks to understand LLMs' decision-making capabilities (Figure 7-2). We expect such methodology to provide novel insights into the limitations of current pretraining paradigms, as well as how to best improve them.

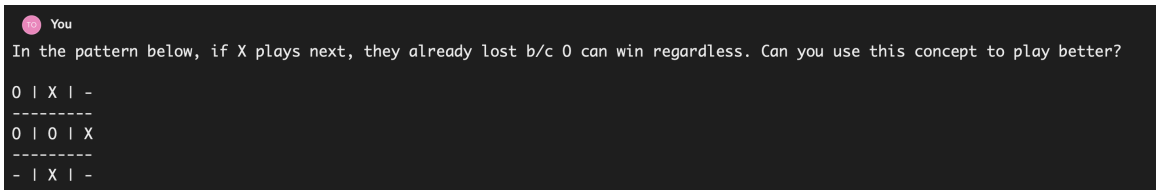

Figure 7-4: While the current LLMs do not play games well (Figure 7-2), how can we best teach them a simple new concept in Tic-Tac-Toe, ideally without much data or supervision, so that they can use it to improve general decision-making performance (*i.e.*, over many different yet similar board scenarios)?

7.2 Adapt pretrained models

The information we have access about the reality is dynamic and constantly increasing. Static models are unlikely to recover the full statistical structure of reality, and to account for the missing information in models pretrained over limited projections. The key question is about *adaptation*:

> **Q:** How can a model **efficiently** interact with the reality, explore, generate and verify hypotheses, and internalize them as knowledge in its representations?

The emphasis is on "**efficiency**". The most interesting and crucial difference about the adaptation setting is that we start with a good pretrained model that already captures the structures of reality to some extent. Proper adaptation should utilize this existing knowledge so that discovering and internalizing new knowledge is both efficient and effective. For example, an LLM is trained on Internet-scale data on various challenging games. If we teach it a new concept for playing Tic-Tac-Toe, the LLM should not need thousands examples or games to understand it. How can an LLM quickly pick up a new piece of knowledge and apply it to many different tasks (Figure 7-4)?

Towards adaptation, some specific questions we can ask are:

1. Can an LLM automatically discover and internalize useful concepts to improve?
2. How do adaptation data and objectives modify model behavior?
3. How to combine different pretrained models?

7.3 Intelligent agent ≡ automating science?

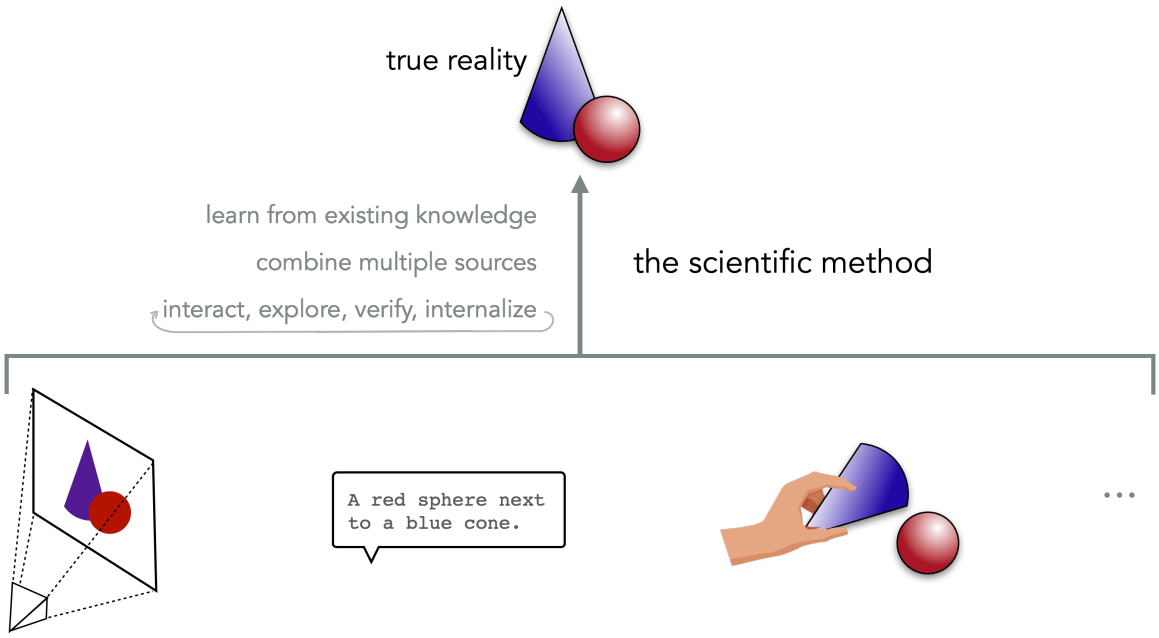

Figure 7-5: A capable intelligent agent should have a good model of the Platonic representation that captures the true reality. The process towards recovering this representation shares similarities with the scientific method in research.

A good model of the Platonic representation that captures the true reality could be a core component of an intelligent agent. As argued in this chapter, we believe that the path towards a Platonic representation of reality involves:

1. pretraining on existing knowledge,
2. combining multiple sources of information with adaptation, and
3. interact with the reality to explore, verify, and internalize.

This process to seek the true reality is strikingly similar to the scientific method for research (Figure 7-5). Both processes perform the *search for truth*, so it may not be too surprising that the best approaches coincide. However, the difference is in how the obtained knowledge is stored. In scientific studies, knowledge about the true reality is stored in human-understandable forms, such as academic papers, textbooks, educational videos, *etc.* In artificial models, we believe that knowledge is stored in the form of *representations*.

The consistent theme throughout this dissertation is a study on the relationship between model representations and knowledge of the world. In future, I strive to continue research towards better machine learning model representations of the reality, models that also assist scientific research, and ultimately an intelligent agent that captures the reality in its representations.

Appendix A

Proofs, Details, and Additional Discussions for Chapter 2

A.1 Proofs and Additional Theoretical Analysis

In this section, we present proofs for propositions and theorems in Sections 2.4.1 and 2.4.2.

The propositions in Section 2.4.1 illustrate the deep relations between the Gaussian kernel $G_t \colon \mathcal{S}^d \times \mathcal{S}^d \to \mathbb{R}$ and the uniform distribution on the unit hypersphere $\mathcal{S}^d$. As we will show below in Appendix A.1.1, these properties directly follow well-known results on strictly positive definite kernels.

In Appendix A.1.2, we present a proof for Theorem 2.4.7. Theorem 2.4.7 describes the asymptotic behavior of $\mathcal{L}_{\mathsf{contrastive}}$ as the number of negative samples M approaches infinity. The theorem is strongly related to empirical contrastive learning, given an error term (deviation from the limit) decaying in $\mathcal{O}(M^{-1/2})$ and that empirical practices often use a large number of negatives (*e.g.*, $M = 65536$ in He et al. (2019)) based on the observation that using more negatives consistently leads to better representation quality (Wu et al., 2018; Tian et al., 2020b; He et al., 2019). Our proof further reveals connections between $\mathcal{L}_{\mathsf{contrastive}}$ and $\mathcal{L}_{\mathsf{uniform}}$ which is defined via the Gaussian kernel.

Finally, also in Appendix A.1.2, we present a weaker result on the setting where only a single negative is used in $\mathcal{L}_{\mathsf{contrastive}}$ (*i.e.*, $M = 1$).

A.1.1 Proofs for Section 2.4.1 and Properties of $\mathcal{L}_{\text{uniform}}$

To prove Proposition 2.4.2 and 2.4.4, we utilize the *strict positive definiteness* (Bochner, 1992; Stewart, 1976) of the Gaussian kernel G_t:

$$G_t(u, v) \triangleq e^{-t\|u-v\|_2^2} = e^{2t \cdot u^\top v - 2t}, \quad t > 0.$$

From there, we apply a known result about such kernels, from which the two propositions directly follow.

Definition A.1.1 (Strict positive definiteness (Bochner, 1992; Stewart, 1976))**.** A symmetric and lower semi-continuous kernel K on $A \times A$ (where A is infinite and compact) is called strictly positive definite if for every finite signed Borel measure μ supported on A whose energy

$$I_K[\mu] \triangleq \int_{\mathcal{S}^d} \int_{\mathcal{S}^d} K(u, v) \, \mathrm{d}\mu(v) \, \mathrm{d}\mu(u)$$

is well defined, we have $I_K[\mu] \geq 0$, where equality holds only if $\mu \equiv 0$ on the σ-algebra of Borel subsets of A.

Definition A.1.2. Let $\mathcal{M}(\mathcal{S}^d)$ be the set of Borel probability measures on $\mathcal{S}^d$.

We are now in the place to apply the following two well-known results, which we present by restating Proposition 4.4.1, Theorem 6.2.1 and Corollary 6.2.2 of Borodachov et al. (2019) in weaker forms. We refer readers to Borodachov et al. (2019) for their proofs.

Lemma A.1.3 (Strict positive definiteness of G_t). For $t > 0$, the Gaussian kernel $G_t(u, v) \triangleq e^{-t\|u-v\|_2^2} = e^{2t \cdot u^\top v - 2t}$ is strictly positive definite on $\mathcal{S}^d \times \mathcal{S}^d$.

Lemma A.1.4 (Strictly positive definite kernels on $\mathcal{S}^d$). Consider kernel $K_f \colon \mathcal{S}^d \times \mathcal{S}^d \to (-\infty, +\infty]$ of the form,

$$K_f(u, v) \triangleq f(\|u - v\|_2^2). \tag{A.1}$$

If K_f is strictly positive definite on $\mathcal{S}^d \times \mathcal{S}^d$ and $I_{K_f}[\sigma_d]$ is finite, then σ_d is the unique measure (on Borel subsets of $\mathcal{S}^d$) in the solution of $\min_{\mu \in \mathcal{M}(\mathcal{S}^d)} I_{K_f}[\mu]$, and the normalized counting measures associated with any K_f-energy minimizing sequence of N-point configurations on $\mathcal{S}^d$ converges weak* to σ_d.

In particular, this conclusion holds whenever f has the property that $-f'(t)$ is strictly completely monotone on $(0, 4]$ and $I_{K_f}[\sigma_d]$ is finite.

We now recall Propositions 2.4.2 and 2.4.4.

Proposition 2.4.2. σ_d is the unique solution (on Borel subsets of $\mathcal{S}^d$) of

$$\min_{\mu \in \mathcal{M}(\mathcal{S}^d)} I_{G_t}[\mu] = \min_{\mu \in \mathcal{M}(\mathcal{S}^d)} \int_{\mathcal{S}^d} \int_{\mathcal{S}^d} G_t(u, v) \, \mathrm{d}\mu(v) \, \mathrm{d}\mu(u). \tag{A.2}$$

Proof of Proposition 2.4.2. This is a direct consequence of Lemmas A.1.3 and A.1.4. □

Proposition 2.4.4. For each $N > 0$, the N point minimizer of the average pairwise potential is

$$\mathbf{u}_N^* = \operatorname*{arg\,min}_{u_1, u_2, \ldots, u_N \in \mathcal{S}^d} \sum_{1 \leq i < j \leq N} G_t(u_i, u_j).$$

The normalized counting measures associated with the $\{\mathbf{u}_N^*\}_{N=1}^{\infty}$ sequence converge weak* to σ_d.

Proof of Proposition 2.4.4. This is a direct consequence of Lemmas A.1.3 and A.1.4. □

More Properties of $\mathcal{L}_{\mathsf{uniform}}$

Range of $\mathcal{L}_{\mathsf{uniform}}$. It's not obvious what the optimal value of $\mathcal{L}_{\mathsf{uniform}}$ is. In the following proposition, we characterize the exact range of the expected Gaussian potential and how it evolves as dimensionality increases. The situation for $\mathcal{L}_{\mathsf{uniform}}$ directly follows as a corollary.

Proposition A.1.5 (Range of the expected pairwise Gaussian potential G_t). For $t > 0$, the expected pairwise Gaussian potential w.r.t. Borel probability measure

$\mu \in \mathcal{M}(\mathcal{S}^d)$

$$I_{G_t}[\mu] = \int_{\mathcal{S}^d} \int_{\mathcal{S}^d} G_t(u,v)\,\mathrm{d}\mu(v)\,\mathrm{d}\mu(u)$$

has range $[e^{-2t}\,{}_0F_1(;\frac{d+1}{2};t^2), 1]$, where ${}_0F_1$ is the confluent hypergeometric limit function defined as

$${}_0F_1(;\alpha;z) \triangleq \sum_{n=0}^{\infty} \frac{z^n}{(\alpha)_n n!}, \tag{A.3}$$

where we have used the Pochhammer symbol

$$(a)_n = \begin{cases} 1 & \text{if } n = 0 \\ a(a+1)(n+2)\ldots(a+n-1) & \text{if } n \geq 1. \end{cases}$$

We have

- The minimum $e^{-2t}\,{}_0F_1(;\frac{d+1}{2};t^2)$ is achieved iff $\mu = \sigma_d$ (on Borel subsets of $\mathcal{S}^d$). Furthermore, this value strictly decreases as d increases, converging to e^{-2t} in the limit of $d \to \infty$.

- The maximum is achieved iff μ is a Dirac delta distribution, *i.e.*, $\mu = \delta_u$ (on Borel subsets of $\mathcal{S}^d$), for some $u \in \mathcal{S}^d$.

Proof of Proposition A.1.5.

- **Minimum.**

  We know from Proposition 2.4.2 that σ_d *uniquely* achieves the minimum, given by the following integral ratio

$$\begin{aligned} I_{G_t}[\sigma_d] &= \frac{\int_0^\pi e^{-t(2\sin\frac{\theta}{2})^2} \sin^{d-1}\theta\,\mathrm{d}\theta}{\int_0^\pi \sin^{d-1}\theta\,\mathrm{d}\theta} \\ &= \frac{\int_0^\pi e^{-2t(1-\cos\theta)} \sin^{d-1}\theta\,\mathrm{d}\theta}{\int_0^\pi \sin^{d-1}\theta\,\mathrm{d}\theta} \\ &= e^{-2t}\frac{\int_0^\pi e^{2t\cos\theta} \sin^{d-1}\theta\,\mathrm{d}\theta}{\int_0^\pi \sin^{d-1}\theta\,\mathrm{d}\theta}. \end{aligned}$$

  The denominator, with some trigonometric identities, can be more straightfor-

wardly evaluated as

$$\int_0^\pi \sin^{d-1}\theta\,\mathrm{d}\theta = \sqrt{\pi}\frac{\Gamma(\frac{d}{2})}{\Gamma(\frac{d+1}{2})}.$$

The numerator is

$$\begin{aligned}
\int_0^\pi e^{2t\cos\theta}\sin^{d-1}\theta\,\mathrm{d}\theta &= -\int_0^\pi e^{2t\cos\theta}\sin^{d-2}\theta\cos'\theta\,\mathrm{d}\theta \\
&= \int_{-1}^1 e^{2ts}(1-s^2)^{d/2-1}\,\mathrm{d}s \\
&= \frac{\Gamma(\frac{d-1}{2}+\frac{1}{2})\sqrt{\pi}}{\Gamma(\frac{d-1}{2}+1)}\,{}_0F_1(;\frac{d-1}{2}+1;-\frac{1}{4}(-2it)^2) \\
&= \frac{\Gamma(\frac{d}{2})\sqrt{\pi}}{\Gamma(\frac{d+1}{2})}\,{}_0F_1(;\frac{d+1}{2};t^2),
\end{aligned}$$

where we have used the following identity based on the Poisson formula for Bessel functions and the relationship between ${}_0F_1$ and Bessel functions:

$$\int_{-1}^1 e^{izs}(1-s^2)^{\nu-\frac{1}{2}}\,\mathrm{d}s = \frac{\Gamma(\nu+\frac{1}{2})\sqrt{\pi}}{(\frac{z}{2})^\nu}J_\nu(z) = \frac{\Gamma(\nu+\frac{1}{2})\sqrt{\pi}}{\Gamma(\nu+1)}\,{}_0F_1(;\nu+1;-\frac{1}{4}z^2).$$

Putting both together, we have

$$\begin{aligned}
I_{G_t}[\sigma_d] &= e^{-2t}\frac{\int_0^\pi e^{2t\cos\theta}\sin^{d-1}\theta\,\mathrm{d}\theta}{\int_0^\pi \sin^{d-1}\theta\,\mathrm{d}\theta} \\
&= e^{-2t}\frac{\frac{\Gamma(\frac{d}{2})\sqrt{\pi}}{\Gamma(\frac{d+1}{2})}\,{}_0F_1(;\frac{d+1}{2};t^2)}{\sqrt{\pi}\frac{\Gamma(\frac{d}{2})}{\Gamma(\frac{d+1}{2})}} \\
&= e^{-2t}\,{}_0F_1(;\frac{d+1}{2};t^2) \\
&= e^{-2t}\sum_{n=0}^\infty \frac{t^{2n}}{(\frac{d+1}{2})_n n!},
\end{aligned}$$

where we have used the definition of ${}_0F_1$ in Equation (A.3) to expand the formula.

Notice that each summand strictly decreases as $d\to\infty$. So must the total sum.

For the asymptotic behavior at $d \to \infty$, it only remains to show that

$$\lim_{d\to\infty} \sum_{n=0}^{\infty} \frac{t^{2n}}{(\frac{d+1}{2})_n n!} = 1. \tag{A.4}$$

For the purpose of applying the Dominated Convergence Theorem (DCT) (on the counting measure). We consider the following summable series

$$\sum_{n=0}^{\infty} \frac{t^{2n}}{n!} = e^{t^2},$$

with each term bounding the corresponding one in Equation (A.4):

$$\frac{t^{2n}}{n!} \geq \frac{t^{2n}}{(\frac{d+1}{2})_n n!}, \qquad \forall n \geq 0, d > 0.$$

Thus,

$$\lim_{d\to\infty} \sum_{n=0}^{\infty} \frac{t^{2n}}{(\frac{d+1}{2})_n n!} = \sum_{n=0}^{\infty} \lim_{d\to\infty} \frac{t^{2n}}{(\frac{d+1}{2})_n n!} = 1 + 0 + 0 + \cdots = 1.$$

Hence, the asymptotic lower range is e^{-2t}.

- **Maximum.**

  Obviously, Dirac delta distributions δ_u, $u \in \mathcal{S}^d$ would achieve a maximum of 1. We will now show that all Borel probability measures μ s.t. $I_{G_t}[\mu] = 1$ are delta distributions.

  Suppose that such a μ is not a Dirac delta distribution. Then, we can take distinct $x, y \in \text{supp}(\mu) \subseteq \mathcal{S}^d$, and open neighborhoods around x and v, $N_x, N_y \in \mathcal{S}^d$ such that they are small enough and disjoint:

$$N_x \triangleq \{u \in \mathcal{S}^d \colon \|u - x\|_2 < \frac{1}{3}\|x - y\|_2\}$$
$$N_y \triangleq \{u \in \mathcal{S}^d \colon \|u - y\|_2 < \frac{1}{3}\|x - y\|_2\}.$$

Then,

$$
\begin{aligned}
I_{G_t}[\mu] &= \int_{\mathcal{S}^d}\int_{\mathcal{S}^d} G_t(u,v)\,\mathrm{d}\mu(v)\,\mathrm{d}\mu(u) \\
&= \int_{\mathcal{S}^d}\int_{\mathcal{S}^d} e^{-t\|u-v\|_2^2}\,\mathrm{d}\mu(v)\,\mathrm{d}\mu(u) \\
&\leq (1-2\mu(N_x)\mu(N_y))e^{-t\cdot 0} + 2\int_{N_x}\int_{N_y} e^{-t\|u-v\|_2^2}\,\mathrm{d}\mu(v)\,\mathrm{d}\mu(u) \\
&< 1-2\mu(N_x)\mu(N_y) + 2\mu(N_x)\mu(N_y)e^{-t(\|x-y\|_2/3)^2} \\
&= 1-2\mu(N_x)\mu(N_y)(1-e^{-\frac{t}{9}\|x-y\|_2^2}) \\
&< 1.
\end{aligned}
$$

Hence, only Dirac delta distributions attain the maximum.

□

Corollary A.1.6 (Range of $\mathcal{L}_{\mathsf{uniform}}$). For encoder $f\colon \mathbb{R}^n \to \mathcal{S}^{m-1}$, $\mathcal{L}_{\mathsf{uniform}}(f;t) \in [-2t + \log{}_0F_1(;\frac{m}{2};t^2), 0]$, where the lower bound $-2t + \log{}_0F_1(;\frac{m}{2};t^2)$ is achieved only by perfectly uniform encoders f, and the upper bound 0 is achieved only by degenerate encoders that output a fixed feature vector almost surely.

Furthermore, the lower bound strictly decreases as the output dimension m increases, attaining the following asymptotic value

$$
\lim_{m\to\infty} -2t + \log{}_0F_1(;\frac{m}{2};t^2) = -2t. \tag{A.5}
$$

Intuition for the optimal $\mathcal{L}_{\mathsf{uniform}}$ value in high dimensions. If we ignore the $\log{}_0F_1(;\frac{m}{2};t^2)$ term, informally, the optimal value of $-2t$ roughly says that any pair of feature vectors on $\mathcal{S}^d$ has distance about $\sqrt{2}$, *i.e.*, are nearly orthogonal to each other. Indeed, vectors of high dimensions are usually nearly orthogonal, which is also consistent with the asymptotic result in Equation (A.5).

Figures A-1 and A-2 visualize how ${}_0F_1$ and the optimal $\mathcal{L}_{\mathsf{uniform}}$ (given by perfectly uniform encoders) evolve.

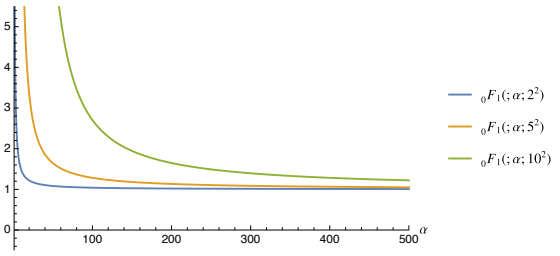

Figure A-1: Asymptotic behavior of ${}_0F_1(;\alpha;z)$. For $z > 0$, as α grows larger, the function converges to 1.

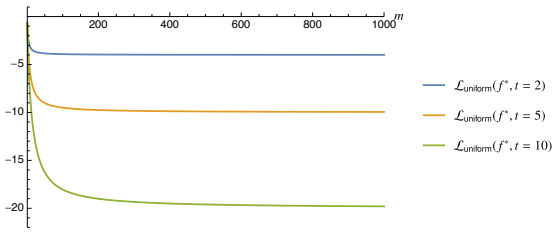

Figure A-2: Asymptotic behavior of optimal $\mathcal{L}_{\text{uniform}}(f, t)$, attained by a perfectly uniform encoder f^*. As the feature dimension m grows larger, the value converges to $-2t$.

Lower bound of $\mathcal{L}_{\text{uniform}}$ estimates. In practice, when $\mathcal{L}_{\text{uniform}}$ calculated using expectation over (a batch of) empirical samples $\{x_i\}_{i=1}^B$, $B > 1$, the range in Corollary A.1.6 is indeed valid, since it bounds over all distributions:

$$\hat{\mathcal{L}}^{(1)}_{\text{uniform}} \triangleq \log \frac{1}{B^2} \sum_{i=1}^{B} \sum_{j=1}^{B} e^{-t\|f(x_i)-f(x_j)\|^2} > -2t + \log {}_0F_1(;\frac{m}{2};t^2). \tag{A.6}$$

However, often $\mathcal{L}_{\text{uniform}}$ is empirically estimated without considering distances between a vector and itself (*e.g.*, in Figure 2-6 and in our experiment settings as described in Appendix A.2):

$$\hat{\mathcal{L}}^{(2)}_{\text{uniform}} \triangleq \log \frac{1}{B(B-1)} \sum_{i=1}^{B} \sum_{j\in\{1,\dots,B\}\setminus\{i\}} e^{-t\|f(x_i)-f(x_j)\|^2}. \tag{A.7}$$

While both quantities converge to the correct value in the limit, the lower bound is not always true for this one, because it is *not* the expected pairwise Gaussian kernel based on some distribution. Note the following relation:

$$\hat{\mathcal{L}}^{(2)}_{\text{uniform}} = \log \left(\frac{B \cdot \exp(\hat{\mathcal{L}}^{(1)}_{\text{uniform}}) - 1}{B-1} \right).$$

We can derive a valid lower bound using Equation (A.6): for ${}_0F_1(;\frac{m}{2};t^2) > \frac{e^{2t}}{B}$,

$$\hat{\mathcal{L}}^{(2)}_{\text{uniform}} > \log \left(\frac{B \cdot \exp(-2t + \log {}_0F_1(;\frac{m}{2};t^2)) - 1}{B-1} \right) = \log \left(\frac{Be^{-2t}\, {}_0F_1(;\frac{m}{2};t^2) - 1}{B-1} \right).$$

Since this approaches fails for cases that ${}_0F_1(;\frac{m}{2};t^2) \leq \frac{e^{2t}}{B}$, we can combine it with the naive lower bound $-4t$, and have

$$\hat{\mathcal{L}}^{(2)}_{\mathsf{uniform}} > \begin{cases} \max(-4t, \log\left(\frac{Be^{-2t}\,{}_0F_1(;\frac{m}{2};t^2)-1}{B-1}\right)) & \text{if } {}_0F_1(;\frac{m}{2};t^2) > \frac{e^{2t}}{B} \\ -4t & \text{otherwise.} \end{cases}$$

Non-negative versions of $\mathcal{L}_{\mathsf{uniform}}$ for practical uses. By definition, $\mathcal{L}_{\mathsf{uniform}}$ always non-positive. As shown above, different $\mathcal{L}_{\mathsf{uniform}}$ empirical estimates may admit different lower bounds. However, in our experience, for reasonably large batch sizes, adding an offset of $2t$ often ensures a non-negative loss that is near zero at optimum. When output dimensionality m is low, it might be useful to add an additional offset of $-\log {}_0F_1(;\frac{m}{2};t^2)$, which can be computed with the help of the SciPy package function `scipy.special.hyp0f1(m/2, t**2)` (Virtanen et al., 2020).

A.1.2 Proofs and Additional Results for Section 2.4.2

The following lemma directly follows Theorem 3.3 and Remarks 3.4 (b)(i) of Serfozo (1982). We refer readers to Serfozo (1982) for its proof.

Lemma A.1.7. Let A be a compact second countable Hausdorff space. Suppose

1. $\{\mu_n\}_{n=1}^{\infty}$ is a sequence of finite and positive Borel measures supported on A that converges weak* to some finite and positive Borel measure μ (which is same as vague convergence since A is compact);
2. $\{f_n\}_{n=1}^{\infty}$ is a sequence of Borel measurable functions that converges continuously to a Borel measurable f;
3. $\{f_n\}_n$ are uniformly bounded over A.

Then, we have the following convergence:

$$\lim_{n\to\infty} \int_{x\in A} f_n(x)\,\mathrm{d}\mu_n(x) = \int_{x\in A} f(x)\,\mathrm{d}\mu(x).$$

We now recall Theorem 2.4.7.

Theorem 2.4.7 (Asymptotics of $\mathcal{L}_{\mathsf{contrastive}}$). For fixed $\tau > 0$, as the number of negative samples $M \to \infty$, the (normalized) contrastive loss converges to

$$\begin{aligned}
&\lim_{M\to\infty} \mathcal{L}_{\mathsf{contrastive}}(f;\tau,M) - \log M \\
&\qquad = \lim_{M\to\infty} \mathop{\mathbb{E}}_{\substack{(x,y)\sim p_{\mathsf{pos}} \\ \{x_i^-\}_{i=1}^M \overset{\text{i.i.d.}}{\sim} p_{\mathsf{data}}}} \left[-\log \frac{e^{f(x)^\mathsf{T} f(y)/\tau}}{e^{f(x)^\mathsf{T} f(y)/\tau} + \sum_i e^{f(x_i^-)^\mathsf{T} f(y)/\tau}} \right] - \log M \\
&\qquad = -\frac{1}{\tau} \mathop{\mathbb{E}}_{(x,y)\sim p_{\mathsf{pos}}} \left[f(x)^\mathsf{T} f(y) \right] + \mathop{\mathbb{E}}_{x\sim p_{\mathsf{data}}} \left[\log \mathop{\mathbb{E}}_{x^-\sim p_{\mathsf{data}}} \left[e^{f(x^-)^\mathsf{T} f(x)/\tau} \right] \right]. \qquad (2.2)
\end{aligned}$$

We have the following results:

1. The first term is minimized iff f is perfectly aligned.

2. If perfectly uniform encoders exist, they form the exact minimizers of the second term.

3. For the convergence in Equation (2.2), the absolute deviation from the limit (*i.e.*, the error term) decays in $\mathcal{O}(M^{-1/2})$.

Proof of Theorem 2.4.7. We first show the convergence stated in Equation (2.2) along with its speed (result 3), and then the relations between the two limiting terms and the alignment and uniformity properties (results 1 and 2).

- **Proof of the convergence in Equation (2.2) and the $\mathcal{O}(M^{-1/2})$ decay rate of its error term (result 3).**

  Note that for any $x, y \in \mathbb{R}^n$ and $\{x_i^-\}_{i=1}^M \overset{\text{i.i.d.}}{\sim} p_{\mathsf{data}}$, we have, almost surely,

  $$\lim_{M\to\infty} \log \left(\frac{1}{M} e^{f(x)^\mathsf{T} f(y)/\tau} + \frac{1}{M} \sum_{i=1}^M e^{f(x_i^-)^\mathsf{T} f(x)/\tau} \right) = \log \mathop{\mathbb{E}}_{x^-\sim p_{\mathsf{data}}} \left[e^{f(x^-)^\mathsf{T} f(x)/\tau} \right], \qquad (A.8)$$

  by the strong law of large numbers (SLLN) and the Continuous Mapping Theorem.

Then, we can derive

$$
\begin{aligned}
&\lim_{M\to\infty} \mathcal{L}_{\mathsf{contrastive}}(f;\tau,M) - \log M \\
&\quad= \mathop{\mathbb{E}}_{(x,y)\sim p_{\mathsf{pos}}}\left[-f(x)^\mathsf{T} f(y)/\tau\right] \\
&\qquad + \lim_{M\to\infty} \mathop{\mathbb{E}}_{\substack{(x,y)\sim p_{\mathsf{pos}} \\ \{x_i^-\}_{i=1}^M \overset{\text{i.i.d.}}{\sim} p_{\mathsf{data}}}} \left[\log\left(\frac{1}{M} e^{f(x)^\mathsf{T} f(y)/\tau} + \frac{1}{M}\sum_{i=1}^M e^{f(x_i^-)^\mathsf{T} f(x)/\tau}\right)\right] \\
&\quad= \mathop{\mathbb{E}}_{(x,y)\sim p_{\mathsf{pos}}}\left[-f(x)^\mathsf{T} f(y)/\tau\right] \\
&\qquad + \mathbb{E}\left[\lim_{M\to\infty} \log\left(\frac{1}{M} e^{f(x)^\mathsf{T} f(y)/\tau} + \frac{1}{M}\sum_{i=1}^M e^{f(x_i^-)^\mathsf{T} f(x)/\tau}\right)\right] \\
&\quad= -\frac{1}{\tau}\mathop{\mathbb{E}}_{(x,y)\sim p_{\mathsf{pos}}}\left[f(x)^\mathsf{T} f(y)\right] + \mathop{\mathbb{E}}_{x\sim p_{\mathsf{data}}}\left[\log \mathop{\mathbb{E}}_{x^-\sim p_{\mathsf{data}}}\left[e^{f(x^-)^\mathsf{T} f(x)/\tau}\right]\right],
\end{aligned}
$$

where we justify the switching of expectation and limit by the convergence stated in Equation (A.8), the boundedness of $e^{u^\mathsf{T} v/\tau}$ (where $u, v \in \mathcal{S}^d, \tau > 0$), and the Dominated Convergence Theorem (DCT).

For convergence speed, we have

$$
\begin{aligned}
&\left|\left(\lim_{M\to\infty} \mathcal{L}_{\mathsf{contrastive}}(f;\tau,M) - \log M\right) - \left(\mathcal{L}_{\mathsf{contrastive}}(f;\tau,M) - \log M\right)\right| \\
&\quad= \left|\mathop{\mathbb{E}}_{\substack{(x,y)\sim p_{\mathsf{pos}} \\ \{x_i^-\}_{i=1}^M \overset{\text{i.i.d.}}{\sim} p_{\mathsf{data}}}} \left[\log \mathop{\mathbb{E}}_{x^-\sim p_{\mathsf{data}}}\left[e^{f(x^-)^\mathsf{T} f(x)/\tau}\right] - \log\left(\frac{1}{M} e^{f(x)^\mathsf{T} f(y)/\tau} + \frac{1}{M}\sum_{i=1}^M e^{f(x_i^-)^\mathsf{T} f(x)/\tau}\right)\right]\right| \\
&\quad\le \mathop{\mathbb{E}}_{\substack{(x,y)\sim p_{\mathsf{pos}} \\ \{x_i^-\}_{i=1}^M \overset{\text{i.i.d.}}{\sim} p_{\mathsf{data}}}} \left[\left|\log \mathop{\mathbb{E}}_{x^-\sim p_{\mathsf{data}}}\left[e^{f(x^-)^\mathsf{T} f(x)/\tau}\right] - \log\left(\frac{1}{M} e^{f(x)^\mathsf{T} f(y)/\tau} + \frac{1}{M}\sum_{i=1}^M e^{f(x_i^-)^\mathsf{T} f(x)/\tau}\right)\right|\right] \\
&\quad\le e^{1/\tau} \mathop{\mathbb{E}}_{\substack{(x,y)\sim p_{\mathsf{pos}} \\ \{x_i^-\}_{i=1}^M \overset{\text{i.i.d.}}{\sim} p_{\mathsf{data}}}} \left[\left|\mathop{\mathbb{E}}_{x^-\sim p_{\mathsf{data}}}\left[e^{f(x^-)^\mathsf{T} f(x)/\tau}\right] - \left(\frac{1}{M} e^{f(x)^\mathsf{T} f(y)/\tau} + \frac{1}{M}\sum_{i=1}^M e^{f(x_i^-)^\mathsf{T} f(x)/\tau}\right)\right|\right] \\
&\quad\le \frac{1}{M} e^{2/\tau} + e^{1/\tau} \mathop{\mathbb{E}}_{x,\{x_i^-\}_{i=1}^M \overset{\text{i.i.d.}}{\sim} p_{\mathsf{data}}} \left[\left|\mathop{\mathbb{E}}_{x^-\sim p_{\mathsf{data}}}\left[e^{f(x^-)^\mathsf{T} f(x)/\tau}\right] - \frac{1}{M}\sum_{i=1}^M e^{f(x_i^-)^\mathsf{T} f(x)/\tau}\right|\right] \\
&\quad= \frac{1}{M} e^{2/\tau} + \mathcal{O}(M^{-1/2}),
\end{aligned}
\tag{A.9}
$$

where the first inequality follows the Intermediate Value Theorem and the $e^{1/\tau}$ upper bound on the absolute derivative of log between the two points, and the last equality follows the Berry-Esseen Theorem given the bounded support of $e^{f(x_i^-)^\intercal f(x)/\tau}$ as following: for i.i.d. random variables Y_i with bounded support $\subset [-a, a]$, zero mean and $\sigma_Y^2 \leq a^2$ variance, we have

$$\begin{aligned}
\mathbb{E}\left[\left|\frac{1}{M}\sum_{i=1}^{M} Y_i\right|\right] &= \frac{\sigma_Y}{\sqrt{M}}\mathbb{E}\left[\left|\frac{1}{\sqrt{M}\sigma_Y}\sum_{i=1}^{M} Y_i\right|\right] \\
&= \frac{\sigma_Y}{\sqrt{M}}\int_0^{\frac{a\sqrt{M}}{\sigma_Y}} \mathbb{P}\left[\left|\frac{1}{\sqrt{M}\sigma_Y}\sum_{i=1}^{M} Y_i\right| > x\right] \mathrm{d}x \\
&\leq \frac{\sigma_Y}{\sqrt{M}}\int_0^{\frac{a\sqrt{M}}{\sigma_Y}} \mathbb{P}\left[|\mathcal{N}(0,1)| > x\right] + \frac{C_a}{\sqrt{M}}\,\mathrm{d}x \qquad \text{(Berry-Esseen)} \\
&\leq \frac{\sigma_Y}{\sqrt{M}}\left(\frac{aC_a}{\sigma_Y} + \int_0^{\infty} \mathbb{P}\left[|\mathcal{N}(0,1)| > x\right]\mathrm{d}x\right) \\
&= \frac{\sigma_Y}{\sqrt{M}}\left(\frac{aC_a}{\sigma_Y} + \mathbb{E}\left[|\mathcal{N}(0,1)|\right]\right) \\
&\leq \frac{C_a}{\sqrt{M}} + \frac{a}{\sqrt{M}}\mathbb{E}\left[|\mathcal{N}(0,1)|\right] \\
&= \mathcal{O}(M^{-1/2}),
\end{aligned}$$

where the constant C_a only depends on a (which controls both the second and the third moment).

- **Proof of result 1: The first term is minimized iff f is perfectly aligned.**

  Note that for $u, v \in \mathcal{S}^d$,

  $$\|u - v\|_2^2 = 2 - 2 \cdot u^T v.$$

  Then the result follows directly the definition of perfect alignment, and the existence of perfectly aligned encoders (*e.g.*, an encoder that maps every input to the same output vector).

- **Proof of result 2: If perfectly uniform encoders exist, they form the exact minimizers of the second term.**

For simplicity, we define the following notation:

Definition A.1.8. $\forall \mu \in \mathcal{M}(\mathcal{S}^d)$, $u \in \mathcal{S}^d$, we define the continuous and Borel measurable function

$$U_\mu(u) \triangleq \int_{\mathcal{S}^d} e^{u^\mathsf{T} v/\tau} \, \mathrm{d}\mu(v). \tag{A.10}$$

with its range bounded in $[e^{-1/\tau}, e^{1/\tau}]$.

Then the second term can be equivalently written as

$$\mathop{\mathbb{E}}_{x \sim p_{\mathsf{data}}} \left[\log \mathop{\mathbb{E}}_{x^- \sim p_{\mathsf{data}}} \left[e^{f(x^-)^\mathsf{T} f(x)/\tau} \right] \right] = \mathop{\mathbb{E}}_{x \sim p_{\mathsf{data}}} \left[\log U_{p_{\mathsf{data}} \circ f^{-1}}(f(x)) \right],$$

where $p_{\mathsf{data}} \circ f^{-1} \in \mathcal{M}(\mathcal{S}^d)$ is the probability measure of features, *i.e.*, the pushforward measure of p_{data} via f.

We now consider the following relaxed problem, where the minimization is taken over $\mathcal{M}(\mathcal{S}^d)$, all possible Borel probability measures on the hypersphere $\mathcal{S}^d$:

$$\min_{\mu \in \mathcal{M}(\mathcal{S}^d)} \int_{\mathcal{S}^d} \log U_\mu(u) \, \mathrm{d}\mu(u). \tag{A.11}$$

Our strategy is to show that the unique minimizer of Equation (A.11) is σ_d, from which the result 2 directly follows. The rest of the proof is structured in three parts.

1. **We show that minimizers of Equation (A.11) exist, *i.e.*, the above infimum is attained for some $\mu \in \mathcal{M}(\mathcal{S}^d)$.**

   Let $\{\mu_m\}_{m=1}^\infty$ be a sequence in $\mathcal{M}(\mathcal{S}^d)$ such that the infimum of Equation (A.11) is reached in the limit:

   $$\lim_{m \to \infty} \int_{\mathcal{S}^d} \log U_{\mu_m}(u) \, \mathrm{d}\mu_m(u) = \inf_{\mu \in \mathcal{M}(\mathcal{S}^d)} \int_{\mathcal{S}^d} \log U_\mu(u) \, \mathrm{d}\mu(u).$$

   From the Helly's Selection Theorem, let μ^* denote some weak* cluster point of this sequence. Then μ_m converges weak* to μ^* along a subsequence

$m \in \mathcal{N} \in \mathbb{N}$. For simplicity and with a slight abuse of notation, we denote this convergent (sub)sequence of measures by $\{\mu_n\}_{n=1}^{\infty}$.

We want to show that μ^* attains the limit (and thus the infimum), *i.e.*,

$$\int_{\mathcal{S}^d} \log U_{\mu^*}(u)\,\mathrm{d}\mu^*(u) = \lim_{n\to\infty} \int_{\mathcal{S}^d} \log U_{\mu_n}(u)\,\mathrm{d}\mu_n(u). \tag{A.12}$$

In view of Lemma A.1.7, since $\mathcal{S}^d$ is a compact second countable Hausdorff space and $\{\log U_{\mu_n}\}_n$ is uniformly bounded over $\mathcal{S}^d$, it remains to prove that $\{\log U_{\mu_n}\}_n$ is continuously convergent to $\log U_{\mu^*}$.

Consider any convergent sequence of points $\{x_n\}_{n=1}^{\infty} \in \mathbb{R}^{d+1}$ s.t. $x_n \to x$ where $x \in \mathcal{S}^d$.

Let $\delta_n = x_n - x$. By simply expanding U_{μ_n} and μ_{μ^*}, we have

$$e^{-\|\delta_n\|/\tau} U_{\mu_n}(x) \le U_{\mu_n}(x_n) \le e^{\|\delta_n\|/\tau} U_{\mu_n}(x).$$

Since both the upper and the lower bound converge to $U_{\mu^*}(x)$ (by the weak * convergence of $\{\mu_n\}_n$ to μ^*), $U_{\mu_n}(x_n)$ must as well. We have proved the continuous convergence of $\{\log U_{\mu_n}\}_n$ to $\log U_{\mu^*}$.

Therefore, the limit in Equation (A.12) holds. The infimum is thus attained at μ^*:

$$\lim_{n\to\infty} \int_u \log U_{\mu_n}(u)\,\mathrm{d}\mu_n = \int_u \log U_{\mu^*}(u)\,\mathrm{d}\mu^*.$$

2. **We show that U_{μ^*} is constant μ^*-almost surely for any minimizer μ^* of Equation (A.11).**

   Let μ^* be any solution of Equation (A.11):

$$\mu^* \in \operatorname*{arg\,min}_{\mu\in\mathcal{M}(\mathcal{S}^d)} \int_u \log U_{\mu}(u)\,\mathrm{d}\mu.$$

   Consider the Borel sets where μ^* has positive measure: $\mathcal{T} \triangleq \{T \in \mathcal{B}(\mathcal{S}^d) \colon \mu^*(T) > 0\}$. For any $T \in \mathcal{T}$, let μ_T^* denote the conditional distribution of μ^* on T,

i.e., $\forall A \in \mathcal{B}(\mathcal{S}^d)$,

$$\mu_T^*(A) = \frac{\mu^*(A \cap T)}{\mu^*(T)}.$$

Note that for any such $T \in \mathcal{T}$, the mixture $(1-\alpha)\mu^* + \alpha\mu_T^*$ is a valid probability distribution (*i.e.*, in $\mathcal{M}(\mathcal{S}^d)$) for $\alpha \in (-\mu^*(T), 1)$, an open interval containing 0.

By the first variation, we must have

$$\begin{aligned}
0 &= \frac{\partial}{\partial\alpha} \int_{\mathcal{S}^d} \log U_{(1-\alpha)\mu^* + \alpha\mu_T^*}(u) \,\mathrm{d}((1-\alpha)\mu^* + \alpha\mu_T^*)(u)\bigg|_{\alpha=0} \\
&= \frac{\partial}{\partial\alpha}(1-\alpha) \int_{\mathcal{S}^d} \log U_{(1-\alpha)\mu^* + \alpha\mu_T^*}(u) \,\mathrm{d}\mu^*(u)\bigg|_{\alpha=0} + \frac{\partial}{\partial\alpha}\alpha \int_{\mathcal{S}^d} \log U_{(1-\alpha)\mu^* + \alpha\mu_T^*}(u) \,\mathrm{d}\mu_T^*(u)\bigg|_{\alpha=0} \\
&= -\int_{\mathcal{S}^d} \log U_{(1-\alpha)\mu^* + \alpha\mu_T^*}(u) \,\mathrm{d}\mu^*(u)\bigg|_{\alpha=0} + \frac{\partial}{\partial\alpha} \int_{\mathcal{S}^d} \log U_{(1-\alpha)\mu^* + \alpha\mu_T^*}(u) \,\mathrm{d}\mu^*(u)\bigg|_{\alpha=0} \\
&\qquad + \int_{\mathcal{S}^d} \log U_{(1-\alpha)\mu^* + \alpha\mu_T^*}(u) \,\mathrm{d}\mu_T^*(u)\bigg|_{\alpha=0} + 0 \cdot \frac{\partial}{\partial\alpha} \int_{\mathcal{S}^d} \log U_{(1-\alpha)\mu^* + \alpha\mu_T^*}(u) \,\mathrm{d}\mu_T^*(u)\bigg|_{\alpha=0} \\
&= -\int_{\mathcal{S}^d} \log U_{\mu^*}(u) \,\mathrm{d}\mu^*(u) + \int_{\mathcal{S}^d} \frac{U_{\mu_T^*}(u) - U_{\mu^*}(u)}{U_{\mu^*}(u)} \,\mathrm{d}\mu^*(u) \\
&\qquad + \int_{\mathcal{S}^d} \log U_{\mu^*}(u) \,\mathrm{d}\mu_T^*(u) + 0 \cdot \int_{\mathcal{S}^d} \frac{U_{\mu_T^*}(u) - U_{\mu^*}(u)}{U_{\mu^*}(u)} \,\mathrm{d}\mu_T^*(u) \\
&= \int_{\mathcal{S}^d} \frac{U_{\mu_T^*}(u)}{U_{\mu^*}(u)} \,\mathrm{d}\mu^*(u) + \int_{\mathcal{S}^d} \log U_{\mu^*}(u) \,\mathrm{d}(\mu_T^* - \mu^*)(u) - 1, \qquad \text{(A.13)}
\end{aligned}$$

where the Leibniz rule along with the boundedness of U_{μ^*} and $U_{\mu_{T_n}^*}$ together justify the exchanges of integration and differentiation.

Let $\{T_n\}_{n=1}^{\infty}$ be a sequence of sets in $\mathcal{T}$ such that

$$\lim_{n\to\infty} \int_{\mathcal{S}^d} U_{\mu^*}(u) \,\mathrm{d}\mu_{T_n}^*(u) = \sup_{T\in\mathcal{T}} \int_{\mathcal{S}^d} U_{\mu^*}(u) \,\mathrm{d}\mu_T^*(u) \triangleq U^*,$$

where the supremum must exist since U_{μ^*} is bounded above.

Because U_{μ^*} is a continuous and Borel measurable function, we have $\{u \colon U_{\mu^*}(u) >$

$U^*\} \in \mathcal{B}(\mathcal{S}^d)$ and thus

$$\begin{aligned} \mu^*(\{u\colon U_{\mu^*}(u) > U^*\}) &= 0, \\ \mu^*_{T_n}(\{u\colon U_{\mu^*}(u) > U^*\}) &= 0, \qquad\qquad \forall n = 1, 2, \ldots, \end{aligned}$$

otherwise $\{u\colon U_{\mu^*}(u) > U^*\} \in \mathcal{T}$, contradicting the definition of U^* as the supremum.

Asymptotically, U_{μ^*} is constant $\mu^*_{T_n}$-almost surely:

$$\begin{aligned} &\int_{\mathcal{S}^d} \left| U_{\mu^*}(u) - \int_{\mathcal{S}^d} U_{\mu^*}(u') \,\mathrm{d}\mu^*_{T_n}(u') \right| \mathrm{d}\mu^*_{T_n}(u) \\ &\qquad = 2 \int_{\mathcal{S}^d} \max\left(0,\ U_{\mu^*}(u) - \int_{\mathcal{S}^d} U_{\mu^*}(u') \,\mathrm{d}\mu^*_{T_n}(u')\right) \mathrm{d}\mu^*_{T_n}(u) \\ &\qquad \leq 2(U^* - \int_{\mathcal{S}^d} U_{\mu^*}(u) \,\mathrm{d}\mu^*_{T_n}(u)) \\ &\qquad \to 0, \qquad\qquad \text{as } n \to \infty, \end{aligned}$$

where the inequality follows the boundedness of U_{μ^*} and that $\mu^*_{T_n}(\{u\colon U_{\mu^*}(u) > U^*\}) = 0$.

Therefore, given the continuity of log and the boundedness of U_{μ^*}, we have

$$\lim_{n\to\infty} \int_{\mathcal{S}^d} \log U_{\mu^*}(u) \,\mathrm{d}\mu^*_{T_n} = \log U^*.$$

Equation (A.13) gives that $\forall n = 1, 2, \ldots,$

$$\begin{aligned} 1 &= \int_{\mathcal{S}^d} \frac{U_{\mu^*_{T_n}}(u)}{U_{\mu^*}(u)} \,\mathrm{d}\mu^* + \int_{\mathcal{S}^d} \log U_{\mu^*}(u) \,\mathrm{d}(\mu^*_{T_n} - \mu^*) \\ &\geq \frac{1}{U^*} \int_{\mathcal{S}^d} U_{\mu^*_{T_n}}(u) \,\mathrm{d}\mu^*(u) + \int_{\mathcal{S}^d} \log U_{\mu^*}(u) \,\mathrm{d}\mu^*_{T_n} - \int_{\mathcal{S}^d} \log U_{\mu^*}(u) \,\mathrm{d}\mu^* \\ &= \frac{1}{U^*} \int_{\mathcal{S}^d} U_{\mu^*}(u) \,\mathrm{d}\mu^*_{T_n}(u) + \int_{\mathcal{S}^d} \log U_{\mu^*}(u) \,\mathrm{d}\mu^*_{T_n} - \int_{\mathcal{S}^d} \log U_{\mu^*}(u) \,\mathrm{d}\mu^*, \end{aligned}$$

where the inequality follows the boundedness of $\frac{U_{\mu^*_{T_n}}}{U_{\mu^*}}$ and that $\mu^*(\{u\colon U_{\mu^*}(u) > U^*\}) = 0$.

Taking the limit of $n \to \infty$ on both sides, we have

$$\begin{aligned}
1 = \lim_{n\to\infty} 1 &\geq \frac{1}{U^*} \lim_{n\to\infty} \int_{\mathcal{S}^d} U_{\mu^*}(u)\,\mathrm{d}\mu^*_{T_n}(u) + \lim_{n\to\infty} \int_{\mathcal{S}^d} \log U_{\mu^*}(u)\,\mathrm{d}\mu^*_{T_n}(u) \\
&\qquad - \int_{\mathcal{S}^d} \log U_{\mu^*}(u)\,\mathrm{d}\mu^*(u) \\
&= 1 + \log U^* - \int_{\mathcal{S}^d} \log U_{\mu^*}(u)\,\mathrm{d}\mu^*(u) \\
&\geq 1 + \log U^* - \log \int_{\mathcal{S}^d} U_{\mu^*}(u)\,\mathrm{d}\mu^*(u) \\
&\geq 1,
\end{aligned}$$

where the last inequality holds because the supremum taken over $\mathcal{T} \supset \{\mathcal{S}^d\}$.

Since $1 = 1$, all inequalities must be equalities. In particular,

$$\int_{\mathcal{S}^d} \log U_{\mu^*}(u)\,\mathrm{d}\mu^*(u) = \log \int_{\mathcal{S}^d} U_{\mu^*}(u)\,\mathrm{d}\mu^*(u).$$

That is, for any solution μ^* of Equation (A.11), U_{μ^*} must be constant μ^*-almost surely.

3. **We show that σ_d is the unique minimizer of the relaxed problem in Equation (A.11).**

Let $S \subset \mathcal{M}(\mathcal{S}^d)$ be the set of measures where the above property holds:

$$S \triangleq \left\{\mu \in \mathcal{M}(\mathcal{S}^d) \colon U_\mu \text{ is constant } \mu\text{-almost surely}\right\}.$$

The problem in Equation (A.11) is thus equivalent to minimizing over S:

$$\begin{aligned}
\arg\min_{\mu\in\mathcal{M}(\mathcal{S}^d)} \int_{\mathcal{S}^d} \log U_\mu(u)\,\mathrm{d}\mu(u) &= \arg\min_{\mu\in S} \int_{\mathcal{S}^d} \log U_\mu(u)\,\mathrm{d}\mu(u) \\
&= \arg\min_{\mu\in S} \log \int_{\mathcal{S}^d} U_\mu(u)\,\mathrm{d}\mu(u) \\
&= \arg\min_{\mu\in S} \log \int_{\mathcal{S}^d}\int_{\mathcal{S}^d} e^{u^\intercal v/\tau}\,\mathrm{d}\mu(v)\,\mathrm{d}\mu(u) \\
&= \arg\min_{\mu\in S} \left(\frac{1}{\tau} + \log \int_{\mathcal{S}^d}\int_{\mathcal{S}^d} e^{-\frac{1}{2\tau}\|u-v\|^2}\,\mathrm{d}\mu(v)\,\mathrm{d}\mu(u)\right) \\
&= \arg\min_{\mu\in S} \int_{\mathcal{S}^d}\int_{\mathcal{S}^d} G_{\frac{1}{2\tau}}(u,v)\,\mathrm{d}\mu(v)\,\mathrm{d}\mu(u).
\end{aligned}$$

By Proposition 2.4.2 and $\tau > 0$, we know that the uniform distribution σ_d is the unique solution to

$$\arg\min_{\mu\in\mathcal{M}(\mathcal{S}^d)} \int_{\mathcal{S}^d}\int_{\mathcal{S}^d} G_{\frac{1}{2\tau}}(u,v)\,\mathrm{d}\mu(v)\,\mathrm{d}\mu(u). \tag{A.14}$$

Since $\sigma_d \in S$, it must also be the unique solution to Equation (A.11).

Finally, if perfectly uniform encoders exist, σ_d is realizable, and they are the exact encoders that realize it. Hence, in such cases, they are the exact minimizers of

$$\min_f \mathop{\mathbb{E}}_{x\sim p_{\mathsf{data}}}\left[\log \mathop{\mathbb{E}}_{x^-\sim p_{\mathsf{data}}}\left[e^{f(x^-)^\intercal f(x)/\tau}\right]\right].$$

□

Relation between Theorem 2.4.7, $\mathcal{L}_{\mathsf{align}}$ and $\mathcal{L}_{\mathsf{uniform}}$. The first term of Equation (2.2) is equivalent with $\mathcal{L}_{\mathsf{align}}$ when $\alpha = 2$, up to a constant and a scaling. In the above proof, we showed that the second term favors uniformity, via the feature distribution that minimizes the pairwise Gaussian kernel (see Equation (A.14)):

$$\arg\min_{\mu\in\mathcal{M}(\mathcal{S}^d)} \int_{\mathcal{S}^d}\int_{\mathcal{S}^d} G_{\frac{1}{2\tau}}(u,v)\,\mathrm{d}\mu(v)\,\mathrm{d}\mu(u), \tag{A.15}$$

which can be alternatively viewed as the relaxed problem of optimizing for the uniformity loss $\mathcal{L}_{\mathsf{uniform}}$:

$$\arg\min_f \mathcal{L}_{\mathsf{uniform}}(f; \frac{1}{2\tau}) = \arg\min_f \mathbb{E}_{x,y \overset{\text{i.i.d.}}{\sim} p_{\mathsf{data}}} \left[G_{\frac{1}{2\tau}}(f(x), f(y)) \right]. \tag{A.16}$$

The relaxation comes from the observation that Equation (A.15) minimizes over all feature distributions on $\mathcal{S}^d$, while Equation (A.16) only considers the realizable ones.

Relation between Equation (A.11) and minimizing average pairwise Gaussian potential (*i.e.*, minimizing $\mathcal{L}_{\mathsf{uniform}}$). In view of the Proposition 2.4.2 and the proof of Theorem 2.4.7, we know that the uniform distribution σ_d is the unique minimizer of both of the following problems:

$$\{\sigma_d\} = \min_{\mu \in \mathcal{M}(\mathcal{S}^d)} \log \int_{\mathcal{S}^d} \int_{\mathcal{S}^d} e^{u^\mathsf{T} v/\tau} \, \mathrm{d}\mu(v) \, \mathrm{d}\mu(u),$$
$$\{\sigma_d\} = \min_{\mu \in \mathcal{M}(\mathcal{S}^d)} \int_{\mathcal{S}^d} \log \int_{\mathcal{S}^d} e^{u^\mathsf{T} v/\tau} \, \mathrm{d}\mu(v) \, \mathrm{d}\mu(u).$$

So pushing the log inside the outer integral doesn't change the solution. However, if we push the log all the way inside the inner integral, the problem becomes equivalent with minimizing the norm of the mean, *i.e.*,

$$\min_{\mu \in \mathcal{M}(\mathcal{S}^d)} \mathbb{E}_{U \sim \mu}[U]^\mathsf{T} \mathbb{E}_{U \sim \mu}[U],$$

which is minimized for any distribution with mean being the all-zeros vector 0, *e.g.*, $\frac{1}{2}\delta_u + \frac{1}{2}\delta_{-u}$ for any $u \in \mathcal{S}^d$ (where δ_u is the Dirac delta distribution at u s.t. $\delta_u(S) = \mathbb{1}_S(u)$, $\forall S \in \mathcal{B}(\mathcal{S}^d)$). Therefore, the location of the log is important.

Theorem A.1.9 (Single negative sample). If perfectly aligned and uniform encoders exist, they form the exact minimizers of the contrastive loss $\mathcal{L}_{\mathsf{contrastive}}(f; \tau, M)$ for fixed $\tau > 0$ and $M = 1$.

Proof of Theorem A.1.9. Since $M = 1$, we have

$$\begin{aligned}
\mathcal{L}_{\mathsf{contrastive}}(f;\tau,1) &= \mathop{\mathbb{E}}_{\substack{(x,y)\sim p_{\mathsf{pos}}\\ x^-\sim p_{\mathsf{data}}}}\left[-\frac{1}{\tau}f(x)^\mathsf{T} f(y) + \log\left(e^{f(x)^\mathsf{T} f(y)/\tau} + e^{f(x^-)^\mathsf{T} f(x)/\tau}\right)\right] \\
&\geq \mathop{\mathbb{E}}_{\substack{x\sim p_{\mathsf{data}}\\ x^-\sim p_{\mathsf{data}}}}\left[-\frac{1}{\tau} + \log\left(e^{1/\tau} + e^{f(x^-)^\mathsf{T} f(x)/\tau}\right)\right] \qquad \text{(A.17)} \\
&\geq -\frac{1}{\tau} + \min_{\mu\in\mathcal{M}(\mathcal{S}^d)} \int_{\mathcal{S}^d}\int_{\mathcal{S}^d} \log\left(e^{1/\tau} + e^{u^\mathsf{T} v/\tau}\right) \mathrm{d}\mu(u)\,\mathrm{d}\mu(v) \qquad \text{(A.18)} \\
&= -\frac{1}{\tau} + \min_{\mu\in\mathcal{M}(\mathcal{S}^d)} \int_{\mathcal{S}^d}\int_{\mathcal{S}^d} \log\left(e^{1/\tau} + e^{(2-\|u-v\|_2^2)/(2\tau)}\right) \mathrm{d}\mu(u)\,\mathrm{d}\mu(v).
\end{aligned}$$

By the definition of perfect alignment, the equality in Equation (A.17) is satisfied iff f is perfectly aligned.

Consider the function $f\colon (0,4] \to \mathbb{R}_+$ defined as

$$f(t) = \log(e^{\frac{1}{\tau}} + e^{\frac{2-t}{2\tau}}).$$

It has the following properties:

- $-f'(t) = \frac{1}{2\tau}\frac{e^{-\frac{t}{2\tau}}}{1+e^{-\frac{t}{2\tau}}} = \frac{1}{2\tau}(1-(1+e^{-\frac{t}{2\tau}})^{-1})$ is strictly completely monotone on $(0,+\infty)$:

  $\forall t \in (0,+\infty)$,

  $$\begin{aligned}
  &\frac{1}{2\tau}(1-(1+e^{-\frac{t}{2\tau}})^{-1}) > 0 \\
  &(-1)^n \frac{\mathrm{d}^n}{\mathrm{d}t^n}\frac{1}{2\tau}(1-(1+e^{-\frac{t}{2\tau}})^{-1}) = \frac{n!}{(2\tau)^{n+1}}(1+e^{-\frac{t}{2\tau}})^{-(n+1)} > 0, \qquad n = 1,2,\ldots.
  \end{aligned}$$

- f is bounded on $(0,4]$.

In view of Lemma A.1.4, we have that the equality in Equation (A.18) is satisfied iff the feature distribution induced by f (*i.e.*, the pushforward measure $p_{\mathsf{data}} \circ f^{-1}$) is σ_d, that is, in other words, f is perfectly uniform.

Therefore,

$$\begin{aligned}\mathcal{L}_{\mathsf{contrastive}}(f;\tau,1) &\geq -\frac{1}{\tau} + \int_{\mathcal{S}^d}\int_{\mathcal{S}^d} \log\left(e^{1/\tau} + e^{u^\intercal v/\tau}\right) \mathrm{d}\sigma_d(u)\,\mathrm{d}\sigma_d(v) \\ &= \text{constant independent of } f,\end{aligned}$$

where equality is satisfied iff f is perfectly aligned and uniform. This concludes the proof. □

Difference between conditions of Theorems 2.4.7 and A.1.9. We remark that the statement in Theorem A.1.9 is weaker than the previous Theorem 2.4.7. Theorem A.1.9 is conditioned on the existence perfectly aligned and uniform encoders. It only shows that $\mathcal{L}_{\mathsf{contrastive}}(f;\tau,M=1)$ favors alignment under the condition that perfect uniformity is realizable, and vice versa. In Theorem 2.4.7, $\mathcal{L}_{\mathsf{contrastive}}$ decomposes into two terms, each favoring alignment and uniformity. Therefore, the decomposition in Theorem 2.4.7 is exempof t from this constraint.

A.2 Experiment Details

All experiments are performed on 1-4 NVIDIA Titan Xp, Titan X PASCAL, Titan RTX, or 2080 Ti GPUs.

A.2.1 CIFAR-10, STL-10 and NYU-Depth-V2 Experiments

For CIFAR-10, STL-10 and NYU-Depth-V2 experiments, we use the following settings, unless otherwise stated in Tables A.3 and A.4 below:

- Standard data augmentation procedures are used for generating positive pairs, including resizing, cropping, horizontal flipping, color jittering, and random grayscale conversion. This follows prior empirical work in contrastive representation learning (Wu et al., 2018; Tian et al., 2020b; Hjelm et al., 2018; Bachman et al., 2019).

- Neural network architectures follow the corresponding experiments on these datasets in Tian et al. (2020b). For NYU-Depth-V2 evaluation, the architecture of the depth prediction CNN is described in Table A.1.

- We use minibatch stochastic gradient descent (SGD) with 0.9 momentum and 0.0001 weight decay.

- We use linearly scaled learning rate (0.12 per 256 batch size) (Goyal et al., 2017).

  - CIFAR-10 and STL-10: Optimization is done over 200 epochs, with learning rate decayed by a factor of 0.1 at epochs 155, 170, and 185.

  - NYU-Depth-V2: Optimization is done over 400 epochs, with learning rate decayed by a factor of 0.1 at epochs 310, 340, and 370.

- Encoders are optimized over the training split. For evaluation, we freeze the encoder, and train classifiers / depth predictors on the training set samples, and test on the validation split.

  - CIFAR-10 and STL-10: We use standard train-val split. Linear classifiers are trained with Adam (Kingma and Ba, 2014) over 100 epochs, with $\beta_1 = 0.5, \beta_2 = 0.999, \epsilon = 10^{-8}$, 128 batch size, and an initial learning rate of 0.001, decayed by a factor of 0.2 at epochs 60 and 80.

  - NYU-Depth-V2: We use the train-val split on the 1449 labeled images from Nathan Silberman and Fergus (2012). Depth predictors are trained with Adam (Kingma and Ba, 2014) over 120 epochs, with $\beta_1 = 0.5, \beta_2 = 0.999, \epsilon = 10^{-8}$, 128 batch size, and an initial learning rate of 0.003, decayed by a factor of 0.2 at epochs 70, 90, 100, and 110.

At each SGD iteration, a minibatch of K positive pairs is sampled $\{(x_i, y_i)\}_{i=1}^{K}$, and the three losses for this minibatch are calculated as following:

- $\mathcal{L}_{\mathsf{contrastive}}$: For each x_i, the sample contrastive loss is taken with the positive being y_i, and the negatives being $\{y_j\}_{j \neq i}$. For each y_i, the sample loss is computed

Operator	Input Spatial Shape	Input #Channel	Kernel Size	Stride	Padding	Output Spatial Shape	Output #Channel
Input	$[h_{\mathsf{in}}, w_{\mathsf{in}}]$	c_{in}	—	—	—	$[h_{\mathsf{in}}, w_{\mathsf{in}}]$	c_{in}
Conv. Transpose + BN + ReLU	$[h_{\mathsf{in}}, w_{\mathsf{in}}]$	c_{in}	3	2	1	$[2h_{\mathsf{in}}, 2w_{\mathsf{in}}]$	$\lfloor c_{\mathsf{in}}/2 \rfloor$
Conv. Transpose + BN + ReLU	$[2h_{\mathsf{in}}, 2w_{\mathsf{in}}]$	$\lfloor c_{\mathsf{in}}/2 \rfloor$	3	2	1	$[4h_{\mathsf{in}}, 4w_{\mathsf{in}}]$	$\lfloor c_{\mathsf{in}}/4 \rfloor$
⋮	⋮	⋮	⋮	⋮	⋮	⋮	⋮
Conv. Transpose + BN + ReLU	$[h_{\mathsf{out}}/2, w_{\mathsf{out}}/2]$	$\lfloor c_{\mathsf{in}}/2^{n-1} \rfloor$	3	2	1	$[h_{\mathsf{out}}, w_{\mathsf{out}}]$	$\lfloor c_{\mathsf{in}}/2^{n} \rfloor$
Conv.	$[h_{\mathsf{out}}, w_{\mathsf{out}}]$	$\lfloor c_{\mathsf{in}}/2^{n} \rfloor$	3	1	1	$[h_{\mathsf{out}}, w_{\mathsf{out}}]$	1

Table A.1: NYU-Depth-V2 CNN depth predictor architecture. Each Conv. Transpose+BN+ReLU block increases the spatial shape by a factor of 2, where BN denotes Batch Normalization (Ioffe and Szegedy, 2015). A sequence of such blocks computes a tensor of the correct spatial shape, from an input containing intermediate activations of a CNN encoder (which downsamples the input RGB image by a power of 2). A final convolution at the end computes the single-channel depth prediction.

similarly. The minibatch loss is calculated by aggregating these $2K$ terms:

$$\frac{1}{2K}\sum_{i=1}^{K}\log\frac{e^{f(x_i)^\intercal f(y_i)/\tau}}{\sum_{j=1}^{K}e^{f(x_i)^\intercal f(y_j)/\tau}}+\frac{1}{2K}\sum_{i=1}^{K}\log\frac{e^{f(x_i)^\intercal f(y_i)/\tau}}{\sum_{j=1}^{K}e^{f(x_j)^\intercal f(y_i)/\tau}}.$$

This calculation follows empirical practices and is similar to Oord et al. (2018); Hénaff et al. (2019), and *end-to-end* in He et al. (2019).

- $\mathcal{L}_{\mathsf{align}}$: The minibatch alignment loss is straightforwardly computed as

$$\frac{1}{K}\sum_{i=1}^{K}\|f(x_i)-f(y_i)\|_2^{\alpha}.$$

- $\mathcal{L}_{\mathsf{uniform}}$: The minibatch uniform loss is calculated by considering each pair of $\{x_i\}_i$ and $\{y_i\}_i$:

$$\frac{1}{2}\log\left(\frac{2}{K(K-1)}\sum_{i\neq j}e^{-t\|f(x_i)-f(x_j)\|_2^2}\right)+\frac{1}{2}\log\left(\frac{2}{K(K-1)}\sum_{i\neq j}e^{-t\|f(y_i)-f(y_j)\|_2^2}\right).$$

Tables A.3 and A.4 below describe the full specifications of all 304 STL-10 and 64 NYU-Depth-V2 encoders. These experiment results are visualized in Figure 2-5, showing a clear connection between representation quality and $\mathcal{L}_{\mathsf{align}}$ & $\mathcal{L}_{\mathsf{uniform}}$ metrics.

ImageNet-100 Classes									
n02869837	n01749939	n02488291	n02107142	n13037406	n02091831	n04517823	n04589890	n03062245	n01773797
n01735189	n07831146	n07753275	n03085013	n04485082	n02105505	n01983481	n02788148	n03530642	n04435653
n02086910	n02859443	n13040303	n03594734	n02085620	n02099849	n01558993	n04493381	n02109047	n04111531
n02877765	n04429376	n02009229	n01978455	n02106550	n01820546	n01692333	n07714571	n02974003	n02114855
n03785016	n03764736	n03775546	n02087046	n07836838	n04099969	n04592741	n03891251	n02701002	n03379051
n02259212	n07715103	n03947888	n04026417	n02326432	n03637318	n01980166	n02113799	n02086240	n03903868
n02483362	n04127249	n02089973	n03017168	n02093428	n02804414	n02396427	n04418357	n02172182	n01729322
n02113978	n03787032	n02089867	n02119022	n03777754	n04238763	n02231487	n03032252	n02138441	n02104029
n03837869	n03494278	n04136333	n03794056	n03492542	n02018207	n04067472	n03930630	n03584829	n02123045
n04229816	n02100583	n03642806	n04336792	n03259280	n02116738	n02108089	n03424325	n01855672	n02090622

Table A.2: 100 randomly selected ImageNet classes forming the ImageNet-100 subset. These classes are the same as the ones used by Tian et al. (2020b).

A.2.2 ImageNet and ImageNet-100 with Momentum Contrast (MoCo) Variants

MoCo and MoCo v2 with $\mathcal{L}_{\mathsf{align}}$ and $\mathcal{L}_{\mathsf{uniform}}$. At each SGD iteration, let

- K be the minibatch size,
- $\{f(x_i)_i\}_{i=1}^K$ be the batched query features encoded by the current up-to-date encoder f (*i.e.*, `q` in Algorithm 1 of He et al. (2019)),
- $\{f_{\mathsf{EMA}}(y_i)\}_{i=1}^K$ be the batched key features encoded by the exponential moving average encoder f_{EMA} (*i.e.*, `k` in Algorithm 1 of He et al. (2019)),
- $\{\mathtt{queue}_j\}_{j=1}^N$ be the feature queue, where N is the queue size.

$\mathcal{L}_{\mathsf{align}}$ and $\mathcal{L}_{\mathsf{uniform}}$ for this minibatch are calculated as following:

- $\mathcal{L}_{\mathsf{align}}$: The minibatch alignment loss is computed as disparity between features from the two encoders:

$$\frac{1}{K}\sum_{i=1}^{K}\|f(x_i) - f_{\mathsf{EMA}}(y_i)\|_2^{\alpha}.$$

- $\mathcal{L}_{\mathsf{uniform}}$: We experiment with two forms of $\mathcal{L}_{\mathsf{uniform}}$:

1. Only computing pairwise distance between $\{f(x_i)\}_i$ and $\{\texttt{queue}_j\}_j$:

$$\log\left(\frac{1}{NK}\sum_{i=1}^{K}\sum_{j=1}^{N} e^{-t\left\|f(x_i)-\texttt{queue}_j\right\|_2^2}\right). \tag{A.19}$$

2. Also computing pairwise distance inside $\{f(x_i)\}_i$:

$$\begin{aligned}\log\Bigg(&\frac{2}{2NK+K(K-1)}\sum_{i=1}^{K}\sum_{j=1}^{N} e^{-t\left\|f(x_i)-\texttt{queue}_j\right\|_2^2} \\ &+\frac{2}{2NK+K(K-1)}\sum_{i\neq j} e^{-t\|f(x_i)-f(x_j)\|_2^2}\Bigg).\end{aligned} \tag{A.20}$$

ImageNet-100 with MoCo

ImageNet-100 details. We use the same ImageNet-100 sampled by Tian et al. (2020b), containing the 100 randomly selected classes listed in Table A.2.

MoCo settings. Our MoCo experiment settings below mostly follow He et al. (2019) and the unofficial implementation by Tian (2019), because the official implementation was not released at the time of performing these analyses:

- Standard data augmentation procedures are used for generating positive pairs, including resizing, cropping, horizontal flipping, color jittering, and random grayscale conversion, following Tian (2019).
- Encoder architecture is ResNet50 (He et al., 2016).
- We use minibatch stochastic gradient descent (SGD) with 128 batch size, 0.03 initial learning rate, 0.9 momentum and 0.0001 weight decay.
- Optimization is done over 240 epochs, with learning rate decayed by a factor of 0.1 at epochs 120, 160, and 200.
- We use 0.999 exponential moving average factor, following He et al. (2019).
- For evaluation, we freeze the encoder, and train a linear classifier on the training set samples, and test on the validation split. Linear classifiers are trained with

minibatch SGD over 60 epochs, with 256 batch size, and an initial learning rate of 10, decayed by a factor of 0.2 at epochs 30, 40, and 50.

Table A.5 below describes the full specifications of all 45 ImageNet-100 encoders. These experiment results are visualized in Figure 2-9a, showing a clear connection between representation quality and $\mathcal{L}_{\mathsf{align}}$ & $\mathcal{L}_{\mathsf{uniform}}$ metrics.

ImageNet with MoCo v2

MoCo v2 settings. Our MoCo v2 experiment settings directly follow Chen et al. (2020b) and the official implementation (Chen et al., 2020c):

- Standard data augmentation procedures are used for generating positive pairs, including resizing, cropping, horizontal flipping, color jittering, random grayscale conversion, and random Gaussian blurring, following Chen et al. (2020c).
- Encoder architecture is ResNet50 (He et al., 2016).
- We use minibatch stochastic gradient descent (SGD) with 256 batch size, 0.03 initial learning rate, 0.9 momentum and 0.0001 weight decay.
- Optimization is done over 200 epochs, with learning rate decayed by a factor of 0.1 at epochs 120 and 160.
- We use 0.999 exponential moving average factor, 65536 queue size, 128 feature dimensions.
- For evaluation, we freeze the encoder, and train a linear classifier on the training set samples, and test on the validation split. Linear classifiers are trained with minibatch SGD over 100 epochs, with 256 batch size, and an initial learning rate of 30, decayed by a factor of 0.1 at epochs 60 and 80.

Unlike the MoCo experiments on ImageNet-100, which were based on unofficial implementations for reasons stated in Sec. A.2.2, the MoCo v2 experiments on full ImageNet were based on the official implementation by Chen et al. (2020c). We

provide a reference implementation that can fully reproduce the results in Table 2.5 at https://github.com/SsnL/moco_align_uniform, where we also provide a model checkpoint (trained using $\mathcal{L}_{\mathsf{align}}$ and $\mathcal{L}_{\mathsf{uniform}}$) of 67.694% validation top1 accuracy.

A.2.3 BookCorpus with Quick-Thought Vectors Variants

BookCorpus details. Since the original BookCorpus dataset (Zhu et al., 2015) is not distributed anymore, we use the unofficial code by Kobayashi (2019) to recreate our copy. Our copy ended up containing 52,799,513 training sentences and 50,000 validation sentences, compared to the original copy used by Quick-Thought Vectors (Logeswaran and Lee, 2018), which contains 45,786,400 training sentences and 50,000 validation sentences.

Quick-Thought Vectors with $\mathcal{L}_{\mathsf{align}}$ and $\mathcal{L}_{\mathsf{uniform}}$. With Quick-Thought Vectors, the positive pairs are the neighboring sentences. At each optimization iteration, let

- $\{x_i\}_{i=1}^{K}$ be the K *consecutive* sentences forming this minibatch, where K be the minibatch size,
- f and g be the two RNN sentence encoders.

The original Quick-Thought Vectors (Logeswaran and Lee, 2018) does not $l2$-normalize on encoder outputs during training the encoder. Here we describe the calculation of $\mathcal{L}_{\mathsf{contrastive}}$, $\mathcal{L}_{\mathsf{align}}$, and $\mathcal{L}_{\mathsf{uniform}}$ for $l2$-normalized encoders, in our modified Quick-Thought Vectors method. Note that this does not affect evaluation since features are $l2$-normalized before using in downstream tasks, following the original Quick-Thought Vectors (Logeswaran and Lee, 2018). For a minibatch, these losses are calculated as following:

- $\mathcal{L}_{\text{contrastive}}$ with temperature:

$$\frac{1}{K}\,\texttt{ce}(\texttt{softmax}(\{f(x_1)^\top g(x_j)\}_j), \{0,1,0,\ldots,0\}) + \frac{1}{K}\sum_{i=2}^{K-1}\texttt{ce}(\texttt{softmax}(\{f(x_i)^\top g(x_j)\}_j), \{\underbrace{0,\ldots,0}_{(i-2)\text{ 0's}}, \frac{1}{2}, 0, \frac{1}{2}, \underbrace{0,\ldots,0}_{(K-i-1)\text{ 0's}}\}) + \frac{1}{K}\,\texttt{ce}(\texttt{softmax}(\{f(x_K)^\top g(x_j)\}_j), \{0,\ldots,1,0\}),$$

  where $\texttt{ce}(p,q)$ is the cross entropy between prediction p and target q.

  This is almost identical with the original contrastive loss used by Quick-Thought Vectors, except that this does not additionally manually masks out the entries $f(x_i)^\top g(x_i)$ with zeros, which is unnecessary with $l2$-normalization.

- $\mathcal{L}_{\text{align}}$: The minibatch alignment loss is computed as disparity between features from the two encoders encoding neighboring sentences (assuming $K >= 2$):

$$\frac{1}{K}\|f(x_1)-g(x_2)\|_2^\alpha + \frac{1}{2K}\sum_{i=2}^{K-2}(\|f(x_{i-1})-g(x_i)\|_2^\alpha + \|f(x_i)-g(x_{i+1})\|_2^\alpha) + \frac{1}{K}\|f(x_{K-1})-g(x_K)\|_2^\alpha.$$

- $\mathcal{L}_{\text{uniform}}$: We combine the uniformity losses for each of f and g by summing them (instead of averaging since f and g are two different encoders):

$$\frac{2}{K(K-1)}\sum_{i\neq j} e^{-t\|f(x_i)-f(x_j)\|_2^2} + \frac{2}{K(K-1)}\sum_{i\neq j} e^{-t\|g(x_i)-g(x_j)\|_2^2}.$$

Our experiment settings below mostly follow the official implementation by Logeswaran and Lee (2018):

- Sentence encoder architecture is bi-directional Gated Recurrent Unit (GRU) (Cho et al., 2014) with inputs from a 620-dimensional word embedding trained jointly from scratch.

- We use Adam (Kingma and Ba, 2014) with $\beta_1 = 0.9, \beta_2 = 0.999, \epsilon = 10^{-8}$, 400

batch size, 0.0005 constant learning rate, and 0.5 gradient norm clipping.

- Optimization is done during 1 epoch over the training data.
- For evaluation on a binary classification task, we freeze the encoder, and fit a logistic classifier with $l2$ regularization on the encoder outputs. A 10-fold cross validation is performed to determine the regularization strength among $\{1, 2^{-1}, \ldots, 2^{-8}\}$, following Kiros et al. (2015) and Logeswaran and Lee (2018). The classifier is finally tested on the validation split.

Table A.6 below describes the full specifications of all 108 BookCorpus encoders along with 6 settings that lead to training instability (*i.e.*, `NaN` occurring). These experiment results are visualized in Figure 2-9b, showing a clear connection between representation quality and $\mathcal{L}_{\mathsf{align}}$ & $\mathcal{L}_{\mathsf{uniform}}$ metrics. For the unnormalized encoders, the features are normalized before calculated $\mathcal{L}_{\mathsf{align}}$ and $\mathcal{L}_{\mathsf{uniform}}$ metrics, since they are nonetheless still normalized before being used in downstream tasks (Logeswaran and Lee, 2018).

Table A.3: Experiment specifications for all 304 STL-10 encoders. We report the encoder representation quality measured by accuracy of linear and k-nearest neighbor (k-NN) with $k = 5$ classifiers on either encoder outputs or fc7 activations, via both a 5-fold cross validation of the training set and the held out validation set.
For encoder initialization, "rand" refers to standard network initialization, and symbols denote finetuning from a pretrained encoder, obtained via the experiment row marked with the same symbol. Initial learning rates (LRs) are usually either fixed as 0.12 or computed via a linear scaling (0.12 per 256 batch size). Dimensionality (abbreviated as "Dim.") shows the ambient dimension of the output features, *i.e.*, they live on the unit hypersphere of one less dimension. The last three rows show encoders that are used to initialize finetuning, but are not part of the 285 encoders plotted in Figure 2-5a, due to their unusual batch size of 786. Their accuracy and $\mathcal{L}_{\mathsf{align}}$ & $\mathcal{L}_{\mathsf{uniform}}$ metrics follow the same trend shown in Figure 2-5a.

Losses			Init.	Epochs	Batch Size	Initial LR	Dim.	Training Set 5-Fold Cross Val. Accuracy ↑				Validation Set Accuracy ↑			
$\mathcal{L}_{\mathsf{contrastive}}$	$\mathcal{L}_{\mathsf{align}}$	$\mathcal{L}_{\mathsf{uniform}}$						Output + Linear	Output + 5-NN	fc7 + Linear	fc7 + 5-NN	Output + Linear	Output + 5-NN	fc7 + Linear	fc7 + 5-NN
—	$1.25 \cdot \mathcal{L}_{\mathsf{a}}(\alpha{=}2)$	$\mathcal{L}_{\mathsf{u}}(t{=}2)$	rand	200	2	0.0009375	128	—	—	—	—	19.31%	22.56%	47.58%	35.30%
—	$1.25 \cdot \mathcal{L}_{\mathsf{a}}(\alpha{=}2)$	$\mathcal{L}_{\mathsf{u}}(t{=}2)$	rand	200	3	0.00140625	128	—	—	—	—	43.97%	42.89%	56.89%	47.63%
—	$1.25 \cdot \mathcal{L}_{\mathsf{a}}(\alpha{=}2)$	$\mathcal{L}_{\mathsf{u}}(t{=}2)$	rand	200	4	0.001875	128	—	—	—	—	53.96%	52.89%	62.86%	55.06%
$\mathcal{L}_{\mathsf{c}}(\tau{=}0.07)$	—	—	rand	200	16	0.0075	128	—	—	—	—	70.46%	70.54%	75.54%	69.63%
$\mathcal{L}_{\mathsf{c}}(\tau{=}0.5)$	—	—	rand	200	16	0.0075	128	—	—	—	—	69.59%	70.04%	76.23%	68.38%
—	$\mathcal{L}_{\mathsf{a}}(\alpha{=}2)$	$\mathcal{L}_{\mathsf{u}}(t{=}2)$	rand	200	16	0.0075	128	—	—	—	—	74.68%	74.34%	79.06%	73.68%
—	$1.25 \cdot \mathcal{L}_{\mathsf{a}}(\alpha{=}1)$	$\mathcal{L}_{\mathsf{u}}(t{=}2)$	rand	200	16	0.0075	128	—	—	—	—	74.75%	73.00%	77.84%	71.70%
—	$1.25 \cdot \mathcal{L}_{\mathsf{a}}(\alpha{=}2)$	$\mathcal{L}_{\mathsf{u}}(t{=}2)$	rand	200	16	0.0075	128	—	—	—	—	73.93%	74.09%	79.25%	73.38%
$\mathcal{L}_{\mathsf{c}}(\tau{=}0.5)$	—	—	rand	200	16	0.12	128	—	—	—	—	67.30%	66.36%	71.53%	66.38%
—	$\mathcal{L}_{\mathsf{a}}(\alpha{=}2)$	$\mathcal{L}_{\mathsf{u}}(t{=}2)$	rand	200	16	0.12	128	—	—	—	—	71.93%	71.24%	75.49%	69.89%
—	$1.25 \cdot \mathcal{L}_{\mathsf{a}}(\alpha{=}1)$	$\mathcal{L}_{\mathsf{u}}(t{=}2)$	rand	200	16	0.12	128	—	—	—	—	71.85%	70.21%	74.65%	69.88%
$\mathcal{L}_{\mathsf{c}}(\tau{=}0.07)$	—	—	rand	200	32	0.015	128	—	—	—	—	71.80%	72.04%	77.29%	70.74%
$\mathcal{L}_{\mathsf{c}}(\tau{=}0.5)$	—	—	rand	200	32	0.015	128	—	—	—	—	73.39%	73.39%	79.43%	73.85%
—	$\mathcal{L}_{\mathsf{a}}(\alpha{=}2)$	$\mathcal{L}_{\mathsf{u}}(t{=}2)$	rand	200	32	0.015	128	—	—	—	—	78.04%	76.60%	82.23%	76.04%
—	$1.25 \cdot \mathcal{L}_{\mathsf{a}}(\alpha{=}1)$	$\mathcal{L}_{\mathsf{u}}(t{=}2)$	rand	200	32	0.015	128	—	—	—	—	78.71%	76.45%	81.66%	76.25%

$\mathcal{L}_{\mathsf{c}}(\tau{=}0.5)$	—	—	rand	200	32	0.12	128	—	—	—	—	70.43%	69.66%	74.95%	69.69%
—	$\mathcal{L}_{\mathsf{a}}(\alpha{=}2)$	$\mathcal{L}_{\mathsf{u}}(t{=}2)$	rand	200	32	0.12	128	—	—	—	—	75.40%	73.70%	78.56%	73.21%
—	$1.25 \cdot \mathcal{L}_{\mathsf{a}}(\alpha{=}1)$	$\mathcal{L}_{\mathsf{u}}(t{=}2)$	rand	200	32	0.12	128	—	—	—	—	75.83%	73.95%	78.48%	73.55%
$\mathcal{L}_{\mathsf{c}}(\tau{=}0.5)$	—	—	rand	200	64	0.03	128	—	—	—	—	74.59%	74.48%	80.64%	75.52%
—	$\mathcal{L}_{\mathsf{a}}(\alpha{=}2)$	$\mathcal{L}_{\mathsf{u}}(t{=}2)$	rand	200	64	0.03	128	—	—	—	—	79.25%	77.84%	82.84%	76.53%
—	$\mathcal{L}_{\mathsf{a}}(\alpha{=}2)$	$\mathcal{L}_{\mathsf{u}}(t{=}2)$	rand	200	64	0.12	128	—	—	—	—	77.80%	75.75%	81.45%	75.49%
—	$1.25 \cdot \mathcal{L}_{\mathsf{a}}(\alpha{=}1)$	$\mathcal{L}_{\mathsf{u}}(t{=}2)$	rand	200	64	0.12	128	—	—	—	—	78.66%	76.19%	81.40%	75.30%
—	$\mathcal{L}_{\mathsf{a}}(\alpha{=}2)$	$\mathcal{L}_{\mathsf{u}}(t{=}2)$	rand	200	64	0.03	512	—	—	—	—	80.44%	78.05%	83.04%	77.29%
—	$0.5 \cdot \mathcal{L}_{\mathsf{a}}(\alpha{=}2)$	$\mathcal{L}_{\mathsf{u}}(t{=}2)$	rand	200	64	0.03	1024	—	—	—	—	81.48%	78.49%	82.88%	77.11%
—	$\mathcal{L}_{\mathsf{a}}(\alpha{=}2)$	$\mathcal{L}_{\mathsf{u}}(t{=}2)$	rand	200	64	0.03	1024	—	—	—	—	80.81%	77.80%	83.18%	77.15%
$\mathcal{L}_{\mathsf{c}}(\tau{=}0.07)$	—	—	rand	200	128	0.06	128	—	—	—	—	73.14%	73.73%	79.90%	72.58%
$\mathcal{L}_{\mathsf{c}}(\tau{=}0.5)$	—	—	rand	200	128	0.06	128	—	—	—	—	75.26%	74.88%	80.98%	75.36%
—	$\mathcal{L}_{\mathsf{a}}(\alpha{=}2)$	$\mathcal{L}_{\mathsf{u}}(t{=}2)$	rand	200	128	0.06	128	—	—	—	—	79.55%	78.09%	83.39%	76.96%
$\mathcal{L}_{\mathsf{c}}(\tau{=}0.07)$	—	—	rand	200	128	0.12	128	—	—	—	—	73.11%	73.84%	78.44%	72.11%
$\mathcal{L}_{\mathsf{c}}(\tau{=}0.5)$	—	—	rand	200	128	0.12	128	—	—	—	—	75.65%	74.80%	80.74%	74.58%
$\mathcal{L}_{\mathsf{c}}(\tau{=}0.687)$	—	—	rand	200	128	0.12	128	—	—	—	—	74.13%	73.14%	79.81%	74.10%
—	$\mathcal{L}_{\mathsf{a}}(\alpha{=}2)$	$\mathcal{L}_{\mathsf{u}}(t{=}2)$	rand	200	128	0.12	128	—	—	—	—	79.74%	77.78%	82.70%	75.23%
—	$1.25 \cdot \mathcal{L}_{\mathsf{a}}(\alpha{=}1)$	$\mathcal{L}_{\mathsf{u}}(t{=}2)$	rand	200	128	0.12	128	—	—	—	—	80.19%	77.91%	82.75%	75.91%
—	$0.75 \cdot \mathcal{L}_{\mathsf{a}}(\alpha{=}2)$	$\mathcal{L}_{\mathsf{u}}(t{=}2)$	rand	200	256	0.12	64	—	—	—	—	78.40%	78.26%	83.46%	76.25%
$\mathcal{L}_{\mathsf{c}}(\tau{=}0.07)$	—	—	rand	200	256	0.12	128	—	—	—	—	75.23%	75.86%	80.64%	73.56%
♡ $\mathcal{L}_{\mathsf{c}}(\tau{=}0.5)$	—	—	rand	200	256	0.12	128	—	—	—	—	76.09%	75.81%	81.49%	75.52%
$\mathcal{L}_{\mathsf{c}}(\tau{=}0.6)$	—	—	rand	200	256	0.12	128	—	—	—	—	75.61%	74.56%	81.09%	75.36%
—	$0.75 \cdot \mathcal{L}_{\mathsf{a}}(\alpha{=}2)$	$\mathcal{L}_{\mathsf{u}}(t{=}2)$	rand	200	256	0.12	128	—	—	—	—	80.54%	78.55%	83.54%	76.81%
—	$\mathcal{L}_{\mathsf{a}}(\alpha{=}2)$	$\mathcal{L}_{\mathsf{u}}(t{=}2)$	rand	200	256	0.12	128	—	—	—	—	80.76%	78.57%	84.24%	76.60%
△ —	$1.25 \cdot \mathcal{L}_{\mathsf{a}}(\alpha{=}1)$	$\mathcal{L}_{\mathsf{u}}(t{=}2)$	rand	200	256	0.12	128	—	—	—	—	81.29%	78.49%	83.55%	74.08%
—	$0.5 \cdot \mathcal{L}_{\mathsf{a}}(\alpha{=}2)$	$\mathcal{L}_{\mathsf{u}}(t{=}2)$	rand	200	256	0.12	256	—	—	—	—	81.79%	79.13%	84.11%	76.60%

—	$0.75 \cdot \mathcal{L}_{\mathsf{a}}(\alpha{=}2)$	$\mathcal{L}_{\mathsf{u}}(t{=}2)$	rand	200	256	0.12	256	—	—	—	—	81.48%	79.61%	83.86%	76.79%
—	$\mathcal{L}_{\mathsf{a}}(\alpha{=}2)$	$\mathcal{L}_{\mathsf{u}}(t{=}2)$	rand	200	256	0.12	256	—	—	—	—	80.95%	78.74%	83.69%	77.11%
—	$\mathcal{L}_{\mathsf{a}}(\alpha{=}2)$	$\mathcal{L}_{\mathsf{u}}(t{=}2)$	rand	200	256	0.12	512	—	—	—	—	81.33%	78.76%	83.81%	76.88%
—	$0.5 \cdot \mathcal{L}_{\mathsf{a}}(\alpha{=}2)$	$\mathcal{L}_{\mathsf{u}}(t{=}2)$	rand	200	360	0.16875	8192	—	—	—	—	82.49%	78.96%	83.86%	76.68%
—	$0.5 \cdot \mathcal{L}_{\mathsf{a}}(\alpha{=}2)$	$\mathcal{L}_{\mathsf{u}}(t{=}2)$	rand	200	512	0.24	4096	—	—	—	—	82.34%	78.84%	84.06%	75.74%
$\mathcal{L}_{\mathsf{c}}(\tau{=}0.07)$	—	—	rand	200	768	0.36	2	—	—	—	—	29.46%	25.50%	59.95%	52.83%
$\mathcal{L}_{\mathsf{c}}(\tau{=}0.5)$	—	—	rand	200	768	0.36	2	—	—	—	—	30.66%	25.39%	48.61%	42.49%
—	$0.5 \cdot \mathcal{L}_{\mathsf{a}}(\alpha{=}2)$	$\mathcal{L}_{\mathsf{u}}(t{=}2)$	rand	200	768	0.36	2	—	—	—	—	27.85%	26.04%	49.29%	43.10%
—	$\mathcal{L}_{\mathsf{a}}(\alpha{=}2)$	$\mathcal{L}_{\mathsf{u}}(t{=}2)$	rand	200	768	0.36	2	—	—	—	—	29.05%	23.94%	45.39%	38.48%
$\mathcal{L}_{\mathsf{c}}(\tau{=}0.07)$	—	—	rand	200	768	0.36	3	—	—	—	—	39.59%	39.66%	63.24%	56.64%
$\mathcal{L}_{\mathsf{c}}(\tau{=}0.5)$	—	—	rand	200	768	0.36	3	—	—	—	—	42.29%	39.70%	68.35%	59.82%
—	$0.5 \cdot \mathcal{L}_{\mathsf{a}}(\alpha{=}2)$	$\mathcal{L}_{\mathsf{u}}(t{=}2)$	rand	200	768	0.36	3	—	—	—	—	41.10%	39.63%	65.64%	56.04%
—	$\mathcal{L}_{\mathsf{a}}(\alpha{=}2)$	$\mathcal{L}_{\mathsf{u}}(t{=}2)$	rand	200	768	0.36	3	—	—	—	—	41.40%	41.45%	67.88%	58.78%
$\mathcal{L}_{\mathsf{c}}(\tau{=}0.07)$	—	—	rand	200	768	0.36	4	—	—	—	—	46.94%	47.08%	64.35%	58.10%
$\mathcal{L}_{\mathsf{c}}(\tau{=}0.5)$	—	—	rand	200	768	0.36	4	—	—	—	—	53.39%	55.41%	73.93%	67.89%
—	$0.5 \cdot \mathcal{L}_{\mathsf{a}}(\alpha{=}2)$	$\mathcal{L}_{\mathsf{u}}(t{=}2)$	rand	200	768	0.36	4	—	—	—	—	47.19%	51.69%	70.00%	62.36%
$\mathcal{L}_{\mathsf{c}}(\tau{=}0.07)$	—	—	rand	200	768	0.36	16	—	—	—	—	64.20%	68.73%	75.66%	69.55%
$\mathcal{L}_{\mathsf{c}}(\tau{=}0.5)$	—	—	rand	200	768	0.36	16	—	—	—	—	71.93%	73.54%	80.53%	74.66%
—	$0.5 \cdot \mathcal{L}_{\mathsf{a}}(\alpha{=}2)$	$\mathcal{L}_{\mathsf{u}}(t{=}2)$	rand	200	768	0.36	16	—	—	—	—	65.41%	70.41%	77.18%	70.55%
—	$\mathcal{L}_{\mathsf{a}}(\alpha{=}2)$	$\mathcal{L}_{\mathsf{u}}(t{=}2)$	rand	200	768	0.36	16	—	—	—	—	70.25%	74.99%	81.59%	74.52%
—	$0.5 \cdot \mathcal{L}_{\mathsf{a}}(\alpha{=}2)$	$\mathcal{L}_{\mathsf{u}}(t{=}2)$	rand	200	768	0.36	32	—	—	—	—	70.30%	73.50%	79.63%	72.21%
—	$\mathcal{L}_{\mathsf{a}}(\alpha{=}2)$	$\mathcal{L}_{\mathsf{u}}(t{=}2)$	rand	200	768	0.36	32	—	—	—	—	73.65%	76.93%	82.81%	75.19%
—	$\mathcal{L}_{\mathsf{a}}(\alpha{=}2.5)$	$\mathcal{L}_{\mathsf{u}}(t{=}2)$	rand	200	768	0.36	32	—	—	—	—	73.71%	77.40%	82.93%	75.86%
—	$0.75 \cdot \mathcal{L}_{\mathsf{a}}(\alpha{=}2)$	$\mathcal{L}_{\mathsf{u}}(t{=}2)$	rand	200	768	0.36	64	—	—	—	—	77.33%	78.35%	84.00%	76.63%
—	$\mathcal{L}_{\mathsf{a}}(\alpha{=}2)$	$\mathcal{L}_{\mathsf{u}}(t{=}2)$	rand	200	768	0.36	64	—	—	—	—	77.94%	78.23%	83.51%	76.59%
$\mathcal{L}_{\mathsf{c}}(\tau{=}0.005)$	—	—	rand	200	768	0.36	128	67.88%	70.15%	74.64%	68.19%	68.14%	71.13%	75.14%	68.88%

$\mathcal{L}_{\mathsf{c}}(\tau{=}0.01)$	—	—	rand	200	768	0.36	128	69.63%	70.62%	75.68%	68.99%	69.86%	70.98%	76.13%	69.65%
$\mathcal{L}_{\mathsf{c}}(\tau{=}0.07)$	—	—	rand	200	768	0.36	128	75.01%	75.11%	80.93%	73.20%	75.46%	75.58%	81.34%	73.93%
$\mathcal{L}_{\mathsf{c}}(\tau{=}0.08)$	—	—	rand	200	768	0.36	128	76.12%	76.06%	81.72%	73.95%	76.58%	76.79%	81.81%	74.43%
$\mathcal{L}_{\mathsf{c}}(\tau{=}0.09)$	—	—	rand	200	768	0.36	128	77.15%	77.15%	82.52%	73.96%	77.74%	77.46%	83.23%	74.81%
$\mathcal{L}_{\mathsf{c}}(\tau{=}0.1)$	—	—	rand	200	768	0.36	128	77.55%	77.40%	82.93%	74.29%	77.83%	77.81%	83.39%	75.19%
$\mathcal{L}_{\mathsf{c}}(\tau{=}0.11)$	—	—	rand	200	768	0.36	128	78.48%	78.20%	83.29%	74.99%	79.01%	78.73%	83.73%	75.60%
$\mathcal{L}_{\mathsf{c}}(\tau{=}0.125)$	—	—	rand	200	768	0.36	128	79.05%	78.06%	83.30%	74.53%	79.59%	78.55%	84.09%	75.55%
$\mathcal{L}_{\mathsf{c}}(\tau{=}0.13)$	—	—	rand	200	768	0.36	128	79.46%	78.55%	**83.98%**	75.16%	79.80%	78.60%	**84.45%**	75.98%
$\mathcal{L}_{\mathsf{c}}(\tau{=}0.15)$	—	—	rand	200	768	0.36	128	79.81%	78.47%	83.62%	74.64%	80.16%	78.99%	84.19%	75.20%
$\mathcal{L}_{\mathsf{c}}(\tau{=}0.16)$	—	—	rand	200	768	0.36	128	79.54%	78.38%	83.35%	74.42%	80.04%	78.68%	83.88%	75.06%
$\mathcal{L}_{\mathsf{c}}(\tau{=}0.175)$	—	—	rand	200	768	0.36	128	79.74%	78.20%	83.56%	74.80%	80.29%	78.49%	83.96%	75.81%
$\mathcal{L}_{\mathsf{c}}(\tau{=}0.19)$	—	—	rand	200	768	0.36	128	80.14%	78.30%	83.52%	75.39%	80.46%	78.75%	83.89%	76.33%
$\mathcal{L}_{\mathsf{c}}(\tau{=}0.2)$	—	—	rand	200	768	0.36	128	79.64%	77.80%	83.37%	75.07%	79.99%	77.96%	83.73%	75.98%
$\mathcal{L}_{\mathsf{c}}(\tau{=}0.25)$	—	—	rand	200	768	0.36	128	79.27%	77.24%	82.70%	75.33%	79.50%	77.49%	83.10%	76.31%
$\mathcal{L}_{\mathsf{c}}(\tau{=}0.3)$	—	—	rand	200	768	0.36	128	78.79%	77.01%	82.58%	75.16%	78.98%	77.18%	82.84%	75.74%
$\mathcal{L}_{\mathsf{c}}(\tau{=}0.5)$	—	—	rand	200	768	0.36	128	76.57%	75.30%	81.18%	75.30%	76.66%	75.61%	81.61%	75.71%
$\mathcal{L}_{\mathsf{c}}(\tau{=}0.75)$	—	—	rand	200	768	0.36	128	74.59%	73.41%	79.72%	74.27%	74.63%	73.52%	80.18%	75.01%
$\mathcal{L}_{\mathsf{c}}(\tau{=}1)$	—	—	rand	200	768	0.36	128	72.88%	72.14%	79.16%	74.08%	73.00%	72.31%	79.54%	74.61%
$\mathcal{L}_{\mathsf{c}}(\tau{=}2)$	—	—	rand	200	768	0.36	128	67.79%	67.15%	77.04%	71.65%	67.13%	66.77%	77.35%	71.84%
★ $\mathcal{L}_{\mathsf{c}}(\tau{=}2.5)$	—	—	rand	200	768	0.36	128	66.11%	65.30%	75.80%	70.59%	65.33%	65.30%	76.31%	70.93%
$\mathcal{L}_{\mathsf{c}}(\tau{=}5)$	—	—	rand	200	768	0.36	128	55.56%	55.74%	70.29%	65.25%	55.75%	55.83%	70.75%	65.58%
$\mathcal{L}_{\mathsf{c}}(\tau{=}0.07)$	$0.5 \cdot \mathcal{L}_{\mathsf{a}}(\alpha{=}2)$	—	rand	200	768	0.36	128	75.13%	75.59%	81.52%	73.55%	75.59%	76.26%	82.10%	74.33%
$\mathcal{L}_{\mathsf{c}}(\tau{=}0.1)$	$0.5 \cdot \mathcal{L}_{\mathsf{a}}(\alpha{=}2)$	—	rand	200	768	0.36	128	77.76%	78.02%	83.28%	74.56%	78.04%	78.44%	83.73%	75.33%
$\mathcal{L}_{\mathsf{c}}(\tau{=}0.5)$	$0.5 \cdot \mathcal{L}_{\mathsf{a}}(\alpha{=}2)$	—	rand	200	768	0.36	128	74.86%	73.92%	80.16%	74.55%	74.96%	73.93%	80.63%	75.13%
$\mathcal{L}_{\mathsf{c}}(\tau{=}0.5)$	$0.5 \cdot \mathcal{L}_{\mathsf{a}}(\alpha{=}2)$	—	rand	200	768	0.36	128	74.69%	74.10%	80.53%	74.77%	74.80%	74.28%	80.91%	75.31%
$\mathcal{L}_{\mathsf{c}}(\tau{=}0.5)$	$\mathcal{L}_{\mathsf{a}}(\alpha{=}2)$	—	rand	200	768	0.36	128	73.31%	72.84%	79.82%	73.73%	73.54%	72.94%	80.26%	74.58%

$\mathcal{L}_{\mathsf{c}}(\tau{=}0.07)$	$0.4 \cdot \mathcal{L}_{\mathsf{a}}(\alpha{=}2)$	$0.2 \cdot \mathcal{L}_{\mathsf{u}}(t{=}2)$	rand	200	768	0.36	128	75.77%	75.98%	81.50%	73.48%	76.11%	76.45%	82.08%	74.00%
$\mathcal{L}_{\mathsf{c}}(\tau{=}0.1)$	$0.4 \cdot \mathcal{L}_{\mathsf{a}}(\alpha{=}2)$	$0.2 \cdot \mathcal{L}_{\mathsf{u}}(t{=}2)$	rand	200	768	0.36	128	78.17%	77.61%	83.04%	74.54%	78.64%	78.10%	83.26%	75.45%
$\mathcal{L}_{\mathsf{c}}(\tau{=}0.5)$	$0.4 \cdot \mathcal{L}_{\mathsf{a}}(\alpha{=}2)$	$0.2 \cdot \mathcal{L}_{\mathsf{u}}(t{=}2)$	rand	200	768	0.36	128	77.73%	76.23%	81.96%	75.10%	77.98%	76.60%	82.38%	75.45%
$\mathcal{L}_{\mathsf{c}}(\tau{=}0.07)$	$0.3 \cdot \mathcal{L}_{\mathsf{a}}(\alpha{=}2)$	$0.4 \cdot \mathcal{L}_{\mathsf{u}}(t{=}2)$	rand	200	768	0.36	128	75.93%	75.55%	81.45%	73.18%	76.13%	76.00%	81.95%	74.11%
$\mathcal{L}_{\mathsf{c}}(\tau{=}0.1)$	$0.3 \cdot \mathcal{L}_{\mathsf{a}}(\alpha{=}2)$	$0.4 \cdot \mathcal{L}_{\mathsf{u}}(t{=}2)$	rand	200	768	0.36	128	77.98%	77.18%	82.77%	74.12%	78.38%	77.79%	83.51%	74.99%
$\mathcal{L}_{\mathsf{c}}(\tau{=}0.5)$	$0.3 \cdot \mathcal{L}_{\mathsf{a}}(\alpha{=}2)$	$0.4 \cdot \mathcal{L}_{\mathsf{u}}(t{=}2)$	rand	200	768	0.36	128	78.69%	76.99%	82.57%	75.12%	79.03%	77.38%	82.93%	75.46%
$\mathcal{L}_{\mathsf{c}}(\tau{=}0.07)$	$0.2 \cdot \mathcal{L}_{\mathsf{a}}(\alpha{=}2)$	$0.6 \cdot \mathcal{L}_{\mathsf{u}}(t{=}2)$	rand	200	768	0.36	128	75.71%	75.22%	80.94%	72.80%	76.05%	75.60%	81.56%	73.46%
$\mathcal{L}_{\mathsf{c}}(\tau{=}0.1)$	$0.2 \cdot \mathcal{L}_{\mathsf{a}}(\alpha{=}2)$	$0.6 \cdot \mathcal{L}_{\mathsf{u}}(t{=}2)$	rand	200	768	0.36	128	78.38%	77.85%	82.87%	74.36%	78.84%	78.54%	83.10%	74.73%
$\mathcal{L}_{\mathsf{c}}(\tau{=}0.5)$	$0.2 \cdot \mathcal{L}_{\mathsf{a}}(\alpha{=}2)$	$0.6 \cdot \mathcal{L}_{\mathsf{u}}(t{=}2)$	rand	200	768	0.36	128	79.72%	77.94%	83.03%	75.32%	80.04%	78.24%	83.28%	75.66%
$\mathcal{L}_{\mathsf{c}}(\tau{=}0.07)$	$0.1 \cdot \mathcal{L}_{\mathsf{a}}(\alpha{=}2)$	$0.8 \cdot \mathcal{L}_{\mathsf{u}}(t{=}2)$	rand	200	768	0.36	128	76.19%	75.62%	81.15%	73.09%	76.90%	76.21%	81.61%	74.48%
$\mathcal{L}_{\mathsf{c}}(\tau{=}0.1)$	$0.1 \cdot \mathcal{L}_{\mathsf{a}}(\alpha{=}2)$	$0.8 \cdot \mathcal{L}_{\mathsf{u}}(t{=}2)$	rand	200	768	0.36	128	78.59%	78.02%	83.18%	74.63%	78.68%	78.48%	83.76%	75.49%
$\mathcal{L}_{\mathsf{c}}(\tau{=}0.5)$	$0.1 \cdot \mathcal{L}_{\mathsf{a}}(\alpha{=}2)$	$0.8 \cdot \mathcal{L}_{\mathsf{u}}(t{=}2)$	rand	200	768	0.36	128	80.25%	78.32%	83.35%	74.26%	80.43%	78.71%	83.76%	75.44%
$\mathcal{L}_{\mathsf{c}}(\tau{=}0.07)$	—	$\mathcal{L}_{\mathsf{u}}(t{=}2)$	rand	200	768	0.36	128	76.31%	75.78%	81.59%	72.79%	76.69%	76.33%	82.23%	73.63%
$\mathcal{L}_{\mathsf{c}}(\tau{=}0.1)$	—	$\mathcal{L}_{\mathsf{u}}(t{=}2)$	rand	200	768	0.36	128	78.55%	77.94%	83.21%	74.67%	79.03%	78.45%	83.75%	75.71%
$\mathcal{L}_{\mathsf{c}}(\tau{=}0.5)$	—	$\mathcal{L}_{\mathsf{u}}(t{=}2)$	rand	200	768	0.36	128	79.93%	78.25%	82.92%	75.22%	80.30%	78.54%	83.34%	76.04%
$\mathcal{L}_{\mathsf{c}}(\tau{=}0.5)$	—	$\mathcal{L}_{\mathsf{u}}(t{=}2)$	rand	200	768	0.36	128	**80.84%**	78.87%	83.72%	75.56%	81.06%	79.05%	84.14%	76.48%
$\mathcal{L}_{\mathsf{c}}(\tau{=}0.5)$	—	$2 \cdot \mathcal{L}_{\mathsf{u}}(t{=}2)$	rand	200	768	0.36	128	77.49%	76.15%	80.99%	74.41%	78.09%	76.83%	81.63%	75.11%
$0.5 \cdot \mathcal{L}_{\mathsf{c}}(\tau{=}0.07)$	$0.5 \cdot \mathcal{L}_{\mathsf{a}}(\alpha{=}2)$	—	rand	200	768	0.36	128	75.40%	75.53%	81.53%	73.91%	75.74%	76.19%	82.00%	74.63%
$0.5 \cdot \mathcal{L}_{\mathsf{c}}(\tau{=}0.1)$	$0.5 \cdot \mathcal{L}_{\mathsf{a}}(\alpha{=}2)$	—	rand	200	768	0.36	128	77.70%	77.70%	83.39%	75.27%	78.06%	78.26%	83.93%	76.21%
$0.5 \cdot \mathcal{L}_{\mathsf{c}}(\tau{=}0.5)$	$0.5 \cdot \mathcal{L}_{\mathsf{a}}(\alpha{=}2)$	—	rand	200	768	0.36	128	73.86%	73.12%	80.08%	74.54%	74.05%	73.18%	80.53%	75.14%
$0.5 \cdot \mathcal{L}_{\mathsf{c}}(\tau{=}0.07)$	$0.4 \cdot \mathcal{L}_{\mathsf{a}}(\alpha{=}2)$	$0.2 \cdot \mathcal{L}_{\mathsf{u}}(t{=}2)$	rand	200	768	0.36	128	76.12%	76.22%	81.75%	73.68%	76.46%	76.75%	82.36%	74.44%
$0.5 \cdot \mathcal{L}_{\mathsf{c}}(\tau{=}0.1)$	$0.4 \cdot \mathcal{L}_{\mathsf{a}}(\alpha{=}2)$	$0.2 \cdot \mathcal{L}_{\mathsf{u}}(t{=}2)$	rand	200	768	0.36	128	78.40%	78.01%	83.39%	75.21%	78.83%	78.30%	83.74%	75.84%
$0.5 \cdot \mathcal{L}_{\mathsf{c}}(\tau{=}0.5)$	$0.4 \cdot \mathcal{L}_{\mathsf{a}}(\alpha{=}2)$	$0.2 \cdot \mathcal{L}_{\mathsf{u}}(t{=}2)$	rand	200	768	0.36	128	78.35%	76.49%	82.02%	75.60%	78.60%	77.18%	82.65%	76.19%
$0.5 \cdot \mathcal{L}_{\mathsf{c}}(\tau{=}0.07)$	$0.3 \cdot \mathcal{L}_{\mathsf{a}}(\alpha{=}2)$	$0.4 \cdot \mathcal{L}_{\mathsf{u}}(t{=}2)$	rand	200	768	0.36	128	76.59%	75.74%	81.48%	73.59%	77.20%	76.43%	82.03%	74.36%
$0.5 \cdot \mathcal{L}_{\mathsf{c}}(\tau{=}0.1)$	$0.3 \cdot \mathcal{L}_{\mathsf{a}}(\alpha{=}2)$	$0.4 \cdot \mathcal{L}_{\mathsf{u}}(t{=}2)$	rand	200	768	0.36	128	78.85%	77.43%	82.98%	74.87%	79.20%	77.95%	83.29%	75.60%
$0.5 \cdot \mathcal{L}_{\mathsf{c}}(\tau{=}0.5)$	$0.3 \cdot \mathcal{L}_{\mathsf{a}}(\alpha{=}2)$	$0.4 \cdot \mathcal{L}_{\mathsf{u}}(t{=}2)$	rand	200	768	0.36	128	79.53%	77.56%	82.84%	75.19%	79.71%	77.95%	83.19%	76.08%

$0.5 \cdot \mathcal{L}_{\mathsf{c}}(\tau{=}0.07)$	$0.2 \cdot \mathcal{L}_{\mathsf{a}}(\alpha{=}2)$	$0.6 \cdot \mathcal{L}_{\mathsf{u}}(t{=}2)$	rand	200	768	0.36	128	77.07%	76.49%	81.78%	73.10%	77.44%	76.98%	82.33%	73.85%
$0.5 \cdot \mathcal{L}_{\mathsf{c}}(\tau{=}0.1)$	$0.2 \cdot \mathcal{L}_{\mathsf{a}}(\alpha{=}2)$	$0.6 \cdot \mathcal{L}_{\mathsf{u}}(t{=}2)$	rand	200	768	0.36	128	78.55%	78.04%	83.20%	74.30%	78.91%	78.38%	83.81%	75.18%
$0.5 \cdot \mathcal{L}_{\mathsf{c}}(\tau{=}0.5)$	$0.2 \cdot \mathcal{L}_{\mathsf{a}}(\alpha{=}2)$	$0.6 \cdot \mathcal{L}_{\mathsf{u}}(t{=}2)$	rand	200	768	0.36	128	80.47%	78.36%	83.42%	75.82%	80.88%	78.51%	83.83%	76.65%
$0.5 \cdot \mathcal{L}_{\mathsf{c}}(\tau{=}0.07)$	$0.1 \cdot \mathcal{L}_{\mathsf{a}}(\alpha{=}2)$	$0.8 \cdot \mathcal{L}_{\mathsf{u}}(t{=}2)$	rand	200	768	0.36	128	76.30%	76.43%	81.72%	73.35%	76.56%	77.11%	82.11%	74.00%
$0.5 \cdot \mathcal{L}_{\mathsf{c}}(\tau{=}0.1)$	$0.1 \cdot \mathcal{L}_{\mathsf{a}}(\alpha{=}2)$	$0.8 \cdot \mathcal{L}_{\mathsf{u}}(t{=}2)$	rand	200	768	0.36	128	78.71%	78.00%	83.35%	74.46%	79.29%	78.44%	83.81%	75.45%
$0.5 \cdot \mathcal{L}_{\mathsf{c}}(\tau{=}0.5)$	$0.1 \cdot \mathcal{L}_{\mathsf{a}}(\alpha{=}2)$	$0.8 \cdot \mathcal{L}_{\mathsf{u}}(t{=}2)$	rand	200	768	0.36	128	80.51%	78.99%	83.57%	75.47%	80.95%	79.44%	83.98%	76.45%
$0.5 \cdot \mathcal{L}_{\mathsf{c}}(\tau{=}0.07)$	—	$\mathcal{L}_{\mathsf{u}}(t{=}2)$	rand	200	768	0.36	128	75.48%	76.10%	81.47%	72.97%	75.80%	76.86%	82.06%	73.81%
$0.5 \cdot \mathcal{L}_{\mathsf{c}}(\tau{=}0.1)$	—	$\mathcal{L}_{\mathsf{u}}(t{=}2)$	rand	200	768	0.36	128	77.78%	78.07%	83.23%	74.51%	78.38%	78.46%	83.89%	75.49%
$0.5 \cdot \mathcal{L}_{\mathsf{c}}(\tau{=}0.5)$	—	$\mathcal{L}_{\mathsf{u}}(t{=}2)$	rand	200	768	0.36	128	78.04%	76.18%	81.89%	73.67%	78.43%	76.44%	82.33%	74.44%
—	$\mathcal{L}_{\mathsf{a}}(\alpha{=}2)$	—	rand	200	768	0.36	128	10.00%	10.36%	11.07%	14.20%	10.00%	9.40%	12.53%	14.27%
—	$0.9875 \cdot \mathcal{L}_{\mathsf{a}}(\alpha{=}2)$	$0.025 \cdot \mathcal{L}_{\mathsf{u}}(t{=}2)$	rand	200	768	0.36	128	10.00%	9.90%	11.04%	13.72%	10.00%	10.94%	13.03%	13.64%
—	$0.975 \cdot \mathcal{L}_{\mathsf{a}}(\alpha{=}2)$	$0.05 \cdot \mathcal{L}_{\mathsf{u}}(t{=}2)$	rand	200	768	0.36	128	10.00%	9.98%	10.65%	14.29%	10.00%	9.75%	12.11%	14.77%
—	$0.9 \cdot \mathcal{L}_{\mathsf{a}}(\alpha{=}2)$	$0.1 \cdot \mathcal{L}_{\mathsf{u}}(t{=}2)$	rand	200	768	0.36	128	10.00%	10.08%	10.10%	13.62%	10.00%	9.95%	10.00%	13.49%
—	$0.95 \cdot \mathcal{L}_{\mathsf{a}}(\alpha{=}2)$	$0.1 \cdot \mathcal{L}_{\mathsf{u}}(t{=}2)$	rand	200	768	0.36	128	10.00%	10.51%	10.15%	13.27%	10.00%	9.85%	10.00%	11.99%
—	$\mathcal{L}_{\mathsf{a}}(\alpha{=}2)$	$0.1 \cdot \mathcal{L}_{\mathsf{u}}(t{=}2)$	rand	200	768	0.36	128	10.00%	9.93%	10.39%	14.38%	10.00%	10.26%	10.00%	14.03%
—	$0.56 \cdot \mathcal{L}_{\mathsf{a}}(\alpha{=}2)$	$0.12 \cdot \mathcal{L}_{\mathsf{u}}(t{=}2)$	rand	200	768	0.36	128	75.93%	75.10%	80.88%	74.87%	75.99%	75.41%	81.40%	75.66%
—	$0.88 \cdot \mathcal{L}_{\mathsf{a}}(\alpha{=}2)$	$0.12 \cdot \mathcal{L}_{\mathsf{u}}(t{=}2)$	rand	200	768	0.36	128	10.00%	10.13%	10.00%	12.89%	10.00%	11.18%	10.03%	12.43%
—	$0.9375 \cdot \mathcal{L}_{\mathsf{a}}(\alpha{=}2)$	$0.125 \cdot \mathcal{L}_{\mathsf{u}}(t{=}2)$	rand	200	768	0.36	128	10.00%	10.52%	10.42%	13.71%	10.00%	9.14%	10.05%	14.26%
—	$0.57 \cdot \mathcal{L}_{\mathsf{a}}(\alpha{=}2)$	$0.14 \cdot \mathcal{L}_{\mathsf{u}}(t{=}2)$	rand	200	768	0.36	128	76.35%	75.51%	81.07%	75.27%	76.55%	75.86%	81.69%	75.70%
—	$0.86 \cdot \mathcal{L}_{\mathsf{a}}(\alpha{=}2)$	$0.14 \cdot \mathcal{L}_{\mathsf{u}}(t{=}2)$	rand	200	768	0.36	128	10.00%	9.07%	10.33%	14.24%	10.00%	9.91%	10.73%	15.08%
—	$0.855 \cdot \mathcal{L}_{\mathsf{a}}(\alpha{=}2)$	$0.145 \cdot \mathcal{L}_{\mathsf{u}}(t{=}2)$	rand	200	768	0.36	128	10.00%	10.67%	10.30%	14.11%	10.00%	9.35%	11.70%	13.30%
—	$0.85 \cdot \mathcal{L}_{\mathsf{a}}(\alpha{=}2)$	$0.15 \cdot \mathcal{L}_{\mathsf{u}}(t{=}2)$	rand	200	768	0.36	128	10.00%	10.17%	10.00%	12.97%	10.00%	10.05%	10.00%	13.16%
—	$0.925 \cdot \mathcal{L}_{\mathsf{a}}(\alpha{=}2)$	$0.15 \cdot \mathcal{L}_{\mathsf{u}}(t{=}2)$	rand	200	768	0.36	128	10.00%	9.79%	10.10%	13.11%	10.00%	9.73%	10.11%	12.91%
—	$0.845 \cdot \mathcal{L}_{\mathsf{a}}(\alpha{=}2)$	$0.155 \cdot \mathcal{L}_{\mathsf{u}}(t{=}2)$	rand	200	768	0.36	128	74.56%	74.06%	80.10%	74.93%	74.99%	74.39%	80.44%	75.83%
—	$0.58 \cdot \mathcal{L}_{\mathsf{a}}(\alpha{=}2)$	$0.16 \cdot \mathcal{L}_{\mathsf{u}}(t{=}2)$	rand	200	768	0.36	128	77.03%	76.34%	81.25%	75.26%	77.33%	76.76%	81.80%	75.89%
—	$0.84 \cdot \mathcal{L}_{\mathsf{a}}(\alpha{=}2)$	$0.16 \cdot \mathcal{L}_{\mathsf{u}}(t{=}2)$	rand	200	768	0.36	128	74.49%	74.03%	80.30%	74.72%	74.73%	74.10%	80.70%	75.13%

—	$0.9125 \cdot \mathcal{L}_{\mathsf{a}}(\alpha{=}2)$	$0.175 \cdot \mathcal{L}_{\mathsf{u}}(t{=}2)$	rand	200	768	0.36	128	10.00%	9.41%	10.39%	13.64%	10.00%	10.14%	10.10%	14.14%
—	$0.59 \cdot \mathcal{L}_{\mathsf{a}}(\alpha{=}2)$	$0.18 \cdot \mathcal{L}_{\mathsf{u}}(t{=}2)$	rand	200	768	0.36	128	77.25%	76.38%	81.39%	75.41%	77.65%	77.06%	81.68%	76.19%
—	$0.82 \cdot \mathcal{L}_{\mathsf{a}}(\alpha{=}2)$	$0.18 \cdot \mathcal{L}_{\mathsf{u}}(t{=}2)$	rand	200	768	0.36	128	76.09%	75.10%	80.99%	75.63%	76.45%	75.48%	81.45%	76.48%
—	$0.91 \cdot \mathcal{L}_{\mathsf{a}}(\alpha{=}2)$	$0.18 \cdot \mathcal{L}_{\mathsf{u}}(t{=}2)$	rand	200	768	0.36	128	75.11%	74.63%	80.50%	75.28%	75.40%	75.04%	80.85%	75.83%
—	$0.9075 \cdot \mathcal{L}_{\mathsf{a}}(\alpha{=}2)$	$0.185 \cdot \mathcal{L}_{\mathsf{u}}(t{=}2)$	rand	200	768	0.36	128	75.29%	74.83%	80.64%	75.04%	75.69%	75.41%	80.93%	75.65%
—	$0.905 \cdot \mathcal{L}_{\mathsf{a}}(\alpha{=}2)$	$0.19 \cdot \mathcal{L}_{\mathsf{u}}(t{=}2)$	rand	200	768	0.36	128	75.69%	74.61%	80.80%	74.98%	75.99%	74.95%	81.21%	75.59%
—	$0.9025 \cdot \mathcal{L}_{\mathsf{a}}(\alpha{=}2)$	$0.195 \cdot \mathcal{L}_{\mathsf{u}}(t{=}2)$	rand	200	768	0.36	128	75.81%	74.93%	80.75%	74.66%	76.06%	75.29%	81.16%	75.14%
—	$0.8 \cdot \mathcal{L}_{\mathsf{a}}(\alpha{=}2)$	$0.2 \cdot \mathcal{L}_{\mathsf{u}}(t{=}2)$	rand	200	768	0.36	128	76.52%	75.96%	81.05%	75.38%	76.75%	76.24%	81.29%	75.83%
—	$0.9 \cdot \mathcal{L}_{\mathsf{a}}(\alpha{=}2)$	$0.2 \cdot \mathcal{L}_{\mathsf{u}}(t{=}2)$	rand	200	768	0.36	128	75.92%	75.02%	80.85%	75.36%	76.15%	75.29%	81.15%	76.24%
—	$\mathcal{L}_{\mathsf{a}}(\alpha{=}2)$	$0.2 \cdot \mathcal{L}_{\mathsf{u}}(t{=}2)$	rand	200	768	0.36	128	75.14%	74.29%	80.39%	74.76%	75.46%	74.44%	80.64%	75.34%
—	$0.7 \cdot \mathcal{L}_{\mathsf{a}}(\alpha{=}2)$	$0.3 \cdot \mathcal{L}_{\mathsf{u}}(t{=}2)$	rand	200	768	0.36	128	78.61%	77.00%	82.14%	75.73%	78.94%	77.50%	82.26%	76.34%
—	$0.6 \cdot \mathcal{L}_{\mathsf{a}}(\alpha{=}2)$	$0.4 \cdot \mathcal{L}_{\mathsf{u}}(t{=}2)$	rand	200	768	0.36	128	79.36%	77.80%	82.63%	75.55%	79.60%	77.93%	82.86%	76.63%
—	$0.8 \cdot \mathcal{L}_{\mathsf{a}}(\alpha{=}2)$	$0.4 \cdot \mathcal{L}_{\mathsf{u}}(t{=}2)$	rand	200	768	0.36	128	79.24%	77.52%	82.44%	75.23%	79.65%	77.89%	82.69%	75.71%
—	$\mathcal{L}_{\mathsf{a}}(\alpha{=}2)$	$0.4 \cdot \mathcal{L}_{\mathsf{u}}(t{=}2)$	rand	200	768	0.36	128	78.45%	77.09%	82.30%	75.38%	78.85%	77.53%	82.86%	76.02%
—	$0.5 \cdot \mathcal{L}_{\mathsf{a}}(\alpha{=}2)$	$0.5 \cdot \mathcal{L}_{\mathsf{u}}(t{=}2)$	rand	200	768	0.36	128	80.03%	78.47%	83.12%	75.14%	80.39%	78.70%	83.56%	75.70%
—	$0.75 \cdot \mathcal{L}_{\mathsf{a}}(\alpha{=}2)$	$0.5 \cdot \mathcal{L}_{\mathsf{u}}(t{=}2)$	rand	200	768	0.36	128	79.72%	77.30%	82.69%	75.44%	79.96%	77.55%	83.35%	76.14%
—	$\mathcal{L}_{\mathsf{a}}(\alpha{=}2)$	$0.5 \cdot \mathcal{L}_{\mathsf{u}}(t{=}2)$	rand	200	768	0.36	128	79.09%	77.50%	82.80%	75.46%	79.27%	77.96%	83.10%	76.45%
—	$0.4 \cdot \mathcal{L}_{\mathsf{a}}(\alpha{=}2)$	$0.6 \cdot \mathcal{L}_{\mathsf{u}}(t{=}2)$	rand	200	768	0.36	128	80.23%	78.67%	83.49%	75.61%	80.45%	78.83%	84.01%	76.61%
—	$0.5 \cdot \mathcal{L}_{\mathsf{a}}(\alpha{=}2)$	$0.6 \cdot \mathcal{L}_{\mathsf{u}}(t{=}2)$	rand	200	768	0.36	128	80.37%	78.82%	83.05%	75.54%	80.48%	79.11%	83.33%	76.50%
—	$0.7 \cdot \mathcal{L}_{\mathsf{a}}(\alpha{=}2)$	$0.6 \cdot \mathcal{L}_{\mathsf{u}}(t{=}2)$	rand	200	768	0.36	128	80.29%	78.16%	83.40%	75.59%	80.59%	78.66%	83.83%	76.24%
—	$0.3 \cdot \mathcal{L}_{\mathsf{a}}(\alpha{=}2)$	$0.7 \cdot \mathcal{L}_{\mathsf{u}}(t{=}2)$	rand	200	768	0.36	128	80.16%	78.91%	83.39%	**76.21%**	80.58%	79.51%	83.78%	77.03%
—	$0.2 \cdot \mathcal{L}_{\mathsf{a}}(\alpha{=}2)$	$0.8 \cdot \mathcal{L}_{\mathsf{u}}(t{=}2)$	rand	200	768	0.36	128	74.67%	78.15%	82.53%	75.83%	75.13%	78.63%	83.03%	76.45%
—	$0.5 \cdot \mathcal{L}_{\mathsf{a}}(\alpha{=}2)$	$0.8 \cdot \mathcal{L}_{\mathsf{u}}(t{=}2)$	rand	200	768	0.36	128	80.59%	78.73%	83.73%	76.05%	81.08%	79.10%	84.04%	76.88%
—	$0.6 \cdot \mathcal{L}_{\mathsf{a}}(\alpha{=}2)$	$0.8 \cdot \mathcal{L}_{\mathsf{u}}(t{=}2)$	rand	200	768	0.36	128	80.29%	78.74%	83.53%	75.75%	80.65%	78.89%	83.89%	76.86%
—	$0.1 \cdot \mathcal{L}_{\mathsf{a}}(\alpha{=}2)$	$0.9 \cdot \mathcal{L}_{\mathsf{u}}(t{=}2)$	rand	200	768	0.36	128	69.77%	75.72%	80.55%	73.38%	70.29%	76.13%	80.88%	74.14%
—	$0.08 \cdot \mathcal{L}_{\mathsf{a}}(\alpha{=}2)$	$0.92 \cdot \mathcal{L}_{\mathsf{u}}(t{=}2)$	rand	200	768	0.36	128	67.65%	73.97%	79.35%	71.86%	68.04%	74.90%	79.84%	72.50%

—	$0.96 \cdot \mathcal{L}_{\mathsf{a}}(\alpha{=}2)$	$0.92 \cdot \mathcal{L}_{\mathsf{u}}(t{=}2)$	rand	200	768	0.36	128	80.74%	78.71%	83.49%	76.14%	81.08%	79.26%	83.95%	77.26%
—	$0.06 \cdot \mathcal{L}_{\mathsf{a}}(\alpha{=}2)$	$0.94 \cdot \mathcal{L}_{\mathsf{u}}(t{=}2)$	rand	200	768	0.36	128	66.88%	73.81%	79.21%	72.32%	67.46%	74.68%	79.56%	73.09%
—	$0.97 \cdot \mathcal{L}_{\mathsf{a}}(\alpha{=}2)$	$0.94 \cdot \mathcal{L}_{\mathsf{u}}(t{=}2)$	rand	200	768	0.36	128	80.28%	78.45%	83.51%	75.68%	80.63%	78.63%	83.83%	76.33%
—	$0.04 \cdot \mathcal{L}_{\mathsf{a}}(\alpha{=}2)$	$0.96 \cdot \mathcal{L}_{\mathsf{u}}(t{=}2)$	rand	200	768	0.36	128	63.89%	70.80%	76.33%	69.55%	64.21%	71.49%	77.10%	70.38%
—	$0.98 \cdot \mathcal{L}_{\mathsf{a}}(\alpha{=}2)$	$0.96 \cdot \mathcal{L}_{\mathsf{u}}(t{=}2)$	rand	200	768	0.36	128	80.76%	78.69%	83.97%	75.63%	81.15%	78.89%	84.43%	76.78%
—	$\mathcal{L}_{\mathsf{a}}(\alpha{=}2)$	$0.975 \cdot \mathcal{L}_{\mathsf{u}}(t{=}2)$	rand	200	768	0.36	128	79.94%	78.45%	83.34%	75.23%	80.44%	78.86%	83.65%	75.83%
—	$0.02 \cdot \mathcal{L}_{\mathsf{a}}(\alpha{=}2)$	$0.98 \cdot \mathcal{L}_{\mathsf{u}}(t{=}2)$	rand	200	768	0.36	128	56.39%	63.06%	69.48%	62.85%	56.78%	63.90%	69.80%	63.82%
—	$0.99 \cdot \mathcal{L}_{\mathsf{a}}(\alpha{=}2)$	$0.98 \cdot \mathcal{L}_{\mathsf{u}}(t{=}2)$	rand	200	768	0.36	128	80.24%	78.90%	83.34%	74.89%	80.45%	79.40%	83.76%	75.55%
—	$\mathcal{L}_{\mathsf{a}}(\alpha{=}2)$	$0.98 \cdot \mathcal{L}_{\mathsf{u}}(t{=}2)$	rand	200	768	0.36	128	80.29%	78.64%	83.46%	75.23%	80.77%	78.84%	83.96%	75.90%
—	—	$\mathcal{L}_{\mathsf{u}}(t{=}2)$	rand	200	768	0.36	128	20.62%	15.96%	24.52%	16.13%	20.50%	16.14%	24.64%	16.24%
—	$0.0025 \cdot \mathcal{L}_{\mathsf{a}}(\alpha{=}2)$	$\mathcal{L}_{\mathsf{u}}(t{=}2)$	rand	200	768	0.36	128	36.14%	33.19%	46.82%	35.22%	36.28%	33.76%	47.04%	36.05%
—	$0.005 \cdot \mathcal{L}_{\mathsf{a}}(\alpha{=}2)$	$\mathcal{L}_{\mathsf{u}}(t{=}2)$	rand	200	768	0.36	128	48.38%	49.74%	59.67%	49.55%	48.69%	50.41%	59.81%	50.40%
—	$0.0125 \cdot \mathcal{L}_{\mathsf{a}}(\alpha{=}2)$	$\mathcal{L}_{\mathsf{u}}(t{=}2)$	rand	200	768	0.36	128	51.31%	57.94%	64.95%	57.49%	51.80%	58.75%	65.40%	58.01%
—	$0.025 \cdot \mathcal{L}_{\mathsf{a}}(\alpha{=}1)$	$\mathcal{L}_{\mathsf{u}}(t{=}2)$	rand	200	768	0.36	128	46.13%	51.81%	58.51%	51.30%	46.61%	52.65%	59.03%	51.99%
—	$0.025 \cdot \mathcal{L}_{\mathsf{a}}(\alpha{=}2)$	$\mathcal{L}_{\mathsf{u}}(t{=}2)$	rand	200	768	0.36	128	57.34%	62.50%	69.09%	61.76%	57.89%	63.43%	69.58%	62.51%
—	$0.25 \cdot \mathcal{L}_{\mathsf{a}}(\alpha{=}1)$	$\mathcal{L}_{\mathsf{u}}(t{=}2)$	rand	200	768	0.36	128	70.80%	75.24%	80.59%	72.59%	71.40%	75.54%	81.20%	73.36%
—	$0.25 \cdot \mathcal{L}_{\mathsf{a}}(\alpha{=}2)$	$\mathcal{L}_{\mathsf{u}}(t{=}2)$	rand	200	768	0.36	128	76.14%	78.45%	82.97%	75.90%	76.83%	78.88%	83.51%	76.74%
—	$0.3 \cdot \mathcal{L}_{\mathsf{a}}(\alpha{=}2)$	$\mathcal{L}_{\mathsf{u}}(t{=}2)$	rand	200	768	0.36	128	76.72%	78.01%	83.26%	75.61%	77.30%	78.43%	83.79%	76.25%
—	$0.4 \cdot \mathcal{L}_{\mathsf{a}}(\alpha{=}2)$	$\mathcal{L}_{\mathsf{u}}(t{=}2)$	rand	200	768	0.36	128	78.71%	77.76%	83.13%	75.42%	79.36%	78.01%	83.64%	76.24%
—	$0.5 \cdot \mathcal{L}_{\mathsf{a}}(\alpha{=}2)$	$\mathcal{L}_{\mathsf{u}}(t{=}2)$	rand	200	768	0.36	128	80.41%	**79.18%**	83.85%	75.54%	80.03%	79.35%	84.20%	76.84%
—	$0.75 \cdot \mathcal{L}_{\mathsf{a}}(\alpha{=}2)$	$\mathcal{L}_{\mathsf{u}}(t{=}2)$	rand	200	768	0.36	128	80.54%	78.84%	83.61%	75.26%	80.89%	79.29%	84.23%	76.28%
—	$\mathcal{L}_{\mathsf{a}}(\alpha{=}2)$	$\mathcal{L}_{\mathsf{u}}(t{=}2)$	rand	200	768	0.36	128	80.32%	78.90%	83.48%	74.97%	80.76%	79.23%	83.75%	76.15%
—	$1.025 \cdot \mathcal{L}_{\mathsf{a}}(\alpha{=}2)$	$\mathcal{L}_{\mathsf{u}}(t{=}2)$	rand	200	768	0.36	128	80.37%	78.69%	83.48%	75.78%	80.74%	79.06%	84.00%	76.56%
—	$1.25 \cdot \mathcal{L}_{\mathsf{a}}(\alpha{=}2)$	$\mathcal{L}_{\mathsf{u}}(t{=}2)$	rand	200	768	0.36	128	80.50%	78.41%	83.54%	75.89%	80.84%	78.65%	83.95%	76.56%
—	$0.4 \cdot \mathcal{L}_{\mathsf{a}}(\alpha{=}2)$	$1.2 \cdot \mathcal{L}_{\mathsf{u}}(t{=}2)$	rand	200	768	0.36	128	75.37%	73.62%	78.88%	71.55%	75.78%	73.83%	79.15%	72.35%
—	$0.3 \cdot \mathcal{L}_{\mathsf{a}}(\alpha{=}2)$	$1.4 \cdot \mathcal{L}_{\mathsf{u}}(t{=}2)$	rand	200	768	0.36	128	72.69%	75.62%	80.67%	73.49%	73.14%	75.99%	81.49%	74.20%

□

—	$0.25 \cdot \mathcal{L}_{\mathsf{a}}(\alpha{=}2)$	$1.5 \cdot \mathcal{L}_{\mathsf{u}}(t{=}2)$	rand	200	768	0.36	128	70.61%	73.50%	78.53%	71.85%	71.03%	74.10%	79.13%	72.50%
—	$0.2 \cdot \mathcal{L}_{\mathsf{a}}(\alpha{=}2)$	$1.6 \cdot \mathcal{L}_{\mathsf{u}}(t{=}2)$	rand	200	768	0.36	128	67.35%	70.98%	76.84%	69.13%	67.69%	71.64%	77.40%	69.91%
—	$0.1 \cdot \mathcal{L}_{\mathsf{a}}(\alpha{=}2)$	$1.8 \cdot \mathcal{L}_{\mathsf{u}}(t{=}2)$	rand	200	768	0.36	128	64.43%	68.89%	74.24%	68.15%	65.01%	69.34%	74.70%	68.80%
—	$0.0875 \cdot \mathcal{L}_{\mathsf{a}}(\alpha{=}2)$	$1.825 \cdot \mathcal{L}_{\mathsf{u}}(t{=}2)$	rand	200	768	0.36	128	63.38%	68.83%	73.56%	67.33%	64.05%	69.76%	73.91%	68.14%
—	$0.075 \cdot \mathcal{L}_{\mathsf{a}}(\alpha{=}2)$	$1.85 \cdot \mathcal{L}_{\mathsf{u}}(t{=}2)$	rand	200	768	0.36	128	63.02%	69.32%	74.49%	68.22%	63.44%	69.91%	75.05%	69.06%
—	$0.0625 \cdot \mathcal{L}_{\mathsf{a}}(\alpha{=}2)$	$1.875 \cdot \mathcal{L}_{\mathsf{u}}(t{=}2)$	rand	200	768	0.36	128	58.73%	64.37%	70.93%	63.74%	59.23%	65.14%	71.54%	64.69%
—	$0.05 \cdot \mathcal{L}_{\mathsf{a}}(\alpha{=}2)$	$1.9 \cdot \mathcal{L}_{\mathsf{u}}(t{=}2)$	rand	200	768	0.36	128	57.61%	64.13%	69.13%	63.09%	58.03%	65.09%	69.43%	64.09%
—	$0.025 \cdot \mathcal{L}_{\mathsf{a}}(\alpha{=}2)$	$1.95 \cdot \mathcal{L}_{\mathsf{u}}(t{=}2)$	rand	200	768	0.36	128	50.89%	57.70%	63.93%	57.83%	51.46%	58.39%	64.45%	58.34%
—	$0.0125 \cdot \mathcal{L}_{\mathsf{a}}(\alpha{=}2)$	$1.975 \cdot \mathcal{L}_{\mathsf{u}}(t{=}2)$	rand	200	768	0.36	128	44.71%	50.89%	57.75%	51.21%	45.14%	51.99%	57.98%	52.11%
—	—	$2 \cdot \mathcal{L}_{\mathsf{u}}(t{=}2)$	rand	200	768	0.36	128	21.99%	19.46%	28.94%	20.10%	21.91%	19.75%	29.65%	20.76%
—	$0.1 \cdot \mathcal{L}_{\mathsf{a}}(\alpha{=}2)$	$2 \cdot \mathcal{L}_{\mathsf{u}}(t{=}2)$	rand	200	768	0.36	128	63.63%	70.70%	75.85%	69.41%	64.14%	71.43%	76.50%	69.99%
—	$0.2 \cdot \mathcal{L}_{\mathsf{a}}(\alpha{=}2)$	$2 \cdot \mathcal{L}_{\mathsf{u}}(t{=}2)$	rand	200	768	0.36	128	66.52%	72.89%	77.66%	70.98%	67.16%	73.52%	78.19%	71.79%
—	$\mathcal{L}_{\mathsf{a}}(\alpha{=}1)$	$2 \cdot \mathcal{L}_{\mathsf{u}}(t{=}2)$	rand	200	768	0.36	128	10.00%	10.00%	10.00%	10.00%	10.00%	10.00%	10.00%	10.00%
—	$\mathcal{L}_{\mathsf{a}}(\alpha{=}1)$	$2.5 \cdot \mathcal{L}_{\mathsf{u}}(t{=}2)$	rand	200	768	0.36	128	10.00%	10.00%	10.00%	10.00%	10.00%	10.00%	10.00%	10.00%
—	$\mathcal{L}_{\mathsf{a}}(\alpha{=}1)$	$3 \cdot \mathcal{L}_{\mathsf{u}}(t{=}2)$	rand	200	768	0.36	128	10.00%	10.00%	10.00%	10.00%	10.00%	10.00%	10.00%	10.00%
—	$\mathcal{L}_{\mathsf{a}}(\alpha{=}1)$	$4 \cdot \mathcal{L}_{\mathsf{u}}(t{=}2)$	rand	200	768	0.36	128	10.00%	10.00%	10.00%	10.00%	10.00%	10.00%	10.00%	10.00%
—	—	$5 \cdot \mathcal{L}_{\mathsf{u}}(t{=}2)$	rand	200	768	0.36	128	19.61%	14.29%	21.70%	14.97%	19.64%	14.19%	21.61%	15.58%
—	$0.05 \cdot \mathcal{L}_{\mathsf{a}}(\alpha{=}2)$	$5 \cdot \mathcal{L}_{\mathsf{u}}(t{=}2)$	rand	200	768	0.36	128	50.49%	55.71%	61.45%	55.15%	50.91%	56.71%	61.58%	56.19%
—	$\mathcal{L}_{\mathsf{a}}(\alpha{=}1)$	$5 \cdot \mathcal{L}_{\mathsf{u}}(t{=}2)$	rand	200	768	0.36	128	10.00%	10.00%	10.00%	10.01%	10.00%	10.00%	10.00%	10.00%
—	$0.5 \cdot \mathcal{L}_{\mathsf{a}}(\alpha{=}2)$	$\mathcal{L}_{\mathsf{u}}(t{=}2)$	rand	200	768	0.36	256	—	—	—	—	82.10%	79.45%	84.15%	77.10%
—	$0.75 \cdot \mathcal{L}_{\mathsf{a}}(\alpha{=}2)$	$\mathcal{L}_{\mathsf{u}}(t{=}2)$	rand	200	768	0.36	256	—	—	—	—	81.53%	79.03%	83.54%	76.35%
—	$\mathcal{L}_{\mathsf{a}}(\alpha{=}2)$	$\mathcal{L}_{\mathsf{u}}(t{=}2)$	rand	200	768	0.36	256	—	—	—	—	81.33%	79.06%	84.03%	75.89%
—	$0.025 \cdot \mathcal{L}_{\mathsf{a}}(\alpha{=}2)$	$\mathcal{L}_{\mathsf{u}}(t{=}2)$	rand	200	768	0.36	512	—	—	—	—	75.76%	72.75%	78.29%	71.04%
—	$0.375 \cdot \mathcal{L}_{\mathsf{a}}(\alpha{=}2)$	$\mathcal{L}_{\mathsf{u}}(t{=}2)$	rand	200	768	0.36	512	—	—	—	—	82.33%	79.18%	83.91%	76.44%
—	$0.5 \cdot \mathcal{L}_{\mathsf{a}}(\alpha{=}2)$	$\mathcal{L}_{\mathsf{u}}(t{=}2)$	rand	200	768	0.36	512	—	—	—	—	82.55%	79.64%	84.29%	75.74%
—	$\mathcal{L}_{\mathsf{a}}(\alpha{=}2)$	$\mathcal{L}_{\mathsf{u}}(t{=}2)$	rand	200	768	0.36	512	—	—	—	—	82.04%	78.79%	83.98%	76.50%

—	$0.025 \cdot \mathcal{L}_{\mathsf{a}}(\alpha{=}2)$	$\mathcal{L}_{\mathsf{u}}(t{=}2)$	rand	200	768	0.36	1024	—	—	—	—	76.39%	72.45%	78.23%	70.59%
—	$0.05 \cdot \mathcal{L}_{\mathsf{a}}(\alpha{=}2)$	$\mathcal{L}_{\mathsf{u}}(t{=}2)$	rand	200	768	0.36	1024	—	—	—	—	79.68%	75.43%	80.81%	73.45%
—	$0.25 \cdot \mathcal{L}_{\mathsf{a}}(\alpha{=}2)$	$\mathcal{L}_{\mathsf{u}}(t{=}2)$	rand	200	768	0.36	1024	—	—	—	—	**83.03%**	79.63%	84.15%	76.10%
—	$0.25 \cdot \mathcal{L}_{\mathsf{a}}(\alpha{=}2)$	$\mathcal{L}_{\mathsf{u}}(t{=}2)$	rand	200	768	0.36	1024	—	—	—	—	82.85%	79.44%	83.91%	75.35%
—	$0.375 \cdot \mathcal{L}_{\mathsf{a}}(\alpha{=}2)$	$\mathcal{L}_{\mathsf{u}}(t{=}2)$	rand	200	768	0.36	1024	—	—	—	—	82.63%	79.33%	83.69%	76.09%
—	$0.5 \cdot \mathcal{L}_{\mathsf{a}}(\alpha{=}2)$	$\mathcal{L}_{\mathsf{u}}(t{=}2)$	rand	200	768	0.36	1024	—	—	—	—	82.85%	**79.75%**	83.85%	76.81%
—	$\mathcal{L}_{\mathsf{a}}(\alpha{=}2)$	$\mathcal{L}_{\mathsf{u}}(t{=}2)$	rand	200	768	0.36	1024	—	—	—	—	81.89%	79.09%	84.03%	75.51%
—	$0.25 \cdot \mathcal{L}_{\mathsf{a}}(\alpha{=}2)$	$\mathcal{L}_{\mathsf{u}}(t{=}2)$	rand	200	768	0.36	1536	—	—	—	—	82.93%	79.55%	84.00%	75.81%
—	$0.5 \cdot \mathcal{L}_{\mathsf{a}}(\alpha{=}2)$	$\mathcal{L}_{\mathsf{u}}(t{=}2)$	rand	200	1024	0.48	512	—	—	—	—	82.20%	79.36%	83.69%	75.73%
—	$\mathcal{L}_{\mathsf{a}}(\alpha{=}2)$	$\mathcal{L}_{\mathsf{u}}(t{=}2)$	rand	200	1024	0.48	512	—	—	—	—	81.66%	79.03%	83.88%	75.49%
—	$0.25 \cdot \mathcal{L}_{\mathsf{a}}(\alpha{=}2)$	$\mathcal{L}_{\mathsf{u}}(t{=}2)$	rand	200	1024	0.48	1024	—	—	—	—	82.40%	78.98%	83.34%	75.85%
—	$0.375 \cdot \mathcal{L}_{\mathsf{a}}(\alpha{=}2)$	$\mathcal{L}_{\mathsf{u}}(t{=}2)$	rand	200	1024	0.48	1024	—	—	—	—	82.74%	79.48%	83.70%	76.59%
—	$0.5 \cdot \mathcal{L}_{\mathsf{a}}(\alpha{=}2)$	$\mathcal{L}_{\mathsf{u}}(t{=}2)$	rand	200	1024	0.48	1024	—	—	—	—	82.51%	79.11%	83.46%	74.94%
$\mathcal{L}_{\mathsf{c}}(\tau{=}0.5)$	—	—	△	12	256	0.12	128	—	—	—	—	79.31%	77.45%	83.34%	76.60%
—	$5e-05 \cdot \mathcal{L}_{\mathsf{a}}(\alpha{=}2)$	—	♣	12	256	0.12	128	—	—	—	—	64.11%	62.45%	77.96%	68.56%
—	$0.0005 \cdot \mathcal{L}_{\mathsf{a}}(\alpha{=}2)$	—	♣	12	256	0.12	128	—	—	—	—	63.90%	62.40%	77.81%	68.55%
—	$0.005 \cdot \mathcal{L}_{\mathsf{a}}(\alpha{=}2)$	—	♣	12	256	0.12	128	—	—	—	—	61.53%	61.66%	76.83%	66.68%
—	$0.5 \cdot \mathcal{L}_{\mathsf{a}}(\alpha{=}2)$	—	♣	12	256	0.12	128	—	—	—	—	10.36%	23.01%	49.19%	39.39%
—	—	$0.01 \cdot \mathcal{L}_{\mathsf{u}}(t{=}2)$	♣	12	256	0.12	128	—	—	—	—	44.75%	41.79%	55.59%	38.59%
—	$0.5 \cdot \mathcal{L}_{\mathsf{a}}(\alpha{=}2)$	$0.01 \cdot \mathcal{L}_{\mathsf{u}}(t{=}2)$	♣	12	256	0.12	128	—	—	—	—	10.03%	32.81%	57.95%	41.53%
—	—	$0.1 \cdot \mathcal{L}_{\mathsf{u}}(t{=}2)$	♣	12	256	0.12	128	—	—	—	—	54.78%	54.05%	65.77%	50.13%
—	—	$\mathcal{L}_{\mathsf{u}}(t{=}2)$	♣	12	256	0.12	128	—	—	—	—	55.74%	52.03%	63.90%	50.59%
—	$0.005 \cdot \mathcal{L}_{\mathsf{a}}(\alpha{=}2)$	$\mathcal{L}_{\mathsf{u}}(t{=}2)$	♣	12	256	0.12	128	—	—	—	—	57.85%	55.18%	65.64%	53.33%
—	$0.05 \cdot \mathcal{L}_{\mathsf{a}}(\alpha{=}2)$	$\mathcal{L}_{\mathsf{u}}(t{=}2)$	♣	12	256	0.12	128	—	—	—	—	68.46%	66.07%	72.88%	64.65%
—	$0.4 \cdot \mathcal{L}_{\mathsf{a}}(\alpha{=}2)$	$\mathcal{L}_{\mathsf{u}}(t{=}2)$	♡	12	256	0.12	128	—	—	—	—	77.63%	76.65%	81.75%	75.95%
—	$0.5 \cdot \mathcal{L}_{\mathsf{a}}(\alpha{=}1)$	$\mathcal{L}_{\mathsf{u}}(t{=}2)$	♠	12	256	0.12	128	—	—	—	—	70.00%	68.21%	74.15%	66.77%

—	$0.5 \cdot \mathcal{L}_{\mathsf{a}}(\alpha{=}2)$	$\mathcal{L}_{\mathsf{u}}(t{=}2)$	♡	12	256	0.12	128	—	—	—	—	77.73%	76.33%	81.61%	76.00%
—	$0.5 \cdot \mathcal{L}_{\mathsf{a}}(\alpha{=}2)$	$\mathcal{L}_{\mathsf{u}}(t{=}2)$	♢	12	256	0.12	128	—	—	—	—	74.23%	72.89%	79.01%	71.46%
—	$0.625 \cdot \mathcal{L}_{\mathsf{a}}(\alpha{=}1)$	$\mathcal{L}_{\mathsf{u}}(t{=}2)$	♢	12	256	0.12	128	—	—	—	—	74.40%	72.84%	79.29%	71.41%
—	$\mathcal{L}_{\mathsf{a}}(\alpha{=}2)$	$\mathcal{L}_{\mathsf{u}}(t{=}2)$	♡	12	256	0.12	128	—	—	—	—	76.48%	75.86%	81.04%	75.43%
—	$\mathcal{L}_{\mathsf{a}}(\alpha{=}2)$	$\mathcal{L}_{\mathsf{u}}(t{=}2)$	♢	12	256	0.12	128	—	—	—	—	73.13%	72.24%	78.33%	71.15%
—	$1.25 \cdot \mathcal{L}_{\mathsf{a}}(\alpha{=}1)$	$\mathcal{L}_{\mathsf{u}}(t{=}2)$	♡	12	256	0.12	128	—	—	—	—	76.80%	75.75%	81.00%	75.11%
—	$1.25 \cdot \mathcal{L}_{\mathsf{a}}(\alpha{=}1)$	$\mathcal{L}_{\mathsf{u}}(t{=}2)$	♢	12	256	0.12	128	—	—	—	—	73.11%	71.73%	78.23%	71.79%
—	$1.25 \cdot \mathcal{L}_{\mathsf{a}}(\alpha{=}1)$	$\mathcal{L}_{\mathsf{u}}(t{=}2)$	♠	12	256	0.12	128	—	—	—	—	69.10%	67.21%	74.19%	66.25%
—	$1.875 \cdot \mathcal{L}_{\mathsf{a}}(\alpha{=}1)$	$\mathcal{L}_{\mathsf{u}}(t{=}2)$	♢	12	256	0.12	128	—	—	—	—	72.63%	71.08%	77.79%	70.98%
$\mathcal{L}_{\mathsf{c}}(\tau{=}0.5)$	—	—	□	12	768	0.36	128	—	—	—	—	75.34%	74.00%	81.09%	73.23%
$\mathcal{L}_{\mathsf{c}}(\tau{=}0.5)$	—	—	★	12	768	0.36	128	—	—	—	—	65.60%	64.25%	70.73%	64.79%
$0.5 \cdot \mathcal{L}_{\mathsf{c}}(\tau{=}0.5)$	—	—	★	12	768	0.36	128	—	—	—	—	69.64%	67.70%	74.89%	68.74%
$0.25 \cdot \mathcal{L}_{\mathsf{c}}(\tau{=}0.5)$	—	—	★	12	768	0.36	128	—	—	—	—	69.11%	68.34%	74.30%	69.30%
$0.05 \cdot \mathcal{L}_{\mathsf{c}}(\tau{=}0.5)$	—	—	★	12	768	0.36	128	—	—	—	—	70.43%	69.70%	76.08%	71.31%
$0.025 \cdot \mathcal{L}_{\mathsf{c}}(\tau{=}0.5)$	—	—	□	12	768	0.36	128	—	—	—	—	80.27%	78.65%	83.93%	77.00%
$0.025 \cdot \mathcal{L}_{\mathsf{c}}(\tau{=}0.5)$	—	—	★	12	768	0.36	128	—	—	—	—	70.00%	68.74%	76.24%	71.86%
$0.01 \cdot \mathcal{L}_{\mathsf{c}}(\tau{=}0.5)$	—	—	□	12	768	0.36	128	—	—	—	—	80.46%	78.88%	83.64%	**77.38%**
$0.01 \cdot \mathcal{L}_{\mathsf{c}}(\tau{=}0.5)$	—	—	★	12	768	0.36	128	—	—	—	—	68.13%	67.38%	75.63%	71.28%
—	$0.00025 \cdot \mathcal{L}_{\mathsf{a}}(\alpha{=}2)$	—	★	12	768	0.36	128	—	—	—	—	65.94%	64.33%	75.14%	70.90%
—	$0.0005 \cdot \mathcal{L}_{\mathsf{a}}(\alpha{=}2)$	—	★	12	768	0.36	128	—	—	—	—	64.88%	63.18%	74.78%	70.88%
—	$0.0005 \cdot \mathcal{L}_{\mathsf{a}}(\alpha{=}2)$	—	★	12	768	0.36	128	—	—	—	—	64.89%	63.53%	74.76%	70.89%
—	$0.001 \cdot \mathcal{L}_{\mathsf{a}}(\alpha{=}2)$	—	★	12	768	0.36	128	—	—	—	—	62.65%	61.93%	74.31%	70.36%
—	$0.0025 \cdot \mathcal{L}_{\mathsf{a}}(\alpha{=}2)$	—	★	12	768	0.36	128	—	—	—	—	59.18%	60.09%	72.98%	69.41%
—	$0.005 \cdot \mathcal{L}_{\mathsf{a}}(\alpha{=}2)$	—	★	12	768	0.36	128	—	—	—	—	52.18%	55.06%	71.40%	67.10%
—	$0.005 \cdot \mathcal{L}_{\mathsf{a}}(\alpha{=}2)$	—	★	12	768	0.36	128	—	—	—	—	52.86%	55.95%	71.63%	67.76%
—	$0.5 \cdot \mathcal{L}_{\mathsf{a}}(\alpha{=}2)$	—	★	12	768	0.36	128	—	—	—	—	10.00%	17.42%	36.69%	34.94%

—	—	$0.0001 \cdot \mathcal{L}_{\mathsf{u}}(t{=}2)$	★	12	768	0.36	128	—	—	—	—	60.32%	59.49%	70.65%	64.70%
—	—	$0.0005 \cdot \mathcal{L}_{\mathsf{u}}(t{=}2)$	★	12	768	0.36	128	—	—	—	—	44.34%	43.41%	61.06%	53.97%
—	$0.0005 \cdot \mathcal{L}_{\mathsf{a}}(\alpha{=}2)$	$0.0005 \cdot \mathcal{L}_{\mathsf{u}}(t{=}2)$	★	12	768	0.36	128	—	—	—	—	66.14%	66.13%	75.29%	70.20%
—	—	$0.001 \cdot \mathcal{L}_{\mathsf{u}}(t{=}2)$	★	12	768	0.36	128	—	—	—	—	41.61%	40.73%	56.91%	48.24%
—	$0.001 \cdot \mathcal{L}_{\mathsf{a}}(\alpha{=}2)$	$0.001 \cdot \mathcal{L}_{\mathsf{u}}(t{=}2)$	★	12	768	0.36	128	—	—	—	—	66.23%	66.55%	75.16%	70.25%
—	$0.5 \cdot \mathcal{L}_{\mathsf{a}}(\alpha{=}2)$	$0.001 \cdot \mathcal{L}_{\mathsf{u}}(t{=}2)$	★	12	768	0.36	128	—	—	—	—	10.00%	17.79%	35.06%	34.11%
—	$0.002 \cdot \mathcal{L}_{\mathsf{a}}(\alpha{=}2)$	$0.002 \cdot \mathcal{L}_{\mathsf{u}}(t{=}2)$	★	12	768	0.36	128	—	—	—	—	66.35%	67.07%	74.50%	70.33%
—	—	$0.01 \cdot \mathcal{L}_{\mathsf{u}}(t{=}2)$	★	12	768	0.36	128	—	—	—	—	44.64%	41.55%	50.75%	42.90%
—	$0.01 \cdot \mathcal{L}_{\mathsf{a}}(\alpha{=}2)$	$0.01 \cdot \mathcal{L}_{\mathsf{u}}(t{=}2)$	★	12	768	0.36	128	—	—	—	—	71.54%	70.71%	75.45%	70.43%
—	$0.5 \cdot \mathcal{L}_{\mathsf{a}}(\alpha{=}2)$	$0.01 \cdot \mathcal{L}_{\mathsf{u}}(t{=}2)$	★	12	768	0.36	128	—	—	—	—	10.00%	18.05%	32.93%	31.53%
—	$0.03 \cdot \mathcal{L}_{\mathsf{a}}(\alpha{=}2)$	$0.02 \cdot \mathcal{L}_{\mathsf{u}}(t{=}2)$	★	12	768	0.36	128	—	—	—	—	72.13%	71.86%	76.33%	71.78%
—	$0.025 \cdot \mathcal{L}_{\mathsf{a}}(\alpha{=}2)$	$0.025 \cdot \mathcal{L}_{\mathsf{u}}(t{=}2)$	★	12	768	0.36	128	—	—	—	—	73.40%	72.58%	76.44%	72.09%
—	$0.0375 \cdot \mathcal{L}_{\mathsf{a}}(\alpha{=}2)$	$0.025 \cdot \mathcal{L}_{\mathsf{u}}(t{=}2)$	★	12	768	0.36	128	—	—	—	—	72.54%	71.56%	76.14%	71.89%
—	$0.05 \cdot \mathcal{L}_{\mathsf{a}}(\alpha{=}2)$	$0.05 \cdot \mathcal{L}_{\mathsf{u}}(t{=}2)$	★	12	768	0.36	128	—	—	—	—	73.94%	72.63%	77.05%	72.36%
—	—	$0.1 \cdot \mathcal{L}_{\mathsf{u}}(t{=}2)$	★	12	768	0.36	128	—	—	—	—	54.51%	48.40%	60.60%	49.00%
—	$0.1 \cdot \mathcal{L}_{\mathsf{a}}(\alpha{=}2)$	$0.1 \cdot \mathcal{L}_{\mathsf{u}}(t{=}2)$	★	12	768	0.36	128	—	—	—	—	73.30%	72.21%	76.54%	72.13%
—	$0.5 \cdot \mathcal{L}_{\mathsf{a}}(\alpha{=}2)$	$0.1 \cdot \mathcal{L}_{\mathsf{u}}(t{=}2)$	★	12	768	0.36	128	—	—	—	—	67.45%	67.03%	74.04%	68.73%
—	$0.25 \cdot \mathcal{L}_{\mathsf{a}}(\alpha{=}2)$	$0.25 \cdot \mathcal{L}_{\mathsf{u}}(t{=}2)$	★	12	768	0.36	128	—	—	—	—	73.09%	71.66%	76.80%	71.16%
—	$0.5 \cdot \mathcal{L}_{\mathsf{a}}(\alpha{=}2)$	$0.5 \cdot \mathcal{L}_{\mathsf{u}}(t{=}2)$	★	12	768	0.36	128	—	—	—	—	72.18%	71.56%	76.38%	70.93%
—	—	$\mathcal{L}_{\mathsf{u}}(t{=}2)$	★	12	768	0.36	128	—	—	—	—	39.45%	35.56%	47.18%	35.60%
—	$0.0005 \cdot \mathcal{L}_{\mathsf{a}}(\alpha{=}2)$	$\mathcal{L}_{\mathsf{u}}(t{=}2)$	★	12	768	0.36	128	—	—	—	—	43.58%	38.19%	49.38%	38.64%
—	$0.005 \cdot \mathcal{L}_{\mathsf{a}}(\alpha{=}2)$	$\mathcal{L}_{\mathsf{u}}(t{=}2)$	★	12	768	0.36	128	—	—	—	—	50.10%	47.36%	56.66%	48.73%
—	$0.05 \cdot \mathcal{L}_{\mathsf{a}}(\alpha{=}2)$	$\mathcal{L}_{\mathsf{u}}(t{=}2)$	★	12	768	0.36	128	—	—	—	—	65.65%	66.15%	71.48%	66.10%
—	$0.5 \cdot \mathcal{L}_{\mathsf{a}}(\alpha{=}2)$	$\mathcal{L}_{\mathsf{u}}(t{=}2)$	★	12	768	0.36	128	—	—	—	—	70.34%	70.04%	74.88%	68.76%
—	$0.5 \cdot \mathcal{L}_{\mathsf{a}}(\alpha{=}2)$	$\mathcal{L}_{\mathsf{u}}(t{=}2)$	★	12	768	0.36	128	—	—	—	—	70.84%	69.88%	75.61%	69.34%
—	$\mathcal{L}_{\mathsf{a}}(\alpha{=}2)$	$\mathcal{L}_{\mathsf{u}}(t{=}2)$	★	12	768	0.36	128	—	—	—	—	66.83%	65.59%	72.09%	65.30%

	—	$1.5 \cdot \mathcal{L}_{\mathsf{a}}(\alpha{=}2)$	$1.5 \cdot \mathcal{L}_{\mathsf{u}}(t{=}2)$	★	12	768	0.36	128	—	—	—	—	65.18%	62.32%	69.77%	62.31%
	—	$\mathcal{L}_{\mathsf{a}}(\alpha{=}2)$	$2 \cdot \mathcal{L}_{\mathsf{u}}(t{=}2)$	★	12	768	0.36	128	—	—	—	—	63.21%	61.86%	68.66%	60.80%
	—	$2 \cdot \mathcal{L}_{\mathsf{a}}(\alpha{=}2)$	$2 \cdot \mathcal{L}_{\mathsf{u}}(t{=}2)$	★	12	768	0.36	128	—	—	—	—	61.93%	60.78%	68.54%	60.18%
♢	$\mathcal{L}_{\mathsf{c}}(\tau{=}1)$	—	—	rand	200	786	0.12	128	—	—	—	—	70.35%	70.11%	80.41%	73.15%
♣	$\mathcal{L}_{\mathsf{c}}(\tau{=}2)$	—	—	rand	200	786	0.12	128	—	—	—	—	64.19%	62.38%	78.11%	68.77%
♠	$\mathcal{L}_{\mathsf{c}}(\tau{=}3)$	—	—	rand	200	786	0.12	128	—	—	—	—	55.04%	53.94%	74.95%	64.04%

Table A.4: Experiment specifications for all 64 NYU-Depth-V2 encoders. We report the encoder representation quality measured by mean squared error (MSE) of a CNN depth predictor trained on conv5 or conv4 activations, via both a 5-fold cross validation of the training set and the held out validation set.
All encoders in this table use standard network initialization (denoted as "rand"). Dimensionality (abbreviated as "Dim.") shows the ambient dimension of the output features, *i.e.*, they live on the unit hypersphere of one less dimension.

Losses			Init.	Epochs	Batch Size	Initial LR	Dim.	Training Set 5-Fold Cross Val. MSE ↓		Validation Set MSE ↓	
$\mathcal{L}_{\text{contrastive}}$	$\mathcal{L}_{\text{align}}$	$\mathcal{L}_{\text{uniform}}$						conv5	conv4	conv5	conv4
—	$0.5 \cdot \mathcal{L}_{\text{a}}(\alpha{=}2)$	$\mathcal{L}_{\text{u}}(t{=}2)$	rand	400	128	0.06	128	0.7405	0.7979	0.7378	0.7969
$\mathcal{L}_{\text{c}}(\tau{=}0.25)$	—	—	rand	400	128	0.06	128	0.7188	0.7747	0.7259	0.7761
—	$4.375 \cdot \mathcal{L}_{\text{a}}(\alpha{=}2)$	$\mathcal{L}_{\text{u}}(t{=}2)$	rand	400	128	0.06	128	0.8039	0.8297	0.8032	0.8281
—	$3.625 \cdot \mathcal{L}_{\text{a}}(\alpha{=}1)$	$\mathcal{L}_{\text{u}}(t{=}2)$	rand	400	128	0.06	128	0.7290	0.7775	0.7303	0.7749
—	$\mathcal{L}_{\text{a}}(\alpha{=}2)$	$\mathcal{L}_{\text{u}}(t{=}2)$	rand	400	128	0.06	128	0.7121	0.7689	0.7191	0.7725
—	$3.5 \cdot \mathcal{L}_{\text{a}}(\alpha{=}2)$	$\mathcal{L}_{\text{u}}(t{=}2)$	rand	400	128	0.06	128	0.7270	0.7741	0.7260	0.7772
$\mathcal{L}_{\text{c}}(\tau{=}4)$	—	—	rand	400	128	0.06	128	0.7592	0.8195	0.7598	0.8175
—	$\mathcal{L}_{\text{a}}(\alpha{=}2)$	$0.3333 \cdot \mathcal{L}_{\text{u}}(t{=}2)$	rand	400	128	0.06	128	0.7165	0.7697	0.7215	0.7693
—	$2 \cdot \mathcal{L}_{\text{a}}(\alpha{=}2)$	$\mathcal{L}_{\text{u}}(t{=}2)$	rand	400	128	0.06	128	0.7300	0.7669	0.7226	0.7699
$\mathcal{L}_{\text{c}}(\tau{=}0.05)$	—	—	rand	400	128	0.06	128	0.7170	0.7672	0.7206	0.7637
$\mathcal{L}_{\text{c}}(\tau{=}1)$	—	—	rand	400	128	0.06	128	0.7505	0.7958	0.7560	0.7965
—	$0.5 \cdot \mathcal{L}_{\text{a}}(\alpha{=}2)$	$7.5 \cdot \mathcal{L}_{\text{u}}(t{=}2)$	rand	400	128	0.06	128	0.8188	0.8556	0.8302	0.8590
—	$1.25 \cdot \mathcal{L}_{\text{a}}(\alpha{=}2)$	$0.5 \cdot \mathcal{L}_{\text{u}}(t{=}2)$	rand	400	128	0.06	128	0.7237	0.7788	0.7224	0.7806
—	$4.625 \cdot \mathcal{L}_{\text{a}}(\alpha{=}1)$	$\mathcal{L}_{\text{u}}(t{=}2)$	rand	400	128	0.06	128	0.8692	0.8820	0.8724	0.8840
—	$3.375 \cdot \mathcal{L}_{\text{a}}(\alpha{=}2)$	$\mathcal{L}_{\text{u}}(t{=}2)$	rand	400	128	0.06	128	0.7663	0.7935	0.7691	0.7938
—	$0.75 \cdot \mathcal{L}_{\text{a}}(\alpha{=}2)$	$0.5 \cdot \mathcal{L}_{\text{u}}(t{=}2)$	rand	400	128	0.06	128	**0.7008**	0.7621	**0.7014**	0.7592
—	$\mathcal{L}_{\text{a}}(\alpha{=}2)$	$0.25 \cdot \mathcal{L}_{\text{u}}(t{=}2)$	rand	400	128	0.06	128	0.7293	0.7997	0.7313	0.8013
$\mathcal{L}_{\text{c}}(\tau{=}0.07)$	—	—	rand	400	128	0.06	128	0.7079	**0.7468**	0.7105	**0.7460**
$\mathcal{L}_{\text{c}}(\tau{=}0.005)$	—	—	rand	400	128	0.06	128	0.7608	0.8109	0.7633	0.8149

—	$4 \cdot \mathcal{L}_{\mathsf{a}}(\alpha{=}2)$	$\mathcal{L}_{\mathsf{u}}(t{=}2)$	rand	400	128	0.06	128	0.7721	0.8195	0.7737	0.8190
—	$1.5 \cdot \mathcal{L}_{\mathsf{a}}(\alpha{=}1)$	$\mathcal{L}_{\mathsf{u}}(t{=}2)$	rand	400	128	0.06	128	0.7231	0.7810	0.7193	0.7889
—	$\mathcal{L}_{\mathsf{a}}(\alpha{=}2)$	$0.5 \cdot \mathcal{L}_{\mathsf{u}}(t{=}2)$	rand	400	128	0.06	128	0.7044	0.7714	0.7047	0.7718
—	$0.5 \cdot \mathcal{L}_{\mathsf{a}}(\alpha{=}2)$	$0.5 \cdot \mathcal{L}_{\mathsf{u}}(t{=}2)$	rand	400	128	0.06	128	0.7329	0.7751	0.7454	0.7786
—	$2.5 \cdot \mathcal{L}_{\mathsf{a}}(\alpha{=}1)$	$\mathcal{L}_{\mathsf{u}}(t{=}2)$	rand	400	128	0.06	128	0.7295	0.7747	0.7304	0.7785
—	$4.125 \cdot \mathcal{L}_{\mathsf{a}}(\alpha{=}2)$	$\mathcal{L}_{\mathsf{u}}(t{=}2)$	rand	400	128	0.06	128	0.7497	0.8129	0.7478	0.8128
—	$0.125 \cdot \mathcal{L}_{\mathsf{a}}(\alpha{=}2)$	$2.5 \cdot \mathcal{L}_{\mathsf{u}}(t{=}2)$	rand	400	128	0.06	128	0.8109	0.8535	0.8092	0.8523
—	$1.25 \cdot \mathcal{L}_{\mathsf{a}}(\alpha{=}2)$	$\mathcal{L}_{\mathsf{u}}(t{=}2)$	rand	400	128	0.06	128	0.7509	0.7892	0.7324	0.7926
—	$3.75 \cdot \mathcal{L}_{\mathsf{a}}(\alpha{=}2)$	$\mathcal{L}_{\mathsf{u}}(t{=}2)$	rand	400	128	0.06	128	0.7514	0.8005	0.7531	0.8003
—	$2.25 \cdot \mathcal{L}_{\mathsf{a}}(\alpha{=}2)$	$\mathcal{L}_{\mathsf{u}}(t{=}2)$	rand	400	128	0.06	128	0.7360	0.7706	0.7413	0.7747
—	$4.875 \cdot \mathcal{L}_{\mathsf{a}}(\alpha{=}1)$	$\mathcal{L}_{\mathsf{u}}(t{=}2)$	rand	400	128	0.06	128	0.8699	0.8882	0.8717	0.8918
—	$3.125 \cdot \mathcal{L}_{\mathsf{a}}(\alpha{=}2)$	$\mathcal{L}_{\mathsf{u}}(t{=}2)$	rand	400	128	0.06	128	0.7203	0.7713	0.7138	0.7682
—	$1.5 \cdot \mathcal{L}_{\mathsf{a}}(\alpha{=}2)$	$\mathcal{L}_{\mathsf{u}}(t{=}2)$	rand	400	128	0.06	128	0.7261	0.7744	0.7259	0.7715
$\mathcal{L}_{\mathsf{c}}(\tau{=}0.5)$	—	—	rand	400	128	0.06	128	0.7334	0.7743	0.7293	0.7701
—	$\mathcal{L}_{\mathsf{a}}(\alpha{=}2)$	$0.2857 \cdot \mathcal{L}_{\mathsf{u}}(t{=}2)$	rand	400	128	0.06	128	0.7456	0.8070	0.7423	0.8030
—	$2.5 \cdot \mathcal{L}_{\mathsf{a}}(\alpha{=}2)$	$\mathcal{L}_{\mathsf{u}}(t{=}2)$	rand	400	128	0.06	128	0.7289	0.7591	0.7250	0.7597
—	$0.5 \cdot \mathcal{L}_{\mathsf{a}}(\alpha{=}2)$	$3 \cdot \mathcal{L}_{\mathsf{u}}(t{=}2)$	rand	400	128	0.06	128	0.7819	0.8352	0.7808	0.8314
—	$0.5 \cdot \mathcal{L}_{\mathsf{a}}(\alpha{=}2)$	$10 \cdot \mathcal{L}_{\mathsf{u}}(t{=}2)$	rand	400	128	0.06	128	0.8422	0.8896	0.8430	0.8857
—	$3 \cdot \mathcal{L}_{\mathsf{a}}(\alpha{=}2)$	$\mathcal{L}_{\mathsf{u}}(t{=}2)$	rand	400	128	0.06	128	0.7203	0.7642	0.7160	0.7643
—	$3.875 \cdot \mathcal{L}_{\mathsf{a}}(\alpha{=}2)$	$\mathcal{L}_{\mathsf{u}}(t{=}2)$	rand	400	128	0.06	128	0.7477	0.7980	0.7476	0.7960
$\mathcal{L}_{\mathsf{c}}(\tau{=}0.4)$	—	—	rand	400	128	0.06	128	0.7181	0.7628	0.7163	0.7651
—	$0.75 \cdot \mathcal{L}_{\mathsf{a}}(\alpha{=}1)$	$\mathcal{L}_{\mathsf{u}}(t{=}2)$	rand	400	128	0.06	128	0.7670	0.8225	0.7700	0.8224
—	$1.25 \cdot \mathcal{L}_{\mathsf{a}}(\alpha{=}1)$	$\mathcal{L}_{\mathsf{u}}(t{=}2)$	rand	400	128	0.06	128	0.7311	0.7922	0.7265	0.7942
—	$1.75 \cdot \mathcal{L}_{\mathsf{a}}(\alpha{=}2)$	$0.5 \cdot \mathcal{L}_{\mathsf{u}}(t{=}2)$	rand	400	128	0.06	128	0.7323	0.7900	0.7297	0.7884
—	$4.5 \cdot \mathcal{L}_{\mathsf{a}}(\alpha{=}2)$	$\mathcal{L}_{\mathsf{u}}(t{=}2)$	rand	400	128	0.06	128	0.7592	0.8350	0.7585	0.8297
—	$0.5 \cdot \mathcal{L}_{\mathsf{a}}(\alpha{=}2)$	$5 \cdot \mathcal{L}_{\mathsf{u}}(t{=}2)$	rand	400	128	0.06	128	0.7909	0.8517	0.7891	0.8526

$0.5 \cdot \mathcal{L}_{\mathsf{c}}(\tau{=}0.07)$	—	—	rand	400	128	0.06	128	0.7068	0.7594	0.7028	0.7624
—	$3.75 \cdot \mathcal{L}_{\mathsf{a}}(\alpha{=}1)$	$\mathcal{L}_{\mathsf{u}}(t{=}2)$	rand	400	128	0.06	128	0.7352	0.7853	0.7294	0.7817
—	$3.125 \cdot \mathcal{L}_{\mathsf{a}}(\alpha{=}1)$	$\mathcal{L}_{\mathsf{u}}(t{=}2)$	rand	400	128	0.06	128	0.7152	0.7661	0.7060	0.7667
—	$3.625 \cdot \mathcal{L}_{\mathsf{a}}(\alpha{=}2)$	$\mathcal{L}_{\mathsf{u}}(t{=}2)$	rand	400	128	0.06	128	0.7420	0.7925	0.7505	0.7970
—	$5 \cdot \mathcal{L}_{\mathsf{a}}(\alpha{=}2)$	$\mathcal{L}_{\mathsf{u}}(t{=}2)$	rand	400	128	0.06	128	0.8072	0.8631	0.8084	0.8617
$\mathcal{L}_{\mathsf{c}}(\tau{=}0.1)$	—	—	rand	400	128	0.06	128	0.7074	0.7539	0.7124	0.7491
—	$1.5 \cdot \mathcal{L}_{\mathsf{a}}(\alpha{=}2)$	$0.5 \cdot \mathcal{L}_{\mathsf{u}}(t{=}2)$	rand	400	128	0.06	128	0.7255	0.7793	0.7199	0.7765
—	$7.5 \cdot \mathcal{L}_{\mathsf{a}}(\alpha{=}2)$	$\mathcal{L}_{\mathsf{u}}(t{=}2)$	rand	400	128	0.06	128	0.8160	0.8512	0.8131	0.8505
—	$4.75 \cdot \mathcal{L}_{\mathsf{a}}(\alpha{=}2)$	$\mathcal{L}_{\mathsf{u}}(t{=}2)$	rand	400	128	0.06	128	0.8102	0.8633	0.8084	0.8721
—	$0.5 \cdot \mathcal{L}_{\mathsf{a}}(\alpha{=}2)$	$2.5 \cdot \mathcal{L}_{\mathsf{u}}(t{=}2)$	rand	400	128	0.06	128	0.7696	0.8208	0.7669	0.8141
—	$2 \cdot \mathcal{L}_{\mathsf{a}}(\alpha{=}1)$	$\mathcal{L}_{\mathsf{u}}(t{=}2)$	rand	400	128	0.06	128	0.7209	0.7839	0.7370	0.7867
$0.5 \cdot \mathcal{L}_{\mathsf{c}}(\tau{=}0.1)$	—	—	rand	400	128	0.06	128	0.7062	0.7586	0.7024	0.7575
$\mathcal{L}_{\mathsf{c}}(\tau{=}10)$	—	—	rand	400	128	0.06	128	0.7860	0.8375	0.7850	0.8335
—	$3.375 \cdot \mathcal{L}_{\mathsf{a}}(\alpha{=}1)$	$\mathcal{L}_{\mathsf{u}}(t{=}2)$	rand	400	128	0.06	128	0.7236	0.7703	0.7230	0.7728
—	$0.25 \cdot \mathcal{L}_{\mathsf{a}}(\alpha{=}2)$	$\mathcal{L}_{\mathsf{u}}(t{=}2)$	rand	400	128	0.06	128	0.7596	0.8122	0.7574	0.8107
$\mathcal{L}_{\mathsf{c}}(\tau{=}0.3)$	—	—	rand	400	128	0.06	128	0.7337	0.7653	0.7361	0.7640
$\mathcal{L}_{\mathsf{c}}(\tau{=}5)$	—	—	rand	400	128	0.06	128	0.7801	0.8278	0.7715	0.8355
—	$3.25 \cdot \mathcal{L}_{\mathsf{a}}(\alpha{=}2)$	$\mathcal{L}_{\mathsf{u}}(t{=}2)$	rand	400	128	0.06	128	0.7495	0.7903	0.7503	0.7941
—	$0.5 \cdot \mathcal{L}_{\mathsf{a}}(\alpha{=}2)$	$4 \cdot \mathcal{L}_{\mathsf{u}}(t{=}2)$	rand	400	128	0.06	128	0.8062	0.8597	0.8042	0.8608

Table A.5: Experiment specifications for all 45 ImageNet-100 ResNet50 encoders trained using methods based on Momentum Contrast (MoCo) (He et al., 2019). We report the encoder representation quality measured by accuracy of a linear classifier on penultimate layer activations, via both a 3-fold cross validation of the training set and the held out validation set.
All encoders in this table use standard network initialization (denoted as "rand"). Dimensionality (abbreviated as "Dim.") shows the ambient dimension of the output features, *i.e.*, they live on the unit hypersphere of one less dimension.
For $\mathcal{L}_{\mathsf{uniform}}$, the "Intra-batch" column denotes whether $\mathcal{L}_{\mathsf{uniform}}$ calculation includes pairwise distances within batch in addition to distances w.r.t. to the queue (*i.e.*, Equation (A.20) vs. Equation (A.19)).

Losses				Init.	Epochs	Batch Size	Queue Size	Initial LR	Dim.	Training Set 3-Fold Cross Val. Accuracy ↑		Validation Set Accuracy ↑	
$\mathcal{L}_{\mathsf{contrastive}}$	$\mathcal{L}_{\mathsf{align}}$	$\mathcal{L}_{\mathsf{uniform}}$								top1	top5	top1	top5
		Form	Intra-batch										
$\mathcal{L}_{\mathsf{c}}(\tau{=}0.01)$	—	—		rand	240	128	16384	0.03	128	62.45%	85.64%	64.14%	86.12%
$\mathcal{L}_{\mathsf{c}}(\tau{=}0.07)$	—	—		rand	240	128	16384	0.03	128	71.68%	91.00%	72.80%	91.64%
$\mathcal{L}_{\mathsf{c}}(\tau{=}0.5)$	—	—		rand	240	128	16384	0.03	128	68.56%	91.21%	69.98%	91.80%
$\mathcal{L}_{\mathsf{c}}(\tau{=}1)$	—	—		rand	240	128	16384	0.03	128	62.19%	87.73%	64.06%	88.32%
$\mathcal{L}_{\mathsf{c}}(\tau{=}2)$	—	—		rand	240	128	16384	0.03	128	53.62%	83.03%	55.46%	84.18%
$\mathcal{L}_{\mathsf{c}}(\tau{=}5)$	—	—		rand	240	128	16384	0.03	128	37.52%	68.93%	39.00%	70.86%
—	$2 \cdot \mathcal{L}_{\mathsf{a}}(\alpha{=}2)$	—		rand	240	128	16384	0.03	128	1.03%	5.12%	1.22%	5.42%
—	$\mathcal{L}_{\mathsf{a}}(\alpha{=}2)$	$0.125 \cdot \mathcal{L}_{\mathsf{u}}(t{=}8)$	✓	rand	240	128	16384	0.03	128	65.89%	88.28%	67.42%	88.96%
—	$\mathcal{L}_{\mathsf{a}}(\alpha{=}2)$	$0.15 \cdot \mathcal{L}_{\mathsf{u}}(t{=}7)$	✓	rand	240	128	16384	0.03	128	67.51%	88.95%	68.90%	89.68%
—	$\mathcal{L}_{\mathsf{a}}(\alpha{=}2)$	$0.17 \cdot \mathcal{L}_{\mathsf{u}}(t{=}6)$	✓	rand	240	128	16384	0.03	128	67.90%	89.83%	69.18%	90.76%
—	$\mathcal{L}_{\mathsf{a}}(\alpha{=}2)$	$0.2 \cdot \mathcal{L}_{\mathsf{u}}(t{=}5)$	✓	rand	240	128	16384	0.03	128	69.27%	90.08%	70.46%	90.86%
—	$1.8 \cdot \mathcal{L}_{\mathsf{a}}(\alpha{=}2)$	$0.2 \cdot \mathcal{L}_{\mathsf{u}}(t{=}2)$	✓	rand	240	128	16384	0.03	128	1.00%	4.94%	1.00%	5.00%
—	$\mathcal{L}_{\mathsf{a}}(\alpha{=}2)$	$0.25 \cdot \mathcal{L}_{\mathsf{u}}(t{=}4)$	✓	rand	240	128	16384	0.03	128	69.77%	90.57%	70.70%	91.14%
—	$\mathcal{L}_{\mathsf{a}}(\alpha{=}2)$	$0.33 \cdot \mathcal{L}_{\mathsf{u}}(t{=}3)$	✓	rand	240	128	16384	0.03	128	70.67%	91.14%	71.86%	91.58%
—	$1.6 \cdot \mathcal{L}_{\mathsf{a}}(\alpha{=}2)$	$0.4 \cdot \mathcal{L}_{\mathsf{u}}(t{=}2)$	✓	rand	240	128	16384	0.03	128	67.34%	90.27%	69.16%	91.00%
—	$\mathcal{L}_{\mathsf{a}}(\alpha{=}2)$	$0.5 \cdot \mathcal{L}_{\mathsf{u}}(t{=}2)$	✗	rand	240	128	16384	0.03	128	70.91%	91.38%	72.34%	91.86%

—	$\mathcal{L}_{\mathsf{a}}(\alpha{=}2)$	$0.5 \cdot \mathcal{L}_{\mathsf{u}}(t{=}2)$	✓	rand	240	128	16384	0.03	128	71.03%	91.61%	71.90%	92.06%
—	$1.4 \cdot \mathcal{L}_{\mathsf{a}}(\alpha{=}2)$	$0.6 \cdot \mathcal{L}_{\mathsf{u}}(t{=}2)$	✓	rand	240	128	16384	0.03	128	71.11%	91.69%	72.06%	92.28%
—	$1.2 \cdot \mathcal{L}_{\mathsf{a}}(\alpha{=}2)$	$0.8 \cdot \mathcal{L}_{\mathsf{u}}(t{=}2)$	✓	rand	240	128	16384	0.03	128	71.76%	91.51%	72.78%	91.90%
—	$0.75 \cdot \mathcal{L}_{\mathsf{a}}(\alpha{=}2)$	$\mathcal{L}_{\mathsf{u}}(t{=}2)$	✓	rand	240	128	16384	0.03	128	70.23%	91.01%	71.40%	91.36%
—	$\mathcal{L}_{\mathsf{a}}(\alpha{=}2)$	$\mathcal{L}_{\mathsf{u}}(t{=}1)$	✓	rand	240	128	16384	0.03	128	68.07%	90.66%	69.54%	91.14%
—	$\mathcal{L}_{\mathsf{a}}(\alpha{=}2)$	$\mathcal{L}_{\mathsf{u}}(t{=}2)$	✗	rand	240	128	16384	0.03	128	69.59%	90.67%	70.64%	91.28%
—	$\mathcal{L}_{\mathsf{a}}(\alpha{=}2)$	$\mathcal{L}_{\mathsf{u}}(t{=}2)$	✓	rand	240	128	16384	0.03	128	70.45%	91.25%	71.48%	91.72%
—	$1.5 \cdot \mathcal{L}_{\mathsf{a}}(\alpha{=}2)$	$\mathcal{L}_{\mathsf{u}}(t{=}2)$	✓	rand	240	128	16384	0.03	128	72.39%	91.71%	73.80%	92.22%
—	$2 \cdot \mathcal{L}_{\mathsf{a}}(\alpha{=}2)$	$\mathcal{L}_{\mathsf{u}}(t{=}2)$	✗	rand	240	128	16384	0.03	128	72.19%	**92.35%**	73.30%	92.74%
—	$2 \cdot \mathcal{L}_{\mathsf{a}}(\alpha{=}2)$	$\mathcal{L}_{\mathsf{u}}(t{=}2)$	✗	rand	240	128	32768	0.03	128	72.41%	92.08%	73.54%	92.74%
—	$2 \cdot \mathcal{L}_{\mathsf{a}}(\alpha{=}2)$	$\mathcal{L}_{\mathsf{u}}(t{=}2)$	✓	rand	240	128	16384	0.03	128	72.69%	92.21%	73.74%	**92.80%**
—	$2 \cdot \mathcal{L}_{\mathsf{a}}(\alpha{=}2)$	$\mathcal{L}_{\mathsf{u}}(t{=}2)$	✓	rand	240	128	32768	0.03	128	72.65%	92.09%	73.68%	92.46%
—	$2.5 \cdot \mathcal{L}_{\mathsf{a}}(\alpha{=}2)$	$\mathcal{L}_{\mathsf{u}}(t{=}2)$	✗	rand	240	128	16384	0.03	128	71.77%	91.99%	73.00%	92.14%
—	$2.5 \cdot \mathcal{L}_{\mathsf{a}}(\alpha{=}2)$	$\mathcal{L}_{\mathsf{u}}(t{=}2)$	✓	rand	240	128	16384	0.03	128	72.31%	91.99%	73.50%	92.38%
—	$3 \cdot \mathcal{L}_{\mathsf{a}}(\alpha{=}2)$	$\mathcal{L}_{\mathsf{u}}(t{=}2)$	✓	rand	240	128	16384	0.03	128	72.03%	92.09%	73.48%	92.56%
—	$3 \cdot \mathcal{L}_{\mathsf{a}}(\alpha{=}2)$	$\mathcal{L}_{\mathsf{u}}(t{=}3)$	✓	rand	240	128	16384	0.03	128	**73.49%**	92.24%	**74.60%**	92.74%
—	$4 \cdot \mathcal{L}_{\mathsf{a}}(\alpha{=}2)$	$\mathcal{L}_{\mathsf{u}}(t{=}4)$	✓	rand	240	128	16384	0.03	128	72.93%	92.03%	74.30%	92.54%
—	$5 \cdot \mathcal{L}_{\mathsf{a}}(\alpha{=}2)$	$\mathcal{L}_{\mathsf{u}}(t{=}5)$	✓	rand	240	128	16384	0.03	128	71.96%	91.67%	73.04%	92.28%
—	$6 \cdot \mathcal{L}_{\mathsf{a}}(\alpha{=}2)$	$\mathcal{L}_{\mathsf{u}}(t{=}6)$	✓	rand	240	128	16384	0.03	128	70.49%	90.63%	72.02%	91.24%
—	$7 \cdot \mathcal{L}_{\mathsf{a}}(\alpha{=}2)$	$\mathcal{L}_{\mathsf{u}}(t{=}7)$	✓	rand	240	128	16384	0.03	128	70.66%	90.83%	72.32%	91.86%
—	$8 \cdot \mathcal{L}_{\mathsf{a}}(\alpha{=}2)$	$\mathcal{L}_{\mathsf{u}}(t{=}8)$	✓	rand	240	128	16384	0.03	128	69.47%	90.33%	70.86%	91.26%
—	$0.8 \cdot \mathcal{L}_{\mathsf{a}}(\alpha{=}2)$	$1.2 \cdot \mathcal{L}_{\mathsf{u}}(t{=}2)$	✓	rand	240	128	16384	0.03	128	70.45%	90.72%	71.22%	91.06%
—	$0.6 \cdot \mathcal{L}_{\mathsf{a}}(\alpha{=}2)$	$1.4 \cdot \mathcal{L}_{\mathsf{u}}(t{=}2)$	✓	rand	240	128	16384	0.03	128	69.03%	90.53%	70.44%	90.92%
—	$0.4 \cdot \mathcal{L}_{\mathsf{a}}(\alpha{=}2)$	$1.6 \cdot \mathcal{L}_{\mathsf{u}}(t{=}2)$	✓	rand	240	128	16384	0.03	128	67.04%	89.24%	68.32%	89.76%
—	$0.2 \cdot \mathcal{L}_{\mathsf{a}}(\alpha{=}2)$	$1.8 \cdot \mathcal{L}_{\mathsf{u}}(t{=}2)$	✓	rand	240	128	16384	0.03	128	66.71%	88.93%	68.10%	89.48%
—	—	$2 \cdot \mathcal{L}_{\mathsf{u}}(t{=}2)$	✓	rand	240	128	16384	0.03	128	2.43%	9.97%	2.92%	10.56%

—	$\mathcal{L}_{\mathsf{a}}(\alpha{=}2)$	$\mathcal{L}_{\mathsf{u}}(t{=}2)$	✓	rand	240	128	16384	0.03	128	58.43%	84.67%	60.36%	85.02%
—	$2 \cdot \mathcal{L}_{\mathsf{a}}(\alpha{=}2)$	$\mathcal{L}_{\mathsf{u}}(t{=}2)$	✗	rand	240	128	32768	0.03	128	69.68%	91.13%	70.80%	91.80%
—	$2 \cdot \mathcal{L}_{\mathsf{a}}(\alpha{=}2)$	$\mathcal{L}_{\mathsf{u}}(t{=}2)$	✓	rand	240	128	16384	0.03	128	69.62%	90.77%	70.92%	91.42%

Table A.6: Experiment specifications for all 108 BookCorpus recurrent encoders trained using methods based on Quick-Thought Vectors (Logeswaran and Lee, 2018). We report the encoder representation quality measured by accuracy of logistic classifiers on encoder outputs for the Movie Review Sentence Polarity (MR) and Customer Product Sentiment (CR) binary classification tasks, via both a 5-fold cross validation of the training set (of the downstream task) and the held out validation set (of the downstream task).
All encoders in this table use standard network initialization (denoted as "`rand`"). Dimensionality (abbreviated as "Dim.") shows the ambient dimension of the output features, *i.e.*, features from $l2$-normalized encoders live on the unit hypersphere of one less dimension. Regardless of whether the encoder is $l2$-normalized (indicated in "Normalization" column), the features are always normalized before being used for downstream tasks, following Logeswaran and Lee (2018).
The only unnormalized encoder is obtained using the unmodified Quick-Thought Vectors algorithm. 6 configurations that suffer from training instability (*i.e.*, `NaN` occurring) are also reported.

Losses			Normalization	Init.	Epochs	Batch Size	Initial LR	Dim.	Training Set 5-Fold Cross Val. Accuracy ↑		Validation Set Accuracy ↑	
$\mathcal{L}_{\text{contrastive}}$	$\mathcal{L}_{\text{align}}$	$\mathcal{L}_{\text{uniform}}$							MR	CR	MR	CR
$\mathcal{L}_{\text{c}}(\tau{=}1)$	—	—	✗	rand	1	400	0.0005	1200	76.33%	81.90%	77.23%	83.07%
$\mathcal{L}_{\text{c}}(\tau{=}0.005)$	—	—	✓	rand	1	400	0.0005	1200	74.97%	82.94%	76.85%	82.54%
$\mathcal{L}_{\text{c}}(\tau{=}0.01)$	—	—	✓	rand	1	400	0.0005	1200	75.02%	82.20%	75.54%	82.28%
$\mathcal{L}_{\text{c}}(\tau{=}0.05)$	—	—	✓	rand	1	400	0.0005	1200	75.48%	**83.64%**	**77.69%**	83.86%
$\mathcal{L}_{\text{c}}(\tau{=}0.075)$	—	—	✓	rand	1	400	0.0005	1200	**76.37%**	83.32%	77.51%	82.28%
$\mathcal{L}_{\text{c}}(\tau{=}0.1)$	—	—	✓	rand	1	400	0.0005	1200	75.82%	81.90%	74.79%	83.86%
$\mathcal{L}_{\text{c}}(\tau{=}0.2)$	—	—	✓	rand	1	400	0.0005	1200	74.33%	81.08%	75.63%	80.16%
$\mathcal{L}_{\text{c}}(\tau{=}0.25)$	—	—	✓	rand	1	400	0.0005	1200	72.33%	79.49%	71.51%	78.84%
$\mathcal{L}_{\text{c}}(\tau{=}0.3)$	—	—	✓	rand	1	400	0.0005	1200	72.85%	78.54%	73.57%	79.10%
$\mathcal{L}_{\text{c}}(\tau{=}0.4)$	—	—	✓	rand	1	400	0.0005	1200	69.72%	77.28%	67.85%	77.51%
$\mathcal{L}_{\text{c}}(\tau{=}0.5)$	—	—	✓	rand	1	400	0.0005	1200	68.97%	76.27%	68.98%	74.07%
$\mathcal{L}_{\text{c}}(\tau{=}0.6)$	—	—	✓	rand	1	400	0.0005	1200	68.61%	75.48%	68.88%	73.81%
$\mathcal{L}_{\text{c}}(\tau{=}0.7)$	—	—	✓	rand	1	400	0.0005	1200	67.89%	74.01%	67.76%	76.46%
$\mathcal{L}_{\text{c}}(\tau{=}0.8)$	—	—	✓	rand	1	400	0.0005	1200	67.02%	74.77%	66.07%	74.34%
$\mathcal{L}_{\text{c}}(\tau{=}0.9)$	—	—	✓	rand	1	400	0.0005	1200	66.78%	74.01%	65.32%	72.75%

$\mathcal{L}_{\mathsf{c}}(\tau{=}1)$	—	—	✓	rand	1	400	0.0005	1200	66.67%	74.12%	65.79%	74.34%
$\mathcal{L}_{\mathsf{c}}(\tau{=}1.5)$	—	—	✓	rand	1	400	0.0005	1200	63.92%	70.47%	65.42%	75.93%
$\mathcal{L}_{\mathsf{c}}(\tau{=}2)$	—	—	✓	rand	1	400	0.0005	1200	63.97%	72.06%	62.79%	71.69%
$\mathcal{L}_{\mathsf{c}}(\tau{=}5)$	—	—	✓	rand	1	400	0.0005	1200	62.21%	69.50%	62.98%	73.54%
$\mathcal{L}_{\mathsf{c}}(\tau{=}0.075)$	$\mathcal{L}_{\mathsf{a}}(\alpha{=}2)$	—	✓	rand	1	400	0.0005	1200	69.16%	73.39%	68.13%	72.75%
$\mathcal{L}_{\mathsf{c}}(\tau{=}1)$	$\mathcal{L}_{\mathsf{a}}(\alpha{=}2)$	—	✓	rand	1	400	0.0005	1200	49.68%	63.81%	49.77%	63.49%
$\mathcal{L}_{\mathsf{c}}(\tau{=}0.075)$	$0.9 \cdot \mathcal{L}_{\mathsf{a}}(\alpha{=}2)$	$0.1 \cdot \mathcal{L}_{\mathsf{u}}(t{=}2)$	✓	rand	1	400	0.0005	1200	71.26%	77.90%	71.42%	76.72%
$\mathcal{L}_{\mathsf{c}}(\tau{=}1)$	$0.9 \cdot \mathcal{L}_{\mathsf{a}}(\alpha{=}2)$	$0.1 \cdot \mathcal{L}_{\mathsf{u}}(t{=}2)$	✓	rand	1	400	0.0005	1200	51.26%	63.78%	52.01%	63.49%
$\mathcal{L}_{\mathsf{c}}(\tau{=}0.075)$	$0.8 \cdot \mathcal{L}_{\mathsf{a}}(\alpha{=}2)$	$0.2 \cdot \mathcal{L}_{\mathsf{u}}(t{=}2)$	✓	rand	1	400	0.0005	1200	76.25%	83.05%	76.48%	83.33%
$\mathcal{L}_{\mathsf{c}}(\tau{=}1)$	$0.8 \cdot \mathcal{L}_{\mathsf{a}}(\alpha{=}2)$	$0.2 \cdot \mathcal{L}_{\mathsf{u}}(t{=}2)$	✓	rand	1	400	0.0005	1200	71.33%	79.31%	70.48%	78.31%
$\mathcal{L}_{\mathsf{c}}(\tau{=}0.075)$	$0.7 \cdot \mathcal{L}_{\mathsf{a}}(\alpha{=}2)$	$0.3 \cdot \mathcal{L}_{\mathsf{u}}(t{=}2)$	✓	rand	1	400	0.0005	1200	75.67%	81.20%	74.60%	81.48%
$\mathcal{L}_{\mathsf{c}}(\tau{=}1)$	$0.7 \cdot \mathcal{L}_{\mathsf{a}}(\alpha{=}2)$	$0.3 \cdot \mathcal{L}_{\mathsf{u}}(t{=}2)$	✓	rand	1	400	0.0005	1200	71.59%	78.72%	73.66%	78.84%
$\mathcal{L}_{\mathsf{c}}(\tau{=}0.075)$	$0.6 \cdot \mathcal{L}_{\mathsf{a}}(\alpha{=}2)$	$0.4 \cdot \mathcal{L}_{\mathsf{u}}(t{=}2)$	✓	rand	1	400	0.0005	1200	75.06%	82.23%	74.41%	81.48%
$\mathcal{L}_{\mathsf{c}}(\tau{=}1)$	$0.6 \cdot \mathcal{L}_{\mathsf{a}}(\alpha{=}2)$	$0.4 \cdot \mathcal{L}_{\mathsf{u}}(t{=}2)$	✓	rand	1	400	0.0005	1200	70.53%	78.43%	68.88%	75.93%
$\mathcal{L}_{\mathsf{c}}(\tau{=}0.075)$	$0.5 \cdot \mathcal{L}_{\mathsf{a}}(\alpha{=}2)$	$0.5 \cdot \mathcal{L}_{\mathsf{u}}(t{=}2)$	✓	rand	1	400	0.0005	1200	74.45%	81.61%	74.51%	**84.66%**
$\mathcal{L}_{\mathsf{c}}(\tau{=}1)$	$0.5 \cdot \mathcal{L}_{\mathsf{a}}(\alpha{=}2)$	$0.5 \cdot \mathcal{L}_{\mathsf{u}}(t{=}2)$	✓	rand	1	400	0.0005	1200	66.06%	72.97%	63.64%	73.02%
$\mathcal{L}_{\mathsf{c}}(\tau{=}0.075)$	$0.4 \cdot \mathcal{L}_{\mathsf{a}}(\alpha{=}2)$	$0.6 \cdot \mathcal{L}_{\mathsf{u}}(t{=}2)$	✓	rand	1	400	0.0005	1200	73.23%	80.61%	74.32%	82.54%
$\mathcal{L}_{\mathsf{c}}(\tau{=}1)$	$0.4 \cdot \mathcal{L}_{\mathsf{a}}(\alpha{=}2)$	$0.6 \cdot \mathcal{L}_{\mathsf{u}}(t{=}2)$	✓	rand	1	400	0.0005	1200	57.75%	67.55%	57.92%	69.84%
$\mathcal{L}_{\mathsf{c}}(\tau{=}0.075)$	$0.3 \cdot \mathcal{L}_{\mathsf{a}}(\alpha{=}2)$	$0.7 \cdot \mathcal{L}_{\mathsf{u}}(t{=}2)$	✓	rand	1	400	0.0005	1200	72.99%	79.46%	74.88%	77.25%
$\mathcal{L}_{\mathsf{c}}(\tau{=}1)$	$0.3 \cdot \mathcal{L}_{\mathsf{a}}(\alpha{=}2)$	$0.7 \cdot \mathcal{L}_{\mathsf{u}}(t{=}2)$	✓	rand	1	400	0.0005	1200	56.96%	64.31%	55.30%	65.34%
$\mathcal{L}_{\mathsf{c}}(\tau{=}0.075)$	$0.2 \cdot \mathcal{L}_{\mathsf{a}}(\alpha{=}2)$	$0.8 \cdot \mathcal{L}_{\mathsf{u}}(t{=}2)$	✓	rand	1	400	0.0005	1200	71.94%	79.43%	70.95%	78.04%
$\mathcal{L}_{\mathsf{c}}(\tau{=}1)$	$0.2 \cdot \mathcal{L}_{\mathsf{a}}(\alpha{=}2)$	$0.8 \cdot \mathcal{L}_{\mathsf{u}}(t{=}2)$	✓	rand	1	400	0.0005	1200	54.90%	64.22%	55.11%	63.76%
$\mathcal{L}_{\mathsf{c}}(\tau{=}0.075)$	$0.1 \cdot \mathcal{L}_{\mathsf{a}}(\alpha{=}2)$	$0.9 \cdot \mathcal{L}_{\mathsf{u}}(t{=}2)$	✓	rand	1	400	0.0005	1200	70.53%	78.25%	69.82%	78.57%
$\mathcal{L}_{\mathsf{c}}(\tau{=}1)$	$0.1 \cdot \mathcal{L}_{\mathsf{a}}(\alpha{=}2)$	$0.9 \cdot \mathcal{L}_{\mathsf{u}}(t{=}2)$	✓	rand	1	400	0.0005	1200	55.56%	64.90%	53.98%	65.08%
$\mathcal{L}_{\mathsf{c}}(\tau{=}0.075)$	—	$\mathcal{L}_{\mathsf{u}}(t{=}2)$	✓	rand	1	400	0.0005	1200	70.13%	77.66%	70.67%	77.25%
$\mathcal{L}_{\mathsf{c}}(\tau{=}1)$	—	$\mathcal{L}_{\mathsf{u}}(t{=}2)$	✓	rand	1	400	0.0005	1200	54.76%	63.45%	53.98%	64.81%

—	$\mathcal{L}_{\mathsf{a}}(\alpha{=}2)$	—	✓	rand	1	400	0.0005	1200	49.85%	63.81%	50.05%	63.49%
—	$\mathcal{L}_{\mathsf{a}}(\alpha{=}2)$	—	✓	rand	1	400	0.0005	1200	50.02%	63.81%	49.30%	63.49%
—	$\mathcal{L}_{\mathsf{a}}(\alpha{=}2)$	—	✓	rand	1	400	0.0005	1200	50.04%	63.81%	49.95%	63.49%
—	$0.9091 \cdot \mathcal{L}_{\mathsf{a}}(\alpha{=}2)$	$0.0909 \cdot \mathcal{L}_{\mathsf{u}}(t{=}2)$	✓	rand	1	400	0.0005	1200	49.67%	63.81%	49.86%	63.49%
—	$0.9 \cdot \mathcal{L}_{\mathsf{a}}(\alpha{=}2)$	$0.1 \cdot \mathcal{L}_{\mathsf{u}}(t{=}2)$	✓	rand	1	400	0.0005	1200	49.71%	63.81%	49.77%	63.49%
—	$0.9 \cdot \mathcal{L}_{\mathsf{a}}(\alpha{=}2)$	$0.1 \cdot \mathcal{L}_{\mathsf{u}}(t{=}5)$	✓	rand	1	400	0.0005	1200	73.42%	81.23%	73.76%	80.95%
—	$0.9 \cdot \mathcal{L}_{\mathsf{a}}(\alpha{=}2)$	$0.1 \cdot \mathcal{L}_{\mathsf{u}}(t{=}7)$	✓	rand	1	400	0.0005	1200	70.59%	78.57%	71.60%	77.51%
—	$0.8889 \cdot \mathcal{L}_{\mathsf{a}}(\alpha{=}2)$	$0.1111 \cdot \mathcal{L}_{\mathsf{u}}(t{=}2)$	✓	rand	1	400	0.0005	1200	50.14%	63.81%	49.86%	63.49%
—	$0.875 \cdot \mathcal{L}_{\mathsf{a}}(\alpha{=}2)$	$0.125 \cdot \mathcal{L}_{\mathsf{u}}(t{=}2)$	✓	rand	1	400	0.0005	1200	50.33%	63.98%	49.86%	63.49%
—	$0.875 \cdot \mathcal{L}_{\mathsf{a}}(\alpha{=}2)$	$0.125 \cdot \mathcal{L}_{\mathsf{u}}(t{=}7)$	✓	rand	1	400	0.0005	1200	64.70%	72.71%	64.10%	71.69%
—	$0.8571 \cdot \mathcal{L}_{\mathsf{a}}(\alpha{=}2)$	$0.1429 \cdot \mathcal{L}_{\mathsf{u}}(t{=}2)$	✓	rand	1	400	0.0005	1200	59.80%	66.52%	59.51%	67.72%
—	$0.8333 \cdot \mathcal{L}_{\mathsf{a}}(\alpha{=}1)$	$0.1667 \cdot \mathcal{L}_{\mathsf{u}}(t{=}2)$	✓	rand	1	400	0.0005	1200	68.42%	76.07%	68.60%	75.13%
—	$0.8333 \cdot \mathcal{L}_{\mathsf{a}}(\alpha{=}2)$	$0.1667 \cdot \mathcal{L}_{\mathsf{u}}(t{=}2)$	✓	rand	1	400	0.0005	1200	66.69%	73.09%	67.95%	71.69%
—	$0.833 \cdot \mathcal{L}_{\mathsf{a}}(\alpha{=}2)$	$0.167 \cdot \mathcal{L}_{\mathsf{u}}(t{=}5)$	✓	rand	1	400	0.0005	1200	54.35%	64.49%	56.33%	63.49%
—	$0.8298 \cdot \mathcal{L}_{\mathsf{a}}(\alpha{=}1)$	$0.1702 \cdot \mathcal{L}_{\mathsf{u}}(t{=}2)$	✓	rand	1	400	0.0005	1200	67.38%	74.68%	67.29%	73.81%
—	$0.8298 \cdot \mathcal{L}_{\mathsf{a}}(\alpha{=}2)$	$0.1702 \cdot \mathcal{L}_{\mathsf{u}}(t{=}2)$	✓	rand	1	400	0.0005	1200	66.24%	73.33%	64.76%	77.25%
—	$0.8261 \cdot \mathcal{L}_{\mathsf{a}}(\alpha{=}1)$	$0.1739 \cdot \mathcal{L}_{\mathsf{u}}(t{=}2)$	✓	rand	1	400	0.0005	1200	65.91%	75.27%	66.82%	74.07%
—	$0.8261 \cdot \mathcal{L}_{\mathsf{a}}(\alpha{=}2)$	$0.1739 \cdot \mathcal{L}_{\mathsf{u}}(t{=}2)$	✓	rand	1	400	0.0005	1200	67.65%	73.56%	67.95%	72.49%
—	$0.8222 \cdot \mathcal{L}_{\mathsf{a}}(\alpha{=}1)$	$0.1778 \cdot \mathcal{L}_{\mathsf{u}}(t{=}2)$	✓	rand	1	400	0.0005	1200	66.73%	75.13%	67.85%	73.54%
—	$0.8222 \cdot \mathcal{L}_{\mathsf{a}}(\alpha{=}2)$	$0.1778 \cdot \mathcal{L}_{\mathsf{u}}(t{=}2)$	✓	rand	1	400	0.0005	1200	69.33%	73.42%	69.54%	74.60%
—	$0.8182 \cdot \mathcal{L}_{\mathsf{a}}(\alpha{=}1)$	$0.1818 \cdot \mathcal{L}_{\mathsf{u}}(t{=}2)$	✓	rand	1	400	0.0005	1200	66.17%	74.36%	65.70%	74.34%
—	$0.8182 \cdot \mathcal{L}_{\mathsf{a}}(\alpha{=}2)$	$0.1818 \cdot \mathcal{L}_{\mathsf{u}}(t{=}2)$	✓	rand	1	400	0.0005	1200	69.61%	75.51%	70.10%	75.40%
—	$0.814 \cdot \mathcal{L}_{\mathsf{a}}(\alpha{=}1)$	$0.186 \cdot \mathcal{L}_{\mathsf{u}}(t{=}2)$	✓	rand	1	400	0.0005	1200	63.43%	72.74%	63.82%	73.28%
—	$0.814 \cdot \mathcal{L}_{\mathsf{a}}(\alpha{=}2)$	$0.186 \cdot \mathcal{L}_{\mathsf{u}}(t{=}2)$	✓	rand	1	400	0.0005	1200	71.32%	77.72%	70.85%	77.25%
—	$0.8095 \cdot \mathcal{L}_{\mathsf{a}}(\alpha{=}1)$	$0.1905 \cdot \mathcal{L}_{\mathsf{u}}(t{=}2)$	✓	rand	1	400	0.0005	1200	63.47%	72.33%	63.82%	73.28%
—	$0.8095 \cdot \mathcal{L}_{\mathsf{a}}(\alpha{=}2)$	$0.1905 \cdot \mathcal{L}_{\mathsf{u}}(t{=}2)$	✓	rand	1	400	0.0005	1200	71.33%	77.19%	71.13%	75.40%

—	$0.8049 \cdot \mathcal{L}_{\mathsf{a}}(\alpha{=}1)$	$0.1951 \cdot \mathcal{L}_{\mathsf{u}}(t{=}2)$	✓	rand	1	400	0.0005	1200	61.17%	70.79%	61.01%	73.54%
—	$0.8049 \cdot \mathcal{L}_{\mathsf{a}}(\alpha{=}2)$	$0.1951 \cdot \mathcal{L}_{\mathsf{u}}(t{=}2)$	✓	rand	1	400	0.0005	1200	72.04%	77.93%	73.38%	77.51%
—	$0.8 \cdot \mathcal{L}_{\mathsf{a}}(\alpha{=}1)$	$0.2 \cdot \mathcal{L}_{\mathsf{u}}(t{=}2)$	✓	rand	1	400	0.0005	1200	60.91%	69.41%	59.14%	70.37%
—	$0.8 \cdot \mathcal{L}_{\mathsf{a}}(\alpha{=}2)$	$0.2 \cdot \mathcal{L}_{\mathsf{u}}(t{=}2)$	✓	rand	1	400	0.0005	1200	72.60%	80.34%	73.48%	79.89%
—	$0.8 \cdot \mathcal{L}_{\mathsf{a}}(\alpha{=}2)$	$0.2 \cdot \mathcal{L}_{\mathsf{u}}(t{=}5)$	✓	rand	1	400	0.0005	1200	54.82%	63.19%	51.64%	64.02%
—	$0.8 \cdot \mathcal{L}_{\mathsf{a}}(\alpha{=}2)$	$0.2 \cdot \mathcal{L}_{\mathsf{u}}(t{=}7)$	✓	rand	1	400	0.0005	1200	53.67%	63.90%	57.92%	65.61%
—	$0.75 \cdot \mathcal{L}_{\mathsf{a}}(\alpha{=}1)$	$0.25 \cdot \mathcal{L}_{\mathsf{u}}(t{=}2)$	✓	rand	1	400	0.0005	1200	55.29%	63.63%	55.11%	70.11%
—	$0.75 \cdot \mathcal{L}_{\mathsf{a}}(\alpha{=}2)$	$0.25 \cdot \mathcal{L}_{\mathsf{u}}(t{=}2)$	✓	rand	1	400	0.0005	1200	72.60%	80.72%	71.88%	79.63%
—	$0.7 \cdot \mathcal{L}_{\mathsf{a}}(\alpha{=}1)$	$0.3 \cdot \mathcal{L}_{\mathsf{u}}(t{=}2)$	✓	rand	1	400	0.0005	1200	54.24%	63.87%	55.01%	68.52%
—	$0.7 \cdot \mathcal{L}_{\mathsf{a}}(\alpha{=}2)$	$0.3 \cdot \mathcal{L}_{\mathsf{u}}(t{=}2)$	✓	rand	1	400	0.0005	1200	71.80%	78.93%	73.76%	77.78%
—	$0.7 \cdot \mathcal{L}_{\mathsf{a}}(\alpha{=}2)$	$0.3 \cdot \mathcal{L}_{\mathsf{u}}(t{=}5)$	✓	rand	1	400	0.0005	1200	55.34%	62.07%	53.51%	63.23%
—	$0.7 \cdot \mathcal{L}_{\mathsf{a}}(\alpha{=}2)$	$0.3 \cdot \mathcal{L}_{\mathsf{u}}(t{=}7)$	✓	rand	1	400	0.0005	1200	54.22%	64.28%	55.20%	60.85%
—	$0.6667 \cdot \mathcal{L}_{\mathsf{a}}(\alpha{=}1)$	$0.3333 \cdot \mathcal{L}_{\mathsf{u}}(t{=}2)$	✓	rand	1	400	0.0005	1200	55.42%	63.25%	54.83%	68.78%
—	$0.6667 \cdot \mathcal{L}_{\mathsf{a}}(\alpha{=}2)$	$0.3333 \cdot \mathcal{L}_{\mathsf{u}}(t{=}2)$	✓	rand	1	400	0.0005	1200	68.49%	76.48%	67.20%	74.60%
—	$0.6 \cdot \mathcal{L}_{\mathsf{a}}(\alpha{=}1)$	$0.4 \cdot \mathcal{L}_{\mathsf{u}}(t{=}2)$	✓	rand	1	400	0.0005	1200	54.86%	63.63%	55.30%	67.46%
—	$0.6 \cdot \mathcal{L}_{\mathsf{a}}(\alpha{=}2)$	$0.4 \cdot \mathcal{L}_{\mathsf{u}}(t{=}2)$	✓	rand	1	400	0.0005	1200	60.60%	69.35%	61.29%	68.25%
—	$0.6 \cdot \mathcal{L}_{\mathsf{a}}(\alpha{=}2)$	$0.4 \cdot \mathcal{L}_{\mathsf{u}}(t{=}5)$	✓	rand	1	400	0.0005	1200	54.64%	63.96%	56.61%	62.43%
—	$0.6 \cdot \mathcal{L}_{\mathsf{a}}(\alpha{=}2)$	$0.4 \cdot \mathcal{L}_{\mathsf{u}}(t{=}7)$	✓	rand	1	400	0.0005	1200	55.28%	63.63%	55.20%	63.76%
—	$0.5 \cdot \mathcal{L}_{\mathsf{a}}(\alpha{=}1)$	$0.5 \cdot \mathcal{L}_{\mathsf{u}}(t{=}2)$	✓	rand	1	400	0.0005	1200	53.61%	64.40%	52.86%	66.14%
—	$0.5 \cdot \mathcal{L}_{\mathsf{a}}(\alpha{=}2)$	$0.5 \cdot \mathcal{L}_{\mathsf{u}}(t{=}2)$	✓	rand	1	400	0.0005	1200	55.42%	64.75%	55.76%	66.40%
—	$0.5 \cdot \mathcal{L}_{\mathsf{a}}(\alpha{=}2)$	$0.5 \cdot \mathcal{L}_{\mathsf{u}}(t{=}5)$	✓	rand	1	400	0.0005	1200	55.49%	63.16%	55.39%	64.29%
—	$0.5 \cdot \mathcal{L}_{\mathsf{a}}(\alpha{=}2)$	$0.5 \cdot \mathcal{L}_{\mathsf{u}}(t{=}7)$	✓	rand	1	400	0.0005	1200	56.06%	63.90%	57.73%	64.81%
—	$0.4 \cdot \mathcal{L}_{\mathsf{a}}(\alpha{=}1)$	$0.6 \cdot \mathcal{L}_{\mathsf{u}}(t{=}2)$	✓	rand	1	400	0.0005	1200	54.27%	64.37%	54.45%	63.49%
—	$0.4 \cdot \mathcal{L}_{\mathsf{a}}(\alpha{=}2)$	$0.6 \cdot \mathcal{L}_{\mathsf{u}}(t{=}2)$	✓	rand	1	400	0.0005	1200	55.22%	63.69%	57.73%	67.72%
—	$0.4 \cdot \mathcal{L}_{\mathsf{a}}(\alpha{=}2)$	$0.6 \cdot \mathcal{L}_{\mathsf{u}}(t{=}5)$	✓	rand	1	400	0.0005	1200	53.26%	63.57%	53.70%	65.87%
—	$0.4 \cdot \mathcal{L}_{\mathsf{a}}(\alpha{=}2)$	$0.6 \cdot \mathcal{L}_{\mathsf{u}}(t{=}7)$	✓	rand	1	400	0.0005	1200	54.53%	63.66%	53.14%	64.55%

—	$0.3 \cdot \mathcal{L}_{\mathsf{a}}(\alpha{=}1)$	$0.7 \cdot \mathcal{L}_{\mathsf{u}}(t{=}2)$	✓	rand	1	400	0.0005	1200	54.75%	63.43%	53.42%	64.02%
—	$0.3 \cdot \mathcal{L}_{\mathsf{a}}(\alpha{=}2)$	$0.7 \cdot \mathcal{L}_{\mathsf{u}}(t{=}2)$	✓	rand	1	400	0.0005	1200	53.64%	63.84%	54.64%	62.70%
—	$0.3 \cdot \mathcal{L}_{\mathsf{a}}(\alpha{=}2)$	$0.7 \cdot \mathcal{L}_{\mathsf{u}}(t{=}5)$	✓	rand	1	400	0.0005	1200	55.13%	63.81%	55.39%	64.81%
—	$0.3 \cdot \mathcal{L}_{\mathsf{a}}(\alpha{=}2)$	$0.7 \cdot \mathcal{L}_{\mathsf{u}}(t{=}7)$	✓	rand	1	400	0.0005	1200	56.56%	63.87%	56.04%	66.67%
—	$0.2 \cdot \mathcal{L}_{\mathsf{a}}(\alpha{=}1)$	$0.8 \cdot \mathcal{L}_{\mathsf{u}}(t{=}2)$	✓	rand	1	400	0.0005	1200	53.86%	64.04%	54.83%	69.31%
—	$0.2 \cdot \mathcal{L}_{\mathsf{a}}(\alpha{=}2)$	$0.8 \cdot \mathcal{L}_{\mathsf{u}}(t{=}2)$	✓	rand	1	400	0.0005	1200	53.73%	65.34%	53.98%	64.55%
—	$0.2 \cdot \mathcal{L}_{\mathsf{a}}(\alpha{=}2)$	$0.8 \cdot \mathcal{L}_{\mathsf{u}}(t{=}5)$	✓	rand	1	400	0.0005	1200	54.76%	64.37%	55.76%	65.87%
—	$0.2 \cdot \mathcal{L}_{\mathsf{a}}(\alpha{=}2)$	$0.8 \cdot \mathcal{L}_{\mathsf{u}}(t{=}7)$	✓	rand	1	400	0.0005	1200	54.86%	63.51%	53.89%	66.40%
—	$0.1 \cdot \mathcal{L}_{\mathsf{a}}(\alpha{=}1)$	$0.9 \cdot \mathcal{L}_{\mathsf{u}}(t{=}2)$	✓	rand	1	400	0.0005	1200	54.60%	65.72%	56.42%	68.52%
—	$0.1 \cdot \mathcal{L}_{\mathsf{a}}(\alpha{=}2)$	$0.9 \cdot \mathcal{L}_{\mathsf{u}}(t{=}2)$	✓	rand	1	400	0.0005	1200	54.60%	64.90%	57.26%	60.85%
—	$0.1 \cdot \mathcal{L}_{\mathsf{a}}(\alpha{=}2)$	$0.9 \cdot \mathcal{L}_{\mathsf{u}}(t{=}5)$	✓	rand	1	400	0.0005	1200	56.23%	63.66%	55.48%	66.14%
—	$0.1 \cdot \mathcal{L}_{\mathsf{a}}(\alpha{=}2)$	$0.9 \cdot \mathcal{L}_{\mathsf{u}}(t{=}7)$	✓	rand	1	400	0.0005	1200	54.65%	65.22%	55.95%	64.02%
—	—	$\mathcal{L}_{\mathsf{u}}(t{=}2)$	✓	rand	1	400	0.0005	1200	55.02%	62.69%	57.36%	67.72%
—	—	$\mathcal{L}_{\mathsf{u}}(t{=}5)$	✓	rand	1	400	0.0005	1200	54.95%	64.04%	56.04%	64.02%
—	—	$\mathcal{L}_{\mathsf{u}}(t{=}7)$	✓	rand	1	400	0.0005	1200	54.55%	63.48%	56.33%	63.49%
—	$\mathcal{L}_{\mathsf{a}}(\alpha{=}1)$	—	✓	rand	1	400	0.0005	1200	NaN occurred			
—	$0.9091 \cdot \mathcal{L}_{\mathsf{a}}(\alpha{=}1)$	$0.0909 \cdot \mathcal{L}_{\mathsf{u}}(t{=}2)$	✓	rand	1	400	0.0005	1200	NaN occurred			
—	$0.9 \cdot \mathcal{L}_{\mathsf{a}}(\alpha{=}1)$	$0.1 \cdot \mathcal{L}_{\mathsf{u}}(t{=}2)$	✓	rand	1	400	0.0005	1200	NaN occurred			
—	$0.8889 \cdot \mathcal{L}_{\mathsf{a}}(\alpha{=}1)$	$0.1111 \cdot \mathcal{L}_{\mathsf{u}}(t{=}2)$	✓	rand	1	400	0.0005	1200	NaN occurred			
—	$0.875 \cdot \mathcal{L}_{\mathsf{a}}(\alpha{=}1)$	$0.125 \cdot \mathcal{L}_{\mathsf{u}}(t{=}2)$	✓	rand	1	400	0.0005	1200	NaN occurred			
—	$0.8571 \cdot \mathcal{L}_{\mathsf{a}}(\alpha{=}1)$	$0.1429 \cdot \mathcal{L}_{\mathsf{u}}(t{=}2)$	✓	rand	1	400	0.0005	1200	NaN occurred			

Appendix B

Proofs, Details, and Additional Discussions for Chapter 3

B.1 Discussions for Section 3.2: Preliminaries on Quasimetrics and Poisson Processes

B.1.1 Quasimetric Spaces

Definition 3.2.1 (Quasimetric Space)**.** A *quasimetric space* is a pair $(\mathcal{X}, d)$, where $\mathcal{X}$ is a set of points and $d\colon \mathcal{X} \times \mathcal{X} \to [0, \infty]$ is the quasimetric, satisfying the following conditions:

$$\forall x, y \in \mathcal{X}, \qquad x = y \iff d(x, y) = 0, \quad \text{(Identity of Indiscernibles)}$$
$$\forall x, y, z \in \mathcal{X}, \qquad d(x, y) + d(y, z) \geq d(x, z). \qquad \text{(Triangle Inequality)}$$

Definition B.1.1 (Quasipseudometric Space)**.** As a further generalization, we say $(\mathcal{X}, d)$ is a *quasipseudometric space* if the *Identity of Indiscernibles* requirement is

only satisfied in one direction:

$$\forall x, y \in \mathcal{X}, \qquad x = y \implies d(x, y) = 0, \quad \text{(Identity of Indiscernibles)}$$
$$\forall x, y, z \in \mathcal{X}, \qquad d(x, y) + d(y, z) \geq d(x, z). \qquad \text{(Triangle Inequality)}$$

Examples of Quasimetric Spaces

Proposition B.1.2 (Expected Hitting Time of a Markov Chain). Let random variables $(X_t)_t$ be a Markov Chain with support $\mathcal{X}$. Then $(\mathcal{X}, d_{\mathsf{hitting}})$ is a quasimetric space, where

$$d_{\mathsf{hitting}}(s, t) \triangleq \mathbb{E}\left[\text{time to hit } t \mid \text{start from } s\right], \tag{B.1}$$

where we define the hitting time of s starting from s to be 0.

Proof of Proposition B.1.2. Obviously d_{hitting} is non-negative. We then verify the following quasimetric space properties:

- **Identity of Indiscernibles.** By definition, we have, $\forall x, y \in \mathcal{X}$, $x \neq y$,

$$d_{\mathsf{hitting}}(x, x) = 0 \tag{B.2}$$
$$d_{\mathsf{hitting}}(x, y) \geq 1. \tag{B.3}$$

- **Triangle Inequality.** For any $x, y, z \in \mathcal{X}$, we have

$$d_{\mathsf{hitting}}(x, y) + d_{\mathsf{hitting}}(y, z) = \mathbb{E}\left[\text{time to hit } y \text{ then hit } z \mid \text{start from } x\right] \tag{B.4}$$
$$\geq \mathbb{E}\left[\text{time to hit } z \mid \text{start from } x\right] \tag{B.5}$$
$$= d_{\mathsf{hitting}}(x, z). \tag{B.6}$$

Hence, $(\mathcal{X}, d_{\mathsf{hitting}})$ is a quasimetric space. □

Proposition B.1.3 (Conditional Shannon Entropy). Let $\mathcal{X}$ be the set of random variables (of some probability space). Then $(\mathcal{X}, d_H)$ is a quasipseudometric space, where

$$d_H(X, Y) \triangleq H(Y \mid X). \tag{B.7}$$

If for all distinct $(X, Y) \in \mathcal{X} \times \mathcal{X}$, X can not be written as (almost surely) a deterministic function of Y, then $(\mathcal{X}, d_H)$ is a quasimetric space.

Proof of Proposition B.1.3. Obviously d_H is non-negative. We then verify the following quasipseudometric space properties:

- **Identity of Indiscernibles.** By definition, we have, $\forall X, Y \in \mathcal{X}$,

$$d_H(X, X) = H(X \mid X) = 0 \tag{B.8}$$
$$d_H(Y, X) = H(Y \mid X) \geq 0, \tag{B.9}$$

  where $\leq$ is $=$ iff Y is a (almost surely) deterministic function of X.

- **Triangle Inequality.** For any $X, Y, Z \in \mathcal{X}$, we have

$$\begin{aligned} d_H(X, Y) + d_H(Y, Z) &= H(Y \mid X) + H(Z \mid Y) && \text{(B.10)} \\ &\geq H(Y \mid X) + H(Z \mid XY) && \text{(B.11)} \\ &= H(YZ \mid X) && \text{(B.12)} \\ &\geq H(Z \mid X) && \text{(B.13)} \\ &= d_H(X, Z). && \text{(B.14)} \end{aligned}$$

Hence, $(\mathcal{X}, d_H)$ is a quasipseudometric space, and a quasimetric space when the last condition is satisfied. □

Conditional Kolmogorov Complexity. From algorithmic information theory, the conditional Kolmogorov complexity $K(y \mid x)$ also similarly measures "the bits needed to create y given x as input" (Kolmogorov, 1963). It is also almost a quasimetric, but the exact definition affects some constant/log terms that may make the quasimetric constraints non-exact. For instance, when defined with the prefix-free version, conditional Kolmogorov complexity is always strictly positive, even for $K(x \mid x) > 0$ (Li et al., 2008). One may remedy this with a definition using a universal Turing machine (UTM) that simply outputs the input on empty program. But to make

triangle inequality work, one needs to reason about how the input and output parts work on the tape(s) of the UTM. Nonetheless, regardless of the definition details, conditional Kolmogorov complexity do satisfy a triangle inequality up to log terms (Grunwald and Vitányi, 2004). So intuitively, it behaves roughly like a quasimetric defined on the space of binary strings.

Optimal Goal-Reaching Plan Costs in Markov Decision Processes (MDPs) We define MDPs in the standard manner: $\mathcal{M} = (\mathcal{S}, \mathcal{A}, \mathcal{R}, \mathcal{P}, \gamma)$ (Puterman, 1994), where $\mathcal{S}$ is the state space, $\mathcal{A}$ is the action space, $\mathcal{R}\colon \mathcal{S} \times \mathcal{A} \to \mathbb{R}$ is the reward function, $\mathcal{P}\colon \mathcal{S} \times \mathcal{A} \to \Delta(\mathcal{S})$ is the transition function (where $\Delta(\mathcal{S})$ is the set of all distributions over $\mathcal{S}$), and $\gamma \in (0, 1)$ is the discount factor.

We define Π as the collection of all stationary policies $\pi\colon \mathcal{S} \to \Delta(\mathcal{A})$ on $\mathcal{M}$. For a particular policy $\pi \in \Pi$, it induces random *trajectories*:

- *Trajectory* starting from state $s \in \mathcal{S}$ is the random variable

$$\xi_\pi(s) = (s_1, a_1, r_1, s_2, a_2, r_2, \dots), \tag{B.15}$$

  distributed as

$$s_1 = s \tag{B.16}$$

$$a_i \sim \pi(s_i), \qquad \forall i \geq 1 \tag{B.17}$$

$$s_{i+1} \sim \mathcal{P}(s_i, a_i), \qquad \forall i \geq 1. \tag{B.18}$$

- *Trajectory* starting from state-action pair $(s, a) \in \mathcal{S} \times \mathcal{A}$ is the random variable

$$\xi_\pi(s, a) = (s_1, a_1, r_1, s_2, a_2, r_2, \dots), \tag{B.19}$$

distributed as

$$s_1 = s \tag{B.20}$$

$$a_1 = a \tag{B.21}$$

$$a_i \sim \pi(s_i), \qquad \forall i \geq 2 \tag{B.22}$$

$$s_{i+1} \sim \mathcal{P}(s_i, a_i), \qquad \forall i \geq 1. \tag{B.23}$$

Proposition B.1.4 (Optimal Goal-Reaching Plan Costs in MDPs). Consider an MDP $\mathcal{M} = (\mathcal{S}, \mathcal{A}, \mathcal{R}, \mathcal{P}, \gamma)$. WLOG, assume that $\mathcal{R}\colon \mathcal{S} \times \mathcal{A} \to (-\infty, 0]$ has only non-positive rewards (*i.e.*, negated costs). Let $\mathcal{X} = \mathcal{S} \cup (\mathcal{S} \times \mathcal{A})$. Then $(\mathcal{X}, d_{\mathsf{sum}})$ and $(\mathcal{X}, d_\gamma)$ are quasipseudometric spaces, where

$$\begin{aligned} & d_{\mathsf{sum}}(x, y) \\ &\triangleq \min_{\pi \in \Pi} \mathbb{E}\left[\text{total costs from } x \text{ to } y \text{ under } \pi\right] \qquad \text{(B.24)} \\ &= \begin{cases} \min_{\pi \in \Pi} \mathbb{E}_{(s_1, a_1, r_1, \dots) = \xi_\pi(x)} \Big[-\sum_t r_t \underbrace{\mathbf{1}_{s' \notin \{s_i\}_{i \in [t]}}}_{\text{not reached } s' \text{ yet}} \Big] & \text{if } \underbrace{y = s' \in \mathcal{S}}_{\text{goal is a state}}, \\ \min_{\pi \in \Pi} \mathbb{E}_{(s_1, a_1, r_1, \dots) = \xi_\pi(x)} \Big[-\sum_t r_t \underbrace{\mathbf{1}_{(s', a') \notin \{(s_i, a_i)\}_{i \in [t-1]}}}_{\text{not reached } s' \underline{\text{ and }} \text{performed } a' \text{ yet}} \Big] & \text{if } \underbrace{y = (s', a') \in \mathcal{S} \times \mathcal{A}}_{\text{goal is a state-action pair}}, \end{cases} \qquad \text{(B.25)} \end{aligned}$$

and

$$d_\gamma(x, y) \triangleq \log_\gamma \max_{\pi \in \Pi} \mathbb{E}\left[\gamma^{\text{total costs from } x \text{ to } y \text{ under } \pi}\right] \tag{B.26}$$

is defined similarly.

If the reward function is always *negative*, $(\mathcal{X}, d_{\mathsf{sum}})$ and $(\mathcal{X}, d_\gamma)$ are *quasimetric* spaces.

Proof of Proposition B.1.4. Obviously both d_{sum} and d_γ are non-negative, and satisfy *Identity of Indiscernibles* (for quasipseudometric spaces). For triangle inequality, note that for each y, we can instead consider alternative MDPs:

- If $y = s' \in \mathcal{S}$, modify the original MDP to make s' a sink state, where performing

any action yields 0 reward (*i.e.*, 0 cost);

- If $y = (s', a') \in \mathcal{S} \times \mathcal{A}$, modify the original MDP such that performing action a' in state s' surely transitions to a new sink state, where performing any action yields 0 reward (*i.e.*, 0 cost).

Obviously, both are Markovian. Furthermore, they are Stochastic Shortest Path problems with no negative costs (Guillot and Stauffer, 2020), implying that there are Markovian (*i.e.*, stationary) optimal policies (respectively w.r.t. either minimizing expected total cost or maximizing expected $\gamma^{\text{total cost}}$). Thus optimizing over the set of stationary policies, Π, gives the optimal quantity over all possible policies, including concatenation of two stationary policies. Thus the triangle inequality is satisfied by both.

Hence, $(\mathcal{X}, d_{\mathsf{sum}})$ and $(\mathcal{X}, d_\gamma)$ are quasipseudometric spaces.

Finally, if the reward function is always *negative*, $x \neq y \implies d_{\mathsf{sum}}(x, y) > 0$ and $d_\gamma(x, y) > 0$, so $(\mathcal{X}, d_{\mathsf{sum}})$ and $(\mathcal{X}, d_\gamma)$ are quasimetric spaces. □

Remark B.1.5. We make a couple remarks:

- Any MDP with a bounded reward function can be modified to have only non-positive rewards by subtracting the maximum reward (or larger);
- We have
$$d_{\mathsf{sum}}(s, (s, a)) = d_\gamma(s, (s, a)) = -\mathcal{R}(s, a). \tag{B.27}$$
- When the dynamics is deterministic, $d_{\mathsf{sum}} \equiv d_\gamma$, $\forall \gamma \in (0, 1)$.
- Unless y is reachable from x with probability 1 under some policy, $d_{\mathsf{sum}}(x, y) = \infty$.
- Unless y is *unreachable* from x with probability 1 under *all* policies, $d_{\mathsf{sum}}(x, y) < \infty$. Therefore, it is often favorable to consider d_γ types.
- In certain MDP formulations, the reward is stochastic and/or dependent on the reached next state. The above definitions readily extend to those cases.

- $\gamma^{d_\gamma((s,a),y)}$ is very similar to Q-functions except that Q-function applies discount based on time, and $\gamma^{d_\gamma((s,a),y)}$ applies discount based on costs. We note that a Q-learning-like recurrence can also be found for $\gamma^{d_\gamma((s,a),y)}$.

  If the cost is constant in the sense for some fixed $c < 0$, $\mathcal{R}(s,a) = c$, $\forall (s,a) \in \mathcal{S} \times \mathcal{A}$, then time and cost are equivalent up to a scale. Therefore, $\gamma^{d_\gamma((s,a),y)}$ coincides with the optimal Q-functions for the MDPs described in proof, and $\gamma^{d_\gamma(s,y)}$ coincides with the optimal value functions for the respective MDPs.

Quasimetric Treewidth and Graph Treewidth

Definition 3.2.2 (Treewidth of Quasimetric Spaces (Mémoli et al., 2018))**.** Consider representations of a quasimetric space M as shortest-path distances on a positively-weighted directed graph. *Treewidth* of M is the minimum over all such graphs' treewidths. (Recall that the treewidth of a graph (after replacing directed edges with undirected ones) is a measure of its complexity.)

Graph treewidth is a standard complexity measure of how "similar" a graph is to a tree (Robertson and Seymour, 1984). Informally speaking, if a graph has low treewidth, we can represent it as a tree, preserving all connected paths between vertices, except that in each tree node, we store a small number of vertices (from the original graph) rather than just 1.

Graph treewidth is widely used by the Theoretical Computer Science and Graph Theory communities, since many NP problems are solvable in polynomial time for graphs with bounded treewidth (Bertele and Brioschi, 1973).

B.1.2 Poisson Processes

Definition 3.2.3 (Poisson Process)**.** For nonatomic measure μ on set A, a *Poisson process* on A with *mean measure* μ is a random countable subset $P \subset A$ (*i.e.*, the random events / points) such that

- for any disjoint measurable subsets $A_1, \ldots, A_n$ of A, the random variables $N(A_1), \ldots, N(A_n)$ are independent, where $N(B) \triangleq \#\{P \cap B\}$ is the number

of points of P in B, and

- $N(B)$ has the Poisson distribution with mean $\mu(B)$, denoted as $\text{Pois}(\mu(B))$.

Poisson processes are usually used to model events that randomly happens "with no clear pattern", *e.g.*, visible stars in a patch of the sky, arrival times of Internet packages to a data center. These events may randomly happen all over the sky / time. To an extent, we can say that their characteristic feature is a property of statistical independence (Kingman, 2005).

To understand this, imagine raindrops hitting the windshield of a car. Suppose that we already know that the rain is heavy, knowing the exact pattern of the raindrops hitting on the left side of the windshield tells you little about the hitting pattern on the right side. Then, we may assume that, as long as we look at regions that are disjoint on the windshield, the number of raindrops in each region are independent.

This is the fundamental motivation of Poisson processes. In a sense, from this characterization, Poisson processes are inevitable (see Sec. 1.4 of (Kingman, 2005)).

Poisson Race Probability $\mathbb{P}[\text{Pois}(\mu_1) \leq \text{Pois}(\mu_2)]$ and Its Gradient Formulas

In Fact 3.2.4 we made several remarks on the Poisson race probability, *i.e.*, for *independent* $X \sim \text{Pois}(\mu_1)$, $Y \sim \text{Pois}(\mu_2)$, the quantity $\mathbb{P}[X \leq Y]$. In this section, we detailedly describe how we arrived at those conclusions, and provide the exact gradient formulas for differentiating $\mathbb{P}[X \leq Y]$ w.r.t. μ_1 and μ_2.

From Skellam distribution CDF to Non-Central χ^2 distribution CDF. Distribution of the difference of two independent Poisson random variables is called the *Skellam* distribution (Skellam, 1946), with its parameter being the rate of the two Poissons. That is, $X - Y \sim \text{Skellam}(\mu_1, \mu_2)$. Therefore, $\mathbb{P}[X \leq Y]$ is essentially the cumulative distribution function (CDF) of this Skellam at 0. In Eq. (4) of (Johnson, 1959), a connection is made between the CDF of $\text{Skellam}(\mu_1, \mu_2)$ distribution, and the CDF of a non-central χ^2 distribution (which is a non-centered generalization of χ^2 distribution) with two parameters $k > 0$ degree(s) of freedom and non-centrality

parameter $\lambda \geq 0$): for integer $n > 0$,

$$\mathbb{P}\left[\text{Skellam}(\mu_1, \mu_2) \geq n\right] = \mathbb{P}\big[\text{NonCentral}\chi^2(\underbrace{2n}_{\text{degree(s) of freedom}}, \underbrace{2\mu_2}_{\text{non-centrality parameter}}) < 2\mu_1\big], \tag{B.28}$$

which can be evaluated using statistical computing packages such as `SciPy` (Virtanen et al., 2020) and `CDFLIB` (Burkardt, 2021; Brown et al., 1994).

Marcum-Q-Function and gradient formulas. To differentiate through Equation (B.28), we consider representing the non-central χ^2 CDF as a Marcum-Q-function (Marcum, 1950). One definition of the Marcum-Q-function $Q_M \colon \mathbb{R} \times \mathbb{R} \to \mathbb{R}$ in statistics is

$$Q_M(a, b) \triangleq \int_b^\infty x \left(\frac{x}{a}\right)^{M-1} \exp\left(-\frac{x^2 + a^2}{2}\right) I_{M-1}(ax)\, \mathrm{d}x, \tag{B.29}$$

where I_{M-1} is the modified Bessel function of order $M - 1$. (When M is non-integer, we refer readers to (Brychkov, 2012; Marcum, 1950) for definitions, which are not relevant to the discussion below.) When used in CDF of non-central χ^2, we have

$$\mathbb{P}\left[\text{NonCentral}\chi^2(k, \lambda) < x\right] = 1 - Q_{\frac{k}{2}}(\sqrt{\lambda}, \sqrt{x}). \tag{B.30}$$

Combining with Equation (B.28), and using the symmetry $\text{Skellam}(\mu_1, \mu_2) \overset{d}{=} -\text{Skellam}(\mu_2, \mu_1)$, we have, for integer n,

$$\mathbb{P}\left[X \leq Y + n\right] = \mathbb{P}\left[\text{Skellam}(\mu_1, \mu_2) \leq n\right] \tag{B.31}$$

$$= \begin{cases} \mathbb{P}\left[\text{NonCentral}\chi^2(-2n, 2\mu_1) < 2\mu_2\right] & \text{if } n < 0 \\ 1 - \mathbb{P}\left[\text{NonCentral}\chi^2(2(n+1), 2\mu_2) < 2\mu_1\right] & \text{if } n \geq 0 \end{cases} \tag{B.32}$$

$$= \begin{cases} 1 - Q_{-n}(\sqrt{2\mu_1}, \sqrt{2\mu_2}) & \text{if } n < 0 \\ Q_{n+1}(\sqrt{2\mu_2}, \sqrt{2\mu_1}) & \text{if } n \geq 0. \end{cases} \tag{B.33}$$

Prior work (Brychkov, 2012) provides several derivative formula for the Marcum-Q-Function:

- For $n < 0$, we have

$$\frac{\partial}{\partial \mu_1}\mathbb{P}\left[X \leq Y + n\right] = \frac{\partial}{\partial \mu_1}\left(1 - Q_{-n}(\sqrt{2\mu_1}, \sqrt{2\mu_2})\right) \tag{B.34}$$

$$= Q_{-n}(\sqrt{2\mu_1}, \sqrt{2\mu_2}) - Q_{-n+1}(\sqrt{2\mu_1}, \sqrt{2\mu_2})$$

(Eq. (16) of (Brychkov, 2012))

$$= -\left(\frac{\mu_2}{\mu_1}\right)^{-\frac{n}{2}} e^{-(\mu_1+\mu_2)} I_{-n}(2\sqrt{\mu_1\mu_2})$$

(Eq. (2) of (Brychkov, 2012))

$$= -\left(\frac{\mu_2}{\mu_1}\right)^{-\frac{n}{2}} e^{-(\sqrt{\mu_1}-\sqrt{\mu_2})^2} I^{(e)}_{-n}(2\sqrt{\mu_1\mu_2}), \tag{B.35}$$

where $I^{(e)}_v(x) \triangleq e^{-|x|} I_v(x)$ is the exponentially-scaled version of I_v that computing libraries often provide due to its superior numerical precision (*e.g.*, `SciPy` (Virtanen et al., 2020)),

$$\frac{\partial}{\partial \mu_2}\mathbb{P}\left[X \leq Y + n\right] = \frac{\partial}{\partial \mu_2}\left(1 - Q_{-n}(\sqrt{2\mu_1}, \sqrt{2\mu_2})\right) \tag{B.36}$$

$$= \left(\frac{\mu_2}{\mu_1}\right)^{-\frac{n+1}{2}} e^{-(\mu_1+\mu_2)} I_{-n-1}(2\sqrt{\mu_1\mu_2})$$

(Eq. (19) of (Brychkov, 2012))

$$= \left(\frac{\mu_2}{\mu_1}\right)^{-\frac{n+1}{2}} e^{-(\sqrt{\mu_1}-\sqrt{\mu_2})^2} I^{(e)}_{-n-1}(2\sqrt{\mu_1\mu_2}), \tag{B.37}$$

- For $n \geq 0$, we have

$$\frac{\partial}{\partial \mu_1}\mathbb{P}\left[X \leq Y + n\right] = \frac{\partial}{\partial \mu_1} Q_{n+1}(\sqrt{2\mu_2}, \sqrt{2\mu_1}) \tag{B.38}$$

$$= -\left(\frac{\mu_1}{\mu_2}\right)^{n} e^{-(\mu_1+\mu_2)} I_n(2\sqrt{\mu_1\mu_2})$$

(Eq. (19) of (Brychkov, 2012))

$$= -\left(\frac{\mu_1}{\mu_2}\right)^{n} e^{-(\sqrt{\mu_1}-\sqrt{\mu_2})^2} I^{(e)}_{n}(2\sqrt{\mu_1\mu_2}), \tag{B.39}$$

and,

$$\frac{\partial}{\partial \mu_2}\mathbb{P}\left[X \leq Y + n\right] = \frac{\partial}{\partial \mu_2} Q_{n+1}(\sqrt{2\mu_2}, \sqrt{2\mu_1}) \tag{B.40}$$

$$= Q_{n+2}(\sqrt{2\mu_2}, \sqrt{2\mu_1}) - Q_{n+1}(\sqrt{2\mu_2}, \sqrt{2\mu_1})$$

(Eq. (16) of (Brychkov, 2012))

$$= \left(\frac{\mu_1}{\mu_2}\right)^{\frac{n+1}{2}} e^{-(\mu_1+\mu_2)} I_{n+1}(2\sqrt{\mu_1\mu_2})$$

(Eq. (2) of (Brychkov, 2012))

$$= \left(\frac{\mu_1}{\mu_2}\right)^{\frac{n+1}{2}} e^{-(\sqrt{\mu_1}-\sqrt{\mu_2})^2} I^{(e)}_{n+1}(2\sqrt{\mu_1\mu_2}). \tag{B.41}$$

Setting $n = 0$ gives the proper forward and backward formulas for $\mathbb{P}\left[X \leq Y\right]$.

B.2 Proofs, Discussions and Additional Results for Section 3.4: Theoretical Analysis of Various Learning Algorithms

Assumptions. Recall that we assumed a quasimetric space, which is stronger than a quasipseudometric space (Definition B.1.1), with finite distances. These are rather mild assumptions, since any quasipseudometric with infinities can always be modified to obey these assumptions by (1) adding a small metric (*e.g.*, $d_\epsilon(x, y) \triangleq \epsilon \mathbf{1}_{x \neq y}$ with small $\epsilon > 0$) and (2) capping the infinite distances to a large value higher than any finite distance.

Worst-case analysis. In this work we focus on the *worst-case* scenario, as is common in standard (quasi)metric embedding analyses (Bourgain, 1985; Johnson and Lindenstrauss, 1984; Indyk, 2001; Mémoli et al., 2018). Such results are important because embeddings are often used as heuristics in downstream tasks (*e.g.*, planning) which are sensitive to any error. While our negative result readily extends to the average-case scenario (since the error (distortion or violation) is arbitrary), we leave a

thorough average-case analysis as future work.

Data-independent bounds. We analyze possible *data-independent* bounds for various algorithms. In this sense, the positive result for PQEs (Theorem B.3.4) is really strong, showing good guarantees *regardless data quasimetric*. The negative result (Theorem 3.4.6) is also revealing, indicating that a family of algorithms should probably not be used, unless we know something more about data. *Data-independent* bounds are often of great interest in machine learning (*e.g.*, concepts of VC-dimension (Vapnik and Chervonenkis, 2015) and PAC learning (Valiant, 1984)). An important future work is to explore data-dependent results, possibly via defining a quasimetric complexity metric that is both friendly for machine learning analysis, and connects well with combinatorics measures such as quasimetric treewidth.

Violation and distortion metrics. The optimal violation has value 1. Specifically, it is 1 iff $\hat{d}$ is a quasimetric on $\mathcal{X}$ (assuming *non-negativity*). Distortion (over training set) and violation together quantify how well $\hat{d}$ learns a quasimetric consistent with the training data. A predictor can fit training data well (low distortion), but ignores basic quasimetric constraints on heldout data (high violation). Conversely, a predictor can perfectly obey the training data constraints (low violation), but doesn't actually fit training data well (high distortion). Indeed, (assuming *non-negativity* and *Identity of Indiscernibles*), perfect distortion (value 1) and violation (value 1) imply that $\hat{d}$ is a quasimetric consistent with training data.

Relation with classical in-distribution generalization studies. Classical generalization studies the prediction error over the underlying data distribution, and often involves complexity of the hypothesis class and/or training data (Vapnik and Chervonenkis, 2015; McAllester, 1999). Our focus on quasimetric constraints violation is, in fact, not an orthogonal problem, but potentially a core part of in-distribution generalization for this setting. Here, the underlying distribution is supported on all pairs of $\mathcal{X} \times \mathcal{X}$. Indeed, if a learning algorithm has large distortion, it must attain large prediction error on $S \subset \mathcal{X} \times \mathcal{X}$; if it has large violation, it must violates the

quasimetric constraints and necessarily admits bad prediction error on some pairs (whose true distances obey the quasimetric constraints). Theorem 3.4.3 (proved below) formalizes this idea, where we characterize generalization with the distortion *over all possible pairs in* $\mathcal{X} \times \mathcal{X}$.

B.2.1 Theorem 3.4.3: Distortion and Violation Lower-Bound Generalization Error

Theorem 3.4.3 (Distortion and Violation Lower-Bound Generalization Error). For non-negative $\hat{d}$, $\mathsf{dis}(\hat{d}) \geq \max(\mathsf{dis}_S(\hat{d}), \sqrt{\mathsf{vio}(\hat{d})})$, where $\mathsf{dis}(\hat{d})$ captures generalization over the entire $\mathcal{X}$ space.

Proof

Proof of Theorem 3.4.3. It is obvious that

$$\mathsf{dis}(\hat{d}) \geq \mathsf{dis}_S(\hat{d}). \tag{B.42}$$

Therefore, it remains to show that $\mathsf{dis}(\hat{d}) \geq \sqrt{\mathsf{vio}(\hat{d})}$.

WLOG, say $\mathsf{vio}(\hat{d}) > 1$. Otherwise, the statement is trivially true.

By the definition of violation (see Definition 3.4.2), we have, for some $x, y, z \in \mathcal{X}$, with $\hat{d}(x, z) > 0$,

$$\frac{\hat{d}(x, z)}{\hat{d}(x, y) + \hat{d}(y, z)} = \mathsf{vio}(\hat{d}). \tag{B.43}$$

If $\hat{d}(x, y) + \hat{d}(y, z) = 0$, then we must have one of the following two cases:

- If $d(x, y) > 0$ or $d(y, z) > 0$, the statement is true because $\mathsf{dis}(\hat{d}) = \infty$.
- If $d(x, y) = d(y, z) = 0$, then $d(x, z) = 0$ and the statement is true since $\mathsf{dis}(\hat{d}) \geq \frac{\hat{d}(x,z)}{d(x,z)} = \infty$.

It is sufficient to prove the case that $\hat{d}(x,y) + \hat{d}(y,z) > 0$. We can derive

$$\hat{d}(x,z) = \mathsf{vio}(\hat{d}) \left(\hat{d}(x,y) + \hat{d}(y,z) \right) \tag{B.44}$$

$$\geq \frac{\mathsf{vio}(\hat{d})}{\mathsf{dis}(\hat{d})} \left(d(x,y) + d(y,z) \right) \tag{B.45}$$

$$\geq \frac{\mathsf{vio}(\hat{d})}{\mathsf{dis}(\hat{d})} \, d(x,z). \tag{B.46}$$

If $d(x,z) = 0$, then $\mathsf{dis}(\hat{d}) = \infty$ and the statement is trivially true.

If $d(x,z) > 0$, above Equation (B.46) implies

$$\mathsf{dis}(\hat{d}) \geq \frac{\hat{d}(x,z)}{d(x,z)} \geq \frac{\mathsf{vio}(\hat{d})}{\mathsf{dis}(\hat{d})} \implies \mathsf{dis}(\hat{d}) \geq \sqrt{\mathsf{vio}(\hat{d})}. \tag{B.47}$$

Combining Equations (B.42) and (B.47) gives the desired statement.

□

B.2.2 Lemma 3.4.5: Examples of OrthEquiv Algorithms

Lemma 3.4.5 (Examples of OrthEquiv Algorithms). k-nearest-neighbor with Euclidean distance, dot-product kernel ridge regression (including min-norm linear regression and MLP trained with squared loss in NTK regime) are OrthEquiv.

Recall the definition of Equivariant Learning Transforms.

Definition 3.4.4 (Equivariant Learning Algorithms)**.** Given training set $\mathcal{D} = \{(z_i, y_i)\}_i$, where $z_i \in \mathcal{Z}$ are inputs and $y_i \in \mathcal{Y}$ are targets, a learning algorithm Alg produces a function $\mathsf{Alg}(\mathcal{D})\colon \mathcal{Z} \to Y$ such that $\mathsf{Alg}(\mathcal{D})(z')$ is the function's prediction on sample z'. Consider $\mathcal{T}$ a set of transformations $\mathcal{Z} \to \mathcal{Z}$. Alg is equivariant to $\mathcal{T}$ iff for all transform $T \in \mathcal{T}$, training set $\mathcal{D}$, $\mathsf{Alg}(\mathcal{D}) = \mathsf{Alg}(T\mathcal{D}) \circ T$, where $T\mathcal{D} = \{(Tz, y)\colon (z,y) \in \mathcal{D}\}$ is the training set with transformed inputs.

Proof

Proof of Lemma 3.4.5. We consider the three algorithms individually:

- **k-nearest neighbor with Euclidean distance.**

  It is evident that if a learning algorithm only depend on pairwise dot products (or distances), it is equivariant to orthogonal transforms, which preserve dot products (and distances). k-nearest-neighbor with Euclidean distance only depends on pairwise distances, which can be written in terms of dot products:

$$\|x - y\|_2^2 = x^\mathsf{T} x + y^\mathsf{T} y - 2x^\mathsf{T} y. \tag{B.48}$$

  Therefore, it is equivariant to orthogonal transforms.

- **Dot-product kernel ridge regression.**

  Since orthogonal transforms preservers dot-products, dot-product kernel ridge regression is equivariant to them.

  As two specific examples, let's look at linear regression and NTK for fully-connected MLPs.

  - **Min-norm least-squares linear regression.**

    Recall that the solution to min-norm least-squares linear regression $Ax = b$ is given by Moore–Penrose pseudo-inverse $x = A^+ b$. For any matrix $A \in \mathbb{R}^{m \times n}$ with SVD $U\Sigma V^* = A$, and $T \in O(n)$ (where $O(n)$ is the orthogonal group in dimension n), we have

$$(AT^\mathsf{T})^+ = (U\Sigma V^* T^\mathsf{T})^+ = TV\Sigma^+ U^* = TA^+, \tag{B.49}$$

    where we used $T^* = T^\mathsf{T}$ for $T \in O(n)$. The solution for the transformed data AT^T and b is thus

$$(AT^\mathsf{T})^+ b = TA^+ b. \tag{B.50}$$

Thus, for any new data point $\tilde{x} \in \mathbb{R}^n$ and its transformed version $T\tilde{x} \in \mathbb{R}^n$,

$$\underbrace{(T\tilde{x})^\mathsf{T}(AT^\mathsf{T})^+ b}_{\text{transformed problem prediction}} = \tilde{x}^\mathsf{T} T^\mathsf{T} T A^+ = \underbrace{\tilde{x}A^+}_{\text{original problem prediction}}. \tag{B.51}$$

Hence, min-norm least-squares linear regression is equivariant to orthogonal transforms.

– **MLP trained with squared loss in NTK regime.**

We first recall the NTK recursive formula from (Jacot et al., 2018).

Denote the NTK for a MLP with L layers with the scalar kernel $\Theta^{(L)} \colon \mathbb{R}^d \times \mathbb{R}^d \to \mathbb{R}$. Let $\beta > 0$ be the (fixed) parameter for the bias strength in the network model, and σ be the activation function. Given $x, z \in \mathbb{R}^d$, it can be recursively defined as following. For $h \in [L]$,

$$\Theta^{(h)}(x,z) \triangleq \Theta^{(h-1)}(x,z)\dot{\Sigma}^{(h)}(x,z) + \Sigma^{(h)}(x,z), \tag{B.52}$$

where

$$\Sigma^{(0)}(x,z) = \frac{1}{d}x^\mathsf{T} z + \beta^2, \tag{B.53}$$

$$\Lambda^{(h-1)}(x,z) = \begin{pmatrix} \Sigma^{(h-1)}(x,x) & \Sigma^{(h-1)}(x,z) \\ \Sigma^{(h-1)}(z,x) & \Sigma^{(h-1)}(z,z) \end{pmatrix}, \tag{B.54}$$

$$\Sigma^{(h)}(x,z) = c \cdot \mathbb{E}_{(u,v)\sim\mathcal{N}(0,\Lambda^{(h-1)})}\left[\sigma(u)\sigma(v)\right] + \beta^2, \tag{B.55}$$

$$\dot{\Sigma}^{(h)}(x,z) = c \cdot \mathbb{E}_{(u,v)\sim\mathcal{N}(0,\Lambda^{(h-1)})}\left[\dot{\sigma}(u)\dot{\sigma}(v)\right], \tag{B.56}$$

for some constant c.

It is evident from the recursive formula, that $\Theta^{(h)}(x,z)$ only depends on $x^\mathsf{T}x$, $z^\mathsf{T}z$ and $x^\mathsf{T}z$. Therefore, the NTK is *invariant* to orthogonal transforms.

Furthermore, training an MLP in NTK regime is the same as kernel regression with the NTK (Jacot et al., 2018), which has a unique solution only depending on the kernel matrix on training set, denoted as $K_{\mathsf{train}} \in \mathbb{R}^{n\times n}$,

where n is the training set size. Specifically, for training data $\{(x_i, y_i)\}_{i\in[n]}$, the solution $f^*_{\mathsf{NTK}}\colon \mathbb{R} \to \mathbb{R}$ can be written as

$$f^*_{\mathsf{NTK}}(x) = \begin{pmatrix} \Theta^{(L)}(x, x_1) & \Theta^{(L)}(x, x_2) & \cdots & \Theta^{(L)}(x, x_n) \end{pmatrix} K^{-1}_{\mathsf{train}} y, \quad \text{(B.57)}$$

where $y = \begin{pmatrix} y_1 & y_2 & \dots & y_n \end{pmatrix}$ is the vector of training labels.

Consider any orthogonal transform $T \in O(d)$, and the NTK regression trained on the transformed data $\{(Tx_i, y_i)\}_{i\in[n]}$. Denote the solution as $f^*_{\mathsf{NTK},T}\colon \mathbb{R} \to \mathbb{R}$. As we have shown, K^{-1}_{train} is invariant to such transforms, and remains the same. Therefore,

$$f^*_{\mathsf{NTK},T}(Tx) = \begin{pmatrix} \Theta^{(L)}(Tx, Tx_1) & \Theta^{(L)}(Tx, Tx_2) & \cdots & \Theta^{(L)}(Tx, Tx_n) \end{pmatrix} K^{-1}_{\mathsf{train}} y \quad \text{(B.58)}$$

$$= \begin{pmatrix} \Theta^{(L)}(x, x_1) & \Theta^{(L)}(x, x_2) & \cdots & \Theta^{(L)}(x, x_n) \end{pmatrix} K^{-1}_{\mathsf{train}} y \quad \text{(B.59)}$$

$$= f^*_{\mathsf{NTK}}(x). \quad \text{(B.60)}$$

Hence, MLPs trained (with squared loss) in NTK regime is equivariant to orthogonal transforms.

Furthermore, we note that there are many variants of MLP NTK formulas depending on details such as the particular initialization scheme and bias settings. However, they usually only lead to slight changes that do not affect our results. For example, while the above recursive NTK formula are derived assuming that the bias terms are initialized with a normal distribution (Jacot et al., 2018), the formulas for initializing bias as zeros (Geifman et al., 2020) does not affect the dependency only on dot product, and thus our results still hold true.

These cases conclude the proof. □

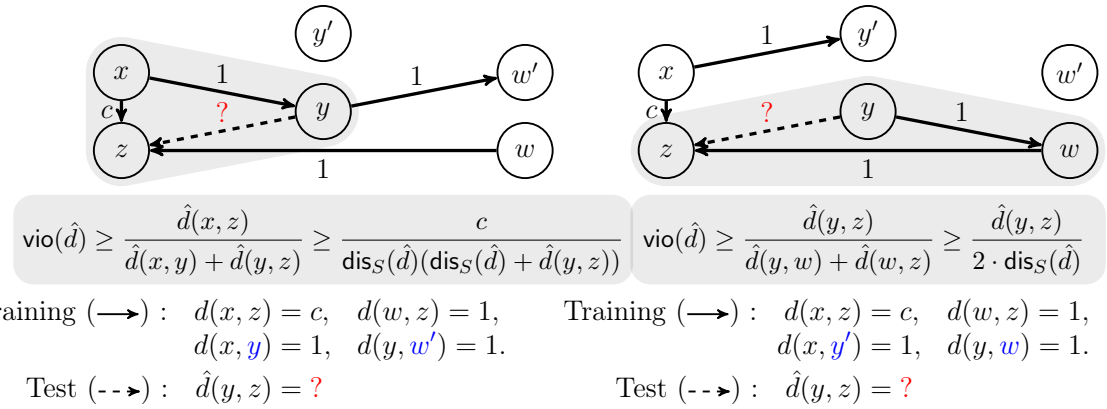

Figure B-1: Two training sets pose incompatible constraints (●) for the test pair distance $d(y,z)$. With one-hot features, an orthogonal transform can exchange $(*,y) \leftrightarrow (*,y')$ and $(*,w) \leftrightarrow (*,w')$, leaving the test pair (y,z) unchanged, but transforming the training set from one scenario to the other. Given either set, an OrthEquiv algorithm must attain same training distortion and predict identically on (y,z). For appropriate c, this implies large distortion (not fitting training set) or violation (not approximately a quasimetric) in one of these cases.

B.2.3 Theorem 3.4.6: Failure of OrthEquiv Algorithms

Theorem 3.4.6 (Failure of OrthEquiv Algorithms). Let $(f_n)_n$ be an *arbitrary* sequence of large values. There is an infinite sequence of quasimetric spaces $((\mathcal{X}_n, d_n))_n$ with $|\mathcal{X}_n| = n$, $\mathcal{X}_n \subset \mathbb{R}^n$ such that, over a random training set S of size m, any OrthEquiv algorithm outputs a predictor $\hat{d}$ that

- $\hat{d}$ fails *non-negativity*, or
- $\max(\mathsf{dis}_S(\hat{d}), \mathsf{vio}(\hat{d})) \geq f_n$ (*i.e.*, $\hat{d}$ approximates training S badly or is far from a quasimetric),

with probability $1/2 - o(1)$, as long as S does not contain almost all of the pairs $1 - m/n^2 = \omega(n^{-1/3})$, and does not only include few pairs $m/n^2 = \omega(n^{-1/2})$.

Recall that the little-Omega notation means $f = \omega(g) \iff g = o(f)$.

Proof

Proof strategy. In our proof below, we will extend the construction discussed in Section 3.4.2 to large quasimetric spaces (reproduced here as Figure B-1). To do so, we

1. Construct large quasimetric spaces containing many copies of the (potentially failing) structure in Figure B-1, where we can consider training sets of certain properties such that

   - we can pair up such training sets,
   - an algorithm equivariant to orthogonal transforms must fail on one of them,
   - for each pair, the two training sets has equal probability of being sampled;

   Then, it remains to show that with probability $1-o(1)$ we end up with a training set of such properties.

2. Consider sampling training set as independently collecting each pair with a certain probability p, and carefully analyze the conditions to sample a training set with the special properties with high probability $1-o(1)$.

3. Extend to fixed-size training sets and show that, under similar conditions, we sample a training set with the special properties with high probability $1-o(1)$.

In the discussion below and the proof, we will freely speak of infinite distances between two elements of $\mathcal{X}$, but really mean a very large value (possibly finite). This allows us to make the argument clearer and less verbose. Therefore, we are not restricting the applicable settings of Theorem 3.4.6 to quasimetrics with (or without) infinite distances.

In Section 3.4.2, we showed how orthogonal-transform-equivariant algorithms can not predict $\hat{d}(y,z)$ differently for the two particular quasimetric spaces and their training sets shown in Figure B-1.

But are these the only bad training sets? Before the proof, let us consider what kinds of training sets are bad for these two quasimetric spaces. Consider the quasimetrics d_{left} and d_{right} over $\mathcal{X} \triangleq \{x, y, y', z, w, w'\}$, with distances as shown in the left and right parts of Figure B-1, where we assume that the unlabeled pairs have infinite distances except in the left pattern $d(x,w') \le 2$, and in the both patterns $d(y,z)$ has some appropriate value consistent with the respective triangle inequality.

Specifically, we ask:

- For what training sets $S_{\mathsf{left}} \subset \mathcal{X} \times \mathcal{X}$ can we interchange $y \leftrightarrow y'$ and $w \leftrightarrow w'$ on 2nd input to obtain a valid training set for d_{right}, regardless of c?

- For what training sets $S_{\mathsf{right}} \subset \mathcal{X} \times \mathcal{X}$ can we interchange $y \leftrightarrow y'$ and $w \leftrightarrow w'$ on 2nd input to obtain a valid training set for d_{left}, regardless of c?

Note that if S_{left} (or S_{right}) satisfies its condition, the predictor $\hat{d}$ from an algorithm equivariant to orthogonal transforms must (1) predict $\hat{d}(y, z)$ identically and (2) attain the same training set distortion on it and its transformed training set. As we will see in the proof for Theorem 3.4.6, this implies large distortion or violation for appropriate c.

Intuitively, all we need is that the transformed data do not break quasimetric constraints. However, its conditions are actually nontrivial as we want to set c to arbitrary:

- We can't have $(x, w) \in S_{\mathsf{right}}$ because it would be transformed into (x, w') which has $d_{\mathsf{left}}(x, w') \leq 2$. Then $d_{\mathsf{right}}(x, w) \leq 2$ and then restricts the possible values of c due to triangle inequality with $d_{\mathsf{right}}(w, z) = 1$. For similar reasons, we can't have $(x, w') \in S_{\mathsf{left}}$. In fact, we can't have a path of finite total distance from x to w (or w') in S_{right} (or S_{left}).

- We can not have $(y', y') \in S_{(\cdot)}$ (which has distance 0), which would get transformed into (y', y) with distance 0, which (on the other pattern) would restrict the possible values of c due to triangle inequality. For similar reasons (w', w'), and cycles containing y' or w' with finite total distance, should be avoided.

- For the theoretical analysis, we assumed that the truth d is a quasimetric rather than just being a quasipseudometric. The difference is that quasipseudometric additionally allows two distinct elements to have 0 distance. This assumptions allows us to freely talk about distance ratios for defining distortion and violation.

  For this particular reason, we can't allow (y, y'), (y', y), (w, w'), (w', w), (y, y) or (w, w), as they break this assumption. However, with metrics more friendly to zero distances (than distortion and violation, which are based on distance

ratios), it might be possible to allow them and obtain better bounds in the second-moment argument below in the proof for Theorem 3.4.6.

With these understandings of the pattern shown in Figure B-1, we are ready to discuss the constructed quasimetric space and training sets.

Proof of Theorem 3.4.6. Our proof follows the outline listed above.

1. **Construct large quasimetric spaces containing many copies of the (potentially failing) structure in Figure B-1.**

   For any $n > 0$, consider the following quasimetric space $(\mathcal{X}_n, d_n)$ of size n, with one-hot features. WLOG, assume $n = 12k$ is a multiple of 12. If it is not, set at most 11 elements to have infinite distance with every other node. This won't affect the asymptotics. Let the $n = 12k$ elements of the space be

$$\begin{aligned}\mathcal{X}_n = \{&x_1^{\mathsf{left}}, \ldots, x_k^{\mathsf{left}}, x_1^{\mathsf{right}}, \ldots, x_k^{\mathsf{right}}, w_1^{\mathsf{left}}, \ldots, w_k^{\mathsf{left}}, w_1^{\mathsf{right}}, \ldots, w_k^{\mathsf{right}},\\ &y_1^{\mathsf{left}}, \ldots, y_k^{\mathsf{left}}, y_1^{\mathsf{right}}, \ldots, y_k^{\mathsf{right}}, w_1'^{\mathsf{left}}, \ldots, w_k'^{\mathsf{left}}, w_{k+1}'^{\mathsf{right}}, \ldots, w_{2k}'^{\mathsf{right}},\\ &y_1'^{\mathsf{left}}, \ldots, y_k'^{\mathsf{left}}, y_{k+1}'^{\mathsf{right}}, \ldots y_{2k}'^{\mathsf{right}}, z_1, \ldots, z_k, \qquad z_{k+1}, \ldots, z_{2k}\},\end{aligned} \tag{B.61}$$

   with quasimetric distances, $\forall i, j$,

$$d_n(x_i^{\mathsf{left}}, z_j) = d_n(x_i^{\mathsf{right}}, z_j) \quad = c \tag{B.62}$$

$$d_n(w_i^{\mathsf{left}}, z_j) = d_n(w_i^{\mathsf{right}}, z_j) \quad = 1 \tag{B.63}$$

$$d_n(x_i^{\mathsf{left}}, y_i^{\mathsf{left}}) = d_n(x_i^{\mathsf{right}}, y_i'^{\mathsf{right}}) = 1 \tag{B.64}$$

$$d_n(y_i^{\mathsf{left}}, w_i'^{\mathsf{left}}) = d_n(y_i^{\mathsf{right}}, w_i^{\mathsf{right}}) = 1 \tag{B.65}$$

$$d_n(x_i^{\mathsf{left}}, w_i'^{\mathsf{left}}) = 2 \tag{B.66}$$

$$d_n(y_i^{\mathsf{left}}, z_j) = c \tag{B.67}$$

$$d_n(y_i^{\mathsf{right}}, z_j) = 2, \tag{B.68}$$

   where subscripts are colored to better show when they are the same (or different), unlisted distances are infinite (except that $d_n(u, u) = 0, \forall u \in \mathcal{X}$).

Essentially, we equally divide the $12k$ nodes into 6 "types", $\{x, y, w, z, w', y'\}$, corresponding to the 6 nodes from Figure B-1, where each type has half of its nodes corresponding to the left pattern (of Figure B-1), and the other half corresponding to the right pattern, except for the z types.

Furthermore,

- Among the left-pattern nodes, each set with the same subscript are bundled together in the sense that x_i^{left} only has finite distance to y_i^{left} which only has finite distance to $w_i'^{\text{left}}$ (instead of other y_j^{left}'s or $w_k'^{\text{left}}$'s). However, since distance to/from y_i^{left} and w_i^{left} are infinite anyways, we can pair

$$(x_i^{\text{left}}, y_i^{\text{left}}, w_i'^{\text{left}}, y_j'^{\text{left}}, w_l^{\text{left}}, z_h) \tag{B.69}$$

  for any i, j, l, h, to obtain a left pattern.

- Among the right-pattern nodes, each set with the same subscript are bundled together in the sense that x_i^{right} only has finite distance to $y_i'^{\text{right}}$, and y_j^{right} which only has finite distance to w_j^{right} (instead of other $y_j'^{\text{right}}$'s or w_k^{right}'s). However, since are distances are infinite anyways, we can pair

$$(x_i^{\text{right}}, y_i'^{\text{right}}, y_j^{\text{right}}, w_j^{\text{right}}, w_l'^{\text{right}}, z_h) \tag{B.70}$$

  for any i, j, l, h, to obtain a right pattern.

We can see that $(\mathcal{X}, d)$ indeed satisfies all quasimetric space requirements (Definition 3.2.1), including triangle inequalities (*e.g.*, by, for each (a, b) with finite distance $d_n(a, b) < \infty$, enumerating finite-length paths from a to b).

Now consider the sampled training set S.

- We say S is *bad* on a left pattern specified by $i_{\mathsf{left}}, j_{\mathsf{left}}, l_{\mathsf{left}}, h_{\mathsf{left}}$, if

$$S \supset \{(x^{\mathsf{left}}_{i_{\mathsf{left}}}, z_{h_{\mathsf{left}}}), (x^{\mathsf{left}}_{i_{\mathsf{left}}}, y^{\mathsf{left}}_{i_{\mathsf{left}}}), (y^{\mathsf{left}}_{i_{\mathsf{left}}}, w'^{\mathsf{left}}_{i_{\mathsf{left}}}), (w^{\mathsf{left}}_{l_{\mathsf{left}}}, z_{h_{\mathsf{left}}})\} \tag{B.71}$$

$$\begin{aligned}\emptyset = S \cap \{&(y^{\mathsf{left}}_{i_{\mathsf{left}}}, z_{h_{\mathsf{left}}}), (y^{\mathsf{left}}_{i_{\mathsf{left}}}, y^{\mathsf{left}}_{i_{\mathsf{left}}}), (w^{\mathsf{left}}_{l_{\mathsf{left}}}, w^{\mathsf{left}}_{l_{\mathsf{left}}}), (y'^{\mathsf{left}}_{j_{\mathsf{left}}}, y'^{\mathsf{left}}_{j_{\mathsf{left}}}), (w'^{\mathsf{left}}_{i_{\mathsf{left}}}, w'^{\mathsf{left}}_{i_{\mathsf{left}}}),\\ &(x^{\mathsf{left}}_{i_{\mathsf{left}}}, w'^{\mathsf{left}}_{i_{\mathsf{left}}}), (y^{\mathsf{left}}_{i_{\mathsf{left}}}, y'^{\mathsf{left}}_{j_{\mathsf{left}}}), (w^{\mathsf{left}}_{l_{\mathsf{left}}}, w'^{\mathsf{left}}_{i_{\mathsf{left}}}), (y'^{\mathsf{left}}_{j_{\mathsf{left}}}, y^{\mathsf{left}}_{i_{\mathsf{left}}}), (w'^{\mathsf{left}}_{i_{\mathsf{left}}}, w^{\mathsf{left}}_{l_{\mathsf{left}}})\}\end{aligned} \tag{B.72}$$

- We say S is *bad* on a right pattern specified by $i_{\mathsf{right}}, j_{\mathsf{right}}, l_{\mathsf{right}}, h_{\mathsf{right}}$, if

$$S \supset \{(x^{\mathsf{right}}_{i_{\mathsf{right}}}, z_{h_{\mathsf{right}}}), (x^{\mathsf{right}}_{i_{\mathsf{right}}}, y'^{\mathsf{right}}_{i_{\mathsf{right}}}), (y'^{\mathsf{right}}_{j_{\mathsf{right}}}, w^{\mathsf{right}}_{j_{\mathsf{right}}}), (w^{\mathsf{right}}_{j_{\mathsf{right}}}, z_{h_{\mathsf{right}}})\} \tag{B.73}$$

$$\begin{aligned}\emptyset = S \cap \{&(y^{\mathsf{right}}_{j_{\mathsf{right}}}, z_{h_{\mathsf{right}}}), (y^{\mathsf{right}}_{j_{\mathsf{right}}}, y^{\mathsf{right}}_{j_{\mathsf{right}}}), (w^{\mathsf{right}}_{j_{\mathsf{right}}}, w^{\mathsf{right}}_{j_{\mathsf{right}}}), (y'^{\mathsf{right}}_{i_{\mathsf{right}}}, y'^{\mathsf{right}}_{i_{\mathsf{right}}}),\\ &(w'^{\mathsf{right}}_{l_{\mathsf{right}}}, w'^{\mathsf{right}}_{l_{\mathsf{right}}}), (x^{\mathsf{right}}_{i_{\mathsf{right}}}, w'^{\mathsf{right}}_{j_{\mathsf{right}}}), (y^{\mathsf{right}}_{j_{\mathsf{right}}}, y'^{\mathsf{right}}_{i_{\mathsf{right}}}), (w^{\mathsf{right}}_{j_{\mathsf{right}}}, w'^{\mathsf{right}}_{l_{\mathsf{right}}}),\\ &(y'^{\mathsf{right}}_{i_{\mathsf{right}}}, y^{\mathsf{right}}_{j_{\mathsf{right}}}), (w'^{\mathsf{right}}_{l_{\mathsf{right}}}, w^{\mathsf{right}}_{j_{\mathsf{right}}})\}\end{aligned} \tag{B.74}$$

Most importantly,

- If S is bad on a left pattern specified by $i_{\mathsf{left}}, j_{\mathsf{left}}, l_{\mathsf{left}}, h_{\mathsf{left}}$, consider the orthogonal transform that interchanges $y^{\mathsf{left}}_{i_{\mathsf{left}}} \leftrightarrow y'^{\mathsf{left}}_{j_{\mathsf{left}}}$ and $w^{\mathsf{left}}_{l_{\mathsf{left}}} \leftrightarrow w'^{\mathsf{left}}_{i_{\mathsf{left}}}$ on 2nd input. In S, the possible transformed pairs are

$$\begin{aligned}
d(x^{\mathsf{left}}_{i_{\mathsf{left}}}, y^{\mathsf{left}}_{i_{\mathsf{left}}}) = 1 \quad &\longrightarrow \quad d(x^{\mathsf{left}}_{i_{\mathsf{left}}}, y'^{\mathsf{left}}_{j_{\mathsf{left}}}) = 1, && \text{(known in } S\text{)}\\
d(y^{\mathsf{left}}_{i_{\mathsf{left}}}, w'^{\mathsf{left}}_{i_{\mathsf{left}}}) = 1 \quad &\longrightarrow \quad d(y^{\mathsf{left}}_{i_{\mathsf{left}}}, w^{\mathsf{left}}_{l_{\mathsf{left}}}) = 1, && \text{(known in } S\text{)}\\
d(u, y^{\mathsf{left}}_{i_{\mathsf{left}}}) = \infty \quad &\longrightarrow \quad d(u, y'^{\mathsf{left}}_{j_{\mathsf{left}}}) = \infty, && \\
& && \text{(poissble in } S \text{ for some } u \neq x^{\mathsf{left}}_{i_{\mathsf{left}}}\text{)}\\
d(u, y'^{\mathsf{left}}_{j_{\mathsf{left}}}) = \infty \quad &\longrightarrow \quad d(u, y^{\mathsf{left}}_{i_{\mathsf{left}}}) = \infty, && \text{(poissble in } S \text{ for some } u\text{)}\\
d(u, w'^{\mathsf{left}}_{i_{\mathsf{left}}}) = \infty \quad &\longrightarrow \quad d(u, w^{\mathsf{left}}_{l_{\mathsf{left}}}) = \infty, && \\
& && \text{(poissble in } S \text{ for some } u \notin \{x^{\mathsf{left}}_{i_{\mathsf{left}}}, y^{\mathsf{left}}_{i_{\mathsf{left}}}\}\text{)}\\
d(u, w^{\mathsf{left}}_{l_{\mathsf{left}}}) = \infty \quad &\longrightarrow \quad d(u, w'^{\mathsf{left}}_{i_{\mathsf{left}}}) = \infty. && \text{(poissble in } S \text{ for some } u\text{)}
\end{aligned}$$

The crucial observation is that the transformed training set just look like

one sampled from a quasimetric space where

- the quasimetric space has one less set of left-pattern elements,
- the quasimetric space has one more set of right-pattern elements, and
- transformed training set is *bad* on that extra right pattern (given by the extra set of right-pattern elements),

which can be easily verified by comparing the transformed training set with the requirements in Equations (B.73) and (B.74).

- Similarly, if S is bad on a right pattern specified by $i_{\mathsf{right}}, j_{\mathsf{right}}, l_{\mathsf{right}}, h_{\mathsf{right}}$, consider the orthogonal transform that interchanges $y^{\mathsf{right}}_{j_{\mathsf{right}}} \leftrightarrow y'^{\mathsf{right}}_{i_{\mathsf{right}}}$ and $w^{\mathsf{right}}_{j_{\mathsf{right}}} \leftrightarrow w'^{\mathsf{right}}_{l_{\mathsf{right}}}$ on 2nd input. In S the possible transformed pairs are

$$
\begin{aligned}
d(x^{\mathsf{right}}_{i_{\mathsf{right}}}, y'^{\mathsf{right}}_{i_{\mathsf{right}}}) = 1 \quad &\longrightarrow \quad d(x^{\mathsf{right}}_{i_{\mathsf{right}}}, y^{\mathsf{right}}_{j_{\mathsf{right}}}) = 1, && \text{(known in } S\text{)} \\
d(y^{\mathsf{right}}_{j_{\mathsf{right}}}, w^{\mathsf{right}}_{j_{\mathsf{right}}}) = 1 \quad &\longrightarrow \quad d(y^{\mathsf{right}}_{j_{\mathsf{right}}}, w'^{\mathsf{right}}_{l_{\mathsf{right}}}) = 1, && \text{(known in } S\text{)} \\
d(u, y^{\mathsf{right}}_{j_{\mathsf{right}}}) = \infty \quad &\longrightarrow \quad d(u, y'^{\mathsf{right}}_{i_{\mathsf{right}}}) = \infty, \\
& && \text{(poissble in } S \text{ for some } u\text{)} \\
d(u, y'^{\mathsf{right}}_{i_{\mathsf{right}}}) = \infty \quad &\longrightarrow \quad d(u, y^{\mathsf{right}}_{j_{\mathsf{right}}}) = \infty, \\
& && \text{(poissble in } S \text{ for some } u \neq x^{\mathsf{right}}_{i_{\mathsf{right}}}\text{)} \\
d(u, w'^{\mathsf{right}}_{l_{\mathsf{right}}}) = \infty \quad &\longrightarrow \quad d(u, w^{\mathsf{right}}_{j_{\mathsf{right}}}) = \infty, \\
& && \text{(poissble in } S \text{ for some } u\text{)} \\
d(u, w^{\mathsf{right}}_{j_{\mathsf{right}}}) = \infty \quad &\longrightarrow \quad d(u, w'^{\mathsf{right}}_{l_{\mathsf{right}}}) = \infty. \\
& && \text{(poissble in } S \text{ for some } u \notin \{x^{\mathsf{right}}_{i_{\mathsf{right}}}, y^{\mathsf{right}}_{j_{\mathsf{right}}}\}\text{)}
\end{aligned}
$$

Again, the crucial observation is that the transformed training set just look like one sampled from a quasimetric space where

- the quasimetric space has one less set of right-pattern elements,
- the quasimetric space has one more set of left-pattern elements, and
- transformed training set is *bad* on that extra left pattern (given by the extra set of left-pattern elements),

which can be easily verified by comparing the transformed training set with the requirements in Equations (B.71) and (B.72).

Therefore, when S is bad on *both a left pattern and a right pattern* (necessarily on disjoint sets of pairs), we consider the following orthogonal transform composed of:

(a) both transforms specified above (which only transforms 2nd inputs),

(so that after this we obtain *another possible training set of same size from the quasimetric space that is only different up to some permutation of* $\mathcal{X}$)

(b) a permutation of $\mathcal{X}$ (on both inputs) so that the bad left-pattern nodes and the bad right-pattern nodes exchange features,

This transforms gives *another possible training set of same size from the same quasimetric space, also is bad on a left pattern and a right pattern*. Moreover, with a particular way of select bad patterns (*e.g.*, by the order of the subscripts), this process is *reversible*. Therefore, we have defined a way to pair up all such bad training sets.

Consider the predictors $\hat{d}_{\mathsf{before}}$ and $\hat{d}_{\mathsf{after}}$ trained on these two training sets (before and after transform) with an learning algorithm equivariant to orthogonal transforms. Assuming that they satisfy non-negativity and Identity of Indiscernibles, we have,

- The predictors have the same distortion over respective training sets.

  Therefore we denote this distortion as $\mathsf{dis}_S(\hat{d})$ without specifying the predictor $\hat{d}$ or training set S.

- the predictors must predict the same on heldout pairs in the sense that

$$\hat{d}_{\mathsf{before}}(y^{\mathsf{left}}_{i_{\mathsf{left}}}, z_{h_{\mathsf{left}}}) = \hat{d}_{\mathsf{after}}(y^{\mathsf{right}}_{j_{\mathsf{right}}}, z_{h_{\mathsf{right}}}) \tag{B.75}$$

$$\hat{d}_{\mathsf{before}}(y^{\mathsf{right}}_{j_{\mathsf{right}}}, z_{h_{\mathsf{right}}}) = \hat{d}_{\mathsf{after}}(y^{\mathsf{left}}_{i_{\mathsf{left}}}, z_{h_{\mathsf{left}}}). \tag{B.76}$$

Focusing on the first, we denote

$$\hat{d}(y,z) \triangleq \hat{d}_{\mathsf{before}}(y^{\mathsf{left}}_{i_{\mathsf{left}}}, z_{h_{\mathsf{left}}}) = \hat{d}_{\mathsf{after}}(y^{\mathsf{right}}_{j_{\mathsf{right}}}, z_{h_{\mathsf{right}}}) \tag{B.77}$$

without specifying the predictor $\hat{d}$ or the specific y and z.

However, the quasimetric constraints on heldout pairs $(y^{\mathsf{left}}_{i_{\mathsf{left}}}, z_{h_{\mathsf{left}}})$ and $(y^{\mathsf{right}}_{j_{\mathsf{right}}}, z_{h_{\mathsf{right}}})$ are completely different (see the left vs. right part of Figure B-1). Therefore, as shown in Figure B-1, assuming *non-negativity*, *one of the two predictors* must have total violation at least

$$\mathsf{vio}(\hat{d}) \geq \max\left(\frac{c}{\mathsf{dis}_S(\hat{d})(\mathsf{dis}_S(\hat{d}) + \hat{d}(y,z))}, \frac{\hat{d}(y,z)}{2 \cdot \mathsf{dis}_S(\hat{d})}\right). \tag{B.78}$$

Fixing a large enough c, two terms in the max of Equation (B.78) can equal for some $\hat{d}(y,z)$, and are respectively decreasing and increasing in $\hat{d}(y,z)$. In that case, we have

$$\mathsf{vio}(\hat{d}) \geq \frac{\delta}{2 \cdot \mathsf{dis}_S(\hat{d})}, \tag{B.79}$$

for $\delta > 0$ such that

$$\frac{c}{\mathsf{dis}_S(\hat{d})(\mathsf{dis}_S(\hat{d}) + \delta)} = \frac{\delta}{2 \cdot \mathsf{dis}_S(\hat{d})}. \tag{B.80}$$

Solving the above quadratic equation gives

$$\delta = \frac{-\mathsf{dis}_S(\hat{d}) + \sqrt{\mathsf{dis}_S(\hat{d})^2 + 8c}}{2}, \tag{B.81}$$

leading to

$$\mathsf{vio}(\hat{d}) \geq \frac{-1 + \sqrt{1 + 8c/\mathsf{dis}_S(\hat{d})^2}}{4}. \tag{B.82}$$

Therefore, choosing $c \geq f_n^2(4f_n+1)^2$ gives

$$\mathsf{dis}_S(\hat{d}) \leq f_n \tag{B.83}$$

$$\implies \mathsf{vio}(\hat{d}) \geq \frac{-1+\sqrt{1+8c/\mathsf{dis}_S(\hat{d})^2}}{4} \tag{B.84}$$

$$\geq \frac{-1+\sqrt{1+8f_n^2(4f_n+1)^2/f_n^2}}{4} \tag{B.85}$$

$$= \frac{-1+\sqrt{1+8(4f_n+1)^2}}{4} \tag{B.86}$$

$$\geq \frac{-1+4f_n+1}{4} \tag{B.87}$$

$$= f_n. \tag{B.88}$$

Hence, for training sets that are *bad* on *both a left pattern and a right pattern*, we have shown a way to pair them up such that

- each pair of training sets have the same size, and
- the algorithm fail on one of each pair by producing a distance predictor that
  - has either distortion over training set $\geq f_n$, or violation $\geq f_n$, and
  - has test MSE $\geq f_n$.

Remark B.2.1. Note that all training sets of size m has equal probability of being sampled. Therefore, to prove the theorem, it suffices to show that with probability $1-o(1)$, we can sample a training set of size m that is *bad* on *both a left pattern and a right pattern*.

2. **Consider sampling training set as individually collecting each pair with a certain probability p, and carefully analyze the conditions to sample a training set with the special properties with high probability $1-o(1)$.**

   In probabilistic methods, it is often much easier to work with independent random variables. Therefore, instead of considering uniform sampling a training set

S of fixed size m, we consider including each pair in S with probability p, chosen independently. We will first show result based on this sampling procedure via a second moment argument, and later extend to the case with a fixed-size training set.

First, let's define some notations that ignore constants:

$$f \sim g \iff f = (1 + o(1))g \tag{B.89}$$

$$f \ll g \iff f = o(g). \tag{B.90}$$

We start with stating a standard result from the second moment method (Alon and Spencer, 2004).

Corollary B.2.2 (Corollary 4.3.5 of (Alon and Spencer, 2004)). Consider random variable $X = X_1 + X_2 + \cdots + X_n$, where X_i is the indicator random variable for event A_i. Write $i \sim j$ if $i \neq j$ and the pair of events (A_i, A_j) are not independent. Suppose the following quantity does not depend on i:

$$\Delta^* \triangleq \sum_{j \sim i} \mathbb{P}\left[A_j \mid A_i\right]. \tag{B.91}$$

If $\mathbb{E}[X] \to \infty$ and $\Delta^* \ll \mathbb{E}[X]$, then $X \sim \mathbb{E}[X]$ with probability $1 - o(1)$.

We will apply this corollary to obtain conditions on p such that S with probability $1 - o(1)$ is *bad* on some left pattern, and conditions such that S with probability $1 - o(1)$ is *bad* on some right pattern. A union bound would then give the desired result.

- **S is *bad* on some left pattern.**

  Recall that a left pattern is specified by $i_{\mathsf{left}}, j_{\mathsf{left}}, l_{\mathsf{left}}, h_{\mathsf{left}}$ all $\in [k]$:

$$(x^{\mathsf{left}}_{i_{\mathsf{left}}}, y^{\mathsf{left}}_{i_{\mathsf{left}}}, w^{\prime\mathsf{left}}_{i_{\mathsf{left}}}, y^{\prime\mathsf{left}}_{j_{\mathsf{left}}}, w^{\mathsf{left}}_{l_{\mathsf{left}}}, z_{h_{\mathsf{left}}}) \tag{B.92}$$

Therefore, we consider $k^4 = (\frac{n}{12})^4$ events of the form

$$A_{i_{\text{left}},j_{\text{left}},l_{\text{left}},h_{\text{left}}} \triangleq \{S \text{ is bad on the } \underline{\text{left pattern}} \text{ at } i_{\text{left}}, j_{\text{left}}, l_{\text{left}}, h_{\text{left}}\}. \tag{B.93}$$

Obviously, these events are symmetrical, and the Δ^* in Equation (B.91) does not depend on i.

By the quasimetric space construction and the requirement for S to be bad on a <u>left pattern</u> in Equations (B.71) and (B.72), we can see that $(i_{\text{left}}, j_{\text{left}}, l_{\text{left}}, h_{\text{left}}) \sim (i'_{\text{left}}, j'_{\text{left}}, l'_{\text{left}}, h'_{\text{left}})$ only if $i_{\text{left}} = i'_{\text{left}}$ or $j_{\text{left}} = j'_{\text{left}}$ or $l_{\text{left}} = l'_{\text{left}}$ or $h_{\text{left}} = h'_{\text{left}}$.

Therefore, we have

$$\begin{aligned}
\mathbb{E}[X] &\sim n^4p^4(1-p)^{10} && \text{(include 4 pairs \& exclude 10 pairs)}\\
\Delta^* &\ll n^3p^4(1-p)^9 && \text{(share } j_{\mathsf{left}}\text{)}\\
&\quad + n^3p^2(1-p)^7 && \text{(share } i_{\mathsf{left}}\text{)}\\
&\quad + n^3p^4(1-p)^9 && \text{(share } l_{\mathsf{left}}\text{)}\\
&\quad + n^3p^4(1-p)^{10} && \text{(share } h_{\mathsf{left}}\text{)}\\
&\quad + n^2p^2(1-p)^4 && \text{(share } j_{\mathsf{left}}, i_{\mathsf{left}}\text{)}\\
&\quad + n^2p^4(1-p)^8 && \text{(share } j_{\mathsf{left}}, l_{\mathsf{left}}\text{)}\\
&\quad + n^2p^4(1-p)^9 && \text{(share } j_{\mathsf{left}}, h_{\mathsf{left}}\text{)}\\
&\quad + n^2p^2(1-p)^4 && \text{(share } i_{\mathsf{left}}, l_{\mathsf{left}}\text{)}\\
&\quad + n^2p(1-p)^6 && \text{(share } i_{\mathsf{left}}, h_{\mathsf{left}}\text{)}\\
&\quad + n^2p^3(1-p)^9 && \text{(share } l_{\mathsf{left}}, h_{\mathsf{left}}\text{)}\\
&\quad + n(1-p)^3 && \text{(share } i_{\mathsf{left}}, l_{\mathsf{left}}, h_{\mathsf{left}}\text{)}\\
&\quad + np^3(1-p)^8 && \text{(share } j_{\mathsf{left}}, l_{\mathsf{left}}, h_{\mathsf{left}}\text{)}\\
&\quad + np(1-p)^3 && \text{(share } j_{\mathsf{left}}, i_{\mathsf{left}}, h_{\mathsf{left}}\text{)}\\
&\quad + np^2(1-p) && \text{(share } j_{\mathsf{left}}, i_{\mathsf{left}}, l_{\mathsf{left}}\text{)}\\
&\sim n^3p^2(1-p)^7 + n^2(p^2(1-p)^4 + p(1-p)^6) && \text{(B.94)}\\
&\quad + n((1-p)^3 + p^2(1-p)). && \text{(B.95)}
\end{aligned}$$

Therefore, to apply Corollary B.2.2, we need to have

$$\begin{aligned}
n^4p^4(1-p)^{10} &\to \infty && \text{(B.96)}\\
n^3p^2(1-p)^7 &\ll n^4p^4(1-p)^{10} && \text{(B.97)}\\
n^2(p^2(1-p)^4 + p(1-p)^6) &\ll n^4p^4(1-p)^{10} && \text{(B.98)}\\
n((1-p)^3 + p^2(1-p)) &\ll n^4p^4(1-p)^{10}, && \text{(B.99)}
\end{aligned}$$

which gives

$$p \gg n^{-1/2} \tag{B.100}$$

$$1 - p \gg n^{-1/3} \tag{B.101}$$

as a sufficient condition to for S to be bad on some left pattern with probability $1 - o(1)$.

- **S is *bad* on some right pattern.**

Recall that a right pattern is specified by $i_{\text{right}}, j_{\text{right}}, l_{\text{right}}, h_{\text{right}}$ all $\in [k]$:

$$(x^{\text{right}}_{i_{\text{right}}}, y^{\prime\text{right}}_{i_{\text{right}}}, y^{\text{right}}_{j_{\text{right}}}, w^{\text{right}}_{j_{\text{right}}}, w^{\prime\text{right}}_{l_{\text{right}}}, z_{h_{\text{right}}}) \tag{B.102}$$

Similarly, we consider $k^4 = (\frac{n}{12})^4$ events of the form

$$A_{i_{\text{right}}, j_{\text{right}}, l_{\text{right}}, h_{\text{right}}} \triangleq \{S \text{ is bad on the left pattern at } i_{\text{right}}, j_{\text{right}}, l_{\text{right}}, h_{\text{right}}\}. \tag{B.103}$$

Again, these events are symmetrical, and Δ^* in Equation (B.91) does not depend on i.

Similarly, we have

$$\begin{aligned}
\mathbb{E}[X] &\sim n^4p^4(1-p)^{10} && \text{(include 4 pairs \& exclude 10 pairs)}\\
\Delta^* &\ll n^3p^3(1-p)^9 && \text{(share } i_{\mathsf{right}}\text{)}\\
&\quad + n^3p^3(1-p)^8 && \text{(share } j_{\mathsf{right}}\text{)}\\
&\quad + n^3p^4(1-p)^{10} && \text{(share } h_{\mathsf{right}}\text{)}\\
&\quad + n^3p^4(1-p)^9 && \text{(share } l_{\mathsf{right}}\text{)}\\
&\quad + n^2p^2(1-p)^4 && \text{(share } i_{\mathsf{right}}, j_{\mathsf{right}}\text{)}\\
&\quad + n^2p^2(1-p)^9 && \text{(share } i_{\mathsf{right}}, h_{\mathsf{right}}\text{)}\\
&\quad + n^2p^3(1-p)^8 && \text{(share } i_{\mathsf{right}}, l_{\mathsf{right}}\text{)}\\
&\quad + n^2p^2(1-p)^7 && \text{(share } j_{\mathsf{right}}, h_{\mathsf{right}}\text{)}\\
&\quad + n^2p^3(1-p)^5 && \text{(share } j_{\mathsf{right}}, l_{\mathsf{right}}\text{)}\\
&\quad + n^2p^4(1-p)^9 && \text{(share } h_{\mathsf{right}}, l_{\mathsf{right}}\text{)}\\
&\quad + np^2(1-p)^4 && \text{(share } j_{\mathsf{right}}, h_{\mathsf{right}}, l_{\mathsf{right}}\text{)}\\
&\quad + np^2(1-p)^8 && \text{(share } i_{\mathsf{right}}, h_{\mathsf{right}}, l_{\mathsf{right}}\text{)}\\
&\quad + np^2(1-p) && \text{(share } i_{\mathsf{right}}, j_{\mathsf{right}}, l_{\mathsf{right}}\text{)}\\
&\quad + n(1-p) && \text{(share } i_{\mathsf{right}}, j_{\mathsf{right}}, h_{\mathsf{right}}\text{)}\\
&\sim n^3p^3(1-p)^8 + n^2p^2(1-p)^4 && \text{(B.104)}\\
&\quad + n(1-p). && \text{(B.105)}
\end{aligned}$$

Therefore, to apply Corollary B.2.2, we need to have

$$n^4p^4(1-p)^{10} \to \infty \tag{B.106}$$

$$n^3p^3(1-p)^8 \ll n^4p^4(1-p)^{10} \tag{B.107}$$

$$n^2p^2(1-p)^4 \ll n^4p^4(1-p)^{10} \tag{B.108}$$

$$n(1-p) \ll n^4p^4(1-p)^{10}, \tag{B.109}$$

which gives

$$p \gg n^{-3/4} \tag{B.110}$$

$$1 - p \gg n^{-1/3} \tag{B.111}$$

as a sufficient condition to for S to be bad on some right pattern with probability $1 - o(1)$.

So, by union bound, as long as

$$p \gg n^{-1/2} \tag{B.112}$$

$$1 - p \gg n^{-1/3}, \tag{B.113}$$

S is bad on some left pattern *and* some right pattern with probability $1 - o(1)$.

3. **Extend to fixed-size training sets and show that, under similar conditions, we sample a training set with the special properties with high probability $1 - o(1)$.**

   To extend to fixed-size training sets, we consider the following alteration procedure:

   (a) Sample training set S by independently include each pair with probability $p \triangleq \frac{m+\delta}{n^2}$, for some $\delta > 0$.

   (b) Show that with high probability $1 - o(1)$, we end up with $[m, m + 2\delta]$ pairs in S.

   (c) Make sure that p satisfy Equation (B.112) and Equation (B.113) so that S is bad on some left pattern *and* some right pattern with high probability $1 - o(1)$.

   (d) Randomly discard the additional pairs, and show that with high probability $1 - o(1)$ this won't affect that S is bad on some left pattern *and* some right pattern.

We now consider each step in details:

(a) **Sample training set S by independently include each pair with probability $p \triangleq \frac{m+\delta}{n^2}$, for some $\delta > 0$.**

For $p \triangleq \frac{m+\delta}{n^2}$, the number of pairs in the training set is distributed as

$$\text{Binomial}(n^2, \frac{m+\delta}{n^2}). \tag{B.114}$$

(b) **Show that with high probability $1-o(1)$, we end up with $[m, m+2\delta]$ pairs in S.**

Standard Binomial concentration tells us that,

$$\delta \gg n\sqrt{p(1-p)} \implies \mathbb{P}\left[\text{Binomial}(n^2, \frac{m+\delta}{n^2}) \notin [m, m+2\delta]\right] \to 0, \tag{B.115}$$

which can be satisfied if

$$\delta \gg n. \tag{B.116}$$

(c) **Make sure that p satisfy Equation (B.112) and Equation (B.113) so that S is bad on some left pattern *and* some right pattern with high probability $1 - o(1)$.**

Therefore, we want

$$\frac{m+\delta}{n^2} \gg n^{-1/2} \tag{B.117}$$

$$1 - \frac{m+\delta}{n^2} \gg n^{-1/3}. \tag{B.118}$$

(d) **Randomly discard the additional pairs, and show that with high probability $1 - o(1)$ this won't affect that S is bad on some left pattern *and* some right pattern.**

Consider any specific bad left pattern *and a* right pattern in S. It is sufficient that we don't break these two patterns during discarding.

Since we only discard pairs, it suffices to only consider the pairs we want

to preserve, which are a total of 8 pairs across two patterns.

Each such pair is discarded the probability $\leq \frac{2\delta}{m}$, since we remove at most 2δ pairs. By union bound,

$$\mathbb{P}\left[\text{all 8 pairs are preserved}\right] \geq 1 - \frac{16\delta}{m}. \tag{B.119}$$

Hence, it suffices to make sure that

$$\delta \ll m. \tag{B.120}$$

Collecting all requirements, we have

$$\delta \gg n \tag{B.121}$$

$$\frac{m+\delta}{n^2} \gg n^{-1/2} \tag{B.122}$$

$$1 - \frac{m+\delta}{n^2} \gg n^{-1/3} \tag{B.123}$$

$$\delta \ll m. \tag{B.124}$$

Assume that

$$\frac{m}{n^2} \gg n^{-1/2} \tag{B.125}$$

$$1 - \frac{m}{n^2} \gg n^{-1/3}. \tag{B.126}$$

It can be easily verified that using $\delta \triangleq n^{1.1}$ satisfies all conditions.

Hence, for a uniformly randomly sampled training set S with size m, S is bad on some left pattern *and* some right pattern with high probability $1 - o(1)$, as long as

$$\frac{m}{n^2} \gg n^{-1/2} \tag{B.127}$$

$$1 - \frac{m}{n^2} \gg n^{-1/3}. \tag{B.128}$$

This is exactly the condition we need to prove the theorem (see Remark B.2.1).

This concludes the proof. □

Discussions

Training set size dependency. Intuitively, when the training set has almost all pairs, violation can be lowered by simply fitting training set well; when it is small and sparse, the learning algorithm may have an easier job finding some consistent quasimetric. Theorem 3.4.6 shows that, outside these two cases, algorithms equivariant to orthogonal transforms can fail. Note that for the latter case, Theorem 3.4.6 requires the training fraction to decrease slower than $n^{-1/2}$, which rules out training sizes that is linear in n. We leave improving this result as future work. Nonetheless, Theorem 3.4.6 still covers common scenarios such as a fixed fraction of all pairs, and highlights that a training-data-agnostic result (such as the ones for PQEs) is not possible for these algorithms.

Proof techniques. In embedding theory, it is quite standard to analyze quasimetrics as directed graphs due to their lack of nice metric structure. In the proof for Theorem 3.4.6, we used abundant techniques from the probabilistic method, which are commonly used for analyzing graph properties in the asymptotic case, including Corollary B.2.2 from the second moment technique, and the alteration technique to extend to fixed-size training sets. While such techniques may be new in learning theory, they are standard for characterizing asymptotic probabilities on graphs, which quasimetrics are often analyzed as (Charikar et al., 2006; Mémoli et al., 2018).

To provide more intuition on why these techniques are useful here, we note that the construction of a training set of pairs is essentially like constructing an Erdős-Rényi random graph on n^2 vertices. Erdős-Rényi (undirected) random graphs come in two kinds:

- Uniformly sampling a fixed number of m edges;
- Adding an edge between each pair with probability p, decided independently.

The latter, due to its independent decisions, is often much easy to analyze and preferred by many. The alteration technique (that we used in the proof) is also a standard way to transfer a result on a random graph of the latter type, to a random graph of the former type (Bollobás and Béla, 2001). Readers can refer to (Alon and Spencer, 2004; Bollobás and Béla, 2001; Erdős and Rényi, 1959) for more in-depth treatment of these topics.

Generalization to other transforms. The core of this construction only relies on the ability to swap (concatenated) inputs between $(x, y) \leftrightarrow (x, y')$ and between $(y, w) \leftrightarrow (y, w')$ via a transform. For instance, here the orthogonal transforms satisfy this requirement on one-hot features. Therefore, the result can also be generalized to other transforms and features with the same property. Our stated theorem focuses on orthogonal transforms because they correspond to several common learning algorithms (see Lemma 3.4.5). If a learning algorithm is equivariant to some other transform family, it would be meaningful to generalize this result to that transform family, and obtain a similar negative result. We leave such extensions as future work.

Corollary of Distortion and Violation for Unconstrained MLPs

Corollary B.2.3 (Distortion and Violation of Unconstrained MLPs). Let $(f_n)_n$ be an arbitrary sequence of desired violation values. There is an infinite collection of quasimetric spaces $((\mathcal{X}_n, d_n))_{n=1,2,\ldots}$ with $|\mathcal{X}_n| = n$, $\mathcal{X}_n \subset \mathbb{R}^n$ such that MLP trained with squared loss in NTK regime converges to a function $\hat{d}$ that either

- fails non-negativity, or
- $\mathsf{vio}(\hat{d}) \geq f_n$,

with probability $1/2 - o(1)$ over the random training set S of size m, as long as S does not contain almost all pairs $1 - m/n^2 = \omega(n^{-1/3})$, and does not only include few pairs $m/n^2 = \omega(n^{-1/2})$.

Proof of Corollary B.2.3. This follows directly from Theorem 3.4.6 and standard NTK convergence results obtained from the kernel regression optimality and the positive-definiteness of the NTK. In particular, Proposition 2 of (Jacot et al., 2018) claims

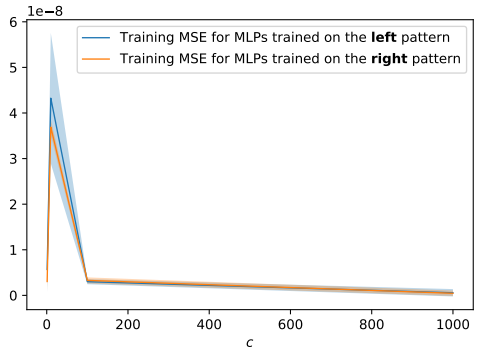

(a) Training losses for varying c. Note the scale of the vertical axis.

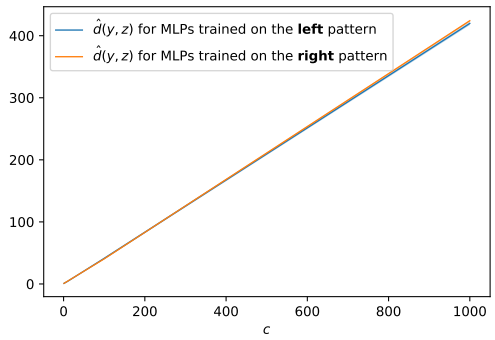

(b) Prediction on heldout pair $\hat{d}(y, z)$ for varying c.

Figure B-2: Training unconstrained MLPs on the toy failure construction discussed in Section 3.4.2 (reproduced as Figure B-1). Two patterns in the construction have different constraints on distance of the heldout pair (y, z). Plots show mean and standard deviations over 5 runs. **Left:** All training conclude with small training error. **Right:** Trained MLPs predict identically for both patterns. Here standard deviation is small compared to mean and thus not very visible.

that the NTK is positive-definite when restricted to a hypersphere. Since the construction in proof of Theorem 3.4.6 uses one-hot features, the input (concatenation of two features) lie on the hypersphere with radius $\sqrt{2}$. Hence, the NTK is guaranteed positive definite. □

Empirical Verification of the Failure Construction

We train unconstrained MLPs on the toy failure construction discussed in Section 3.4.2 (reproduced as Figure B-1). The MLP uses 12-1024-1 architecture with ReLU activations, takes in the concatenated one-hot features, and directly outputs predicted distances. Varying $c \in \{1, 10, 100, 1000\}$, we train the above MLP 5 times on each of the two patterns in Figure B-1, by regressing towards the training distances via MSE loss.

In Figure B-2, we can see that all training runs conclude with small training error, and indeed the trained MLPs predict very similarly on the heldout pair, regardless whether it is trained on the left or right pattern of Figure B-1, which restricts the heldout pair distance differently.

This verifies our theory (Theorem 3.4.6 and Corollary B.2.3) that algorithms equiv-

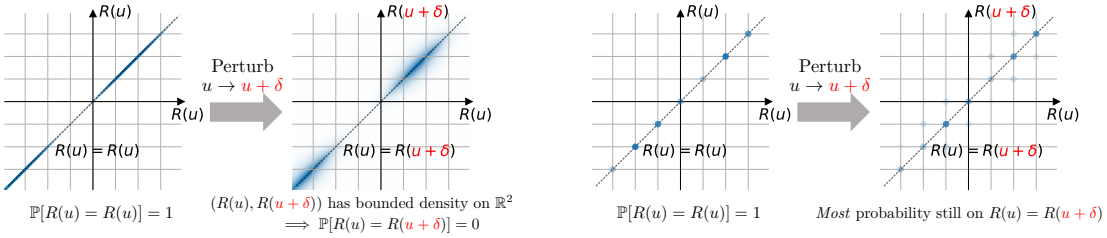

(a) Continuous-valued stochastic process. (b) Discrete-valued stochastic process.

Figure B-3: Bivariate distributions from different stochastic processes. **Left:** In a continuous-valued process (where $(N_\theta, N_{\theta'})$ has bounded density if $\theta \neq \theta'$), perturbing one $\theta \to \theta + \epsilon$ leaves $\mathbb{P}[N_\theta = N_{\theta+\epsilon}] = 0$. Then one of $\mathbb{P}\big[N_\theta \leq N_{\theta+\epsilon}\big]$ and $\mathbb{P}\big[N_{\theta+\epsilon} \leq N_\theta\big]$ must be far away from 1 (as they sum to 1), breaking differentiability at either $\mathbb{P}[N_\theta \leq N_\theta] = 1$ or $\mathbb{P}[N_{\theta+\epsilon} \leq N_{\theta+\epsilon}] = 1$. **Right:** For discrete-valued processes, most probability can still be left on $N_\theta = N_{\theta+\epsilon}$ and thus do not break differentiability.

ariant to orthogonal transforms (including MLPs in NTK regime) cannot distinguish these two cases and thus must fail on one of them.

B.3 Proofs and Discussions for Section 3.5: Poisson Quasimetric Embeddings (PQEs)

B.3.1 Non-differentiability of Continuous-Valued Stochastic Processes

In this section we formalize the argument presented in Section 3.5.3 to show why continuous-valued stochastic processes lead to non-differentiability. Figure B-3 also provides a graphical illustration of the general idea.

Proposition B.3.1 (Quasimetric Embeddings with Continuous-Valued Stochastic Processes are not Differentiable). Consider any $\mathbb{R}^k$-valued stochastic process $\{R(u)\}_{u \in \mathbb{R}^d}$ such that $u \neq u' \implies \mathbb{P}[R(u) = R(u')] < c$ for some universal constant $c < 1$. Then $\mathbb{P}[R(u) \leq R(u')]$ is not differentiable at any $u = u'$.

Proof of Proposition B.3.1. Assume that the quantity is differentiable. Then it must be continuous in u and v.

We will use the (ϵ, δ)-definition of continuity.

At any $u \in \mathbb{R}^d$, consider small $\epsilon \in (0, \frac{1-c}{3})$. By continuity, since

$$\mathbb{P}\left[R(u) \leq R(u)\right] = \mathbb{P}\left[R(u+\delta) \leq R(u+\delta)\right] = 1 \tag{B.129}$$

we can find $\epsilon \in \mathbb{R}^d$ such that

$$\mathbb{P}\left[R(u) \leq R(u+\delta)\right] \geq 1 - \epsilon \tag{B.130}$$

$$\mathbb{P}\left[R(u+\delta) \leq R(u)\right] \geq 1 - \epsilon. \tag{B.131}$$

However, by assumption, $\mathbb{P}\left[R(u) = R(u+\delta)\right] < c$. Therefore,

$$\mathbb{P}\left[R(u) \leq R(u+\delta)\right] \geq 1 - \epsilon \tag{B.132}$$

$$\mathbb{P}\left[R(u+\delta) < R(u)\right] \geq 1 - \epsilon - c, \tag{B.133}$$

which implies

$$1 = \mathbb{P}\left[R(u) \leq R(u+\delta)\right] + \mathbb{P}\left[R(u+\delta) < R(u)\right] \geq 2 - 2\epsilon - c \geq \frac{5}{3} - \frac{2}{3}c > 1. \tag{B.134}$$

By contradiction, the quantity must not be differentiable at any $u = u'$. □

B.3.2 PQE-GG: Gaussian-based Measure and Gaussian Shapes

In Section 3.5.1, we presented the following PQE-LH formulation for Lebesgue measures and half-lines:

$$d_z^{\mathsf{PQE\text{-}LH}}(u, v) \triangleq \sum_i \alpha_i \cdot \Big(1 - \exp\big(-\sum_j (u_{i,j} - v_{i,j})^+\big)\Big). \tag{3.10}$$

Here, $u_{i,j}$ and $v_{i,j}$ receive zero gradient when $u_{i,j} \leq v_{i,j}$.

Gaussian shapes parametrization. We therefore consider a set parametrization where no one set is entirely contained in a different set— the regions regions $\subset \mathbb{R}^2$ between an axis and a 1D Gaussian density function of fixed variance $\sigma^2_{\mathsf{shape}} = 1$. That

is, for each given $u \in R$, we consider sets

$$A_{\mathcal{N}}(\mu) \triangleq \{(a, b) \colon b \in [0, f_{\mathcal{N}}(a; \mu, 1)]\}, \tag{B.135}$$

where $f_{\mathcal{N}}(b; \mu, \sigma^2)$ denotes the density of 1D Gaussian $\mathcal{N}(\mu, \sigma^2)$ with mean μ and variance σ^2 evaluated at b. Since the Gaussian density function have unbounded support, these sets, which are translated versions of each other, never have one set fully contained in another. For latent $u \in \mathbb{R}^{h \times k}$ reshaped as 2D, our set parametrizations are,

$$u \to A_{i,j}(u) \triangleq A_{\mathcal{N}}(u_{i,j}), \qquad i \in [h], j \in [k]. \tag{B.136}$$

A Gaussian-based measure. These subsets of $\mathbb{R}^2$ always have Lebesgue measure 1, which would make PQE symmetrical (if used with a (scaled) Lebesgue measure). Thus, we use an alternative $\mathbb{R}^2$ measure given by the product of a $\mathbb{R}$ Lebesgue measure on the b-dimension (*i.e.*, dimension of the function value of the Gaussian density) and a $\mathbb{R}$ Gaussian measure on the a-dimension (*i.e.*, dimension on the input of the Gaussian density) centered at 0 with *learnable* variances $(\sigma^2_{\mathsf{measure}})_{i,j}$. To avoid being constrained by the bounded total measure of 1, we also optimize learnable positive scales $c_{i,j} > 0$. Hence, the each Poisson process has a mean measure as the product of a $\mathbb{R}$ Lebesgue measure and a $\mathbb{R}$ Gaussian with learnable standard deviation, then scaled with a learnable scale.

Note that the Gaussian measure should not be confused with the Gaussian shape. Their parameters also are fully independent with one another.

Computing measures of Gaussian shapes and their intersections. The intersection of two such Gaussian shapes is formed by two Gaussian tail shapes, reflected around the middle point of the two Gaussian means (since they have the same standard deviation $\sigma^{\mathsf{shape}} = 1$). Hence, it is sufficient to describe how to integrate a Gaussian density on a Gaussian measure over an interval. Applying this with different intervals would give the measure of the intersection, and the measures of the two Gaussian shapes. Omit indices i, j for clarity. Formally, we integrate the Gaussian density

$f_{\mathcal{N}}(a; u, \sigma^2_{\mathsf{shape}})$ over the centered Gaussian measure with variance $\sigma^2_{\mathsf{measure}}$, which has density $f_{\mathcal{N}}(a; 0, \sigma^2_{\mathsf{measure}})$:

$$\int c \cdot f_{\mathcal{N}}(a; u, \sigma^2_{\mathsf{shape}}) f_{\mathcal{N}}(a; 0, \sigma^2_{\mathsf{measure}}) \, \mathrm{d}a, \tag{B.137}$$

which is also another Gaussian integral (*e.g.*, considered as integrating the product measure along the a line of the form $y = x+u$). After standard algebraic manipulations (omitted here), we obtain

$$\int c \cdot f_{\mathcal{N}}(a; u, \sigma^2_{\mathsf{shape}}) f_{\mathcal{N}}(a; 0, \sigma^2_{\mathsf{measure}}) \, \mathrm{d}a \tag{B.138}$$

$$= \frac{c \cdot \exp\left(-u^2/\sigma^2_{\mathsf{total}}\right)}{\sqrt{2\pi\sigma^2_{\mathsf{total}}}} \int f_{\mathcal{N}} \left(a; u\frac{\sigma^2_{\mathsf{measure}}}{\sigma^2_{\mathsf{total}}}, \frac{\sigma^2_{\mathsf{shape}}\sigma^2_{\mathsf{measure}}}{\sigma^2_{\mathsf{total}}} \right) \mathrm{d}a, \tag{B.139}$$

for

$$\sigma^2_{\mathsf{total}} \triangleq \sigma^2_{\mathsf{shape}} + \sigma^2_{\mathsf{measure}}. \tag{B.140}$$

This can be easily evaluated using statistical computing packages that supports computing the error function and/or Gaussian CDF. Moreover, this final form is also readily differentiable with standard gradient formulas. To summarize,

- each set $A(u)$ has total measure

$$\frac{c}{\sqrt{2\pi\sigma^2_{\mathsf{total}}}} \exp\left(-u^2/\sigma^2_{\mathsf{total}}\right); \tag{B.141}$$

- the intersection of $A(v)$ and $A(u_2)$, for $v \leq u_2$ has measure

$$\frac{c \cdot \exp\left(-u_2^2/\sigma^2_{\mathsf{total}}\right)}{\sqrt{2\pi\sigma^2_{\mathsf{total}}}} \int_{-\infty}^{\frac{v+u_2}{2}} f_{\mathcal{N}} \left(a; u_2\frac{\sigma^2_{\mathsf{measure}}}{\sigma^2_{\mathsf{total}}}, \frac{\sigma^2_{\mathsf{shape}}\sigma^2_{\mathsf{measure}}}{\sigma^2_{\mathsf{total}}} \right) \mathrm{d}a \tag{B.142}$$

$$+ \frac{c \cdot \exp\left(-v^2/\sigma^2_{\mathsf{total}}\right)}{\sqrt{2\pi\sigma^2_{\mathsf{total}}}} \int_{\frac{v+u_2}{2}}^{+\infty} f_{\mathcal{N}} \left(a; v\frac{\sigma^2_{\mathsf{measure}}}{\sigma^2_{\mathsf{total}}}, \frac{\sigma^2_{\mathsf{shape}}\sigma^2_{\mathsf{measure}}}{\sigma^2_{\mathsf{total}}} \right) \mathrm{d}a. \tag{B.143}$$

Interpretation and representing any total order. Consider two Gaussian shapes $A(v)$ and $A(u_2)$. Note that the Gaussian-based measure μ_{Gaussian} is symmetric

around and centered at 0. Therefore,

$$|v| < |u_2| \implies \mu_{\mathsf{Gaussian}}(A(v)) > \mu_{\mathsf{Gaussian}}(A(u_2)) \tag{B.144}$$

$$\implies \mu_{\mathsf{Gaussian}}(A(v) \setminus A(u_2)) > \mu_{\mathsf{Gaussian}}(A(u_2) \setminus A(v)). \tag{B.145}$$

Moreover, scaling the rates of a Poisson makes it more concentrated (as a Poisson's mean grows as the square of its standard deviation) so that $\lim_{c\to\infty} \mathbb{P}\left[\mathrm{Pois}(c\mu_1) \leq \mathrm{Pois}(c\mu_2)\right] = \mathbf{1}_{\mu_1<\mu_2}$ for $\mu_1 \neq \mu_2$. Then any total order can be represented as the limit of a Poisson process with Gaussian shapes, with the shapes' having their means arranged according to the total order, as the scale on the Gaussian-based measure grows to infinity.

B.3.3 Theoretical Guarantees for PQEs

Theorem 3.5.2 (Distortion and violation of PQEs). Under the assumptions of Section 3.4, *any* quasimetric space with size n and treewidth t admits a PQE-LH and a PQE-GG with distortion $\mathcal{O}(t \log^2 n)$ and violation 1, with an expressive encoder (*e.g.*, a ReLU network with ≥ 3 layers and polynomial width).

In Section 3.5.4, we presented the above theoretical distortion and violation guarantees for PQE-LH and PQE-GG. Furthermore, we commented that the same guarantees apply to more generally to PQEs satisfying a mild condition. Here, we first precisely describe this condition, show that PQE-LH and PQE-GG do satisfy it, state and prove the general result, and then show the above as a straightforward corollary.

The Concentration Property

Recall that PQEs are generally defined with measures μ and set parametrizations A as

$$d_z^{\mathsf{PQE}}(u, v; \mu, A, \alpha) \triangleq \sum_i \alpha_i \cdot \mathbb{E}_{\pi_z \sim \Pi_z^{\mathsf{PQE}}(\mu_i, A_i)} \left[\pi_z(u, v)\right], \tag{3.14}$$

where

$$\mathbb{E}_{\pi_z \sim \Pi_z^{\mathsf{PQE}}(\mu, A)}[\pi_z(u, v)] \triangleq 1 - \prod_j \mathbb{P}\left[N_j(A_j(u)) \leq N_j(A_j(v))\right]. \tag{3.13}$$

Because the measures μ and set parametrizations A themselves may have parameters (*e.g.*, as in PQE-GG), we consider them as classes of PQEs. *E.g.*, PQE-GG is a class of PQEs such that the μ is the specific Gaussian-based form, and A is the specific Guassian-shape.

Definition B.3.2 (Concetration Property of PQEs)**.** Consider a PQE class with h mixtures of quasipartition distributions, each from k Poisson processes. We say that it has concentration property if it satisfies the following. Consider any finite subset of $\mathcal{X}' \subset \mathcal{X}$, and arbitrary function $g\colon \mathcal{X} \to \mathbb{R}^{h\times k}$. There exists a sequence of $((f^{(n)}, \mu^{(n)}, A^{(n)})_n$ such that

- $f^{(n)}\colon \mathcal{X}' \to \mathbb{R}^d$,
- $\mu^{(n)}, A^{(n)}$ are valid members of this PQE,
- $\mathbb{E}_{\pi_z\sim\Pi_z^{\mathsf{PQE}}(\mu_i,A_i)}\left[\pi_z(f^{(n)}(x'), f^{(n)}(y'))\right]$ uniformly converges to $1-\prod_j \mathbf{1}_{g(x)_{i,j}\le g(y)_{i,j}}$, over all mixtures i and pairs $x, y \in \mathcal{X}'$.

A sufficient condition. It suffices to make the probabilities

$$(x, y, i, j) \to \mathbb{P}\left[N_j(A_j(u)) \le N_j(A_j(v))\right], \tag{B.146}$$

along some PQE sequence uniformly converge to the indicators

$$(x, y, i, j) \to \mathbf{1}_{g(x')_{i,j}\le g(y')_{i,j}}. \tag{B.147}$$

This is sufficient since product of bounded functions is uniformly convergent, if each function is. Both statements below together form **a sufficient condition** for Equation (B.146) to uniformly converge to Equation (B.147):

1. For any g, there exists a specific PQE of this class satisfying
   - Measures (of set differences) are consistent with g with some margin $\epsilon > 0$:

$\forall i \in [h], j \in [k], x \in \mathcal{X}', y \in \mathcal{X}',$

$$\begin{aligned}
& g(x)_{i,j} < g(y)_{i,j} \\
\iff & \mu_{i,j}(A_{i,j}(f(x)) \setminus A_{i,j}(f(y))) + \epsilon < \mu_{i,j}(A_{i,j}(f(y)) \setminus A_{i,j}(f(x))) \\
& g(x)_{i,j} = g(y)_{i,j} \\
\iff & \mu_{i,j}(A_{i,j}(f(x)) \setminus A_{i,j}(f(y))) = \mu_{i,j}(A_{i,j}(f(y)) \setminus A_{i,j}(f(x))) = 0.
\end{aligned}$$

- Either of the following:

  - One side must be zero: $\forall i \in [h], j \in [k], x \in \mathcal{X}, y \in \mathcal{X},$

$$(\mu_{i,j}(A_{i,j}(f(x)) \setminus A_{i,j}(f(y)))) (\mu_{i,j}(A_{i,j}(f(y)) \setminus A_{i,j}(f(x)))) = 0, \tag{B.148}$$

  - Max measure is bounded by some constant $c > 0$:

$$\max_{x,y,i,j} \mu_{i,j}(A_{i,j}(f(x)) \setminus A_{i,j}(f(y))) \leq c. \tag{B.149}$$

2. For any given specific PQE of this class, for any positive scale $d > 0$, there is another PQE (with same formulation) whose measures (of set differences) equal exactly those of the given PQE scaled by d.

We now show that this is a sufficient condition. Note that a Poisson distribution has standard deviation equal to square root of its mean. This means that as we scale the rate of a Poisson, it becomes more concentrated. Applying to Poisson race probability, we have, for $0 \leq \mu_1 + \epsilon < \mu_2$,

- one direction of Poisson race probability:

$$\mathbb{P}\left[\text{Pois}(d\cdot\mu_1) \le \text{Pois}(d\cdot\mu_2)\right] \tag{B.150}$$

$$\ge \mathbb{P}\left[|\text{Pois}(d\cdot\mu_2) - \text{Pois}(d\cdot\mu_1) - d(\mu_2-\mu_1)| \le d(\mu_2-\mu_1)\right] \tag{B.151}$$

$$\ge 1 - \frac{\mu_1+\mu_2}{d(\mu_2-\mu_1)^2} \tag{B.152}$$

$$\ge \begin{cases} 1-\frac{2}{d\epsilon} & \text{if } \mu_1 = 0 \\ 1-\frac{2c}{d\epsilon^2} & \text{if } \mu_2 < c; \end{cases} \tag{B.153}$$

- the other direction of Poisson race probability:

$$\mathbb{P}\left[\text{Pois}(d\cdot\mu_2) \le \text{Pois}(d\cdot\mu_1)\right] \tag{B.154}$$

$$\le \mathbb{P}\left[|\text{Pois}(d\cdot\mu_2) - \text{Pois}(d\cdot\mu_1) - d(\mu_2-\mu_1)| \ge d(\mu_2-\mu_1)\right] \tag{B.155}$$

$$\le \frac{\mu_1+\mu_2}{d(\mu_2-\mu_1)^2} \tag{B.156}$$

$$\le \begin{cases} \frac{2}{d\epsilon} & \text{if } \mu_1 = 0 \\ \frac{2c}{d\epsilon^2} & \text{if } \mu_2 < c. \end{cases} \tag{B.157}$$

Therefore, applying to scaled versions of the PQE from Item 1 above, we have thus obtained the desired sequence, where Equation (B.146) uniformly converges to Equation (B.147) with rate $\mathcal{O}(1/d)$.

Lemma B.3.3. PQE-LH and PQE-GG both have the concentration property.

Proof of Lemma B.3.3. We show that both classes satisfy the above sufficient condition.

- PQE-LH: Lebesgue measure λ and half-lines.

  WLOG, since $\mathcal{X}$ is countable, we assume that g satisfies

$$g(x)_{i,j} \ne g(y)_{i,j} \implies |g(x)_{i,j} - g(y)_{i,j}| > 1, \qquad \forall i \in [h], j \in [k], x \in \mathcal{X}', y \in \mathcal{X}'. \tag{B.158}$$

The encoder in Item 1 above $f\colon \mathcal{X} \to \mathbb{R}^{h\times k}$ can simply be g. We then have

$$\mu_{i,j}(A_{i,j}(f(y))\backslash A_{i,j}(f(x))) = \mathrm{Leb}((-\infty, g(y)]\backslash(-\infty, g(x)]) = (g(y)_{i,j} - g(x)_{i,j})^+. \tag{B.159}$$

This ensures that one side is always zero. Furthermore, scaling can be done by simply scaling the encoder f. Hence, PQE-LH satisfies this constraint.

- PQE-GG: Gaussian-based measure and Gaussian shapes (see Appendix B.3.2).

  Because $\mathcal{X}'$ is finit, we can have positive constant margin for the PQE requirements in Item 1. (Infinite $\mathcal{X}'$ does not work because the total measure is finite (for a specific PQE-GG with specific values of the scaling).) Concretely, we satisfy both requirements via

  - in descending order of $g(\cdot)_{i,j}$ we assign Gaussian shapes increasingly further from the origin;
  - scaling comes from that we allow scaling the Gaussian-based measure.

  Hence, PQE-GG satisfies this constraint for finite $\mathcal{X}$.

□

A General Statement

We now state the general theorem for PQEs with the above concentration property.

Theorem B.3.4 (Distortion and violation of PQEs (General)). Consider any PQE class with the concentration property. Under the assumptions of Section 3.4, *any* quasimetric space with size n and treewidth t admits such a PQE with distortion $\mathcal{O}(t \log^2 n)$ and violation 1, with an expressive encoder (*e.g.*, a ReLU network with ≥ 3 hidden layers, $\mathcal{O}(n)$ hidden width, and $\mathcal{O}(n^2)$ quasipartition distributions, each with $\mathcal{O}(n)$ Poisson processes.).

Before proving this more general theorem, let us extend a result from Mémoli et al. (2018).

Lemma B.3.5 (Quasimetric Embeddings with Low Distortion; Adapted from Corollary 2 in Mémoli et al. (2018)). Let $M = (X, d)$ be a quasipseudometric space with treewidth t, and $n = |X|$. Then M admits an embedding into a convex combination (*i.e.*, scaled mixture) of $\mathcal{O}(n^2)$ quasipartitions with distortion $\mathcal{O}(t \log^2 n)$.

Proof of Lemma B.3.5. The distortion bound is proved in Corollary 2 in (Mémoli et al., 2018), which states that any quasipseudometric space with n elements and t treewidth admits an embedding into a convex combination of quasipartitions with distortion $\mathcal{O}(t \log^2 n)$.

To see that n^2 quasipartitions suffice, we scrutinize their construction of quasipartitions in Algorithm 2 of (Mémoli et al., 2018), reproduced below as Algorithm 2.

Algorithm 2 Random quasipartition of a graph with bounded treewidth. Algorithm 2 of (Mémoli et al., 2018).

Input: A digraph G of treewidth t, a hierarchical tree of separators of G (H, f) with width t, and $r > 0$.

Output: A random r-bounded quasipartition R.

Initialization: Set $G^* = G$, $H^* = H$ and $R = E(G)$. Perform the following recursive algorithm on G^* and H^*.

Step 1. Pick $z \in [0, r/2]$ uniformly at random.

Step 2. If $|V(G^*)| \leq 1$,terminate the current recursive call. Otherwise pick the set of vertices $K = G^*$. Let $H_1, \ldots, H_m$ be the sub-trees of H^* below $\mathsf{root}(H^*)$ that are hierarchical trees of separators of $C_1, \ldots, C_m$ respectively.

Step 3. For all $(u, v) \in E(G^*)$ remove (u, v) from R if one of the following holds:

(a) $d_G(u, x) > z$ and $d_G(v, x) \leq z$ for some vertex $x \in K$.

(b) $d_G(x, v) > z$ and $d_G(x, u) \leq z$ for some vertex $x \in K$.

Step 4. For all $i \in \{1, \ldots, m\}$ perform a recursive call of Steps 2-4 setting $G^* = G^*[C_i]$ and $H^* = H_i$.

Step 5. Once all branches of the recursive terminate, enforce transitivity on R: For all $u, v, w \in V(G)$ if $(u, v) \in R$ and $(v, w) \in R$, add (u, w) to R.

Many concepts used in Algorithm 2 are not relevant for our purpose (*e.g.*, r-bounded quasipartition). Importantly, we observe that for a given quasimetric space, the produced quasipartition is entirely determined by the random choice of z in Step 1, which is only used to compare with distance values between node pairs. Note that there are n^2 node pairs, whose minimum distance is exactly 0 (*i.e.*, distance from a node to itself). Since $z \geq 0$, there are at most n^2 choices of z that lead to at most n^2 different quasipartitions, for all possible values of r.

The construction used to prove Corollary 2 of (Mémoli et al., 2018) uses exactly quasipartitions given by this algorithm. Therefore, the lemma is proved. □

Lemma B.3.5 essentially proves the first half of Theorem B.3.4. Before proving the full Theorem B.3.4, we restate the following result from (Hiraguchi, 1951), which gives us a bound on how many total orders are needed to represent a general partial order (*i.e.*, quasipartition).

Theorem B.3.6 (Hiraguchi's Theorem (Hiraguchi, 1951; Bogart, 1973)). Let (X, P) be a partially ordered set such that $|X| \geq 4$. Then there exists a mapping $f\colon X \to \mathbb{R}^{\lfloor |X|/2 \rfloor}$ such that

$$\forall x, y \in X, \qquad xPy \iff f(x) \leq f(y) \text{ coordinate-wise}. \tag{B.160}$$

Proof of Theorem B.3.4. It immediately follows from Lemma B.3.5 and Theorem B.3.6 that any quasimetric space with n elements and treewidth t admits an embedding with distortion $\mathcal{O}(t \log^2 n)$ into a convex combination of n^2 quasipartitions, each represented with an intersection of $\mathcal{O}(n)$ total orders.

Because the PQE class has concentration property, for any finite quasimetric space, we can simply select a PQE that is close enough to the desired convex combination of n^2 quasipartitions, to obtain distortion $\mathcal{O}(t \log^2 n)$. Since each Poisson process in PQE takes a constant number of latent dimensions, we can have such a PQE with $\mathcal{O}(n^3)$-dimensional latents and n^2 quasipartition distributions.

It remains only to prove that we can compute such required latents using the described architecture.

Consider any $x \in \mathcal{X} \subset \mathbb{R}^d$. Since $\mathcal{X}$ is finite, we can always find direction $u_x \in \mathbb{R}^d$ such that $\forall y \in \mathcal{X} \setminus \{x\}$, $y^\mathsf{T} u_x \neq x^\mathsf{T} u_x$. That is, x has a unique projection onto u_x. Therefore, we can have $c, b_+, b_- \in \mathbb{R}$ such that

$$c \cdot u_x^\mathsf{T} x + b_+ = 1 \tag{B.161}$$

$$-c \cdot u_x^\mathsf{T} x + b_- = 1, \tag{B.162}$$

but for $y \in \mathcal{X} \setminus \{x\}$, we have, for some $a > 0$, either

$$c \cdot u_x^\mathsf{T} y + b_+ = -a \tag{B.163}$$

$$-c \cdot u_x^\mathsf{T} y + b_- = a + 2, \tag{B.164}$$

or

$$c \cdot u_x^\mathsf{T} y + b_+ = a + 2 \tag{B.165}$$

$$-c \cdot u_x^\mathsf{T} y + b_- = -a. \tag{B.166}$$

Then, consider computing two of the first layer features as, on input z,

$$[\mathrm{ReLU}(c \cdot u_x^\mathsf{T} z + b_+) \quad \mathrm{ReLU}(-c \cdot u_x^\mathsf{T} z + b_-)], \tag{B.167}$$

which, if $z = x$, is $[1, 1]$; if $z \neq x$, is either $[0, 2 + a]$ or $[2 + a, 0]$, for some $a > 0$.

Then, one of the second layer features may sum these two features and threshold it properly would single out x, *i.e.*, activate only when input is x.

After doing this for all $x \in \mathcal{X}$, we obtain an n-dimensional second layer feature space that is just one-hot features.

The third layer can then just be a simple embedding look up, able to represent any embedding, including the one allowing a PQE to have distortion $\mathcal{O}(t \log n)$, as described above.

Because quasimetric embeddings naturally have violation 1, this concludes the proof. □

Proof of Theorem 3.5.2: Distortion and violation of PQEs

Proof of Theorem 3.5.2. Lemma B.3.3 and Theorem B.3.4 imply the result. To see that polynomial width is sufficient, note that the hidden width are polynomial by Theorem B.3.4, and that the embedding dimensions needed to represent each of the $\mathcal{O}(n^3)$ Poisson processes is constant 1 in both PQE-LH and PQE-GG. Hence the latent space is also polynomial. This concludes the result. □

Discussions

Dependency on $\log n$. $\log n$ dependency frequently occurs in distortion results. Perhaps the most well-known ones are Bourgain's Embedding Theorem (Bourgain, 1985) and the Johnson-Lindenstrauss Lemma (Johnson and Lindenstrauss, 1984), which concern *metric* embeddings into Euclidean spaces.

Dependency on treewidth t. Treewidth t here works as a complexity measure of the quasimetric. We will use a simple example to illustrate why low-treewidth is easy. Consider the extreme case where the quasimetric is the shortest-path distance on a tree, whose each edge is converted into two opposing directed ones and assigned arbitrary non-negative weights. Such a quasimetric space has treewidth 1 (see Definition 3.2.2). On a tree,

1. the shortest path between two points is fixed, regardless of the weights assigned,
2. for each internal node u and one of its child c, the followings are quasipartitions:

$$d'_{01}(x, y) \triangleq \mathbf{1}_{\text{shortest path from } x \text{ to } y \text{ passes } (u,c)}$$
$$d''_{01}(x, y) \triangleq \mathbf{1}_{\text{shortest path from } x \text{ to } y \text{ passes } (c,u)}.$$

Hence it can be *exactly* represented as a convex combination of quasipartitions. However, both of observations becomes false when the graph structure becomes more complex (higher treewidth) and the shortest paths can are less well represented as tree paths of the tree composition.

Comparison with unconstrained MLPs. Theorem B.3.4 requires a poly-width encoder to achieve low distortion. This is comparable with deep unconstrained MLPs trained in NTK regime, which can reach 0 training error (distortion 1 on training set) in the limit but also requires polynomial width (Arora et al., 2019b).

Quasipseudometrics and infinite distances. Theorem B.3.4 relies on our assumptions that $(\mathcal{X}, d)$ is not a quasipseudometric space and has all finite distances. In fact, if we allow a PQE to have infinite convex combination weights, it can readily represent quasipseudometric spaces with infinite distances. Additionally, PQE can still well approximate the quasimetric space with infinities replaced with any sufficiently large finite value (*e.g.*, larger than the maximum finite distance). Thus, this limit is generally not important in practice (*e.g.*, learning γ-discounted distances), where a large value and infinity are usually not treated much differently.

Optimizing quasimetric embeddings. From Theorem B.3.4, we know that optimizing PQEs over the training set S w.r.t. distortion achieves low distortion (and optimal violation by definition). While directly optimizing distortion (or error on log distance or distance ratios, equivalently) seems a valid choice, such objectives do not always train stably in practice, with possible infinities and zeros. Often more stable losses are used, such as MSE over raw distances or γ-discounted distances γ^d, for $\gamma \in (0, 1)$. These objectives do not directly relate to distortion, except for some elementary loose bounds. To better theoretically characterize their behavior, an alternative approach with an average-case analysis might be necessary.

B.3.4 Implementing Poisson Quasimetric Embeddings (PQEs)

Section 3.5.2 mentioned a couple implementation techniques for PQEs. In this section, we present them in full details.

Normalized Measures

Consider a PQE whose each of j expected quasipartitions is defined via k Poisson processes, with set parametrizations $u \to A_{i,j}(u), i \in [h], j \in [k]$. To be robust to the choice of k, we instead use the normalized set parametrizations $A'_{i,j}$'s:

$$A'_{i,j}(u) \triangleq A_{i,j}(u)/k, \qquad i \in [h], j \in [k]. \quad \text{(B.168)}$$

This does not change the PQE's concentration property (Definition B.3.2) or its theoretical guarantees (*e.g.*, Theorems 3.5.2 and B.3.4).

Outputting γ-Discounted Distances

Recall the PQE quasimetric formulation in Equation (3.14), for $\alpha_i \geq 0$, and encoder $f\colon \mathcal{X} \to \mathbb{R}^d$ (with set parametrizations $A_{i,j}$'s and measures $\mu_{i,j}$'s):

$$\hat{d}(x,y) \triangleq \sum_i \alpha_i \left(1 - \prod_j \mathbb{P}\left[\mathrm{Pois}(\mu_{i,j}(A^f_{i,j}(x) \setminus A^f_{i,j}(y)) \leq \mathrm{Pois}(\mu_{i,j}(A^f_{i,j}(y) \setminus A^f_{i,j}(x))\right]\right), \tag{3.14}$$

where we used shorthands $A^f_{i,j}(x) \triangleq A_{i,j}(f(x))$.

With discount factor $\gamma \in (0,1)$, we can write the γ-discounted PQE distance as

$$\gamma^{\hat{d}(x,y)} = \prod_i \Big(\underbrace{\gamma^{\alpha_i}}_{\text{a scalar that can take value in any } (0,1)}\Big)^{1 - \prod_j \mathbb{P}\left[\mathrm{Pois}(\mu_{i,j}(A^f_{i,j}(x) \setminus A^f_{i,j}(y)) \leq \mathrm{Pois}(\mu_{i,j}(A^f_{i,j}(y) \setminus A^f_{i,j}(x))\right]}. \tag{B.169}$$

Therefore, instead of learning $\alpha_i \in [0, \infty)$, we can learn bases $\beta_i \in (0,1)$ such and define the γ-discounted PQE distance as

$$\gamma^{\hat{d}(x,y)} \triangleq \prod_i \beta_i^{1 - \prod_j \mathbb{P}\left[\mathrm{Pois}(\mu_{i,j}(A^f_{i,j}(x) \setminus A^f_{i,j}(y)) \leq \mathrm{Pois}(\mu_{i,j}(A^f_{i,j}(y) \setminus A^f_{i,j}(x))\right]}. \tag{B.170}$$

These bases $\beta_i \in (0,1)$ can be parametrized via a sigmoid transform. Consider quasimetric learning w.r.t. errors on γ-discounted distances (*e.g.*, MSE). Unlike the parametrization with directly learning the convex combination weights α_i's, such a parametrization (that learns the bases β_i's) does not explicitly include γ and thus can

potentially be more stable for a wider range of γ choices.

Initialization. Consider learning bases β_i's via a sigmoid transform: learning b_i and defining $\beta_i \triangleq \sigma(b_i)$. We must take care in initializing these b_i's so that $\sigma(b_i)$'s are not too close to 0 or 1, since we take a product of powers with these bases. To be robust to different h numbers of quasipartition distributions, we initialize the each b_i to be from the uniform distribution

$$\mathcal{U}[\sigma^{-1}(0.5^{2/h}), \sigma^{-1}(0.75^{2/h})], \tag{B.171}$$

which means that, at initialization,

$$\prod_{i\in[h]} \beta_i^{0.5} = \prod_{i\in[h]} \sigma(b_i)^{0.5} \in [0.5, 0.75], \tag{B.172}$$

providing a good range of initial outputs, assuming that the exponents (expected outputs of quasipartition distributions) are close to 0.5. Alternatively, b_i's maybe parametrized by a deep linear network, a similar initialization is employed. See Appendix B.3.4 below for details.

Learning Linear/Convex Combinations with Deep Linear Networks

Deep linear networks have the same expressive power as regular linear models, but enjoy many empirical and theoretical benefits in optimization (Saxe et al., 2013; Pennington et al., 2018; Huh et al., 2021). Specifically, instead of directly learning a matrix $\in \mathbb{R}^{m\times n}$, a deep linear network (with bias) of l layers learns a sequence of

matrices

$$M_1 \in \mathbb{R}^{m_1 \times n} \tag{B.173}$$

$$M_2 \in \mathbb{R}^{m_2 \times m_1} \tag{B.174}$$

$$\vdots \quad \vdots \tag{B.175}$$

$$M_{l-1} \in \mathbb{R}^{m_{l-1} \times m_{l-2}} \tag{B.176}$$

$$M_l \in \mathbb{R}^{m \times m_{l-1}} \tag{B.177}$$

$$B \in \mathbb{R}^{m \times n}, \tag{B.178}$$

where the linear matrix can be obtained with

$$M_l \; M_{l-1} \ldots M_2 \; M_1 + B, \tag{B.179}$$

and we require

$$\min(m_1, m_2, \ldots, m_{l-1}) \geq \min(m, n). \tag{B.180}$$

In our case, the convex combination weights for the quasipartition distributions often need to be large, in order to represent large quasimetric distances; in Poisson process mean measures with learnable scales (*e.g.*, the Gaussian-based measure described in Appendix B.3.2), the scales may also need to be large to approximate particular quasipartitions (see Appendix B.3.3).

Therefore, we choose to use deep linear networks to optimize these parameters. In particular,

- **For the convex combination weights for h quasipartition distributions,**
  - When learning the convex combination weights $\{\alpha_i\}_{i \in [h]}$, we use a deep linear network to parametrize a matrix $\in \mathbb{R}^{1 \times h}$ (*i.e.*, a linear map from $\mathbb{R}^h$ to $\mathbb{R}$), which is then viewed as a vector $\in \mathbb{R}^h$ and applied an element-wise square transform $a \to a^2$ to obtain non-negative weights $\alpha \in [0, \infty)^h$;
  - When learning the bases for discounted quasimetric distances β_i's (see Appendix B.3.4), we use a deep linear network to parametrize a matrix

$\in \mathbb{R}^{h\times 1}$, which is then viewed as a vector $\in \mathbb{R}^h$ and applied an element-wise sigmoid transform $a \to \sigma(a)$ to obtain bases $\beta \in (0,1)^h$.

Note that here we parametrize a matrix $\in \mathbb{R}^{h\times 1}$ rather than $\mathbb{R}^{1\times h}$ as above for α_i's. The reason for this choice is entirely specific to the initialization scheme we use (*i.e.*, (fully-connected layer weight matrix initialization, as discussed below). Here the interpretation of a linear map is no longer true. If we use $\mathbb{R}^{1\times h}$, the initialization method would lead to the entries distributed with variance roughly $1/n$, which only makes sense if they are then added together. Therefore, we use $\mathbb{R}^{h\times 1}$, which would lead to constant variance.

- **For scales of the Poisson process mean measure, such as PQE-GG,** we consider a slightly different strategy.

  Consider a PQE formulation with $h \times k$ independent Poisson processes, from which we form h quasipartition distributions, each from k total orders parametrized by k Poisson processes. The Poisson processes are defined on sets

  $$\{A_{i,j}\}_{i\in[h],j\in[k]}, \tag{B.181}$$

  use mean measures

  $$\{\mu_{i,j}\}_{i\in[h],j\in[k]}, \tag{B.182}$$

  and set parametrizations

  $$\{u \to A_{i,j}(u)\}_{i\in[h],j\in[k]}, \tag{B.183}$$

  to compute quantities

  $$\mu_{i,j}(A_{i,j}(u) \setminus A_{i,j}(v)) \qquad \text{for } u \in \mathbb{R}^d, v \in \mathbb{R}^d, i \in [h], j \in [k]. \tag{B.184}$$

  Scaling each mean measure independently. Essentially, adding learnable scales (of mean measures) $w \in [0,\infty)^{h\times k}$ (or, equivalently, $\{w_{i,j} \in [0,\infty)\}_{i,j}$)

gives a scaled set of measures

$$\{w_{i,j} \cdot \mu_{i,j}\}_{i\in[h],j\in[k]}. \tag{B.185}$$

This means that the quantities in Equation (B.184) becomes respectively scaled as

$$w_{i,j} \cdot \mu_{i,j}(A_{i,j}(u) \setminus A_{i,j}(v)) \qquad \text{for } u \in \mathbb{R}^d, v \in \mathbb{R}^d, i \in [h], j \in [k]. \tag{B.186}$$

Convex combinations of *all* measures. However, we can be more flexible here, and allow not just scaling each measure independently, but also *convex combinations of all measures*. Instead of having w as a collection of $h \times k$ scalar numbers $\in [0, \infty)$, we have a collection of $(h \times k)$ vectors each having length $(h \times k)$ (or $h \times k$-shape tensors)

$$\{w_{i,j} \in [0, \infty)^{h\times k}\}_{i\in[h],j\in[k]}, \tag{B.187}$$

and have the quantities in Equation (B.184) respectively scaled and combined as

$$\sum_{i',j'} w_{i,j,i',j'} \cdot \mu_{i',j'}(Ai', j'(u) \setminus A_{i',j'}(v)) \qquad \text{for } u \in \mathbb{R}^d, v \in \mathbb{R}^d, i \in [h], j \in [k]. \tag{B.188}$$

Note that these still are valid Poisson processes for a PQE. Specifically, the new Poisson processes now all use the same set parametrization (as the collection of original ones), with different measures (as different weighted combinations of the original measures). This generalizes the case where each mean measure is scaled independently (as w can be diagonal).

Therefore, we will apply this more general strategy using **convex combinations of *all* measures**.

Similarly to learning the convex combination weights of quasipartition distribu-

tions, we collapse a deep linear network into a tensor $\in \mathbb{R}^{h\times k\times h\times k}$, and apply an element-wise square $a \to a^2$, result of which is used as the convex combination weights w to ensure non-negativity.

Initialization. For initializing the matrices $(M_1, M_2, \ldots, M_l)$ of a deep linear network (Equation (B.177)), we use the standard weight matrix initialization of fully-connected layers in PyTorch (Paszke et al., 2019). The bias matrix B (Equation (B.178)) is initialized to all zeros.

When used for learning the bases for discounted quasimetric distances β_i's (as described in Appendix B.3.4), we have a deep linear network parametrizing a matrix $\in \mathbb{R}^{h\times 1}$, initialized in the same way as above (including initializing B as all zeros). Consider the matrix up to before the last one:

$$M^* \triangleq M_{l-1} \cdot M_2 \; M_1 \in \mathbb{R}^{m_{l-1}\times 1}. \tag{B.189}$$

M^* is essentially a projection to be applied on each row of the last matrix $M_l \in \mathbb{R}^{h\times m_{l-1}}$, to obtain b_i (which is then used to obtain bases $\beta_i \triangleq \sigma(b_i)$). Therefore, we simply rescale the M^* subspace for each row of M_l and keep the orthogonal space intact, such that the projections would be distributed according to the distribution specified in Equation (B.171):

$$\mathcal{U}[\sigma^{-1}(0.5^{2/h}), \sigma^{-1}(0.75^{2/h})], , \tag{B.171}$$

which has good initial value properties, as shown in Appendix B.3.4.

Choosing h the Number of Quasipartition Distributions and k the Number of Poisson Processes for Each Quasipartition Distribution

A PQE (class) is defined with $h \times k$ independent Poisson processes with means $\{\mu_{i,j}\}_{i\in[h],j\in[k]}$ along with $h \times k$ set parametrizations $\{A_{i,j}\}_{i\in[h],j\in[k]}$. For k pairs of means and set parametrizations, we obtain a random quasipartition. A mixture (convex combination) of the resulting h random quasipartitions gives the quasimetric. The choices of μ and A are flexible. In this work we explore PQE-LH and PQE-GG

as two options, both using essentially the same measure and parametrization across all i, j (up to individual learnable scales). These two instantiations both perform well empirically. In this section we aim to provide some intuition on choosing these two hyperparameters h and k.

h the Number of Quasipartition Distributions Theoretical result Theorem B.3.4 suggest thats, for a quasimetric space with n elements, n^2 quasipartition distributions suffice to learn a low distortion embedding. Since this is a worst-case result, the practical scenario may require much fewer quasipartitions. For instance, Appendix B.3.3 shows that $\mathcal{O}(n)$ quasipartitions is sufficient for any quasimetric space with a tree structure. In our experiments, $h \in [8, 128]$ quasipartition distributions are used.

k the Number of Poisson Processes for Each Quasipartition Distribution (Random Partial Order) It is well-known that such intersection of sufficiently many total orders can represent *any* partial order (Trotter, 1995; Hiraguchi, 1951). This idea is equivalent with the dominance drawing dimension of directed graphs (Ortali and Tollis, 2019), which concerns an order embedding of the vertices to preserve the poset specified by the reachability relation. In this graph theoretical view, several results are known. (Felsner et al., 2010) prove that planar graphs have at most 8 dimension. (Ortali and Tollis, 2019) show that the dimension of any graph with n vertices is at most $\min(w_P, \frac{n}{2})$, where w_P the maximum size of a set of incomparable vertices. A simpler and more fundamental result can be traced to Hiraguchi from 1951:

Theorem B.3.6 (Hiraguchi's Theorem (Hiraguchi, 1951; Bogart, 1973)). Let (X, P) be a partially ordered set such that $|X| \geq 4$. Then there exists a mapping $f\colon X \to \mathbb{R}^{\lfloor |X|/2 \rfloor}$ such that

$$\forall x, y \in X, \qquad xPy \iff f(x) \leq f(y) \text{ coordinate-wise}. \tag{B.160}$$

Theorem B.3.6 states that $\frac{n}{2}$ dimensions generally suffice for any poset of size $n \geq 4$.

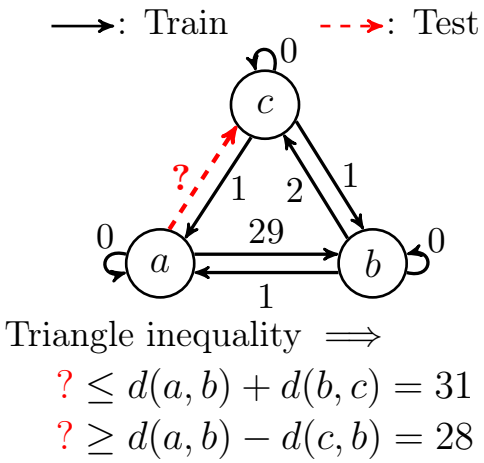

Figure B-4: The 3-element quasimetric space, and the training pairs. Training set contains all pairs except for (a, c). Arrows show quasimetric distances (rather than edge weights of some graph).

In our formulation, this means that using $k = \frac{n}{2}$ Poisson processes (giving $\frac{n}{2}$ random total orders) will be maximally expressive. In practice, this is likely unnecessary and sometimes impractical. In our experiments, we choose a small fixed number $k = 4$.

B.4 Experiment Settings and Additional Results

Computation power. All our experiments run on a single GPU and finish within 3 hours. GPUs we used include NVIDIA 1080, NVIDIA 2080 Ti, NVIDIA 3080 Ti, NVIDIA Titan Xp, NVIDIA Titan RTX, and NVIDIA Titan V.

B.4.1 Experiments from Section 3.3.2: A Toy Example

In Section 3.3.2 and Figure 3-2, we show experiment results on a simple 3-element quasimetric space.

Quasimetric space. The quasimetric space has 3 elements with one-hot features $\in \mathbb{R}^3$. Thequasimetric and training pairs are shown in Figure B-4.

Unconstrained network. The unconstrained network has architecture 6-128-128-32-1, with ReLU activations.

Metric embedding. The embedding space is 32-dimensional, upon which corresponding metric is applied. The encoder network has architecture 6-128-128-32, with ReLU activations.

Asymmetric dot products. The embedding space is 32-dimensional. The two inputs are encoded with a *different* encoder of architecture 6-128-128-32, with ReLU activations. Then the dot product of the two 32-dimensional vector is taken, which parametrizes a distance estimate

Poisson Quasimetric Embeddings. The embedding space is 32-dimensional, which parametrizes 8 quasimetric distributions, each from 4 independent Poisson processes using (scaled) Lebesgue measure and half-lines. We use deep linear networks, as described in Appendix B.3.4. A deep linear network (without bias) of architecture 8-32-32-1 parametrizes the convex combination weights $\{\alpha_i\}_{i\in[8]}$. Another deep linear network (without bias) of architecture 32-64-64-32 parametrizes convex combination weights of the mean measures $d \in [0,\infty)^{32\times 32}$. Note that these *do not* give many more effective parameters to PQEs as they are equivalent with simple linear transforms.

Optimization. All models are trained w.r.t. MSE on distances with the Adam optimizer (Kingma and Ba, 2014) with learning rate 0.0003 for 1000 iterations (without mini-batching since the training set has size 8).

Additional results. Results with additional formulations (together with the ones presented in Figure 3-2) are shown in Figure B-5.

B.4.2 Experiments from Section 3.5.5: Experiments

Triangle inequality regularizer. For methods that do not inherently respect triangle inequalities (*e.g.*, unconstrained networks and asymmetrical dot products), we explore training with a regularizer that encourages following these inequalities. By sampling random triplets uniformly over the training set, the regularizer is formulated

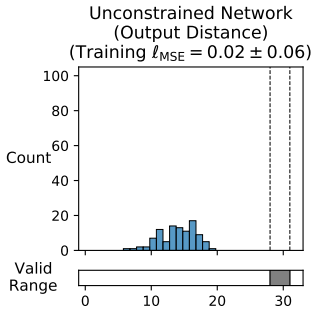

(a) Unconstrained network that directly predicts distance.

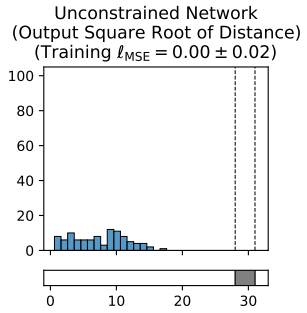

(b) Unconstrained network that predicts distance with a square $a \to a^2$ transform.

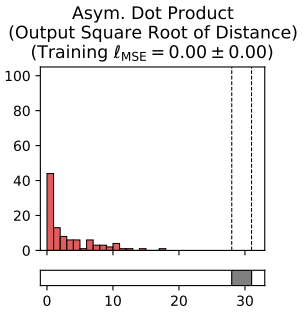

(c) Asymmetrical dot product that predicts distance with a square $a \to a^2$ transform.

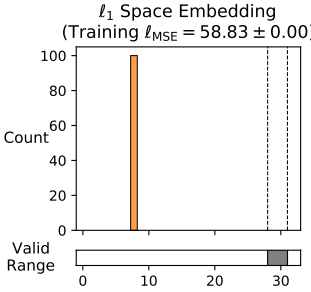

(d) Metric embedding into an ℓ_1 space.

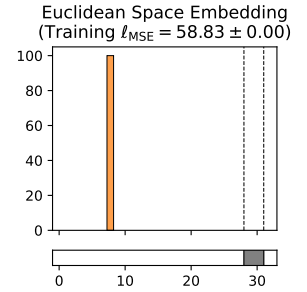

(e) Metric embedding into an Euclidean space.

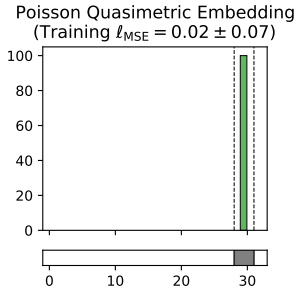

(f) Poisson Quasimetric Embedding specified in Appendix B.4.1.

Figure B-5: Training different formulations to fit training pairs distances via MSE, and using them to predict on the test pair. Plots show distribution of the prediction over 100 runs. Standard deviations of the training error are shown.

as,

$$\mathbb{E}_{x,y,z}\big[\max(0, \gamma^{\hat{d}(x,y)+\hat{d}(y,z)} - \gamma^{\hat{d}(x,z)})^2\big], \tag{B.190}$$

where the γ-discounted terms and the squared form allows easier balancing with the training loss, which, across all experiments, are MSEs on some γ-discounted distances.

PQE settings. Across all experiments of this section, when given an encoder architecture mapping input to an $\mathbb{R}^d$ latent space, we construct PQEs according to the following general recipe, to obtain the two PQEs settings used across all experiments: PQE-LH (PQE with Lebesgue measure and half-lines) and PQE-GG (PQE with Gaussian-based measure and Gaussian shapes, see see Appendix B.3.2):

- (Assuming d is a multiple of 4,) We use $h \triangleq= d/4$ quasipartition distributions, each given by $k \triangleq 4$ Poisson processes;
- A deep linear network (see Appendix B.3.4), is used for parametrizing the convex combination weights $\alpha \in \mathbb{R}^{d/4}$ or the bases $\beta \in \mathbb{R}^{d/4}$ (see Appendix B.3.4), we follow the initialization and parametrization described in Appendix B.3.4, with hidden sizes $[n_{\mathsf{hidden}}, n_{\mathsf{hidden}}, n_{\mathsf{hidden}}]$ (*i.e.*, 4 matrices/layers), where $n_{\mathsf{hidden}} \triangleq \max(64, 2^{1+\lceil \log_2(d/4) \rceil})$.
- For PQE-GG,
  - The learnable $\sigma^2_{\mathsf{measure}} \in (0, \infty)^d$ (one for each Poisson Process) is achieved by optimizing the log variance, which is initialized as all zeros.
  - The Gaussian-based measures need learnable scales. We use a deep linear network to parametrize the $[0, \infty)^{d \times d}$ weights for the convex combinations of measures, as described in Appendix B.3.4. Similarly, it has hidden sizes $[n_{\mathsf{hidden}}, n_{\mathsf{hidden}}, n_{\mathsf{hidden}}]$ (*i.e.*, 4 matrices/layers), where $n_{\mathsf{hidden}} \triangleq \max(64, 2^{1+\lceil \log_2 d \rceil})$.

Note that the PQEs add only a few extra effective parameters on top of the encoder (d for PQE-LH, and $d + d^2$ for PQE-GG), as the deep linear networks do not add extra effective parameters.

Mixed space metric embedding settings. Across all experiments of this section, when given an encoder architecture mapping input to an $\mathbb{R}^d$ latent space, we construct the metric embedding into mixed space as follows:

- (Assuming d is a multiple of 4,) We use (1) a $(d/2)$-dimensional Euclidean space (2) a $(d/4)$-dimensional ℓ_1 space, and a $(d/4)$-dimensional spherical distance space (without scale).

- Additionally, we optimize three scalar values representing the log weights of the convex combination to mix these spaces.

DeepNorm and WideNorm method overview and parameter count comparison with PQEs. Both DeepNorm and WideNorm parametrize asymmetrical norms. When used to approximate quasimetrics, they are applied as $\hat{d}(x, y) \triangleq f_{\mathsf{AsymNorm}}(f_{\mathsf{Enc}}(x) - f_{\mathsf{Enc}}(y))$, where f_{Enc} is the encoder mapping from data space to an $\mathbb{R}^d$ latent space and f_{AsymNorm} is either the DeepNorm or the WideNorm predictor on that latent space (Pitis et al., 2020).

- **DeepNorm** is a modification from Input Convex Neural Network (ICNN; Amos et al. (2017)), with restricted weight matrices and activation functions for positive homogeneity (a requirement of asymmetrical norms), and additional concave function for expressivity.

  For an input latent space of $\mathbb{R}^d$, consider an n-layer DeepNorm with width w (*i.e.*, ICNN output size) and the suggested intermediate MaxReLU activation and MaxMean final aggregation (see (Pitis et al., 2020) for details of these

functions). This DeepNorm predictor f_{DeepNorm} (on latent space) has

$$\begin{aligned}\#\text{parmaters of } f_{\mathsf{DeepNorm}} = & \underbrace{n \times (d \times w)}_{U \text{ matrices from input to each layer}} \\ & + \underbrace{(n-1) \times w^2}_{W \text{ matrices between neighboring layer activations}} \\ & + \underbrace{n \times w}_{\text{intermediate MaxReLU activations}} \\ & + \underbrace{w \times (4+5)}_{\text{concave function (with 5 components) parameters}} \\ & + \underbrace{1}_{\text{final MaxMean aggregation}} ,\end{aligned}$$

which is on the order of $\mathcal{O}(nw \max(d, w))$. In the common case where the hidden size w is chosen to be on the same magnitude as d, this becomes $\mathcal{O}(nd^2)$.

- **WideNorm** is based on the observation that

$$x \to \|W \text{ ReLU}(x :: -x)\|_2 \tag{B.191}$$

is an asymmetric norm when W is non-negative, where :: denotes vector concatenation. WideNorm then learns many such norms each with a different W matrix parameter, before (again) feeding the norm values into a concave function and aggregating them together with MaxMean.

For an input latent space of $\mathbb{R}^d$, consider a WideNorm with c such learned norms with W matrices of shape $\mathbb{R}_{\geq 0}^{(2d) \times w}$. This WideNorm predictor f_{WideNorm}

(on latent space), has

$$\begin{aligned}\#\text{parmaters of } f_{\mathsf{WideNorm}} = &\underbrace{c \times (2d \times w)}_{W \text{ matrices}} \\ &+ \underbrace{c \times (4+5)}_{\text{concave function (with 5 components) parameters}} \\ &+ \underbrace{1}_{\text{final MaxMean aggregation}},\end{aligned}$$

which is on the order of $\mathcal{O}(cdw)$. In the common case where both the number of components c and the output size of each component (before applying the $l2$-norm) are chosen to be on the same magnitude as d, this becomes $\mathcal{O}(d^3)$.

For both DeepNorm and WideNorm, their parameter counts are much larger than the number of effective parameters of PQEs (d for PQE-LH and $d + d^2$ for PQE-GG). For a 256-dimensional latent space, this difference can be on the order of $10^6 \sim 10^7$.

DeepNorm and WideNorm settings. Across all experiments of this section, we evaluate 2 DeepNorm settings and 3 WideNorm settings, all derived from the experiment setting of the original paper (Pitis et al., 2020). For both DeepNorm and WideNorm, we use MaxReLU activations, MaxMean aggregation, and concave function of 5 components. For DeepNorm, we use 3-layer networks with 2 different hidden sizes: 48 and 128 for the 48-dimensional latent space in random directed graphs experiments, 512 and 128 for the 512-dimensional latent space in the large-scale social graph experiments, 128 and 64 for the 128-dimensional latent space in offline Q-learning experiments. For WideNorm, we components of size 32 and experiment with 3 different numbers of components: 32, 48, and 128.

Error range. Results are gathered across 5 random seeds, showing both averages and population standard deviations.

Random Directed Graphs Quasimetric Learning

Graph generation. The random graph generation is controlled by three parameters d, ρ_{un} and ρ_{di}. d is the dimension of the vertex features. ρ_{un} specifies the fraction of pairs that should have at least one (directed) edge between them. ρ_{di} specifies the fraction of *such* pairs that should *only* have one (directed) edge between them. Therefore, if $\rho_{\mathsf{un}} = 1, \rho_{\mathsf{di}} = 0$, we have a fully connected graph; if $\rho_{\mathsf{un}} = 0.5, \rho_{\mathsf{di}} = 1$, we have a graph where half of the vertex pairs have exactly one (directed) edge between them, and the other half are not connected. For completeness, the exact generation procedure for a graph of n vertices is the following:

1. randomly add $\rho_{\mathsf{un}} \cdot n^2$ undirected edges, each represented as two opposite directed edges;
2. optimize $\mathbb{R}^{n \times d}$ vertex feature matrix using Adam (Kingma and Ba, 2014) w.r.t. $\mathcal{L}_{\mathsf{align}}(\alpha = 2) + 0.3 \cdot \mathcal{L}_{\mathsf{uniform}}(t = 3)$ from (Wang and Isola, 2020), where each two node is considered a positive pair if they are connected;
3. randomly initialize a network f of architecture d-4096-4096-4096-4096-1 with tanh activations;
4. for each connected vertex pair (u, v), obtain $d_{u \to v} \triangleq f(\mathsf{feature}(u)) - f(\mathsf{feature}(v))$ and $d_{v \to u} = -d_{u \to v}$;
5. for each (u, v) such that $d_{u \to v}$ is among the top $1 - \rho_{\mathsf{di}}/2$ of such values (which is guaranteed to not include both directions of the same pair due to symmetry of $d_{u \to v}$), make $v \to u$ the only directed edge between u and v.

We experiment with three graphs of 300 vertices and 64-dimensional vertex features:

- **Figure B-6:** A graph generated with $\rho_{\mathsf{un}} = 0.15, \rho_{\mathsf{di}} = 0.85$;
- **Figure B-7:** A sparser graph generated with $\rho_{\mathsf{un}} = 0.05, \rho_{\mathsf{di}} = 0.85$;
- **Figure B-8:** A sparse graph with block structure by

1. generating 10 small dense graphs of 30 vertices and 32-dimensional vertex features, using $\rho_{\mathsf{un}} = 0.18, \rho_{\mathsf{di}} = 0.15$,
2. generating a sparse 10-vertex "supergraph" with 32-dimensional vertex features, using $\rho_{\mathsf{un}} = 0.22, \rho_{\mathsf{di}} = 0.925$,
3. for each supergraph vertex
   (a) associating it with a different small graph,
   (b) for all vertices of the small graph, concatenate the supergraph vertex's feature to the existing feature, forming 64-dimensional vertex features for the small graph vertices,
   (c) picking a random representative vertex from the small graph,
4. connecting all 10 representative vertices in the same way as their respective supergraph vertices are connected in the supergraph.

Architecture. All encoder based methods (PQEs, metric embeddings, dot products) use 64-128-128-128-48 network with ReLU activations, mapping 64-dimensional inputs to a 48-dimensional latent space. Unconstrained networks use a similar 128-128-128-128-48-1 network, mapping concatenated the 128-dimensional input to a scalar output.

Data. For each graph, we solve the groundtruth distance matrix and obtain 300^2 pairs, from which we randomly sample the training set, and use the rest as the test set. We run on 5 training fractions evenly spaced on the logarithm scale, from 0.01 to 0.7.

Training. We use 2048 batch size with the Adam optimizer (Kingma and Ba, 2014), with learning rate decaying according to the cosine schedule without restarting (Loshchilov and Hutter, 2016) starting from 10^{-4} to 0 over 3000 epochs. All models are optimized w.r.t. MSE on the γ-discounted distances, with $\gamma = 0.9$. When running with the triangle inequality regularizer, $683 \approx 2048/3$ triplets are uniformly sampled at each iteration.

Full results and ablation studies. Figures B-6 to B-8 show full results of all methods running on all three graphs. In Figure B-9, we perform ablation studies on the implementation techniques for PQEs mentioned in Appendix B.3.4: outputting discounted distance and deep linear networks. On the simple directed graphs such as the dense graph, the basic PQE-LH without theses techniques works really well, even surpassing the results with both techniques. However, on graphs with more complex structures (*e.g.*, the sparse graph and the sparse graph with block structure), basic versions of PQE-LH and PQE-GG starts to perform badly and show large variance, while the versions with both techniques stably trains to the best results. Therefore, for robustness, we use both techniques in other experiments.

Large-Scale Social Graphs Quasimetric Learning

Data source. We choose the Berkeley-StanfordWebGraph (Leskovec and Krevl, 2014) as the large-scale *directed* social graph, which consists of 685,230 pages as nodes, and 7,600,595 hyperlinks as directed edges. Additionally, we also use the Youtube social network (Leskovec and Krevl, 2014; Mislove et al., 2007) as a *undirected* social graph, which consists of 1,134,890 users as nodes, and 2,987,624 friendship relations as undirected edges. Both datasets are available from the SNAP website (Leskovec and Krevl, 2014) under the BSD license.

Data processing. For each graph, we use node2vec to obtain 128-dimensional node features (Grover and Leskovec, 2016). Since the graph is large, we use the landmark method (Rizi et al., 2018) to construct training and test sets. Specifically, we randomly choose 150 nodes, called landmarks, and compute the distances between these landmarks and all nodes. For directed graph, this means computing distances of both directions. From the obtained pairs and distances, we randomly sample 2,500,000 pairs to form the training set. Similarly, we form a test set of 150,000 from a disjoint set of 50 landmarks. For the undirected graph, we double the size of each set by reversing the pairs, since the distance is symmetrical.

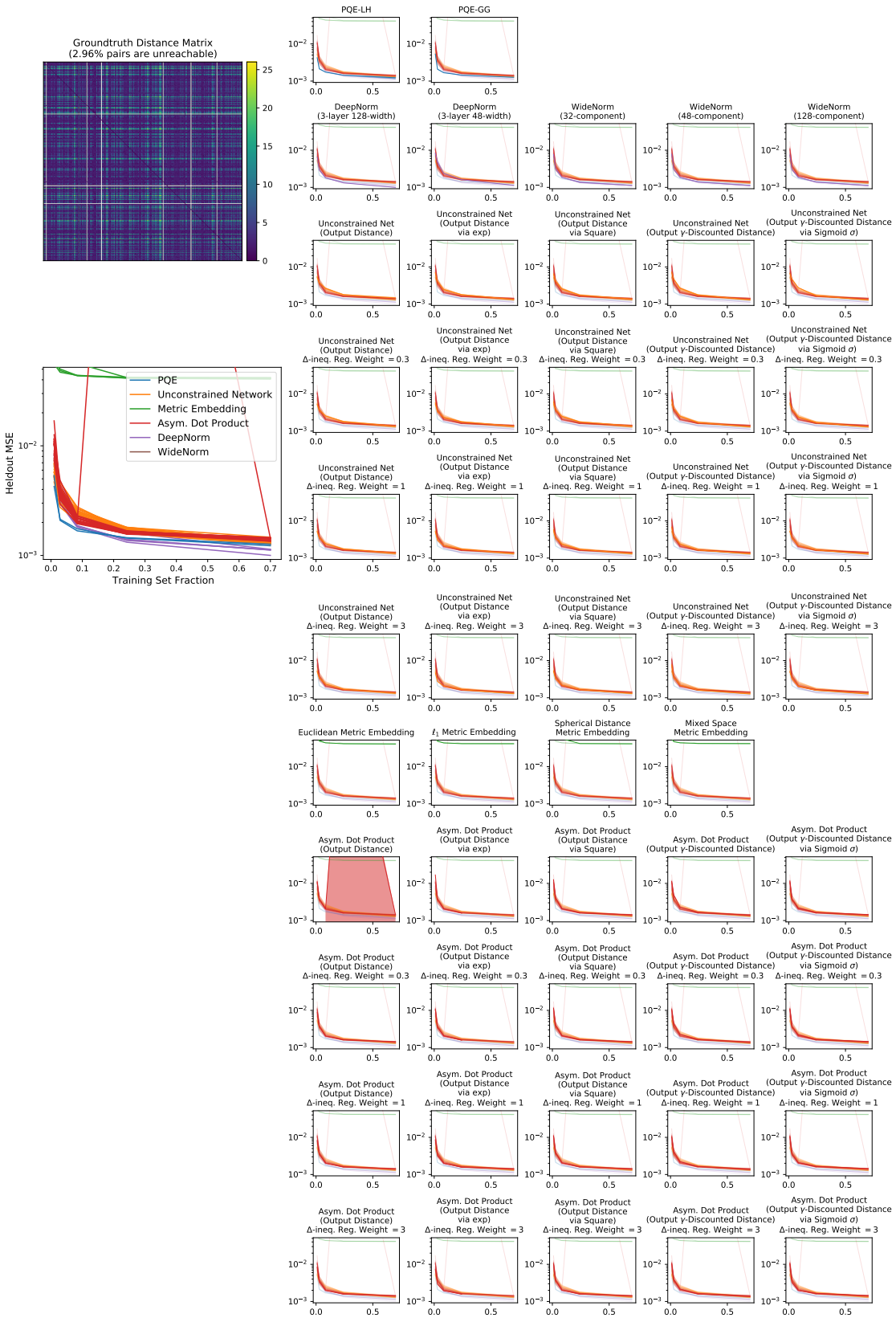

Figure B-6: Approximating a dense graph. Individual plots on the right show standard deviations.

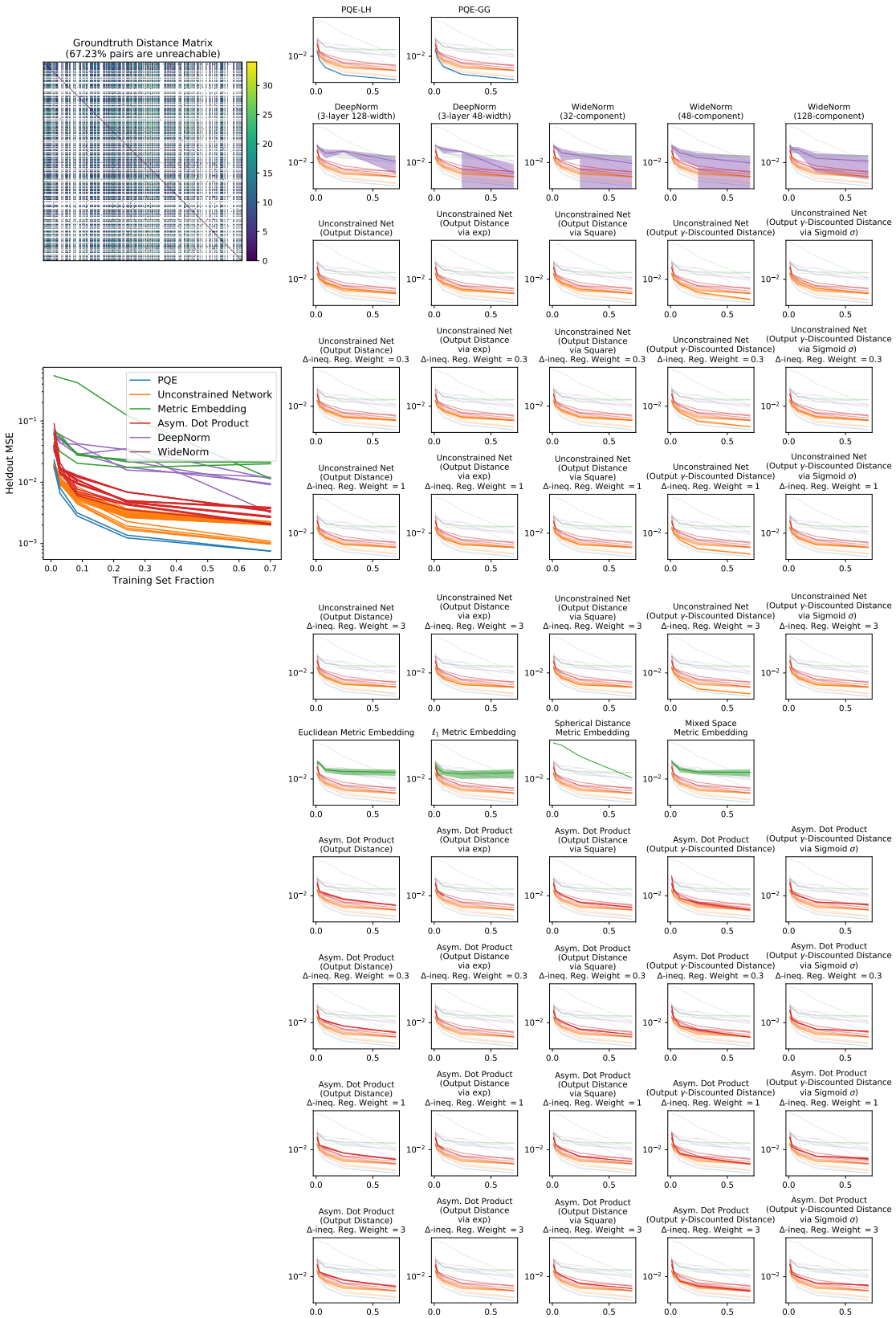

Figure B-7: Approximating a sparse graph. Individual plots on the right show standard deviations.

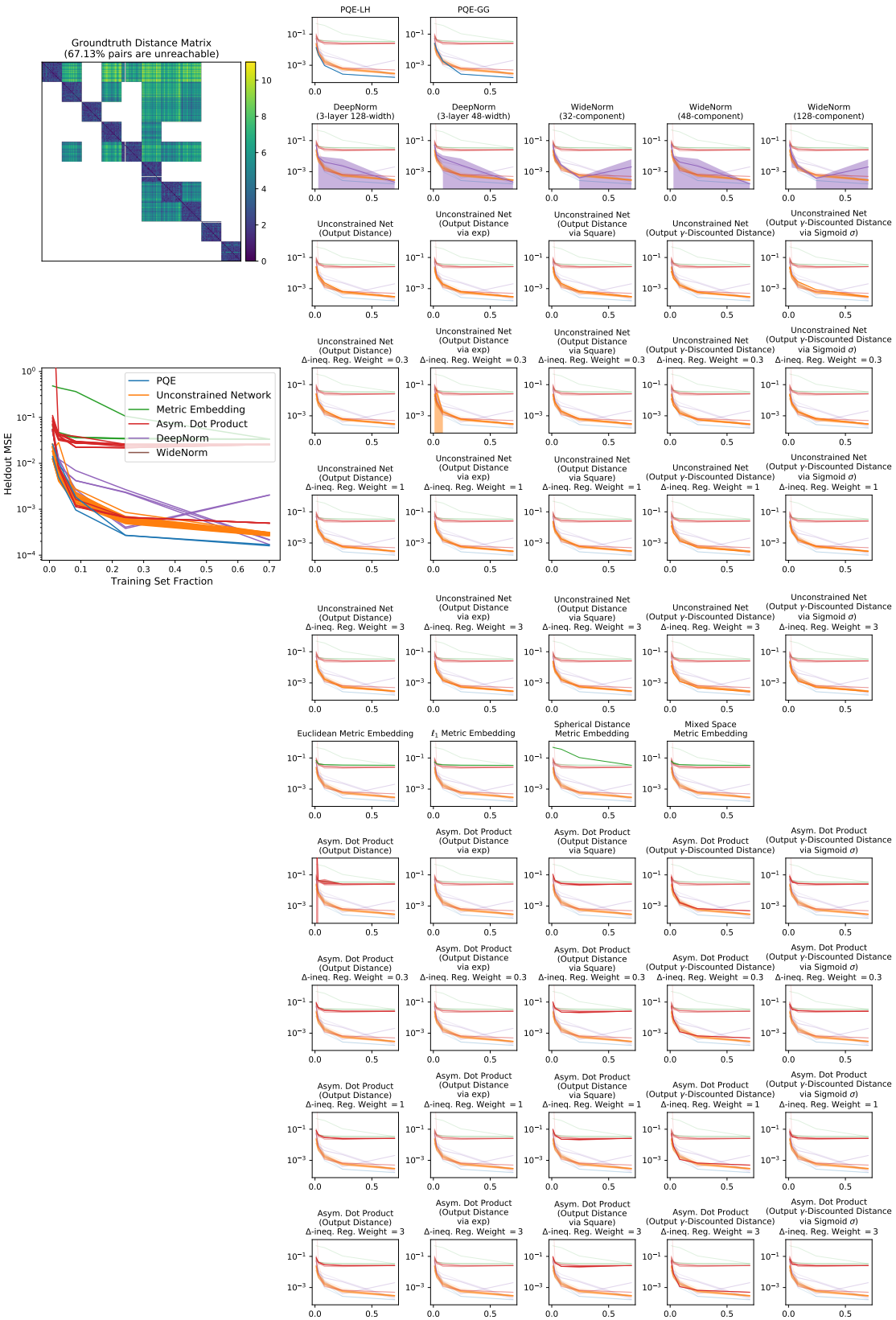

Figure B-8: Approximating a sparse graph with block structure. Individual plots on the right show standard deviations.

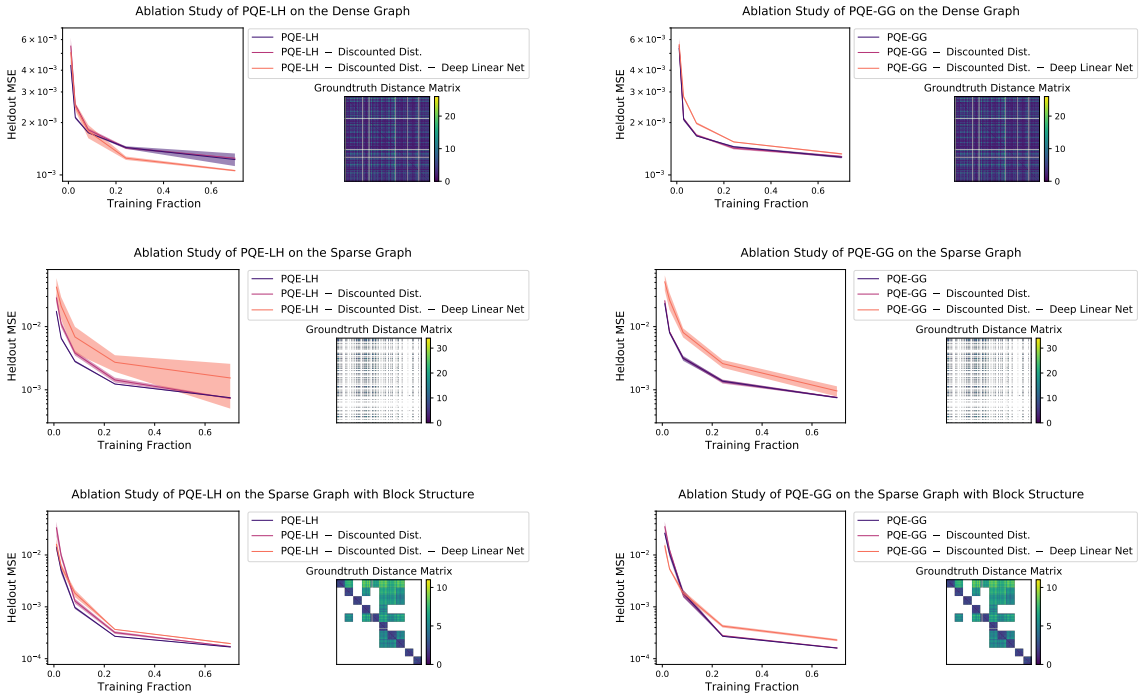

Figure B-9: Ablation studies of PQE-LH and PQE-GG on three random graphs.

Architecture. All encoder based methods (PQEs, metric embeddings, dot products) use 128-2048-2048-2048-512 network with ReLU activations and Batch Normalization (Ioffe and Szegedy, 2015) after each activation, mapping 128-dimensional inputs to a 512-dimensional latent space. Unconstrained networks use a similar 256-2048-2048-2048-512-1 network, mapping concatenated the 256-dimensional input to a scalar output.

Training. We use 1024 batch size with the Adam optimizer (Kingma and Ba, 2014), with learning rate decaying according to the cosine schedule without restarting (Loshchilov and Hutter, 2016) starting from 10^{-4} to 0 over 80 epochs. All models are optimized w.r.t. MSE on the γ-discounted distances, with $\gamma = 0.9$. When running with the triangle inequality regularizer, $342 \approx 1024/3$ triplets are uniformly sampled at each iteration.

Full results. Tables B.1 and B.2 show full results of distance learning on these two graphs. On the *directed* Berkeley-StanfordWebGraph, PQE-LH performs the best

Method Family	Formulation		MSE w.r.t. γ-discounted distances ($\times 10^{-3}$) $\downarrow$	L1 Error when true $d < \infty$ $\downarrow$	Prediction $\hat{d}$ when true $d = \infty$ $\uparrow$
PQEs	PQE-LH		3.0427 ± 0.1527	1.6263 ± 0.0550	69.9424 ± 0.4930
	PQE-GG		3.9085 ± 0.1258	1.8951 ± 0.0336	101.8240 ± 10.3970
Unconstrained Nets (without Triangle Inequality Regularizer)	Output distance	$\hat{d}(x,y) \triangleq f(x,y)$	3.0862 ± 0.0392	2.1151 ± 0.0241	59.5243 ± 0.3700
	Output distance via $\exp(\cdot)$	$\hat{d}(x,y) \triangleq \exp(f(x,y))$	3.3541 ± 0.1759	1.0090×10^{23} ± 2.0179×10^{23}	5.3583×10^{5} ± 1.0582×10^{6}
	Output distance via squaring $a \to a^2$	$\hat{d}(x,y) \triangleq (f(x,y))^2$	4.5663 ± 0.2294	3.3459 ± 0.2494	68.2613 ± 11.6061
	Output γ-discounted distance	$\gamma^{\hat{d}(x,y)} \triangleq f(x,y)$	NaN ± NaN	NaN ± NaN	NaN ± NaN
	Output γ-discounted distance via sigmoid $\sigma(\cdot)$	$\gamma^{\hat{d}(x,y)} \triangleq \sigma(f(x,y))$	3.1823 ± 0.1133	∞ ± NaN	65.8630 ± 0.4287
Unconstrained Nets (Triangle Inequality Regularizer Weight = 0.3)	Output distance	$\hat{d}(x,y) \triangleq f(x,y)$	2.8128 ± 0.0625	2.2109 ± 0.0341	61.3709 ± 0.3936
	Output distance via $\exp(\cdot)$	$\hat{d}(x,y) \triangleq \exp(f(x,y))$	2.9344 ± 0.0455	∞ ± NaN	∞ ± NaN
	Output distance via squaring $a \to a^2$	$\hat{d}(x,y) \triangleq (f(x,y))^2$	4.9947 ± 0.4198	16.5445 ± 29.3175	58.9205 ± 6.4216
	Output γ-discounted distance	$\gamma^{\hat{d}(x,y)} \triangleq f(x,y)$	NaN ± NaN	NaN ± NaN	NaN ± NaN
	Output γ-discounted distance via sigmoid $\sigma(\cdot)$	$\gamma^{\hat{d}(x,y)} \triangleq \sigma(f(x,y))$	2.9178 ± 0.1351	∞ ± NaN	∞ ± NaN
Unconstrained Nets (Triangle Inequality Regularizer Weight = 1)	Output distance	$\hat{d}(x,y) \triangleq f(x,y)$	3.0481 ± 0.1272	2.3729 ± 0.1378	60.4040 ± 0.1890
	Output distance via $\exp(\cdot)$	$\hat{d}(x,y) \triangleq \exp(f(x,y))$	3.0161 ± 0.0718	∞ ± NaN	3.1289×10^{16} ± 6.2579×10^{16}
	Output distance via squaring $a \to a^2$	$\hat{d}(x,y) \triangleq (f(x,y))^2$	4.4921 ± 0.3534	3.6930 ± 0.4896	90.6206 ± 66.5704
	Output γ-discounted distance	$\gamma^{\hat{d}(x,y)} \triangleq f(x,y)$	4.4046 ± 0.5167	2.7873 ± 0.0770	31.3195 ± 0.9929
	Output γ-discounted distance via sigmoid $\sigma(\cdot)$	$\gamma^{\hat{d}(x,y)} \triangleq \sigma(f(x,y))$	2.9314 ± 0.1022	2.2634 ± 0.1147	∞ ± NaN
Unconstrained Nets (Triangle Inequality Regularizer Weight = 3)	Output distance	$\hat{d}(x,y) \triangleq f(x,y)$	5.2955 ± 0.5279	3.8060 ± 0.2908	58.1193 ± 0.4383
	Output distance via $\exp(\cdot)$	$\hat{d}(x,y) \triangleq \exp(f(x,y))$	3.5713 ± 0.2002	212.5421 ± 416.9256	∞ ± NaN
	Output distance via squaring $a \to a^2$	$\hat{d}(x,y) \triangleq (f(x,y))^2$	4.3745 ± 0.3709	2.9491 ± 0.2228	53.1119 ± 5.5452
	Output γ-discounted distance	$\gamma^{\hat{d}(x,y)} \triangleq f(x,y)$	7.3416 ± 0.6486	3.5232 ± 0.1352	26.9200 ± 0.4697
	Output γ-discounted distance via sigmoid $\sigma(\cdot)$	$\gamma^{\hat{d}(x,y)} \triangleq \sigma(f(x,y))$	3.5818 ± 0.3565	∞ ± NaN	65.7709 ± 0.8646
Asym. Dot Products (without Triangle Inequality Regularizer)	Output distance	$\hat{d}(x,y) \triangleq f(x)^\mathsf{T} g(y)$	3.1622×10^{19} ± NaN	23.4270 ± NaN	0.1529 ± NaN
	Output distance via $\exp(\cdot)$	$\hat{d}(x,y) \triangleq \exp(f(x)^\mathsf{T} g(y))$	NaN ± NaN	NaN ± NaN	NaN ± NaN
	Output distance via squaring $a \to a^2$	$\hat{d}(x,y) \triangleq (f(x)^\mathsf{T} g(y))^2$	48.1056 ± 0.0056	2.5195×10^{11} ± 2.1751×10^{11}	2.6794×10^{11} ± 2.5398×10^{11}
	Output γ-discounted distance	$\gamma^{\hat{d}(x,y)} \triangleq f(x)^\mathsf{T} g(y)$	NaN ± NaN	NaN ± NaN	NaN ± NaN
	Output γ-discounted distance via sigmoid $\sigma(\cdot)$	$\gamma^{\hat{d}(x,y)} \triangleq \sigma(f(x)^\mathsf{T} g(y))$	48.1073 ± 0.0112	∞ ± NaN	∞ ± NaN
Asym. Dot Products (Triangle Inequality Regularizer Weight = 0.3)	Output distance	$\hat{d}(x,y) \triangleq f(x)^\mathsf{T} g(y)$	NaN ± NaN	NaN ± NaN	NaN ± NaN
	Output distance via $\exp(\cdot)$	$\hat{d}(x,y) \triangleq \exp(f(x)^\mathsf{T} g(y))$	NaN ± NaN	NaN ± NaN	NaN ± NaN
	Output distance via squaring $a \to a^2$	$\hat{d}(x,y) \triangleq (f(x)^\mathsf{T} g(y))^2$	48.1041 ± 0.0035	1.9498×10^{11} ± 7.9641×10^{10}	1.6049×10^{11} ± 3.7099×10^{10}
	Output γ-discounted distance	$\gamma^{\hat{d}(x,y)} \triangleq f(x)^\mathsf{T} g(y)$	NaN ± NaN	NaN ± NaN	NaN ± NaN
	Output γ-discounted distance via sigmoid $\sigma(\cdot)$	$\gamma^{\hat{d}(x,y)} \triangleq \sigma(f(x)^\mathsf{T} g(y))$	48.1103 ± 0.0110	∞ ± NaN	∞ ± NaN
Asym. Dot Products (Triangle Inequality Regularizer Weight = 1)	Output distance	$\hat{d}(x,y) \triangleq f(x)^\mathsf{T} g(y)$	NaN ± NaN	NaN ± NaN	NaN ± NaN
	Output distance via $\exp(\cdot)$	$\hat{d}(x,y) \triangleq \exp(f(x)^\mathsf{T} g(y))$	NaN ± NaN	NaN ± NaN	NaN ± NaN
	Output distance via squaring $a \to a^2$	$\hat{d}(x,y) \triangleq (f(x)^\mathsf{T} g(y))^2$	48.1021 ± 0.0002	2.2986×10^{11} ± 9.1970×10^{10}	2.5002×10^{11} ± 1.4464×10^{11}
	Output γ-discounted distance	$\gamma^{\hat{d}(x,y)} \triangleq f(x)^\mathsf{T} g(y)$	NaN ± NaN	NaN ± NaN	NaN ± NaN
	Output γ-discounted distance via sigmoid $\sigma(\cdot)$	$\gamma^{\hat{d}(x,y)} \triangleq \sigma(f(x)^\mathsf{T} g(y))$	58.4894 ± 23.2224	∞ ± NaN	∞ ± NaN
Asym. Dot Products (Triangle Inequality Regularizer Weight = 3)	Output distance	$\hat{d}(x,y) \triangleq f(x)^\mathsf{T} g(y)$	NaN ± NaN	NaN ± NaN	NaN ± NaN
	Output distance via $\exp(\cdot)$	$\hat{d}(x,y) \triangleq \exp(f(x)^\mathsf{T} g(y))$	NaN ± NaN	NaN ± NaN	NaN ± NaN
	Output distance via squaring $a \to a^2$	$\hat{d}(x,y) \triangleq (f(x)^\mathsf{T} g(y))^2$	48.1031 ± 0.0020	2.3522×10^{11} ± 2.6429×10^{11}	1.7025×10^{11} ± 1.0700×10^{11}
	Output γ-discounted distance	$\gamma^{\hat{d}(x,y)} \triangleq f(x)^\mathsf{T} g(y)$	NaN ± NaN	NaN ± NaN	NaN ± NaN
	Output γ-discounted distance via sigmoid $\sigma(\cdot)$	$\gamma^{\hat{d}(x,y)} \triangleq \sigma(f(x)^\mathsf{T} g(y))$	48.3034 ± 0.4485	∞ ± NaN	∞ ± NaN
Metric Embeddings	Euclidean space	$\hat{d}(x,y) \triangleq \|f(x) - f(y)\|_2$	17.5952 ± 0.2667	7.5399 ± 0.0742	53.8500 ± 3.8430
	ℓ_1 space	$\hat{d}(x,y) \triangleq \|f(x) - f(y)\|_1$	18.0521 ± 0.3546	7.1154 ± 0.1835	66.2507 ± 3.3308
	Spherical distance space w/ learnable scale α	$\hat{d}(x,y) \triangleq \alpha \cdot \arccos(\frac{f(x)^\mathsf{T} f(y)}{\|f(x)\|_2 \|f(y)\|_2})$	19.2990 ± 0.2032	6.9545 ± 0.0887	32.1458 ± 0.4562
	Mixing above three spaces w/ learnable weights		17.8312 ± 0.3099	7.3493 ± 0.1086	51.7481 ± 3.6248
DeepNorms	3-layer 128-width		7.0862 ± 0.3170	2.4498 ± 0.0617	111.2209 ± 2.5045
	3-layer 512-width		5.0715 ± 0.1348	2.0853 ± 0.0633	120.0452 ± 4.3525
WideNorms	32-component (each of size 32)		3.5328 ± 0.2120	1.7694 ± 0.0213	124.6580 ± 2.8678
	48-component (each of size 32)		3.6842 ± 0.2385	1.8081 ± 0.0680	122.6833 ± 5.5026
	128-component (each of size 32)		3.8125 ± 0.2331	1.8096 ± 0.0765	128.5427 ± 5.1412

Table B.1: Quasimetric learning on the large-scale *directed* Berkeley-StanfordWebGraph.

Method Family	Formulation		MSE w.r.t. γ-discounted distances ($\times 10^{-3}$) ↓	L1 Error when true $d < \infty$ ↓	Prediction $\hat{d}$ when true $d = \infty$ ↑
PQEs	PQE-LH		2.4400 ± 0.0695	0.6480 ± 0.0119	NaN ± NaN
	PQE-GG		2.5895 ± 0.0318	0.6697 ± 0.0042	NaN ± NaN
Unconstrained Nets (without Triangle Inequality Regularizer)	Output distance	$\hat{d}(x,y) \triangleq f(x,y)$	1.4883 ± 0.0168	0.5084 ± 0.0029	NaN ± NaN
	Output distance via $\exp(\cdot)$	$\hat{d}(x,y) \triangleq \exp(f(x,y))$	1.5223 ± 0.0160	0.4910 ± 0.0151	NaN ± NaN
	Output distance via squaring $a \to a^2$	$\hat{d}(x,y) \triangleq (f(x,y))^2$	2.2955 ± 1.1674	0.6185 ± 0.1409	NaN ± NaN
	Output γ-discounted distance	$\gamma^{\hat{d}(x,y)} \triangleq f(x,y)$	1.5069 ± 0.0228	0.4975 ± 0.0211	NaN ± NaN
	Output γ-discounted distance via sigmoid $\sigma(\cdot)$	$\gamma^{\hat{d}(x,y)} \triangleq \sigma(f(x,y))$	1.4802 ± 0.0197	0.5082 ± 0.0036	NaN ± NaN
Unconstrained Nets (Triangle Inequality Regularizer Weight = 0.3)	Output distance	$\hat{d}(x,y) \triangleq f(x,y)$	1.5009 ± 0.0208	0.5107 ± 0.0032	NaN ± NaN
	Output distance via $\exp(\cdot)$	$\hat{d}(x,y) \triangleq \exp(f(x,y))$	1.5206 ± 0.0444	0.4935 ± 0.0098	NaN ± NaN
	Output distance via squaring $a \to a^2$	$\hat{d}(x,y) \triangleq (f(x,y))^2$	1.7398 ± 0.3896	0.5488 ± 0.0600	NaN ± NaN
	Output γ-discounted distance	$\gamma^{\hat{d}(x,y)} \triangleq f(x,y)$	1.5005 ± 0.0148	0.4986 ± 0.0121	NaN ± NaN
	Output γ-discounted distance via sigmoid $\sigma(\cdot)$	$\gamma^{\hat{d}(x,y)} \triangleq \sigma(f(x,y))$	1.4851 ± 0.0168	0.5089 ± 0.0026	NaN ± NaN
Unconstrained Nets (Triangle Inequality Regularizer Weight = 1)	Output distance	$\hat{d}(x,y) \triangleq f(x,y)$	1.4999 ± 0.0243	0.5107 ± 0.0046	NaN ± NaN
	Output distance via $\exp(\cdot)$	$\hat{d}(x,y) \triangleq \exp(f(x,y))$	1.5224 ± 0.0376	0.4948 ± 0.0169	NaN ± NaN
	Output distance via squaring $a \to a^2$	$\hat{d}(x,y) \triangleq (f(x,y))^2$	1.8875 ± 0.5078	0.5692 ± 0.0683	NaN ± NaN
	Output γ-discounted distance	$\gamma^{\hat{d}(x,y)} \triangleq f(x,y)$	1.4769 ± 0.0176	0.4919 ± 0.0128	NaN ± NaN
	Output γ-discounted distance via sigmoid $\sigma(\cdot)$	$\gamma^{\hat{d}(x,y)} \triangleq \sigma(f(x,y))$	1.4846 ± 0.0115	0.5088 ± 0.0021	NaN ± NaN
Unconstrained Nets (Triangle Inequality Regularizer Weight = 3)	Output distance	$\hat{d}(x,y) \triangleq f(x,y)$	1.4939 ± 0.0110	0.5099 ± 0.0018	NaN ± NaN
	Output distance via $\exp(\cdot)$	$\hat{d}(x,y) \triangleq \exp(f(x,y))$	1.5154 ± 0.0389	0.4871 ± 0.0174	NaN ± NaN
	Output distance via squaring $a \to a^2$	$\hat{d}(x,y) \triangleq (f(x,y))^2$	2.4747 ± 1.0850	0.6505 ± 0.1357	NaN ± NaN
	Output γ-discounted distance	$\gamma^{\hat{d}(x,y)} \triangleq f(x,y)$	1.4915 ± 0.0127	0.4983 ± 0.0160	NaN ± NaN
	Output γ-discounted distance via sigmoid $\sigma(\cdot)$	$\gamma^{\hat{d}(x,y)} \triangleq \sigma(f(x,y))$	1.4829 ± 0.0153	0.5084 ± 0.0029	NaN ± NaN
Asym. Dot Products (without Triangle Inequality Regularizer)	Output distance	$\hat{d}(x,y) \triangleq f(x)^\mathsf{T} g(y)$	2633.7907 ± NaN	11.3879 ± NaN	NaN ± NaN
	Output distance via $\exp(\cdot)$	$\hat{d}(x,y) \triangleq \exp(f(x)^\mathsf{T} g(y))$	NaN ± NaN	NaN ± NaN	NaN ± NaN
	Output distance via squaring $a \to a^2$	$\hat{d}(x,y) \triangleq (f(x)^\mathsf{T} g(y))^2$	339.1550 ± 0.0022	7.8948×10^{11} ± 7.4010×10^{11}	NaN ± NaN
	Output γ-discounted distance	$\gamma^{\hat{d}(x,y)} \triangleq f(x)^\mathsf{T} g(y)$	2.6920 ± 1.2655	0.7062 ± 0.2156	NaN ± NaN
	Output γ-discounted distance via sigmoid $\sigma(\cdot)$	$\gamma^{\hat{d}(x,y)} \triangleq \sigma(f(x)^\mathsf{T} g(y))$	182.2068 ± 1.2382	∞ ± NaN	NaN ± NaN
Asym. Dot Products (Triangle Inequality Regularizer Weight = 0.3)	Output distance	$\hat{d}(x,y) \triangleq f(x)^\mathsf{T} g(y)$	9.9748×10^5 ± NaN	8.1867 ± NaN	NaN ± NaN
	Output distance via $\exp(\cdot)$	$\hat{d}(x,y) \triangleq \exp(f(x)^\mathsf{T} g(y))$	NaN ± NaN	NaN ± NaN	NaN ± NaN
	Output distance via squaring $a \to a^2$	$\hat{d}(x,y) \triangleq (f(x)^\mathsf{T} g(y))^2$	339.1560 ± 0.0010	6.8658×10^{11} ± 3.4985×10^{11}	NaN ± NaN
	Output γ-discounted distance	$\gamma^{\hat{d}(x,y)} \triangleq f(x)^\mathsf{T} g(y)$	NaN ± NaN	NaN ± NaN	NaN ± NaN
	Output γ-discounted distance via sigmoid $\sigma(\cdot)$	$\gamma^{\hat{d}(x,y)} \triangleq \sigma(f(x)^\mathsf{T} g(y))$	183.3337 ± 1.0384	∞ ± NaN	NaN ± NaN
Asym. Dot Products (Triangle Inequality Regularizer Weight = 1)	Output distance	$\hat{d}(x,y) \triangleq f(x)^\mathsf{T} g(y)$	NaN ± NaN	NaN ± NaN	NaN ± NaN
	Output distance via $\exp(\cdot)$	$\hat{d}(x,y) \triangleq \exp(f(x)^\mathsf{T} g(y))$	NaN ± NaN	NaN ± NaN	NaN ± NaN
	Output distance via squaring $a \to a^2$	$\hat{d}(x,y) \triangleq (f(x)^\mathsf{T} g(y))^2$	339.1552 ± 0.0021	7.4588×10^{11} ± 3.7277×10^{11}	NaN ± NaN
	Output γ-discounted distance	$\gamma^{\hat{d}(x,y)} \triangleq f(x)^\mathsf{T} g(y)$	NaN ± NaN	NaN ± NaN	NaN ± NaN
	Output γ-discounted distance via sigmoid $\sigma(\cdot)$	$\gamma^{\hat{d}(x,y)} \triangleq \sigma(f(x)^\mathsf{T} g(y))$	191.0928 ± 9.7137	∞ ± NaN	NaN ± NaN
Asym. Dot Products (Triangle Inequality Regularizer Weight = 3)	Output distance	$\hat{d}(x,y) \triangleq f(x)^\mathsf{T} g(y)$	NaN ± NaN	NaN ± NaN	NaN ± NaN
	Output distance via $\exp(\cdot)$	$\hat{d}(x,y) \triangleq \exp(f(x)^\mathsf{T} g(y))$	NaN ± NaN	NaN ± NaN	NaN ± NaN
	Output distance via squaring $a \to a^2$	$\hat{d}(x,y) \triangleq (f(x)^\mathsf{T} g(y))^2$	339.1556 ± 0.0020	9.0283×10^{11} ± 6.0203×10^{11}	NaN ± NaN
	Output γ-discounted distance	$\gamma^{\hat{d}(x,y)} \triangleq f(x)^\mathsf{T} g(y)$	NaN ± NaN	NaN ± NaN	NaN ± NaN
	Output γ-discounted distance via sigmoid $\sigma(\cdot)$	$\gamma^{\hat{d}(x,y)} \triangleq \sigma(f(x)^\mathsf{T} g(y))$	228.0300 ± 37.0632	∞ ± NaN	NaN ± NaN
Metric Embeddings	Euclidean space	$\hat{d}(x,y) \triangleq \|f(x) - f(y)\|_2$	1.3131 ± 0.0671	0.4833 ± 0.0128	NaN ± NaN
	ℓ_1 space	$\hat{d}(x,y) \triangleq \|f(x) - f(y)\|_1$	3.5993 ± 1.5986	0.7787 ± 0.1842	NaN ± NaN
	Spherical distance space w/ learnable scale α	$\hat{d}(x,y) \triangleq \alpha \cdot \arccos(\frac{f(x)^\mathsf{T} f(y)}{\|f(x)\|_2 \|f(y)\|_2})$	6.7731 ± 0.1915	1.0829 ± 0.0177	NaN ± NaN
	Mixing above three spaces w/ learnable weights		2.1014 ± 0.0685	0.5923 ± 0.0109	NaN ± NaN
DeepNorms	3-layer 128-width		8.0192 ± 0.2476	1.1834 ± 0.0213	NaN ± NaN
	3-layer 512-width		5.4366 ± 0.0855	0.9666 ± 0.0072	NaN ± NaN
WideNorms	32-component (each of size 32)		3.0841 ± 0.0667	0.7272 ± 0.0068	NaN ± NaN
	48-component (each of size 32)		3.0438 ± 0.1322	0.7247 ± 0.0173	NaN ± NaN
	128-component (each of size 32)		2.9964 ± 0.1363	0.7173 ± 0.0166	NaN ± NaN

Table B.2: Metric learning on the large-scale *undirected* Youtube graph. This graph does not have unreachable pairs so the last column is always NaN.

(w.r.t. discounted distance MSE). While PQE-GG has larger discounted distance MSE than some other baselines, it accurately predicts finite distances and outputs large values for unreachable pairs. On the *undirected* Youtube graph, perhaps as expected, metric embedding methods have an upper hand, with the best performing method being an Euclidean space embedding. Notably, DeepNorms and WideNorms do much worse than PQEs on this symmetric graph.

Offline Q-Learning

As shown in Proposition B.1.4 and Remark B.1.5, we know that a quasimetric is formed with the optimal goal-reaching plan costs in a MDP $\mathcal{M} = (\mathcal{S}, \mathcal{A}, \mathcal{R}, \mathcal{P}, \gamma)$ where each action has *unit cost* (*i.e.*, negated reward). The quasimetric is defined on $\mathcal{X} \triangleq \mathcal{S} \cup (\mathcal{S} \times \mathcal{A})$.

Similarly, Tian et al. (2020a) also make this observation and propose to optimize a distance function by Q-learning on a collected set of trajectories. The optimized distance function (*i.e.*, Q-function) is then used with standard planning algorithms such as the Cross Entropy Method (CEM) (De Boer et al., 2005). The specific model they used is an unconstrained network $f\colon (s, a, s') \to \mathbb{R}$, outputting discounted distances (Q-values).

Due to the existing quasimetric structure, we explore using PQEs as the distance function formulation. We mostly follow the algorithm in Tian et al. (2020a) except for the following minor differences:

- Tian et al. (2020a) propose to sample half of the goal from future steps of the same trajectory, and half of the goal from similar states across the entire dataset, defined by a nearest neighbor search. For simplicity, in the latter case, we instead sample a random state across the entire dataset.

- In Tian et al. (2020a), target goals are defined as single states, and the Q-learning formulation only uses quantities distances from state-action pairs $(s, a) \in \mathcal{S} \times \mathcal{A}$ to states s': $\hat{d}((s, a), s')$.

  However, if we only train on $\hat{d}((s, a), s')$, quasimetric embeddings might not

learn much about the distance to state-action pairs, or from states, because it may simply only assign finite distances to $\hat{d}((s,a),s')$, and set everything else to infinite. To prevent such issues, we choose to use state-action pairs as target goals, by adding a random action. Then, the embedding methods only need to embed state-action pairs.

In planning when the target is actually a single goal $s' \in \mathcal{S}$, we use the following distance/Q-function

$$\hat{d}((s,a),s') \triangleq -1 + \frac{1}{|\mathcal{A}|}\sum_{a' \in \mathcal{A}} \hat{d}((s,a),(s',a')). \tag{B.192}$$

Such a modification is used for all embedding methods (PQEs, metric embeddings, asymmetrical dot products). For unconstrained networks, we test both the original formulation (of using single state as goals) and this modification.

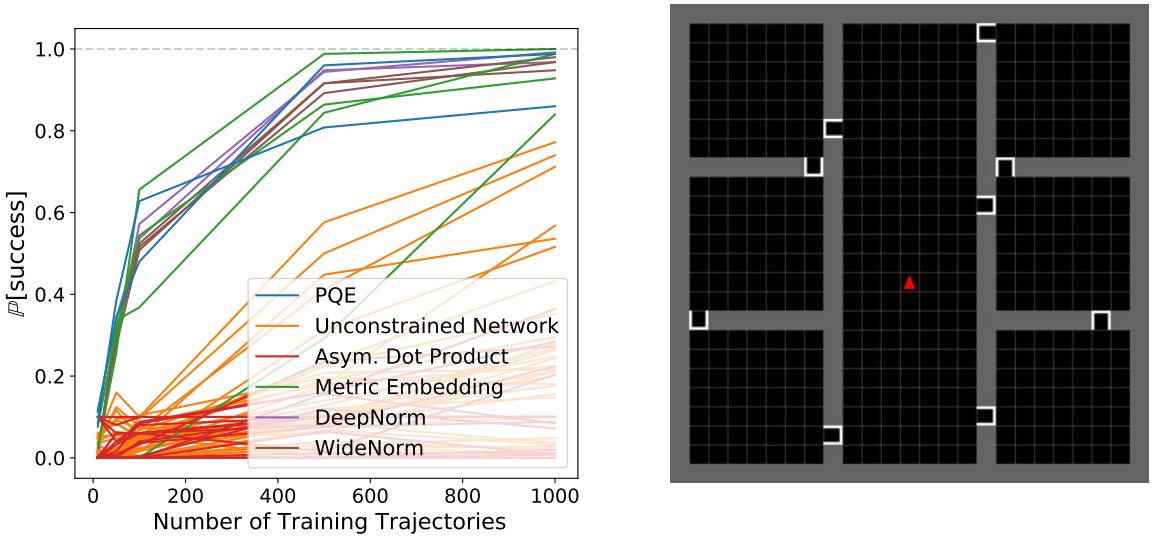

Figure B-10: Grid-world offline Q-learning average planning success rates in the environment shown right.

Environment. The environment is a grid-world with one-way doors, as shown in of Figure B-10, which is built upon `gym-minigrid` (Chevalier-Boisvert et al., 2018) (a project under Apache 2.0 License). The agent has 4 actions corresponding to moving towards 4 directions. When it moves toward a direction that is blocked by a wall or

an one-way door, it does not move. States are represented as 18-dimensional vectors, containing the 2D location of the agent (normalized to be within $[-1, 1]^2$). The other dimensions are always constant in our enviroment as they refer to information that can not be changed in this particular environment (*e.g.*, the state of the doors). The agent always starts at a random location in the center room (*e.g.*, the initial position of the red triangle in Figure B-10). The environment also defines a goal sampling distribution as a random location in one of the rooms on the left or right side. Note that this goal distribution is only used for data collection and evaluation. In training, we train goal-conditional policies using the goal sampling mechanism adapted from Tian et al. (2020a), as described above.

Training trajectories. To collect the training trajectories, we use an ϵ-greedy planner with groundtruth distance toward the environment goal, with a large $\epsilon = 0.6$. Each trajectory is capped to have at most 200 steps.

Architecture. All encoder based methods (PQEs, metric embeddings, dot products) use 18-2048-2048-2048-1024 network with ReLU activations and Batch Normalization (Ioffe and Szegedy, 2015) after each activation, mapping a 18-dimensional state to four 256-dimensional latent vectors, corresponding to the embeddings for all four state-action pairs. Unconstrained networks use a similar architecture and take in concatenated 36-dimensional inputs. With the original formulation with states as goals, we use a 36-2048-2048-2048-256-4 network to obtain a $\mathbb{R}^{|\mathcal{A}|}$ output, representing the distance/Q-values from each state-action pair to the goal; with the modified formulation with state-action pairs as goals, we use a 36-2048-2048-2048-256-16 network to obtain a $\mathbb{R}^{|\mathcal{A}|\times|\mathcal{A}|}$ output.

Training. We use 1024 batch size with the Adam optimizer (Kingma and Ba, 2014), with learning rate decaying according to the cosine schedule without restarting (Loshchilov and Hutter, 2016) starting from 10^{-4} to 0 over 1000 epochs. Since we are running Q-learning, all models are optimized w.r.t. MSE on the γ-discounted distances, with $\gamma = 0.95$. When running with the triangle inequality regularizer, $341 \approx 1024/3$

triplets are uniformly sampled at each iteration.

Planning details. To use the learned distance/Q-function for planning towards a given goal, we perform greedy 1-step planning, where we always select the best action in $\mathcal{A}$ according to the learned model, without any lookahead. In each of 50 runs, the planner is asked to reach a goal given by the environment within 300 steps. The set of 50 initial location and goal states is entirely decided by the seed used, regardless of the model. We run each method 5 times using the same set of 5 seeds.

Full results. Average results across 5 runs are shown in Figure B-10, with full results (with standard deviations) shown in Figure B-11. Planning performance across the formulations vary a lot, with PQEs and the Euclidean metric embedding being the best and most data-efficient ones. Using either formulation (states vs. state-action pairs as goals) does not seem to affect the performance of unconstrained networks. We note that the the asymmetrical dot product formulation outputting discounted distance is similar to Universal Value Function Approximators (UVFA) formulation (Schaul et al., 2015); the unconstrained network outputting discounted distance with states as goals is the same formulation as the method from Tian et al. (2020a).

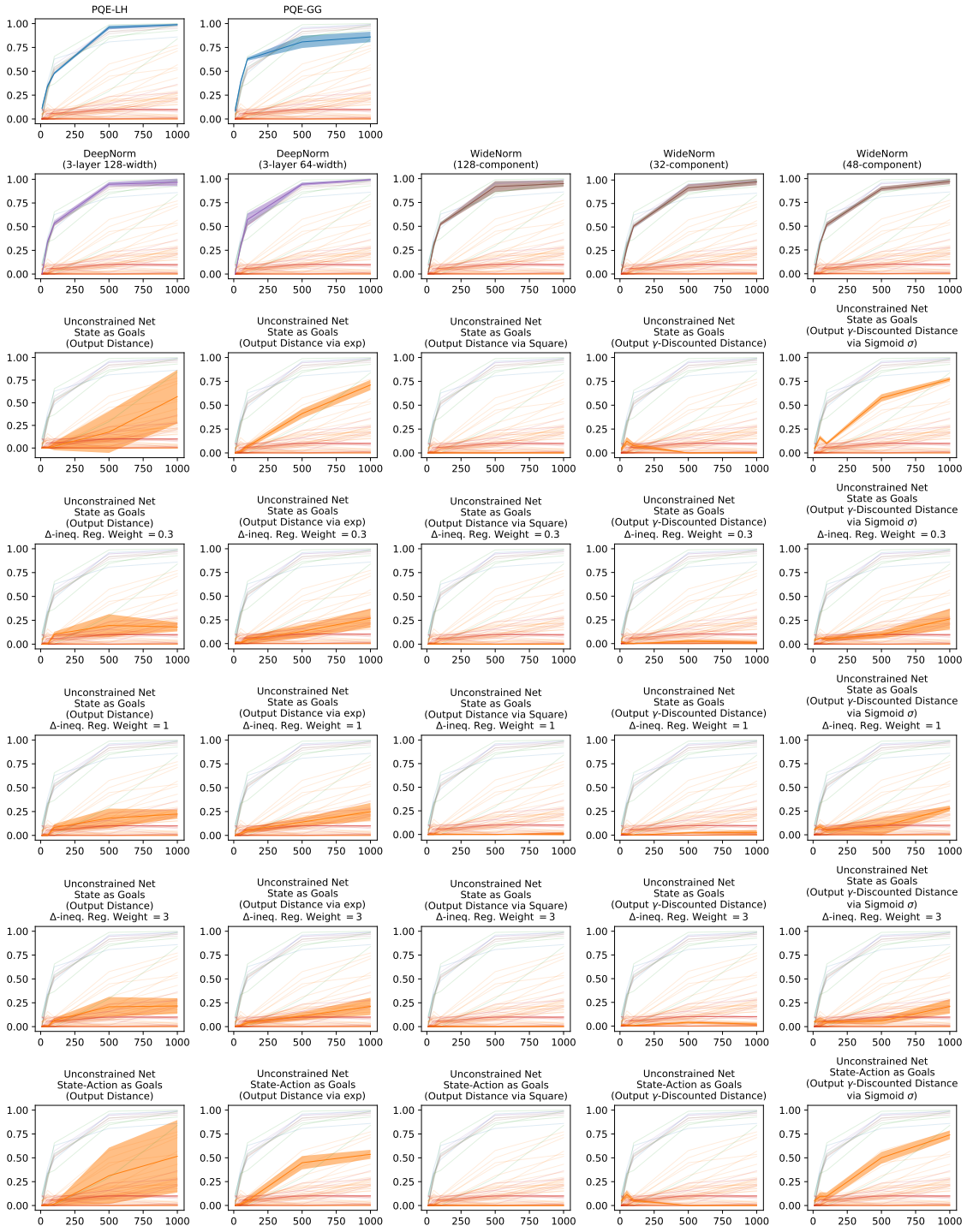

Figure B-11: Grid-world offline Q-learning full results. Individual plots on show standard deviations.

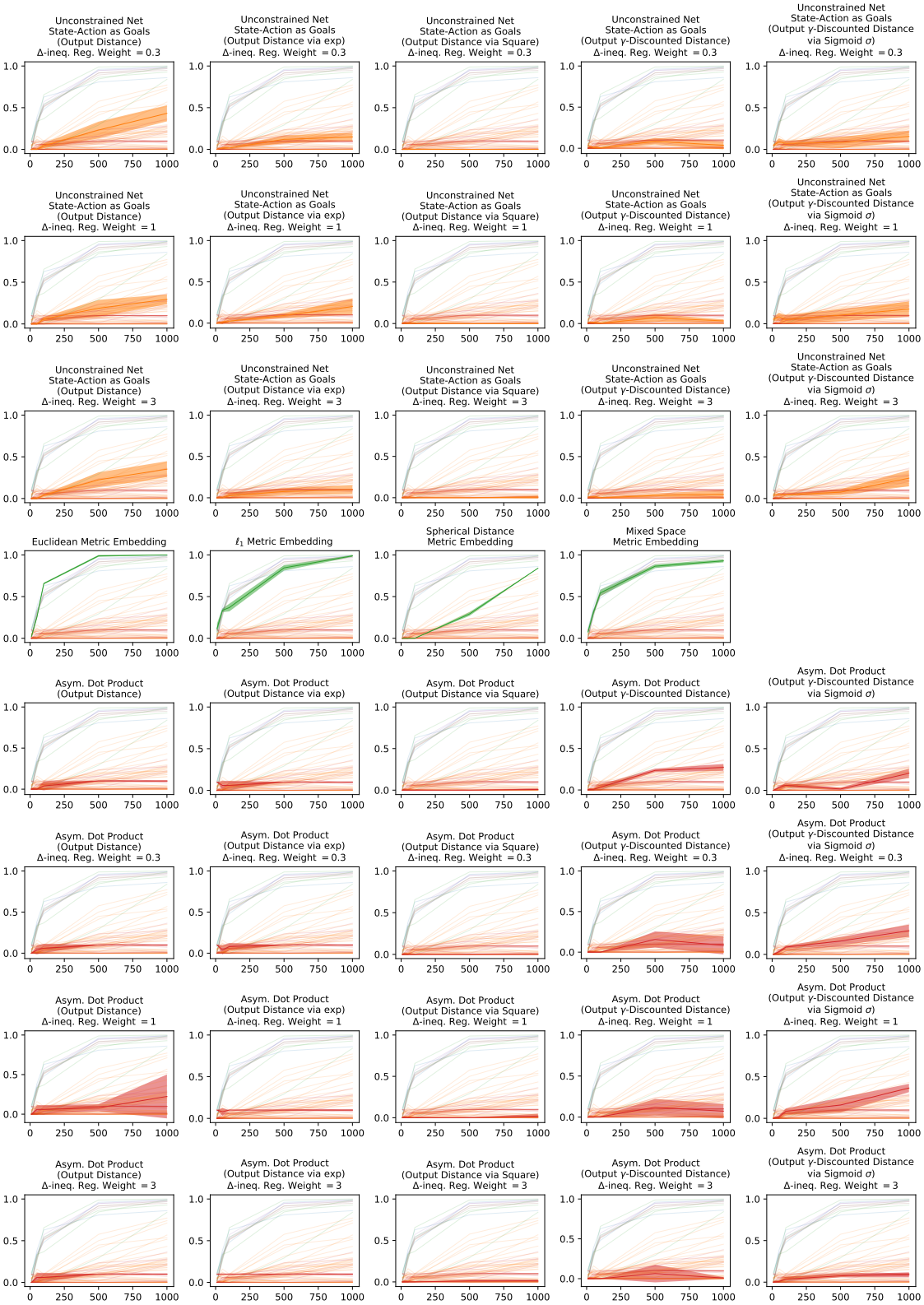

Figure B-11: Grid-world offline Q-learning full results (cont.). Individual plots on show standard deviations.

B.5 Deriving IQE From PQE

Here we will derive IQE via modifying the PQE-LH formula to scale linearly with latent (*i.e.*, to have latent positive homogeneity).

Recall the PQE-LH formula:

$$d_{\mathsf{PQE\text{-}LH}}(u, v; \alpha) = \sum_i \alpha_i \cdot (1 - \exp(-\sum_j (u_{ij} - v_{ij})^+)). \tag{B.193}$$

To make it scale linearly with latents, we must avoid the exponentiation transform on latent vector values, and instead use the latent vector to control a linear quantity. Therefore, we will reformulate the outer sum as an integral, and use latent vector to indicate where the summand (now integrand) has non-zero values.

First, we reformulate Equation (B.193) with an integration without weighting (by α), and obtain PQE-LH:

$$d_{\mathsf{Integral\text{-}PQE\text{-}LH}}(u, v) = \int_x (1 - \exp(-\sum_j (h_j(u; x) - h_j(v; x))^+)) \, \mathrm{d}x. \tag{B.194}$$

PQE-LH is derived by considering processes only activated on sets of the form $[x, \infty)$ (half-lines). Inspired by this choice, we consider $h_j(u; x) = \begin{cases} c & \text{if } x > u_j \\ 0 & \text{otherwise} \end{cases}$, for some $c > 0$.

Then

$$d_{\mathsf{Integral\text{-}PQE\text{-}LH}}(u, v; c) = \int_x (1 - \exp(-c \cdot |\{j \colon x \in [u_j, \max(u_j, v_j)]\}|) \, \mathrm{d}x. \tag{B.195}$$

Take $c \to \infty$, we have

$$d_{\mathsf{Integral\text{-}PQE\text{-}LH}}(u, v) = \int_x \mathbf{1}_{\exists j, x \in [u_j, \max(u_j, v_j)]} \, \mathrm{d}x \tag{B.196}$$

$$= \left| \bigcup_j [u_j, \max(u_j, v_j)] \right|, \tag{B.197}$$

which is exactly the IQE component.

Then, for expressivity, we combine several such components and obtain IQEs.

B.6 Proofs for Section 3.6: Interval Quasimetric Embeddings (IQEs)

Theorem 3.6.1.

- **Proof for IQE-maxmean.**

  At $l = 1$, IQE-maxmean formula can exactly recover the MRN asymmetrical component d_{asym}. By Theorem 2 of Liu et al. (2022), (f_1, d_{asym}) can exactly represent d for some f_1. Therefore, the same results apply to $d_{\mathsf{IQE\text{-}maxmean}}$.

- **Proof for IQE-sum.**

  For $d_{\mathsf{IQE\text{-}sum}}$, we present a novel construction that allows it to represent any quasipartition, and thus any convex combination of quasipartitions. Then, by Lemma B.3.5, some convex combination of quasipartitions admits a $\mathcal{O}(t \log^2 n)$ embedding.

  WLOG, consider any quasipartition π represented as an order embedding $g \colon \mathcal{X} \to [n]^m$. That is,

  $$\pi(u, v) = \begin{cases} 0 & \text{if } g(u) \leq g(v) \text{ coordinate-wise} \\ 1 & \text{otherwise.} \end{cases} \tag{B.198}$$

  Consider vectors $e_i \in \{0, 1\}^n$, where only the first i dimensions are 0's, and the rest are 1's. These vector nicely connect the IQE component structure (union of intervals) with the order embedding structure (conjunction over coordinate-wise comparisons).

  For any latent u, v and any $i \in [m]$,

  $$\bigcup_{j=1}^{n} \left[(e_{g_i(u)})_j, \max((e_{g_i(u)})_j, (e_{g_i(v)})_j)\right] = \begin{cases} \varnothing & \text{if } g_i(u) \leq g_i(v) \\ [0, 1] & \text{otherwise.} \end{cases} \tag{B.199}$$

Construct mapping

$$f(u) \triangleq [e_{g_1(u)} :: e_{g_2(u)} :: \cdots :: e_{g_m(u)}] \in \{0,1\}^{mn}, \tag{B.200}$$

where :: denotes concatenation.

Then, for any latent u, v,

$$\bigcup_{j=1}^{n} \left[f_i(u), \max(f_i(u), f_i(v))\right] = \begin{cases} \varnothing & \text{if } g(u) \leq g(v) \text{ coordinate-wise} \\ [0,1] & \text{otherwise.} \end{cases} \tag{B.201}$$

By using scaled f, each IQE component can thus represent arbitrary scaled quasipartition. Thus IQE-sum can exactly represent any convex of quasipartitions using a polynomial-sized neural encoder.

□

Theorem 3.6.2. In proof of Theorem 3.6.1, a reduction from MRN asymmetrical part to IQE-maxmean is given. The same reduction can be applied here. Invoking Theorem 2 of Liu et al. (2022) leads to the desired result. □

Theorem 3.6.3. MRN approximation results (same as Theorems 3.6.1 and 3.6.2) are proved showing that an asymmetric norm (*i.e.*, semi-norm) universally approximate quasimetrics (Theorem 2 of Liu et al., 2022). Deep Norm and Wide Norm can approximate any semi-norm (Theorem 2 of Pitis et al., 2020) and thus have the same properties. □

Appendix C

Proofs, Details, and Additional Discussions for Chapter 4

C.1 Discussions and Generalizations of QRL

Self-Transitions are in fact already handled by the QRL objective presented in this paper (Equations (4.6) and (4.12)). For any state s (with or without self-transition), we have $V^*(s; s) = 0$, since the optimal cost to first reach s start from s is given by the empty trajectory. This is naturally enforced by our value function model $-d_\theta$, since it is enforced to be a quasimetric. For self-transitions (s, a, s, r) in the training data (where $r \leq 0$ is the reward), their contribution to the constraint loss term will always be $\texttt{relu}(d_\theta(s, s) + r)^2 = \texttt{relu}(0 + r)^2 = \texttt{relu}(r)^2 = 0^2 = 0$. Therefore, the constraints are inherently satisfied for self-transitions. So our theoretical results from Section 4.3.1 also hold for such cases.

Constant Costs. In many cases (and most goal-reaching benchmarks), each environment transition has a fixed constant cost C. In other words, the task is to reach the given goal as quickly as possible. Then, in the QRL constrained optimization, we can drop the $\texttt{relu}(\cdot)$ and essentially, since we know that $-V^*(s; s') = C$ for sure, and thus we should have $d_\theta(s, s') = C$. Technically speaking, the $\texttt{relu}(\cdot)$ formulation should be able to find the same solution. In our experience, even when it is known

that the transition cost is constant, adding this information in the objective, *i.e.*, removing $\texttt{relu}(\cdot)$, does not significantly change the results.

General Goals (Sets of States). We can easily extend QRL to general goals, which are sets of states. Let $G \subset \mathcal{S}$ be such a general goal. We augment our models to operate not just on $\mathcal{S}$, but on $\mathcal{S} \bigcup \{G\}$ (which can be simply achieved by, *e.g.*, adding an indicator dimension). When we encounter transition that ends within some $s' \in G$, we simultaneously add a transition (s', G) to the dataset.

C.2 Proofs

C.2.1 Theorem 4.2.1: Value-Quasimetric Equivalence

Proof of Theorem 4.2.1. We have shown already $-V^* \in \mathfrak{Qmet}(\mathcal{S})$. (See also Proposition B.1.4.)

For any $d \in \mathfrak{Qmet}(\mathcal{S})$, define

$$\begin{aligned} \mathcal{A} &\triangleq \mathcal{S} \\ P(s, s_{\mathsf{act}}) &\triangleq \delta_{s_{\mathsf{act}}} && (\delta_x \text{ is the Dirac measure at } x) \\ R(s, s') &\triangleq -d(s, s'). \end{aligned}$$

Then the optimal value of $(\mathcal{S}, \mathcal{A}, P, R)$ is $-d$, regardless of discounting factor (if any).

For the on-policy values, consider action space $\mathcal{A} = \{a_{\mathsf{self}}, a_{\mathsf{next}}\}$. Assume that state-space $|\mathcal{S}| > 2$. Let s_1, s_2, s_3 be three distinct states in $\mathcal{S}$, all transitions have

reward -1, and

$$
\begin{aligned}
P(s_1, a_{\mathsf{self}}) &= \delta_{s_1} \\
P(s_2, a_{\mathsf{self}}) &= \delta_{s_2} \\
P(s_3, a_{\mathsf{self}}) &= \delta_{s_3} && (a_{\mathsf{self}} \text{ is always a self-transition}) \\
P(s_1, a_{\mathsf{next}}) &= \delta_{s_2} \\
P(s_2, a_{\mathsf{next}}) &= \delta_{s_3} \\
P(s_3, a_{\mathsf{next}}) &= \delta_{s_1} && (a_{\mathsf{next}} \text{ goes to the next state cyclically}) \\
\pi(s_1; s_2) &= \delta_{a_{\mathsf{next}}} && (\pi \text{ always takes } a_{\mathsf{next}} \text{ when tasked to go to } s_2 \text{ from } s_1) \\
\pi(s_2; s_3) &= \delta_{a_{\mathsf{next}}} \\
\pi(s_1; s_2) &= \delta_{a_{\mathsf{self}}}.
\end{aligned}
$$

So

$$
\begin{aligned}
-V^{\pi}(s_1; s_2) = -V^{\pi}(s_2; s_3) &= 1 \\
-V^{\pi}(s_3; s_1) &= \infty,
\end{aligned}
$$

violating triangle-inequality. □

C.2.2 Theorem 4.3.1: Exact Recovery

Proof of Theorem 4.3.1. Since the transition dynamics is deterministic, we can say that states s_0 is locally connected to state s_1 if $\exists a \in \mathcal{A}$ such that $P(s_1 \mid s_0, a) = 1$. We say a path $(s_0^{\mathsf{path}}, s_1^{\mathsf{path}}, s_2^{\mathsf{path}}, \ldots, s_T^{\mathsf{path}})$ connects s_0 to s_1 if

$$
\begin{aligned}
&s_0^{\mathsf{path}} = s_0 \\
&s_i^{\mathsf{path}} \text{ is locally connected to } s_{i+1}^{\mathsf{path}}, \quad \forall i \in \{0, 1, \ldots, T-1\} \\
&s_T^{\mathsf{path}} = s_1.
\end{aligned}
$$

And we say the total cost of this path is the total rewards over all $T-1$ transitions, *i.e.*, $T-1$.

From the definition of V^* and Theorem 4.2.1, We know that,

$$-V^* \in \mathfrak{Qmet}(\mathcal{S})$$
$$-V^*(s;g) = \text{total cost of shortest path connecting } s \text{ to } g, \qquad \forall s, g.$$

Therefore, the constraints stated in Equation (4.9) is feasible. The rest of this proof focuses only on d_θ's that satisfy the constraints, which includes $-V^*$.

Due to triangle inequality, we have $\forall s, g$,

$$d_\theta(s,g) \leq \text{total cost of shortest path connecting } s \text{ to } g = -V^*(s;g). \tag{C.1}$$

Therefore,

$$\mathbb{E}_{s,g}[d_\theta(s,g)] \leq \mathbb{E}_{s,g}[-V^*(s;g)], \tag{C.2}$$

with equality iff $d_\theta(s,g) = -V^*(s;g)$ almost surely.

Hence, $d_{\theta^*}(s,g) = -V^*(s;g)$ almost surely.

□

C.2.3 Theorem 4.3.2: Function Approximation

We first state the more general and formal version of Theorem 4.3.2.

Theorem C.2.1 (Function Approximation; General; Formal). Assume that $\mathcal{S}$ is compact and V^* is continuous.

Consider a quasimetric model family that is a universal approximator of $\mathfrak{Qmet}(\mathcal{S})$ in terms of L_∞ error (*e.g.*, IQE (Section 3.6) and MRN (Liu et al., 2022)). Concretely, this means that $\forall \epsilon > 0$, we can have $\{d_\theta^{(\epsilon)}\}_\theta$ such that, there exists some θ where

$$\forall s_0, s_1 \in \mathcal{S}, \quad \left| d_\theta^{(\epsilon)}(s_0, s_1) + V(s_0; s_1) \right| \leq \epsilon. \tag{C.3}$$

Now for some small $\epsilon > 0$, consider solving Equation (4.9) over $\{d_\theta^{(\epsilon/2)}\}_\theta$ with the

relaxed constraint that

$$\forall (s, a, s', r) \text{ transition}, \quad \texttt{relu}(d_\theta^{(\epsilon/2)}(s, s') + r) \leq \epsilon, \tag{C.4}$$

then for $s \sim p_{\mathsf{state}}, g \sim p_{\mathsf{goal}}$, and for all $\delta > 0$, we have

$$|d_{\theta^*}(s, g) + (1 + \epsilon)V^*(s; g)| \in [-\delta, 0],$$

with probability $1 - \mathcal{O}\left(\frac{\epsilon}{\delta} \cdot (-\mathbb{E}[V^*])\right)$.

As a special case with $\delta = \sqrt{\epsilon}$, we have

$$\mathbb{P}\left[\left|d_{\theta^*}(s, g) + (1 + \epsilon)V^*(s; g)\right| \in [-\sqrt{\epsilon}, 0]\right] = 1 - \mathcal{O}\left(-\sqrt{\epsilon} \cdot \mathbb{E}[V^*]\right), \tag{C.5}$$

which is exactly Theorem 4.3.2.

Note that the compactness and continuity assumptions ensure that V^* is bounded. We start by proving a lemma.

Lemma C.2.2. With the assumptions of Theorem C.2.1, there exists a $d_{\theta^\dagger}^{(\epsilon/2)}$ that satisfies the constraint with

$$\forall s, g, \quad d_{\theta^\dagger}^{(\epsilon/2)}(s, g) \geq -V^*(s; g). \tag{C.6}$$

Proof of Lemma C.2.2. Let the underlying MDP of V^* be $\mathcal{M} = (\mathcal{S}, \mathcal{A}, P, R)$. Consider another MDP $\tilde{\mathcal{M}} = (\mathcal{S}, \mathcal{A}, P, R - \frac{\epsilon}{2})$, with optimal goal-reaching value function $\tilde{V}^* \in \mathfrak{Qmet}(\mathcal{S})$.

Obviously, transitions (s, a, s', r) in $\mathcal{M}$ bijectively correspond to transitions $(s, a, s', r - \frac{\epsilon}{2})$ in $\tilde{\mathcal{M}}$.

For any s and g, let $s \to s_1 \to s_2 \to \cdots \to s_{n-1} \to g$ be the shortest path

connecting s to g in $\tilde{\mathcal{M}}$ via n transitions.

$$-\tilde{V}^*(s;g) = \text{total cost of } s \to s_1 \to s_2 \to \cdots \to s_{n-1} \to g \text{ according to } R - \frac{\epsilon}{2} \text{ as reward} \tag{C.7}$$

$$= \frac{n \cdot \epsilon}{2} + \text{total cost of } s \to s_1 \to s_2 \to \cdots \to s_{n-1} \to g \text{ according to } R \text{ as reward} \tag{C.8}$$

$$\geq \frac{n \cdot \epsilon}{2} + \text{total cost of shortest path connecting } s \text{ to } g \text{ in } \mathcal{M} \text{ according to } R \text{ as reward} \tag{C.9}$$

$$= \frac{n \cdot \epsilon}{2} - V^*(s;g). \tag{C.10}$$

Since $n > 0$ iff $s \neq g$, we have

$$-\tilde{V}^*(s;g) \geq \frac{\epsilon}{2} \cdot \mathbb{1}_{s \neq g} - V^*(s;g), \qquad \forall s, g. \tag{C.11}$$

By universal approximation, there exists $d_{\theta^\dagger}^{(\epsilon/2)}$ such that

$$\forall s, g, \quad \left| d_{\theta^\dagger}^{(\epsilon/2)}(s,g) + \tilde{V}^*(s;g) \right| \leq \frac{\epsilon}{2}. \tag{C.12}$$

In particular,

- for $s \neq g$, by Equations (C.11) and (C.12), we have

$$d_{\theta^\dagger}^{(\epsilon/2)}(s,g) \geq -\tilde{V}^*(s;g) - \frac{\epsilon}{2} \geq -V^*(s;g); \tag{C.13}$$

- for $s = g$, by Equation (C.12), we have

$$d_{\theta^\dagger}^{(\epsilon/2)}(s,g) = d_{\theta^\dagger}^{(\epsilon/2)}(s,s) = 0 = -V^*(s;s) = -V^*(s;g). \tag{C.14}$$

Hence, $d_{\theta^\dagger}^{(\epsilon/2)} \geq -V^*$ globally. Now it only remains to show that $d_{\theta^\dagger}^{(\epsilon/2)}$ satisfies the constraint.

For any transition $(s, a, s', r = R(s, s'))$ in $\mathcal{M}$, by Equation (C.12),

$$d_{\theta^\dagger}^{(\epsilon/2)}(s, s') \leq -\tilde{V}^*(s; s') + \frac{\epsilon}{2} \tag{C.15}$$

$$\leq \frac{\epsilon}{2} - R(s, s') + \frac{\epsilon}{2}$$

(since $s \to s'$ is also a valid path in $\tilde{\mathcal{M}}$ with cost $\frac{\epsilon}{2} - R(s, s')$)

$$= -r + \epsilon, \tag{C.16}$$

which means that $d_{\theta^\dagger}^{(\epsilon/2)}$ satisfies the constraint.

Hence the desired $d_{\theta^\dagger}^{(\epsilon/2)}$ exists.

□

Now we are ready to prove Theorems 4.3.2 and C.2.1.

Proof of Theorems 4.3.2 and C.2.1. Let $d_{\theta^*}^{(\epsilon/2)}$ be the solution to the relaxed problem. By the definition of the universal approximator, such solutions exist. Moreover, we have

$$\forall s, g, \quad d_{\theta^*}^{(\epsilon/2)}(s, g) \leq -(1 + \epsilon)V^*(s; g), \tag{C.17}$$

by the constraint and triangle inequality.

Define

$$p \triangleq \mathbb{P}[d_{\theta^*}^{(\epsilon/2)}(s, g) < -(1 + \epsilon)V^*(s; g) - \delta]. \tag{C.18}$$

Then

$$\mathbb{E}[d_{\theta^*}^{(\epsilon/2)}(s, g)] \leq -(1 + \epsilon)\mathbb{E}[V^*(s; g)] - p\delta, \tag{C.19}$$

where we used Equations (C.17) and (C.18).

Let $d_{\theta^\dagger}^{(\epsilon/2)}$ be the quasimetric from Lemma C.2.2. Then, by optimality, we must have

$$\mathbb{E}[d_{\theta^*}^{(\epsilon/2)}(s, g)] \geq \mathbb{E}[d_{\theta^\dagger}^{(\epsilon/2)}(s, g)] \geq -\mathbb{E}[V^*(s; g)]. \tag{C.20}$$

Combining Equations (C.19) and (C.20), we have

$$-(1 + \epsilon)\mathbb{E}[V^*(s; g)] - p\delta \geq -\mathbb{E}[V^*(s; g)]. \tag{C.21}$$

Rearranging the terms, we have

$$p \leq \frac{\epsilon}{\delta} \cdot (-\mathbb{E}[V^*]). \tag{C.22}$$

Combining Equations (C.17) and (C.22) gives the desired result. □

C.3 Experiment Details and Additional Results

All our results are aggregation from 5 runs with different seeds.

We first discuss general design details that holds across all settings. For task-specific details, we discuss them in separate subsections below.

QRL. Across all experiments, we use $\epsilon = 0.25$, initialize Lagrange multiplier $\lambda = 0.01$, and use Adam (Kingma and Ba, 2014) to optimize all parameters. λ is optimized via a softplus transform to ensure non-negativity. Our latent transition model T is implemented in a residual manner, where

$$T(z, a) \triangleq g_\phi(z, a) + z, \tag{C.23}$$

and g_ϕ being a generic MLP with weights and biases of the last fully-connected layer initialized to all zeros. Unless otherwise noted, all networks are implemented as simple ReLU MLPs. p_{state} is taken to be the beginning state of a random transition sampled from dataset / replay buffer. Unless otherwise noted, p_{goal} is taken to be the resulting state of a random transition sampled from dataset / replay buffer. For maximizing d_θ, unless otherwise noted, we use the strictly monotonically increasing convex function

$$\phi(x) \triangleq -\text{softplus}(500 - x, \beta = 0.01) = -100 \times \text{softplus}(5 - \frac{x}{100}). \tag{C.24}$$

MSG. We follow the authors'suggestions, use 64-critics, and tune the two regularizer hyperparameters over $\alpha \in \{0, 0.1, 0.5, 1\}$ and $\beta \in \{-4, -8\}$. For other hyperparameters, we use the same default values used in the original paper (Ghasemipour et al.,

2022).

C.3.1 Discretized `MountainCar`

Discretization. `MountainCar` state is parametrized by position $\in [-1.2, 0.6]$ and velocity $\in [-0.07, 0.07]$. For a dimension with values in interval $[l, u]$, we consider 160 evenly spaced bins of length $(u - l)/159$, with centers being

$$\left\{ l + \frac{u-l}{159} \times k \colon k = 0, 1, 2, \ldots, 159 \right\}. \tag{C.25}$$

After each reset and transition, we discretize each dimension of the state vector, so that future dynamics start from the discretized vector. To discretize a value, we find the bin it falls into, and replace it with the value of bin center. Note that the two bins at the two ends are centered at u and l, respectively. So the two ends are exactly represented. Discretizing each dimension this way leads to 160×160 discrete states.

Data. In `MountainCar`, the original environment goal (top of hill) is a set of states with position $\in [0.5, 0.6]$ and velocity $\in [0, 0.07]$, where the agent is considered reaching that goal if it reaches any of those states. We adapt QRL and other goal-reaching methods to support this general goal following the procedure outlined in Appendix C.1. Specifically, we augment the observation space to include an additional indicator dimension, which is 1 only when representing this general goal. In summary, any original (discretized) state $s \triangleq [u, v]$ becomes $\tilde{s} \triangleq [u, v, 0]$, and $G \triangleq [0.5, 0, 1]$ refers to this general goal. All critics and policies now takes in this augmented 3-dimensional vector as input. For each encountered state $\tilde{s}$ that falls in this set, a new transition $(\tilde{s}, G)$ is added to the offline dataset. The dataset includes 240 such added transitions and 199,888 transitions generated by running a random actor for 1,019 episodes, where each episode terminate when the agent reaches top of hill or times out at 250 timesteps.

Evaluation. For each target goal, we evaluate the planning performance starting from each of 160×160 states, with a budget of 200 steps. At each step, the agent

receives -1 reward until it reaches the goal. The episode return is then averaged over 160×160 states to compute the statistics. For the task of planning towards 9 specific states, we say that agent reaches the goal if it reaches a 13×13 neighborhood centered around the goal state, and average the metrics over 9 target goal states. For QRL and Q-Learning, we did not train any policy network. Instead, the agents take the action that maximizes Q value (or minimizes distance) for simplicity.

Goal Distribution. For all multi-goal methods, wherever possible, we adopt a goal-sampling distribution as following: for $s_{\mathsf{goal}} \sim p_{\mathsf{goal}}$,

$$s_{\mathsf{goal}} = \begin{cases} \mathsf{resulting\ state\ from\ a\ random\ transition} & \text{with probability } 0.95 \\ [0.5, 0, 1] & \text{with probability } 0.05. \end{cases} \tag{C.26}$$

QRL. We use 3-1024-1024-1024-256 network for f and (256+3)-1024-1024-1024-256 residual network for T, where 3 represents the one-hot encoding of 3 discrete actions. For d_θ, we use a 256-1024-1024-1024-256 projector followed by an IQE-maxmean head with 16 components, each of size 32. $\mathcal{L}_{\mathsf{transition}}$ is optimized with a weight of 75. Our learning rate is 0.3 for λ and 5×10^{-4} for the model parameters. We use a batch size of 4096 to train 5×10^5 gradient steps. For all parameters except λ, we used cosine learning rate scheduling without restarting, decaying to 0 at the end of training.

Q-Learning. We use x-1024-1024-1024-1024-1024-1024-3 networks for vanilla Q-Learning, where $x = 3$ in the single-goal setting, and $x = 6$ in the multi-goal setting. The 3 outputs represents estimated Q values for all 3 actions.

Q-Learning with Quasimetrics. We use the same encoder and projector architecture as QRL, as well as the same IQE specification. Additionally, to model the Q-function, we also add a 256-1024-1024-1024-(3×256) transition model (which outputs the residual for each of the 3 actions), and adopt QRL's transition loss with a weight of 5. In other words, we replace the QRL's value learning objective with the Q-Learning temporal-difference objective (and keep the transition loss). We use

a discount factor of 0.95, and update the target Q model every 2 iterations with a exponential moving average factor of 0.005. We use a learning rate of 0.001 and a batch size of 4096 to train 5×10^5 gradient steps.

Contrastive RL. We mostly follow the author's parameters for their offline experiments, using x-1024-1024-1024-d_z encoders, where $x = (3 + 3)$ for the state-action encoder, $x = 3$ for the goal encoder, and d_z is the latent dimension. We tune $d_z \in \{16, 64\}$ and choose 64 for better performance. The policy training is modified to compute exactly the expected Q-value (rather than using a reparametrized sample) from the policy's output action distribution, to accommodate the discrete action space. Since the dataset is generated from a random actor policy, we disable the behavior cloning loss. We train over 10^5 gradient steps using a batch size of 1024. We note that Contrastive RL requires a specific goal-sampling distribution, which we use instead of p_{goal} from Equation (C.26).

Contrastive RL with Quasimetrics. We use the same encoder and projector architecture as QRL, as well as the same IQE specification. Similar to Q-Learning, we also add a residual transition model, which uses the same (256+3)-1024-1024-256 architecture as QRL's transition model, and adopt QRL's transition loss with a weight of 5. In other words, we replace the QRL's value learning objective with the contrastive objective from Contrastive RL (and keep the transition loss). Contrastive RL objective estimates the on-policy Q-function with an extra goal-specific term determined by p_{goal} (Eysenbach et al., 2022). Thus, we also learn a 256-1024-1024-1 model $c(z_g)$, where z_g is the latent of goal g. Contrastive RL loss is computed with the sum of $c(z_g)$ and quasimetric output. Other hyperparameters are identical to the vanilla Contrastive RL choices.

MSG. We follow the original paper and tune $\alpha \in \{0, 0.1, 0.5, 1\}$ and $\beta \in \{-4, -8\}$. After tuning, we select $\alpha = 0.1$, $\beta = -4$ for both the single-goal and multi-goal setting. For relabelling, we find using random goals hurting performance. Hence, instead of p_{goal} from Equation (C.26), we use $[0.5, 0.5, 1]$ with probability 0.05, and a future state

from the same trajectory with probability 0.95, where the future state is taken to be $\Delta t \geq 1$ steps away, where $\Delta t \sim \text{Geometric}(0.3)$.

Diffuser. Diffuser's training horizon defines the length of trajectory segment used in training. Any trajectory with length shorter than this number won't be sampled at all for training. We tune the training horizon between 16 (which includes almost all training trajectories) and 200 (which excludes shorter trajectories from training but may better capture long-term dependencies), and choose 16 due to its better performance in both evaluations.

C.3.2 Offline `d4rl maze2d`

Evaluation. For each method, we evaluate both single-goal and multi-goal planning over 100 episodes.

QRL. We use 4-1024-1024-1024-256 network for f and (256+2)-1024-1024-1024-256 residual network for T, where 2 is the action dimension. For d_θ, we use a 256-1024-1024-2048 projector followed by an IQE-maxmean head with 64 components, each of size 32. $\mathcal{L}_{\mathsf{transition}}$ is optimized with a weight of 1. Our learning rate is 0.01 for λ, 5×10^{-4} for the critic parameters, and 3×10^{-5} for the policy parameters. We use a batch size of 4096 to train 2×10^5 gradient steps. Inspired by Contrastive RL (Eysenbach et al., 2022), we augment policy training with an additional behavior cloning loss of weight 0.05 (towards a goal that is $\Delta t \geq 1$ steps in the future from the same trajectory, for $\Delta t \sim \text{Geometric}(0.99)$).

Contrastive RL. We mostly follow the author's parameters for their offline experiments, using x-1024-1024-1024-16 encoders, where $x = (4 + 2)$ for the state-action encoder, and $x = 4$ for the goal encoder, and d_z is the latent dimension, as well as a behavior cloning loss of weight 0.05. We train over 1.5×10^5 gradient steps using a batch size of 1024. We note that Contrastive RL requires a specific goal-sampling distribution, which we use instead of p_{goal} from Equation (C.26).

MSG. For single-goal results, we report the evaluations from the original paper. For multi-goal tasks, we use the same architectures with relabelling, and tune $\alpha \in \{0, 0.1, 0.5, 1\}$ and $\beta \in \{-4, -8\}$, following the procedure from original paper. After tuning, we use $\alpha = 0.1$ and $\beta = -8$ for the `large` maze, $\alpha = 0.5$ and $\beta = -4$ for the `medium` maze, and $\alpha = 0.1$ and $\beta = -8$ for the `umaze` maze. For relabelling, we sample goal state a future state from the same trajectory, where the future state is taken to be $\Delta t \geq 1$ steps away, where $\Delta t \sim \text{Geometric}(0.3)$.

MPPI with QRL Value. We run MPPI in the QRL's learned dynamics and value function with a planning horizon of 5 steps, 10,000 samples per step, and the QRL Q-function (via the QRL dynamics and value function) as reward in each step. The noise variance to sample and explore actions is $\sigma^2 = 1$. We experimented $\lambda \in \{0.1, 0.01\}$, a regularizer penalizing the cost of control noise, and use $\lambda = 0.01$ due to its slightly superior performance.

Diffuser. We strictly follow the original paper's parameters for `maze2d` experiments. For planning with sampled actions, each Diffuser sample yields many actions, so we replan after using up all previously sampled actions (similar to open-loop planning). In our experience, replanning at every timestep is extremely computationally costly without observed improvements. For QRL value planning, we guide Diffuser sampling for minimizing the learned quasimetric distance towards goal state (in addition to its existing goal-conditioning) with a weight of 0.1 over 4 guidance steps at each sampling iteration. Since each Diffuser sample is a long-horizon trajectories refined over many iterations, guiding at each timestep of the trajectory is computationally expensive. Therefore, we gather state-action pairs from every 5 timesteps as well as the last step of the trajectory, and feed these pairs into learned QRL value function to compute the average QRL values as guidance.

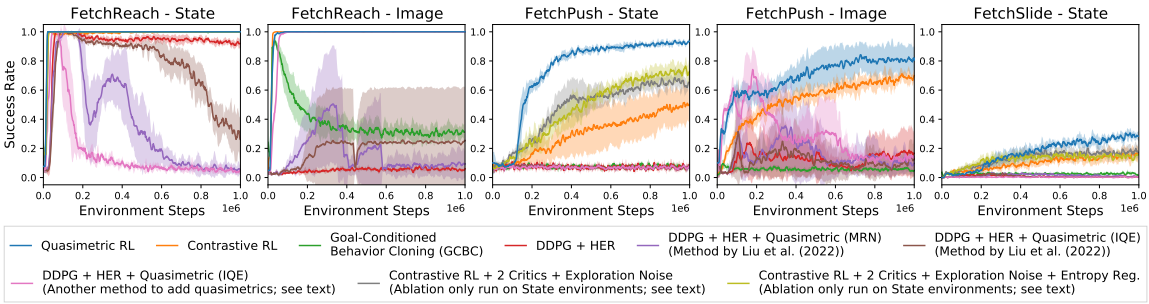

Figure C-1: Online learning performance on GCRL benchmarks, including an alternative method to integrate quasimetrics in DDPG and a variant of Contrastive RL trained with two critics and exploration action noise on state-based settings. No method has access to ground truth reward function. QRL still consistently outperforms the baseline methods, learning both faster and better. `FetchSlide` with image observation is not shown because no method reaches a non-trivial success rate. See Appendix C.3.3 for details of the additional baselines.

C.3.3 Online GCRL

Environment. For `FetchReach` and `FetchPush`, we strictly follow Contrastive RL experimental setups (Eysenbach et al., 2022) to generate initial and goal states/images. The image observations are RGB with 64×64 resolution. For `FetchSlide`, we adopt a similar strategy and generate goal states where object position dimensions are set to the target location and other dimensions are set to zeros. We are unable to get any method to reach a non-trivial success rate on `FetchSlide` with image observation despite tuning hyperparamteres and image rendering. We thus omit this setting in results.

Evaluation. We evaluate each method for 50 episodes every 2000 environment steps (*i.e.*, 40 episodes). Following standard practice, we mark an episode as successful if the agent completes the task at any timestep within the time limit (50 steps). For clearer visualizations in Figures 4-5 and C-1, the success rates curves are smoothed with a sliding window of length 5 before gathering across 5 seeds, similar to visualizations in (Liu et al., 2022). For comparing sample efficiencies between Contrastive RL and QRL, we look at the smoothed success rates from both methods, find the sample size where QRL first exceeds Contrastive RL's final performance at 10^6 samples, and compute the sample size ratio.

Processing Image Observations. To process image inputs, all compared methods use the same backbone convolutional architecture from (Mnih et al., 2013) to encode the input image into a 1024-dimensional flat vector. We adopt this approach from Contrastive RL (Eysenbach et al., 2022). For different modules in a method, each module uses an independent copy of this backbone (of same architecture but different set of parameters). For modules that takes in two observations (*e.g.*, policy network in all methods and monolithic Q-functions in vanilla DDPG), the same backbone processes each input into a flat vector, and the concatenated 2048-dimensional vector is fed into later parts of the module (which is usually an MLP). Other modules only take in a single observation and simply maps the processed 1024-dimensional vector to the output in a fashion similar to the fully-connected head of convolutional nets (*i.e.*, passing through an activation function and then an MLP). In architecture descriptions below, we omit this backbone part for simplicity, and use x to denote the state dimension for state-based observations and backbone output dimension (*i.e.*, 1024) for image-based observations .

QRL (State-based Observations). We use a x-512-512-128 network for f and a (128+4)-512-512-128 residual network for T, where 4 is the action dimension. For d_θ, we use a 128-512-2048 projector followed by an IQE-maxmean head with 64 components, each of size 32. We use x-512-512-8 network for policy, where x is the input size and 8 parametrizes a tanh-transformed diagonal Normal distribution. $\mathcal{L}_{\mathsf{transition}}$ is optimized with a weight of 0.2. Our learning rates are 0.01 for λ, 1×10^{-4} for the model parameters, and 3×10^{-5} for the policy parameters. We use a batch size of 256 in training. We prefill the replay buffer with 200 episodes from a random actor, and then iteratively perform (1) generating 10 rollouts and (2) optimizing QRL objective for 500 gradients steps. We use $\mathcal{N}(0, 0.3^2)$-perturbed action noise in exploration. For the adaptive entropy regularizer (Haarnoja et al., 2018), we regularize policy to have target entropy $-\dim(\mathcal{A})$, where the entropy regularizer weight is initialized to be 1 and optimized in log-space with a learning rate of 3×10^{-4}. Since the environment has much shorter horizon (each episodes ends at 50 timesteps), we instead use a different

affine-transformed softplus for maximizing d_θ, where $\phi(x) \triangleq -\text{softplus}(15-x, \beta = 0.1)$.

QRL (Image-based Observations). All settings are the same as QRL for state-based observations *except* a few changes:

- We use the convolutional backbone followed by a x-512-128 network for encoder f.
- We optimize $\mathcal{L}_{\mathsf{transition}}$ with an relaxed weight of 0.1 (since the dynamics aren't fully deterministic).
- We update the models less frequently with 125 gradient steps every 10 roll-outs. Contrastive RL uses the same reduced update frequency for image-based observations (Eysenbach et al., 2022), which we observe also has benefits for QRL[1].

Contrastive RL. We strictly follow the original paper's experiment settings (Eysenbach et al., 2022), which does not use two critics or action noise for exploration, and only uses entropy regularizer for image-based observations. For a comparison, we also run Contrastive RL with these techniques added on the state-based environments. As shown in Figure C-1, while they do sometimes improve performance, they do not completely explain the gap between QRL and Contrastive RL. Hence, the improvement of QRL over Contrastive RL indeed (partly) comes from fundamental algorithmic differences. Since Contrastive RL estimates on-policy values, it could be more sensitive adding exploration noises, which degrades the dataset. QRL, however, is conceptually exempt from this issue, since it estimates optimal values.

Goal-Conditioned Behavior Cloning (GCBC). We strictly follow the hyper-parameter setups for the GCBC baseline in the Contrastive RL paper (Eysenbach et al., 2022).

[1]This is potentially related to the lost of capacity phenomenon observed generally in RL algorithms (D'Oro et al., 2023)

DDPG + HER. We mostly follow the experiment setup in the MRN paper (Liu et al., 2022). However, we do not give HER access to reward functions for fair comparison. Instead, HER relabels transition rewards based on whether the state equals the target goal state, which is exactly the same reward structure other method uses (QRL, Contrastive RL and GCBC).

DDPG + HER + Quasimetrics (Method by Liu et al. (2022)). We strictly follow the MRN paper (Liu et al., 2022) to modify DDPG to include quasimetrics, which is slightly different from our modifications to Q-Learning on offline `MountainCar`, but was also shown to be empirically beneficial in online learning (Liu et al., 2022). We follow Liu et al. (2022) for MRN hyperparameters, and use the same IQE hyperparameters as QRL.

DDPG + HER + Quasimetrics (Another method to add quasimetrics). We show *additional* results comparing QRL to a different approach to integrate quasimetrics into DDPG. This approach is different from the one by Liu et al. (2022) but similar to our modifications to Q-Learning on offline `MountainCar` that attain good performance in that task. We adapt the architecture choices by Liu et al. (2022) and QRL. Specifically, we use a x-512-512-128 network for encoder f and (128+4)-512-512-128 residual network for T. For d_θ, we use a 128-2048-2048-2048 projector followed by an IQE-maxmean head with 64 components, each of size 32. We adopt QRL's transition loss with a weight of 5. In other words, we replace the QRL's value learning objective with the DDPG temporal-difference objective (and keep the transition loss). All other hyperparameters follow the same choices in method by Liu et al. (2022). This approach performs extremely poorly on this more challenging set of environments, suggesting that it is unable to scale to more complex continuous-control settings.

As shown in Figure C-1, QRL greatly outperforms both approaches to integrate DDPG and quasimetrics, showing consistent advantage of the QRL objective over Q-Learning's temporal-difference objective.

Appendix D

Details and Additional Discussions for Chapter 5

D.1 Denoised MDP Discussions

D.1.1 Loss Derivation

To apply our mutual information regularizer $I(\boldsymbol{x}; \boldsymbol{s} \mid \boldsymbol{a})$, we can consider a form using another variational distribution ρ (see, *e.g.*, Poole et al. (2019)),

$$\begin{aligned} I(\boldsymbol{x}; \boldsymbol{s} \mid \boldsymbol{a}) &= \min_{\rho} \mathbb{E}_{\boldsymbol{a}} \mathbb{E}_{p_\theta(\boldsymbol{s}|\boldsymbol{a})} \left[D_{\mathsf{KL}}(p_\theta(\boldsymbol{x} \mid \boldsymbol{s}, \boldsymbol{a}) \parallel \rho(\boldsymbol{x} \mid \boldsymbol{a})) \right] \\ &\approx \min_{\rho} \mathbb{E}_{\boldsymbol{a}} \mathbb{E}_{q_\psi(\boldsymbol{s}|\boldsymbol{a})} \left[D_{\mathsf{KL}}(q_\psi(\boldsymbol{x} \mid \boldsymbol{s}, \boldsymbol{a}) \parallel \rho(\boldsymbol{x} \mid \boldsymbol{a})) \right] \\ &\qquad\qquad \text{(assume } q_\psi \text{ is roughly the posterior of } p_\theta) \\ &= \min_{\theta'} \mathcal{L}_{\mathsf{KL}\text{-}x}(\psi, \theta'). \end{aligned} \tag{D.1}$$

The assumption that q_ψ is roughly the posterior of p_θ is acceptable because it is the natural consequence of optimizing the variational MLE objective in Equation (5.1) over θ, ψ.

Alternatively, we can consider the MI defined by a joint conditional distribution $P(\boldsymbol{x}, \boldsymbol{s} \mid a)$ not from the forward model p_θ, but from the data distribution and posterior model $q_\psi(\boldsymbol{x} \mid \boldsymbol{s}, \boldsymbol{a})$. This is also sensible because the variational MLE objective in

Equation (5.1) optimizes for compatible p_θ and q_ψ that both fit data and consistently describe (conditionals of) the same underlying distribution. Thus regularizing either can encourage a low MI. This approach leads to exactly Equation (D.1), without approximation.

Then, the total loss in Equation (5.3) from combining Equations (5.1) and (D.1) is given by

$$\begin{aligned}
&\min_\theta \mathcal{L}_{\mathsf{MLE}}(\theta) + c \cdot I(\boldsymbol{x}; \boldsymbol{s} \mid \boldsymbol{a}) \\
=&\min_{\theta,\theta',\psi} \mathcal{L}_{\mathsf{recon}}(\theta,\psi) + \mathcal{L}_{\mathsf{KL}\text{-}x}(\theta,\psi) + \mathcal{L}_{\mathsf{KL}\text{-}y}(\theta,\psi) + \mathcal{L}_{\mathsf{KL}\text{-}z} + c \cdot + \mathcal{L}_{\mathsf{KL}\text{-}x}(\theta',\psi) \\
=&\min_{\theta,\psi} \mathcal{L}_{\mathsf{recon}}(\theta,\psi) + (1+c) \cdot \mathcal{L}_{\mathsf{KL}\text{-}x}(\theta,\psi) + \mathcal{L}_{\mathsf{KL}\text{-}y}(\theta,\psi) + \mathcal{L}_{\mathsf{KL}\text{-}z}(\theta,\psi).
\end{aligned}$$

D.1.2 Discussions

We discuss some algorithmic choices of Denoised MDP below. Specific implementation details (*e.g.*, architectures) can be found at Appendix D.2.1.

Posterior distributions of r_x and r_y. The p_θ reward distributions $p_\theta(r_x \mid x_t)$ and $p_\theta(r_y \mid y_t)$ are modelled via Gaussians (as is done usually in world models, such as Dreamer (Hafner et al., 2019a)). By the transition structure of Denoised MDPs, these distributions are inherently independent. Recall that $r = r_x + r_y$. Therefore, we can easily compute the distribution of $p_\theta(r \mid x_t, y_t)$ and its log likelihoods. This enables easy optimization of the variational MLE objective, without requiring the posterior model to also infer r_x and r_y from observed r subject to the addition relation.

Partial observability. Sections 5.2 and 5.3 discussions are mostly based in the fully observable setting. Yet most benchmarks and real-world tasks are partially observable, *e.g.*, robot joint speeds that can not be inferred from a single frame. Fortunately, the transition models used in Denoised MDP are fully capable of handle such cases, as long as the encoder q_ψ is not deterministic and the observation model $p_\theta(s \mid \dots)$ does not have the block structure (Du et al., 2019) (which would make x, y, z fully determined from s). In practice, we let both components to be generic conditional

		$\mathbf{Ctrl} + \mathbf{Rew}$	$\mathbf{Ctrl} + \overline{\mathbf{Rew}}$	$\overline{\mathbf{Ctrl}} + \mathbf{Rew}$	$\overline{\mathbf{Ctrl}} + \overline{\mathbf{Rew}}$
DMC	**Noiseless**	Agent	—	—	—
	Video Background	Agent	—	—	Background
	Video Background + Noisy Sensor	Agent	—	Background	—
	Video Background + Camera Jittering	Agent	—	—	Background, Jittering camera
	`RoboDesk`	Agent, Button, Light on desk, Green hue of TV	Blocks on desk, Handle on desk, Other movable objects	TV content, Button sensor noise	Jittering and flickering environment lighting, Jittering camera

Table D.1: Categorization of various information in the evaluated environments.

distributions (parameterized by regular deep neural networks). Therefore, Denoised MDP does not require full observability.

Hyperparameter choice. The loss in Equation (5.4) has two hyperparameters: $\alpha \in (0, \infty)$ and $\beta \in (0, 1)$. To maintain relative ratio with the observation reconstruction loss, we recommend scaling α roughly proportionally with dimensionality of the observation space, as is done in our experiments presented in this chapter. A smaller β means stronger regularization. Therefore, β can be chosen based on training stability and the level of noise distractors in the task.

D.2 Experiment Details

All code (including code for our environment variants and code for our Denoised MDP method) will be released upon publication.

D.2.1 Implementation Details

Environments and Tasks

In all environments, trajectories are capped at 1000 timesteps. Table D.1 shows a summary of what kinds of information exist in each environment.

DeepMind Control Suite (DMC). Our **Video Background** implementation follows Deep Bisimulation for Control (Zhang et al., 2020a) on most environments, using `Kinetics-400` grayscale videos (Smaira et al., 2020), and replacing pixels where blue channel is strictly the greatest of three. This method, however, does not cleanly remove most of background in the Walker Walk environment, where we use an improved mask that replaces all pixels where the blue channel is *among the greatest* of three. For **Camera Jittering**, we shift the observation image according to a smooth random walk, implemented as, at each step, Gaussian-perturbing acceleration, decaying velocity, and adding a pulling force if the position is too far away from origin. For **Sensor Noise**, we select one sensor, and perturb it according to intensity of a patch of the natural video background (*i.e.*, adding average patch value -0.5). We perturb the `speed` sensor for Cheetah Run, the `torso_height` sensor for Walker Walk, and the normalized `finger_to_target_dist` sensor for Reacher Easy. These sensor values undergo non-linear (mostly piece-wise linear) transforms to compute rewards. While they can not be perfectly modelled by additive reward noise, such a model is usually sufficient in most cases when the sensor values are not too extreme and stay in one linear region.

`RoboDesk`. We modify the original `RoboDesk` environment by adding a TV screen and two neighboring desks. The TV screen places (continuously horizontally shifting) natural RGB videos from the `Kinetics-400` dataset (Smaira et al., 2020). The environment has three light sources from the above, to which we added random jittering and flickering. The viewing camera is placed further to allow better view of the noise distractors. Resolution is increased from 64×64 to 96×96 to compensate this change. Camera jittering is implemented by a 3D smooth random walk. Finally, the button sensor (*i.e.*, detected value of how much the button is pressed) is also offset by a random walk. Each of the three button affects the corresponding light on the desk. Additionally, pressing the green button also shifts the TV screen content to a green hue. Following `RoboDesk` reward design, we reward the agent for (1) placing arm close to the button, (2) pressing the button, and (3) how green the TV screen

content is.

`RoboDesk` Joint Position Regression Datasets. To generate training and test set, we use four policies trained by state-space SAC at different stages of training (which is not related to any of the compared methods) and a uniform random actor, to obtain five policies of different qualities. For each policy, we sample 100 trajectories, each containing 1001 pairs (from 1000 interactions) of image observation and groundtruth joint position (of dimension 9). This leads to a total of 500.5×10^3 samples from each policy. From these, 100×10^3 samples are randomly selected as test set. Training sets of sizes $5 \times 10^3, 10 \times 10^3, 25 \times 10^3, 50 \times 10^3, 100 \times 10^3, 150 \times 10^3$ are sampled from the rest. For all test sets and training sets, we enforce each policy to strictly contribute an equal amount.

Model Learning Methods

For all experiments, we let the algorithms use 10^6 environment steps. For PI-SAC and CURL, we follow the original implementations (Laskin et al., 2020a; Lee et al., 2020) and use an action repeat of 4 for Cheetah Run and Reacher Easy, and an action repeat of 2 for Walker Walk. For Denoised MDP, Dreamer, TIA and DBC, we always use an action repeat of 2, following prior works (Hafner et al., 2019a; Fu et al., 2021; Zhang et al., 2020a).

Denoised MDP, Dreamer, and TIA. Both Dreamer and TIA use the same training schedule and the Recurrent State-Space Model (RSSM) as the base architecture (Hafner et al., 2019b). Following them, Denoised MDP also uses these components, and follow the same prefilling and training schedule (see Dreamer (Hafner et al., 2019b) for details). These three model learning methods take in 64×64 RGB observations for DMC, and 96×96 RGB observations for `RoboDesk`. Dreamer only implements encoder and decoder for the former resolution. To handle the increased resolution, we modify the 64×64 architectures and obtain convolutional encoder and decoder shown in Tables D.2 and D.3. For fair comparison, we ensure that each method has

Operator	Input Shape	Kernel Size	Stride	Padding
Input	$[3, 96, 96]$	—	—	—
Conv. + ReLU	$[k, 47, 47]$	4	2	0
Conv. + ReLU	$[2k, 22, 22]$	4	2	0
Conv. + ReLU	$[4k, 10, 10]$	4	2	0
Conv. + ReLU	$[8k, 4, 4]$	4	2	0
Conv. + ReLU	$[8k, 2, 2]$	3	1	0
Reshape + FC	$[m]$	—	—	—

Table D.2: Encoder architecture for (96×96)-resolution observation. The output of this encoder is then fed to other network for inferring posteriors. m and k are two architectural hyperparameters. m controls the output size (unrelated to the actual latent variable sizes). k controls the network width.

Operator	Input Shape	Kernel Size	Stride	Padding
Input	`[input_size]`	—	—	—
FC + ReLU + Reshape	$[m, 1, 1]$	—	—	—
Conv. Transpose + ReLU	$[4k, 3, 3]$	5	2	0
Conv. Transpose + ReLU	$[4k, 9, 9]$	5	2	0
Conv. Transpose + ReLU	$[2k, 21, 21]$	5	2	0
Conv. Transpose + ReLU	$[k, 46, 46]$	6	2	0
Conv. Transpose + ReLU	$[3, 96, 96]$	6	2	0

Table D.3: Decoder architecture for (96×96)-resolution observation. m and k are two architectural hyperparameters. m controls width the fully connected part. k controls width of the convolutional part. They are the same values as in Table D.2.

roughly equal number of parameters by using different latent variable sizes, encoder output sizes (m of Table D.2) and convolutional net widths (k of Table D.3). Details are shown in Table D.4.

KL clipping (free nats). For Denoised MDP, we follow Dreamer (Hafner et al., 2019b,a) and TIA (Fu et al., 2021), and allow 3 free nats for the $\mathcal{L}_{\mathsf{KL}\text{-}x}$ term. In other words, for each element of a batch, we do not optimize the KL term if it is less than 3 (*e.g.*, implemented via clipping). However, we do not allow this for the $\mathcal{L}_{\mathsf{KL}\text{-}y}$ and $\mathcal{L}_{\mathsf{KL}\text{-}z}$ terms, as these variables are to be discarded and information is not allowed to hide in them unless permitted by the structure. An alternative strategy, which we find also empirically effective, is to consider $\mathcal{L}_{\mathsf{KL}\text{-}x} = \underbrace{\beta \cdot \mathcal{L}_{\mathsf{KL}\text{-}x}}_{\text{VAE KL term}} + \underbrace{(1-\beta) \cdot \mathcal{L}_{\mathsf{KL}\text{-}x}}_{\text{MI regularizer term}}$, and to allow free nats only for the first term that is a part of the variational model fitting objective. All results presented in this chapter use the first strategy. Both strategies are implemented in our open source code repository: `github.com/facebookresearch/denoised_mdp`.

Policy Optimization Algorithms Used with Model Learning

Backpropagate via Dynamics. We use the same setting as Dreamer (Hafner et al., 2019a), optimizing a λ-return over 15-step-long rollouts with $\lambda = 0.95$, clipping

	DMC				RoboDesk			
	Latent Sizes	m	k	Total Number of Parameters	Latent Sizes	m	k	Total Number of Parameters
Dreamer	$(220 + 33)$	1024	32	7,479,789	$(220 + 33)$	1024	32	6,385,511
TIA	$(120 + 20) + (120 + 20)$	490	24	7,475,567	$(120 + 20) + (120 + 20)$	490	24	6,384,477
Denoised MDP	$(120 + 20) + (120 + 20)$	1024	32	7,478,826	$(120 + 20) + (120 + 20)$	1024	32	6,384,248

Table D.4: Specific architecture parameters for model learning methods. Since RSSM uses a deterministic part and a stochastic part to represent each latent variable, we use (`deterministic_size` + `stochastic_size`) to indicate size of a latent variable. TIA and Denoised MDP have more than one latent variable. Note that while TIA has lower m and k, it has multiple encoder and decoders, whereas Dreamer and Denoised MDP only have one encoder and one decoder. The total number of parameters is measured with the actor model, but without any additional components from policy optimization algorithm (*e.g.*, critics in SAC). Total number of parameters is lower for `RoboDesk` as the encoder and decoder architecture is narrower than those of DMC for the purpose of reducing memory usage, despite with a higher resolution.

gradients with norm greater than 100. TIA uses the same strategy, except that it groups different models together for gradient clipping. We strictly follow the official TIA implementation.

Latent-Space SAC. We use the regular SAC with automatic entropy tuning, without gradient clipping. This works well for almost all settings, except for Walker Walk variant of DMC, where training often collapses after obtaining good return, regardless of the model learning algorithm. To address instability in this case, we reduce learning rates from 3×10^{-4} to 1×10^{-4} and clip gradients with norm greater than 100 for all latent-space SAC run on these variants.

Model-Free Methods

DBC. For DMC, we used 84×84-resolution observation following original work (even though other methods train on 64×64-resolution observations). For `RoboDesk`, DBC uses the encoder in Table D.2 for 96×96-resolution observation, for fair comparison with other methods. Following the original work, we stack 3 consecutive frames to approximate the required full observability. In the robot arm joint position regression experiment Section 5.5.1, DBC encoders also see stacked observations. For DMC evaluations, we use the data provided by Zhang et al. wherever possible, and run the

official repository for other cases.

State-Space SAC. The state space usually contains robot joint states, including position, velocity, *etc.* For DMC, when **Sensor Noise** is present, this is not the true optimal state space, as we do not supply it with the noisy background that affects the noisy reward. However, it still works well in practice. For `RoboDesk`, the TV's effect on reward is likely stronger and direct state-space SAC fails to learn. Since this evaluation is to obtain a rough "upper bound", we train state-space SAC with a modified reward with less noise— the agent is rewarded by pressing the button, independent of the TV content. This still encourages the optimal strategy of the task allows achieving good policies.

Non-RL methods

Contrastive Learning. We used the Alignment+Uniformity contrastive learning loss from Wang and Isola (2020). The hyperparameters and data augmentations strictly follow their experiments on STL-10 (Coates et al., 2011), which also is of resolution 96×96. The exact loss form is $\mathcal{L}_{\mathsf{align}}(\alpha = 2) + \mathcal{L}_{\mathsf{uniform}}(t = 2)$, a high-performance setting for STL-10.

D.2.2 Compute Resources

All our experiments are run on a single GPU, requiring 8GB memory for DMC tasks, and 16GB memory for `RoboDesk` tasks. We use NVIDIA GPUs of the following types: 1080 Ti, 2080 Ti, 3080 Ti, P100, V100, Titan XP, Titan RTX. For `MuJoCo` (Todorov et al., 2012), we use the `EGL` rendering engine. Training time required for each run heavily depends on the CPU specification and availability. In general, a Denoised MDP run needs $12 \sim 36$ hours on DMC and $24 \sim 50$ hours on `RoboDesk`. TIA uses about $1.5\times$ of these times, due to the adversarial losses. For a comparison between the two Denoised MDP variants, running the same DMC task on the same machine, the Figure 5-2b variant used 23 hours while the Figure 5-2c variant used 26 hours.

D.2.3 Visualization Details

Visualizations of components in learned models. We use different methods to visualize signal and noise information learned by TIA and Denoised MDP in Figures 5-4 and 5-7. For TIA, we used the reconstructions from the two latent (before mask-composing them together as the full reconstruction). For Denoised MDP, we only have one decoder (instead of three for TIA), and thus we decode $(x_t, \texttt{const})$ and $(\texttt{const}, y_t)$ to visualize information contained in each variable, with `const` chosen by visual clarity (usually as value of the other variable at a fixed timestep). Due to the fundamental different ways to obtain these visualizations, in DMC, TIA can prevent the agent from showing up in noise visualizations, while Denoised MDP cannot. However, as stated in Section 5.5.2, our focus should be on what evolves/changes in these images, rather than what is visually present, as static components are essentially not modelled by the corresponding transition dynamics. Visualizations in Figures 5-4 and 5-7 use trajectories generated by a policy trained with state-space SAC. To obtain diverse behaviors, policy outputs are randomly perturbed before being used as actions. From the same trajectory, we use the above described procedure to obtain visualizations. The specific used trajectory segments are chosen to showcase both the modified environment and representative behavior of each method. Please see the supplementary video for clearer visualizations.

D.2.4 `RoboDesk` Result Details

Environment modifications. The agent controls a robotic arm placed in front of a desk and a TV, and is tasked to push down the green button on the desk, which turns on a small green light and makes the TV display have a green hue. The intensity of the TV image's green channel is given to the agent as part of their reward, in addition to distance between the arm to the button, and how much the button is pressed. Additionally, the environment contains other noise distractors, including moveable blocks on the desk ($\mathbf{Ctrl} + \overline{\mathbf{Rew}}$), flickering environment light and camera jittering ($\overline{\mathbf{Ctrl}} + \overline{\mathbf{Rew}}$), TV screen hue ($\mathbf{Ctrl} + \mathbf{Rew}$), TV content ($\overline{\mathbf{Ctrl}} + \mathbf{Rew}$),

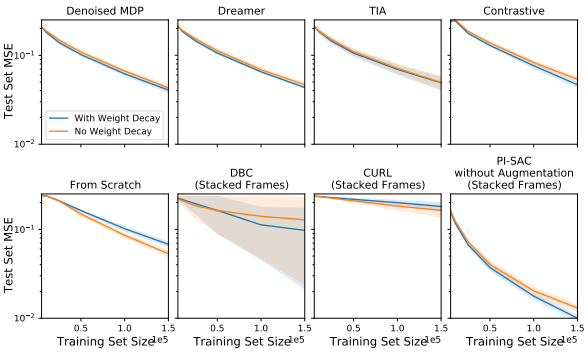

Figure D-1: Effect of weight decay on RoboDesk joint position regression. The curves show final test MSE for various training set sizes. Weight decay generally helps when finetuning from a pretrained encoder, but hurts when training from scratch.

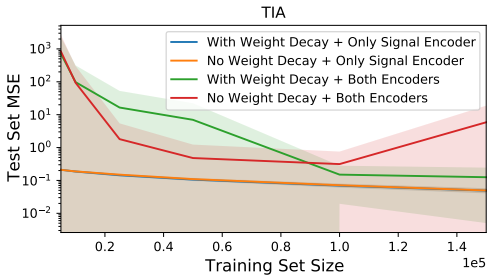

Figure D-2: Performance of all TIA settings on RoboDesk joint position regression. Only using the signal encoder is necessary for good performance.

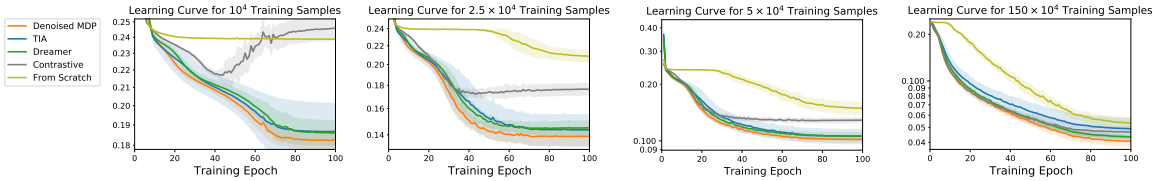

Figure D-3: Training curve comparisons for the RoboDesk joint position regression task across many training set sizes.

and noisy button sensors ($\overline{\textbf{Ctrl}} + \textbf{Rew}$).

Denoised MDP hyperparameters. RoboDesk has roughly twice as many pixels as DMC has. For Denoised MDP, we scale α with the observation space dimensionality (see Section 5.3) and use $\alpha = 2$, with a fixed $\beta = 0.125$. When using the alternative KL free nats strategy discussed in Appendix D.2.1 (results not shown in this chapter), we find $\alpha = 1$ and $\beta = 0.25$ also effective.

TIA hyperparameters. We follow recommendations in the TIA paper, setting $\lambda_{\text{Radv}} = 25{,}000$ to match reconstruction loss in magnitude, and setting $\lambda_{O_s} = 2$ where training is stable.

Robot Arm Joint Position Regression.

Training details. For this task, we jointly train the pre-trained backbone and a three-layer MLP head that has 256 hidden units at each layer, with a learning rate

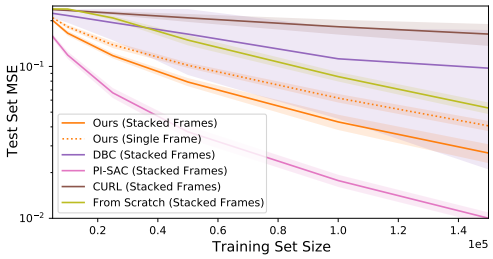

Figure D-4: Performance comparison of finetuning from Denoised MDP encoders and frame-stacked encoders that take in 3 consecutive frames, on `RoboDesk` joint position regression. For Denoised MDP and training from scratch, the encoders *take in only a single frame* and are applied for each of the frame, with output concatenated together before feeding to the prediction head.

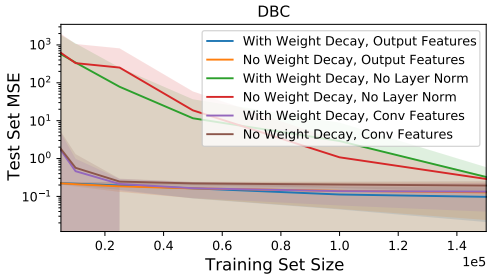

Figure D-5: Performance of all DBC settings on `RoboDesk` joint position regression. Using the output features (after layer normalization) is necessary for good performance.

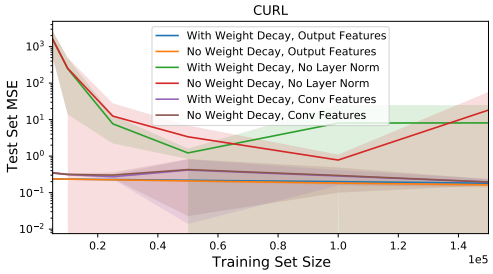

Figure D-6: Performance of all CURL settings on `RoboDesk` joint position regression. Using the output features (after layer normalization) is necessary for good performance.

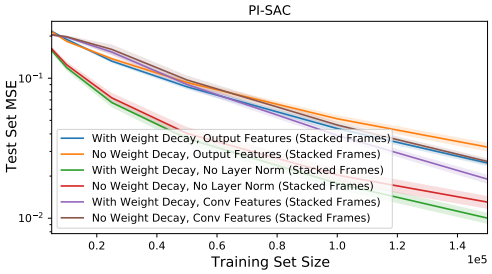

Figure D-7: Performance of all PI-SAC settings on `RoboDesk` joint position regression. Using the activations *before layer normalization* gives best performance.

of 8×10^{-5}. For finetuning from pretrained encoders, we follow common finetuning practice and apply a weight decay of 3×10^{-5} whenever it is helpful (all cases except CURL and training from scratch). See Figure D-1 for comparisons for weight decay options over all methods.

- For model-based RL, we take encoders trained with backpropagating via dynamics as the policy optimization algorithm.
- In training the contrastive encoder, for a (more) fair comparison with RL-trained encoders that are optimized over 10^6 environment steps, we train contrastive encoders on 10^6 samples, obtained in the exact same method of the training sets of this task. In a sense, these contrastive encoders have the advantage of training

on the exact same distribution, and seeing more samples (since RL-trained encoders use action repeat of 2 and thus only ever see 0.5×10^6 samples).

- TIA has two sets of encoders. Using concatenated latents from both unfortunately hurts performance greatly (see Figure D-2). So we use only the encoder for the signal latent.

We also compare training speeds over a wide range of training set sizes in Figure D-3. Denoised MDP encoders lead to faster and better training in all settings.

Additional comparison with frame-stacking encoders. Other pretrained encoders (DBC, CURL and PI-SAC) take in stacked 3 consecutive frames, and are not directly comparable with the other methods. To compare, we also try running Denoised MDP encoders on the 3 consecutive frames, whose feature vector is concatenated before feeding into the head. The result in Figure D-4 shows that our encoder outperforms all but PI-SAC encoders. Finally, for DBC, CURL and PI-SAC, we attempted evaluating intermediate features, features before the final layer normalization, and the output space, and find the last option best-performing for DBC and CURL, and the second option best-performing for PI-SAC (see Figures D-5 to D-7). Therefore, we use these respective spaces, which arguably gives a further edge to these methods, as we essentially tune this additional option on test results. Notably, these respective choices are often the only one achieving relatively good performance, highlighting the necessity of tuning for these methods.

D.2.5 DeepMind Control Suite (DMC) Result Details

Full policy optimization results. Figure D-8 presents the full results on each DMC environment (task + variant). For environment, a comparison plot is made based on which policy learning algorithm is used with the model learning method (with model-free baselines duplicated in both). Such separation is aimed to highlight the performance difference caused by model structure (rather than policy learning algorithm). Across most noisy environments, Denoised MDP performs the best. It

also achieves high return on noiseless environments.

Visualization of learned models. Figure D-9 is the extended version of Figure 5-7 in main text, with full reconstructions from all three models. Please see the supplementary video for clearer visualizations.

Comparison between Denoised MDP variants. We compare the two Denoised MDP variants based Figures 5-2b and 5-2c on Cheetah Run environments with policy trained by packpropagating via learned dynamics. The comparison is shown in the top row of Figure D-8, where we see the Figure 5-2b variant often performing a bit better. We hypothesize that this may due to the more complex prior and posterior structure of Figure 5-2c, which may not learn as efficiently. This also makes Figure 5-2c variant needing longer (wall-clock) time to optimize, as mentioned above in Appendix D.2.2.

TIA hyperparameters and instability. We strictly follow recommendations of the original paper, and use their suggested value for each DMC task. We also note that TIA runs sometimes collapse during training, leading to sharp drops in rewards. After closely inspecting the models before and after collapses, we note that in many cases, such collapses co-occur with sudden spikes in TIA's reward disassociation loss, which is implemented as an adversarial minimax loss, and the noise latent space instantly becomes degenerate (*i.e.*, not used in reconstruction). We hypothesize that this adversarial nature can cause training instability. However, a few collapses do not co-occur with such loss spikes, which maybe alternatively due to that TIA model structure cannot model the respective noise types and that better fitting the model naturally means a degenerate noise latent space.

PI-SAC hyperparameters. For each task, we use the hyperparameters detailed in the original paper (Lee et al., 2020). PI-SAC is usually run with augmentations. However, unlike CURL, augmentation is not an integral part of the PI-SAC algorithm and is completely optional. For a fair comparisons with other methods and to highlight

the effect of the predictive information regularizer, the main mechanism proposed by PI-SAC, we do not use augmentations for PI-SAC.

Denoised MDP hyperparameters. For DMC, we always use fixed $\alpha = 1$. β can be tune according to amount of noises in environment, and to training stability. In Figure D-10, we compare effects of choosing different β's. On noiseless environments, larger β (*i.e.*, less regularization) performs often better. Whereas on noisy environments, sometimes stronger regularization can boost performance. However, overall good performance can be obtained by usually several β values. In Table D.5, we summarize our β choices for each environment in Table D.5.

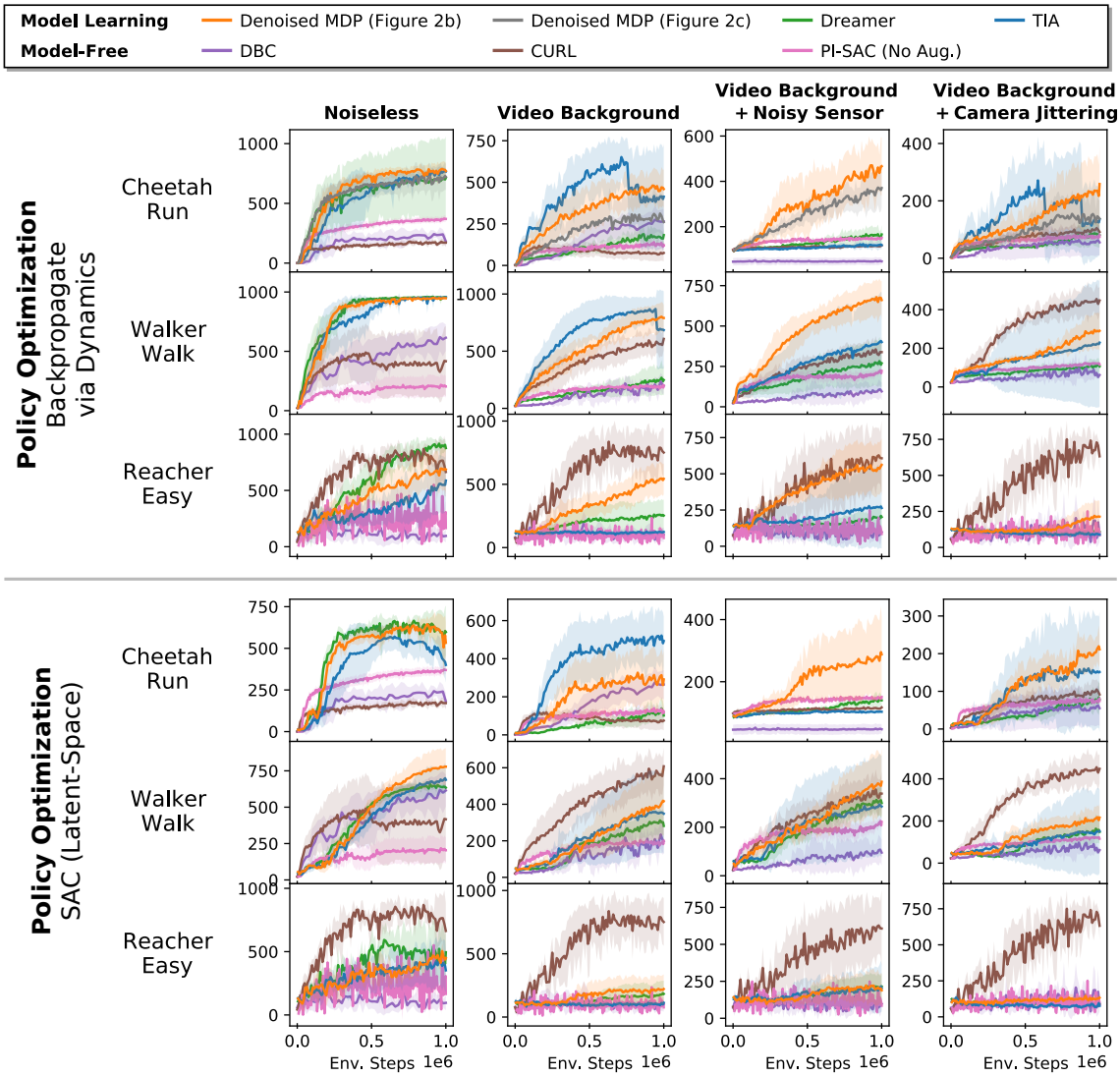

Figure D-8: Complete policy optimization results on DMC. Each plot focuses on a single task variant, showing total episode return versus environment steps taken. For three model-based approaches, we use two policy optimization choices to train on the learned model: **(top half)** backpropagate via learned dynamics and **(bottom half)** SAC on the learned MDP. We also compare with DBC, a model-free baseline. For an "upper bound" (not plotted due to presentation clarity), SAC on true state-space (*i.e.*, optimal representation) in 10^6 environment steps reaches episode return ≈ 800 on Cheetah Run variants, ≈ 980 on Walker Walk variants, and ≈ 960 on Reacher Easy variants. CURL's specific augmentation choice (random crop) potentially helps significantly for Reacher Easy (where the reacher and the target appear in random spatial locations) and **Camera Jittering**. However, unlike Denoised MDP, it does not generally perform well across all environments and noise variants.

Figure D-9: Complete visualization of the different DMC variants and factorizations learned by TIA and Denoised MDP. In addition to visualizations of Figure 5-7, we also visualize full reconstructions from Dreamer, TIA, and Denoised MDP.

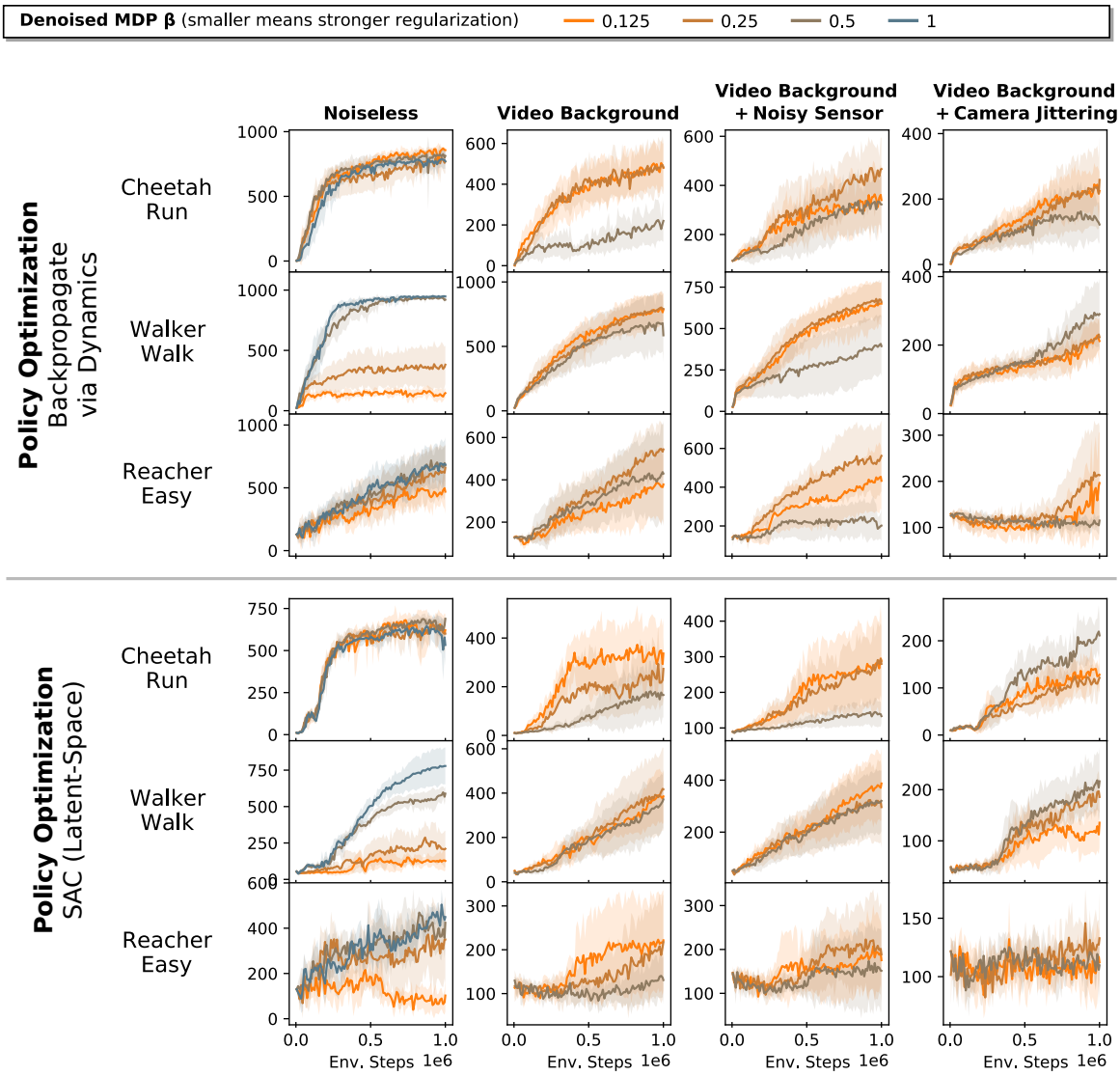

Figure D-10: Effect of choosing β in Denoised MDP on DMC policy optimization results. Setting $\beta = 1$ disables regularization and is *only run on noiseless variants*.

		Noiseless	Video Background	Video Background + Noisy Sensor	Video Background + Camera Jittering
Policy Learning: Backprop via Dynamics	Cheetah Run	1	0.125	0.25	0.25
	Walker Walk	1	0.25	0.25	0.5
	Reacher Easy	1	0.25	0.25	0.25
Policy Learning: SAC (Latent-Space)	Cheetah Run	1	0.125	0.125	0.25
	Walker Walk	1	0.25	0.125	0.5
	Reacher Easy	1	0.125	0.25	0.25

Table D.5: β choices for Denoised MDP results shown in Table 5.1 and Figure D-8. We choose $\beta = 1$ (*i.e.*, disabling regularization) for all noiseless environments, and tuned others. However, as seen in Figure D-10, the results often are not too sensitive to small β changes.

Appendix E

Details and Additional Discussions for Chapter 6

E.1 Mutual k-Nearest Neighbor Alignment Metric

For two models with representations f, g the mutual k-nearest neighbor metric measures the average overlap of their respective nearest neighbor sets. In this section, we refer to this metric as m_{NN}, which we will formally define below.

For cross-modal domains, define $(x_i, y_i) \in \mathcal{X}$ as a sample from the data distribution $\mathcal{X}$ (*e.g.* image-caption dataset). For the single domain alignment measurements, the samples are equivalent $x_i = y_i$ (*e.g.*, images for vision, and text for language). Let $\{x_i, y_i\}_{i=1}^{b}$ be the corresponding mini-batch sampled from this data distribution. Then given two model representations f and g the corresponding features are: $\phi_i = f(x_i)$ and $\psi_i = g(y_i)$, where the collection of these features are denoted as $\Phi = \{\phi_1, \ldots, \phi_b\}$ and $\Psi = \{\psi_1, \ldots, \psi_b\}$. Then for each feature pair (ϕ_i, ψ_i), we compute the respective nearest neighbor sets $\mathcal{S}(\phi_i)$ and $\mathcal{S}(\psi_i)$.

$$d_{\mathsf{knn}}(\phi_i, \Phi \setminus \phi_i) = \mathcal{S}(\phi_i) \tag{E.1}$$

$$d_{\mathsf{knn}}(\psi_i, \Psi \setminus \psi_i) = \mathcal{S}(\psi_i) \tag{E.2}$$

where d_{knn} returns the set of indices of its k-nearest neighbors. Then we measure its

average intersection via

$$m_{\mathsf{NN}}(\phi_i, \psi_i) = \frac{1}{k}|\mathcal{S}(\phi_i) \cap \mathcal{S}(\psi_i)| \tag{E.3}$$

where $|\cdot|$ is the size of the intersection.

The choice to use mutual nearest-neighbors Our initial efforts to measure alignment with CKA revealed a very weak trend of alignment between models, even when comparing models within their own modality. This has also been observed by Bansal et al. (2021), which had relied on alternative metrics such as model-stitching as it "reveals aspects of representations that measures such as centered kernel alignment (CKA) cannot" Bansal et al. (2021).

We chose to use nearest-neighbor as a metric, as methods like CKA has a very strict definition of alignment, which may not fit our current needs. For instance, understanding the precise similarity between unrelated items, such as an orange and Bill Gates, may not be critical.

Relationship between CKA and Mutual Nearest-Neighbors Let $\phi_i \in \mathbb{R}^n$ and $\psi_i \in \mathbb{R}^m$ be vectorized features of two models (*e.g.* language and vision models). Let $\mathbf{K}_{ij} = \kappa(\phi_i, \phi_j)$ and $\mathbf{L}_{ij} = \kappa(\psi_i, \psi_j)$ be the kernel matrices computed from a dataset using some kernel-function κ. Using an inner-product kernel, the ij-th entry of the centered counterpart of these Kernel matrices is:

$$\bar{\mathbf{K}}_{ij} = \langle \phi_i, \phi_j \rangle - \mathbb{E}_l[\langle \phi_i, \phi_l \rangle] \qquad \bar{\mathbf{L}}_{ij} = \langle \psi_i, \psi_j \rangle - \mathbb{E}_l[\langle \psi_i, \psi_l \rangle] \tag{E.4}$$

Then, the cross-covariance of $\mathbf{K}$ and $\mathbf{L}$ is given by:

$$\mathsf{HSIC}(\mathbf{K}, \mathbf{L}) = \frac{1}{(n-1)^2}(\bar{\mathbf{K}}\bar{\mathbf{L}}) \tag{E.5}$$

which serves as an empirical estimator of the Hilbert-Schmidt Independence Criterion Gretton et al. (2005). The Centered Kernel Alignment (CKA) Kornblith et al.

(2019) is then its normalized counterpart:

$$\mathsf{CKA}(\mathbf{K}, \mathbf{L}) = \frac{\mathsf{HSIC}(\mathbf{K}, \mathbf{L})}{\sqrt{\mathsf{HSIC}(\mathbf{K}, \mathbf{K})\mathsf{HSIC}(\mathbf{L}, \mathbf{L})}} \tag{E.6}$$

CKA measures the congruence between two random variables, with a maximum alignment of 1 and a minimum of 0. It is invariant to isotropic scaling and offers a strict notion of alignment, measuring alignment across all samples. Hence, the CKA score reflects the global similarities of the models. This can be illustrated by expanding the trace term in HSIC:

$$(\bar{\mathbf{K}}\bar{\mathbf{L}}) = \sum_i \sum_j \left(\langle \phi_i, \phi_j \rangle - \mathbb{E}_l[\langle \phi_i, \phi_l \rangle]\right) \left(\langle \psi_i, \psi_j \rangle - \mathbb{E}_l[\langle \psi_i, \psi_l \rangle]\right) \tag{E.7}$$

One can modify the definition of alignment to restrict the cross-covariance measurement to samples considered to be nearest neighbors of the current sample i. This emphasizes similarity over dissimilarity, biasing the measure toward local alignment:

$$\mathsf{Align}_{\mathsf{knn}}(\mathbf{K}, \mathbf{L}) = \sum_i \sum_j \alpha(i, j) \cdot \left(\langle \phi_i, \phi_j \rangle - \mathbb{E}_l[\langle \phi_i, \phi_l \rangle]\right) \left(\langle \psi_i, \psi_j \rangle - \mathbb{E}_l[\langle \psi_i, \psi_l \rangle]\right) \tag{E.8}$$

$$\text{where} \qquad \alpha(i, j) = \mathbb{1}[\phi_j \in \mathsf{knn}(\phi_i) \wedge \psi_j \in \mathsf{knn}(\psi_i) \wedge i \neq j] \tag{E.9}$$

Where $\alpha(i, j)$ is a scalar weighting that assigns 1 if j is a mutual nearest neighbors to both ϕ_i and ψ_i, and 0 otherwise. We refer to this metric as the Centered Kernel Nearest-Neighbor Alignment (CKNNA) metric. As the number of nearest neighbors $k \to \dim(\mathbf{K})$, we recover the original CKA metric.

$$\mathsf{CKNNA}(\mathbf{K}, \mathbf{L}) = \frac{\mathsf{Align}_{\mathsf{knn}}(\mathbf{K}, \mathbf{L})}{\sqrt{\mathsf{Align}_{\mathsf{knn}}(\mathbf{K}, \mathbf{K}), \mathsf{Align}_{\mathsf{knn}}(\mathbf{L}, \mathbf{L})}} \tag{E.10}$$

We can further relax the metric to treat the cross-covariance term identically across all nearest-neighbor samples. This is equivalent to the assumption that all nearby

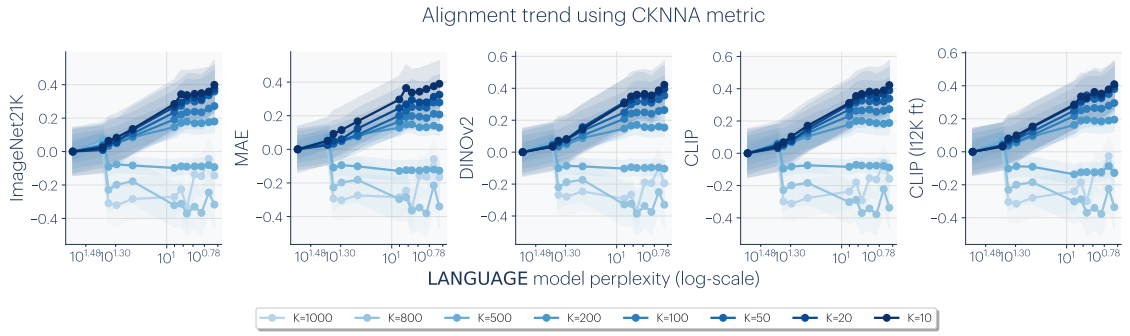

Figure E-1: **Cross-modal alignment increases locally:** Alignment trend when varying the top-k nearest neighbors in the CKNNA metrics (eqn:cknna). We center alignment score to the smallest language model and divide the total trend by the standard deviation. When $k = 1024$, we recover the original CKA metric, and when $k < |\mathcal{X}|$ it closely resembles the mutual nearest-neighbor metric m_{NN}. Each line represents the average of all LLM models for a specific k. As we decrease k, the alignment becomes more pronounced.

samples have the same distance. This simplification leads us back to the mutual nearest neighbor metric:

$$\sum_i \sum_j \alpha(i,j) \cdot 1 = n \cdot k \cdot m_{\text{NN}}(\phi_i, \psi_i) \tag{E.11}$$

By equating these metrics, we analyze the changes in alignment between language and vision models as we vary the number of neighbors k in Equation (E.10). In Figure E-1, we compute the average alignment score across all LLM models. For each k, we center the scores to the smallest vision model and divide by the standard deviation of the scores. We find that high values of k show less conclusive alignment across tasks while decreasing k shows a coherent trend across both models and tasks.

E.2 Consistency across various metrics

We describe the metrics in tbl:metrics and their corresponding properties. The *symmetric* property implies that the metric is symmetric with respect to the data points $d(x, y) = d(y, x)$. The *global* property means all samples are used to compute the distance with respect to every sample. The *ordinal* property is when the ordering of the distance is taken into consideration. For example, mutual nearest neighbor is not ordinal since the nearest neighbors $\{a, b, c\}$ and $\{c, a, b\}$ are treated equally. The *batchable* property is a computational property that makes it feasible to compute in a reasonable time frame.

Vision-vision comparison In Figure E-3, we evaluate Spearman's rank correlation among different metrics and hyperparameters over 78 vision models (details in Appendix E.3.1). We find most metrics highly correlated with each other.

Cross-modal comparison We measure vision-language alignment using a range of alternative metrics. We visualize the corresponding alignment results in Figures E-4 and E-5. Our findings indicate that alignment sensitivity not only depends on the metric used to compute it but also varies according to the specific tasks on which the vision models are trained.

Metric	Property				Description
	symmetric	global	ordinal	batchable	
CKA	✓	✓	✓	✓	Centered Kernel Alignment (CKA; Kornblith et al. (2019)) measures the similarity of neural networks by comparing the alignment of their kernel induced by their feature spaces.
Unbiased CKA	✓	✓	✓	✓	Unbiased estimator of CKA that corrects for sample bias in HSIC Song et al. (2012).
SVCCA	✓	✓	✓	✓	Singular Value Canonical Correlation Analysis (SVCCA; Raghu et al. (2017)) compares neural networks by decomposing their activities into singular vectors and measuring correlation.
Mutual k-NN	✓			✓	Measures the intersection over union (IoU) of nearest neighbors between two models.
CKNNA	✓	✓*	✓	✓	Modified CKA measure that computes the kernel alignment only for its nearest neighbors. See sec:align-metric.
Cycle k-NN				✓	Measures whether the nearest neighbor in one domain also considers the original sample as its nearest neighbor in the other domain.
Edit k-NN	✓	✓*	✓		Computes the edit distance required to match the nearest neighbors between two datasets. The score is normalized by the maximum edit distance.
LCS k-NN	✓	✓*	✓		Calculates the longest common subsequence of nearest neighbors and is normalized by the sequence length.

Figure E-2: Comparative analysis of neural network similarity metrics. ✓* indicates the metric is global and still meaningful when the nearest neighbor k is set to maximum batch-size $k = |\mathcal{X}|$.

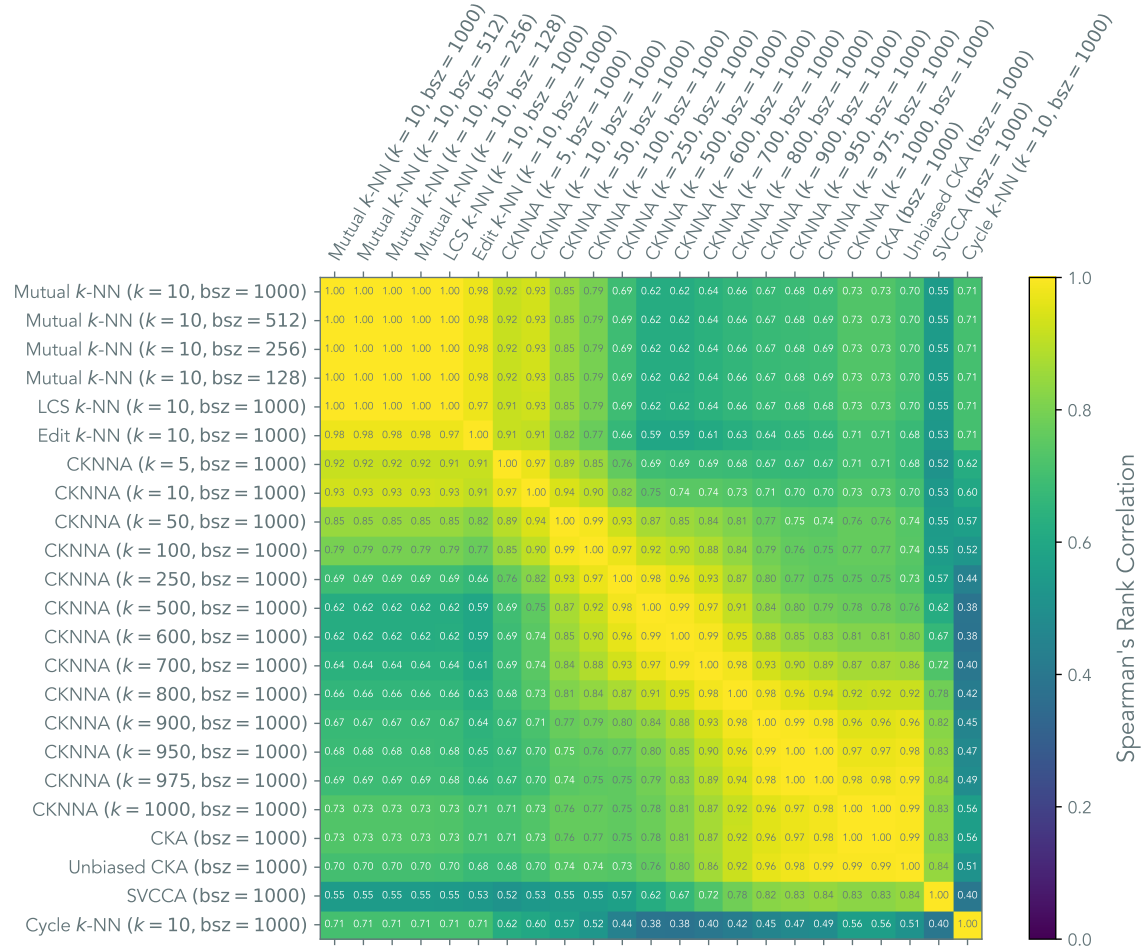

Figure E-3: **Vision-vision alignment measured with various metrics.** Spearman's rank correlation among different metrics and batch sizes (bsz) when used to measure alignment among 78 vision models (see Appendix E.3.1 for details of these models). All p-values are below 2.24×10^{-105}. Our vision-vision analysis in Figure 6-2 is based on the first metric (Mutual k-NN with $k = 10$ and bsz $= 1000$).

E.3 Experiments on Evaluating Alignment and Convergence

To demonstrate representational convergence, we take off-the-shelf models at multiple scales and multiple modalities and measure their representational alignment.

E.3.1 Vision-Vision Alignment and Representation Quality

We consider 78 vision models in total:

- 17 ViT models ranging from ViT-tiny to ViT-giant, trained on tasks including ImageNet-21k (Dosovitskiy et al., 2020) classification, Masked Autoencoders (He et al., 2021), DINO (Caron et al., 2021), and CLIP (Radford et al., 2021), including some finetuned on ImageNet-12k.

- 1 randomly initialized ResNet-50.

- 11 ResNet-50 models trained with contrastive learning on ImageNet-1k, Places-365 (Zhou et al., 2017; López-Cifuentes et al., 2020), and 9 synthetic image datasets used in Baradad et al. (2022).

- 49 ResNet-18 models trained with Alignment and Uniformity contrastive loss (**?**) on ImageNet-100, Places-365, and 47 realistic and synthetic image datasets from Baradad et al. (2021).

To test representation quality, we evaluate linear probing performance on all 19 VTAB classification tasks (Zhai et al., 2019), which is a standard multi-task transfer learning benchmark containing structured, specialized, and natural datasets covering diverse domains. To reduce compute requirements, we subsample training and validation datasets to have at most 10,000 samples. We consider a representation solves a task if its performance is $\geq 80\%$ of the best performance on that task across all 78 models.

To compute the alignment metric, we use $k = 10$ nearest neighbors over 1000 image representations computed on Places-365's validation dataset (Zhou et al., 2017). This dataset is disjoint from VTAB datasets, although both contain natural images.

E.3.2 Cross-Modal Alignment

We compare the representation of an image in a vision model to the representation of a caption describing that image in a language model. The language model families we consider are BLOOM (BigScience et al., 2022), OpenLLaMA (Geng and Liu, 2023), and LLaMA (Touvron et al., 2023). For Figure 6-4, we included more recent model families such as OLMo Groeneveld et al. (2024), LLaMA3 (Meta, 2024), Gemma (Team et al., 2024), and Mistral/Mixtral (Jiang et al., 2023, 2024). These models were downloaded from Huggingface (Wolf et al., 2019).

For vision models, we consider ViT models (Dosovitskiy et al., 2020) of various sizes trained on various data and objectives. We mainly consider the popular vision models: classification on ImageNet-21K (Russakovsky et al., 2015), MAE (He et al., 2021), DINOv2 (Oquab et al., 2023), CLIP (Radford et al., 2021), and CLIP finetuned on ImageNet-12K. These models were downloaded from PyTorch Image Models (TIMM; timm). This is a subset of the models used in vision-vision comparison.

To compute the alignment metric, we use $k = 10$ nearest neighbors over 1024 samples from WIT (Wikipedia-based Image Text)(Srinivasan et al., 2021). For the vision model, we use class token of each layer, and for the language model, we average pool each layer to a single token. Since it is not trivial to determine where the alignment might occur, we draw inspiration from BrainScoreSchrimpf et al. (2018) and compute pairwise alignment scores, then take the maximum. One of these pairwise comparisons also includes concatenated features. We apply l_2 normalization to the features before measuring the distance. As transformer architectures have "emergent outliers" (Dettmers et al., 2022), we truncate the elements in the features that are above the 95-th percentile.

Simply taking the last token did not show any strong alignment signal. We also experimented with prompting the language model and taking the last token

representation. The prompt we used was

```
An image with the caption '<caption>'. This is an image of a <fill>
```

Using prompting showed similar trends to average pooling but had slightly lower alignment scores.

E.4 Color Cooccurrence Experiment

Here we describe the details of how we created the four color representations visualized in Figure 6-8, from left to right.

Perceptual representation from CIELAB color space We embed pixels taken from the CIFAR-10 image dataset (Krizhevsky et al., 2009; Torralba et al., 2008) based on the CIELAB color space, which is designed as a *perceptually uniform* space that changes numerical values correspond to similar perceived changes in color.

Three representations from cooccurrence in VISION and LANGUAGE For these three representations, we first obtain a dissimilarity matrix over colors (in different ways detailed below), then use multidimensional scaling (Shepard, 1980) to find a 3-dimensional embedding in which Euclidean distance between the embeddings for A and B, z_A and z_B, best matches this dissimilarity matrix. We use 1,000 fits and take the best match. Afterward, we visually align it with the CIELAB space by finding the best rotation, translation, scaling, and flipping, by running the Kabsch-Umeyama algorithm (Kabsch, 1976, 1978; Umeyama, 1991) twice, once on $\mathbf{z}$ and once on $-\mathbf{z}$, to account for flipping. The dissimilarity matrix we used in each case is described as following:

- **VISION: Pixel cooccurrence.** We collect color cooccurrence statistics from the CIFAR-10 dataset, and estimate a joint distribution $p(A, B)$ over 300,000 randomly sampled pixel colors A and B that occur within a radius of at most 4 pixels of one another. Colors are quantized on a grid in RGB space and

represented as discrete variables, and $p(A, B)$ is modeled as a table of normalized counts, from which we compute the empirical pointwise mutual information matrix $K_{\mathsf{PMI}}(A, B)$. Quantization ensures that there is no bias from how color distances are represented in RGB space. Dissimilarity matrix is defined as $-K_{\mathsf{PMI}}(A, B) + c$, where $c = \max_{A,B} K_{\mathsf{PMI}}(A, B)$ is an offset to ensure non-negativity (similar to the constant in Section 6.4.2 and Proposition E.6.1 that ensures neural networks can express K_{PMI}).

- **LANGUAGE.** We used an approach similar to Abdou et al. (2021).
  - We take 20 pairs of (color, word) appeared in the dataset collected by Lindsey and Brown (2014), where 51 participants were asked to free name each of the 330 colors from the Munsell Color Chart. We filtered words that appeared less than 100 times, and computed each word's associate color by taking the centroid in CIELAB space. Our filtering process followed Abdou et al. (2021) exactly, but resulted in 20 colors, a slightly different set than the 18 colors they claimed.
  - For each of the 20 color words `<col>`, we construct three sentences:

    ```
    The color <col>.
    This color is <col>.
    The color of this thing is <col>.
    ```

    and obtain the average sentence embedding from the language encoder, as the embedding for `<col>` (details below). We find this approach more effective than Abdou et al. (2021), which uses object names that potentially have color biases, even though the objects may appear in multiple colors.
  - Unlike Abdou et al. (2021), we did not perform linear regression from language embedding to CIELAB space, which distorts distances and easily overfits with only 20 samples. Instead, we used multidimensional scaling to best preserve distances, as described above.

– **Masked language contrastive learning (SimCSE) embedding:** We used sentence embedding from the unsupervised SimCSE RoBERTa-L (Gao et al., 2021) to encode the above sentences into 1024-dimensional embeddings, and used the pairwise Euclidean distances among `<col>` embeddings as the dissimilarity matrix.

– **Masked language predictive learning (RoBERTa) embedding:** We concatenated hidden states of the last four layers of RoBERTa-L (Liu et al., 2019), following (Devlin et al., 2018). We averaged across token dimensions, and obtained a 4096-dimensional embedding for each of the above sentences, and used the pairwise Euclidean distances among `<col>` embeddings as the dissimilarity matrix.

E.5 Caption Density Experiments

We use LLaMA3-8B-Instruct (Meta, 2024) to generate summary captions at various densities for images in the Densely Captioned Images dataset (Urbanek et al., 2023) from the train split. Following Urbanek et al. (2023), we prompt the language model with the following instructions to generate captions at differing granularity:

```
system: You are given a full-text description of an image. You should summarize it into about <num_words> words, being sure to include as much salient visual information as possible given the <num_words> word constraint, especially information from the start of the original description. The new description should apply for the original image. Respond with only the summary, in one line.

user: <original_caption>
```

We measure the alignment with this generated caption to test our hypothesis that denser captations would result in higher alignment scores. In Figure 6-9, we find that the alignment score also improves as caption length increases.

E.6 Analysis of Contrastive Learners

E.6.1 Contrastive objectives learn pointwise mutual information

There are two widely used forms of contrastive objectives. We now discuss each form in detail and show how they both are minimized by the pointwise mutual information (PMI) as stated in Equation (6.5). To simplify notation, we consider learning the bivariate model $g(x_a, x_b) \in \mathbb{R}$. In Section 6.4, such g is optimized within the family of $\{g = \langle f_X, f_X \rangle \colon f_X \in \mathcal{F}_X\}$.

Recall that our positive pairs are sampled from $(x, x_+) \sim P_{\mathsf{coor}}$, and that the negative pairs are sampled independently from its marginals which we denote as $(x, x_-) \overset{\text{i.i.d.}}{\sim} P$ where $P(x) = \sum_{x_+} P_{\mathsf{coor}}(x, x_+)$.

1. **The binary NCE loss (Gutmann and Hyvärinen, 2010)** is defined with a certain prior over sampling positive vs. negative pairs. Let p_{pos} be the probability of sampling a positive pair. Then the loss is given by

$$\mathcal{L}_{\mathsf{binary\text{-}NCE}}(g) \triangleq p_{\mathsf{pos}} \cdot \mathbb{E}_{(x,x_+)\sim P_{\mathsf{coor}}} \left[-\log \sigma(g(x, x_+)) \right] + (1 - p_{\mathsf{pos}}) \cdot \mathbb{E}_{(x,x_-) \overset{\text{i.i.d.}}{\sim} P} \left[-\log \sigma(-g(x, x_-)) \right]. \tag{E.12}$$

   The Bayes optimal solution is given by

$$\begin{aligned} g(x_a, x_b) &= \log \frac{P(\mathsf{pos} \mid x_a, x_b)}{1 - P(\mathsf{pos} \mid x_a, x_b)} && \text{(E.13)} \\ &= \log \frac{P(\mathsf{pos}, x_a, x_b)}{P(\mathsf{neg}, x_a, x_b)} && \text{(E.14)} \\ &= \log \frac{p_{\mathsf{pos}} \cdot P_{\mathsf{coor}}(x_a, x_b)}{(1 - p_{\mathsf{pos}}) P(x_a) P(x_b)} && \text{(E.15)} \\ &= \log \frac{P_{\mathsf{coor}}(x_a, x_b)}{P(x_a) P(x_b)} + \log \frac{p_{\mathsf{pos}}}{1 - p_{\mathsf{pos}}} && \text{(E.16)} \\ &= K_{\mathsf{PMI}}(x_a, x_b) + c_X. && \text{(E.17)} \end{aligned}$$

2. **The InfoNCE loss (Oord et al., 2018)** is defined with randomly sampling one positive pair along with K negative ones. With some hyperparameter $\tau > 0$,

the loss is given by

$$\mathcal{L}_{\mathsf{InfoNCE}}(g) \triangleq \mathbb{E}_{\substack{(x,x_+)\sim P_{\mathsf{coor}} \\ (x_-^{(1)},x_-^{(2)},\ldots,x_-^{(K)}) \overset{\text{i.i.d.}}{\sim} P}} \left[-\log \frac{e^{g(x,x_+)/\tau}}{e^{g(x,x_+)/\tau} + \sum_{i=1}^{K} e^{g(x,x_-^{(i)})/\tau}} \right]. \quad \text{(E.18)}$$

The Bayes optimal solution is given by

$$\frac{e^{g(x,x_+)/\tau}}{e^{g(x,x_+)/\tau} + \sum_{i=1}^{K} e^{g(x,x_-^{(i)})/\tau}} = \frac{P_{\mathsf{coor}}(x_+ \mid x) \prod_j P(x_-^{(j)})}{P_{\mathsf{coor}}(x_+ \mid x) \prod_j P(x_-^{(j)}) + \sum_i P_{\mathsf{coor}}(x_-^{(i)} \mid x) P(x_+) \prod_{j \neq i} P(x_-^{(j)})} \quad \text{(E.19)}$$

$$= \frac{P_{\mathsf{coor}}(x_+ \mid x)/P(x_+)}{P_{\mathsf{coor}}(x_+ \mid x)/P(x_+) + \sum_i P_{\mathsf{coor}}(x_-^{(i)} \mid x)/P(x_-^{(i)})}. \quad \text{(E.20)}$$

For $\tau = 1$, this optima corresponds to g choices where

$$g(x_a, x_b) = \log \frac{P_{\mathsf{coor}}(x_b \mid x_a)}{P(x_b)} + c_X(x_a) \quad \text{(E.21)}$$

$$= K_{\mathsf{PMI}}(x_a, x_b) + c_X(x_a). \quad \text{(E.22)}$$

For the general $\tau \neq 1$ case, we have g (and corresponding f_X) recovers K_{PMI} up to an offset and a scale. Our main argument in Section 6.4 that f_X recovers K_{PMI} still holds.

E.6.2 Contrastive learners can represent K_{PMI} exactly under smoothness conditions

We want to express $K_{\mathsf{PMI}} + C$ using some representation function $f_X \colon \mathcal{X} \to \mathbb{R}^n$ so that

$$\langle f_X(x_a), f_X(x_b) \rangle = K_{\mathsf{PMI}}(x_a, x_b) + C, \qquad \text{for some } C. \quad \text{(E.23)}$$

For such an f_X to exist, an equivalent criterion is that $K_{\mathsf{PMI}} + C$ is positive semi-definite (PSD), as can be seen from eigendecomposition.

Proposition E.6.1. Suppose that the off-diagonal elements of K_{PMI} are bounded within $[\log \rho_{\mathsf{min}}, \log \rho_{\mathsf{min}} + \delta] \in (-\infty, 0]$. We have $K_{\mathsf{PMI}} + C$ is positive semi-definite (PSD) for some C if the joint distribution is sufficiently smooth:

$$\frac{P_{\mathsf{coor}}(z_i \mid z_i)}{P_{\mathsf{coor}}(z_i)} \geq e^{N\delta} \rho_{\mathsf{min}}, \qquad \forall i. \tag{E.24}$$

Proof. Note that $K_{\mathsf{PMI}} + C$ still only has non-positive off-diagonal elements if

$$-C \geq \log \rho_{\mathsf{min}} + \delta. \tag{E.25}$$

For such C, it is diagonally dominant (and thus PSD) if,

$$\forall i, \qquad K_{\mathsf{PMI}}(z_i, z_i) + C \geq \sum_{j \neq i} |K_{\mathsf{PMI}}(z_i, z_j) + C| = -(N-1)C - \sum_{j \neq i} K_{\mathsf{PMI}}(z_i, z_j), \tag{E.26}$$

or equivalently,

$$\forall i, \qquad NC + \sum_j K_{\mathsf{PMI}}(z_i, z_j) \geq 0. \tag{E.27}$$

The following choice of C readily satisfies the above Equation (E.27):

$$C \triangleq -\min_i \frac{1}{N} \sum_j K_{\mathsf{PMI}}(z_i, z_j). \tag{E.28}$$

Therefore, it remains to show that Equation (E.25) is true. Note that

$$-C \triangleq \min_i \frac{1}{N} \sum_j K_{\mathsf{PMI}}(z_i, z_j) \geq \frac{N-1}{N} \log \rho_{\mathsf{min}} + \frac{1}{N} (\min_i K_{\mathsf{PMI}}(z_i, z_i)). \tag{E.29}$$

Therefore, it suffices to have

$$\log \rho_{\mathsf{min}} + \delta \leq \frac{N-1}{N} \log \rho_{\mathsf{min}} + \frac{1}{N} (\min_i K_{\mathsf{PMI}}(z_i, z_i)). \tag{E.30}$$

Rearranging terms gives the desired condition

$$\frac{P_{\mathsf{coor}}(z_i \mid z_i)}{P_{\mathsf{coor}}(z_i)} \geq e^{N\delta} \rho_{\mathsf{min}}, \qquad \forall i. \tag{E.31}$$

□

Remark E.6.2. Proposition E.6.1 is one example that a sufficiently smooth world or a sufficiently high sampling rate allows the PMI kernel K_{PMI} to be *exactly* represented as inner products of a learned feature space (up to a scale). The condition here can be satisfied, for example, if the off-diagonal terms decay linearly with respect to N and stay sufficiently close to each other. While the condition is somewhat strict, it captures the essence that smoothness and continuity allow easier learning. Nonetheless, we note that exact representation is not necessary for convergence, and thus this requirement can likely be relaxed. Please see Section 6.6 for discussions on practical settings.

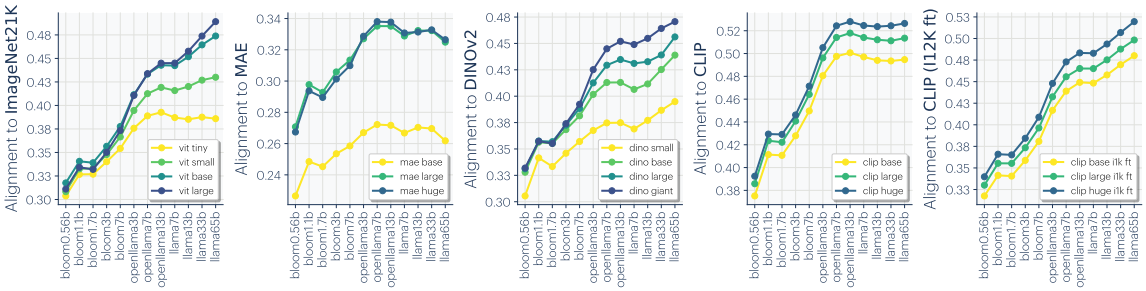

(a) CKA

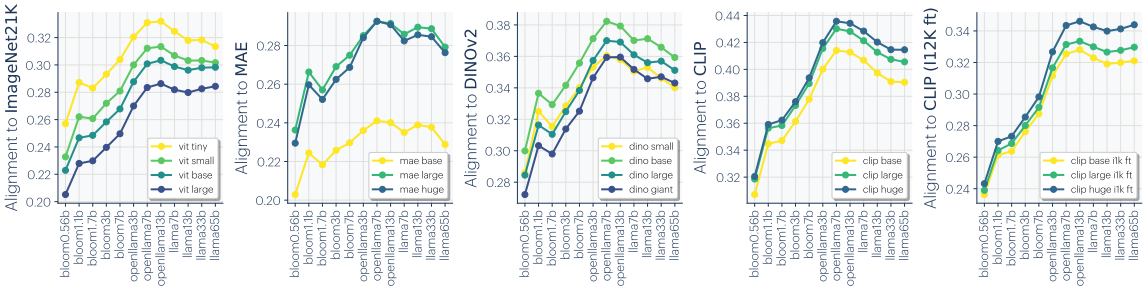

(b) Unbiased CKA

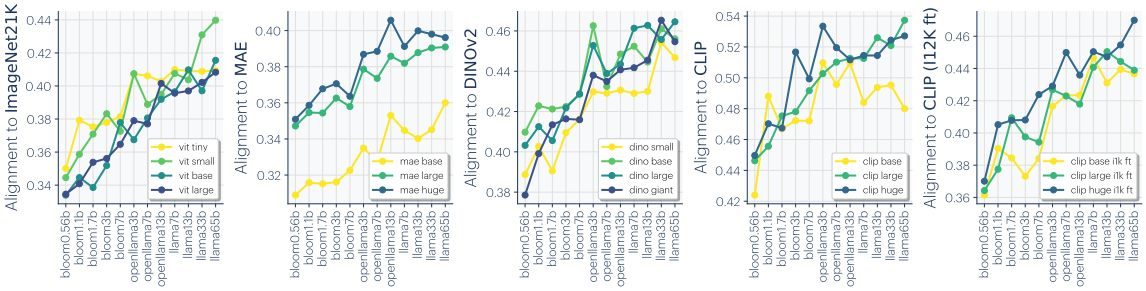

(c) SVCCA

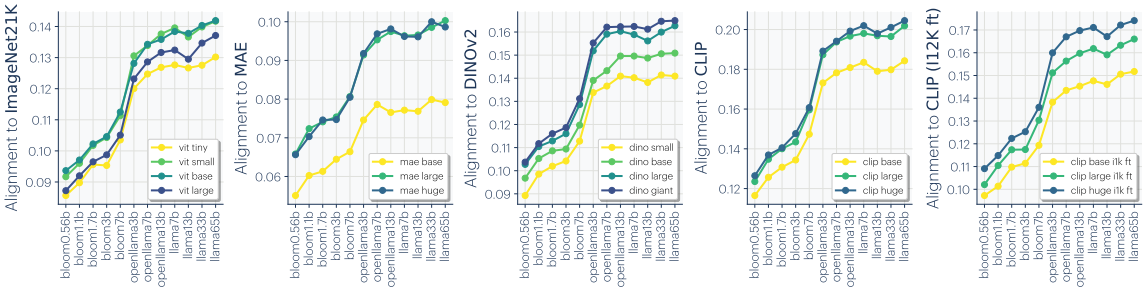

(d) Mutual k-NN ($k = 10$)

Figure E-4: Cross-modal alignment for various metrics (Figure 1 of 2).

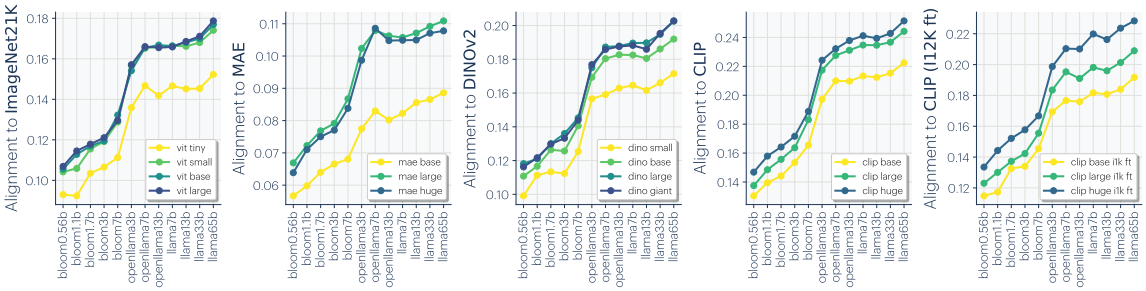

(a) CKNNA ($k = 10$)

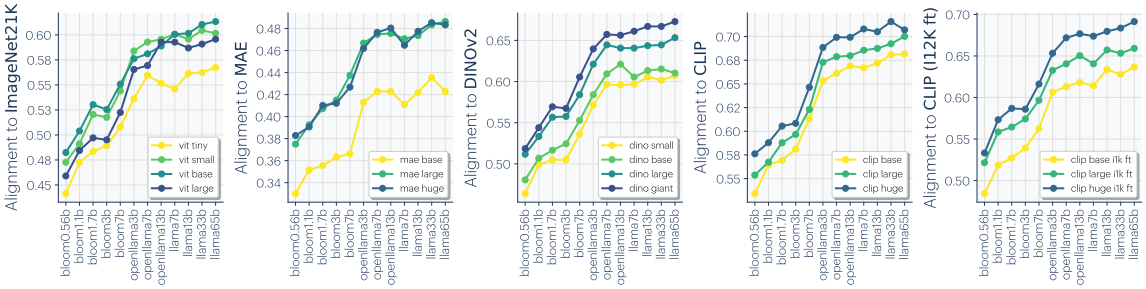

(b) Cycle k-NN ($k = 10$)

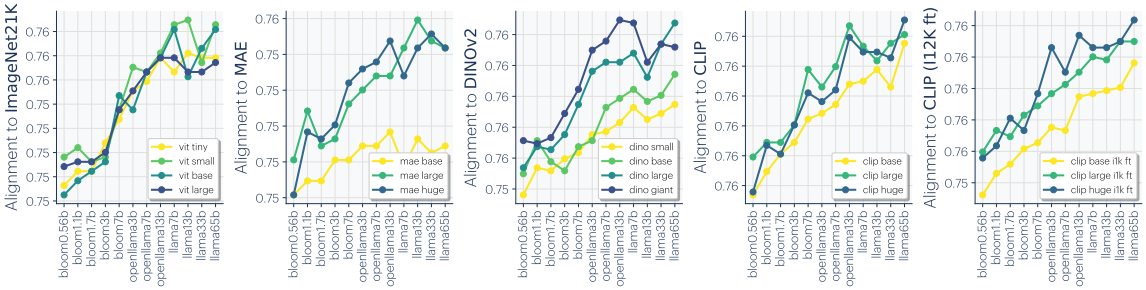

(c) Edit-distance k-NN ($k = 10$)

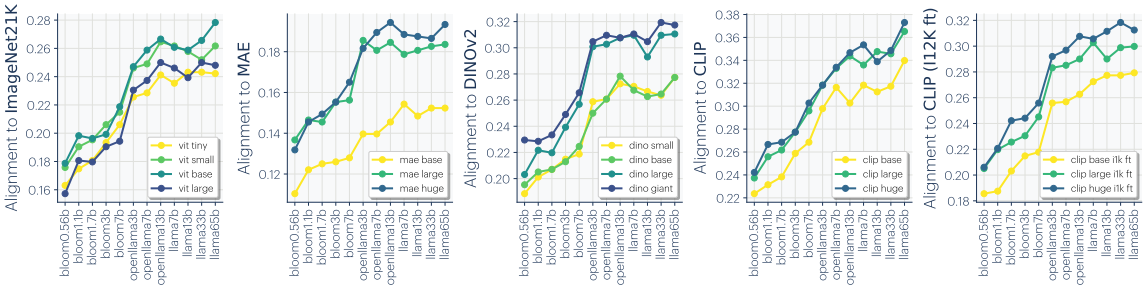

(d) Longest-Common-Subsequence k-NN ($k = 10$)

Figure E-5: Cross-modal alignment for various metrics (Figure 2 of 2).

Bibliography

Mostafa Abdou, Artur Kulmizev, Daniel Hershcovich, Stella Frank, Ellie Pavlick, and Anders Søgaard. Can language models encode perceptual structure without grounding? a case study in color. *arXiv preprint arXiv:2109.06129*, 2021.

Alekh Agarwal, Sham Kakade, Akshay Krishnamurthy, and Wen Sun. FLAMBE: Structural complexity and representation learning of low rank mdps. *arXiv preprint arXiv:2006.10814*, 2020.

Ibrahim Ahmad and Pi-Erh Lin. A nonparametric estimation of the entropy for absolutely continuous distributions (corresp.). *IEEE Transactions on Information Theory*, 22(3):372–375, 1976.

Samuel K Ainsworth, Jonathan Hayase, and Siddhartha Srinivasa. Git re-basin: Merging models modulo permutation symmetries. *arXiv preprint arXiv:2209.04836*, 2022.

Noga Alon and Joel H Spencer. *The probabilistic method*. John Wiley & Sons, 2004.

Brandon Amos, Lei Xu, and J Zico Kolter. Input convex neural networks. In *International Conference on Machine Learning*, pages 146–155. PMLR, 2017.

Marcin Andrychowicz, Filip Wolski, Alex Ray, Jonas Schneider, Rachel Fong, Peter Welinder, Bob McGrew, Josh Tobin, OpenAI Pieter Abbeel, and Wojciech Zaremba. Hindsight experience replay. *Advances in neural information processing systems*, 30, 2017.

Richard Antonello and Alexander Huth. Predictive coding or just feature discovery? an alternative account of why language models fit brain data. *Neurobiology of Language*, 5(1):64–79, 2024.

Nachman Aronszajn. Theory of reproducing kernels. *Transactions of the American mathematical society*, 68(3):337–404, 1950.

Sanjeev Arora, Nadav Cohen, Wei Hu, and Yuping Luo. Implicit regularization in deep matrix factorization. *Advances in Neural Information Processing Systems*, 32, 2019a.

Sanjeev Arora, Simon S Du, Wei Hu, Zhiyuan Li, Ruslan Salakhutdinov, and Ruosong Wang. On exact computation with an infinitely wide neural net. *arXiv preprint arXiv:1904.11955*, 2019b.

Sanjeev Arora, Hrishikesh Khandeparkar, Mikhail Khodak, Orestis Plevrakis, and Nikunj Saunshi. A theoretical analysis of contrastive unsupervised representation learning. *arXiv preprint arXiv:1902.09229*, 2019c.

Philip Bachman, R Devon Hjelm, and William Buchwalter. Learning representations by maximizing mutual information across views. In *Advances in Neural Information Processing Systems*, pages 15509–15519, 2019.

Ananth Balashankar and Lakshminarayanan Subramanian. Learning faithful representations of causal graphs. In *Proceedings of the 59th Annual Meeting of the Association for Computational Linguistics and the 11th International Joint Conference on Natural Language Processing (Volume 1: Long Papers)*, pages 839–850, 2021.

Randall Balestriero and Richard G Baraniuk. A spline theory of deep learning. In *International Conference on Machine Learning*, pages 374–383. PMLR, 2018.

Yamini Bansal, Preetum Nakkiran, and Boaz Barak. Revisiting model stitching to compare neural representations. *Advances in neural information processing systems*, 34:225–236, 2021.

Manel Baradad, Jonas Wulff, Tongzhou Wang, Phillip Isola, and Antonio Torralba. Learning to see by looking at noise. In *Advances in Neural Information Processing Systems*, 2021.

Manel Baradad, Richard Chen, Jonas Wulff, Tongzhou Wang, Rogerio Feris, Antonio Torralba, and Phillip Isola. Procedural image programs for representation learning. *Advances in Neural Information Processing Systems*, 35:6450–6462, 2022.

Horace B Barlow et al. Possible principles underlying the transformation of sensory messages. *Sensory communication*, 1(01):217–233, 1961.

Marc Bellemare, Will Dabney, Robert Dadashi, Adrien Ali Taiga, Pablo Samuel Castro, Nicolas Le Roux, Dale Schuurmans, Tor Lattimore, and Clare Lyle. A geometric perspective on optimal representations for reinforcement learning. *Advances in neural information processing systems*, 32, 2019.

Yoshua Bengio et al. Quick training of probabilistic neural nets by importance sampling.

Umberto Bertele and Francesco Brioschi. On non-serial dynamic programming. *J. Comb. Theory, Ser. A*, 14(2):137–148, 1973.

Dimitri P Bertsekas and John N Tsitsiklis. An analysis of stochastic shortest path problems. *Mathematics of Operations Research*, 16(3):580–595, 1991.

James Betker, Gabriel Goh, Li Jing, Tim Brooks, Jianfeng Wang, Linjie Li, Long Ouyang, Juntang Zhuang, Joyce Lee, Yufei Guo, et al. Improving image generation with better captions. *Computer Science. https://cdn. openai. com/papers/dall-e-3. pdf*, 2(3):8, 2023.

BigScience, Teven Le Scao, Angela Fan, Christopher Akiki, Ellie Pavlick, Suzana Ilić, Daniel Hesslow, Roman Castagné, Alexandra Sasha Luccioni, François Yvon, et al. Bloom: A 176b-parameter open-access multilingual language model. *arXiv preprint arXiv:2211.05100*, 2022.

S Bochner. Monotone funktionen, stieltjessche integrale und harmonische analyse. *Collected Papers of Salomon Bochner*, 2:87, 1992.

Kenneth P Bogart. Maximal dimensional partially ordered sets i. hiraguchi's theorem. *Discrete Mathematics*, 5(1):21–31, 1973.

Piotr Bojanowski and Armand Joulin. Unsupervised learning by predicting noise. In *Proceedings of the 34th International Conference on Machine Learning-Volume 70*, pages 517–526. JMLR. org, 2017.

Béla Bollobás and Bollobás Béla. *Random graphs*. Number 73. Cambridge university press, 2001.

Rishi Bommasani, Drew A Hudson, Ehsan Adeli, Russ Altman, Simran Arora, Sydney von Arx, Michael S Bernstein, Jeannette Bohg, Antoine Bosselut, Emma Brunskill, et al. On the opportunities and risks of foundation models. *arXiv preprint arXiv:2108.07258*, 2021.

Sergiy V Borodachov, Douglas P Hardin, and Edward B Saff. *Discrete energy on rectifiable sets*. Springer, 2019.

Jean Bourgain. On lipschitz embedding of finite metric spaces in hilbert space. *Israel Journal of Mathematics*, 52(1-2):46–52, 1985.

Anthony Brohan, Noah Brown, Justice Carbajal, Yevgen Chebotar, Xi Chen, Krzysztof Choromanski, Tianli Ding, Danny Driess, Avinava Dubey, Chelsea Finn, et al. Rt-2: Vision-language-action models transfer web knowledge to robotic control. *arXiv preprint arXiv:2307.15818*, 2023.

Barry Brown, James Lovato, and Kathy Russell. CDFLIB: library of fortran routines for cumulative distribution functions, inverses, and other parameters, 1994.

Yury Brychkov. On some properties of the marcum q function. *Integral Transforms and Special Functions*, 23:177–182, 03 2012. doi: 10.1080/10652469.2011.573184.

John Burkardt. C++ source code for CDFLIB. https://people.sc.fsu.edu/~jburkardt/cpp_src/cdflib/cdflib.html, 2021.

Rosa Cao and Daniel Yamins. Explanatory models in neuroscience: Part 2–constraint-based intelligibility. *Cognitive Systems Research*, 85, 2024.

Mathilde Caron, Hugo Touvron, Ishan Misra, Hervé Jégou, Julien Mairal, Piotr Bojanowski, and Armand Joulin. Emerging properties in self-supervised vision transformers. In *Proceedings of the IEEE/CVF international conference on computer vision*, pages 9650–9660, 2021.

Pablo Samuel Castro. Scalable methods for computing state similarity in deterministic markov decision processes. In *Proceedings of the AAAI Conference on Artificial Intelligence*, volume 34, pages 10069–10076, 2020.

Nathanael Chambers and Dan Jurafsky. Unsupervised learning of narrative event chains. In *Proceedings of ACL-08: HLT*, pages 789–797, 2008.

Moses Charikar, Konstantin Makarychev, and Yury Makarychev. Directed metrics and directed graph partitioning problems. In *SODA*, volume 6, pages 51–60. Citeseer, 2006.

Lili Chen, Kevin Lu, Aravind Rajeswaran, Kimin Lee, Aditya Grover, Misha Laskin, Pieter Abbeel, Aravind Srinivas, and Igor Mordatch. Decision transformer: Reinforcement learning via sequence modeling. *Advances in neural information processing systems*, 34:15084–15097, 2021.

Patrick H Chen, Si Si, Sanjiv Kumar, Yang Li, and Cho-Jui Hsieh. Learning to screen for fast softmax inference on large vocabulary neural networks. 2018.

Ting Chen, Simon Kornblith, Mohammad Norouzi, and Geoffrey Hinton. A simple framework for contrastive learning of visual representations. In *International conference on machine learning*, pages 1597–1607. PMLR, 2020a.

Xinlei Chen, Haoqi Fan, Ross Girshick, and Kaiming He. Improved baselines with momentum contrastive learning. *arXiv preprint arXiv:2003.04297*, 2020b.

Xinlei Chen, Haoqi Fan, Ross Girshick, and Kaiming He. Improved baselines with momentum contrastive learning. GitHub repository https://github.com/facebookresearch/moco/tree/78b69cafae80bc74cd1a89ac3fb365dc20d157d3, 2020c.

Maxime Chevalier-Boisvert, Lucas Willems, and Suman Pal. Minimalistic gridworld environment for openai gym. https://github.com/maximecb/gym-minigrid, 2018.

Kyunghyun Cho, Bart van Merriënboer, Caglar Gulcehre, Dzmitry Bahdanau, Fethi Bougares, Holger Schwenk, and Yoshua Bengio. Learning phrase representations using RNN encoder–decoder for statistical machine translation. In *Proceedings of the 2014 Conference on Empirical Methods in Natural Language Processing (EMNLP)*, pages 1724–1734, Doha, Qatar, October 2014. Association for Computational Linguistics. doi: 10.3115/v1/D14-1179.

Sumit Chopra, Raia Hadsell, and Yann LeCun. Learning a similarity metric discriminatively, with application to face verification. In *2005 IEEE Computer Society Conference on Computer Vision and Pattern Recognition (CVPR'05)*, volume 1, pages 539–546. IEEE, 2005.

Adam Coates, Andrew Ng, and Honglak Lee. An analysis of single-layer networks in unsupervised feature learning. In *Proceedings of the fourteenth international conference on artificial intelligence and statistics*, pages 215–223, 2011.

Karl Cobbe, Vineet Kosaraju, Mohammad Bavarian, Mark Chen, Heewoo Jun, Lukasz Kaiser, Matthias Plappert, Jerry Tworek, Jacob Hilton, Reiichiro Nakano, Christopher Hesse, and John Schulman. Training verifiers to solve math word problems. *arXiv preprint arXiv:2110.14168*, 2021.

Henry Cohn and Abhinav Kumar. Universally optimal distribution of points on spheres. *Journal of the American Mathematical Society*, 20(1):99–148, 2007.

Colin Conwell, Jacob S Prince, Kendrick N Kay, George A Alvarez, and Talia Konkle. What can 1.8 billion regressions tell us about the pressures shaping high-level visual representation in brains and machines? *BioRxiv*, pages 2022–03, 2022.

Kenneth James Williams Craik. *The nature of explanation*, volume 445. CUP Archive, 1952.

Tim R. Davidson, Luca Falorsi, Nicola De Cao, Thomas Kipf, and Jakub M. Tomczak. Hyperspherical variational auto-encoders. *34th Conference on Uncertainty in Artificial Intelligence (UAI-18)*, 2018.

Pieter-Tjerk De Boer, Dirk P Kroese, Shie Mannor, and Reuven Y Rubinstein. A tutorial on the cross-entropy method. *Annals of operations research*, 134(1):19–67, 2005.

Eric V Denardo. On linear programming in a markov decision problem. *Management Science*, 16(5):281–288, 1970.

Daniel C Dennett. Why the law of effect will not go away. *Journal for the Theory of Social Behaviour*, 1975.

Tim Dettmers, Mike Lewis, Younes Belkada, and Luke Zettlemoyer. Gpt3. int8 (): 8-bit matrix multiplication for transformers at scale. *Advances in Neural Information Processing Systems*, 35:30318–30332, 2022.

Jacob Devlin, Ming-Wei Chang, Kenton Lee, and Kristina Toutanova. Bert: Pre-training of deep bidirectional transformers for language understanding. *arXiv preprint arXiv:1810.04805*, 2018.

Jared M Diamond. *Guns, germs and steel: a short history of everybody for the last 13,000 years*. Vintage London, 1998.

Kamaludin Dingle, Chico Q Camargo, and Ard A Louis. Input–output maps are strongly biased towards simple outputs. *Nature communications*, 9(1):761, 2018.

Jeff Donahue, Yangqing Jia, Oriol Vinyals, Judy Hoffman, Ning Zhang, Eric Tzeng, and Trevor Darrell. Decaf: A deep convolutional activation feature for generic visual recognition. In *International conference on machine learning*, pages 647–655. PMLR, 2014.

Gerald Doppelt. Reconstructing scientific realism to rebut the pessimistic meta-induction. *Philosophy of Science*, 74(1):96–118, 2007.

Pierluca D'Oro, Max Schwarzer, Evgenii Nikishin, Pierre-Luc Bacon, Marc G Bellemare, and Aaron Courville. Sample-efficient reinforcement learning by breaking the replay ratio barrier. In *International Conference on Learning Representations*, 2023.

Alexey Dosovitskiy, Lucas Beyer, Alexander Kolesnikov, Dirk Weissenborn, Xiaohua Zhai, Thomas Unterthiner, Mostafa Dehghani, Matthias Minderer, Georg Heigold, Sylvain Gelly, et al. An image is worth 16x16 words: Transformers for image recognition at scale. *arXiv preprint arXiv:2010.11929*, 2020.

Amil Dravid, Yossi Gandelsman, Alexei A Efros, and Assaf Shocher. Rosetta neurons: Mining the common units in a model zoo. In *Proceedings of the IEEE/CVF International Conference on Computer Vision*, pages 1934–1943, 2023.

Danny Driess, Fei Xia, Mehdi SM Sajjadi, Corey Lynch, Aakanksha Chowdhery, Brian Ichter, Ayzaan Wahid, Jonathan Tompson, Quan Vuong, Tianhe Yu, et al. Palm-e: An embodied multimodal language model. *arXiv preprint arXiv:2303.03378*, 2023.

Simon Du, Akshay Krishnamurthy, Nan Jiang, Alekh Agarwal, Miroslav Dudik, and John Langford. Provably efficient RL with rich observations via latent state decoding. In *International Conference on Machine Learning*, pages 1665–1674. PMLR, 2019.

Ishan Durugkar, Mauricio Tec, Scott Niekum, and Peter Stone. Adversarial intrinsic motivation for reinforcement learning. *Advances in Neural Information Processing Systems*, 34:8622–8636, 2021.

Yonathan Efroni, Dipendra Misra, Akshay Krishnamurthy, Alekh Agarwal, and John Langford. Provable RL with exogenous distractors via multistep inverse dynamics. *arXiv preprint arXiv:2110.08847*, 2021.

Jeffrey L Elman. Finding structure in time. *Cognitive science*, 14(2):179–211, 1990.

Scott Emmons, Benjamin Eysenbach, Ilya Kostrikov, and Sergey Levine. Rvs: What is essential for offline RL via supervised learning? *arXiv preprint arXiv:2112.10751*, 2021.

Paul Erdős and Alfréd Rényi. On random graphs. i. *Publicationes Mathematicae Debrecen*, 6:290–297, 1959.

Benjamin Eysenbach, Ruslan Salakhutdinov, and Sergey Levine. Robust predictable control. *arXiv preprint arXiv:2109.03214*, 2021.

Benjamin Eysenbach, Tianjun Zhang, Ruslan Salakhutdinov, and Sergey Levine. Contrastive learning as goal-conditioned reinforcement learning. *arXiv preprint arXiv:2206.07568*, 2022.

Linxi Fan, Guanzhi Wang, Yunfan Jiang, Ajay Mandlekar, Yuncong Yang, Haoyi Zhu, Andrew Tang, De-An Huang, Yuke Zhu, and Anima Anandkumar. Minedojo: Building open-ended embodied agents with internet-scale knowledge. In *Thirty-sixth Conference on Neural Information Processing Systems Datasets and Benchmarks Track*, 2022.

Stefan Felsner, Ching Man Li, and William T. Trotter. Adjacency posets of planar graphs. *Discrete Mathematics*, 310(5):1097–1104, 2010. ISSN 0012-365X.

Norm Ferns, Prakash Panangaden, and Doina Precup. Metrics for finite markov decision processes. In *UAI*, volume 4, pages 162–169, 2004.

Norman Ferns and Doina Precup. Bisimulation metrics are optimal value functions. In *UAI*, pages 210–219, 2014.

Justin Fu, Aviral Kumar, Ofir Nachum, George Tucker, and Sergey Levine. D4rl: Datasets for deep data-driven reinforcement learning, 2020.

Xiang Fu, Ge Yang, Pulkit Agrawal, and Tommi Jaakkola. Learning task informed abstractions. In *International Conference on Machine Learning*, pages 3480–3491. PMLR, 2021.

Scott Fujimoto and Shixiang Shane Gu. A minimalist approach to offline reinforcement learning. *Advances in neural information processing systems*, 34:20132–20145, 2021.

Scott Fujimoto, Herke Hoof, and David Meger. Addressing function approximation error in actor-critic methods. In *International Conference on Machine Learning*, pages 1587–1596. PMLR, 2018.

Scott Fujimoto, David Meger, Doina Precup, Ofir Nachum, and Shixiang Shane Gu. Why should I trust you, Bellman? the Bellman error is a poor replacement for value error. *arXiv preprint arXiv:2201.12417*, 2022.

Octavian Ganea, Gary Bécigneul, and Thomas Hofmann. Hyperbolic entailment cones for learning hierarchical embeddings. In *International Conference on Machine Learning*, pages 1646–1655. PMLR, 2018.

Tianyu Gao, Xingcheng Yao, and Danqi Chen. SimCSE: Simple contrastive learning of sentence embeddings. In *Empirical Methods in Natural Language Processing (EMNLP)*, 2021.

Timur Garipov, Pavel Izmailov, Dmitrii Podoprikhin, Dmitry P Vetrov, and Andrew G Wilson. Loss surfaces, mode connectivity, and fast ensembling of dnns. *Advances in neural information processing systems*, 31, 2018.

Amnon Geifman, Abhay Yadav, Yoni Kasten, Meirav Galun, David Jacobs, and Ronen Basri. On the similarity between the Laplace and neural tangent kernels. *arXiv preprint arXiv:2007.01580*, 2020.

Carles Gelada, Saurabh Kumar, Jacob Buckman, Ofir Nachum, and Marc G Bellemare. Deepmdp: Learning continuous latent space models for representation learning. In *International Conference on Machine Learning*, pages 2170–2179. PMLR, 2019.

Murray Gell-Mann. *The Quark and the Jaguar: Adventures in the Simple and the Complex*. Macmillan, 1995.

Xinyang Geng and Hao Liu. OpenLLaMA: An open reproduction of LLaMA, May 2023. URL https://github.com/openlm-research/open_llama.

Seyed Kamyar Seyed Ghasemipour, Shixiang Shane Gu, and Ofir Nachum. Why so pessimistic? Estimating uncertainties for offline RL through ensembles, and why their independence matters. *arXiv preprint arXiv:2205.13703*, 2022.

Dibya Ghosh, Abhishek Gupta, Ashwin Reddy, Justin Fu, Coline Devin, Benjamin Eysenbach, and Sergey Levine. Learning to reach goals via iterated supervised learning. *arXiv preprint arXiv:1912.06088*, 2019.

Robert Givan, Thomas Dean, and Matthew Greig. Equivalence notions and model minimization in markov decision processes. *Artificial Intelligence*, 147(1-2):163–223, 2003.

Aaron Gokaslan and Vanya Cohen. Openwebtext corpus. http://Skylion007.github.io/OpenWebTextCorpus, 2019.

Micah Goldblum, Marc Finzi, Keefer Rowan, and Andrew Gordon Wilson. The no free lunch theorem, Kolmogorov complexity, and the role of inductive biases in machine learning. *arXiv preprint arXiv:2304.05366*, 2023.

Joshua Goodman. Classes for fast maximum entropy training. In *2001 IEEE International Conference on Acoustics, Speech, and Signal Processing. Proceedings (Cat. No. 01CH37221)*, volume 1, pages 561–564. IEEE, 2001.

Google. Gemini: a family of highly capable multimodal models. *arXiv preprint arXiv:2312.11805*, 2023.

Mario Götz and Edward B Saff. Note on d—extremal configurations for the sphere in r d+1. In *Recent Progress in Multivariate Approximation*, pages 159–162. Springer, 2001.

Priya Goyal, Piotr Dollár, Ross Girshick, Pieter Noordhuis, Lukasz Wesolowski, Aapo Kyrola, Andrew Tulloch, Yangqing Jia, and Kaiming He. Accurate, large minibatch sgd: Training imagenet in 1 hour. *arXiv preprint arXiv:1706.02677*, 2017.

Edouard Grave, Armand Joulin, Moustapha Cissé, Hervé Jégou, et al. Efficient softmax approximation for gpus. In *Proceedings of the 34th International Conference on Machine Learning-Volume 70*, pages 1302–1310. JMLR. org, 2017.

Arthur Gretton, Olivier Bousquet, Alex Smola, and Bernhard Schölkopf. Measuring statistical dependence with hilbert-schmidt norms. In *International conference on algorithmic learning theory*, pages 63–77. Springer, 2005.

Dirk Groeneveld, Iz Beltagy, Pete Walsh, Akshita Bhagia, Rodney Kinney, Oyvind Tafjord, Ananya Harsh Jha, Hamish Ivison, Ian Magnusson, Yizhong Wang, et al. Olmo: Accelerating the science of language models. *arXiv preprint arXiv:2402.00838*, 2024.

Aditya Grover and Jure Leskovec. node2vec: Scalable feature learning for networks. In *Proceedings of the 22nd ACM SIGKDD international conference on Knowledge discovery and data mining*, pages 855–864, 2016.

Peter Grunwald and Paul Vitányi. Shannon information and kolmogorov complexity. *arXiv preprint cs/0410002*, 2004.

Shuyang Gu, Jianmin Bao, Hao Yang, Dong Chen, Fang Wen, and Lu Yuan. Mask-guided portrait editing with conditional gans. In *Proceedings of the Conference on Computer Vision and Pattern Recognition*, pages 3436–3445, 2019.

Matthieu Guillot and Gautier Stauffer. The stochastic shortest path problem: a polyhedral combinatorics perspective. *European Journal of Operational Research*, 285(1):148–158, 2020.

Suriya Gunasekar, Jason D Lee, Daniel Soudry, and Nati Srebro. Implicit bias of gradient descent on linear convolutional networks. In *Advances in Neural Information Processing Systems*, pages 9461–9471, 2018.

Michael Gutmann and Aapo Hyvärinen. Noise-contrastive estimation: A new estimation principle for unnormalized statistical models. In *Proceedings of the thirteenth international conference on artificial intelligence and statistics*, pages 297–304. JMLR Workshop and Conference Proceedings, 2010.

David Ha and Jürgen Schmidhuber. World models. *arXiv preprint arXiv:1803.10122*, 2018.

Tuomas Haarnoja, Aurick Zhou, Kristian Hartikainen, George Tucker, Sehoon Ha, Jie Tan, Vikash Kumar, Henry Zhu, Abhishek Gupta, Pieter Abbeel, et al. Soft actor-critic algorithms and applications. *arXiv preprint arXiv:1812.05905*, 2018.

Raia Hadsell, Sumit Chopra, and Yann LeCun. Dimensionality reduction by learning an invariant mapping. In *2006 IEEE Computer Society Conference on Computer Vision and Pattern Recognition (CVPR'06)*, volume 2, pages 1735–1742. IEEE, 2006.

Danijar Hafner, Timothy Lillicrap, Jimmy Ba, and Mohammad Norouzi. Dream to control: Learning behaviors by latent imagination. *arXiv preprint arXiv:1912.01603*, 2019a.

Danijar Hafner, Timothy Lillicrap, Ian Fischer, Ruben Villegas, David Ha, Honglak Lee, and James Davidson. Learning latent dynamics for planning from pixels. In *International Conference on Machine Learning*, pages 2555–2565. PMLR, 2019b.

David Hahn, Pol Banzet, James M Bern, and Stelian Coros. Real2sim: Visco-elastic parameter estimation from dynamic motion. *ACM Transactions on Graphics (TOG)*, 38(6):1–13, 2019.

Melissa Hall, Laurens van der Maaten, Laura Gustafson, Maxwell Jones, and Aaron Adcock. A systematic study of bias amplification. *arXiv preprint arXiv:2201.11706*, 2022.

Clyde L Hardin and Alexander Rosenberg. In defense of convergent realism. *Philosophy of Science*, 49(4):604–615, 1982.

DP Hardin and EB Saff. Minimal riesz energy point configurations for rectifiable d-dimensional manifolds. *Advances in Mathematics*, 193(1):174–204, 2005.

Peter E Hart, Nils J Nilsson, and Bertram Raphael. A formal basis for the heuristic determination of minimum cost paths. *IEEE transactions on Systems Science and Cybernetics*, 4(2):100–107, 1968.

Md Hasnat, Julien Bohné, Jonathan Milgram, Stéphane Gentric, Liming Chen, et al. von mises-fisher mixture model-based deep learning: Application to face verification. *arXiv preprint arXiv:1706.04264*, 2017.

Nozomi Hata, Shizuo Kaji, Akihiro Yoshida, and Katsuki Fujisawa. Nested subspace arrangement for representation of relational data. In *International Conference on Machine Learning*, pages 4127–4137. PMLR, 2020.

Kaiming He, Xiangyu Zhang, Shaoqing Ren, and Jian Sun. Deep residual learning for image recognition. In *Proceedings of the IEEE conference on computer vision and pattern recognition*, pages 770–778, 2016.

Kaiming He, Haoqi Fan, Yuxin Wu, Saining Xie, and Ross Girshick. Momentum contrast for unsupervised visual representation learning. *arXiv preprint arXiv:1911.05722*, 2019.

Kaiming He, Haoqi Fan, Yuxin Wu, Saining Xie, and Ross Girshick. Momentum contrast for unsupervised visual representation learning. In *Proceedings of the IEEE/CVF conference on computer vision and pattern recognition*, pages 9729–9738, 2020.

Kaiming He, Xinlei Chen, Saining Xie, Yanghao Li, Piotr Doll'ar, and Ross B Girshick. Masked autoencoders are scalable vision learners. 2022 ieee. In *CVF Conference on Computer Vision and Pattern Recognition (CVPR)*, pages 15979–15988, 2021.

Richard Held, Yuri Ostrovsky, Beatrice de Gelder, Tapan Gandhi, Suma Ganesh, Umang Mathur, and Pawan Sinha. The newly sighted fail to match seen with felt. *Nature neuroscience*, 14(5):551–553, 2011.

Olivier J Hénaff, Ali Razavi, Carl Doersch, SM Eslami, and Aaron van den Oord. Data-efficient image recognition with contrastive predictive coding. *arXiv preprint arXiv:1905.09272*, 2019.

Peter Henderson, Riashat Islam, Philip Bachman, Joelle Pineau, Doina Precup, and David Meger. Deep reinforcement learning that matters. In *Proceedings of the AAAI Conference on Artificial Intelligence*, volume 32, 2018.

Joel Hestness, Sharan Narang, Newsha Ardalani, Gregory Diamos, Heewoo Jun, Hassan Kianinejad, Md Mostofa Ali Patwary, Yang Yang, and Yanqi Zhou. Deep learning scaling is predictable, empirically. *arXiv preprint arXiv:1712.00409*, 2017.

Irina Higgins, David Amos, David Pfau, Sebastien Racaniere, Loic Matthey, Danilo Rezende, and Alexander Lerchner. Towards a definition of disentangled representations. *arXiv preprint arXiv:1812.02230*, 2018.

Toshio Hiraguchi. On the dimension of partially ordered sets. *The science reports of the Kanazawa University*, 1(2):77–94, 1951.

R Devon Hjelm, Alex Fedorov, Samuel Lavoie-Marchildon, Karan Grewal, Phil Bachman, Adam Trischler, and Yoshua Bengio. Learning deep representations by mutual information estimation and maximization. *arXiv preprint arXiv:1808.06670*, 2018.

Elad Hoffer and Nir Ailon. Deep metric learning using triplet network. In *International workshop on similarity-based pattern recognition*, pages 84–92. Springer, 2015.

Sara Hooker. The hardware lottery. *Communications of the ACM*, 64(12):58–65, 2021.

Saihui Hou, Xinyu Pan, Chen Change Loy, Zilei Wang, and Dahua Lin. Learning a unified classifier incrementally via rebalancing. In *Proceedings of the IEEE Conference on Computer Vision and Pattern Recognition*, pages 831–839, 2019.

Minyoung Huh, Pulkit Agrawal, and Alexei A Efros. What makes ImageNet good for transfer learning? *arXiv preprint arXiv:1608.08614*, 2016.

Minyoung Huh, Hossein Mobahi, Richard Zhang, Brian Cheung, Pulkit Agrawal, and Phillip Isola. The low-rank simplicity bias in deep networks. *arXiv preprint arXiv:2103.10427*, 2021.

Minyoung Huh, Hossein Mobahi, Richard Zhang, Brian Cheung, Pulkit Agrawal, and Phillip Isola. The low-rank simplicity bias in deep networks. *Transactions on Machine Learning Research*, 2023. ISSN 2835-8856. URL https://openreview.net/forum?id=bCiNWDmlY2.

Minyoung Huh, Brian Cheung, Tongzhou Wang, and Phillip Isola. The platonic representation hypothesis. In *International Conference on Machine Learning*, 2024.

Piotr Indyk. Algorithmic applications of low-distortion geometric embeddings. In *Proceedings 42nd IEEE Symposium on Foundations of Computer Science*, pages 10–33. IEEE, 2001.

Sergey Ioffe and Christian Szegedy. Batch normalization: Accelerating deep network training by reducing internal covariate shift. In *International Conference on Machine Learning*, pages 448–456, 2015.

Phillip Isola. The discovery of perceptual structure from visual co-occurrences in space and time. In *MIT Ph.D. Thesis*, 2015a.

Phillip Isola, Daniel Zoran, Dilip Krishnan, and Edward H. Adelson. Crisp boundary detection using pointwise mutual information. In *ECCV*, 2014.

Phillip Isola, Daniel Zoran, Dilip Krishnan, and Edward H. Adelson. Learning visual groups from co-occurrences in space and time. In *ICLR, Workshop paper*, 2016.

Phillip John Isola. *The Discovery of perceptual structure from visual co-occurrences in space and time*. PhD thesis, Massachusetts Institute of Technology, 2015b.

Arthur Jacot, Franck Gabriel, and Clément Hongler. Neural tangent kernel: Convergence and generalization in neural networks. *arXiv preprint arXiv:1806.07572*, 2018.

William James. *The principles of psychology*. 1890.

Michael Janner, Qiyang Li, and Sergey Levine. Offline reinforcement learning as one big sequence modeling problem. *Advances in neural information processing systems*, 34:1273–1286, 2021.

Michael Janner, Yilun Du, Joshua Tenenbaum, and Sergey Levine. Planning with diffusion for flexible behavior synthesis. In *International Conference on Machine Learning*, 2022.

Albert Q Jiang, Alexandre Sablayrolles, Arthur Mensch, Chris Bamford, Devendra Singh Chaplot, Diego de las Casas, Florian Bressand, Gianna Lengyel, Guillaume Lample, Lucile Saulnier, et al. Mistral 7b. *arXiv preprint arXiv:2310.06825*, 2023.

Albert Q Jiang, Alexandre Sablayrolles, Antoine Roux, Arthur Mensch, Blanche Savary, Chris Bamford, Devendra Singh Chaplot, Diego de las Casas, Emma Bou Hanna, Florian Bressand, et al. Mixtral of experts. *arXiv preprint arXiv:2401.04088*, 2024.

N. L. Johnson. On an extension of the connexion between poisson and χ^2 distributions. *Biometrika*, 46(3/4):352–363, 1959. ISSN 00063444.

William B Johnson and Joram Lindenstrauss. Extensions of lipschitz mappings into a hilbert space. *Contemporary mathematics*, 26(189-206):1, 1984.

Keller Jordan, Hanie Sedghi, Olga Saukh, Rahim Entezari, and Behnam Neyshabur. Repair: Renormalizing permuted activations for interpolation repair. *arXiv preprint arXiv:2211.08403*, 2022.

Wolfgang Kabsch. A solution for the best rotation to relate two sets of vectors. *Acta Crystallographica Section A: Crystal Physics, Diffraction, Theoretical and General Crystallography*, 32(5):922–923, 1976.

Wolfgang Kabsch. A discussion of the solution for the best rotation to relate two sets of vectors. *Acta Crystallographica Section A: Crystal Physics, Diffraction, Theoretical and General Crystallography*, 34(5):827–828, 1978.

Harini Kannan, Danijar Hafner, Chelsea Finn, and Dumitru Erhan. RoboDesk: A multi-task reinforcement learning benchmark. https://github.com/google-research/robodesk, 2021.

Jared Kaplan, Sam McCandlish, Tom Henighan, Tom B Brown, Benjamin Chess, Rewon Child, Scott Gray, Alec Radford, Jeffrey Wu, and Dario Amodei. Scaling laws for neural language models. *arXiv preprint arXiv:2001.08361*, 2020.

Seung Wook Kim, Yuhao Zhou, Jonah Philion, Antonio Torralba, and Sanja Fidler. Learning to Simulate Dynamic Environments with GameGAN. In *IEEE Conference on Computer Vision and Pattern Recognition (CVPR)*, Jun. 2020.

Diederik P Kingma and Jimmy Ba. Adam: A method for stochastic optimization. *arXiv preprint arXiv:1412.6980*, 2014.

John Frank Charles Kingman. Poisson processes. *Encyclopedia of biostatistics*, 6, 2005.

Ryan Kiros, Yukun Zhu, Ruslan Salakhutdinov, Richard S Zemel, Antonio Torralba, Raquel Urtasun, and Sanja Fidler. Skip-thought vectors. *arXiv preprint arXiv:1506.06726*, 2015.

Max Klabunde, Tobias Schumacher, Markus Strohmaier, and Florian Lemmerich. Similarity of neural network models: A survey of functional and representational measures. *arXiv preprint arXiv:2305.06329*, 2023.

Sosuke Kobayashi. Homemade bookcorpus. GitHub repository https://github.com/soskek/bookcorpus/tree/5fe0cec8d7fd83940e48c799739496dc68ab2798, 2019.

Jing Yu Koh, Ruslan Salakhutdinov, and Daniel Fried. Grounding language models to images for multimodal inputs and outputs. In *International Conference on Machine Learning*, pages 17283–17300. PMLR, 2023.

Andrei N Kolmogorov. On tables of random numbers. *Sankhyā: The Indian Journal of Statistics, Series A*, pages 369–376, 1963.

Simon Kornblith, Mohammad Norouzi, Honglak Lee, and Geoffrey Hinton. Similarity of neural network representations revisited. In *International conference on machine learning*, pages 3519–3529. PMLR, 2019.

Ilya Kostrikov, Denis Yarats, and Rob Fergus. Image augmentation is all you need: Regularizing deep reinforcement learning from pixels. *arXiv preprint arXiv:2004.13649*, 2020.

Alex Krizhevsky, Geoffrey Hinton, et al. Learning multiple layers of features from tiny images. 2009.

Alex Krizhevsky, Ilya Sutskever, and Geoffrey E Hinton. Imagenet classification with deep convolutional neural networks. In *Advances in neural information processing systems*, pages 1097–1105, 2012.

Aviral Kumar, Xue Bin Peng, and Sergey Levine. Reward-conditioned policies. *arXiv preprint arXiv:1912.13465*, 2019.

Aviral Kumar, Aurick Zhou, George Tucker, and Sergey Levine. Conservative Q-learning for offline reinforcement learning. *Advances in Neural Information Processing Systems*, 33:1179–1191, 2020.

Guillaume Lample, Myle Ott, Alexis Conneau, Ludovic Denoyer, and Marc'Aurelio Ranzato. Phrase-based & neural unsupervised machine translation. In Ellen Riloff, David Chiang, Julia Hockenmaier, and Jun'ichi Tsujii, editors, *Proceedings of the 2018 Conference on Empirical Methods in Natural Language Processing*, Brussels, Belgium, October-November 2018. Association for Computational Linguistics.

Naum Samoĭlovich Landkof. *Foundations of modern potential theory*, volume 180. Springer, 1972.

Michael Laskin, Aravind Srinivas, and Pieter Abbeel. CURL: Contrastive unsupervised representations for reinforcement learning. In *International Conference on Machine Learning*, pages 5639–5650. PMLR, 2020a.

Misha Laskin, Kimin Lee, Adam Stooke, Lerrel Pinto, Pieter Abbeel, and Aravind Srinivas. Reinforcement learning with augmented data. *Advances in Neural Information Processing Systems*, 33:19884–19895, 2020b.

Alex X Lee, Anusha Nagabandi, Pieter Abbeel, and Sergey Levine. Stochastic latent actor-critic: Deep reinforcement learning with a latent variable model. *arXiv preprint arXiv:1907.00953*, 2019.

Kuang-Huei Lee, Ian Fischer, Anthony Liu, Yijie Guo, Honglak Lee, John Canny, and Sergio Guadarrama. Predictive information accelerates learning in rl. *Advances in Neural Information Processing Systems*, 33:11890–11901, 2020.

Karel Lenc and Andrea Vedaldi. Understanding image representations by measuring their equivariance and equivalence. In *Proceedings of the IEEE conference on computer vision and pattern recognition*, pages 991–999, 2015.

Jure Leskovec and Andrej Krevl. SNAP Datasets: Stanford large network dataset collection. http://snap.stanford.edu/data, June 2014.

Ming Li, Paul Vitányi, et al. *An introduction to Kolmogorov complexity and its applications*, volume 3. Springer, 2008.

Tianhong Li, Dina Katabi, and Kaiming He. Return of unconditional generation: A self-supervised representation generation method. *arXiv:2312.03701*, 2023.

Long Lian, Boyi Li, Adam Yala, and Trevor Darrell. LLM-grounded diffusion: Enhancing prompt understanding of text-to-image diffusion models with large language models. *arXiv preprint arXiv:2305.13655*, 2023a.

Long Lian, Baifeng Shi, Adam Yala, Trevor Darrell, and Boyi Li. LLM-grounded video diffusion models. *arXiv preprint arXiv:2309.17444*, 2023b.

Timothy P Lillicrap, Jonathan J Hunt, Alexander Pritzel, Nicolas Heess, Tom Erez, Yuval Tassa, David Silver, and Daan Wierstra. Continuous control with deep reinforcement learning. *arXiv preprint arXiv:1509.02971*, 2015.

Delwin T Lindsey and Angela M Brown. The color lexicon of american english. *Journal of vision*, 14(2):17–17, 2014.

Ralph Linsker. Self-organization in a perceptual network. *Computer*, 21(3):105–117, 1988.

Bo Liu, Yihao Feng, Qiang Liu, and Peter Stone. Metric residual networks for sample efficient goal-conditioned reinforcement learning. *arXiv preprint arXiv:2208.08133*, 2022.

Haotian Liu, Chunyuan Li, Qingyang Wu, and Yong Jae Lee. Visual instruction tuning. In *NeurIPS*, 2023.

Steven Liu, Tongzhou Wang, David Bau, Jun-Yan Zhu, and Antonio Torralba. Diverse image generation via self-conditioned gans. In *Conference on Computer Vision and Pattern Recognition (CVPR)*, 2020.

Weiyang Liu, Yandong Wen, Zhiding Yu, Ming Li, Bhiksha Raj, and Le Song. Sphereface: Deep hypersphere embedding for face recognition. In *Proceedings of the IEEE conference on computer vision and pattern recognition*, pages 212–220, 2017.

Weiyang Liu, Rongmei Lin, Zhen Liu, Lixin Liu, Zhiding Yu, Bo Dai, and Le Song. Learning towards minimum hyperspherical energy. In *Advances in Neural Information Processing Systems*, pages 6222–6233. 2018.

Yinhan Liu, Myle Ott, Naman Goyal, Jingfei Du, Mandar Joshi, Danqi Chen, Omer Levy, Mike Lewis, Luke Zettlemoyer, and Veselin Stoyanov. Roberta: A robustly optimized bert pretraining approach. *arXiv preprint arXiv:1907.11692*, 2019.

John Locke. *An Essay Concerning Human Understanding*. 1690.

Lajanugen Logeswaran and Honglak Lee. An efficient framework for learning sentence representations. In *International Conference on Learning Representations*, 2018.

Alejandro López-Cifuentes, Marcos Escudero-Vinolo, Jesús Bescós, and Álvaro García-Martín. Semantic-aware scene recognition. *Pattern Recognition*, 102:107256, 2020.

Ilya Loshchilov and Frank Hutter. SGDR: Stochastic gradient descent with warm restarts. *arXiv preprint arXiv:1608.03983*, 2016.

David G Lowe. Object recognition from local scale-invariant features. In *Proceedings of the seventh IEEE international conference on computer vision*, volume 2, pages 1150–1157. Ieee, 1999.

Kevin Lu, Aditya Grover, Pieter Abbeel, and Igor Mordatch. Pretrained transformers as universal computation engines. *arXiv preprint arXiv:2103.05247*, 1, 2021.

Ekdeep Singh Lubana, Eric J Bigelow, Robert P Dick, David Krueger, and Hidenori Tanaka. Mechanistic mode connectivity. In *International Conference on Machine Learning*, pages 22965–23004. PMLR, 2023.

Clare Lyle, Mark Rowland, Will Dabney, Marta Kwiatkowska, and Yarin Gal. Learning dynamics and generalization in reinforcement learning. *arXiv preprint arXiv:2206.02126*, 2022.

Jun Ma, Yuting He, Feifei Li, Lin Han, Chenyu You, and Bo Wang. Segment anything in medical images. *Nature Communications*, 15(1):654, 2024.

Yecheng Jason Ma, Shagun Sodhani, Dinesh Jayaraman, Osbert Bastani, Vikash Kumar, and Amy Zhang. VIP: Towards universal visual reward and representation via value-implicit pre-training. *arXiv preprint arXiv:2210.00030*, 2022.

Sridhar Mahadevan and Mauro Maggioni. Proto-value functions: A Laplacian framework for learning representation and control in markov decision processes. *Journal of Machine Learning Research*, 8(10), 2007.

Mayug Maniparambil, Raiymbek Akshulakov, Yasser Abdelaziz Dahou Djilali, Mohamed El Amine Seddik, Sanath Narayan, Karttikeya Mangalam, and Noel E O'Connor. Do vision and language encoders represent the world similarly? In *Proceedings of the IEEE/CVF Conference on Computer Vision and Pattern Recognition*, pages 14334–14343, 2024.

Alan S Manne. Linear programming and sequential decisions. *Management Science*, 6(3):259–267, 1960.

Lucas Manuelli, Wei Gao, Peter Florence, and Russ Tedrake. kpam: Keypoint affordances for category-level robotic manipulation. *arXiv preprint arXiv:1903.06684*, 2019.

J. I. Marcum. *Table of Q Functions.* RAND Corporation, Santa Monica, CA, 1950.

David A McAllester. Some pac-bayesian theorems. *Machine Learning*, 37(3):355–363, 1999.

Leland McInnes, John Healy, and James Melville. Umap: Uniform manifold approximation and projection for dimension reduction. *arXiv preprint arXiv:1802.03426*, 2018.

Facundo Mémoli, Anastasios Sidiropoulos, and Vijay Sridhar. Quasimetric embeddings and their applications. *Algorithmica*, 80(12):3803–3824, 2018.

Jack Merullo, Louis Castricato, Carsten Eickhoff, and Ellie Pavlick. Linearly mapping from image to text space. *arXiv preprint arXiv:2209.15162*, 2022.

Meta. Meta LLaMA 3, 2024. URL https://ai.meta.com/blog/meta-llama-3/.

Pascal Mettes, Elise van der Pol, and Cees Snoek. Hyperspherical prototype networks. In *Advances in Neural Information Processing Systems*, pages 1485–1495, 2019.

Vincent Micheli, Karthigan Sinnathamby, and François Fleuret. Multi-task reinforcement learning with a planning quasi-metric. *arXiv preprint arXiv:2002.03240*, 2020.

Tomas Mikolov, Kai Chen, Greg Corrado, and Jeffrey Dean. Efficient estimation of word representations in vector space. *arXiv preprint arXiv:1301.3781*, 2013.

Suvir Mirchandani, Fei Xia, Pete Florence, Brian Ichter, Danny Driess, Montserrat Gonzalez Arenas, Kanishka Rao, Dorsa Sadigh, and Andy Zeng. Large language models as general pattern machines. *arXiv preprint arXiv:2307.04721*, 2023.

Mehdi Mirza and Simon Osindero. Conditional generative adversarial nets. *arXiv preprint arXiv:1411.1784*, 2014.

Alan Mislove, Massimiliano Marcon, Krishna P. Gummadi, Peter Druschel, and Bobby Bhattacharjee. Measurement and Analysis of Online Social Networks. In *Proceedings of the 5th ACM/Usenix Internet Measurement Conference (IMC'07)*, San Diego, CA, October 2007.

Volodymyr Mnih, Koray Kavukcuoglu, David Silver, Alex Graves, Ioannis Antonoglou, Daan Wierstra, and Martin Riedmiller. Playing Atari with deep reinforcement learning. *arXiv preprint arXiv:1312.5602*, 2013.

Aditya Modi, Nan Jiang, Ambuj Tewari, and Satinder Singh. Sample complexity of reinforcement learning using linearly combined model ensembles. In *International Conference on Artificial Intelligence and Statistics*, pages 2010–2020. PMLR, 2020.

Luca Moschella, Valentino Maiorca, Marco Fumero, Antonio Norelli, Francesco Locatello, and Emanuele Rodolà. Relative representations enable zero-shot latent space communication. *arXiv preprint arXiv:2209.15430*, 2022.

Vaishnavh Nagarajan and J Zico Kolter. Uniform convergence may be unable to explain generalization in deep learning. *Advances in Neural Information Processing Systems*, 32, 2019.

Pushmeet Kohli Nathan Silberman, Derek Hoiem and Rob Fergus. Indoor segmentation and support inference from rgbd images. In *ECCV*, 2012.

Richard Lewis Nettleship. *Lectures on the 'Republic' of Plato*, volume 2. Macmillan, 1897.

W. Newton-Smith. *The Rationality of Science*. International Library of Philosophy, Psychology, and Scientific Method. Routledge & Kegan Paul, 1981. ISBN 9780710009135.

Evonne Ng, Sanjay Subramanian, Dan Klein, Angjoo Kanazawa, Trevor Darrell, and Shiry Ginosar. Can language models learn to listen? In *Proceedings of the IEEE/CVF International Conference on Computer Vision*, pages 10083–10093, 2023.

Jerry Ngo and Yoon Kim. What do language models hear? probing for auditory representations in language models, 2024.

Tianwei Ni, Benjamin Eysenbach, Erfan Seyedsalehi, Michel Ma, Clement Gehring, Aditya Mahajan, and Pierre-Luc Bacon. Bridging state and history representations: Understanding self-predictive rl. *arXiv preprint arXiv:2401.08898*, 2024.

Bruno A Olshausen and David J Field. Emergence of simple-cell receptive field properties by learning a sparse code for natural images. *Nature*, 381(6583):607–609, 1996.

Bruno A Olshausen and David J Field. Sparse coding with an overcomplete basis set: A strategy employed by v1? *Vision research*, 37(23):3311–3325, 1997.

Aaron van den Oord, Yazhe Li, and Oriol Vinyals. Representation learning with contrastive predictive coding. *arXiv preprint arXiv:1807.03748*, 2018.

OpenAI. GPT-4 technical report. *arXiv preprint arXiv:2303.08774*, 2023.

Maxime Oquab, Timothée Darcet, Theo Moutakanni, Huy V. Vo, Marc Szafraniec, Vasil Khalidov, Pierre Fernandez, Daniel Haziza, Francisco Massa, Alaaeldin El-Nouby, Russell Howes, Po-Yao Huang, Hu Xu, Vasu Sharma, Shang-Wen Li, Wojciech Galuba, Mike Rabbat, Mido Assran, Nicolas Ballas, Gabriel Synnaeve, Ishan Misra, Herve Jegou, Julien Mairal, Patrick Labatut, Armand Joulin, and Piotr Bojanowski. Dinov2: Learning robust visual features without supervision, 2023.

Shaul Oron, Tali Dekel, Tianfan Xue, William T Freeman, and Shai Avidan. Best-buddies similarity—robust template matching using mutual nearest neighbors. *IEEE transactions on pattern analysis and machine intelligence*, 40(8):1799–1813, 2017.

Giacomo Ortali and Ioannis G Tollis. Multidimensional dominance drawings. *arXiv preprint arXiv:1906.09224*, 2019.

Bo Pang and Lillian Lee. Seeing stars: Exploiting class relationships for sentiment categorization with respect to rating scales. In *Proceedings of the 43rd annual meeting on association for computational linguistics*, pages 115–124. Association for Computational Linguistics, 2005.

Vardan Papyan, XY Han, and David L Donoho. Prevalence of neural collapse during the terminal phase of deep learning training. *Proceedings of the National Academy of Sciences*, 117(40):24652–24663, 2020.

Young-Jin Park, Hao Wang, Shervin Ardeshir, and Navid Azizan. Quantifying representation reliability in self-supervised learning models. In *Conference on Uncertainty in Artificial Intelligence*, 2024.

Omkar M Parkhi, Andrea Vedaldi, and Andrew Zisserman. Deep face recognition. 2015.

Keiran Paster, Sheila McIlraith, and Jimmy Ba. You can't count on luck: Why decision transformers fail in stochastic environments. *arXiv preprint arXiv:2205.15967*, 2022.

Adam Paszke, Sam Gross, Francisco Massa, Adam Lerer, James Bradbury, Gregory Chanan, Trevor Killeen, Zeming Lin, Natalia Gimelshein, Luca Antiga, Alban Desmaison, Andreas Kopf, Edward Yang, Zachary DeVito, Martin Raison, Alykhan Tejani, Sasank Chilamkurthy, Benoit Steiner, Lu Fang, Junjie Bai, and Soumith Chintala. Pytorch: An imperative style, high-performance deep learning library. In H. Wallach, H. Larochelle, A. Beygelzimer, F. d'Alché-Buc, E. Fox, and R. Garnett, editors, *Advances in Neural Information Processing Systems 32*, pages 8026–8037. 2019.

Deepak Pathak, Pulkit Agrawal, Alexei A. Efros, and Trevor Darrell. Curiosity-driven exploration by self-supervised prediction. In *ICML*, 2017.

Judea Pearl. *Heuristics: intelligent search strategies for computer problem solving*. Addison-Wesley Longman Publishing Co., Inc., 1984.

Jeffrey Pennington, Samuel Schoenholz, and Surya Ganguli. The emergence of spectral universality in deep networks. In *International Conference on Artificial Intelligence and Statistics*, pages 1924–1932. PMLR, 2018.

Silviu Pitis, Harris Chan, Kiarash Jamali, and Jimmy Ba. An inductive bias for distances: Neural nets that respect the triangle inequality. In *Proceedings of the Eighth International Conference on Learning Representations*, 2020.

Matthias Plappert, Marcin Andrychowicz, Alex Ray, Bob McGrew, Bowen Baker, Glenn Powell, Jonas Schneider, Josh Tobin, Maciek Chociej, Peter Welinder, et al. Multi-goal reinforcement learning: Challenging robotics environments and request for research. *arXiv preprint arXiv:1802.09464*, 2018.

Plato. Republic. c. 375 BC.

Ben Poole, Sherjil Ozair, Aaron Van Den Oord, Alex Alemi, and George Tucker. On variational bounds of mutual information. In *International Conference on Machine Learning*, pages 5171–5180. PMLR, 2019.

DJ de S Price. *Networks of scientific papers*. Princeton University Press, 2011.

Martin L. Puterman. *Markov Decision Processes: Discrete Stochastic Dynamic Programming*. John Wiley & Sons, Inc., USA, 1st edition, 1994. ISBN 0471619779.

Hilary Putnam. Three kinds of scientific realism. *The Philosophical Quarterly (1950-)*, 32(128):195–200, 1982.

Alec Radford, Rafal Jozefowicz, and Ilya Sutskever. Learning to generate reviews and discovering sentiment. *arXiv preprint arXiv:1704.01444*, 2017.

Alec Radford, Jeffrey Wu, Rewon Child, David Luan, Dario Amodei, Ilya Sutskever, et al. Language models are unsupervised multitask learners. *OpenAI blog*, 1(8):9, 2019.

Alec Radford, Jong Wook Kim, Chris Hallacy, Aditya Ramesh, Gabriel Goh, Sandhini Agarwal, Girish Sastry, Amanda Askell, Pamela Mishkin, Jack Clark, et al. Learning transferable visual models from natural language supervision. In *International conference on machine learning*, pages 8748–8763. PMLR, 2021.

Maithra Raghu, Justin Gilmer, Jason Yosinski, and Jascha Sohl-Dickstein. Svcca: Singular vector canonical correlation analysis for deep learning dynamics and interpretability. *Advances in neural information processing systems*, 30, 2017.

Jonathan Richens and Tom Everitt. Robust agents learn causal world models. *ICLR*, 2024.

Iasonas Kokkinos Rıza Alp Güler, Natalia Neverova. Densepose: Dense human pose estimation in the wild. 2018.

Fatemeh Salehi Rizi, Joerg Schloetterer, and Michael Granitzer. Shortest path distance approximation using deep learning techniques. In *2018 IEEE/ACM International Conference on Advances in Social Networks Analysis and Mining (ASONAM)*, pages 1007–1014. IEEE, 2018.

Neil Robertson and Paul D Seymour. Graph minors. iii. planar tree-width. *Journal of Combinatorial Theory, Series B*, 36(1):49–64, 1984.

Geoffrey Roeder, Luke Metz, and Durk Kingma. On linear identifiability of learned representations. In *International Conference on Machine Learning*, pages 9030–9039. PMLR, 2021.

Sam T Roweis and Lawrence K Saul. Nonlinear dimensionality reduction by locally linear embedding. *science*, 290(5500):2323–2326, 2000.

Olga Russakovsky, Jia Deng, Hao Su, Jonathan Krause, Sanjeev Satheesh, Sean Ma, Zhiheng Huang, Andrej Karpathy, Aditya Khosla, Michael Bernstein, et al. Imagenet large scale visual recognition challenge. *International journal of computer vision*, 115:211–252, 2015.

Axel Sauer, Katja Schwarz, and Andreas Geiger. StylegGAN-XL: Scaling StyleGAN to large diverse datasets. In *ACM SIGGRAPH 2022 conference proceedings*, pages 1–10, 2022.

Nikunj Saunshi, Orestis Plevrakis, Sanjeev Arora, Mikhail Khodak, and Hrishikesh Khandeparkar. A theoretical analysis of contrastive unsupervised representation learning. In *International Conference on Machine Learning*, pages 5628–5637, 2019.

Andrew M Saxe, James L McClelland, and Surya Ganguli. Exact solutions to the nonlinear dynamics of learning in deep linear neural networks. *arXiv preprint arXiv:1312.6120*, 2013.

Tom Schaul, Daniel Horgan, Karol Gregor, and David Silver. Universal value function approximators. In *International conference on machine learning*, pages 1312–1320. PMLR, 2015.

Martin Schrimpf, Jonas Kubilius, Ha Hong, Najib J Majaj, Rishi Rajalingham, Elias B Issa, Kohitij Kar, Pouya Bashivan, Jonathan Prescott-Roy, Franziska Geiger, et al. Brain-score: Which artificial neural network for object recognition is most brain-like? *BioRxiv*, page 407007, 2018.

Florian Schroff, Dmitry Kalenichenko, and James Philbin. Facenet: A unified embedding for face recognition and clustering. In *Proceedings of the IEEE conference on computer vision and pattern recognition*, pages 815–823, 2015.

Richard Serfozo. Convergence of lebesgue integrals with varying measures. *Sankhyā: The Indian Journal of Statistics, Series A*, pages 380–402, 1982.

Pierre Sermanet, Corey Lynch, Yevgen Chebotar, Jasmine Hsu, Eric Jang, Stefan Schaal, Sergey Levine, and Google Brain. Time-contrastive networks: Self-supervised learning from video. In *2018 IEEE international conference on robotics and automation (ICRA)*, pages 1134–1141. IEEE, 2018.

Pratyusha Sharma, Tamar Rott Shaham, Manel Baradad, Stephanie Fu, Adrian Rodriguez-Munoz, Shivam Duggal, Phillip Isola, and Antonio Torralba. A vision check-up for language models. In *arXiv preprint*, 2024.

Roger N Shepard. Multidimensional scaling, tree-fitting, and clustering. *Science*, 210 (4468):390–398, 1980.

Yuyang Shi, Valentin De Bortoli, Andrew Campbell, and Arnaud Doucet. Diffusion schrödinger bridge matching. *Advances in Neural Information Processing Systems*, 36, 2024.

J. G. Skellam. The frequency distribution of the difference between two poisson variates belonging to different populations. *Journal of the Royal Statistical Society. Series A (General)*, 109(Pt 3):296–296, 1946.

Lucas Smaira, João Carreira, Eric Noland, Ellen Clancy, Amy Wu, and Andrew Zisserman. A short note on the kinetics-700-2020 human action dataset. *arXiv preprint arXiv:2010.10864*, 2020.

Alex J Smola and Bernhard Schölkopf. *Learning with kernels*, volume 4. Citeseer, 1998.

Ray J Solomonoff. A formal theory of inductive inference. part i. *Information and control*, 7(1):1–22, 1964.

Le Song, Alex Smola, Arthur Gretton, Justin Bedo, and Karsten Borgwardt. Feature selection via dependence maximization. *Journal of Machine Learning Research*, 13 (5), 2012.

Eduardo Sontag. An abstract approach to dissipation. In *Proceedings of 1995 34th IEEE Conference on Decision and Control*, volume 3, pages 2702–2703. IEEE, 1995.

Ben Sorscher, Surya Ganguli, and Haim Sompolinsky. Neural representational geometry underlies few-shot concept learning. *Proceedings of the National Academy of Sciences*, 119(43):e2200800119, 2022.

Elizabeth S Spelke and Katherine D Kinzler. Core knowledge. *Developmental science*, 10(1):89–96, 2007.

Krishna Srinivasan, Karthik Raman, Jiecao Chen, Michael Bendersky, and Marc Najork. Wit: Wikipedia-based image text dataset for multimodal multilingual machine learning. In *Proceedings of the 44th International ACM SIGIR Conference on Research and Development in Information Retrieval*, pages 2443–2449, 2021.

Aarohi Srivastava, Abhinav Rastogi, Abhishek Rao, Abu Awal Md Shoeb, Abubakar Abid, Adam Fisch, Adam R Brown, Adam Santoro, Aditya Gupta, Adrià Garriga-Alonso, et al. Beyond the imitation game: Quantifying and extrapolating the capabilities of language models. *arXiv preprint arXiv:2206.04615*, 2022.

Ethan Steinberg, Ken Jung, Jason A Fries, Conor K Corbin, Stephen R Pfohl, and Nigam H Shah. Language models are an effective representation learning technique for electronic health record data. *Journal of biomedical informatics*, 113:103637, 2021.

Dave Steiner and Rory Pilgrim. Health-specific embedding tools for dermatology and pathology, Mar 2024. URL https://research.google/blog/health-specific-embedding-tools-for-dermatology-and-pathology/.

James Stewart. Positive definite functions and generalizations, an historical survey. *The Rocky Mountain Journal of Mathematics*, 6(3):409–434, 1976.

George Stoica, Daniel Bolya, Jakob Bjorner, Taylor Hearn, and Judy Hoffman. Zipit! merging models from different tasks without training. *arXiv preprint arXiv:2305.03053*, 2023.

Ilia Sucholutsky, Lukas Muttenthaler, Adrian Weller, Andi Peng, Andreea Bobu, Been Kim, Bradley C. Love, Erin Grant, Iris Groen, Jascha Achterberg, Joshua B. Tenenbaum, Katherine M. Collins, Katherine L. Hermann, Kerem Oktar, Klaus Greff, Martin N. Hebart, Nori Jacoby, Qiuyi Zhang, Raja Marjieh, Robert Geirhos, Sherol Chen, Simon Kornblith, Sunayana Rane, Talia Konkle, Thomas P. O'Connell, Thomas Unterthiner, Andrew K. Lampinen, Klaus-Robert Müller, Mariya Toneva, and Thomas L. Griffiths. Getting aligned on representational alignment, 2023.

Richard S Sutton. An adaptive network that constructs and uses and internal model of its world. *Cognition and Brain Theory*, 4(3):217–246, 1981.

Richard S Sutton. Dyna, an integrated architecture for learning, planning, and reacting. *ACM Sigart Bulletin*, 2(4):160–163, 1991.

Richard S Sutton and Andrew G Barto. *Reinforcement learning: An introduction*. MIT press, 2018.

Richard S Sutton, Joseph Modayil, Michael Delp, Thomas Degris, Patrick M Pilarski, Adam White, and Doina Precup. Horde: A scalable real-time architecture for learning knowledge from unsupervised sensorimotor interaction. In *The 10th International Conference on Autonomous Agents and Multiagent Systems-Volume 2*, pages 761–768, 2011.

Ryota Suzuki, Ryusuke Takahama, and Shun Onoda. Hyperbolic disk embeddings for directed acyclic graphs. In *International Conference on Machine Learning*, pages 6066–6075. PMLR, 2019.

Pieter Merkus Lambertus Tammes. On the origin of number and arrangement of the places of exit on the surface of pollen-grains. *Recueil des travaux botaniques néerlandais*, 27(1):1–84, 1930.

Gemma Team, Thomas Mesnard, Cassidy Hardin, Robert Dadashi, Surya Bhupatiraju, Shreya Pathak, Laurent Sifre, Morgane Rivière, Mihir Sanjay Kale, Juliette Love, et al. Gemma: Open models based on gemini research and technology. *arXiv preprint arXiv:2403.08295*, 2024.

Joshua B Tenenbaum, Vin De Silva, and John C Langford. A global geometric framework for nonlinear dimensionality reduction. *science*, 290(5500):2319–2323, 2000.

Joseph John Thomson. Xxiv. on the structure of the atom: an investigation of the stability and periods of oscillation of a number of corpuscles arranged at equal intervals around the circumference of a circle; with application of the results to the theory of atomic structure. *The London, Edinburgh, and Dublin Philosophical Magazine and Journal of Science*, 7(39):237–265, 1904.

Stephen Tian, Suraj Nair, Frederik Ebert, Sudeep Dasari, Benjamin Eysenbach, Chelsea Finn, and Sergey Levine. Model-based visual planning with self-supervised functional distances. *arXiv preprint arXiv:2012.15373*, 2020a.

Yonglong Tian. Contrastive multiview coding. GitHub repository https://github.com/HobbitLong/CMC/tree/58d06e9a82f7fea2e4af0a251726e9c6bf67c7c9, 2019.

Yonglong Tian, Dilip Krishnan, and Phillip Isola. Contrastive multiview coding. In *Computer Vision–ECCV 2020: 16th European Conference, Glasgow, UK, August 23–28, 2020, Proceedings, Part XI 16*, pages 776–794. Springer, 2020b.

Yonglong Tian, Yue Wang, Dilip Krishnan, Joshua B Tenenbaum, and Phillip Isola. Rethinking few-shot image classification: a good embedding is all you need? In *Computer Vision–ECCV 2020: 16th European Conference, Glasgow, UK, August 23–28, 2020, Proceedings, Part XIV 16*, pages 266–282. Springer, 2020c.

Emanuel Todorov, Tom Erez, and Yuval Tassa. Mujoco: A physics engine for model-based control. In *2012 IEEE/RSJ International Conference on Intelligent Robots and Systems*, pages 5026–5033. IEEE, 2012.

Leo Tolstoy. *Anna Karenina*. The Russian Messenger, 1877.

Antonio Torralba, Rob Fergus, and William T Freeman. 80 million tiny images: A large data set for nonparametric object and scene recognition. *IEEE transactions on pattern analysis and machine intelligence*, 30(11):1958–1970, 2008.

Hugo Touvron, Louis Martin, Kevin Stone, Peter Albert, Amjad Almahairi, Yasmine Babaei, Nikolay Bashlykov, Soumya Batra, Prajjwal Bhargava, Shruti Bhosale, et al. LLaMA 2: Open foundation and fine-tuned chat models. *arXiv preprint arXiv:2307.09288*, 2023.

Dustin Tran, Yura Burda, and Ilya Sutskever. Feature-matching auto-encoders. 2017.

William T Trotter. Partially ordered sets. *Handbook of combinatorics*, 1:433–480, 1995.

Michael Tschannen, Josip Djolonga, Paul K Rubenstein, Sylvain Gelly, and Mario Lucic. On mutual information maximization for representation learning. *arXiv preprint arXiv:1907.13625*, 2019.

Saran Tunyasuvunakool, Alistair Muldal, Yotam Doron, Siqi Liu, Steven Bohez, Josh Merel, Tom Erez, Timothy Lillicrap, Nicolas Heess, and Yuval Tassa. dm_control: Software and tasks for continuous control. *Software Impacts*, 6:100022, 2020.

Shinji Umeyama. Least-squares estimation of transformation parameters between two point patterns. *IEEE Transactions on Pattern Analysis & Machine Intelligence*, 13 (04):376–380, 1991.

Jack Urbanek, Florian Bordes, Pietro Astolfi, Mary Williamson, Vasu Sharma, and Adriana Romero-Soriano. A picture is worth more than 77 text tokens: Evaluating CLIP-style models on dense captions, 2023.

Leslie G Valiant. A theory of the learnable. *Communications of the ACM*, 27(11): 1134–1142, 1984.

Guillermo Valle-Perez, Chico Q Camargo, and Ard A Louis. Deep learning generalizes because the parameter-function map is biased towards simple functions. In *International Conference on Learning Representations*, 2019.

Vladimir N Vapnik and A Ya Chervonenkis. On the uniform convergence of relative frequencies of events to their probabilities. In *Measures of complexity*, pages 11–30. Springer, 2015.

Ivan Vendrov, Ryan Kiros, Sanja Fidler, and Raquel Urtasun. Order-embeddings of images and language. *arXiv preprint arXiv:1511.06361*, 2015.

Pauli Virtanen, Ralf Gommers, Travis E. Oliphant, Matt Haberland, Tyler Reddy, David Cournapeau, Evgeni Burovski, Pearu Peterson, Warren Weckesser, Jonathan Bright, Stéfan J. van der Walt, Matthew Brett, Joshua Wilson, K. Jarrod Millman, Nikolay Mayorov, Andrew R. J. Nelson, Eric Jones, Robert Kern, Eric Larson, C J Carey, İlhan Polat, Yu Feng, Eric W. Moore, Jake VanderPlas, Denis Laxalde, Josef Perktold, Robert Cimrman, Ian Henriksen, E. A. Quintero, Charles R. Harris, Anne M. Archibald, Antônio H. Ribeiro, Fabian Pedregosa, Paul van Mulbregt, and SciPy 1.0 Contributors. SciPy 1.0: Fundamental Algorithms for Scientific Computing in Python. *Nature Methods*, 17:261–272, 2020. doi: 10.1038/s41592-019-0686-2.

Feng Wang, Xiang Xiang, Jian Cheng, and Alan Loddon Yuille. Normface: L2 hypersphere embedding for face verification. In *Proceedings of the 25th ACM international conference on Multimedia*, pages 1041–1049, 2017.

Jiang Wang, Yang Song, Thomas Leung, Chuck Rosenberg, Jingbin Wang, James Philbin, Bo Chen, and Ying Wu. Learning fine-grained image similarity with deep ranking. In *Proceedings of the IEEE conference on computer vision and pattern recognition*, pages 1386–1393, 2014.

Ruosong Wang, Dean P Foster, and Sham M Kakade. What are the statistical limits of offline RL with linear function approximation? *arXiv preprint arXiv:2010.11895*, 2020.

Ruosong Wang, Yifan Wu, Ruslan Salakhutdinov, and Sham Kakade. Instabilities of offline rl with pre-trained neural representation. In *International Conference on Machine Learning*, pages 10948–10960. PMLR, 2021.

Sida Wang and Christopher D Manning. Baselines and bigrams: Simple, good sentiment and topic classification. In *Proceedings of the 50th annual meeting of the association for computational linguistics: Short papers-volume 2*, pages 90–94. Association for Computational Linguistics, 2012.

Tongzhou Wang and Phillip Isola. Understanding contrastive representation learning through alignment and uniformity on the hypersphere. In *Proceedings of the 37th International Conference on Machine Learning*, volume 119 of *Proceedings of Machine Learning Research*, pages 9929–9939. PMLR, 13–18 Jul 2020.

Tongzhou Wang and Phillip Isola. Improved representation of asymmetrical distances with interval quasimetric embeddings. In *Workshop on Symmetry and Geometry in Neural Representations at Conference on Neural Information Processing Systems (NeurReps Workshop at NeurIPS)*, 2022a. Proceedings Track.

Tongzhou Wang and Phillip Isola. On the learning and learnability of quasimetrics. In *International Conference on Learning Representations (ICLR)*, 2022b.

Tongzhou Wang, Simon S. Du, Antonio Torralba, Phillip Isola, Amy Zhang, and Yuandong Tian. Denoised MDPs: Learning world models better than the world itself. In *International Conference on Machine Learning (ICML)*, 2022.

Tongzhou Wang, Antonio Torralba, Phillip Isola, and Amy Zhang. Optimal goal-reaching reinforcement learning via quasimetric learning. In *International Conference on Machine Learning (ICML)*, 2023.

Christopher John Cornish Hellaby Watkins. Learning from delayed rewards. 1989.

Kilian Q Weinberger, John Blitzer, and Lawrence K Saul. Distance metric learning for large margin nearest neighbor classification. In *Advances in neural information processing systems*, pages 1473–1480, 2006.

Paul J Werbos. Learning how the world works: Specifications for predictive networks in robots and brains. In *Proceedings of IEEE International Conference on Systems, Man and Cybernetics, NY*, 1987.

Grady Williams, Andrew Aldrich, and Evangelos Theodorou. Model predictive path integral control using covariance variable importance sampling. *arXiv preprint arXiv:1509.01149*, 2015.

Thomas Wolf, Lysandre Debut, Victor Sanh, Julien Chaumond, Clement Delangue, Anthony Moi, Pierric Cistac, Tim Rault, Rémi Louf, Morgan Funtowicz, et al. Huggingface's transformers: State-of-the-art natural language processing. *arXiv preprint arXiv:1910.03771*, 2019.

Mitchell Wortsman, Gabriel Ilharco, Samir Ya Gadre, Rebecca Roelofs, Raphael Gontijo-Lopes, Ari S Morcos, Hongseok Namkoong, Ali Farhadi, Yair Carmon, Simon Kornblith, et al. Model soups: averaging weights of multiple fine-tuned models improves accuracy without increasing inference time. In *International Conference on Machine Learning*, pages 23965–23998. PMLR, 2022.

Mike Wu, Chengxu Zhuang, Daniel Yamins, and Noah Goodman. On the importance of views in unsupervised representation learning. 2020.

Tsung-Han Wu, Long Lian, Joseph E Gonzalez, Boyi Li, and Trevor Darrell. Self-correcting LLM-controlled diffusion models. *arXiv preprint arXiv:2311.16090*, 2023.

Zhirong Wu, Yuanjun Xiong, Stella X Yu, and Dahua Lin. Unsupervised feature learning via non-parametric instance discrimination. In *Proceedings of the IEEE Conference on Computer Vision and Pattern Recognition*, pages 3733–3742, 2018.

Shaoan Xie, Qirong Ho, and Kun Zhang. Unsupervised image-to-image translation with density changing regularization. *Advances in Neural Information Processing Systems*, 35:28545–28558, 2022.

Eric P Xing, Andrew Y Ng, Michael I Jordan, and Stuart Russell. Distance metric learning with application to clustering with side-information. In *NIPS*, volume 15, page 12. Citeseer, 2002.

Jiacheng Xu and Greg Durrett. Spherical latent spaces for stable variational autoencoders. In *Proceedings of the 2018 Conference on Empirical Methods in Natural Language Processing*, pages 4503–4513, 2018.

Sonnet Xu, Haiwen Gui, Veronica Rotemberg, Tongzhou Wang, Yiqun Chen, and Roxana Daneshjou. A framework for evaluating the efficacy of foundation embedding models in healthcare. *medRxiv*, pages 2024–04, 2024.

Daniel LK Yamins, Ha Hong, Charles F Cadieu, Ethan A Solomon, Darren Seibert, and James J DiCarlo. Performance-optimized hierarchical models predict neural responses in higher visual cortex. *Proceedings of the national academy of sciences*, 111(23):8619–8624, 2014.

Ge Yang, Amy Zhang, Ari Morcos, Joelle Pineau, Pieter Abbeel, and Roberto Calandra. Plan2vec: Unsupervised representation learning by latent plans. In *Learning for Dynamics and Control*, pages 935–946. PMLR, 2020.

Mengjiao Yang, Dale Schuurmans, Pieter Abbeel, and Ofir Nachum. Dichotomy of control: Separating what you can control from what you cannot. *arXiv preprint arXiv:2210.13435*, 2022.

Denis Yarats, Rob Fergus, Alessandro Lazaric, and Lerrel Pinto. Mastering visual continuous control: Improved data-augmented reinforcement learning. *arXiv preprint arXiv:2107.09645*, 2021.

Lin Yen-Chen, Pete Florence, Jonathan T. Barron, Alberto Rodriguez, Phillip Isola, and Tsung-Yi Lin. iNeRF: Inverting neural radiance fields for pose estimation. In *IEEE/RSJ International Conference on Intelligent Robots and Systems (IROS)*, 2021.

Rowan Zellers, Ari Holtzman, Yonatan Bisk, Ali Farhadi, and Yejin Choi. HellaSwag: Can a machine really finish your sentence? In Anna Korhonen, David Traum, and Lluís Màrquez, editors, *Proceedings of the 57th Annual Meeting of the Association for Computational Linguistics*, pages 4791–4800, Florence, Italy, July 2019. Association for Computational Linguistics. doi: 10.18653/v1/P19-1472. URL https://aclanthology.org/P19-1472.

Xiaohua Zhai, Joan Puigcerver, Alexander Kolesnikov, Pierre Ruyssen, Carlos Riquelme, Mario Lucic, Josip Djolonga, Andre Susano Pinto, Maxim Neumann, Alexey Dosovitskiy, et al. The visual task adaptation benchmark. 2019.

Amy Zhang, Rowan McAllister, Roberto Calandra, Yarin Gal, and Sergey Levine. Learning invariant representations for reinforcement learning without reconstruction. *arXiv preprint arXiv:2006.10742*, 2020a.

Richard Zhang, Phillip Isola, Alexei A Efros, Eli Shechtman, and Oliver Wang. The unreasonable effectiveness of deep features as a perceptual metric. In *Proceedings of the IEEE conference on computer vision and pattern recognition*, pages 586–595, 2018.

Tianren Zhang, Shangqi Guo, Tian Tan, Xiaolin Hu, and Feng Chen. Generating adjacency-constrained subgoals in hierarchical reinforcement learning. *Advances in Neural Information Processing Systems*, 33:21579–21590, 2020b.

Bolei Zhou, Agata Lapedriza, Aditya Khosla, Aude Oliva, and Antonio Torralba. Places: A 10 million image database for scene recognition. *IEEE transactions on pattern analysis and machine intelligence*, 40(6):1452–1464, 2017.

Jun-Yan Zhu, Taesung Park, Phillip Isola, and Alexei A Efros. Unpaired image-to-image translation using cycle-consistent adversarial networks. In *Computer Vision (ICCV), 2017 IEEE International Conference on*, 2017.

Yukun Zhu, Ryan Kiros, Richard Zemel, Ruslan Salakhutdinov, Raquel Urtasun, Antonio Torralba, and Sanja Fidler. Aligning books and movies: Towards story-like visual explanations by watching movies and reading books. In *arXiv preprint arXiv:1506.06724*, 2015.

Roland S Zimmermann, Yash Sharma, Steffen Schneider, Matthias Bethge, and Wieland Brendel. Contrastive learning inverts the data generating process. In *International Conference on Machine Learning*, pages 12979–12990. PMLR, 2021.